THREE-DIMENSIONAL BOUNDARY ELEMENT AND EXPERIMENTAL ANALYSIS OF LUBRICATED CERAMIC SURFACE RING CRACKS IN ROLLING CONTACT

PING ZHAO

A thesis submitted in partial fulfilment of the requirements of Bournemouth University for the degree of Doctor of Philosophy

July 2006

Bournemouth University
In collaboration with
SKF Research and Development Company, The Netherlands

ABSTRACT

Surface defects such as ring cracks are located on silicon nitride ceramic rolling elements. The random nature of ring crack position creates difficulties in predicting rolling contact fatigue (RCF) life. The influence of the lubricant, contact pressure and crack geometry on the RCF mechanism is difficult to determine due to the variable nature of RCF life when the crack location is not defined. In this study, rolling contact fatigue was tested using a novel experimental technique. The test ceramic ball specimen with identified surface ring cracks was precisely located in the contact path. The rolling contact fatigue tests were conducted using a modified four-ball machine in a hybrid ceramic/steel combination with five different types of lubricating mediums at various contact pressures. Detailed analysis of damage progression was carried out to study the mechanisms of fatigue failure. A boundary element analysis was used to determine the stress intensity factors around the crack front and stress distributions on the surface in the presence of the surface crack.

The RCF tests of silicon nitride balls with surface ring cracks showed that fatigue life was strongly influenced by load/contact stress, crack size, lubricant and material type. Ring crack spalling failure is not only influenced by sub-surface fatigue crack propagation but also strongly influenced by secondary surface cracks. The formation of the secondary surface cracks is a key factor which dominates spalling of rolling contact fatigue. Modelling work showed that the crack length was an important parameter. Increasing the crack length for given crack radius resulted in higher tensile surface stresses ahead of the original ring crack and also gave higher absolute K_{II} values. In addition, the crack gap and crack face friction had a significant effect on the formation of secondary surface cracks and fatigue crack propagation behaviour. Increasing the crack face friction decreased both the surface tensile stress and absolute magnitude of K_{II}. Numerical calculation results were consistent with the experimental observations.

PUBLICATIONS RESULTING FROM THESIS

Refereed Journal:

[1] "The influence of test lubricants on the rolling contact fatigue failure mechanisms of silicon nitride ceramic"
By P. Zhao, M. Hadfield, Y. Wang and C. Vieillard
Wear Journal, 257, 1047-1057, 2004

[2] "Subsurface propagation of partial ring cracks under rolling contact: Part I, experimental studies"
By P. Zhao, M. Hadfield, Y. Wang and C. Vieillard
Wear Journal, 261, 382-389, 2006

[3] "Subsurface propagation of partial ring cracks under rolling contact: Part II, fracture mechanics analysis"
By P. Zhao, M. Hadfield, Y. Wang and C. Vieillard
Wear Journal, 261, 390-397, 2006

[4] "A study of surface and subsurface geometries of partial ring crack using a defect generating device"
By P. Zhao, M. Hadfield, Y. Wang and C. Vieillard
Submitted to Materials & Design, 2006

Conference Presentation:

[1] "Experimental investigation of lubricated surface ring crack fatigue in rolling contact"
By P. Zhao, M. Hadfield, Y. Wang, C. Vieillard, R. Cundill and S. Ioannides
International Conference on Tribology in Environment Design 2003, p301-310, Professional Engineering Publishing

[2] "The influence of lubrication oil on ceramic rolling contact fatigue failure"
By P. Zhao, M. Hadfield, Y. Wang and C. Vieillard
Mission of Tribology Research 13. IMechE, 2004

ACKNOWLEDGEMENTS

Many people have encouraged and supported my research during the period of my PhD study.

First of all, my very grateful thanks are expressed to Professor Mark Hadfield, my supervisor, who has always been ready to provide encouragement, inspiration and guidance. Every step in the progress of my study reflects his solid support and patient help.

I must also acknowledge the financial support provided by SKF Engineering & Research Centre - The Netherlands.

During the postgraduate studying I was also privileged to spend time at SKF Engineering & Research Centre - The Netherlands. A special thanks goes to S. Ioannides, C. Vieillard, R. Cundill for their professional advice and timely discussion.

My industrial supervisor at SKF (ERC) Ltd, C. Vieillard, has given much advice on material aspects of technical ceramics. Dr R. Cundill has also been an invaluable source of information on material aspects and provided much expert knowledge. Staff from SKF (ERC) Ltd have all contributed to this study by giving support and enthusiasm.

My appreciation also goes to all the staff I have worked with so closely at Bournemouth University, especially laboratory staff.

Finally, last but not least, friends, family and my husband have all contributed support and encouragement.

CONTENTS

LIST OF FIGURES

LIST OF TABLES

NOMENCLATURE

A_0	surface area of ceramic ball
A	area of contact track
a	radius of contact circle
E_1	elasticity modulus of ceramic ball
E_2	elasticity modulus of steel ball
E	elasticity modulus
E^*	effective elasticity modulus
f	traction coefficient
f_c	frictional coefficient of crack face contact
h	height of the segment which cuts through the contact track (Chapter 3), distance between the steel base and the platform (Chapter 2)
H	lifted height of the pendulum
K_I	mode I stress intensity factor
K_{II}	mode II stress intensity factor
K_{IC}	fracture toughness
ΔK_{th}	fatigue crack propagation threshold
l	crack length (Chapter 5), distance between the contact point and the central line (Chapter 2)
L	applied load (shaft load)
P	contact load
p_0	maximum contact pressure
p_m	mean contact pressure
$p(x,y)$	contact pressure
$q(x,y)$	shear traction
r	coordinate in local crack front coordinate system
R	radius of ring crack circle
R_1	radius of ceramic ball
R_2	radius of steel ball
R^*	effective radius
v_t	tangential velocity
(x,y)	Cartesian coordinate system with origin at the centre of Hertzian contact circle
(x,y,z)	Cartesian coordinate system with origin at the centre of Hertzian contact circle
α	angle of the crack path (line P_1P_2 in figure 4.8) to the ball surface (Chapter 4), the initial angle between the pendulum and the central line (Chapter 2)
ϕ	angle of an element position on crack faces
ϕ_0	half angle of ring crack arc AB
φ	contact angle
μ	shear modulus of elasticity
ν	Poisson's ratio
ν_1	Poisson's ratio of ceramic ball
ν_2	Poisson's ratio of steel ball
θ	swing angle (chapter 2), angle in global co-ordinate polar angle in the local crack front coordinate system (Chapter 5)
ρ	contacted crack probability

ABBREVIATIONS

BEM	Boundary Element Method
BEASY	Boundary Element Analysis System
DBEM	Dual Boundary Element Method
EHL	Elasto-Hydrodynamic Lubrication
HIP	Hot Isostatically Pressed
RCF	Rolling Contact Fatigue
SEM	Scanning Electron Microscope
SIF	Stress Intensity Factor
UV	Ultra Violet
WC	Tungsten Carbide

CHAPTER 1
INTRODUCTION

1.1 GENERAL BACKGROUND

High quality silicon nitride (Si_3N_4) ceramics have low densities, low friction coefficients, low thermal expansions, high strengths, and high temperature capability and chemical stability. The combination of these properties makes Si_3N_4 an attractive material for rolling element bearings applications. The advantage of silicon nitride roller bearings has been confirmed (Hamburg et al. 1981, Miner et al. 1981, Bhushan and Sibley 1981, Aramaki et al. 1988). Hybrid rolling element bearings are now offered as a standard component in the ball bearing manufacturing industry. A significant breakthrough made by SKF Aeroengine, through its partnerships with key customers, was the development of a process to manufacture ceramics (silicon nitride) roller in production quantities. These hybrid roller bearings with their combination of ceramic rolling elements in traditional bearing configurations offer many advantages and are expected to constitute a significant proportion of SKF Aeroengines's future products.

One of the major factors limiting widespread use of ceramic rolling elements in advanced industrial applications is the presence of ring crack defects on the surface (Wang and Hadfield 2002a). Surface ring cracks caused by manufacturing pressing faults or blunt impact loads are one of the most common types of defects on ceramic ball surfaces. Surface ring cracks formed prior to, or during, the final lapping or polishing stage are particularly difficult to detect (Cundill 1990). Numerous experimental studies have confirmed that ceramic balls typically fail by crack propagation from the pre-existing surface cracks (Hadfield et al. 1993a, 1993b, Hadfield and Stolarski 1993c, 1994a, 1995, Hadfield 1998, Wang and Hadfield 2000a, 2000b, 2001, 2002a 2004). Research has revealed the role played by a lubricating medium in the process of fatigue failure. Lubricated pre-cracked ceramic balls fail in a non-catastrophic spalling mode (Hadfield et al 1993a). In the previous studies, rolling contact fatigue tests were performed regardless of the crack orientation effect due to the greatest difficulties in performing such tests. As a result, it is difficult to identify the most crucial factors for quality control and life

prediction. In a recent study (Wang and Hadfield 2000a), a novel rolling contact fatigue test method was developed for locating the ring crack. The worst position was located and the test results showed that the 'natural' ring crack failure is heavily dependent on the crack orientations within the contact path. Fatigue failure occurred only in some favourite positions. A numerical fracture mechanics approach was used in the calculation of the stress intensity factor in order to explain why the fatigue life showed big difference as the crack location varies within the contact path (Wang and Hadfield 2000b). The calculations showed that mode I stress intensity (K_I) play an important role in propagating a natural crack. The different crack locations demonstrated different stress intensity values and as a result of that the silicon nitride balls exhibited different rolling contact fatigue life.

In a more recent study, Wang and Hadfield (2001, 2004) demonstrated that the rolling contact fatigue failure of silicon nitride was involved in fatigue crack propagation from the pre-existing ring crack and the secondary surface crack induced as the subsurface fatigue crack grows. In that study, the investigations were concentrated on the natural crack (small crack) and mode I stress intensity was considered as a main factor which governs fatigue crack propagation. The calculations showed that the K_I stress intensity may propagate fatigue crack to a certain spalling size, e.g. 0.3 mm in diameter. However, the modelling was not suitable for the case with a larger size spall. To date, there are no such models to predict various spalling scales due to the limited fundamental understanding of the history of fatigue failure processes starting from various initial sizes of the surface crack. A detailed investigation is now needed.

Therefore, a detailed failure analysis is necessary in order to fully understand the failure mechanisms of rolling contact fatigue in ceramics. Accurate predictive modelling will therefore be based on full exploitation of fatigue behaviour of ceramic rolling elements with various geometries of the crack and it is the subject of this thesis.

1.2 OBJECTIVE AND SCOPE OF RESEARCH WORK

The first main objective of the study presented in this thesis is to investigate experimentally and analytically the fatigue mechanisms and durability of silicon

nitride rolling elements that have surface crack defects. A second main objective is to model these fatigue mechanisms. The scope of this study is:

(1) To perform a comprehensive programme of three-dimensional boundary element analysis of surface ring cracks within ceramic ball rolling elements. This will be achieved by concentrating on crack/contact path orientation with variations of crack dimensions. As part of this process the research will determine the extent of subsurface crack growth in relation to loads ranging from 4.0 to 6.6 GPa to assess critical crack location, geometry and lubricant properties.

(2) To carry out experimental studies using the Plint TE92HS Rotary Tribometer to verify numerical analysis. Natural and artificial cracks are to be located and positioned using dye penetration and optical methods. Experimental RCF tests are carried out using critical positions, defect shape and lubricants (traction and viscosity variants) to establish critical operating conditions.

(3) To develop a fundamental understanding of the ring crack failure and to perform detailed post-test studies including surface and subsurface observations of ring crack spalling failure processes.

1.3 OUTLINE OF THESIS

In Chapter 1, general background and previous research work related to this subject are described. Chapter 2 describes the design of an artificial crack generator. Chapter 3 describes the main programme of experimental testing. Section 3.1 of this Chapter gives details of test materials. Section 3.2 is concerned with crack geometry studies. Section 3.3 describes experimental methods and procedure. Section 3.4 outlines experimental observations during fatigue testing. In Section 3.5, Scanning Electron Microscopy (SEM) analysis is described. In the final Section, Profilometering analysis is shown.

In Chapter 4, experimental results are presented. Surface appearance of surface ring cracks is described in Section 4.1.1. Statistical analysis of surface ring

cracks is shown in Section 4.1.2. Subsurface geometry of the ring cracks is studied in Section 4.1.3 and the mathematical model of the crack is presented in Section 4.1.4. Section 4.2 of this Chapter gives details of the rolling contact fatigue (RCF) performance with natural ring cracks. The effect of test lubricants on the fatigue life is also addressed. Section 4.3 describes the RCF performance with artificial cracks. Section 4.4 describes surface studies of ring crack failure processes. Subsurface studies of crack propagation are shown in Section 4.5. A summary from the experimental work is given in Section 4.6.

An analytical study of ceramic rolling contact fatigue is given in Chapter 5. A boundary element analysis is carried out to increase understanding of fatigue failure processes. The analytical model is presented and described in Section 5.1. The physical considerations and modelling strategies are addressed. A three-dimensional boundary element model is developed and described in Section 5.2. Contact stresses due to surface ring cracks are analysed. The impacting factors such as crack face friction, crack geometry and contact stresses are described in Section 5.3. The calculation results predict the conditions for the secondary surface cracks and interpret the failure mechanism of ceramic rolling contact fatigue. Stress intensity factors (SIF) are computed according to the three-dimensional fracture model. SIF solutions along the crack front are described in Section 5.4. The calculated results are given in Sections 5.4.1 to 5.4.7.

Discussion, conclusions and recommendations for further research topics resulting from this present study are outlined in Chapter 6.

1.4 LITERATURE SURVEY

1.4.1 Failure modes with nominal defect free surfaces

Early investigations on hot-pressed silicon nitride as a rolling bearing material were performed by Scott and Blackwell (1973). Both lubricated and unlubricated contacts were studied using a modified four ball machine. The tests were conducted at 1500 rpm and a maximum Hertzian stress of 5.8GPa for lubricated contact and 7.7 GPa for unlubricated contact. Under lubricated contact, the failure mode was wear and fracture and the upper ball failure was only after a few seconds of testing. For unlubricated conditions upper ball wear was fast and the

wear track on the ball surface retained modest surface quality. The silicon nitride balls were also tested in contact with steel lower balls and the time to failure was increased to minutes. The test results were not promising due to the poor quality of the silicon nitride balls. Parker and Zaretsky (1975) investigated the fatigue life of high-speed-ball bearings with hot pressed silicon nitride balls using a five-ball fatigue test machine. The tests were conducted at a shaft speed of 9600 rpm and the maximum Hertzian contact stresses ranging from 4.3 to 6.2 GPa. No evidence of a wear mode of failure was seen and only fatigue spalls were observed. Also, Lucek and Cowley (1978) investigated the failure mode of hot-pressed ceramic using a disc-on-rod machine at the contact stresses from 4.1 to 5.5 GPa. The results demonstrated that the failure mode was a non-catastrophic spalling for all tests.

Fatigue of silicon nitride hybrid bearings was tested by Morrison et al. (1984), using 12.7 mm diameter silicon nitride balls, M50 steel rings and a brass cage. The lambda value was approximately 3.5 for all tests and the tests were performed at the maximum contact stresses of 1.95 to 2.44 GPa. The failure mode was fatigue spalling and no cases of the silicon nitride balls fracturing were seen. Dry rolling tests on several ceramics were performed by Kim et al. (1986) concluding that the silicon nitride wear rate was the smallest. Wear tests were performed at the stresses ranging from 2.5 GPa to 5 GPa, using a ring-on-disc testing machine. The results indicted that the wear mode is mainly dominated by brittle fracture. Also, wear properties of silicon nitride in dry rolling-sliding contact were investigated by Akazawa and Kato (1988). They selected the ring on roller tester to perform wear tests. It was found that the roughness of the contact surfaces determined the characteristics of the wear particles. Additionally, rolling and sliding wear mechanism were studied by Braza et al. (1989a) using a disc-on-rod tester. Three types of silicon nitride (hot pressed, pressureless sintered and reaction bonded) were tested at a Hertz contact pressure of 1.37 GPa. The reaction bonded type showed a higher wear rate with the failure mode of grain pullout. The other two types showed similar wear rates with the wear mode of submicron chipping. Experimental work (Fujiwara et al.1989), using a ball-on-plate machine, examined the dynamic and static load rating of silicon nitride as a bearing material. Three modes of failure, spalling, cave-in and peeling, were found. Spalling was identified

as the most common mode in long-term test and two other modes were 'cave-in' and peeling in short time tests.

The rolling contact fatigue of hot-pressed silicon nitride was studied using a ball-on-rod tester (Lucek 1990). The specimen (rod) speed was set at 3600 rpm (8600 stress cycles per minute) at a contact stress of 6.4 GPa. A synthetic turbine oil was used and the lubrication regime was boundary lubrication. The predominant failure mechanism in silicon nitride involves the slow growth of circumferential crack from the edges of the contact path driven by tensile stresses. Spalling occurred when material in the compressive zone was insufficiently supported. Allen (1994) studied the effect of composition and physical properties of silicon nitride on rolling wear and fatigue performance using a ball-on-rod machine. Different commercial bearing materials were tested to compare wear and fatigue properties at a contact pressure of 6.4 GPa. The fatigue life and wear resistance were not influenced significantly by the fracture toughness. The results showed that grain boundary composition had no effect on the wear mechanism of these hot-isostatically-pressed materials. In a study (Burrier 1996), the effect of the microstructure on ceramic rolling contact fatigue was investigated using eleven silicon nitride bearing materials. A ball-on-rod tester was adopted and fatigue tests were performed at the contact stress of 5.93 GPa and rod rotation speed of 3600 rpm. It was found that the materials exhibited huge differences in fatigue life and failure mode was spalling. A wide range of rolling contact fatigue endurance was seen in those silicon nitride materials. The materials that contain the microstructure of finer and more equiaxed grains demonstrated good fatigue durability under the relatively high stress contact. In another study (Chao et al. 1998), the wear properties of silicon nitride in lubricated rolling contact was studied. A ball-on-rod tester was used and tests were performed with stresses ranging from 5 to 6.5 GPa. It was found that the initial surface roughness was the important factor which determines the wear rate and behaviour.

Wang and Hadfield (2002a) discussed rolling contact fatigue of ceramics. The RCF life performance and failure modes were influenced by the test-rig type and failure modes could be changed according to contact geometry. The experimental evaluation of silicon nitride should be conducted on a number of

model tests before predicting its performance for rolling element applications. Several failure modes of silicon nitride in rolling contact have been reported, i.e. spalling fatigue failure, delamination failure and rolling contact wear. A recent innovation is the ball-on-flat machine (Kalin and Vizintin 2004) which is useful as sample preparation time is reduced. A study (Hus and Shen 2004) reviewed the various wear models over the years to predict wear, wear transitions, and wear under different mechanisms for ceramics. They also investigated the feasibility of modelling across a range of materials and operating condition using a concept of contact severity and material property normalisation process. Materials failure mechanisms of hybrid bearings with silicon nitride balls were investigated by Thoma et al. (2004), using a modified Shell four-ball apparatus. Five kinds of silicon nitride ceramics, which differed in terms of surface roughness, porosity as well as the amount and chemical composition of additives, were investigated. Lifetime and failure mechanisms varied between the five bearings with silicon nitride balls. Different failure modes on the tested ball surfaces were found which are dependent upon the porosity and chemical composition of the materials.

1.4.2 Failure modes with surface defects

Since Si_3N_4 has a covalently bonded (hexagonal crystalline) structure, difficulties in sintering became a major barrier to its manufacture. Machining was also extremely difficult because of the hardness of Si_3N_4. The difficulties in both sintering and machining resulted in the fact that it was impossible to limit all defects, such as porosity, large inclusions, surface damage, and sintering flaws in Si_3N_4 products. The presence of the surface defects often leads to an uncertainty in failure modes of silicon nitride elements. Even though many investigators explored damage mechanisms of Si_3N_4 under contact loading and have documented their attempts (Akazawa and Kato 1988, Galbato et al. 1992), the damage processes of Si_3N_4 have not been precisely explained. This is because most of the failures resulted from random, external factors (such as defects caused by manufacturing and machining or improper preparation and improper selection of tests) rather than from aspects of material structure. Therefore, the fundamental understanding of the failures initiated from various surface defects is important to the prediction of modern advanced

ceramic rolling elements.

1.4.2.1 Sharp indentation flaw

Vickers hardness tester is usually used to produce sharp indentation flaws. Such flaws are often selected to investigate their effect on rolling contact fatigue failure although it is not possible to find the defect size like the indentation flaw. A very small indentation defect may be used as to simulate the specific defect such as 'star defect', which is occasionally found on the ball surfaces.

The effect of sharp indentation defects on ceramic rolling contact fatigue was studied by Hadfield et al. (Hadfield et al. 1993a, 1993b and 1994b), using a modified four ball machine. The upper ball was a steel ball and contacted with three lower ceramic balls. Each lower ceramic ball contains certain numbers of indentation defects made by Vickers hardness machines. Tests were conducted at a maximum contact stress of 6.4 GPa and spindle speed of 5000 rpm. The lubricants investigated were high viscosity mineral oil and low viscosity synthetic oil. The results showed that silicon nitride balls failed in a non-catastrophic way. Several damage modes were seen on the tested ceramic balls. They were lateral crack spall, radial crack propagation and delamination.

1.4.2.2 Artificial ring crack

Artificial ring cracks (large ring crack) are induced through indentation with a blunt indenter. The effect of such surface cracks on rolling contact fatigue of silicon nitride balls were extensively investigated by Hadfield et al. (1993a), Hadfield et al. (1993b) and Hadfield et al. (1993c). The use of a modified four-ball tester showed that good quality ceramic balls in hybrid contacts did not fail in a catastrophic mode. Fatigue tests were conducted at maximum contact stresses of 6.4 GPa and spindle speed of 5000 rpm. The lubricants investigated were high viscosity mineral oil, low viscosity synthetic oil and high penetration kerosene. Test results on artificially induced crack revealed the role played by a lubricating medium in the process of fatigue failure. Experimental results showed that the artificially produced cracks failed in a non-catastrophic way, the pattern of failure was strongly influenced by the lubricating fluid. The pre-cracks were initiated by an impact

indentation process in which fully developed cone cracks were formed and the rolling contact fatigue mode was spalling. In that study, the artificially produced ring crack depth within the silicon nitride subsurface typically reached 20 μm before developing into a cone crack.

Hadfield (1998) has also performed preliminary experiments on surface ring cracks (small ring crack) found on silicon nitride as purchased from manufacturers to observe the failure mode from such crack defects. A modified four ball machine was used to perform the test and the ceramic balls were placed on the bottom. Experimental results were given a pre-test surface analysis using a dye penetration technique and identified some failure modes of the silicon nitride rolling elements. In that study, it was found that the ring cracks did not develop into cone cracks but failed due to delamination.

1.4.2.3 Natural ring crack

In the previous section, all those RCF test results relied heavily on random crack location and did not consider the importance of specific crack locations. In practice, surface cracks distribute randomly on the ball surface and they can occur in any positions when two balls are in contact. For example, when a modified four ball machine is used to perform a fatigue test, the probability for the crack being in the contact area is only two percent (Wang and Hadfield 2000a). Therefore it is nearly impossible to ensure that the crack is on the contact track if the ceramic ball is just randomly placed in the collet. Wang and Hadfield (2000a) have developed a novel rolling contact fatigue test method for positioning the ring crack (Appendix 1). The ring crack can be located precisely within the contact path. Twelve typical locations were tested experimentally and it was found that silicon nitride balls do not always fail when the contact loading traverses the crack although the cracks are entirely in the contact region. The life of balls in rolling contact fatigue varied considerably as the crack orientation was changed. There were a small number of locations which led to fatigue failure. Therefore, the cracks must be located in the same position so that the test results are comparable and predictable.

A numerical fracture mechanics approach was used in the calculation of the stress intensity factor in order to explain why the fatigue life showed big difference

as the crack location varies within the contact path (Wang and Hadfield 2000b). The calculations of the stress intensity factors, K_I, K_{II} and K_{III}, were made to determine which mode is important for crack propagation. The calculations showed that mode I stress intensity (K_I) dominated natural crack growth. The different crack locations demonstrated different stress intensity values. As a result, the rolling elements with the natural ring cracks exhibited different rolling contact fatigue life.

Wang and Hadfield (2004) investigated the failure processes starting from a natural surface ring crack. Experimental observations identified the importance of the secondary surface cracks in fatigue failure. The fatigue failure process was influenced not only by fatigue crack propagation but also strongly influenced by the crack face contact. The process of the surface crack failure was analysed using a boundary element analysis. In the numerical simulations, the mode I stress intensity (K_I) was assumed to be the most influential factor. No attempt was made to compute the mode II stress intensity (K_{II}) for the crack being in the compressive zone. As a result, the observed spall size was larger than the numerical prediction. To overcome this problem, the mode II stress intensity (K_{II}) has to be considered in the analysis. Effects of various initial crack sizes on secondary surface cracks are also important to determine surface ring crack failure.

1.4.2.4 Line defect

Unlike the surface ring crack defects, line defects are not often observed in silicon nitride balls. The percent for the line defect is approximately 8 % (Wang and Hadfield 2002b). Line defects are also difficult to detect under the normal light source and they only are able to see under the illumination of UV light source. The line defects are approximately straight, extending for 0.5-0.6 mm for the long line defect and extending for about 0.1mm for the short line defect. The subsurface profile of the line defect is like a straight line and the angle between the line and the ball surface ranges from 40° to 90° (Wang and Hadfield 2002b). Recently, this type of defects was studied experimentally and numerically by Wang and Hadfield (2002b, 2003). Rolling contact tests were performed on silicon nitride / steel elements. A modified four-ball machine was used to carry out fatigue tests. The tests were conducted at 5000 rpm and a maximum Hertzian stress of 5.58 and 6.63GPa

respectively. The defect was placed in the worst position using the crack orientation determination procedures (Wang and Hadfield 2000a). The test results confirmed that the failure mode was fatigue spalling. Post-test analysis showed that fatigue cracks that initiated from pre-existing line defect propagated either in the same direction of the motion of the load or opposite to the direction of the motion of the load.

1.4.3 Mechanics of ring cracks

Surface ring cracks are normally caused by manufacturing pressing faults or blunt impact loads. The ring cracks on flat silicate glass plate have been studied extensively in the past (Roesler 1956, Chaudhri and Phillips 1990). The Hertz theory of elastic contact is widely used to explain the ring and cone fracture. Studies on ceramics are becoming more prevalent and the theory of Hertzian fracture has been significantly developed during recent years (Lawn 1998). The contact stress fields are well documented (Huber 1904, Wilshaw 1971, Johnson 1985). The ring and cone fracture tests involve pressing a tungsten carbide ball into the ceramic surface with a progressively increasing load and observing the pattern of fracture. The ring crack pops up first when the load exceeds the critical value and a well-defined cone shaped crack is developed as the normal load further increases. For the Hertz fracture, due to the small volume acted upon by the contact induced tensile stress, the tensile stress for generating ring cracks is much greater than that required for fracture in bulk tensile tests specimens (Roesler 1956, Tillett 1956).

To predict both the fracture load and the subsequent length of the cracks numerous theoretical models have been developed using fracture mechanics approach (Frank and Lawn 1967, Wilshaw 1971, Warren 1978, Mouginot and Maugis 1985, Li and Hills 1991, Warren et al. 1995). In these models, it was assumed that the inclined sides of the cone crack were perpendicular to the maximum principal stress. Under the action of a combined normal and tangential load, a partial cone crack will be generated if the indent slides over the surface. The cracks are initiated at the trailing edge of the contact, and propagate almost perpendicular to the surface (Lawn 1967, Bethune 1971). Warren (Warren et al. 1995) analysed ring crack initiation and propagation using analytical techniques and

concluded that several stages were involved in the formation of the cone cracks. The first two stages of surface defect growth form the complete rings and in the final phase the crack develops into a cone.

Experimental observations were made to identify impact cracking (Cundill 1997). Results demonstrated that the impact resistance to surface ring cracks was sensitive to the material microstructures and some material types were found to be more resistant to impact cracks than others. The ball sizes also showed a significant effect in the impact resistance to the surface ring cracks. For ball sizes of 6.35 mm, a contact stress of 20-25 GPa was required to form surface ring cracks; for ball sizes of 12.7 mm, 10-15 GPa was required; for ball sizes of more than 20 mm, 10-12 GPa was required. The ring crack initiation load of HIP silicon nitride balls was also experimentally studied by some researchers (Ichikawa et al. 1995a, Ichikawa et al. 1995b, Ohgushi and Ichikawa 1996). A maximum contact stress of 14 -18 GPa was required to produce surface ring cracks.

1.4.4 Modelling of crack growth

Modelling of fatigue crack propagation is important to predict fatigue life precisely. Many attempts have been made to relate crack propagation rate with RCF life performance. Braza et al. (1989b) discussed the importance of modelling work for wear mechanisms and indicated that the modes must be described mechanistically to better understand how they occur and to develop formulae for wear material removal. Since Fleming and Suh (1977) discussed the mechanics of crack propagation in delamination wear, fracture mechanics has been applied in the analysis of modelling in a number of studies (Hills and Ashelby 1979, Rosenfield 1980, Keer et al. 1982). In those studies, a subsurface crack parallel to the surface of a half-plane subjected to a Hertzian surface load was analysed and the stress intensity factors were calculated based on the contact induced stress field with no cracks. Also, a crack at an angle to a surface acted on by a Hertzian contact load was also analysed by Keer and Bryant (1983) and Bryant et al. (1984). In Keer and Bryant, lubrication pressure was assumed to be the crack driven force; in Bryant et al., the crack face friction was assumed to be zero due to the existence of the sufficient lubrication oil in the crack. The mode II stress intensity is responsible for

crack growth. Additionally, the surface pitting crack was thoroughly analysed by Bower (1988). The effects of crack face friction and lubrication pressures on crack propagation were summarised.

Numerous studies have been completed to explain the wear mechanisms in ceramic materials (Keer and Worden 1990, Thomsen and Karihaloo 1996). For brittle materials, cracks often occur on the surface due to tension. In Keer and Worden, the stress distribution due to a Hertzian contact was considered to be the main cause for the microchipping cracks. A mode for wear material removal was proposed. The microchipping cracks at the surface link or branch to turn parallel to the surface due to the rapid change in the direction of principal stresses at the indentation contact. In Thomsen and Karihaloo, near-surface cracks subjected to contact loading were modelled. The frictional contact between the crack faces was considered as a significant impact factor in a phase transforming material. This is because the closing effect on the crack tips resulted in significant compressive stresses at the crack tip(s). Consequently, these compressive stresses would induce a frictional resistance to the sliding deformation of the crack tips.

The cracks found on ceramic rolling elements are very small. Currently, experimental results on small fatigue cracks in ceramics are limited. Dauskardt et al. (1992) investigated the subcritical growth behaviour during cyclic-fatigue loading in a SiC-whisker-reinforced alumina ceramic composite. Experimental observations were carried out on both long and micro-structurally small cracks. For the long crack experiments, cyclic fatigue crack growth rates were dependent on the applied stress intensity range and load ratio. The long crack fatigue threshold, ΔK_{th}, was approximately in the order of 60% of K_c. This result was similar to the observations in other ceramic materials. For small surface cracks, cyclic fatigue crack growth rates were significantly smaller than the nominal long-crack threshold ΔK_{th} at the applied stress-intensity levels. Another experiment on the cyclic fatigue behaviour was performed by Reece and Guiu (1991). They studied the effect of environment on the cyclic fatigue behaviour of a high-purity alumina bioceramic using the repeated indentation technique. Tests were conducted in the presence of water, a variety of alcohols, toluene and simulated physiological fluid environments. The experimental results indicated that these environments did not demonstrate any

detectable effect on the damage produced by single indentations, but those containing water cause a significant degradation in cyclic fatigue resistance which cannot be quantified in terms of subcritical crack growth behaviour in static fatigue. A review paper by Ritchie and Dauskardt (1991) summarised the fracture mechanics approach to subcritical crack growth and life prediction during cyclic fatigue of ceramics.

1.5 STATE OF THE ART

Fatigue of silicon nitride elements in rolling contact is almost always initiated from surface crack defects. Many attempts have been made to identify the role of the surface defects and failure mechanisms in rolling contact fatigue using various test machines. Experiments conducted on silicon nitride elements generally exhibited considerable scatter in number of stress cycles to failure. This difficulty arises as a consequence of the variability associated with initial crack size and testing techniques. Available experimental results by Wang and Hadfield (2000a, 2004) pointed to the effects of the crack orientations/locations on time to spall. As the experimental tests were only concentrated on natural cracks, there was little information on the effect of initial crack sizes on contact fatigue and therefore further experimental tests using various crack sizes and geometries are crucial important for predicting contact fatigue. It is necessary to develop an understanding of failure modes starting from various crack sizes. Currently, there is little fundamental understanding of failure mechanisms. Although the numerical analysis has been widely used in fracture modelling, the damage processes of surface cracks are still not fully understood. In recent studies (Wang and Hadfield 2000b, 2004), the natural crack was adopted in the model and crack growth was analysed using a dual boundary element method. No attempt was made to compute the stress intensity factors where the crack lies in the contact circle due to the limitation of the numerical method. The calculations could not explain why the spall size is often larger than the numerical prediction. Detailed experimental and analytical studies on silicon nitride elements with various crack sizes have not been carried out adequately at this stage. Micro-mechanics in ceramic rolling contact have not been adequately studied. Clearly, much effort must be devoted to these aspects.

CHAPTER 2
SURFACE RING CRACK GENERATING DEVICE

This chapter describes the design of a crack generating device and the results obtained from it. The aim of the design and manufacture of the crack generator was to produce various sizes and shapes of the surface ring/cone cracks. The mechanisms of rolling contact fatigue failure may be identified with the help of well-controlled crack sizes. In section 2.1, contact stress fields are described according to classic solutions. Crack generator design is described in section 2.2. The principles of crack geometry control are discussed and test conditions are presented. In the final section, test results are discussed. Surface and subsurface appearances of the artificial ring/cone cracks are also illustrated.

2.1 CONTACT STRESS FIELDS

The most common type of defects found on ceramic ball surfaces are surface ring or cone cracks, which are normally caused by manufacturing pressing faults or blunt impact loads (Cundill 1990). These surface cracks are of partial circular feature, and the arc length is approximately one forth to one third of the circumference of the circle. The phenomena of the ring and cone fracture are normally explained by the Hertz theory of elastic contact. In the past decades, the study on the ring and cone fracture was most widely carried out in flat silicate glass plates. It is becoming more prevalent in ceramics and the damage theory associated with Hertzian fracture has been significantly developed during recent years (Lawn 1998).

For the frictionless contact of a sphere, the basic Hertzian elasticity solutions for a sphere of radius R at normal load P are well documented (Huber 1904, Lawn and Wilshaw 1975, Timoshenko and Goodier 1951, Johnson 1985). The contact radius a is given by:

$$a = \left(\frac{4\kappa P R}{3E} \right)^{1/3} . \qquad (2.1)$$

κ is a factor composed of the elastic constants of the indenter (E_1, ν_1) and the specimen (E, ν):

$$\kappa = \frac{9}{16}[(1-\nu^2)+\frac{E}{E_1}(1-\nu_1^2)]. \qquad (2.2)$$

In these equations, E and E_1 are Young's modulus, and ν and ν_1 are the Poisson ratio of the specimen and the indenter respectively. Figure 2.1 shows the geometry of the contact. The mean contact pressure is given by:

$$p_m = \frac{P}{\pi a^2}. \qquad (2.3)$$

The maximum tensile stress in the specimen occurs at the contact circle:

$$\sigma_{max} = \frac{1}{2}(1-2\nu)p_m. \qquad (2.4)$$

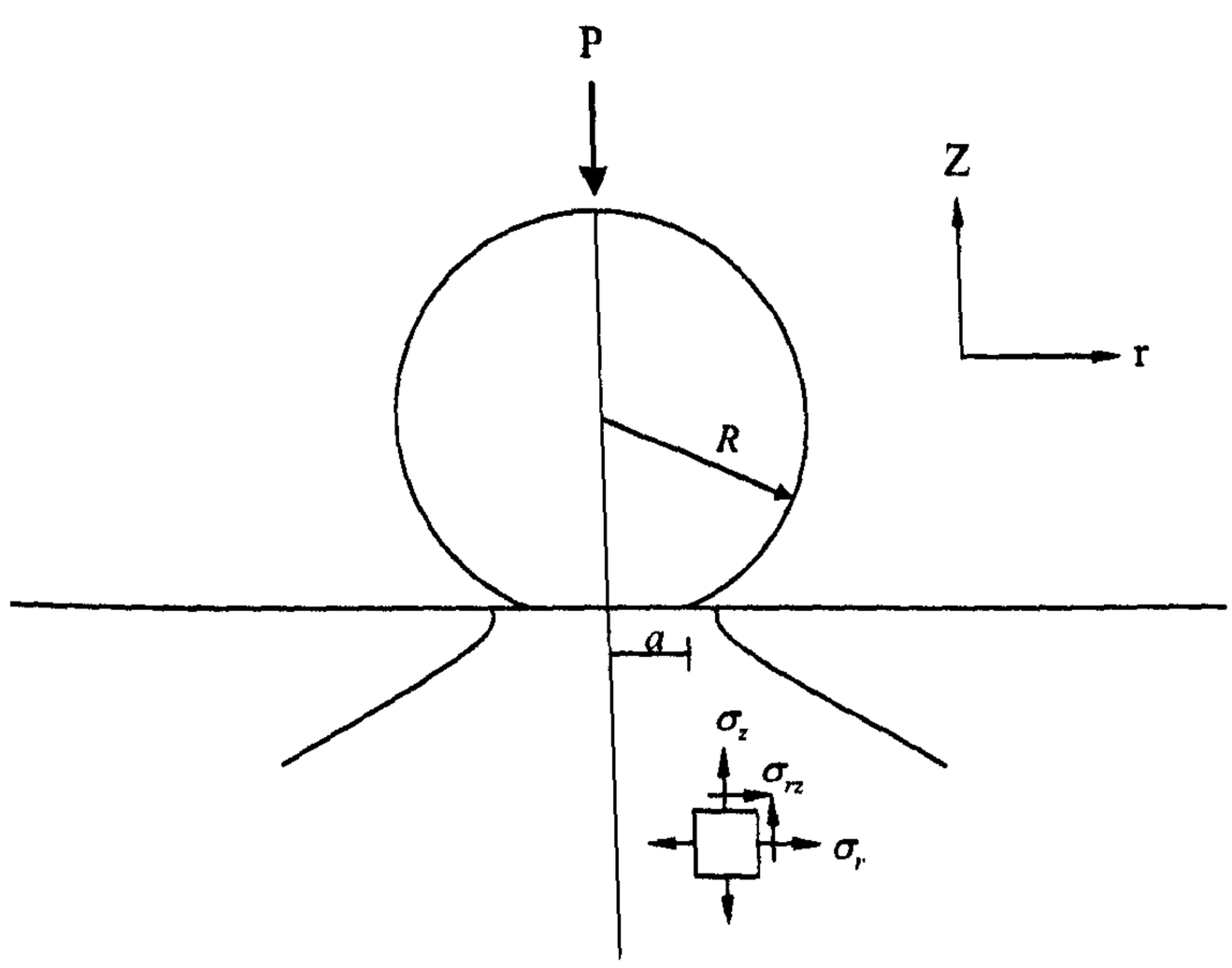

Figure 2.1 Geometry of indentation fracture (Zeng et al. 1992)

The stresses within the Hertzian elastic contact field are given by the equations described in Appendix 2.

The surface friction force has a significant effect not only on the magnitude of the maximum tensile stress but also on the crack path (stresses σ_1 and σ_3 trajectories) as shown in figure 2.2 (Hamilton and Goodman 1966). Hence, the crack geometry and sizes may be controlled using various combinations of surface traction. The effect of surface friction force on crack geometry will be discussed in the next section.

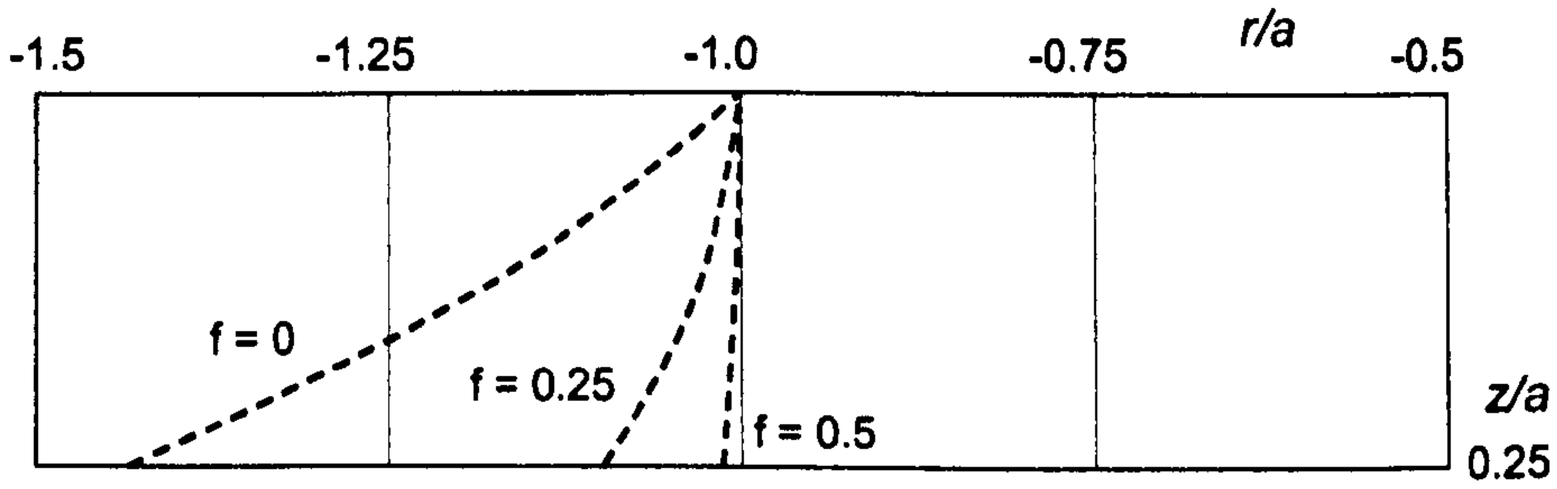

Figure 2.2 Influence of friction coefficients on σ_3 trajectory

2.2 DESIGN OF CRACK GENERATING DEVICE

2.2.1 Description of the device

As discussed in the previous section, the contact radius defines the spatial scale of the contact field and the mean contact stress defines the intensity of the contact field. Therefore, different dimensions of ring/cone cracks may be obtained using the specific combination of traction and indenter sizes. The design of the crack generating device is based on these principles.

A finished ceramic ball was placed into the hole of the mild-steel base facing towards the impacting pendulum, as shown in figure 2.3. A tungsten carbide ball or silicon nitride ceramic ball with collet was mounted on the holder. A mass was dropped under gravity through the hammer. Figure 2.4 systematically illustrates the geometry of the crack generating device. The symbol α represents the initial angle between the pendulum and the central line. The symbol 0 represents the swing angle where the holder is lifted to a height of *H*. Figure 2.5 shows the relationship between the height and the swing angle. The letter *l* stands for the distance between the contact point and the central line and the *h* stands for the distance between the steel base and the platform

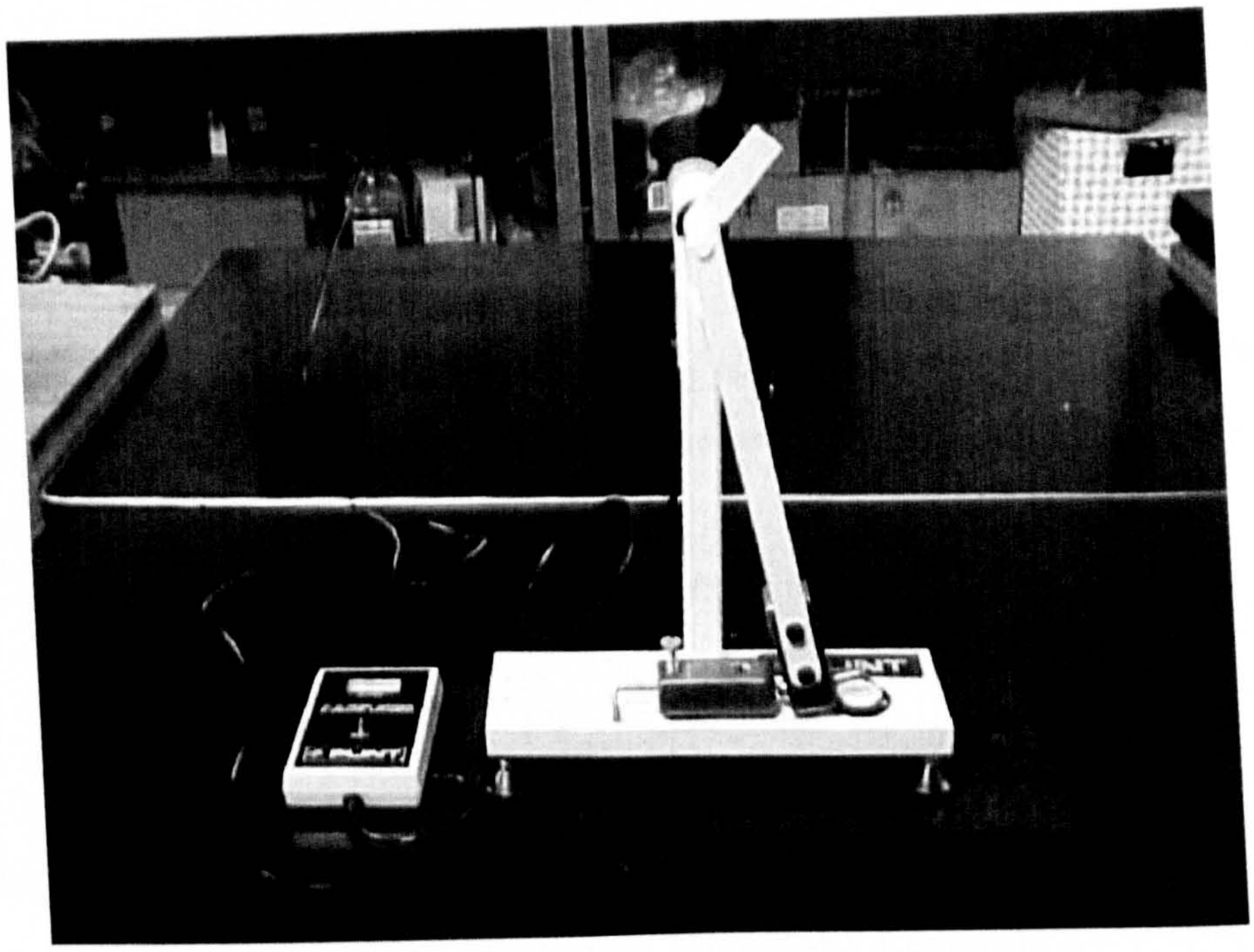

Figure 2.3 Views of the crack generating device

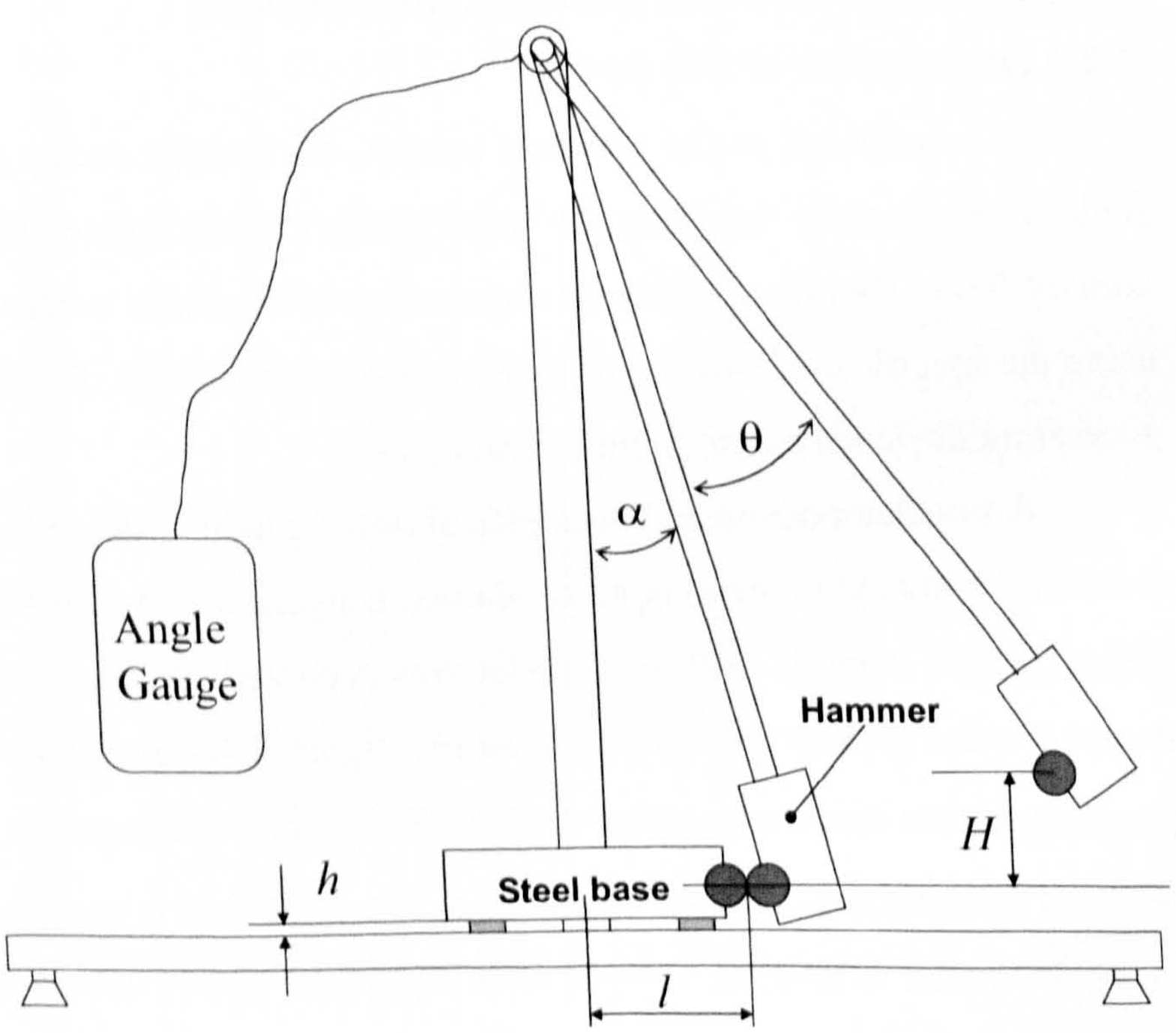

Figure 2.4 Configuration of the crack generating device

An electronic device was used to record the swing angle of the pendulum hanging in the vertical position and the switch was held while the pendulum was raised to the required position. The angle was recorded, and the pendulum was released to perform an impact of the balls. The height of the mild-steel base or the height (or angle) of the pendulum can be adjusted to obtain various surface tractions.

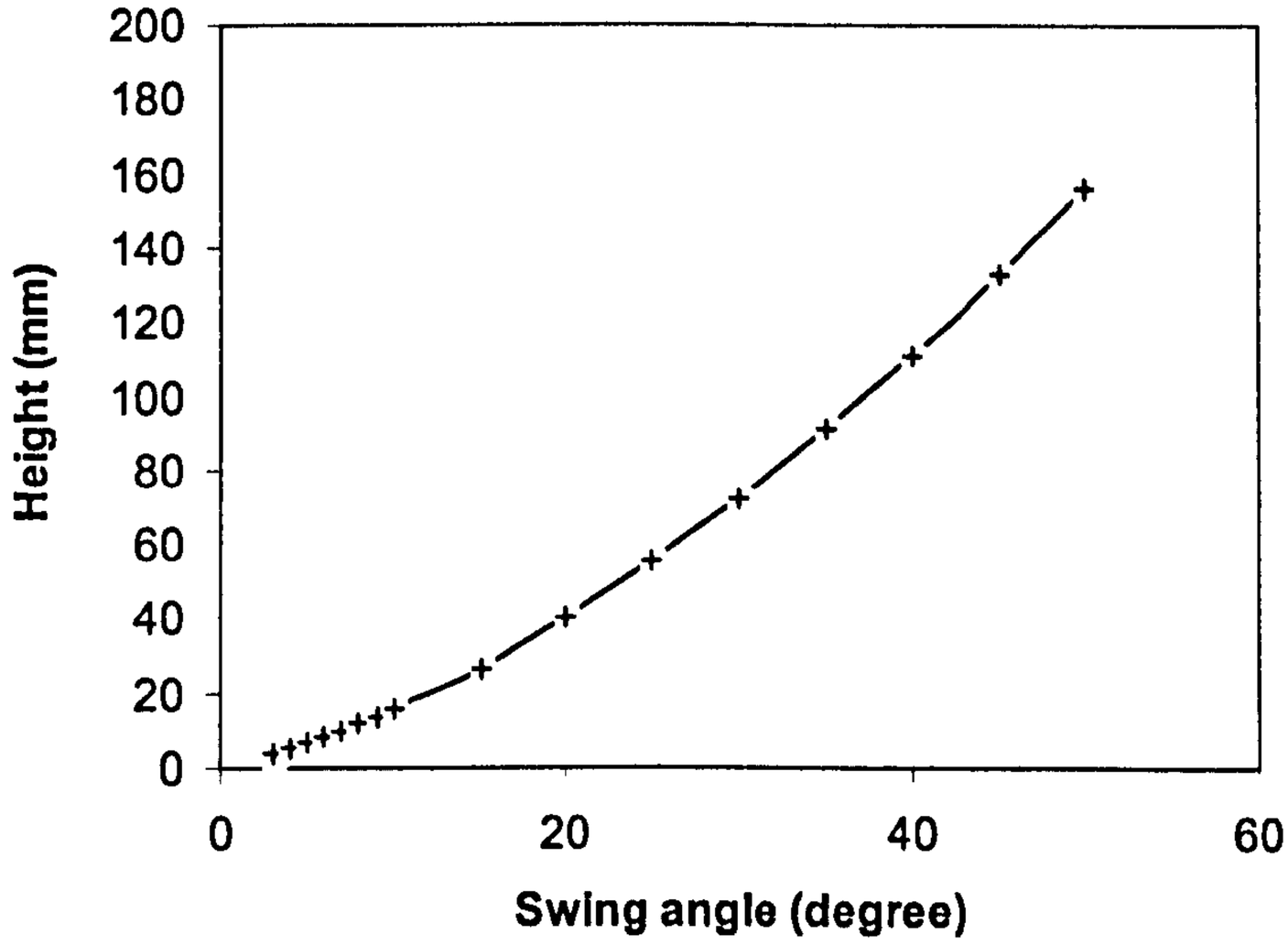

Figure 2.5 Height of the pendulum against swing angle

2.2.2 Principle of crack geometry control

Consider the case of figure 2.6. The collision point is in the centre of the balls and velocity v is at an angle α to the x axis. The angle α depends on the magnitude of l (see figure 2.4). The various values of l can be modified by moving the steel base to the left or the right. The tangential velocity at the moment of collisions can be expressed as follows:

$$v_t = v\sin\alpha \qquad (2.5)$$

Tangential traction will be produced as a result of this tangential velocity. The surface tensile stresses are increased compared to the impact without tangential traction. Consequently, it is easy to produce smaller size cracks.

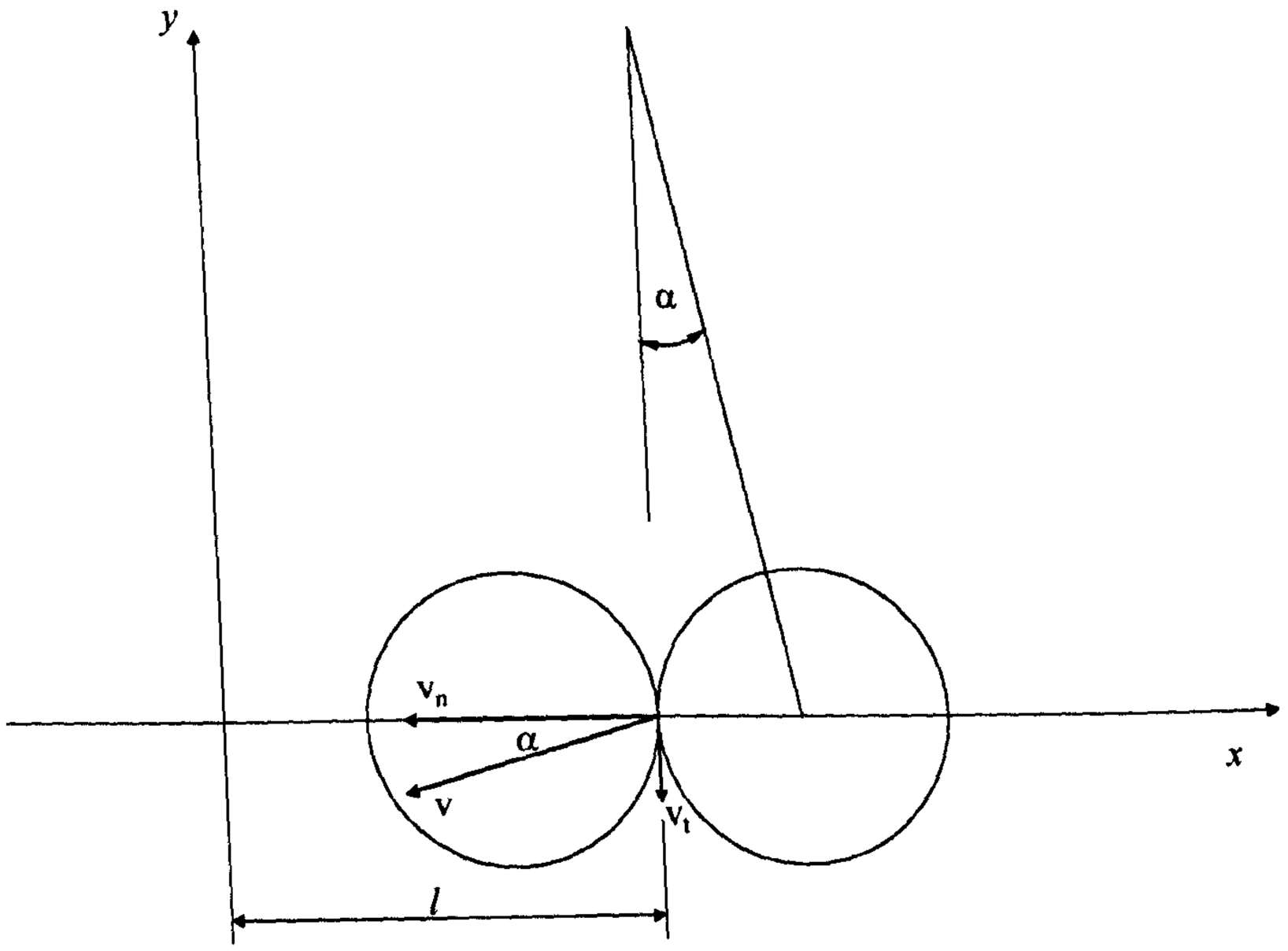

Figure 2.6 Geometry of ball collisions with no off-centre

Figure 2.7 shows the case of off-centre collisions. The tangential velocity at the moment of collisions is:

$$v_t = v\sin(\alpha + \beta)\,. \qquad (2.6)$$

The results indicate that the tangential velocity is larger than that in the case of figure 2.6. The equation (2.6) is a common form, which may represent all situations. Generally speaking, it is hard to keep $\beta = 0$. In practice, an off-centre effect always exists.

We can change the values of α and β to gain the crack geometry required. This crack generator is employed to produce surface cracks as it may simulate the processes of crack formation in the real lapping phases (rotation and impact). The lower ball (held in the steel base) will rotate when the collision starts. The

conditions for impact testing are listed in table 2.1.

Table 2.1 Test conditions for generating surface cracks

Off-centre position	α (Degrees)	β (Degrees)	$\alpha + \beta$ (Degrees)
1	12.4	5.42	17.82
2	12.4	10.89	23.29
3	12.4	16.47	28.87

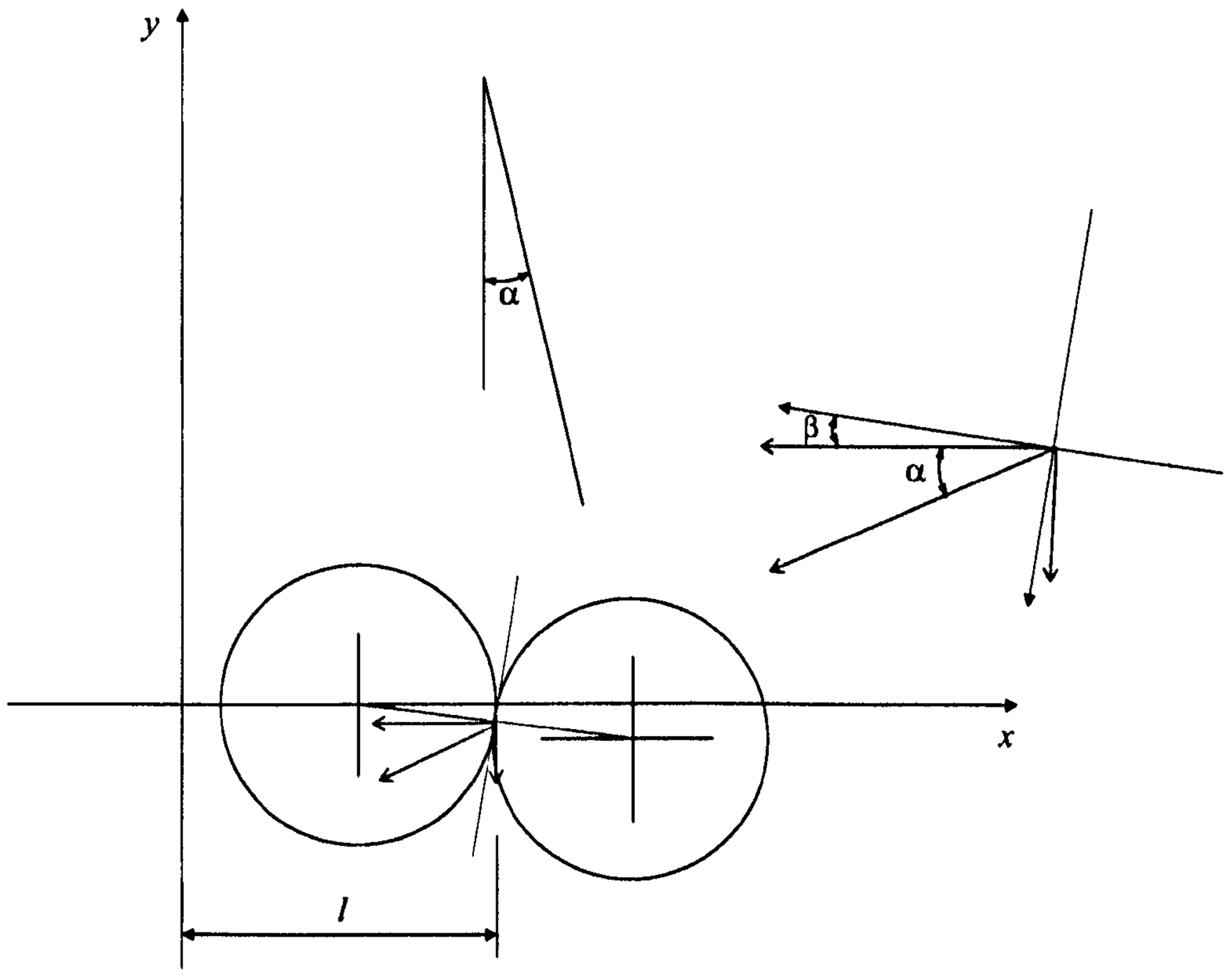

Figure 2.7 Geometry of ball collisions with off-centre

2.3 TEST RESULTS

2.3.1 Surface and subsurface characterisation

The tests of impact resistance were carried out on silicon nitride ceramic balls. The lower ball was located on the mild-steel base and the dropping ball was held by a collet mounted on the holder. Various heights (or swing angles) of the pendulum were selected in order to produce various sizes (length and radius) of cracks. The crack angles (subsurface profile) were controlled by changing the magnitude of angle α and β values. This was done by changing l and h. The initial value of the angle α was 12.4^{o}. The mild-steel base was raised by putting an adjustment washer underneath the mild-steel base. In this way, different values of angle β were obtained.

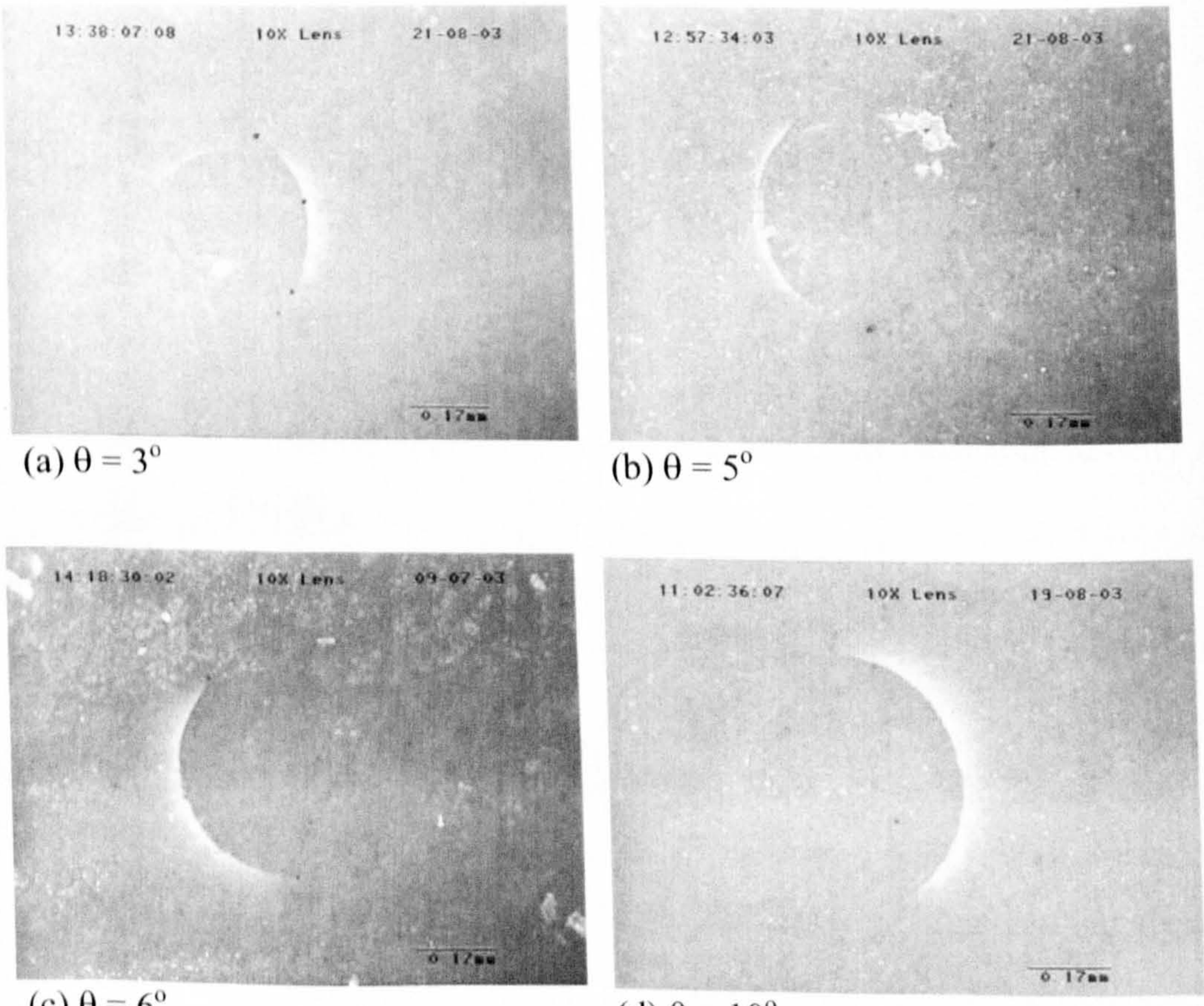

(a) $\theta = 3^{o}$ (b) $\theta = 5^{o}$

(c) $\theta = 6^{o}$ (d) $\theta = 10^{o}$

Figure 2.8 Surface appearances of artificial ring/cone cracks

The dropping angle of the pendulum was progressively reduced from the maximum value until no surface crack was observed on the ball surface under a light

microscope. The dye penetrant method, described in Chapter 3, was used to enhance the ability of surface crack inspections. Detailed analysis of subsurface cracks will be discussed in Chapter 4, section 4.1.3.

The surface ring/cone crack, produced by using a 6.3mm tungsten carbide ball impacting a 12.7mm silicon nitride ball (material A, Chapter 3, Table 3.1) are shown in figure 2.8. The cracks, produced by using 12.7mm balls impacting each other, are shown in figure 2.9. Clearly, the radius of the ring crack increases as the swing angle increases. For the impact of ceramic balls, when the swing angle is too big, slight surface damage may be observed on the central zone. This minor damage looks like small pits removed from the surface. This is only happens when the drop height is large. It is interesting to note that the bigger the crack radius the easier the crack is to observe. This implies that the gap between the faces of the crack increases as the crack radius increases.

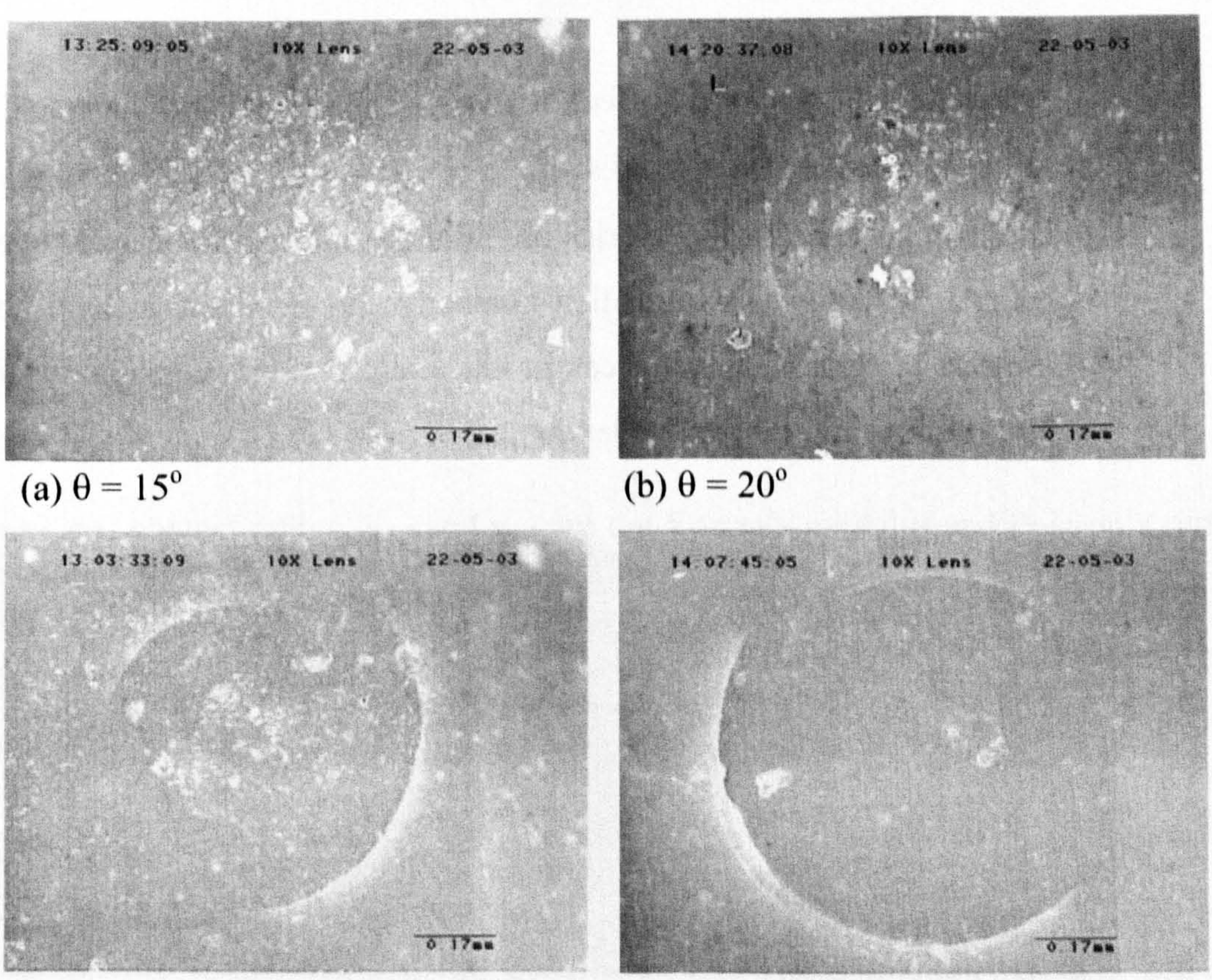

(a) $\theta = 15^{o}$ (b) $\theta = 20^{o}$

(c) $\theta = 30^{o}$ (d) $\theta = 40^{o}$

Figure 2.9 Surface appearances of artificial ring/cone cracks
(12.7mm balls (material A) impacting against each other at position 3)

Subsurface images of the crack are shown in figure 2.10. The subsurface observations show that the length of the cracks increases as the swing angle increases. Note that the crack radius also increases as the swing angle increases. Therefore, a large radius crack leads to a large length crack.

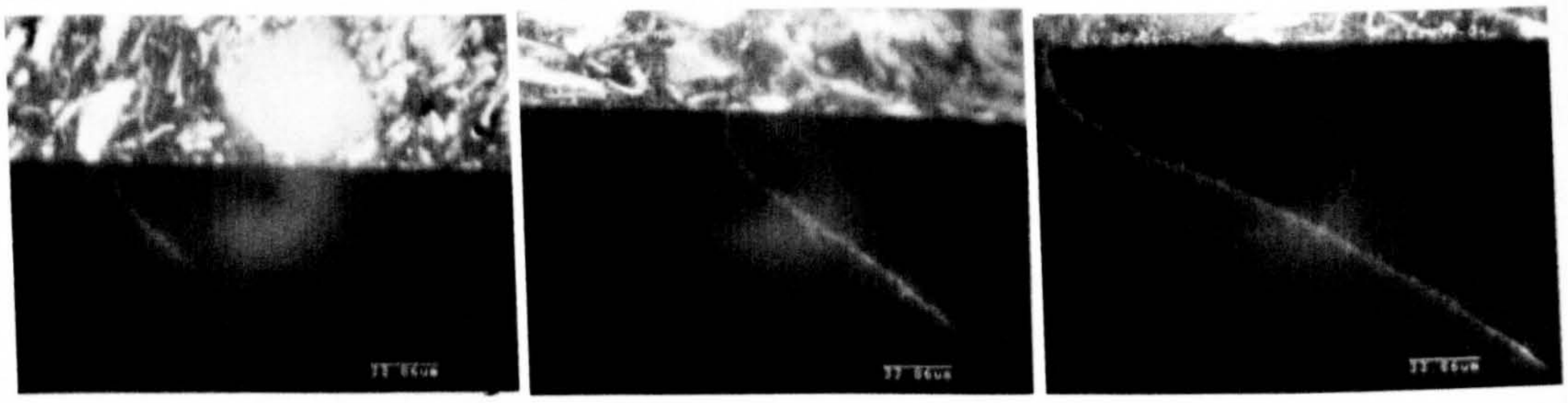

(a) $\theta = 15^{o}$ (b) $\theta = 20^{o}$ (c) $\theta = 30^{o}$

Figure 2.10 Subsurface appearances of artificial ring/cone cracks
(12.7mm balls (material A) impacting against each other at position 3)

Figure 2.11 shows the effect of an off-centre impact on the crack path. Both cracks are generated at the same swing angle ($\theta = 15^{o}$) and are of the same crack radius. As expected, the trajectories are slightly different. Generally speaking, the crack angle increases as the position number increases. Experimental observations confirm that the crack generator can produce different crack geometry. In addition, the sizes of the crack are well under control.

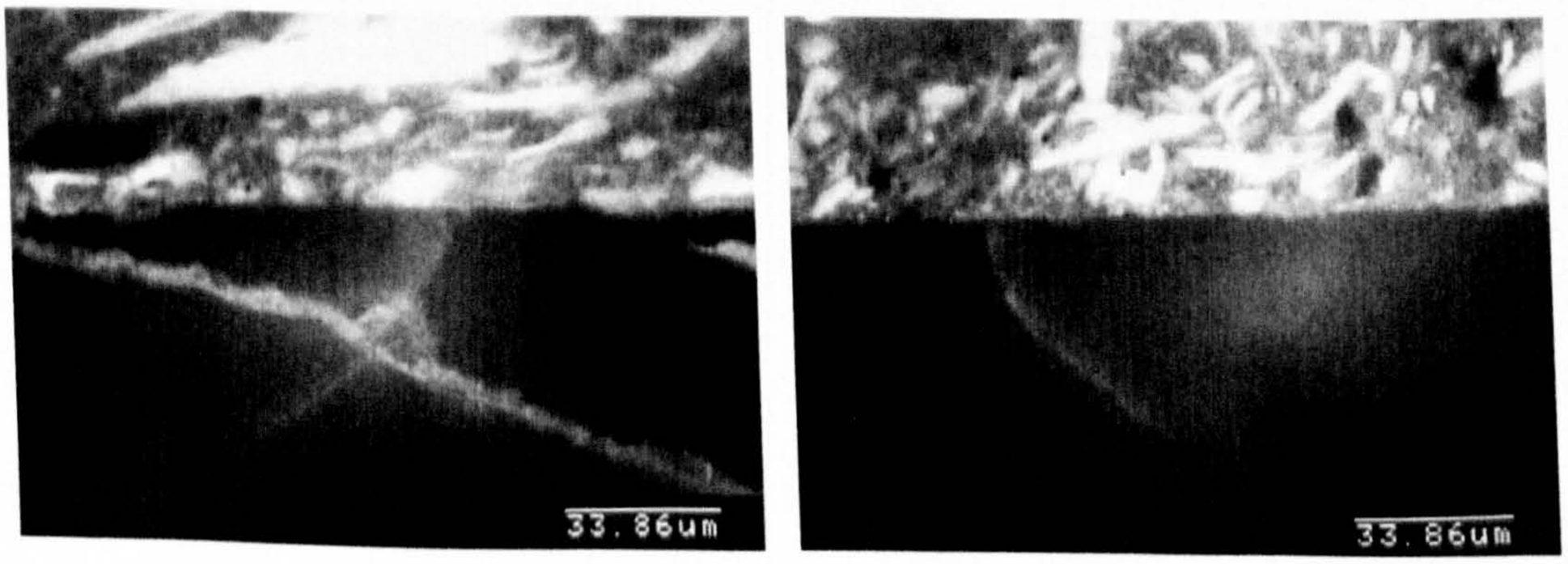

(a) Position 2 (b) Position 3

Figure 2.11 Comparison of subsurface observations on the Material A ball

2.3.2 Hertz fracture strength of surface ring cracks

According to the size of the circular contact zone, the impact force can be simply calculated using a quasi-static Hertzian model owing to the low impact velocity. The surface ring crack is generated when the swing angle (pendulum drop height) reaches a critical value. If the radius of the surface ring cracks is taken as the radius of the contact zone, the tensile stress required to produce the surface cracks can be calculated according to the minimum contact radius. Note that the contact radius and the ring crack radius are not exactly the same. The radius of a ring crack is slightly bigger (Frank and Lawn 1967).

The impact force P, the maximum contact pressure p_0 and the contact radius a are computed using the expression (Johnson 1985):

$$P = \frac{4E^* a^3}{3R^*} \tag{2.7}$$

$$p_0 = \frac{3P}{2\pi a^2} \tag{2.8}$$

$$E^* = \left(\frac{1-\nu_1^2}{E_1} + \frac{1-\nu_2^2}{E_2} \right)^{-1} \tag{2.9}$$

$$R^* = \left(\frac{1}{R_1} + \frac{1}{R_2} \right)^{-1} \tag{2.10}$$

where a is contact radius, $E_{1,2}$ and $\nu_{1,2}$ are the Young's modulus and Poisson's ratios of two impact balls, and $R_{1,2}$ is the radius of the balls respectively. The maximum tensile stresses at the surface, which occur just outside of the contact zone, are given by:

$$\sigma = \frac{(1-2\nu)}{3} p_0 \tag{2.11}$$

When this maximum tensile stress reaches a critical value (Hertz fracture strength), the ring crack will be generated. The Hertz fracture strength can be obtained by experimental tests. The observed circular contact zone at the critical drop height is shown in figure 2.12(a). The crack is just on the edge of the circle. The radius of the circle is approximately 0.28mm and the radius of the ring crack is

0.28mm (figure 2.12(b)). It can be seen from the results that both radii are nearly the same. Therefore, it is reasonable to use the ring crack radius in the calculation. Test results show that the crack radius generated at the critical drop height is 0.38mm for material B (Chapter 3, Table 3.1) balls and 0.28mm for material A balls. Hence, the calculated surface tensile strength is 2.07GPa for material B and 1.51GPa for material A.

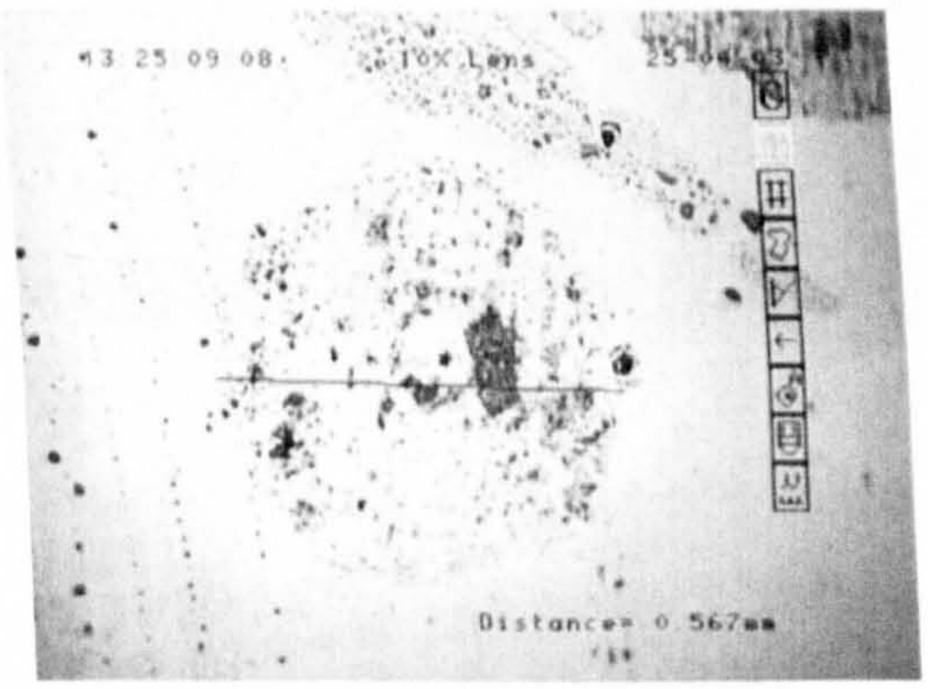

(a) Circular contact zone

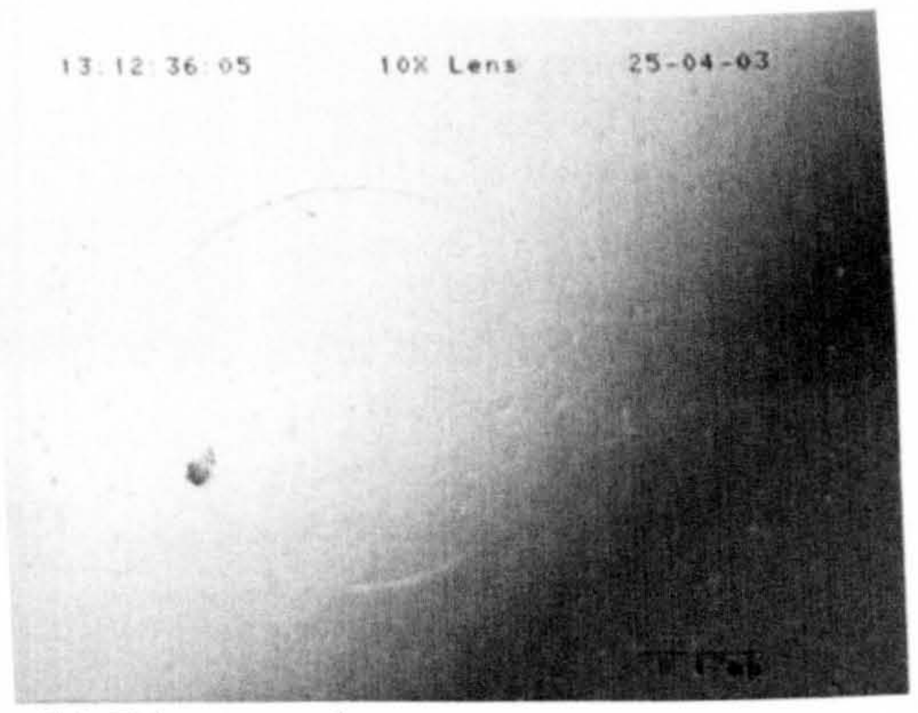

(b) Ring cracks

Figure 2.12 Photographs of artificial cracks

2.3.3 Relationship between the crack radius and swing angles

The relationship between the swing angle and crack radius is shown in figures 2.13 to 2.15. The results, produced by 6.3mm tungsten carbide balls impacting 12.7mm balls (material A) at position one, are shown in figure 2.13, and figure 2.14 for position two. As can be seen from figures 2.13 and 2.14, when a swing angle is less than 5^{o}, the radius approaches to the mean of natural cracks (see Chapter 4). Figure 2.15 illustrates the comparison of crack radius at different swing angles for different materials. Material A and B balls were adopted for this purpose to create the artificial cracks. A natural crack size can be created on material A balls surface when the swing angle is less than a certain value, for example, 15^{o}. However, it is difficult to see the cracks on a material B ball when the swing angle is less than 30^{o}. The results also indicate that the radius of the cracks varies as the swing angles change. The radius of the crack increases as the swing angle increases for all the impact positions.

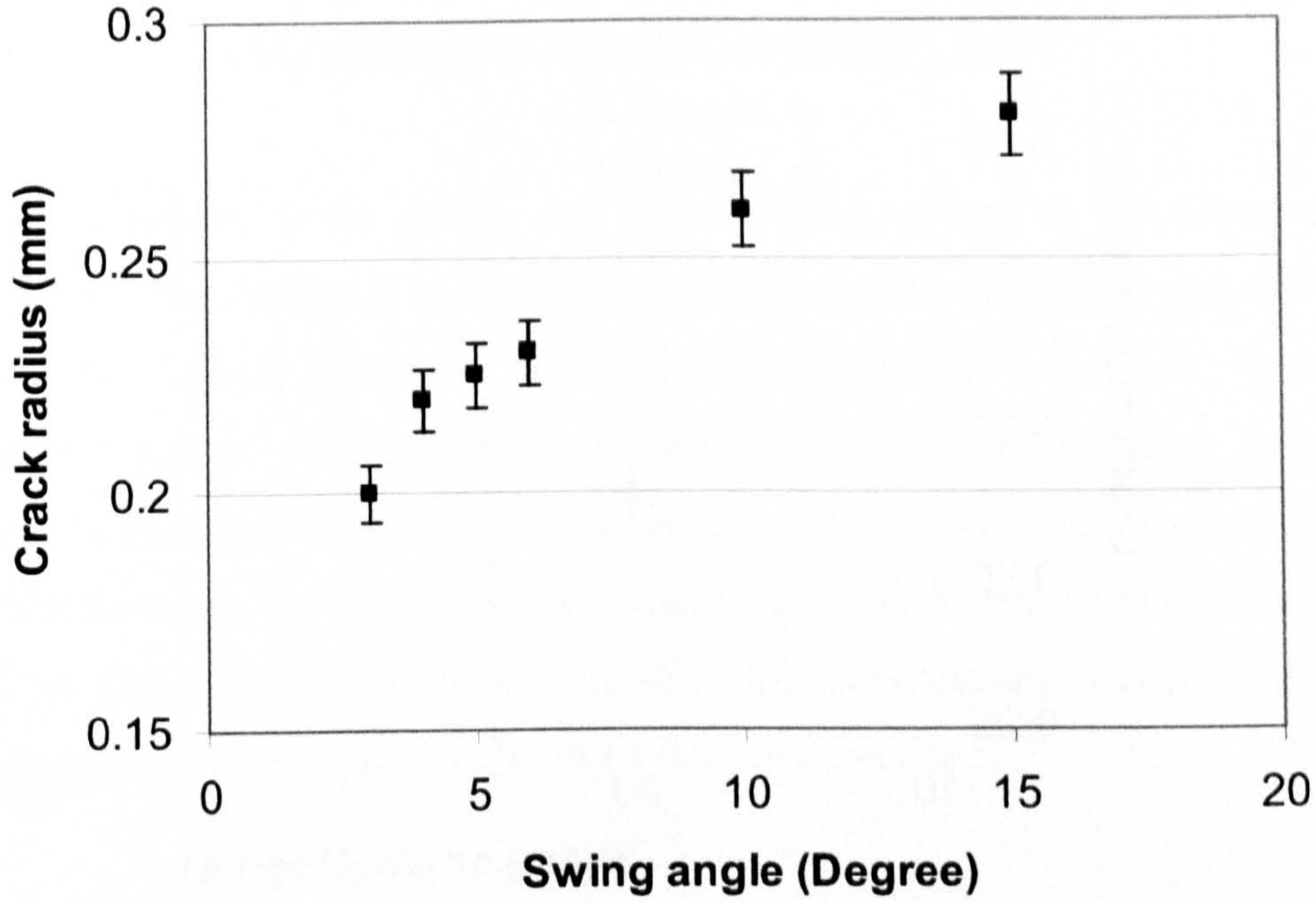

Figure 2.13 Crack radius against swing angle at position 1(different sizes and types of ball impacting each other)

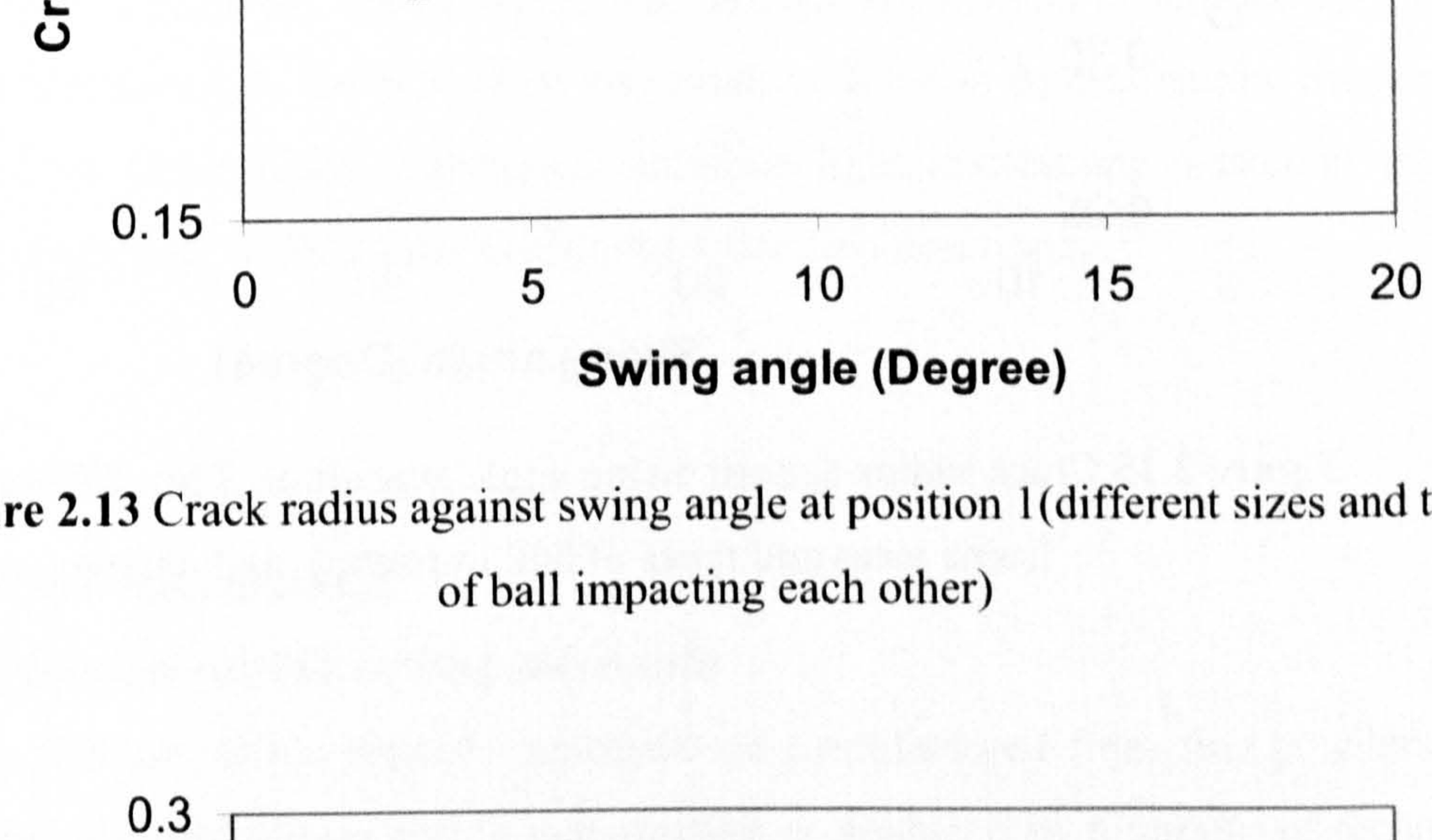

Figure 2.14 Crack radius against swing angle at position 2 (different sizes and types of ball impacting each other)

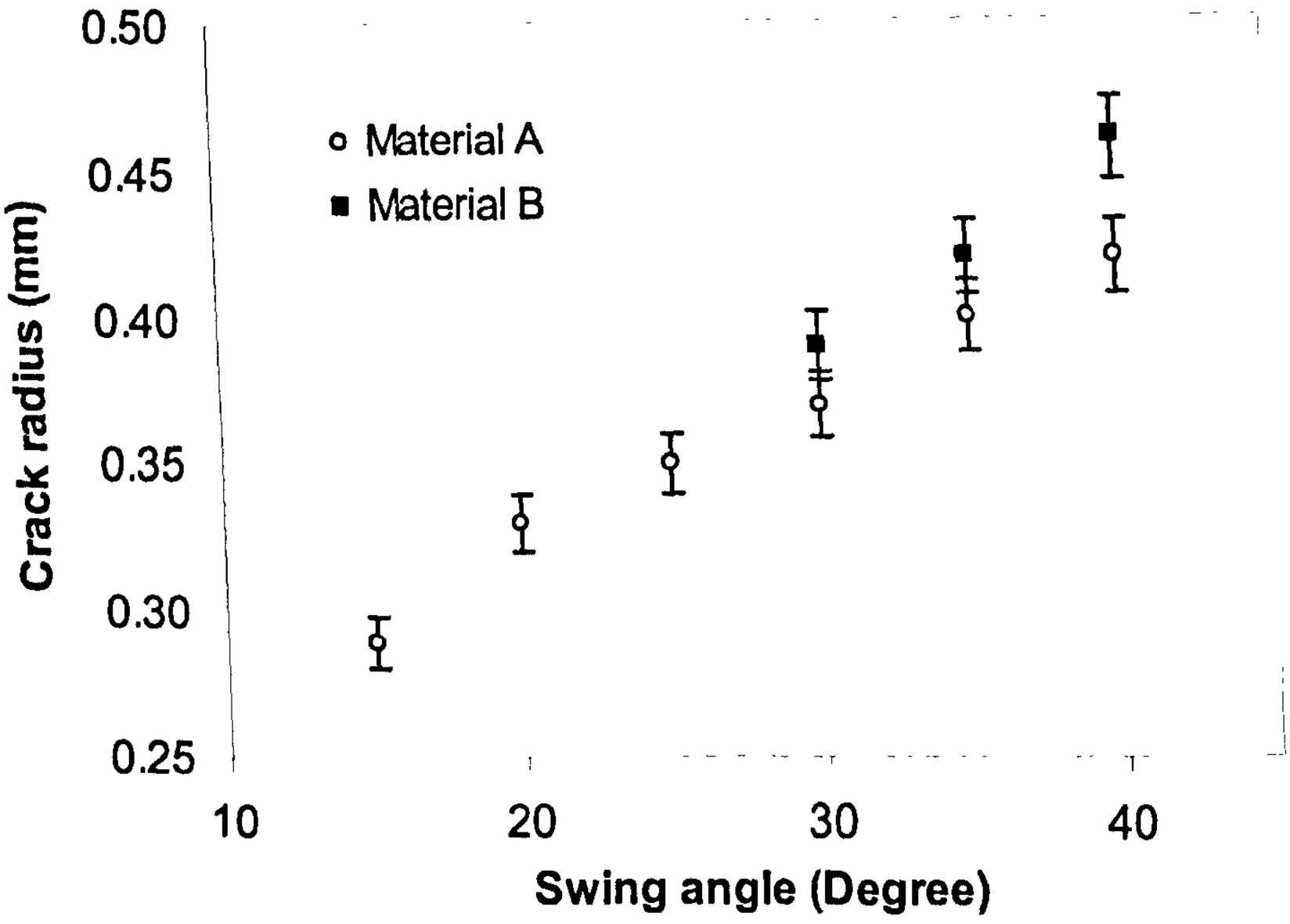

Figure 2.15 Crack radius against swing angle at position 3 for different materials (same sizes and types of ball impacting each other)

CHAPTER 3
EXPERIMENTAL METHODOLOGY

This chapter gives details and specifications related to the experimental methodology. Test materials are described with regard to manufacture and details of silicon nitride rolling elements, steel balls and lubricants are given. Specimen preparation, surface inspection and subsurface examination for crack geometry studies are described. The rolling contact fatigue test method is outlined with regard to the test machine, test procedure and crack orientation determination. Surface and subsurface examination techniques including light microscopy, scanning electron microscopy and WYKO laser profilometer are also described.

3.1 TEST MATERIALS

3.1.1 Silicon nitride rolling elements

Silicon nitride ceramic materials are manufactured from fine powders. The powder used for silicon nitride manufacture is produced by a variety of techniques such as direct nitridation, vapour phase reaction and carbothermal reduction. Powder particle size is particularly interesting from an engineering viewpoint due to its influence on mechanical properties. Good quality silicon-nitride powder is one to two microns in size (Cundill 1992).

Silicon nitride describes a family of materials which include α- or β- sialons as well as pure silicon nitride. In addition, silicon nitride materials can contain significant amounts of both crystalline and glassy oxynitride phases whose composition is determined by compounds added to promote densification. There are also a number of different fabrication and densification processes used to manufacture components. In most cases the starting material is silicon nitride powder, which after preforming can be densified by various processes, including low and high pressure sintering, hot pressing and hot isostatic pressing (Lee and Rainforth 1994).

Silicon nitride materials are classified according to the processing techniques used to prepare the solid form. The categories include sintered, hot-pressed, reaction-bonded and hot isostatically pressed. It is important to recognise that the composition, microstructure, and properties of silicon nitrides vary strongly depending on the processing route used in the fabrication of the product as shown in Appendix 3 (Jahanmir 1994).

Two types of silicon nitride bearing materials were used in the present study. They were manufactured both from the hot isostatic pressing (HIP). The test silicon nitride balls for both materials were 12.7 mm in diameter. The average surface roughness (R_a) is 0.005 to 0.01μm. Typical physical and mechanical properties of silicon nitride ceramic balls for materials A and B are listed in tables 3.1 (Jahanmir 1994).

Table 3.1 Physical and mechanical properties of silicon nitride bearing materials

Material	A	B
Density (g /cm^3)	3.16	3.24
Young's modulus (GPa)	320	310
Poisson's ratio	0.26	0.26
Fracture toughness (MPam$^{1/2}$)	6.05	6.41
Hardness (Vickers indentation) kg/mm^2 @10kg	1660	1600
Coefficient of thermal expansion (×10^{-6} m /m °C), 20-800 °C	2.9	3.0
Thermal conductivity (W / m °C)	29.3 (at 20°C)	30(at 20°C)

3.1.2 Steel balls

Steel balls used in this research were made from carbon chromium steel. The diameter and surface roughness were 12.7 mm and 0.02 μm R_a respectively. The average hardness of the steel balls was 851 H_{v10}. The elastic modulus of the steel ball was 210 GPa and Poisson ratio was 0.3.

3.1.3 Test lubricants

Five lubricants were used to study their influence in the rolling contact fatigue process. The physical properties of the test lubricants are listed in table 3.2. The mineral oil was typical oil used in bearings. Gearbox oil is a hypoid oil with EP additives. The grease is a synthetic ester base-oil with polyurea soap. The traction fluid is a synthetic oil with ZDDP EP additives.

Table 3.2 Test lubricant and properties

Lubricant	Viscosity @ 40^{0}C (cSt)	Viscosity @ 100^{0}C (cSt)
Mineral oil	9.4	2.4
Gearbox oil	101.2	15.24
Grease	70	9.4
Traction oil	31.9	5.4
Kerosene	2.7	n/a

3.2 CRACK INSPECTION

3.2.1 Specimen preparation

Ceramics are brittle materials. Manufacturing processing faults or impact loads often cause surface cracks, which are difficult to observe even under high microscopic magnification. Although several non-destructive evaluation (NDE) techniques, e.g. X-ray microfocus radiography, high frequency ultrasonic and acoustic microscopy, are being developed for detection, measurement and classification of defects and non-conformities in ceramic components, most of the advanced techniques are not sufficiently developed for use in routine inspection of silicon nitride balls (Galbato et al 1992). To inspect these small surface cracks, a fluorescent dye penetration technique was adopted to examine silicon nitride balls.

The fluorescent dye penetration method is very effective in detecting surface

defects on ceramic balls. Use of high resolution penetrants combined with advanced illumination and examination techniques permits detection of very fine, artificially induced, often optically invisible, ball surface crack defects. The sample preparation is the key to effectively detecting surface ring cracks. First of all, the silicon nitride balls are thoroughly cleaned with acetone in an ultrasonic bath to remove any surface grease and debris. Secondly, the samples are soaked for a period of time in the dye penetrants. Thirdly, the samples are put in a dye remover for a very short time to remove any dye from the ball surface and then washed thoroughly with water and then dried carefully. The silicon nitride balls are now ready for inspection.

3.2.2 Surface inspection

Figure 3.1 shows typical surface ring cracks found on the ceramic ball surface using fluorescent dye penetration method. These micrographs are used to determine the crack radius and length of the ring cracks. The fluorescent dye penetration inspection is supplemented by visual examination using bright or dark field illumination for detection of defects that do not retain dye penetrants.

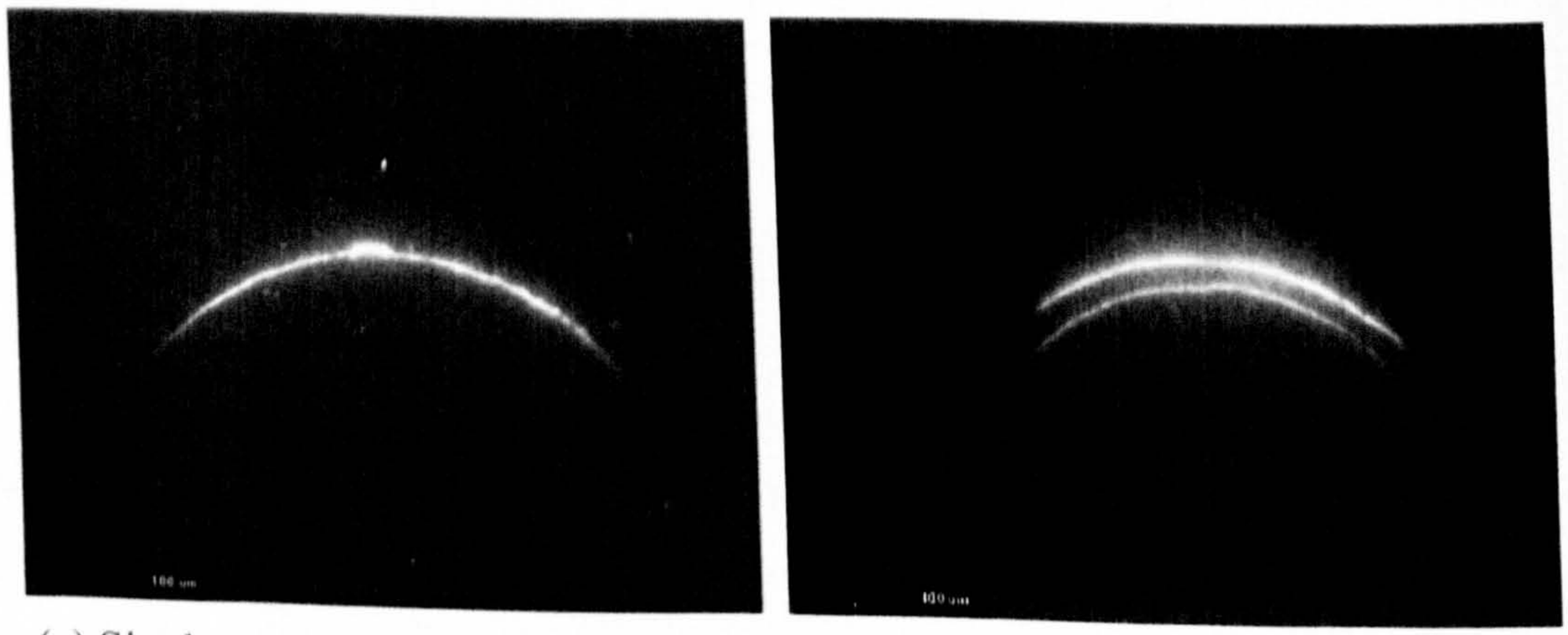

(a) Single crack (b) double cracks

Figure 3.1 Typical ring cracks found on a ceramic ball surface under ultraviolet light

3.2.3 Subsurface examination

Subsurface geometry is important for evaluating contact fatigue of silicon

nitride balls. To examine the subsurface geometry, the ball was sectioned near the crack. The position for sectioning the ball is crucial important to obtain the real subsurface profile. To reach the purpose, the direction of the cutting wheel movement must be straight to the chord of the ring crack. The specimen is a ball and it is not possible to cut through the crack straight away and therefore the ball is required to cut several times. After final cutting, the specimen is mounted and then polished gradually across the ring crack to examine the subsurface profile. The section images are then taken at various distances away from the centre of the ring crack in order to obtain whole images of the subsurface.

As it is difficult to section and polish ceramics due to its high hardness, a Sturers cutting machine incorporating a diamond wheel with sample rotation was used to section ceramic balls. A light microscope with UV light source is employed to inspect the specimen.

3.3 ROLLING CONTACT FATIGUE TEST

3.3.1 Test machine

A Plint TE92/HS Rolling Tribometer (figure 3.2) was used to perform the rolling contact fatigue tests. The test system includes a bench-mounting test machine, a micro-controller and a computer. The computer is connected to the micro-controller via the serial port. The control information is displayed on the computer screen and all test parameters are set up through various screen menus. In this way, it is very easy to set up test conditions and to store test results in the computer.

The test machine consists of an assembly which simulates an angular contact ball-bearing. The stationary steel cup represents the bearing out-race, the three lower balls represent the rolling elements within a bearing-race and the upper ball represents a bearing inner-race. The assembly was loaded via a piston below the steel cup from a pneumatic actuator. Three steel balls were driven by the upper ceramic ball which was assembled to a drive shaft via a collet. The steel cup is filled with the lubrication oil. A heater beneath the cup may be used to control lubricating oil bulk temperature. Spindle speed may be varied up to 10,000 rpm from high or low speed drives. Test time and spindle revolutions are recorded by a timer and

tachometer. The tests were terminated automatically at a set number of drive-shaft revolutions measured by a tachometer. The test machine is equipped with a vibration-sensitive shutoff transducer. When the machine vibrates such that the diode remains in the on mode for more than 1 second the drive motor will cut out and the timer will stop. An increase in the general bearing vibration level is indicative of spalling fatigue failure of a bearing component. When an increase is sensed by the transducer, the test machine is shut down automatically to prevent the progression of the damage and loss of failure initiation data. This machine can test materials and lubricants at shaft speeds between 100 and 10,000 rpm. All of the present tests were conducted at a shaft speed of 5000 rpm.

Figure 3.2 Rolling contact fatigue bench test

The core of the machine is composed of two rigid vertical columns which ensure accurate location of the drive spindle with respect to the normal loading axis. The test adapters are mounted on a cross beam which is guided by linear bearings on the columns and loaded by a pneumatic actuator. The load actuator assembly includes an in-line force measurement for direct feedback control of load.

3.3.2 Crack orientation

Figure 3.3 demonstrates the loading geometry of the test machine and a ring crack within the contact track. The ring crack distribute randomly on the ball surface and they can occur in any positions when two balls contact each other. For example, when a modified four ball machine is used to perform a fatigue test, the probability for the crack being in the contact area is only two percent (Wang and Hadfield 2000a). Therefore it is nearly impossible to ensure that the crack is on the contact track if the ceramic ball is just randomly placed in the collet (Wang and Hadfield 2000a).

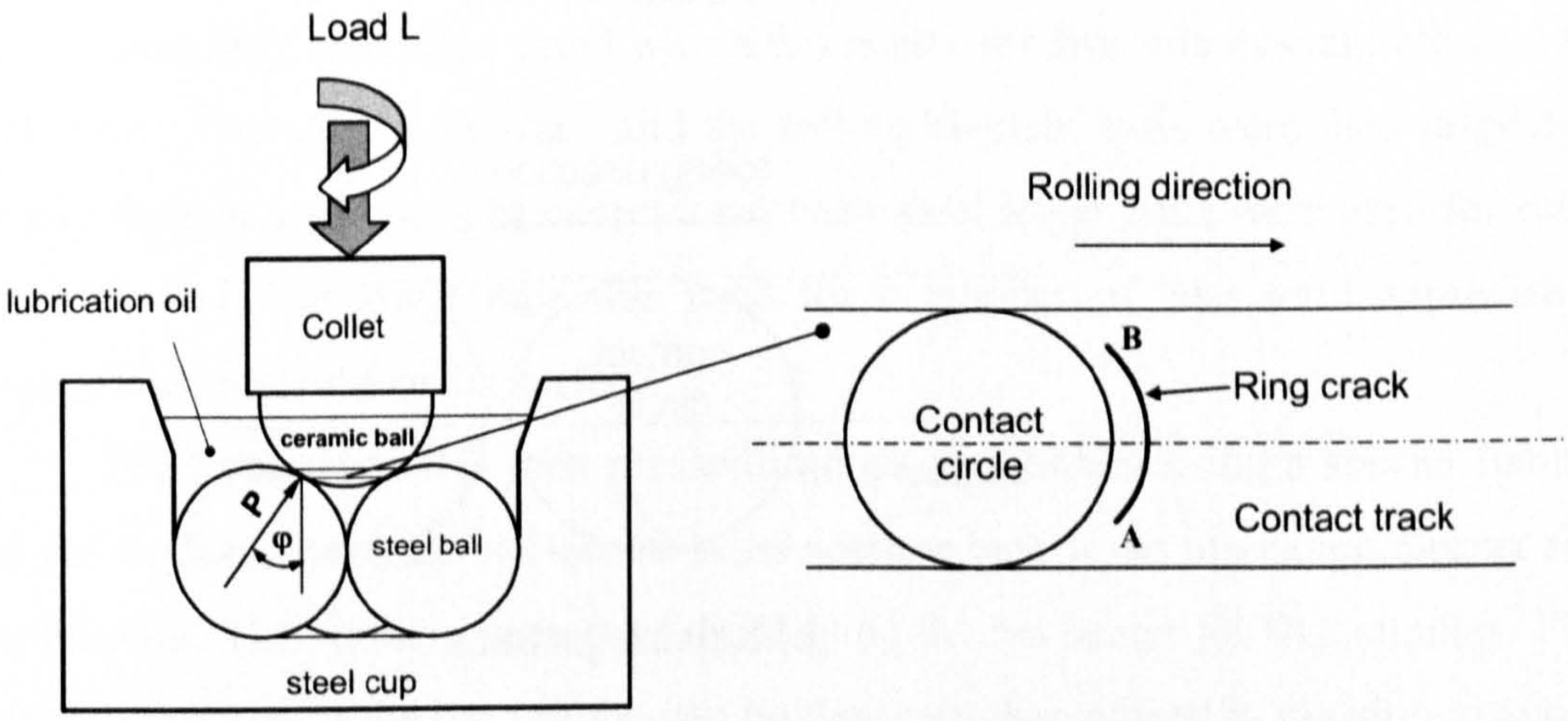

Figure 3.3 Schematic illustration showing the loading configuration (Wang and Hadfield 2000a)

To position the ring crack into the proper orientation, rolling contact fatigue tests were performed using the experimental procedure developed by Wang and Hadfield (2000a). Detailed description of the test procedures can be found in Appendix 1. In this way, the ring crack can be located precisely within the contact path. In the present study, the ring cracks are located in the same position so that the

test results are comparable and predictable. Two crack orientations, normal position (figure 3.4(a)) and reverse position (figure 3.4(b)) were selected to investigate fatigue modes and failure mechanisms.

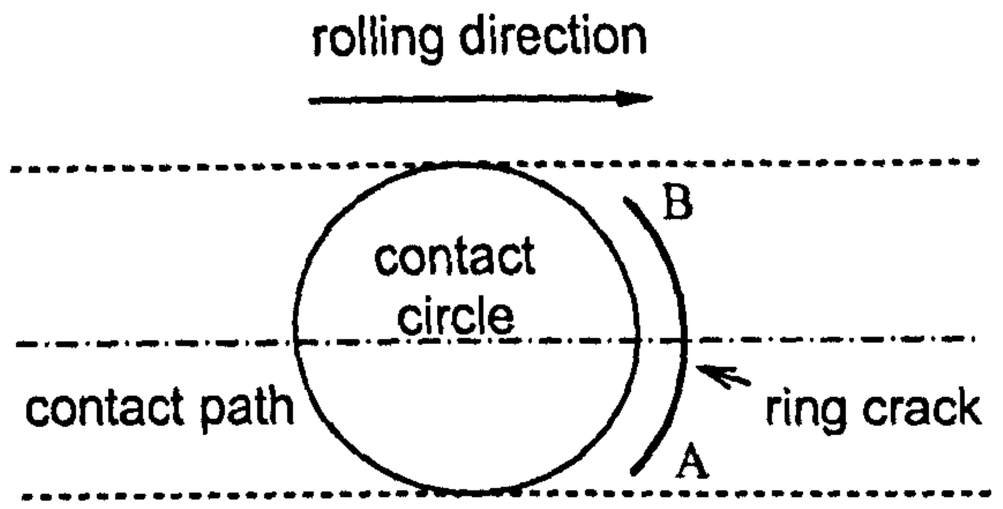

(a) Normal position

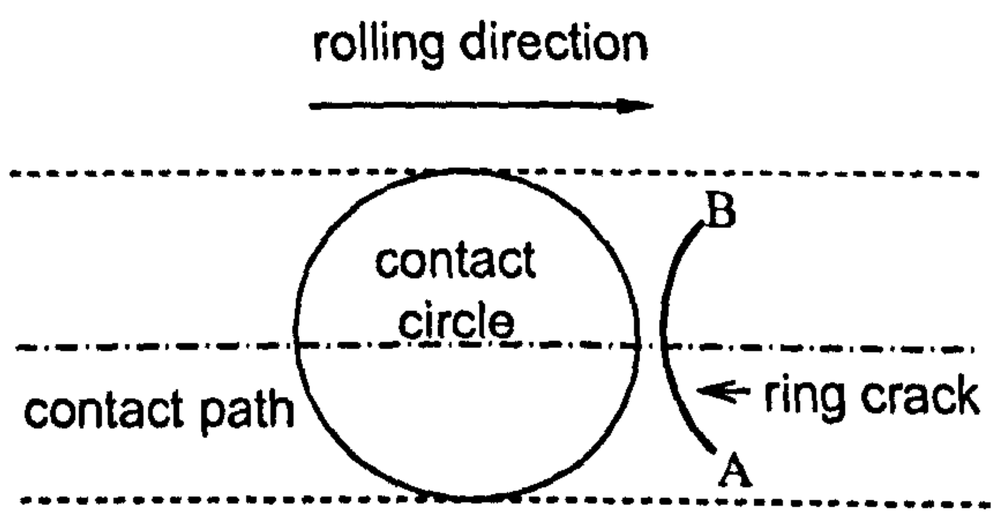

(b) Reverse position

Figure 3.4 Crack orientation used in rolling contact fatigue test

3.3.3 Test preparation

Each test was preceded by checks on the four-ball machine and cleaning of cup assembly components. Periodic checks were made to maintain the belt tension in the high speed driving belt of the modified four-ball machine and the accuracy of the proximity sensors. In addition, the steel cup, which is pressed into the heater assembly, was checked for flatness with a dial indicator and results showed that

there was no deviation. The electric mains supply was switched on after checking the initial control settings were safe. The vibration cut-out mode was selected and spindle bearing temperature cut-out reset. The motor speed controller was set to zero and 'motor enable' switch selected. The vibration potentiometer was then set by adjustment and the LED was illuminated, the control was turned backward one revolution.

Consistent cleaning and degreasing procedures were adopted to prepare the rolling elements and the cup assembly before each RCF test. The driving rolling element and the collet, the driven balls, the cup, the cup holder and the cup holder plate were initially cleaned in an acetone bath in the ultrasonic cleaner for five minutes. The surfaces were then cleaned and dried with tissues. The components of the cup assembly were then dried with a fan heater for five minutes and allowed to cool down. The steel lower race and the rolling element balls were then inspected for any damage under a light microscope. New steel lower balls were used for each test. However, the lower race was used for a number of tests until appreciable damage was observed on its surface.

The lower race was then pressed into the cup holder using a special fixture and the surfaces were again cleaned in an acetone bath in an ultrasonic cleaner for five minutes. The surfaces were then dried using the fan heater for five minutes. The three grub screws at the base of the cup holder were then placed in position to avoid any oil leakage from the base of the cup during the test. The driving spindle was then cleaned with acetone and dried using the fan heater.

3.3.4 Test procedure

The upper-ball was pushed into a spring steel tapered collet after locating the crack and then the collet assembly was placed in the drive spindle. Before the lower steel balls were fitted, the cup assembly was finally cleaned with acetone and was fitted onto the heater pad and loading piston slots. The lubrication oil level should immerse three lover steel balls when the machine is stationary. Place the safety guard in position and start the tests.

This test machine is designed to be able to perform a long term test. During

the long term tests, the oil needs to be replenished due to the loss of the lubrication oils. To perform the direct observations of the surface crack during the fatigue testing, the collet assembly with the ceramic ball was taken off the test machine, cleaned in acetone using an ultrasonic bath for a period of 5-10 minutes, and then examine under the light microscopy. After each observation, the collet was put back to the test machine to continue the fatigue test until failure or expiry of the allocated experiment time. Occasionally, a lower ball failed in which case the set of lower balls was replaced, and the test was continued.

The collet was taken off the machine after test completion. The upper ceramic ball was cleaned in acetone and then was stored in a desiccator for the further analysis. The steel balls were also stored after they were cleaned. The steel cup was inspected for surface damage and replaced if necessary.

3.4 OBSERVATION OF DAMAGE PROGRESSION

3.4.1 Apparatus

A light microscope was used to examine surface damage and crack growth. Due to the nature of the dynamic observations, the optical microscope is the only way to carry out the observation although there is a limitation in magnification. Different illumination methods, e.g. bright field, dark field and Normasky interference, were used in order to improve visibility of surface damage. The UV light illumination was also used to inspect the ring crack and crack growth.

3.4.2 Observation procedure

Observation of ring crack propagation during testing is performed using optical microscopy. To perform the direct observations of the surface crack during the fatigue testing, the collet assembly with the ceramic ball was taken off the test machine, cleaned in acetone using an ultrasonic bath for a period of 15-20 minutes, and then examine under the light microscopy. After each observation, the collet was put back to the test machine to continue the fatigue test until failure or expiry of the allocated experiment time (Wang and Hadfield 2000a).

3.5 SURFACE SCANNING ELECTRON MICROSCOPE STUDIES

3.5.1 Sample preparation

Since the SEM uses electrons to produce an image, most conventional SEM requires that the samples be electrically conductive. In order to view non-conductive samples such as ceramics, we must cover the sample with a thin layer of a conductive material. Coating used in SEM analysis is mainly to prevent the charge-up on the specimen surface and to increase secondary electron emission. Sample preparation is important in the quality of electron microscopic analysis. It is important to remove all water, solvents, or other materials that could vaporize while in the vacuum.

For coating, the sputtering method is generally used. Various substances are being used i.e., carbon (for general analysis) and gold, which must be selected depending on the purpose and magnification. It is necessary to select a coating suitable for the observation magnification. If the coating is too thick, its particles become visible while at the same time the structures of interest are may be obscured. In the present study, carbon was selected as a coating material.

The silicon nitride ball was firmly attached to the specimen support before being viewed in the SEM. The mounting procedure is very important in order to obtain a high quality SEM result. The support must be clean before use. The specimen was placed on the stub before the sputter coating procedure. This will increase the conductivity and the quality of the SEM images.

3.5.2 Equipment description

A scanning electron microscope (SEM), PHILIPS SEM525M EDAX9900, was used for surface studies. The SEM creates the magnified images by using electrons instead of light waves. There are many advantages to using the SEM instead of a light microscope. The SEM has a large depth of field, which allows a large amount of the sample to be in focus at one time. The SEM also produces images of high resolution, which means that closely spaced features can be examined at a high magnification. The combination of higher magnification, larger depth of focus, greater resolution, and ease of sample observation makes the SEM

one of the most heavily used instruments in research areas today.

3.5.3 Surface examination

Thorough visual surface examination of all ball failures was performed using the scanning electron microscope. A standard development method of failure analysis was adopted. All images were recorded by taking photographs of the display.

3.6 SURFACE WYKO ANALYSIS

3.6.1 Machine description

A WYKO laser profilometer was employed to measure the profile of the spalls. The WYKO is a surface profilometer using fast 3D laser measurement in quality assurance and process control. The profilometer uses non-contact interferometry for surface topography measurements. The WYKO laser profilometer does not rely on any one technology to solve complex engineering problems; instead, it comes with the option of two different laser measurement sensors, making it a useful tool to meet various measuring requirements.

3.6.2 Sample preparation

The samples are thoroughly cleaned with acetone in an ultrasonic bath. It is important to remove any surface grease and debris because it is directly related to the quality of surface topography measurement.

CHAPTER 4
EXPERIMENTAL RESULTS

This chapter presents the results of rolling contact fatigue tests. The aim of the experimental tests was to investigate the failure modes of ceramic rolling elements that contain surface ring cracks under various tribological conditions. The observations include the subsurface at the stages of incipient spall, with a spall and without a spall. Surface appearance of surface ring cracks is described in Section 4.1.1. Statistical analysis of surface ring cracks is presented in Section 4.1.2. Subsurface geometry of the ring cracks is studied in Section 4.1.3 and the mathematical model of the crack is presented in Section 4.1.4.

Five test lubricants were used to examine the possible effects on the failure modes of natural ring cracks and the results are described in Sections 4.2.1 to 4.2.5. The rolling contact fatigue performance was tested with various load ranges. A comparison of RCF life at different loads for different lubricants was carried out and the results are described in Section 4.2.6.

The results of experimental tests carried out on artificial pre-cracked silicon nitride balls are given in Section 4.3. The influence of lubricants on RCF life is described in Section 4.3.1. The influence of ceramic materials on RCF is discussed in Section 4.3.2. The results show that the different ceramic materials can strongly influence rolling contact fatigue performance. The influence of rolling directions, crack geometry (crack angles and crack size) is discussed in Sections 4.3.3 to 4.3.5. In the final section the influence of contact load on RCF failure modes is described.

Surface observations of fatigue failure were carried out and results are discussed in Section 4.4. Investigation into the formation of secondary surface cracks is presented in Section 4.4.1. Characterisation of fatigue spall is outlined in Section 4.4.2. Subsurface observations of crack failure processes are described in Section 4.5. Finally, summary and discussion of experimental work are given in Section 4.6.

4.1 CHARACTERISATION OF SURFACE RING CRACKS

4.1.1 Surface appearance

The manufacturing pressing faults or blunt impact loads are the main causes to generate surface ring cracks which are often seen on the ceramic ball surfaces. The present studies on 12.7mm diameter silicon nitride balls showed that 90% of the balls were found to contain surface defects. The majority of these defects were surface ring cracks. Lateral and radial surface cracks are not often observed and they are normally caused by a poor sintering mixture or a sharp indentation load.

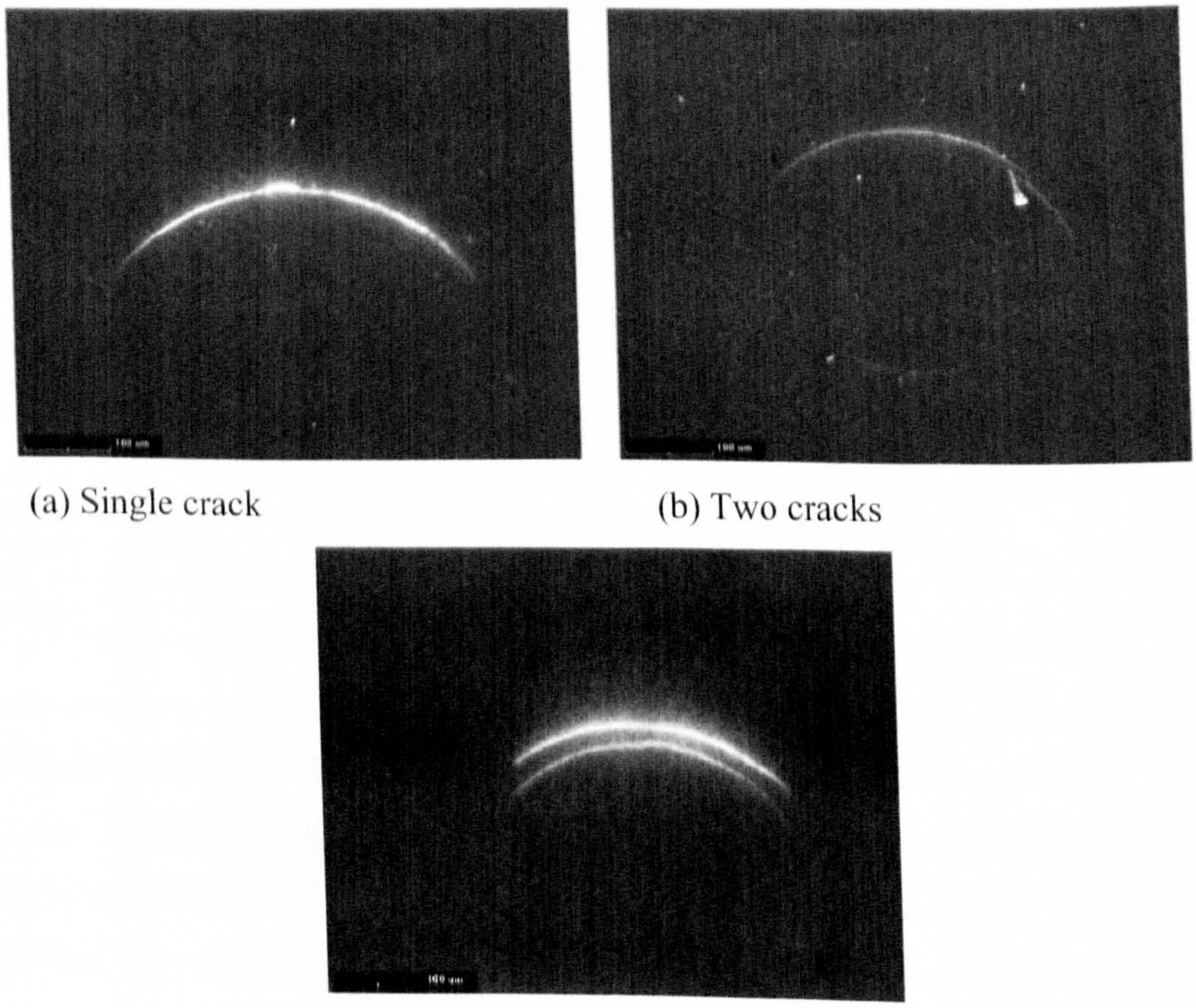

(a) Single crack

(b) Two cracks

(c) Double cracks

Figure 4.1 Surface ring cracks found on silicon nitride ball surface

Figure 4.1 illustrates three types of surface ring cracks normally found on the surfaces of ceramic balls. As can be seen from figure 4.1, these surface ring cracks are of partial circular feature. The arc length is approximately 1/4 of the circumference of a circle.

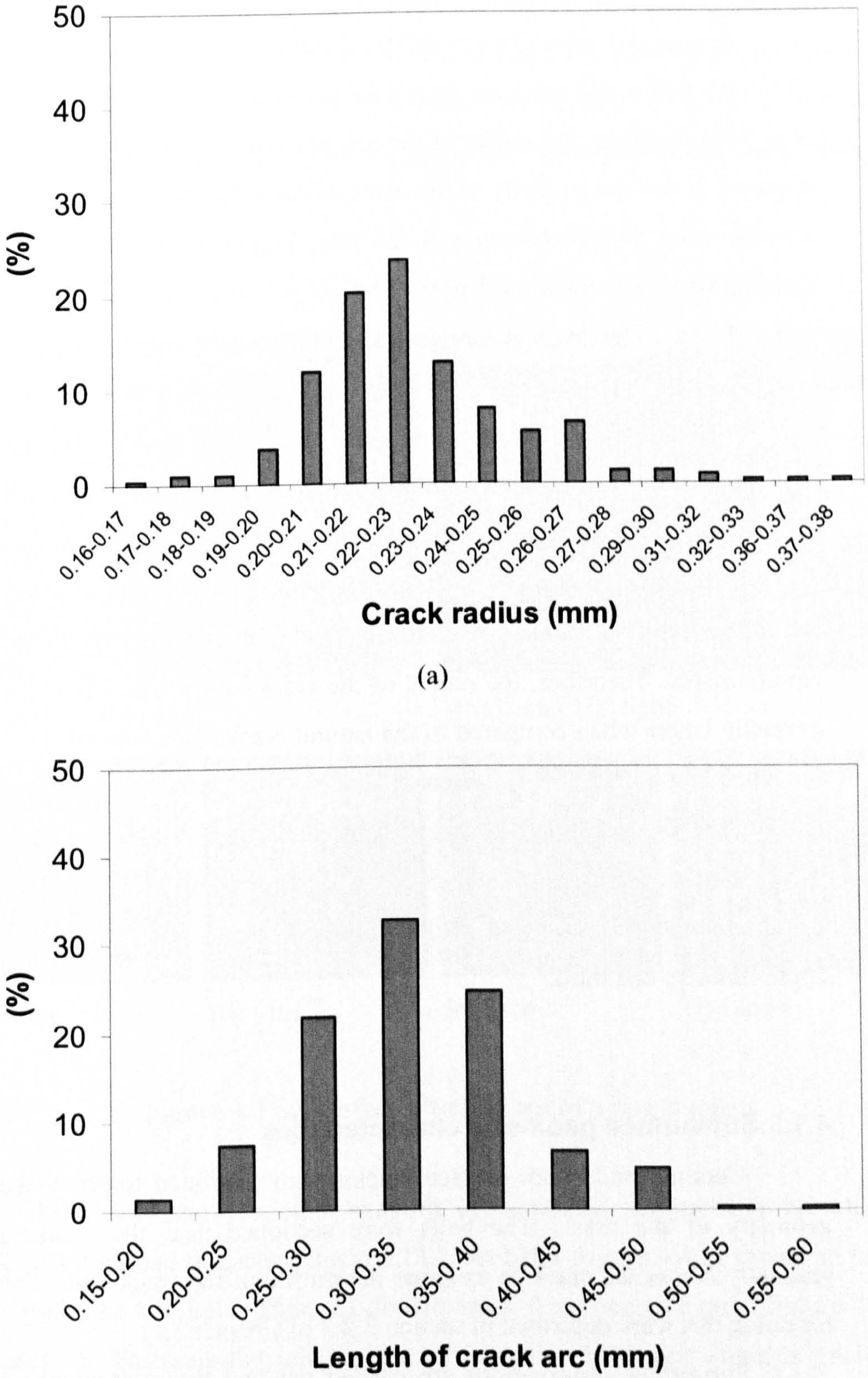

Figure 4.2 Statistical distributions of detected cracks

4.1.2 Analysis of crack sizes

Figure 4.2 shows the statistical distributions of the detected surface cracks. The crack radius and crack arc length are measured from the micrographs. As can be seen from the plots, the radius of the cracks varies in the range of 0.16 to 0.38 mm (figure 4.2(a)). The majority of the crack radius falls between 0.2 and 0.25 mm. The average value is approximately 0.228 mm. Figure 4.2(b) illustrates the statistical distribution of the crack arc length. 79 % of the crack arc lengths are between 0.25 and 0.4 mm. The average arc length is 0.334mm, which is approximately one quarter of the circumference of a circle. The length of natural cracks ranges from 0.03 to 0.06 mm. The distribution of the crack sizes implies that the most of the natural cracks are generated in similar conditions.

For the artificially produced cracks, the sizes of the cracks can be well controlled by means of different drop heights of the pendulum together with an off-centre position. Tangential traction is smaller than that in finishing or lapping environments. Therefore, the radius of the cracks for artificially induced cracks is normally larger when compared to the natural cracks (see Chapter 2). The radius of the crack can be reduced to the same size if a small size ball is adopted. However, the ratio of the arc length to the circumference is still larger if compared to the natural cracks. The ratio of the arc length to the circumference is approximately one quarter for the natural cracks, while for the artificial produced cracks the ratio is approximately one third.

4.1.3 Subsurface geometry characteristics

Ceramic balls with surface cracks were sectioned to study the subsurface geometry of the crack. The balls were sectioned near the crack and polished gradually across the crack to examine the profile of the crack path. The procedures for doing this were described in section 3.2.3 of Chapter 3.

Subsurface observations are carried out and the micrographs are taken at section lines indicated by the lines. Figure 4.3 shows an example of the subsurface images from artificial cracks (12.7mm balls impacting each other). Figure 4.3(a) shows a dark field image of a double crack on two sides. Figure 4.3(b) indicates the

positions where the images are taken. The crack on the right side is the observation object. The *z* axis value is gradually increased when the sections are moved to the middle (Compare figures 4.3(c) to (f)). Therefore the face of the crack must be a crescent shape. Figure 4.3(f) shows the subsurface geometry of the crack observed from the middle of the crack.

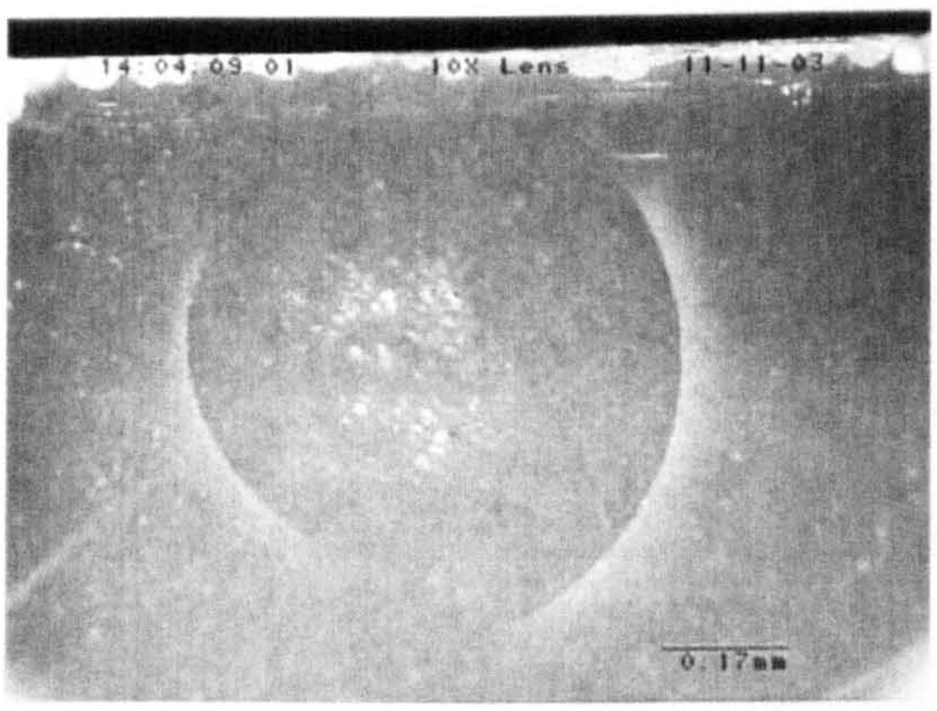

(a) Dark field image

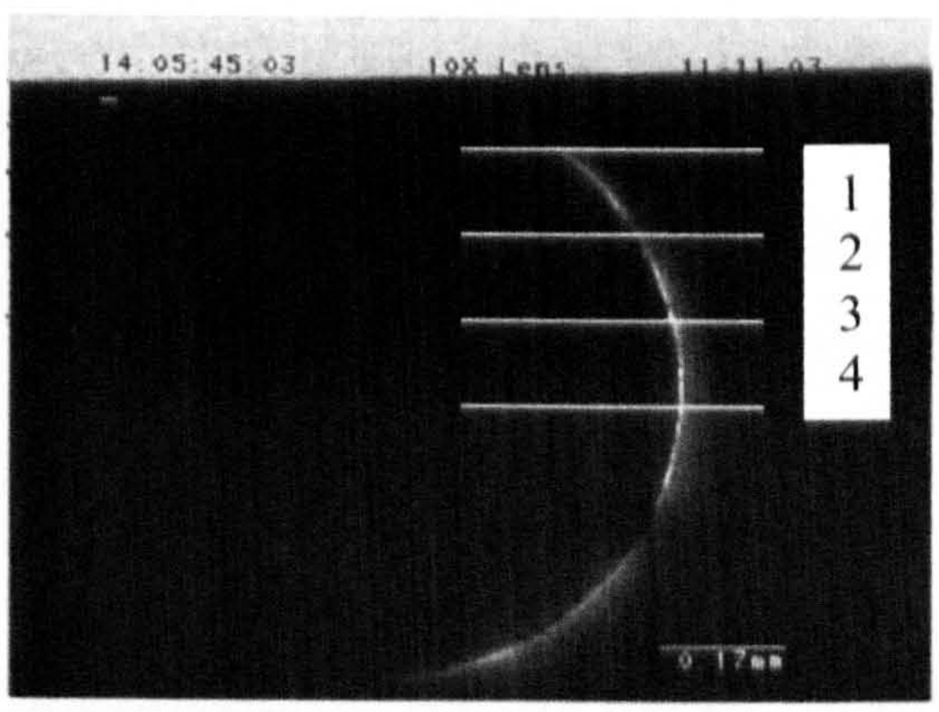

(b) Under UV light

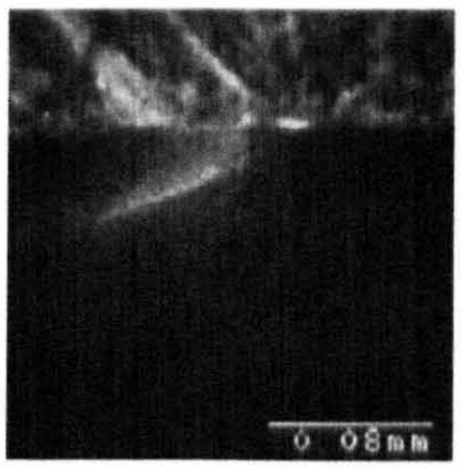

(c) Line 1

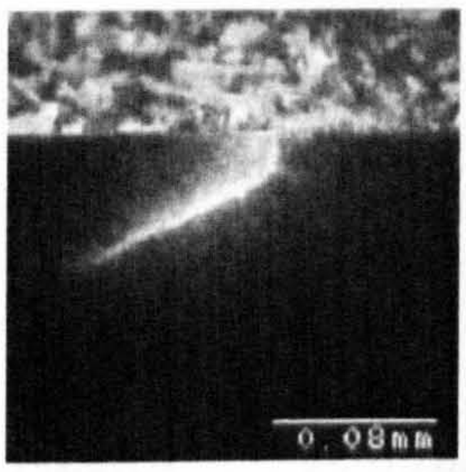

(d) Line 2

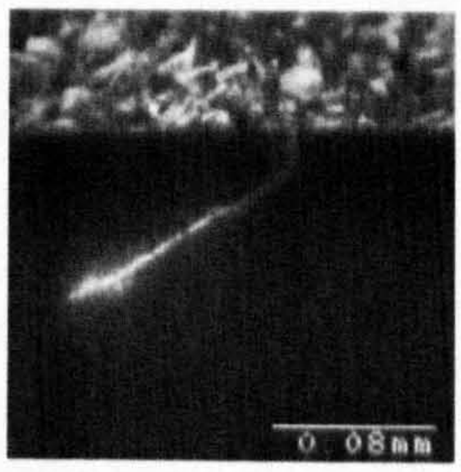

(e) Line 3

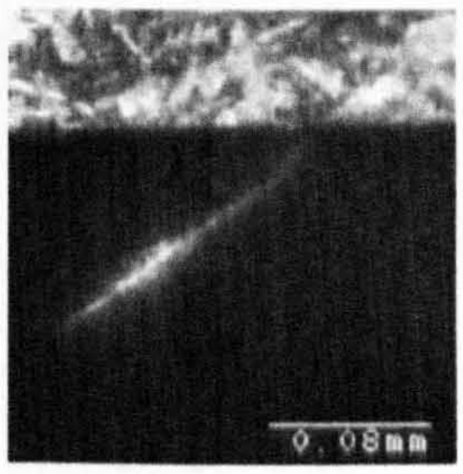

(f) Line 4

Figure 4.3 Subsurface observations of a ring crack

Figure 4.4 shows another example of subsurface images from an artificial crack (6.35mm ball impacting against 12.7mm ball). Figure 4.4(a) shows an image taken under an UV light. This is a double crack from one side only. Figure 4.4(b) indicates the positions the images relate to. Again, the *z* axis value is gradually increased when the sections are moved to the middle (Compare figures 4.4(c) to (f)). Figure 4.4(f) displays the subsurface geometry observed from the middle section of the crack.

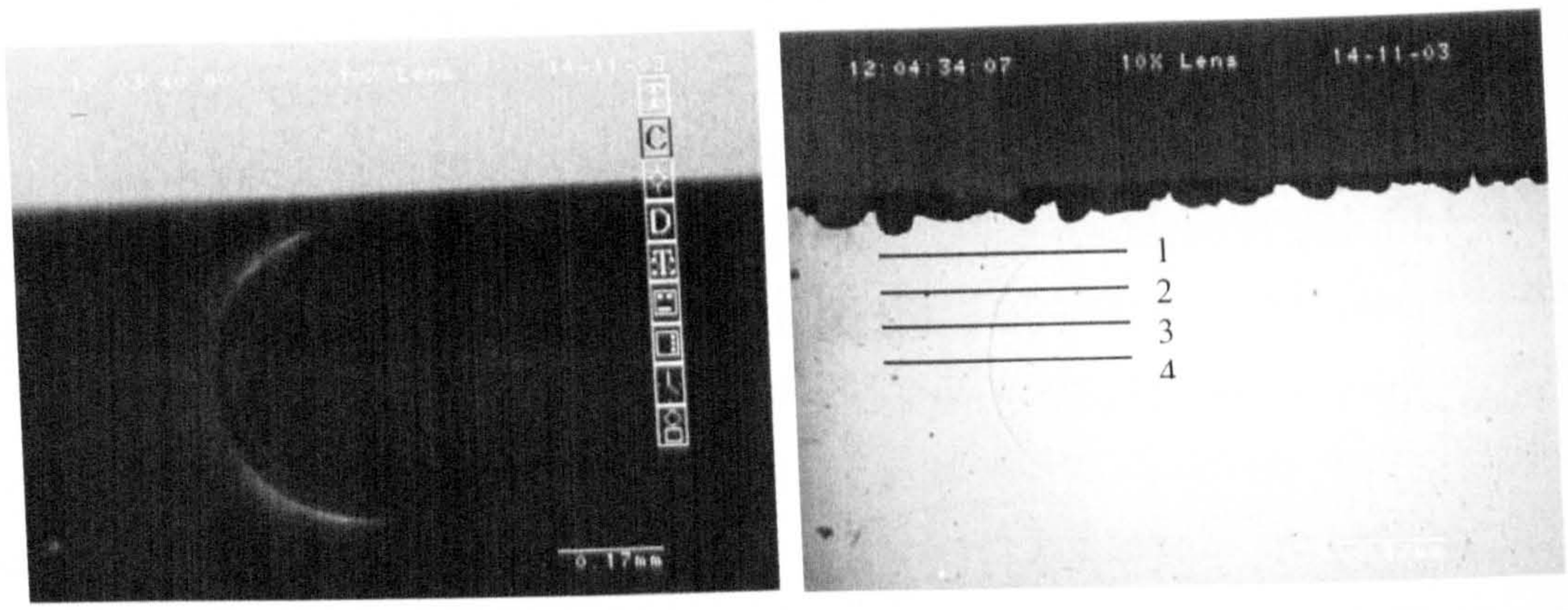

(a) Under UV light (b) White light

(c) Line 1 (d) Line 2 (e) Line 3 (f) Line 4

Figure 4.4 Subsurface observations of a ring crack

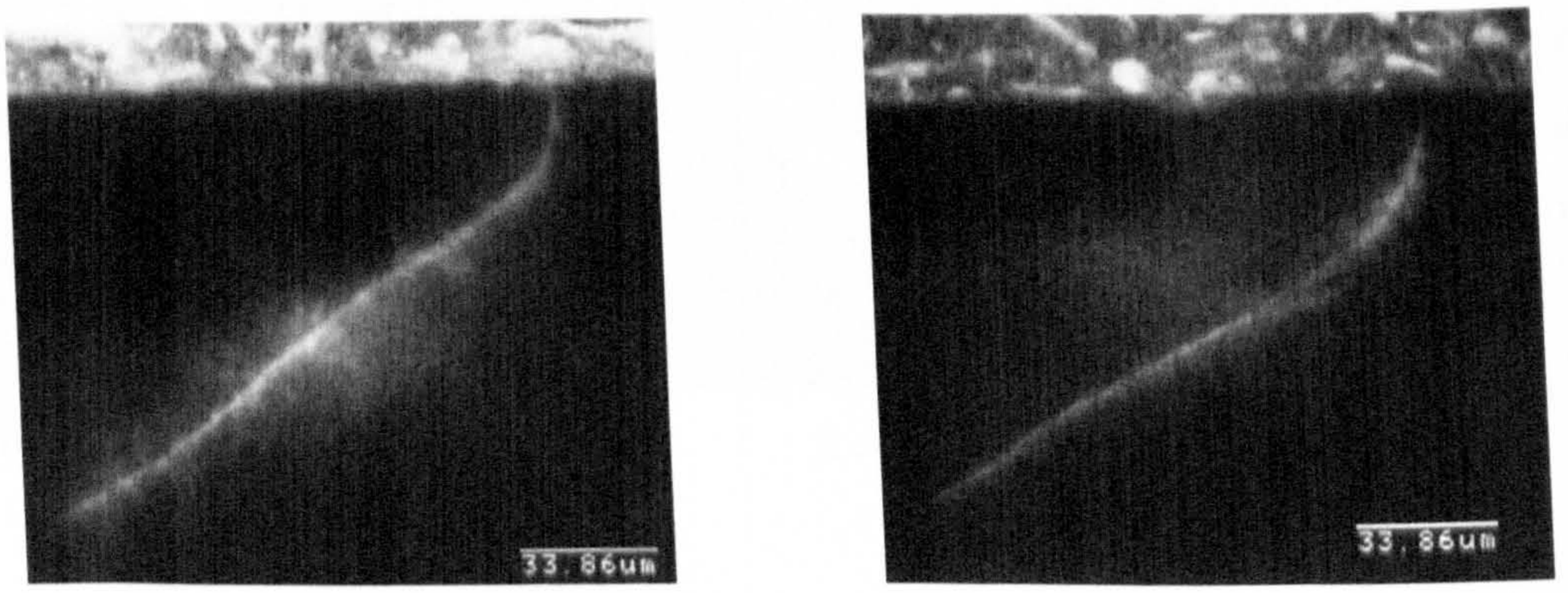

(a) Material A (R=0.42mm) (b) Material B (R=0.42mm)

Figure 4.5 Comparison of subsurface geometry of two types of material

In figure 4.5, the subsurface geometry observed from two types of silicon nitride ball (Material A and B) is exhibited. The impact was performed using the same size balls (12.7mm ball impacting against 12.7 mm ball). Figure 4.5(a) is the image from material A balls and figure 4.5(b) is from material B balls. No significant difference is seen when the crack radius is the same. The angles of the cracks were between approximately 32° and 35°.

Subsurface observations from various impact conditions were carried out to identify the characteristics of the subsurface geometry of the cracks and the results are shown in figure 4.6. All the micrographs were taken from the middle plane of the crack. Figures 4.6(a) and 4.6(b) are the results from the artificial cracks. In figure 4.6(a), the crack was generated using two different sizes of ball (6.35mm and 12.7mm). The crack forms at the critical drop height of the pendulum (at the swing angle 4^{o}). In figure 4.6(b) the crack was produced using the same size balls. Again, the crack was formed at the critical swing angle. It can be seen that the crack angle in figure 4.6(b) is larger than that in figure 4.6(a).

Figures 4.6(c) and 4.6(d) are from the natural cracks. The crack angles for these natural cracks are larger compared to the artificial cracks. Note that the lengths of these cracks are very similar, approximately 40 to 50 microns.

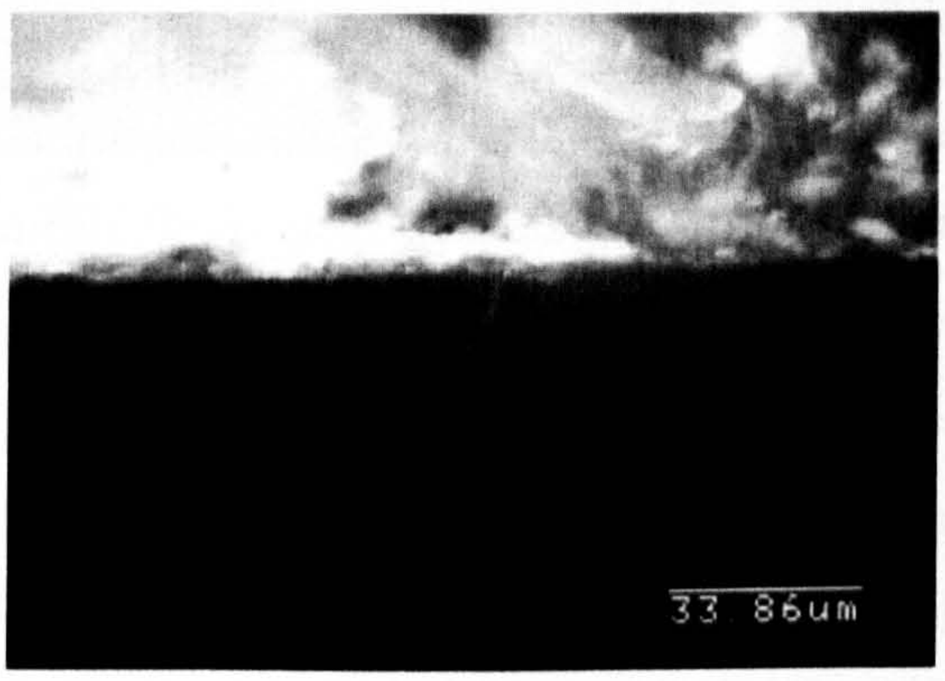

(a) Different size impact (6.35 to 12.7)

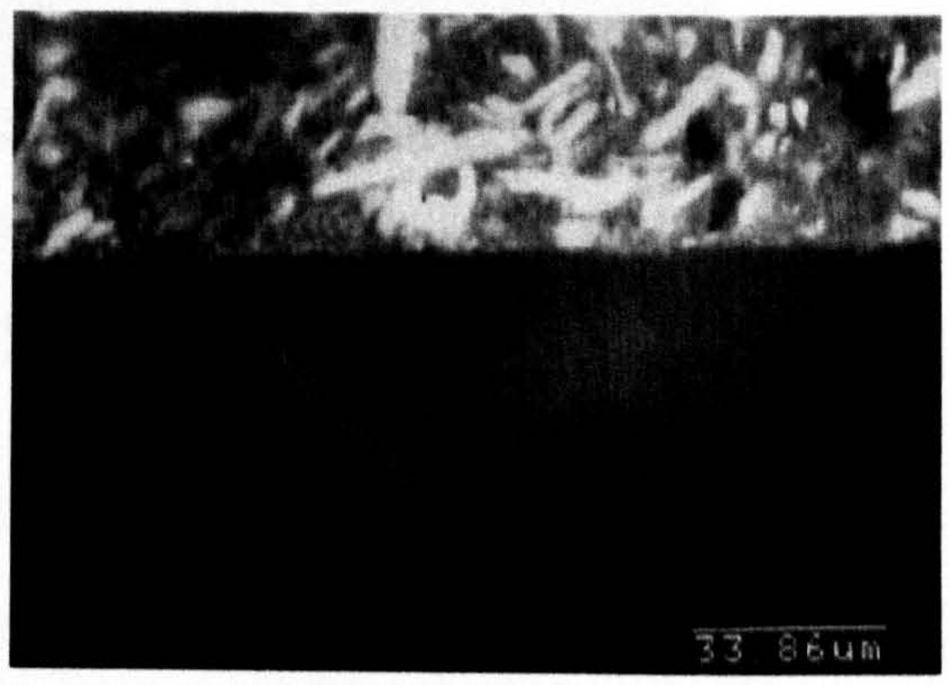

(b) Same size impact (12.7 to 1.27)

(c) Natural crack

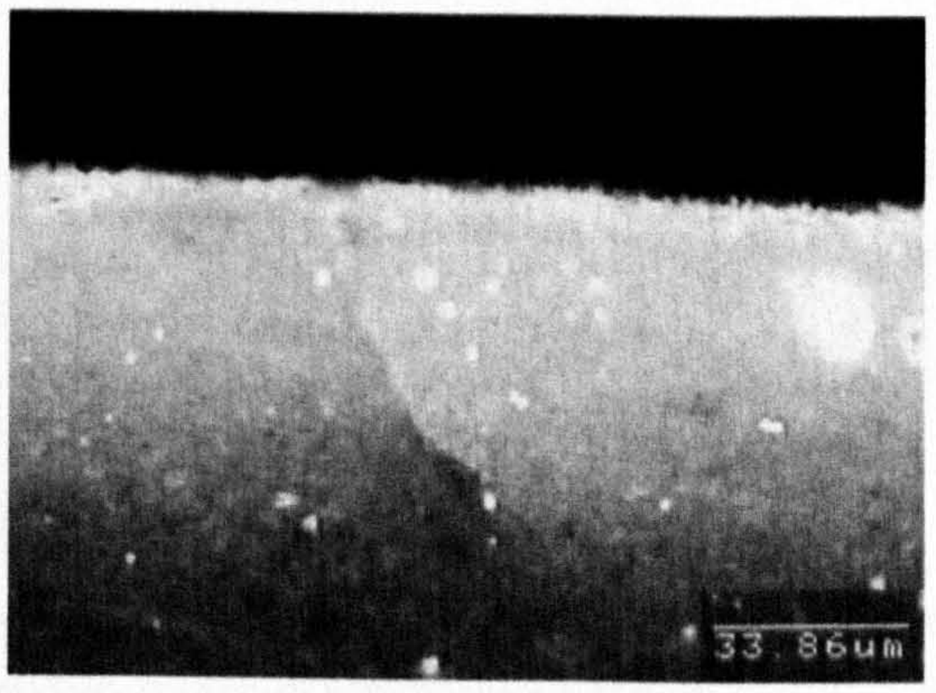

(d) Natural crack

Figure 4.6 Subsurface geometry of the crack generated at different conditions.

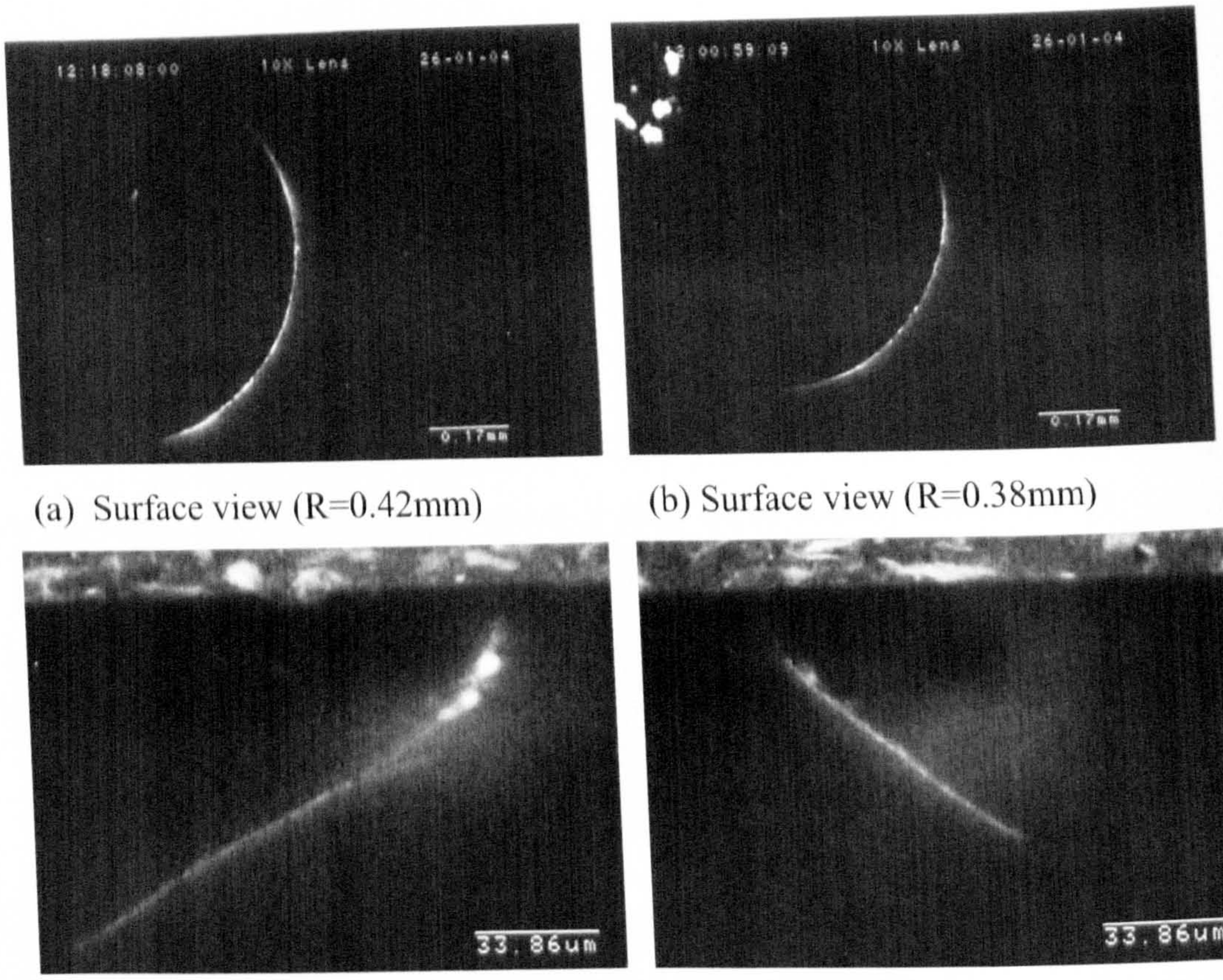

(a) Surface view (R=0.42mm)

(b) Surface view (R=0.38mm)

(c) Subsurface view (R=0.42mm)

(d) Subsurface view (R=0.38mm)

Figure 4.7 Comparison of crack geometry with different radii

Figure 4.7 shows experimental observations from different radii of the crack. It appears that lengths increase with the radius of artificial cracks. Therefore, it is important to select the same radius cracks as test specimens.

4.1.4 Mathematical model

A mathematical model of the ring crack is very important in the numerical analysis and life prediction. Previous study on ring crack geometry was completed by Wang and Hadfield (2000a). In that study, the geometry of a natural ring crack (figure 4.8(a)) was described using following expressions (Wang and Hadfield 2000a):

$$x = \left(R + l\sqrt{1-\left(\frac{\phi}{\phi_0}\right)^2}\cos\alpha\right)\cos\phi \qquad (4.1)$$

$$y = (R + l\sqrt{1 - (\frac{\phi}{\phi_0})^2}\cos\alpha)\sin\phi \qquad (4.2)$$

$$z = \sqrt{\frac{l\cos\alpha}{20}\sqrt{1-(\frac{\phi}{\phi_0})^2}} \qquad (4.3)$$

Where R = crack radius

l = crack length, $0 < l <=$ maximum length (line P_1P_2)

α = angle of line P_1P_2 to the ball surface, $0 < \alpha < \pi/2$

ϕ = angle of an element position on the crack face, $-\phi_0 < \phi < \phi_0$

ϕ_0 = half angle of ring crack arc AB, $0 < \phi_0 < \pi/2$

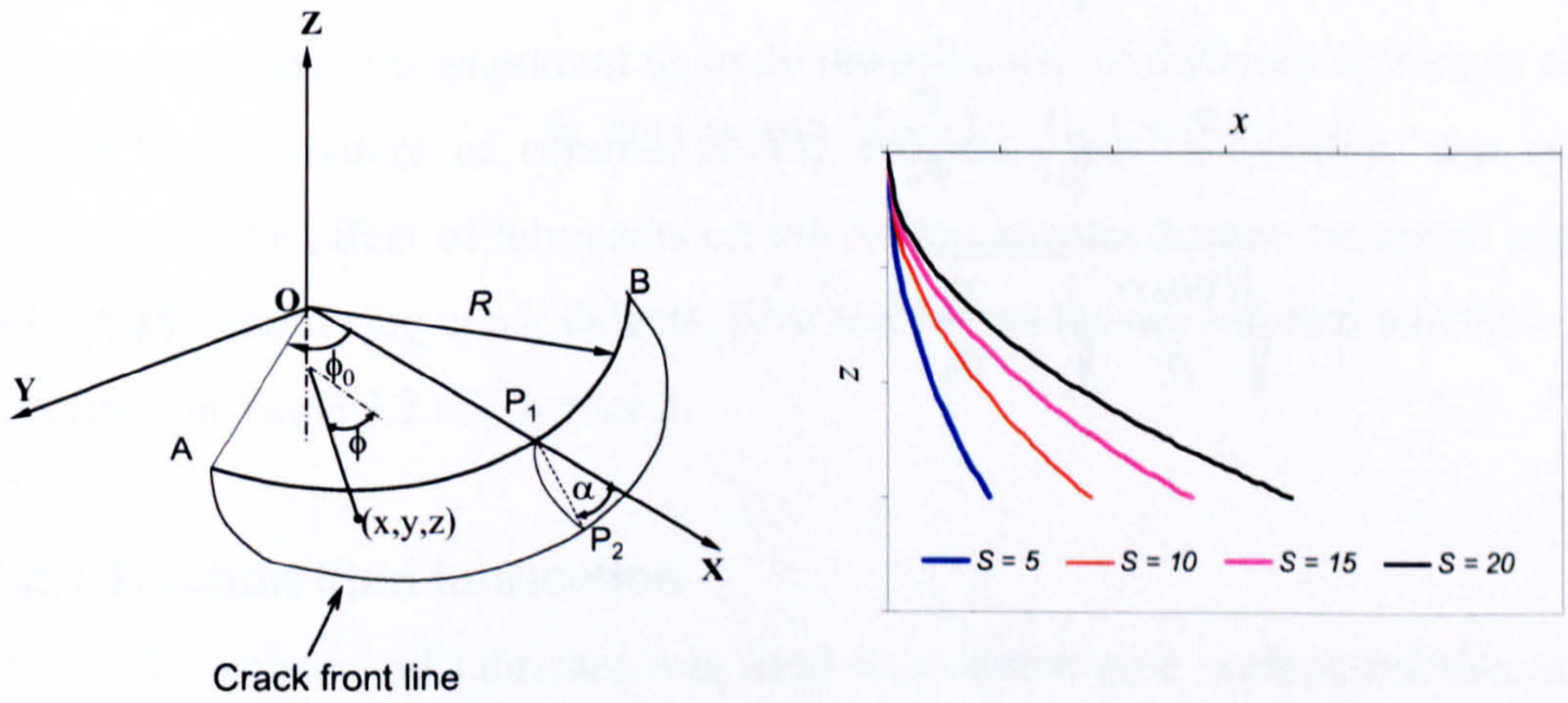

Figure 4.8 Geometry of a surface ring crack: (a) coordinate system of a surface ring crack (Wang and Hadfield 2000a); (b) subsurface path of the crack at the plane of y=0.

In practice, the shape of the crack is changed as the surface traction varies. The above expressions are only suitable for some certain conditions. The shape of the crack is mainly determined by the equation (4.3). A shape constant is induced here to represent various shapes and the modified equation (4.3) is now rewritten as

$$z = \sqrt{\frac{l\cos\alpha}{S}\sqrt{1-(\frac{\phi}{\phi_0})^2}} \qquad (4.4)$$

Where S is a shape constant which is used to describe various shapes of the ring crack. Experimental observations showed *S* ranges from 5 to 20 depending on the condition when the crack was formed. Figure 4.8(b) demonstrates the effect of the shape constant on the subsurface profile of the crack. Using equation (4.4) instead of (4.3), the modified expressions (4.5) to (4.7) can be used to describe almost all the geometries of surface ring cracks formed in the lapping or finishing processes.

$$x = (R + l\sqrt{1-(\frac{\phi}{\phi_0})^2}\cos\alpha)\cos\phi \qquad (4.5)$$

$$y = (R + l\sqrt{1-(\frac{\phi}{\phi_0})^2}\cos\alpha)\sin\phi \qquad (4.6)$$

$$z = \sqrt{\frac{l\cos\alpha}{S}\sqrt{1-(\frac{\phi}{\phi_0})^2}} \qquad (4.7)$$

4.2 RCF PERFORMANCE WITH NATURAL RING CRACKS

Although rolling contact fatigue can be attributed to the stresses and the properties of the material, it is now recognised that the nature of the lubricant and environment it creates also have very important effect on the rolling contact fatigue failure. Lubrication is essential in ceramic-steel contacts, where the presence of lubricants reduces not only the adhesion and friction of the pairing material but also the brittle micro-fracture of ceramic materials during sliding. Under unlubricated conditions, ceramics cause undesirable high wear on the mating metallic parts.

Lubricants have received much attention in rolling contact fatigue of steels and many studies have been done (Tourret and Wright 1977, Wang et al. 1996). However, there is little information on the effect of lubricants on ceramic rolling contact fatigue. For a better understanding and proper use of lubricants in rolling contact problems, it is important to study the influence of different lubricants on the rolling fatigue failure of ceramic rolling elements. For this reason, this section investigates the effect of lubricants on the rolling contact fatigue failure of ceramic balls with natural ring crack defects. Five test lubricants are selected and have been described in Table 3.2 of Chapter 3.

4.2.1 Traction fluid lubrication

A synthetic oil lubricant was used to examine how surface traction affects the fatigue failure modes of ceramic rolling elements. Balls (Material A) were used for these tests. Each test was conducted at a speed of 5,000 rpm. The crack orientation was in the normal position as shown in figure 3.4(a) in Section 3.3.2 of Chapter 3. Test conditions and results were listed in table 4.1. As can be seen from the table, the fatigue life changes with the contact stresses. To compare fatigue life at contact stresses more clearly, the results are plotted in a bar chart as shown in figure 4.9. The contact fatigue life decreased as the contact stress increased. The results indicate that the fatigue failure may not occur if the stress level is less than a certain value. For example, no fatigue failure is seen when the maximum contact stress is less than 4.0 GPa in the 20.25×10^7 stress cycles.

Table 4.1 Test conditions and results for traction oil

Test No.	Contact stress (GPa)	Average oil Temperature (^{o}C)	Time to failure or end of test (Hours)	Stress cycles ($\times 10^{7}$)
TOL-1	4.00	30	300*	20.25*
TOL-2	4.44	33	117	7.898
TOL-3	5.03	40	68.5	4.624
TOL-4	5.58	44	21	1.418
TOL-5	6.63	53	17	1.148

* Test suspended without spalling

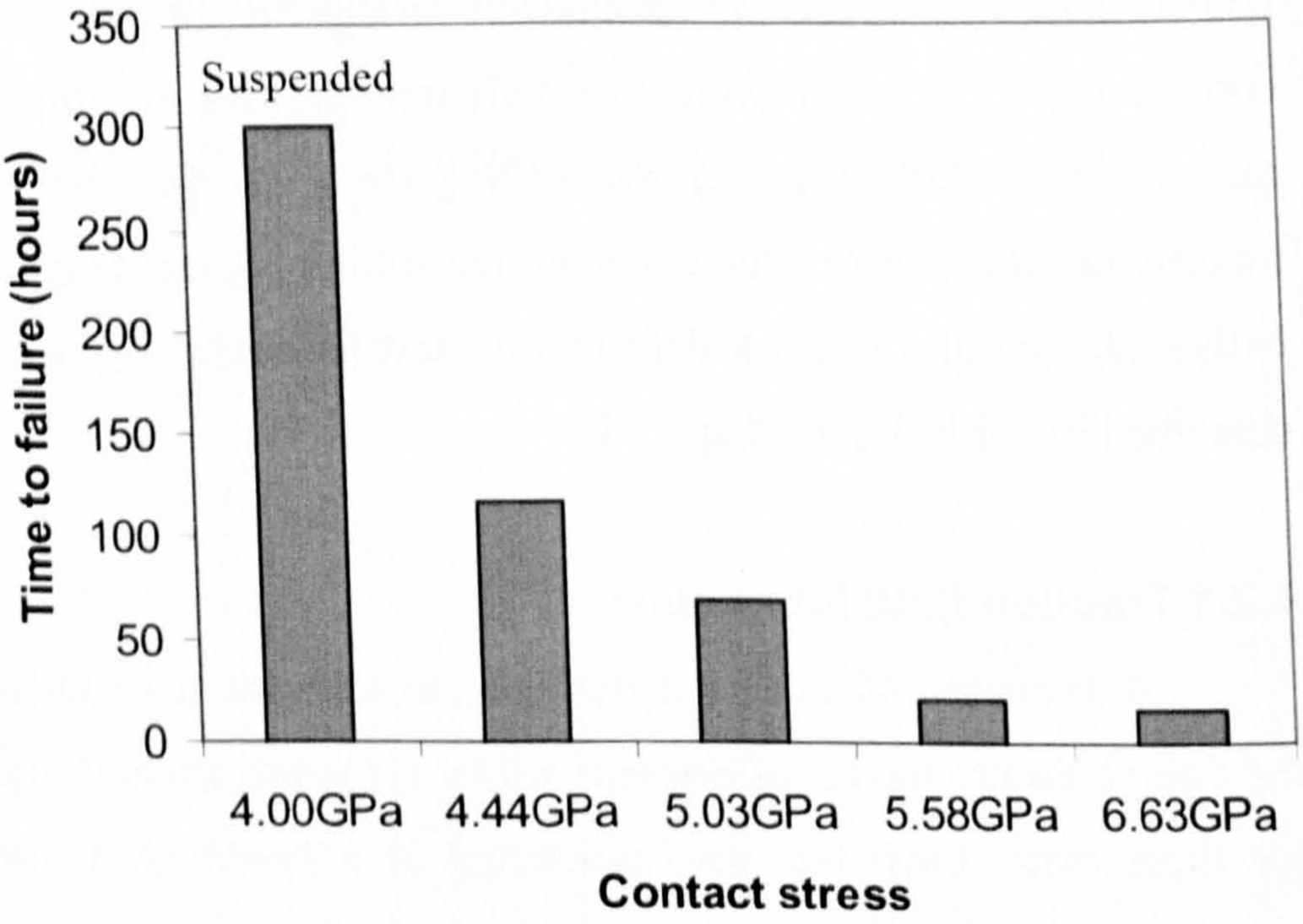

Figure 4.9 Rolling contact fatigue life at different loads lubricated with traction oil.

Observations of damage progression were carried out to determine the mechanisms of rolling contact fatigue failure associated with surface ring cracks. In general the natural surface ring crack is not visible without an ultra-violet light source. The crack can only be detected by using a dye-penetrant method under ultra-violet light. During the fatigue tests, however, the cracks can be seen under normal light conditions.

Figure 4.10(a) showed a surface ring crack before testing under UV light (Test TOL-1). Figure 4.10(b) showed the contact track and ring crack after 300 hours of testing, where the contact track was covered by a dark lubricant deposit. No surface damage was seen. Figure 4.11(a) shows the ring crack image after 23 hours of testing (Test TOL-2). Compared with figure 4.10(b), the width of the contact track was increased because the contact stress was increased from 4.0 to 4.44 GPa. The crack is clearly visible under a normal light source. Spalling fatigue failure occurred after 117 hours of testing shown in figure 4.11(b).

Observations of silicon nitride ball surfaces from Test TOL-3 at the contact pressure of 5.03 GPa are illustrated in figure 4.12. The surface ring crack can only be seen under UV light source before testing (figure 4.12(a)). As the fatigue test proceeds the crack becomes visible under the white light source (figure 4.12(b)). The micro-cracks are present on the ball surface after 46 hours of testing as shown in figure 4.12(c). An overview of the spall obtained after 68.5 hours of testing is illustrated in figure 4.12(d). The spall contour resembles an ellipse. The longer semi-axis is always parallel to the rolling direction, and the short axis is perpendicular to the rolling direction.

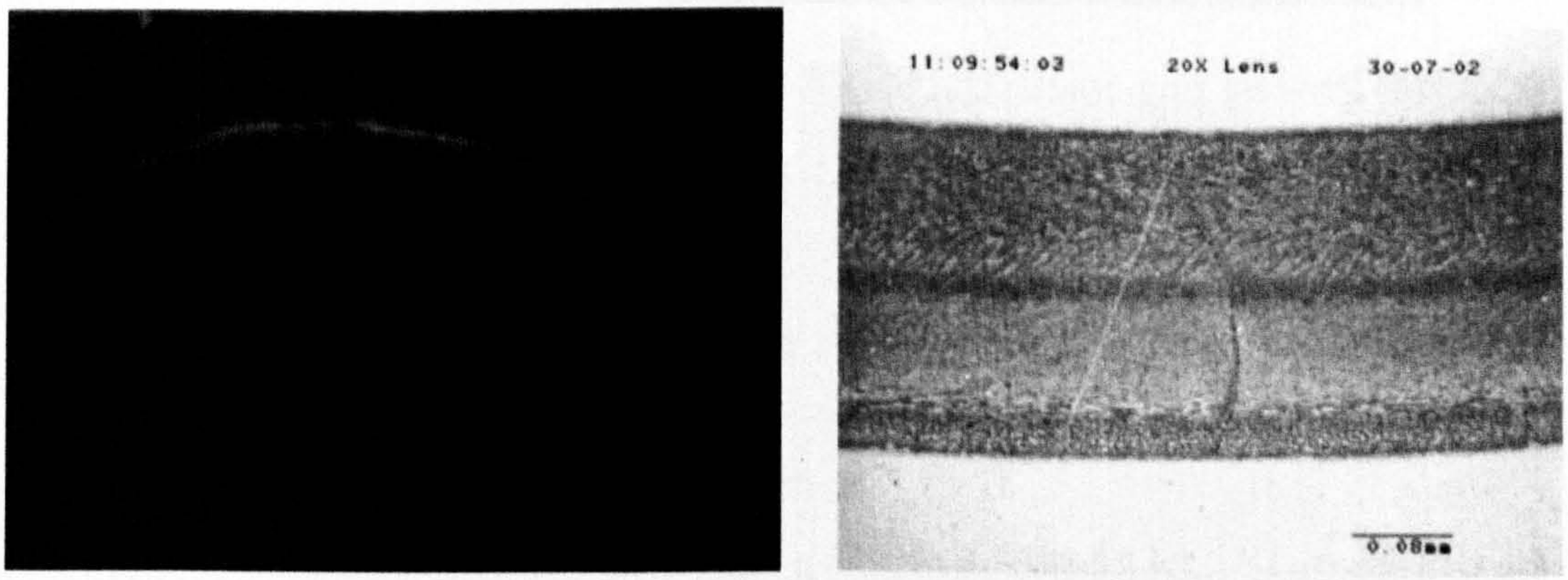

(a) Pre-test ring crack (UV light) (b) 300 hours of testing (white light)

Figure 4.10 Surface observations of silicon nitride ball (Test TOL-1)

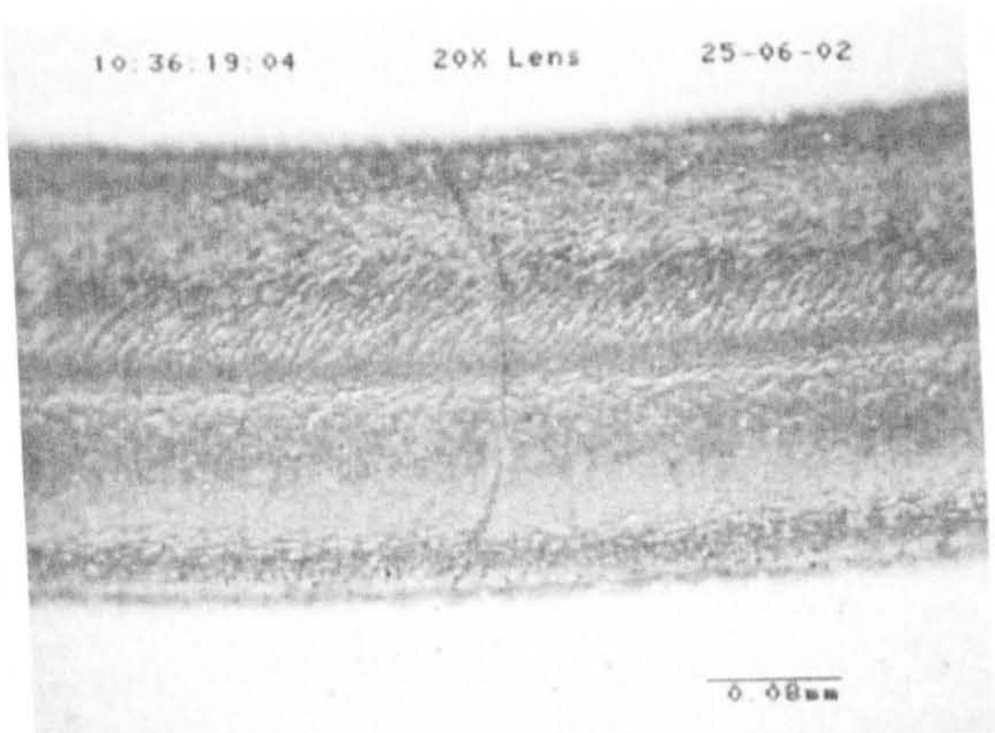

(a) After 23 hours of testing

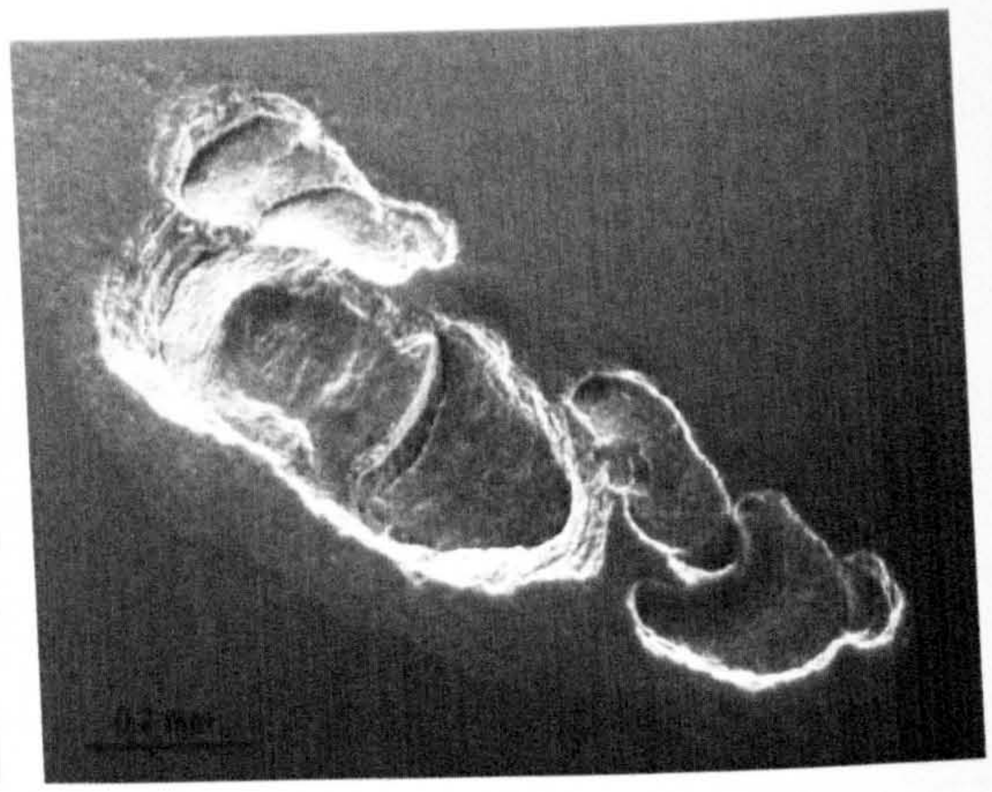

(b) An overview of spall (SEM)

Figure 4.11 Surface observations of silicon nitride ball (Test TOL-2)

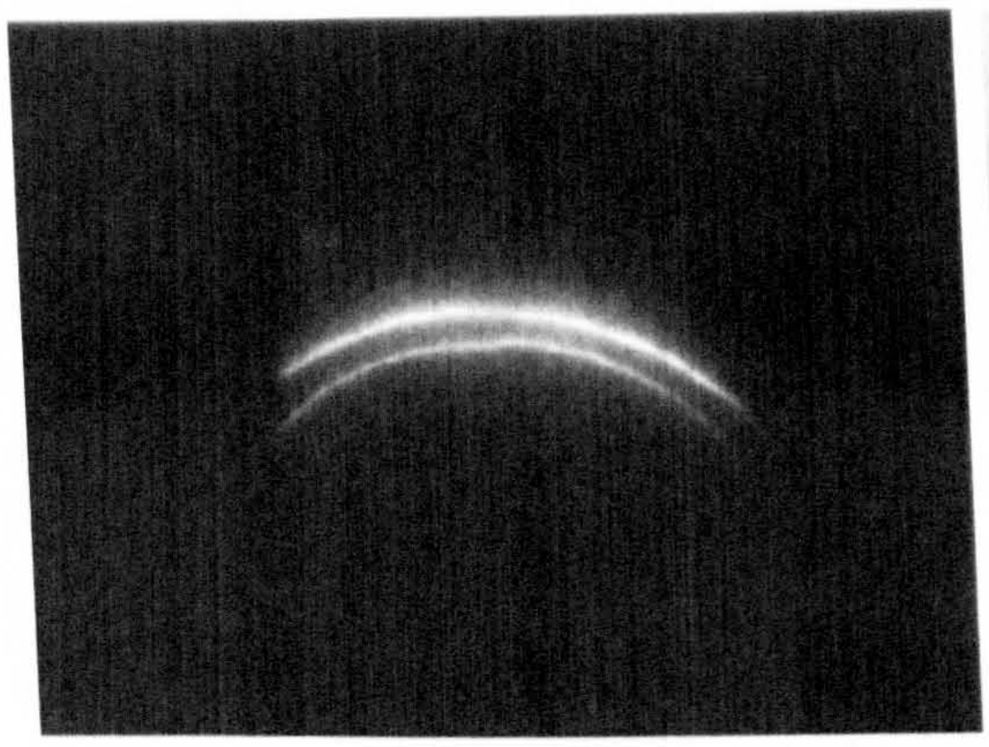

(a) Pre-test ring crack (UV light)

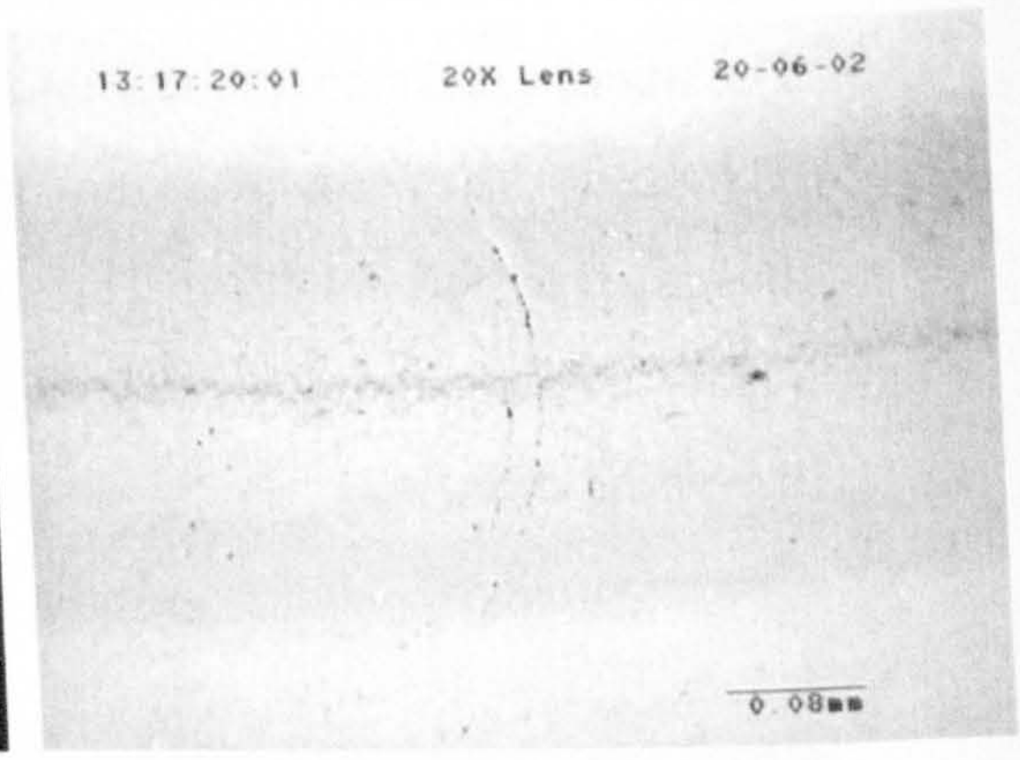

(b) 46 hours of testing

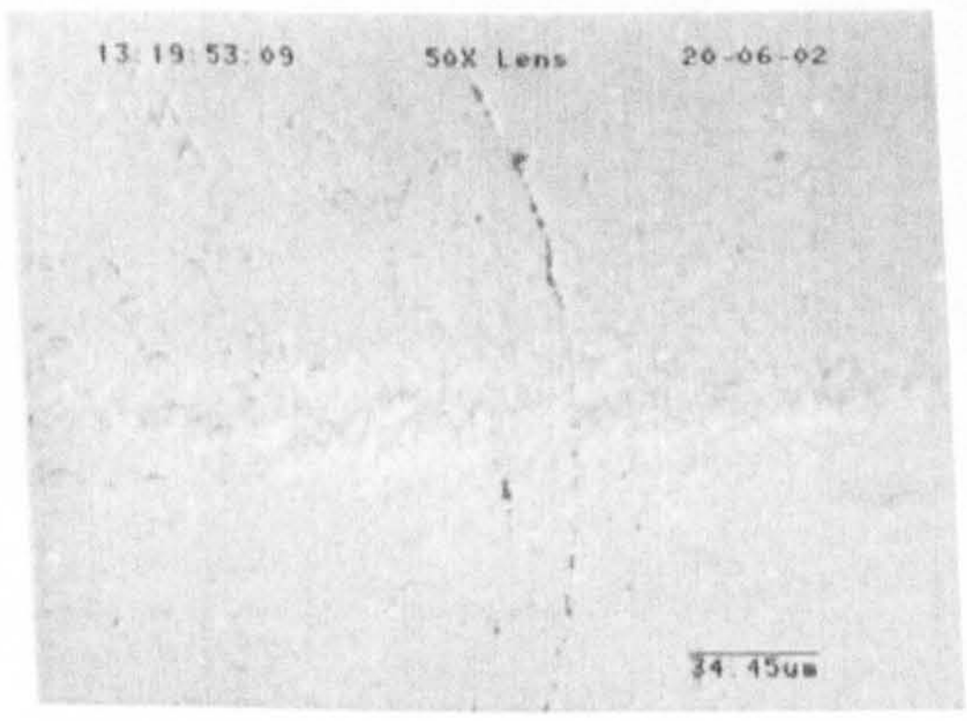

(c) Micro-cracks observed on the path

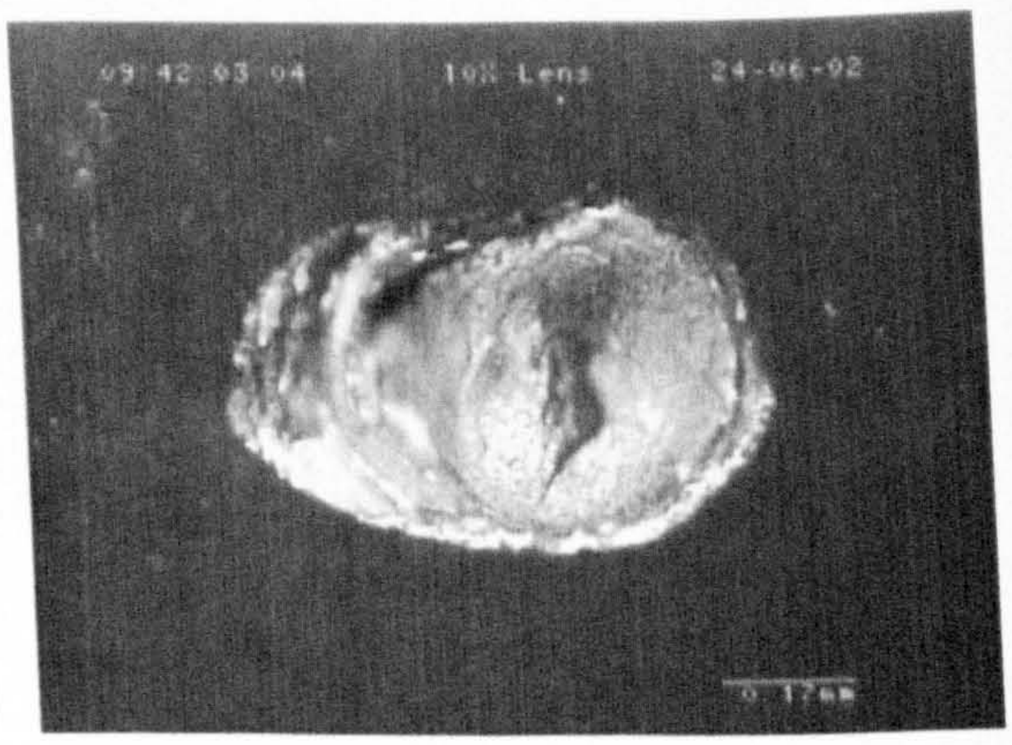

(d) Overview of the spall (dark field)

Figure 4.12 Surface observations of silicon nitride ball (Test TOL-3)

Figure 4.13 shows the result from Test TOL-4. The contact pressure was 5.58 GPa in this case. Figure 4.13(a) shows the surface ring crack before the test. Figure 4.13(b) shows the overview of fatigue spall. The contact stress is increased to 6.63 GPa (Test TOL-5) to attempt high stress failure modes. Figure 4.14(a) shows a surface ring crack before testing under UV light. Figure 4.14(b) shows the fatigue spall optical image after 17 hours of testing. There is no difference in failure modes for the stress range of 4.0 to 6.63 GPa. Failure modes are fatigue spalling. Surface wear is often seen when the contact stress is at high level.

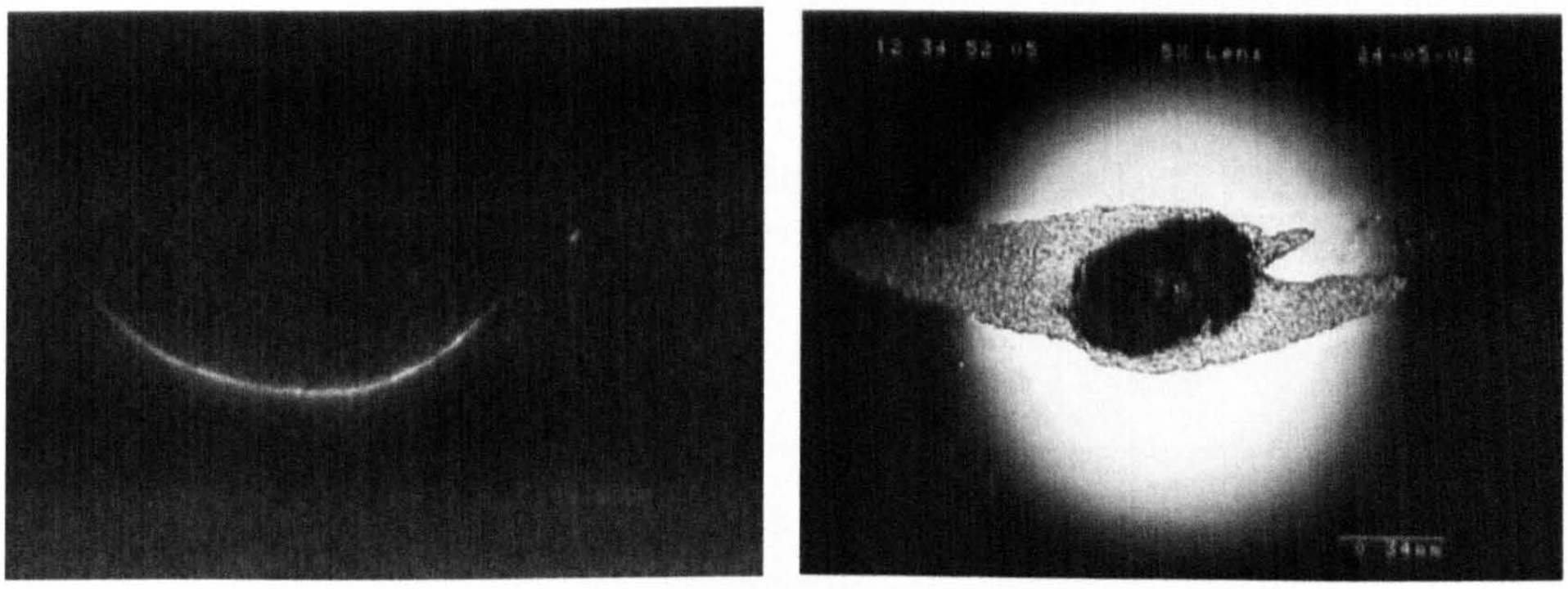

(a) Pre-test ring crack (UV light) (b) Fatigue spall optical image

Figure 4.13 Surface observations of silicon nitride ball (Test TOL-4)

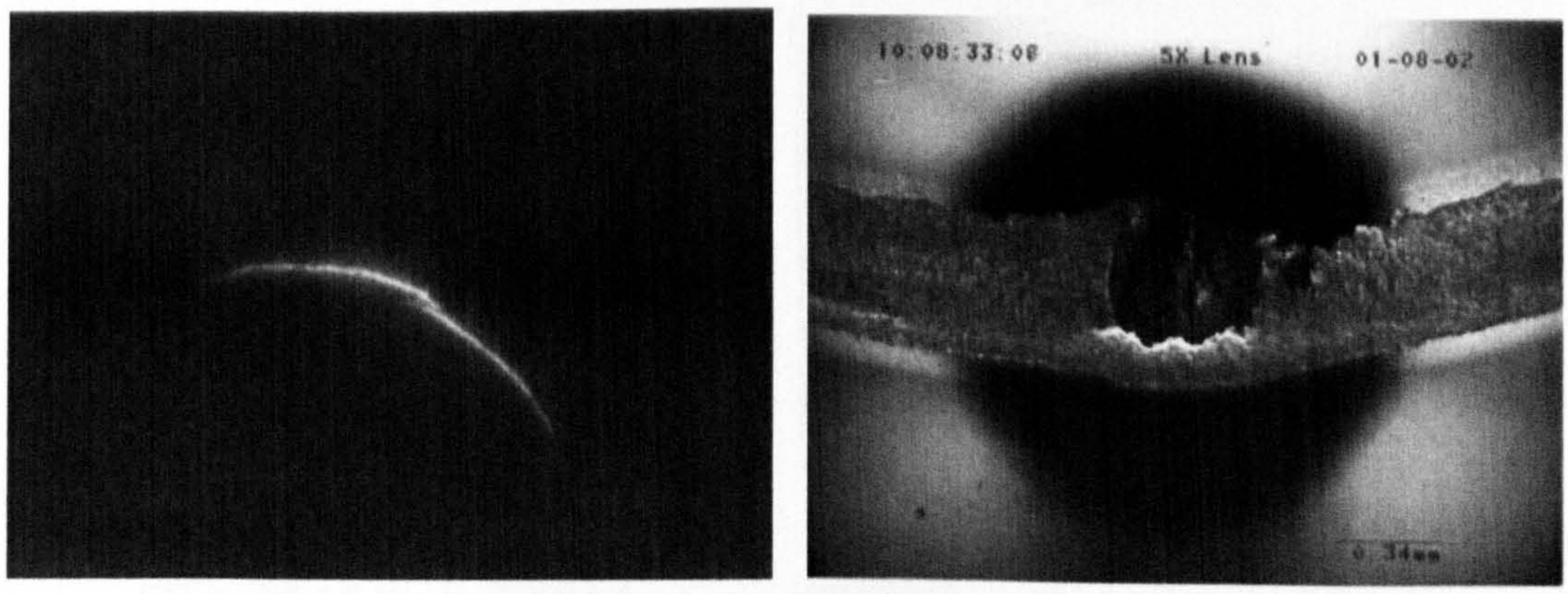

(a) Pre-test ring crack (UV light) (b) Fatigue spall optical image

Figure 4.14 Surface observations of silicon nitride ball (Test TOL-5)

4.2.2 Gearbox oil lubrication

A high viscosity lubricant, gearbox oil, was also used in determining the effect of lubricants on RCF performance. All of the tests were conducted at a speed of 5000 rpm. The crack was placed in the normal position as shown in figure 3.4(a) in Section 3.3.2 of Chapter 3. The type A material was used for these tests. Test conditions and results were shown in table 4.2. Lubricant temperature was recorded after equilibrium was reached. As temperature gradually increases with contact load, film thickness reduces due to the effects of the viscosity. Figure 4.15 shows fatigue life at different loads. It is obvious that the fatigue life decreases with the increase of the contact stresses.

Table 4.2 Test conditions and results for gearbox oil

Test No.	Contact stress (GPa)	Average oil Temperature (^{o}C)	Time to failure or end of test (Hours)	Stress cycles ($\times 10^{7}$)
GOL-1	5.03	38	300*	20.25*
GOL-2	5.58	41	134.33	9.067
GOL-3	6.63	54	78.72	5.314

*Test suspended without spalling

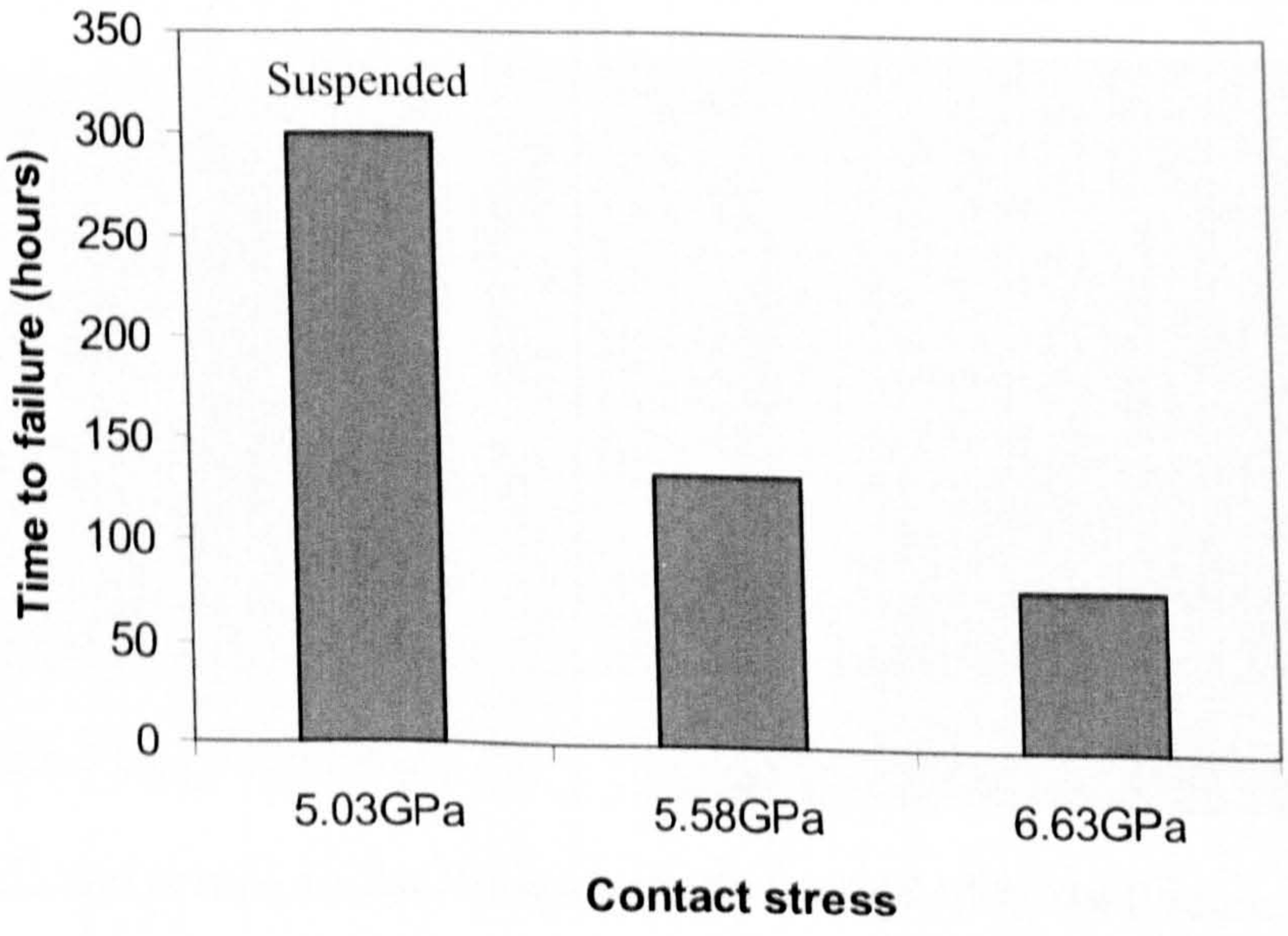

Figure 4.15 Rolling contact fatigue life at different loads lubricated with gearbox oil

Test GOL-1 was suspended after reaching 300 hours (approximately 200 million stress cycles). No damage was observed after microscopic analysis under white light. Figure 4.16(a) shows the surface ring crack after 63 hours of testing. Figure 4.16(b) is the surface ring crack after 227.7 hours of testing. Comparison of figure 4.16(a) and (b) reveals that there is no significant change in the ring crack size and the crack does not propagate along the ring crack circle. The crack becomes more visible.

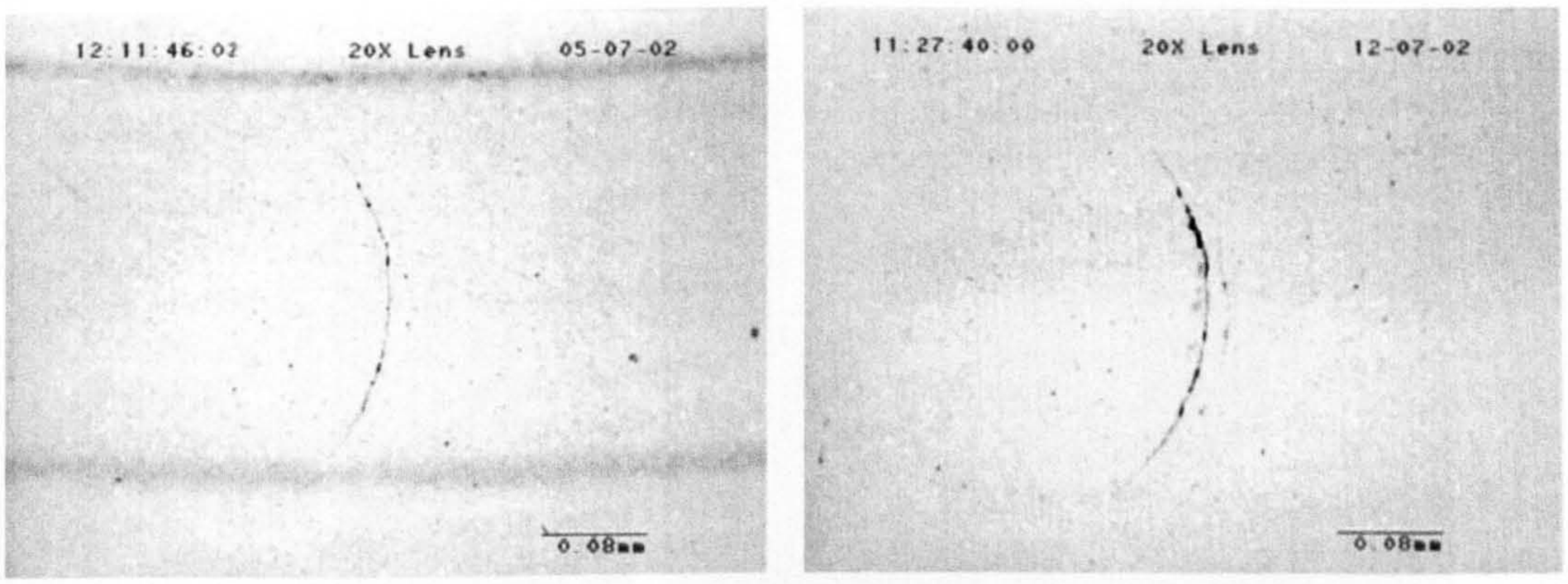

(a) After 63 hours of testing (b) After 227.7 hours of testing

Figure 4.16 Surface observations of silicon nitride ball (Test GOL-1)

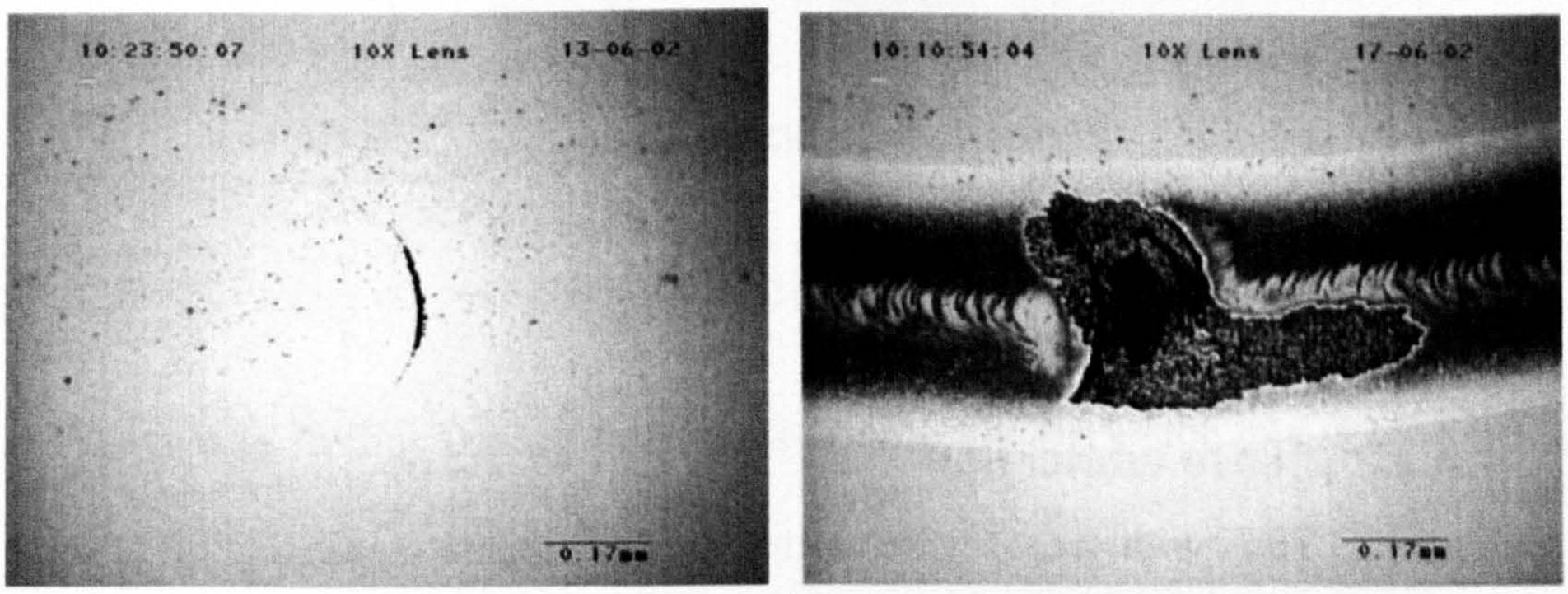

(a) After 39.8 hours of testing (b) Failure overview

Figure 4.17 Surface observations of silicon nitride ball (Test GOL-2)

Figure 4.17 shows the surface observations from Test GOL-2. The maximum contact pressure was 5.58 GPa. After 39.8 hours of testing the ring crack becomes more visible (figure 4.17(a)) and the micro-cracks are observed on the contact track. These micro-cracks are distributed in a regular pattern. The overview of the spall is

shown in figure 4.17(b), where the original ring crack is still clear after the fatigue spall was formed. The delaminated failure characteristic on the wear track is also found

Observations from Test GOL-3 are shown in figure 4.18. The optical and SEM images are shown in figure 4.18(a) and (b) respectively. This test differs from Test GOL-2 in that the contact stress is different. The maximum contact pressure is increased from 5.58 GPa to 6.63 GPa, and the crack remains in the same position. The spall is formed after 78.72 hours of testing. Failure modes are fatigue spalling.

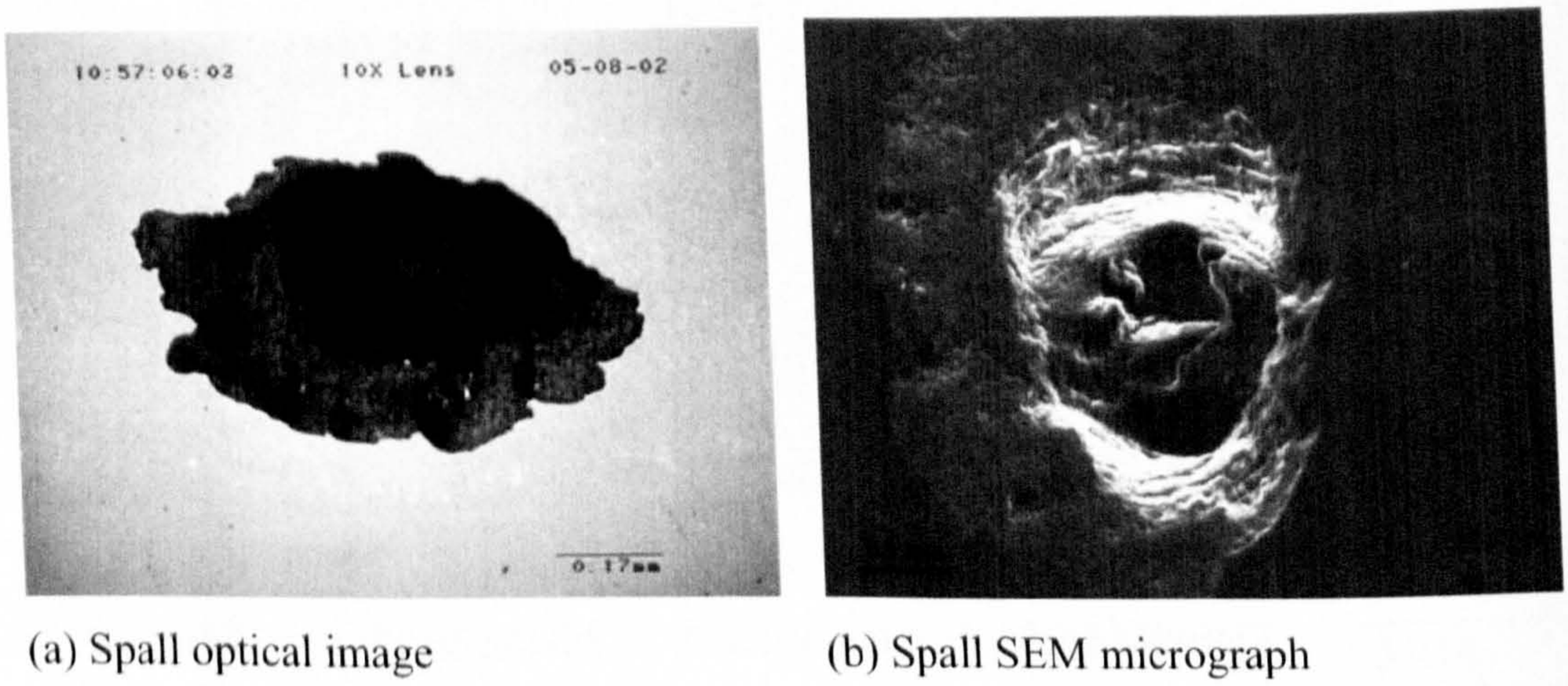

(a) Spall optical image (b) Spall SEM micrograph

Figure 4.18 Overview of the spall (Test GOL-3)

4.2.3 Grease lubrication

Tests with grease were carried out to compare grease and oil lubrication. All of the tests were conducted at a speed of 5000 rpm. The crack orientation was in the normal position as shown in figure 3.4(a) in Section 3.3.2 of Chapter 3. The type A material was used for these tests. Test conditions and results were listed in table 4.3.

Figure 4.19 shows the comparison of RCF life performance. It is clear that the rolling contact fatigue life increases as the contact load decreases. When contact stress is less than 5.03 GPa, there is no fatigue failure in 200 million stress cycles.

Therefore, 5.03 GPa is indicated as the minimum load for likely fatigue failure with grease lubrication.

Table 4.3 Test conditions and results for grease

Test No.	Contact stress (GPa)	Average oil Temperature (^{o}C)	Time to failure or end of test (Hours)	Stress cycles ($\times 10^{7}$)
Grease-1	5.03	44	300*	20.25*
Grease-2	5.58	46	231.67	15.64
Grease-3	6.63	58	60.58	4.09

* Test suspended without spalling

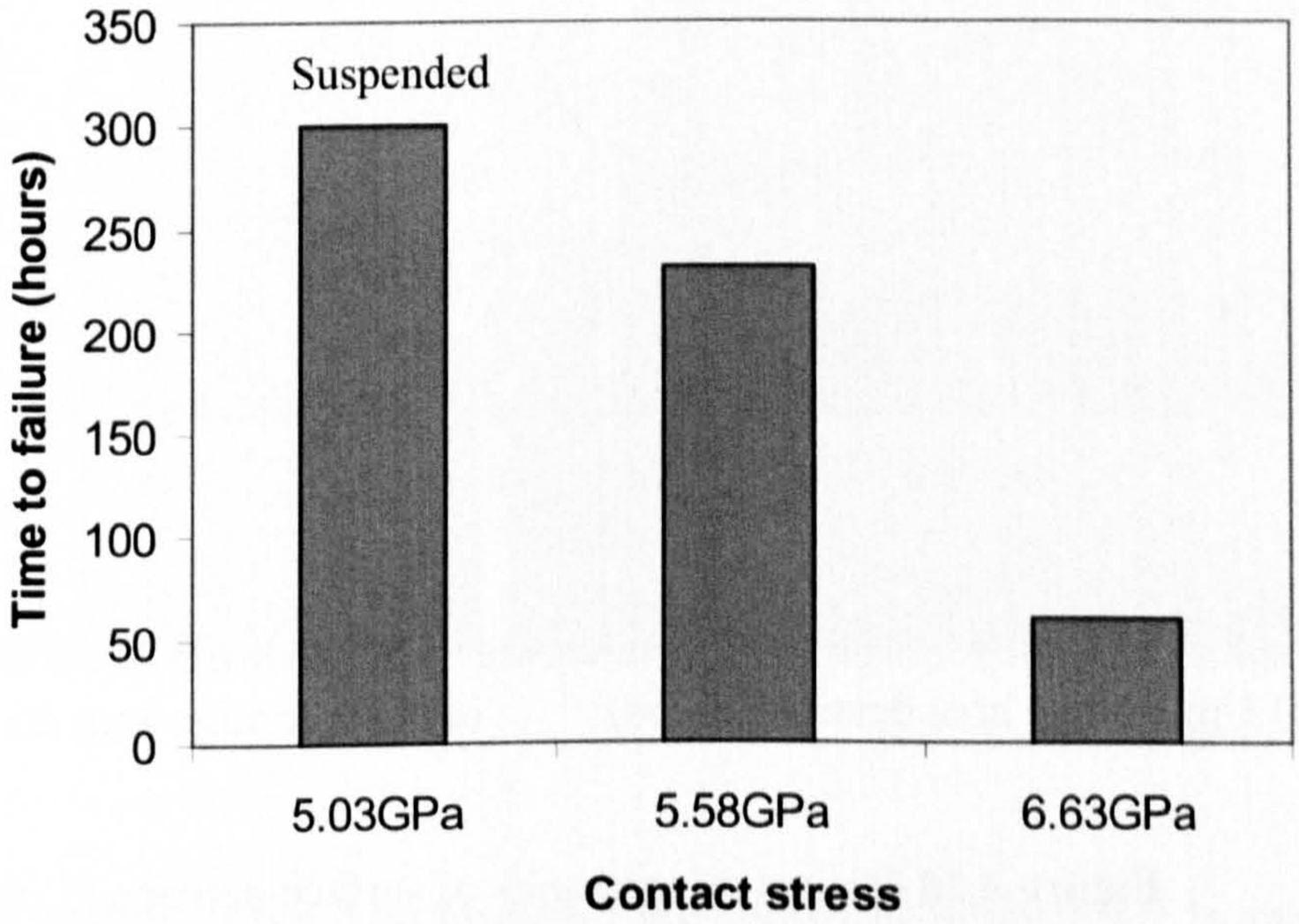

Figure 4.19 Rolling contact fatigue life at different loads with grease lubrication

Figure 4.20 shows the microscopic analysis results from Test Grease-1. The ring cracks after 143.6 hours and 300 hours of testing are shown in figure 4.20(a) and (b), respectively. Comparison reveals that there is no significant change in the ring crack and contact path. The crack still stays at the original crack length. The contact surface remained in good condition even though it had been subjected to 300

hours of testing. Micro-chips are found on the upper and lower edge contact track as detailed in figure 4.20 (c) and figure 4.20 (d).

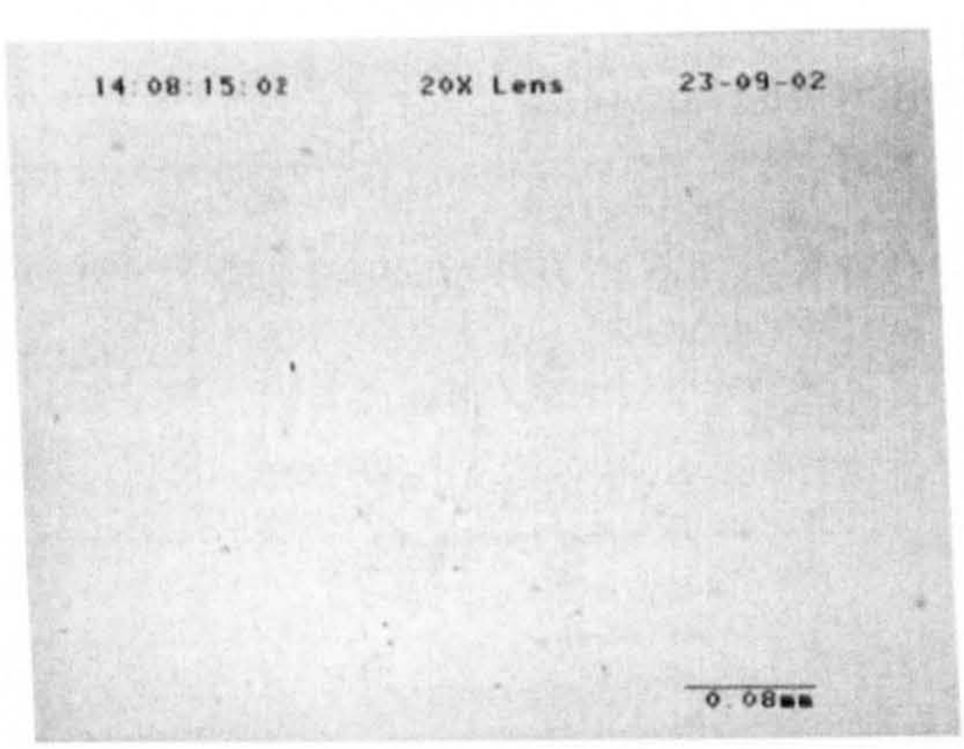

(a) After 143.6 hours of testing

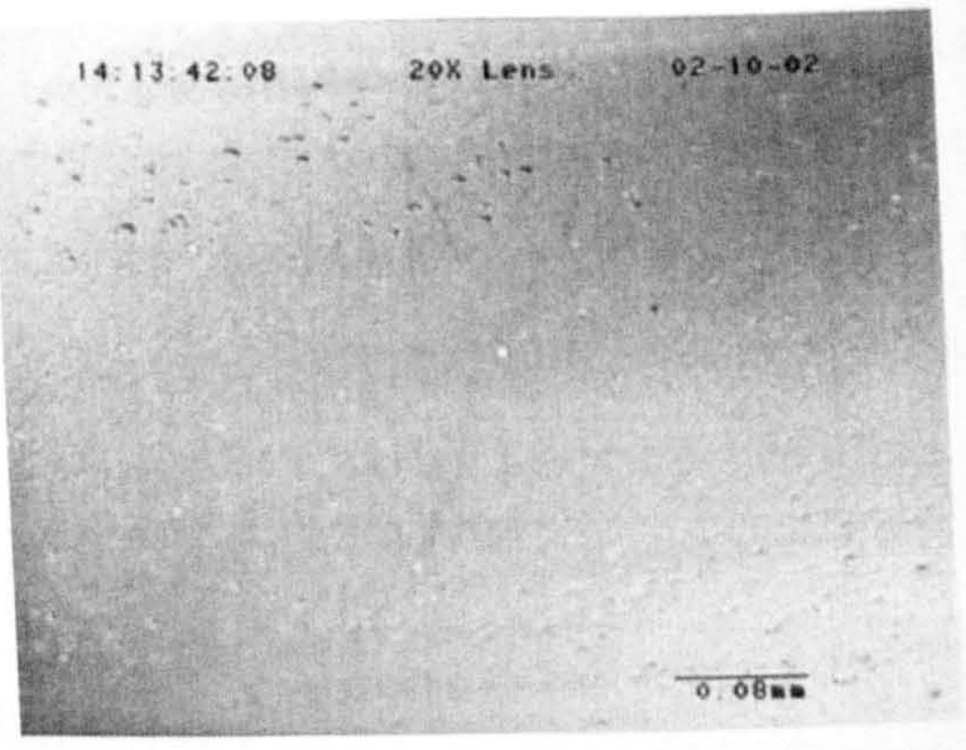

(b) After 300 hours of testing

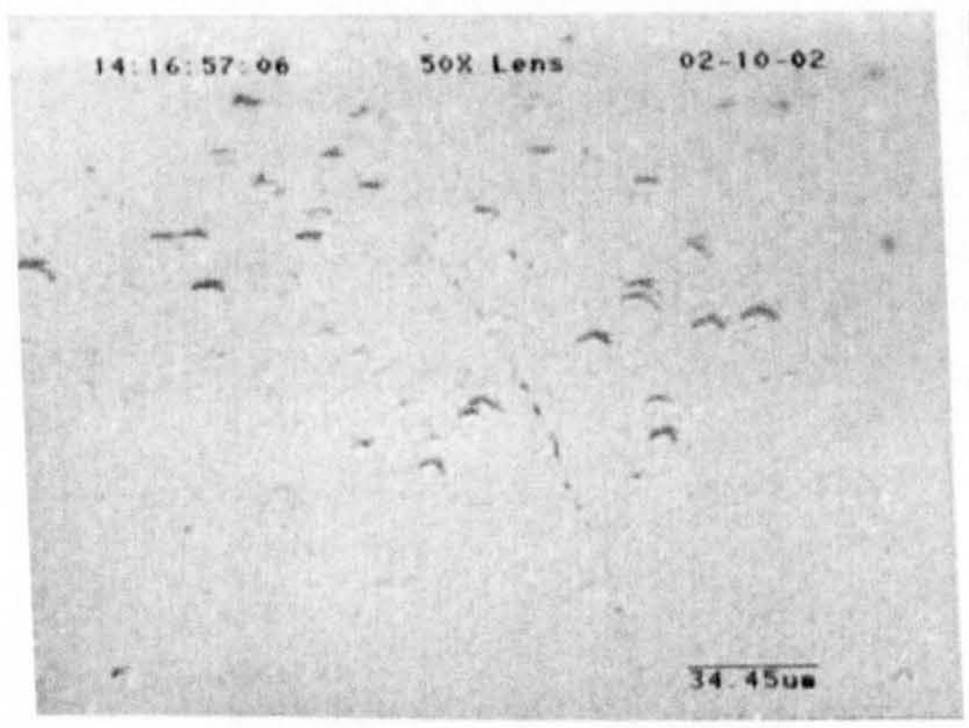

(c) Upper edge area detail (300 hrs)

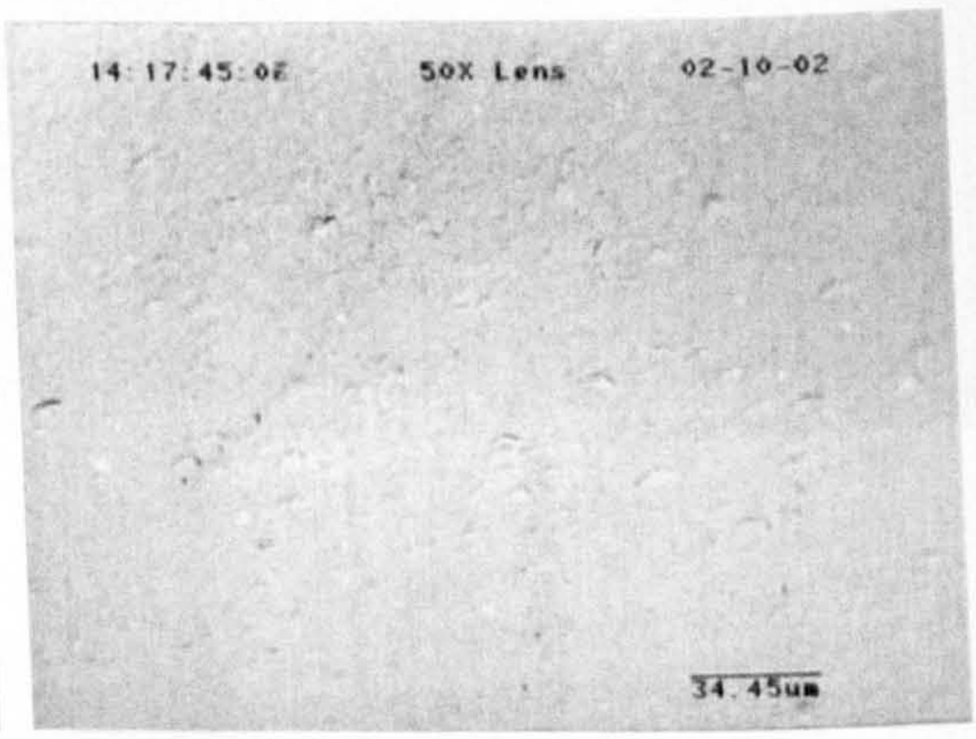

(d) Lower edge area detail (300 hrs)

Figure 4.20 Optical micrographs of surface damage (Test Grease-1)

In figure 4.21, surface observations are presented (Test Grease-2). The ring crack can only be seen under UV light source (figure 4.21(a)). After 23.5 hours of testing the contact track is covered by a bright substance (figure 4.21(b)). The ring-crack becomes visible as well. This bright substance (or deposit) can be removed using publishing power. No surface damage is seen after removing the deposit. The optical micrograph of fatigue spall is shown in figure 4.21(c) and the SEM micrograph in figure 4.21(d). Detailed SEM analysis will be presented in Section 4.4.1.

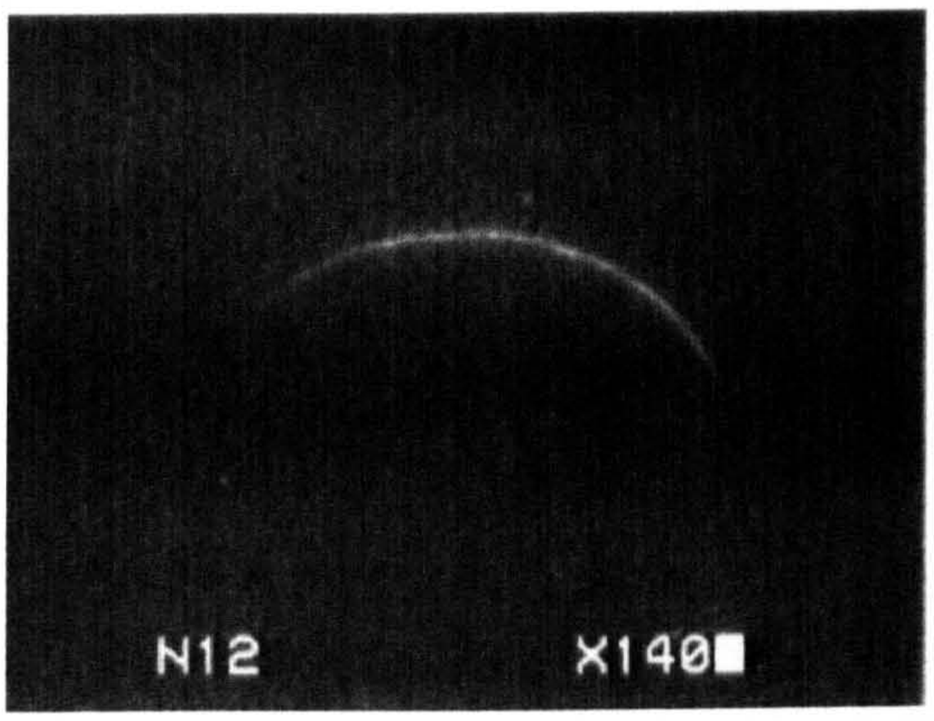

(a) Before test

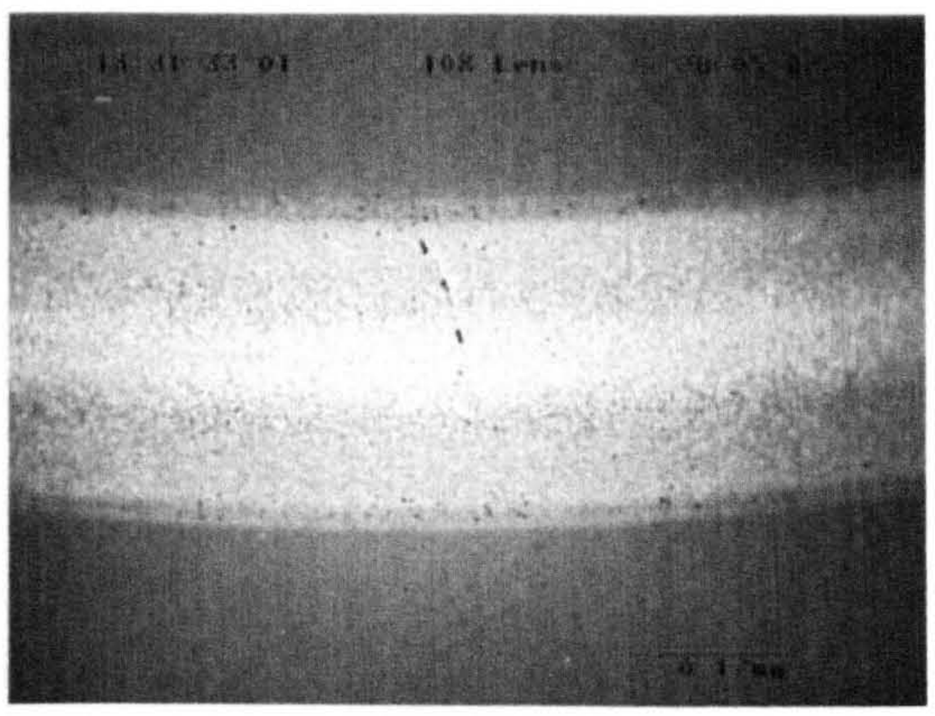

(b) After 23.5 hours of testing

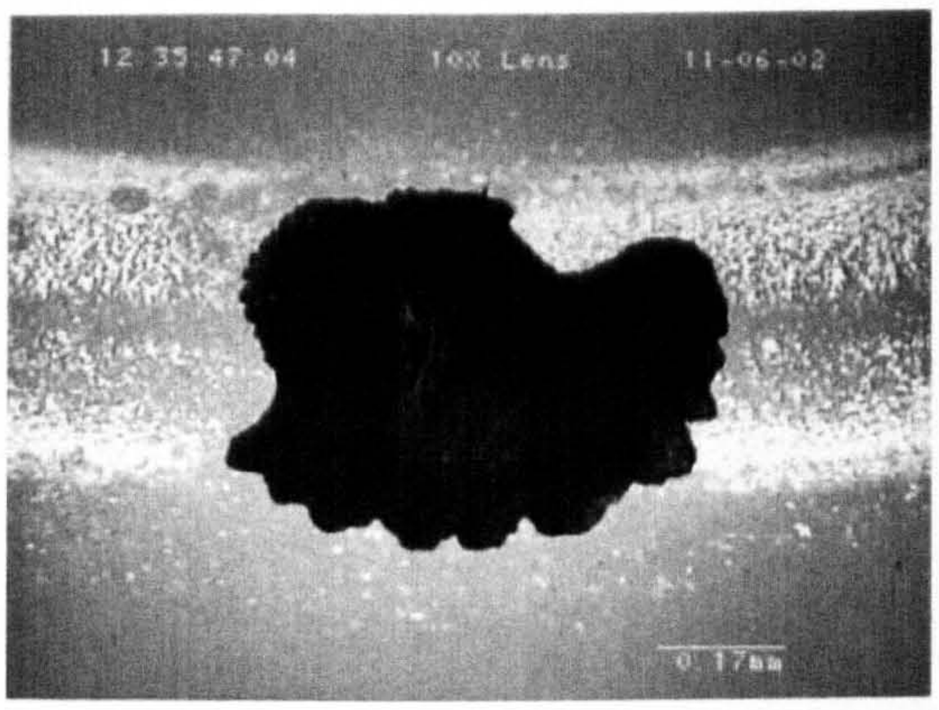

(c) Spall optical image (231.67 hours)

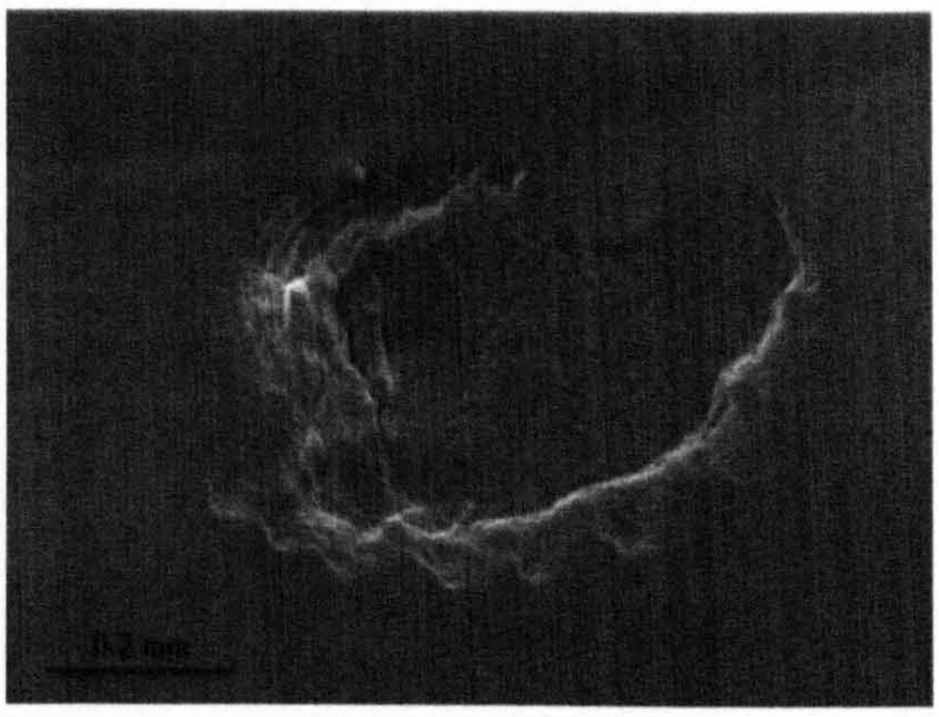

(d) SEM micrograph

Figure 4.21 Surface observations of silicon nitride ball (Test Grease-2)

Observations from Test Grease-3 are shown in figure 4.22. In this test, the contact stress increased to a high level (6.63GPa). The aim is to compare the failure modes among various contact stresses. Figure 4.22(a) shows the contact path and ring-crack after 1.3 hours of testing. Figure 4.22(b) shows an overview of the spalling formation after 60.58 hours of testing. Detailed SEM investigation of test balls was carried out as shown in figure 4.22(c) and figure 4.22(d). Again, the failure mode at high contact stresses is fatigue spalling.

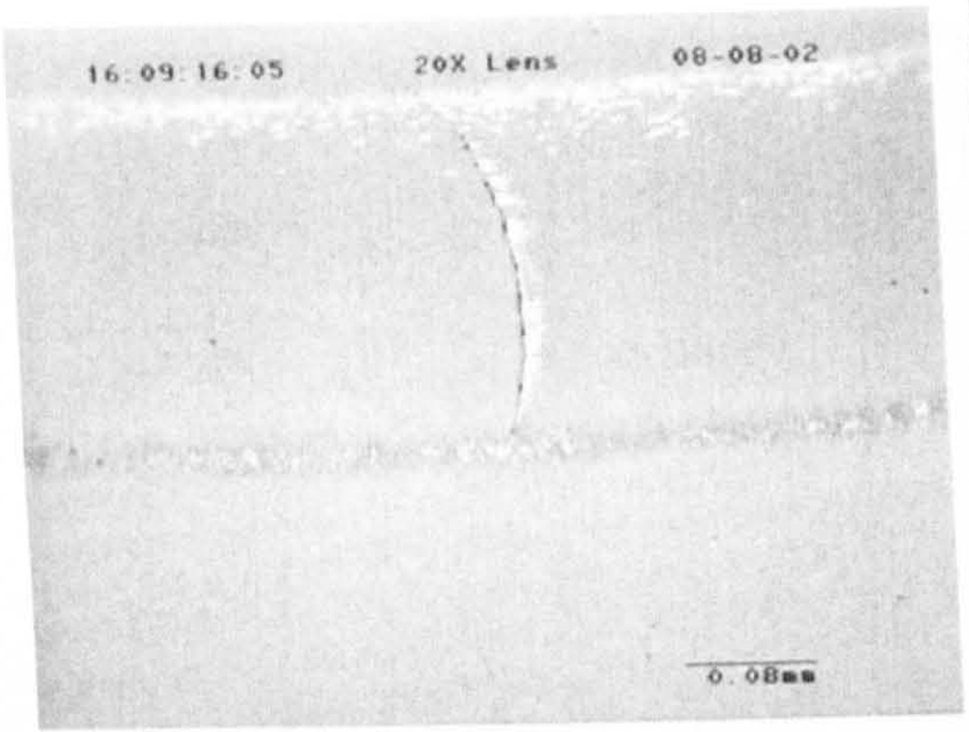

(a) 1.3 hours of testing

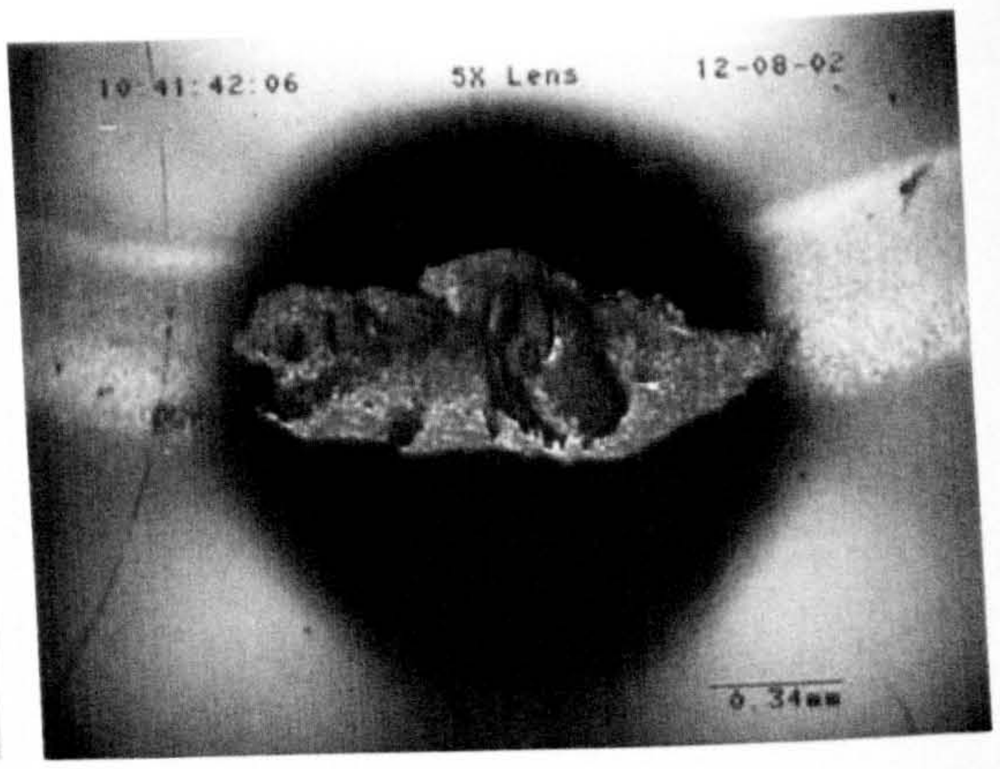

(b) An overview of the spall

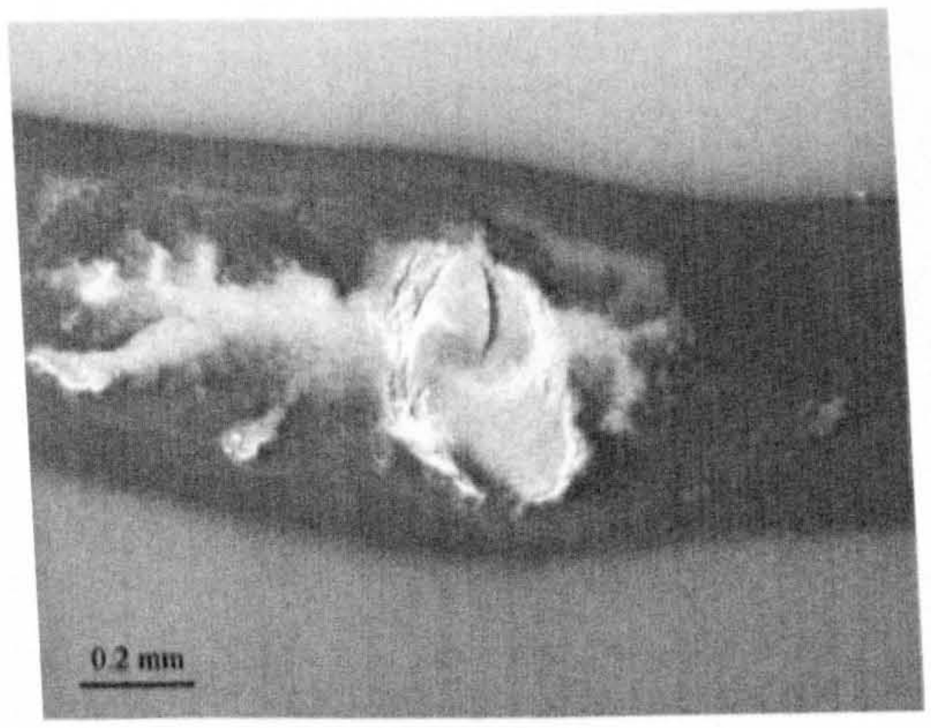

(c) SEM Micrograph of spall

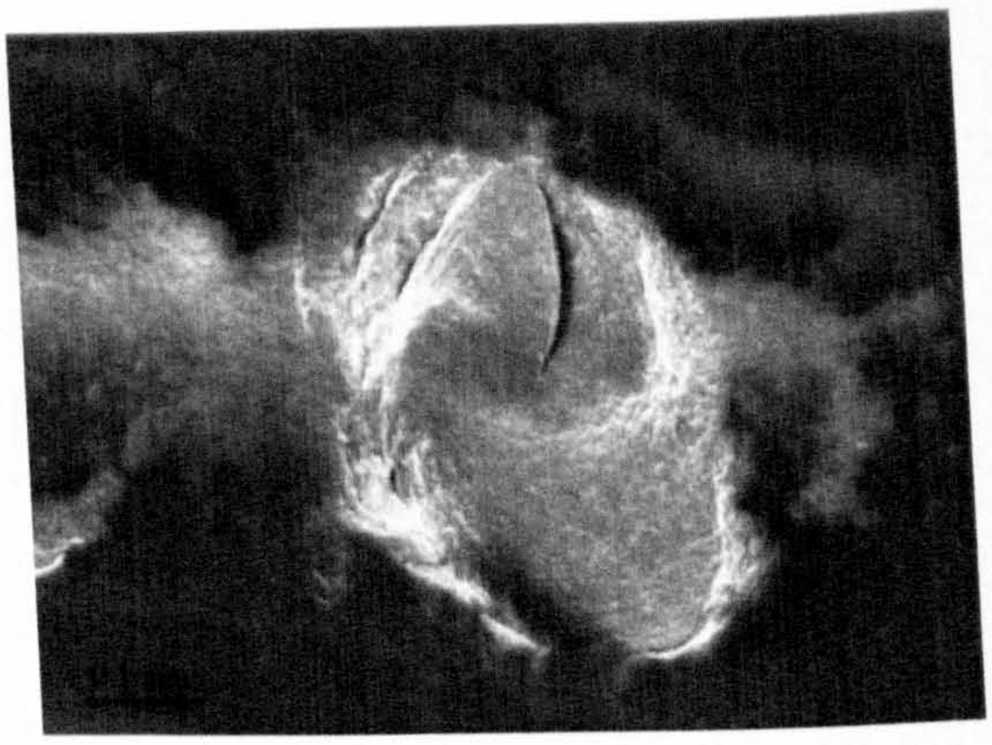

(d) High magnification of the spall

Figure 4.22 Surface observations of silicon nitride ball (Test Grease-3)

4.2.4 Kerosene lubrication

Kerosene is not normally used as a lubricating fluid. The use of kerosene is due to its strong penetration capacity. The purpose of using kerosene as a lubrication fluid is to examine whether or not trapped fluid has a significant effect on the RCF performance. The crack orientation was in the normal position as shown in figure 3.4(a) in Section 3.3.2 of Chapter 3. The test conditions and results are listed in table 4.4. All tests, conducted at different contact stresses, were terminated due to excessive wear, although test time did not reach the maximum length of the test time. During the whole test time, three steel lower balls were changed twice due to the fatigue spall which appeared on one of the steel ball surfaces for all these three tests

at different test times. The test temperatures can reach 60°C when the contact stress is 6.63 GPa. The tests were suspended due to wear. No fatigue spalls were seen.

Table 4.4 Test conditions and results for kerosene

Test No.	Contact stress (GPa)	Average oil temperature (°C)	Time to failure or end of test (Hours)	Stress cycles ($\times 10^7$)
Kerosene-1	5.03	33	20.35*	1.37*
Kerosene-2	5.58	44	55.62*	3.75*
Kerosene-3	6.63	60	38.35*	2.59*

* Test suspended due to wear

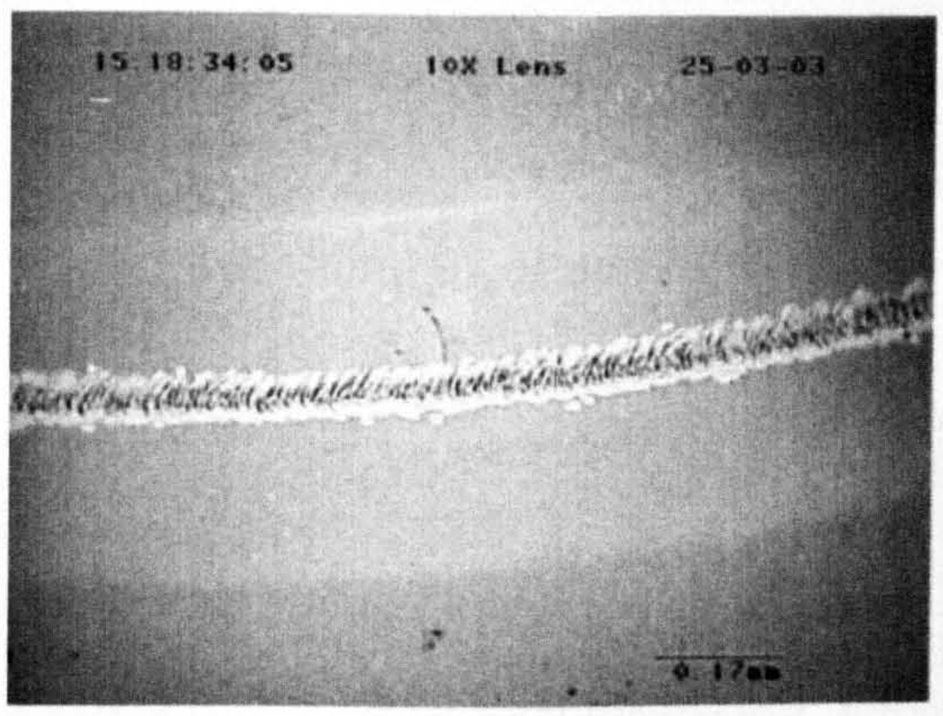

(a) After 6.77 hours of testing

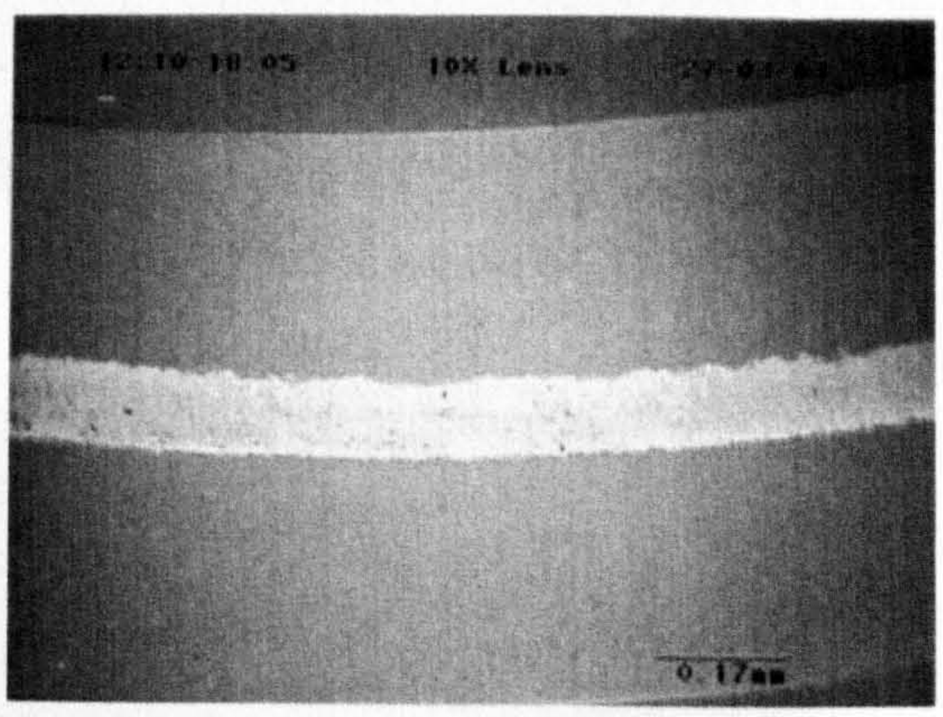

(b) After 16.35 hours of testing

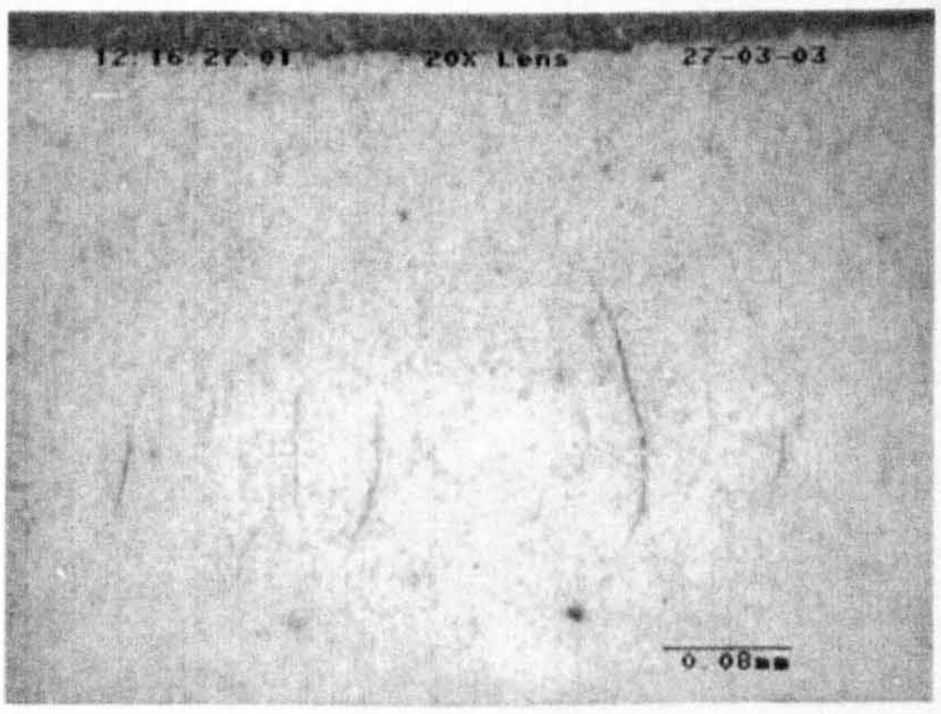

(c) Bottom of the contact track

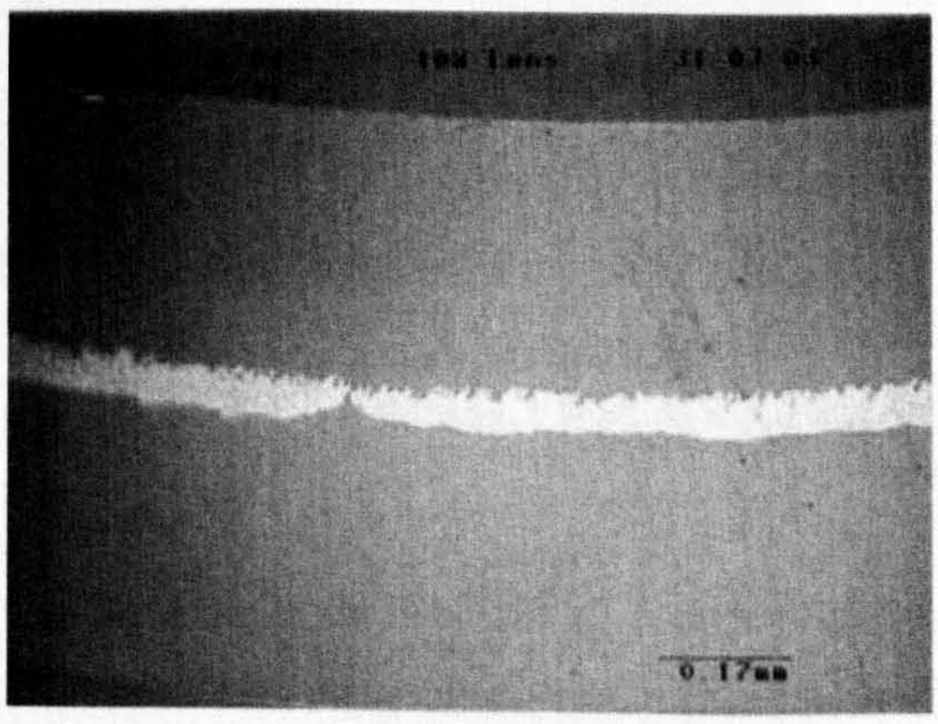

(d) After 20.35 hours of testing

Figure 4.23 Observations of surface damage from Test Kerosene-1

Observations of surface damage from Test Kerosene-1 are shown in figure 4.23. The severe wear dominated the failure mode. The surface ring crack is becoming smaller (figure 4.23(a)) and the contact track is becoming wider (figure 4.23(b). This development is caused by material removed from the contact track. The traction cracks are found everywhere along the contact track (figure 4.23(c)). After 20.35 hours of testing, the ring crack disappears (figure 4.23(d)) and the test was ended.

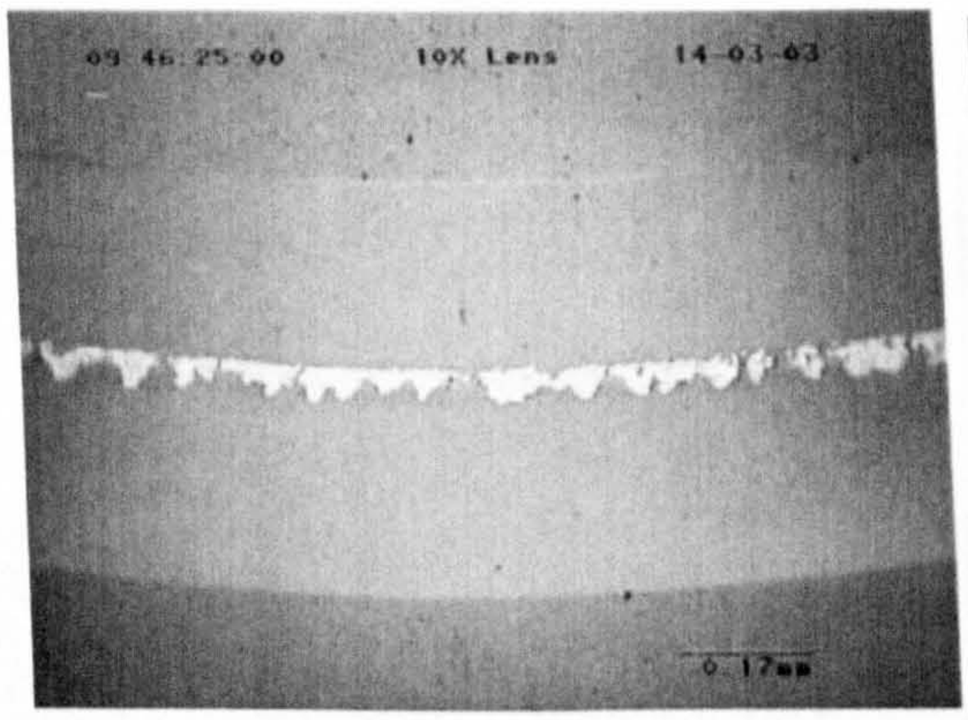

(a) After 18 hours of testing

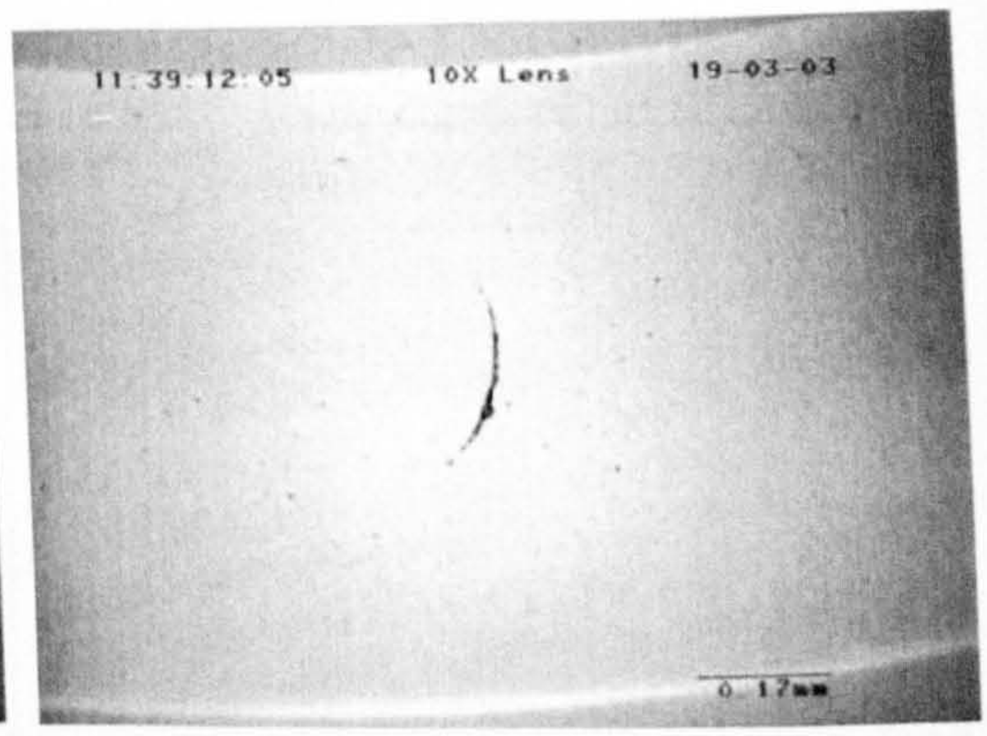

(b) After 46.78 hours of testing

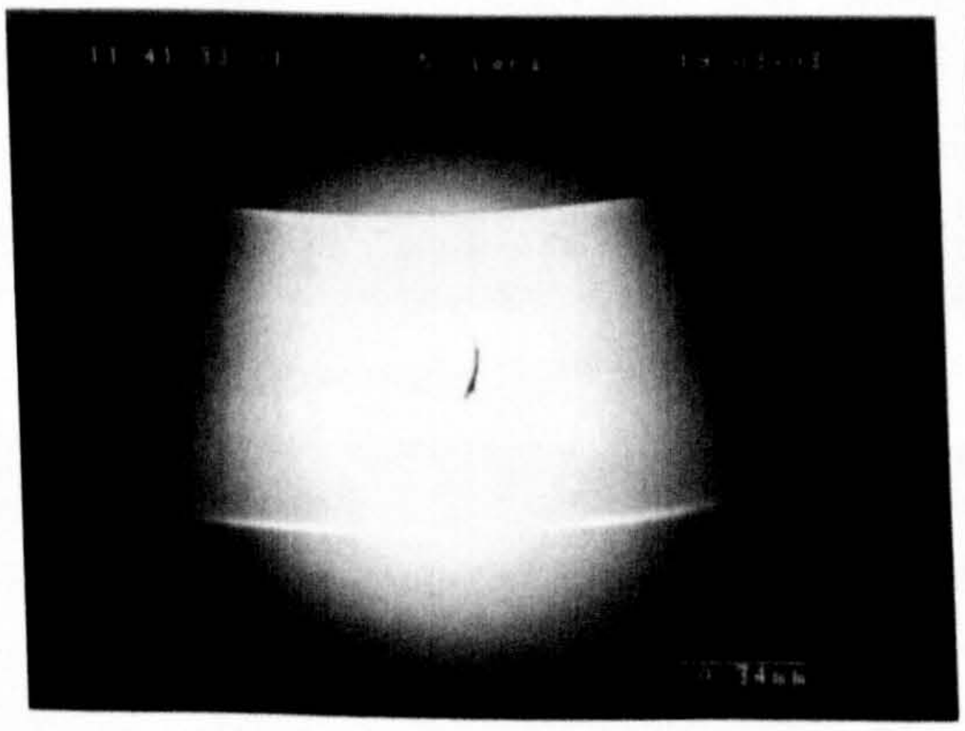

(c) After 46.78 hours of testing

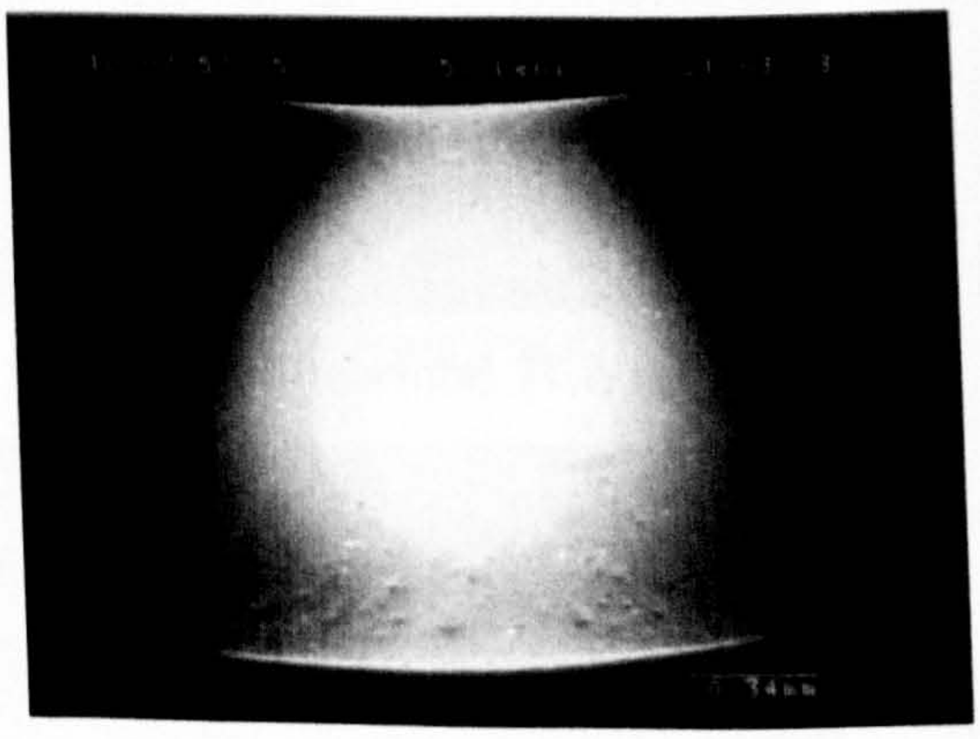

(d) After 55.62 hours of testing

Figure 4.24 Observations of surface damage from Test Kerosene-2

The result of surface examinations from Test Kerosene- 2 is shown in figure 4.24. Again, the severe wear dominates failure modes. The ring cracks after 18 hours and 46.78 hours of testing are shown in figure 4.24(a) and figure 4.24(b),

respectively. Comparison of figure 4.24(a) and figure 4.24(b) reveals that there is significant change on the contact path. The width of the contact path (figure 4.24(b)), is much wider than the width of contact path (figure 4.24(a)) due to wear. Figures 4.24(c) and (d) show the surface damage after different hours of testing, and it can be seen that the ring crack disappears and the contact track presents a smooth shallow groove. The test was suspended.

Test Kerosene-3 was suspended due to excessive wear (Figure 4.25(a) to (d)). The traction cracks and micro-cracks (chips) were found everywhere along the contact track. The opposed orientation of traction cracks on either side of the track is clearly seen (figure 4.25(c)). The starvation in lubrication fluid and slip may be the reason for the formation of these traction cracks.

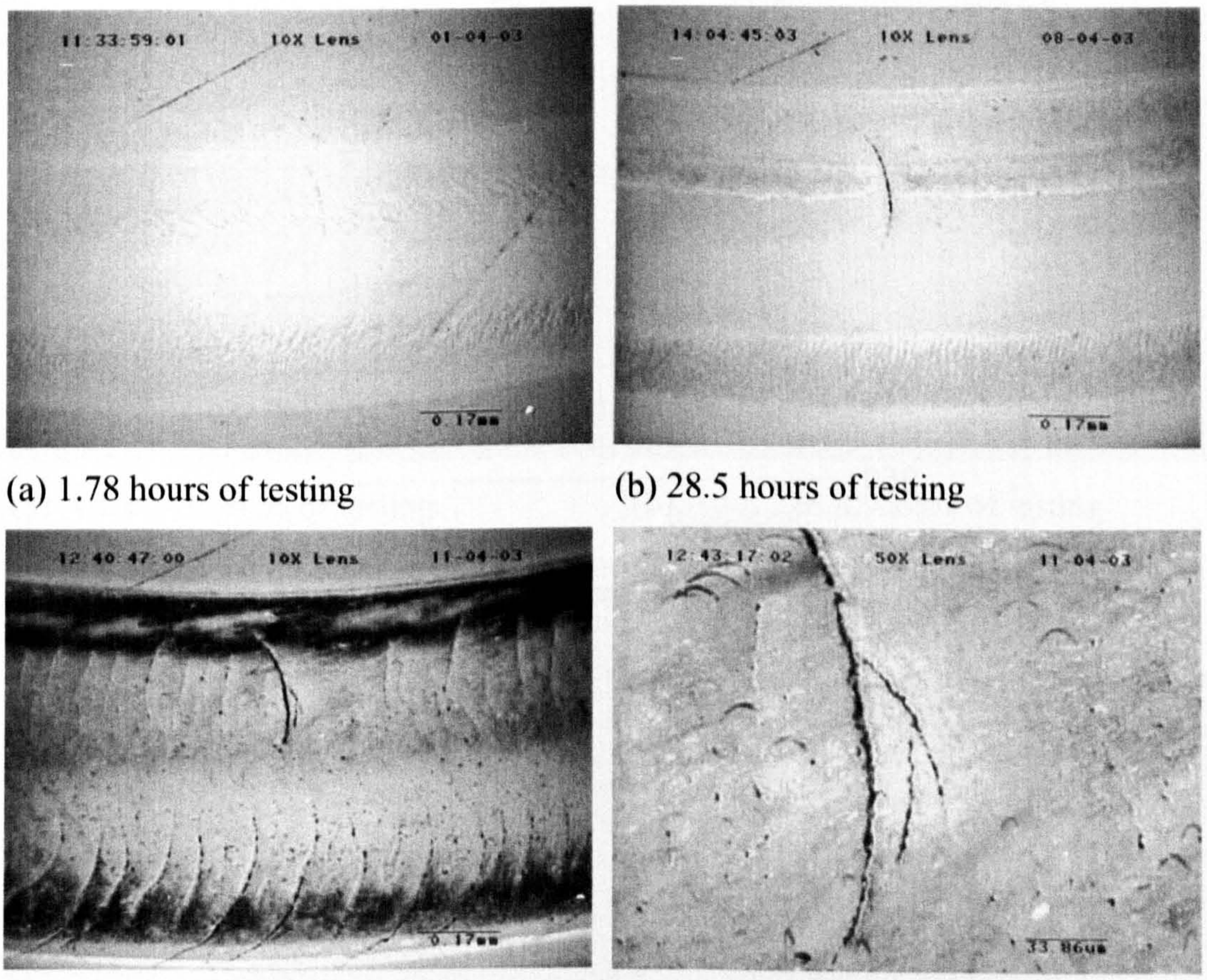

(a) 1.78 hours of testing

(b) 28.5 hours of testing

(c) 38.35 hours of testing

(d) Detail of ring crack and micro-chips

Figure 4.25 Observations of surface damage from Test Kerosene-3

4.2.5 Mineral oil lubrication

A summary of the rolling contact fatigue test with mineral oil is given in table 4.5. All of the tests were conducted at a speed of 5000 rpm. Balls (Material A) were used for these tests. Figure 4.26 shows the comparison of RCF life performance. It is clear that the rolling contact fatigue life increases as the contact load increases.

Table 4.5 Test conditions and results for mineral oil

Test No.	Contact stress (GPa)	Average oil Temperature (^{o}C)	Time to failure or end of test (Hours)	Stress cycles ($\times 10^{7}$)
TT9-1	4.00	32	300*	20.25*
TT9-2	4.44	34	278.32	18.8
TT9-3	5.03	36	106.42	7.2
TT9-4	5.58	42	28.17	1.9
TT9-5	6.63	51	17.87	1.2
TT9-6	5.03	35	116.2**	7.89**

* Test suspended without spalling, **TT9-6 was stopped for cutting

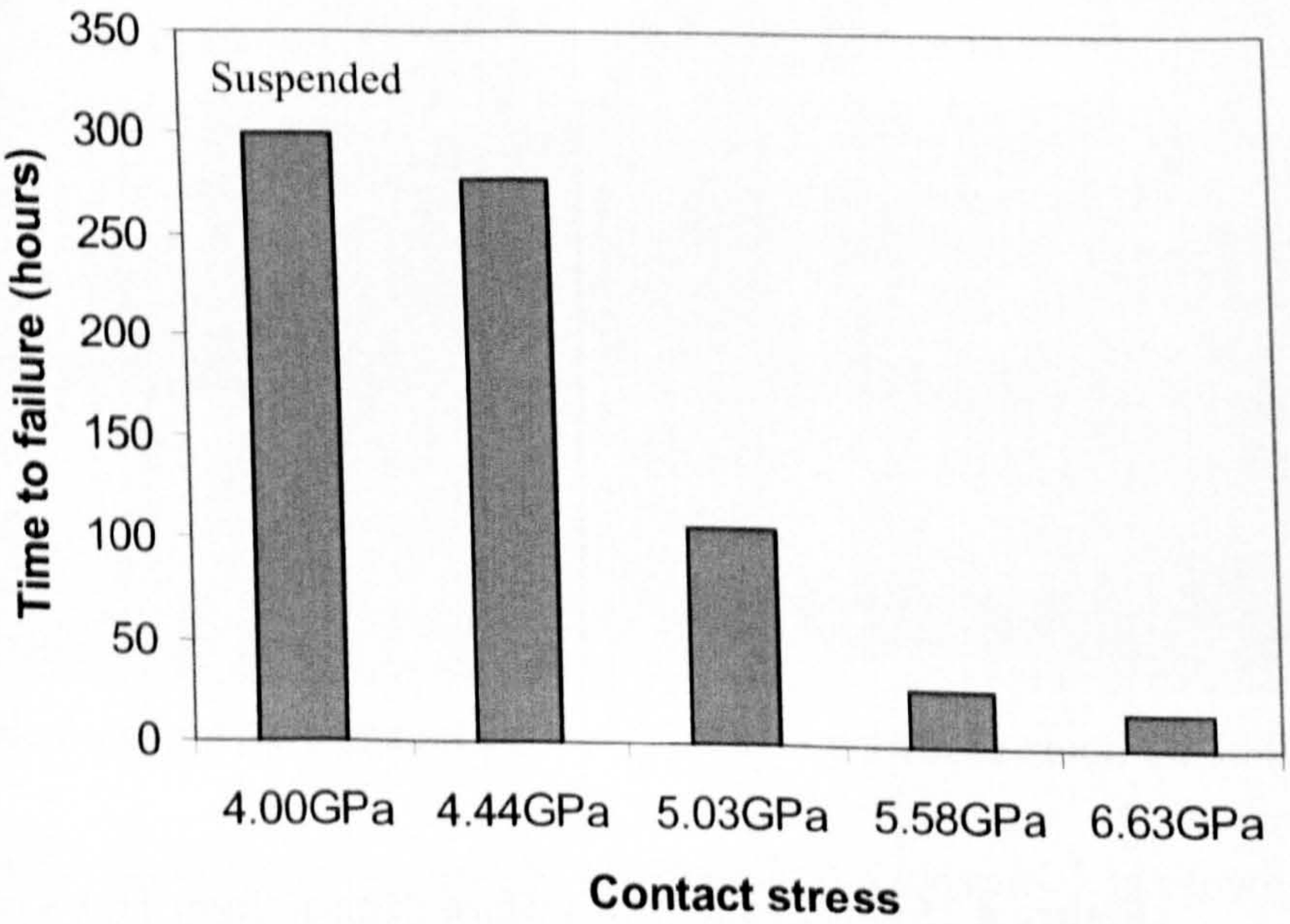

Figure 4.26 Rolling contact fatigue life at different loads with mineral oil

Direct observations of surface damage have been carried out and the results are shown in figures 4.27 to 4.30. Like previous tests, the pre-test ring crack only can be seen under the ultra-violet light. After a few hours of testing, the cracks can be seen under the normal light conditions.

Figure 4.27(a) shows the surface ring crack after 241 hours of testing (Test TT9-2). The contact track is seen clearly and the crack gap is getting bigger. No other surface damage is observed. The overview of the fatigue spall is shown in figure 4.27(b). Observations from Test TT9-3 are shown in figure 4.28. Figure 4.28(a) shows the ring crack image after 55 hours of testing (Test TT9-3). The crack is clearly seen under a normal light source. Spalling fatigue failure occurred after 106.42 hours of testing shown in figure 4.28(b).

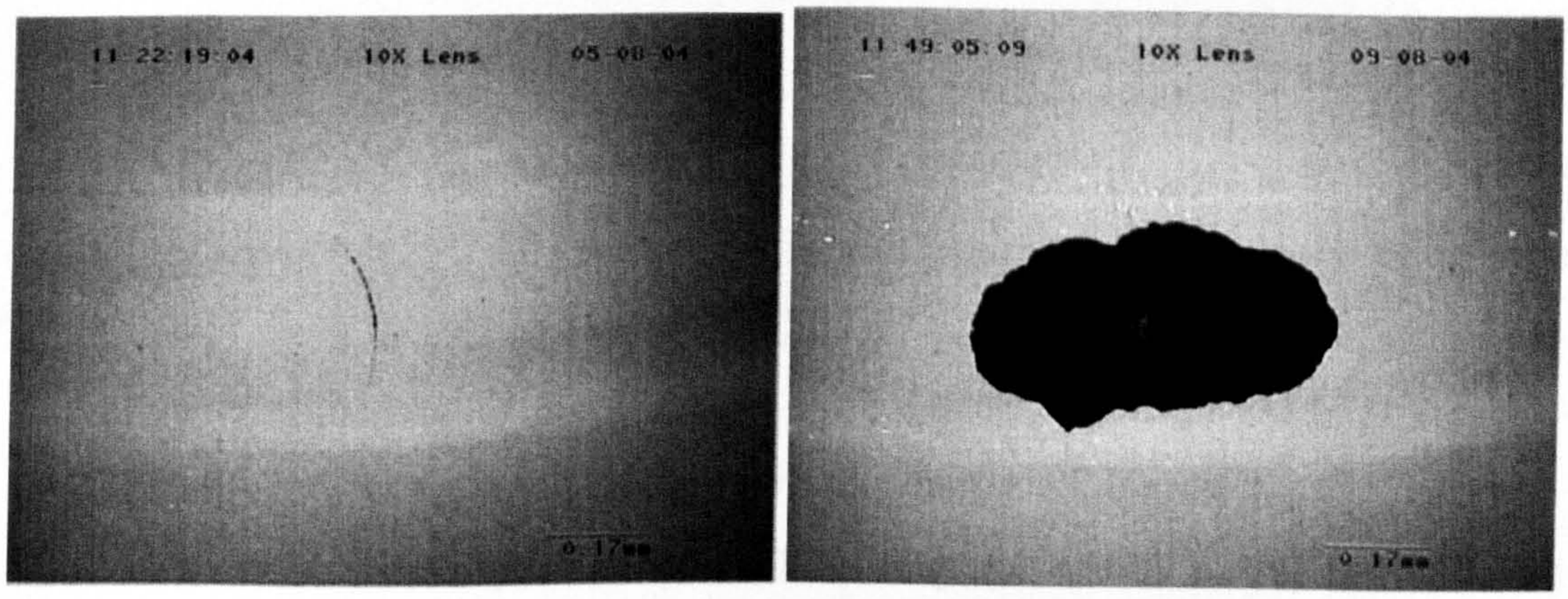

(a) After 241 hours of testing (b) After 278.32 hours of testing

Figure 4.27 Surface observations of silicon nitride ball (Test TT9-2)

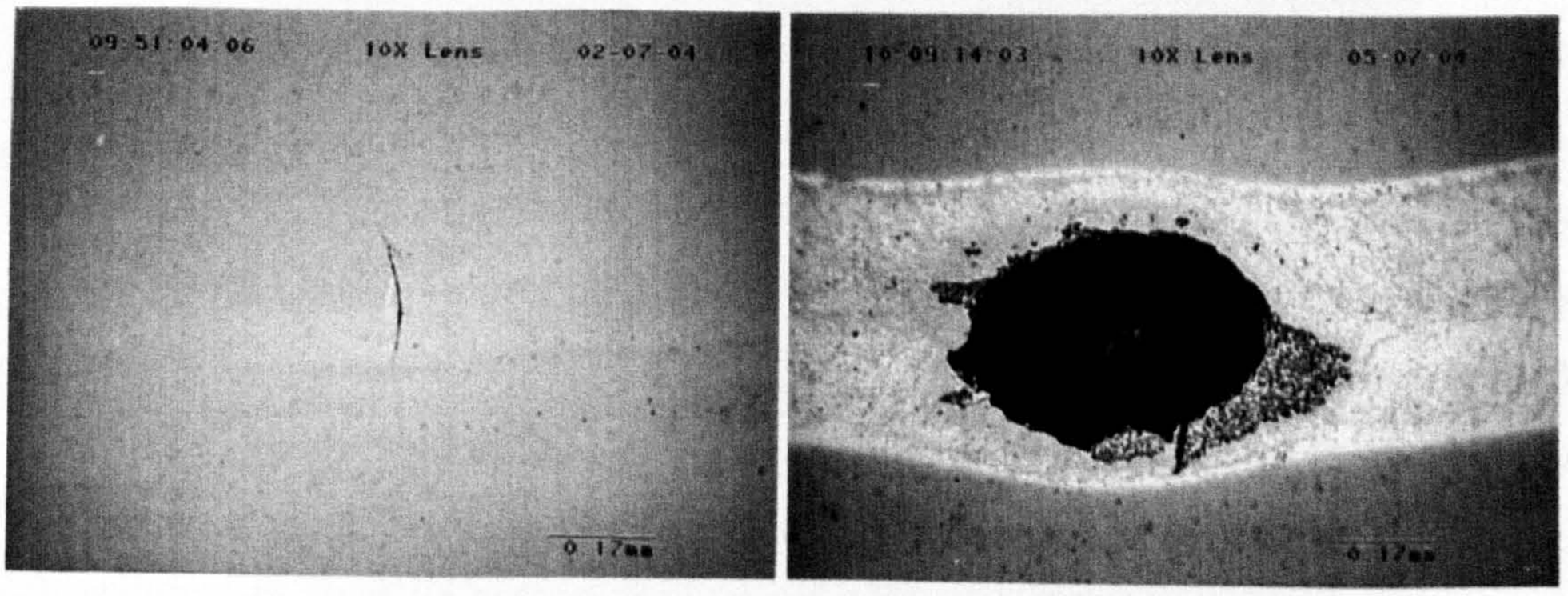

(a) After 55 hours of testing (b) 106.42 hours of testing

Figure 4.28 Surface observations of silicon nitride ball (Test TT9-3)

Observations of silicon nitride ball surfaces from Test TT9-4 at the contact pressure of 5.58 GPa are illustrated in figure 4.29. The surface ring crack only can be seen under UV light source before testing. As the fatigue test proceeds the crack becomes visible under a white light source (figure 4.29(a)). An overview of the spall obtained after 28.17 hours of testing is illustrated in figure 4.29(b).

Figure 4.30(a) shows the surface ring crack after 2.2 hours of testing. The contact loading is increased to 6.63 GPa (Test TT9-5). Figure 4.30(b) shows the fatigue spall optical image after 17.87 hours of testing.

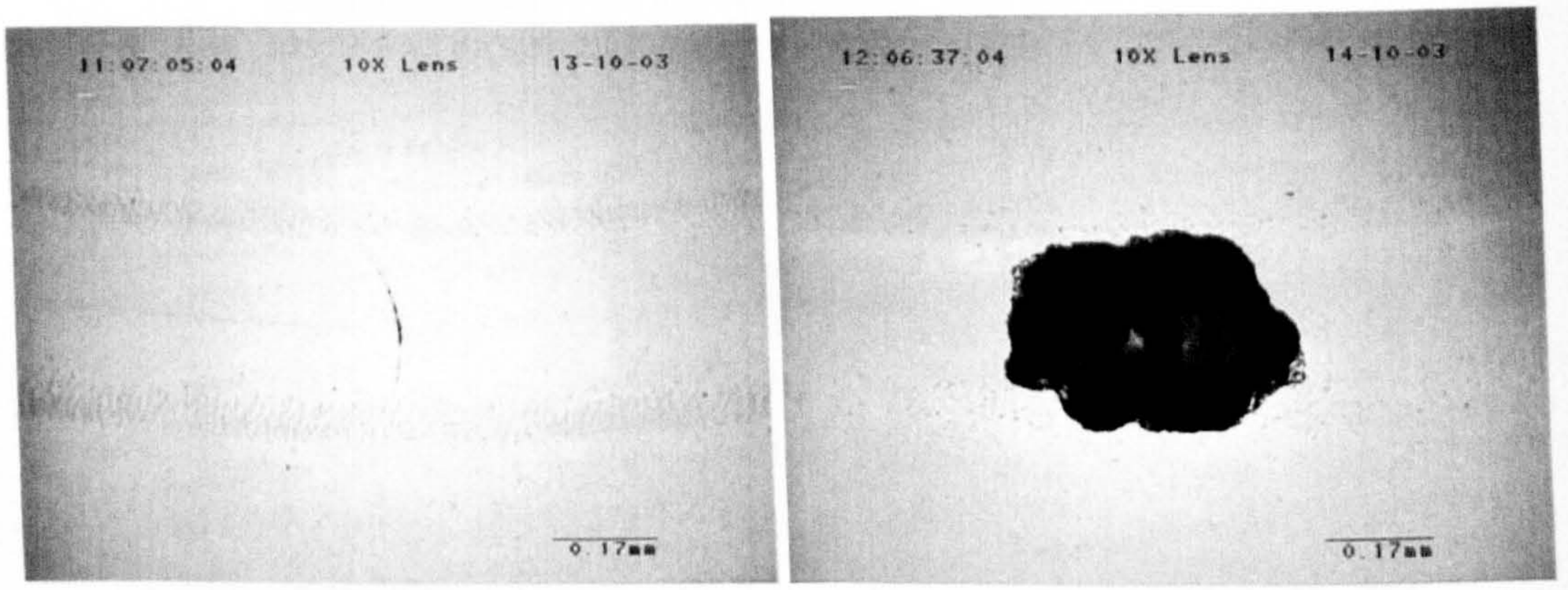

(a) After 21 hours of testing (b) 28.17 hours of testing

Figure 4.29 Surface observations of silicon nitride ball (Test TT9-4)

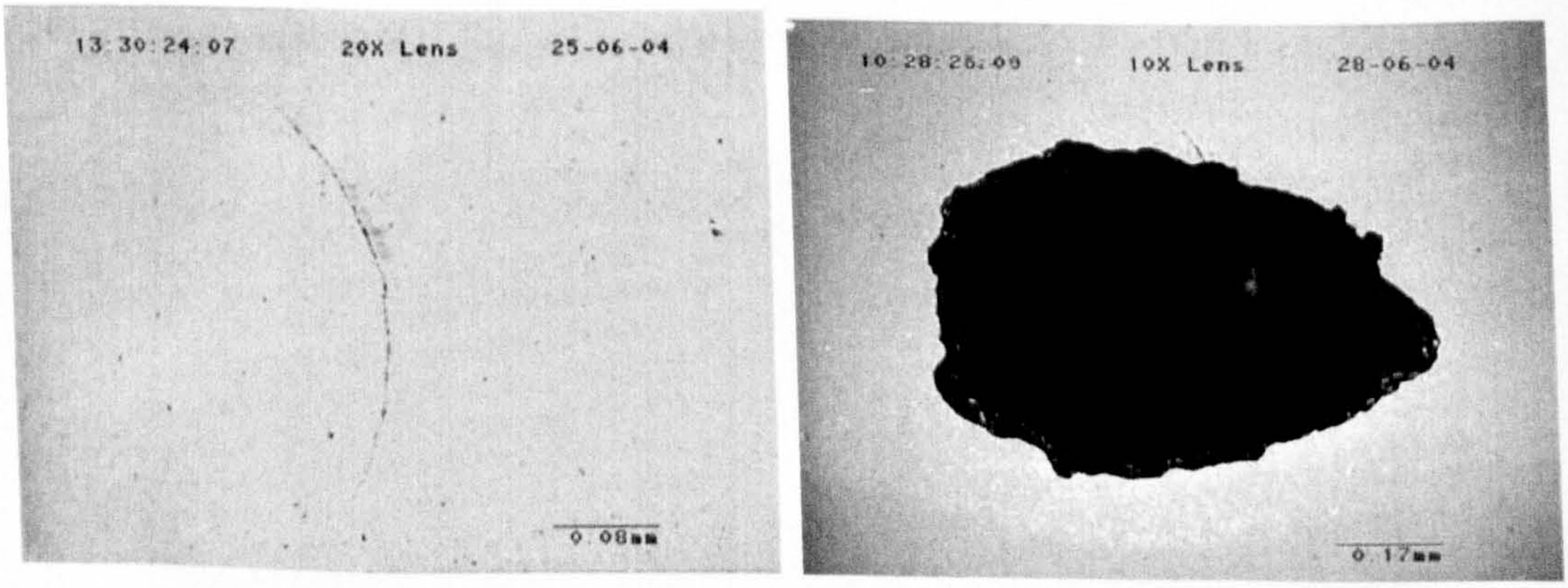

(a) After 2.2 hours of testing (b) 17.87 hours of testing

Figure 4.30 Surface observations of silicon nitride ball (Test TT9-5)

It can be seen from the above observations that the spall contour resembles an ellipse. The bigger the contact stress, the larger the spall contour. Also, the longer semi-axis is always parallel to the rolling direction, and the short axis is perpendicular to the rolling direction.

4.2.6 Comparison of RCF performance with different lubricants

The RCF life performance for each lubricant has been described in previous sections and the results were listed in tables 4.1 to 4.5. As can be seen from the tables, fatigue life changes with the contact stresses and lubricants. For example, in table 4.3, the fatigue life at the maximum contact pressure of 6.68 GPa is 40.9 million stress cycles, and 156.4 million stress cycles at the maximum contact pressure of 5.58 GPa for grease lubricant. The lubricants had a significant effect on the RCF life performance, e.g., at the maximum contact pressure of 5.58 GPa, the fatigue life for grease is 156.4 million stress cycles and for traction oil it is 14.18 million stress cycles. Rolling contact fatigue failure modes show spalling type failure except for kerosene lubrication, which was dominated by surface wear. Therefore, comparison of fatigue life performance does not include kerosene lubrication.

To compare the experimental results clearly, the results are plotted in the bar chart as shown in figure 4.31, which illustrates the relationship between the fatigue life and contact stresses with various lubricants. The contact fatigue life decreased with the increase of the contact stresses for all lubricants. For gearbox oil and grease, when the maximum contact pressure was less than 5.0 GPa, there was no fatigue failure in 300 hours of testing (approximately 20.25×10^7 fatigue cycles). However, for traction oil, fatigue failure appeared after 68.5 hours of testing, and 106.42 hours for mineral oil. Obviously, the lubricants have a significant effect on ceramic balls which have pre-existing surface cracks. Different mechanisms have been proposed to explain why lubrication fluid influences rolling contact fatigue since Way (1935) published his work. For example, lubricating oil penetrates into the crack to produce a hydraulic effect. The lubrication pressure was assumed to prise the crack open and to force the crack to grow back to the surface (Keer and Bryant 1983, Murakami et

al. 1985, Kaneta and Murakami 1987). Also sufficient lubrication fluid was taken to exist in the crack so that the crack face friction was zero which increased Mode II crack propagation.

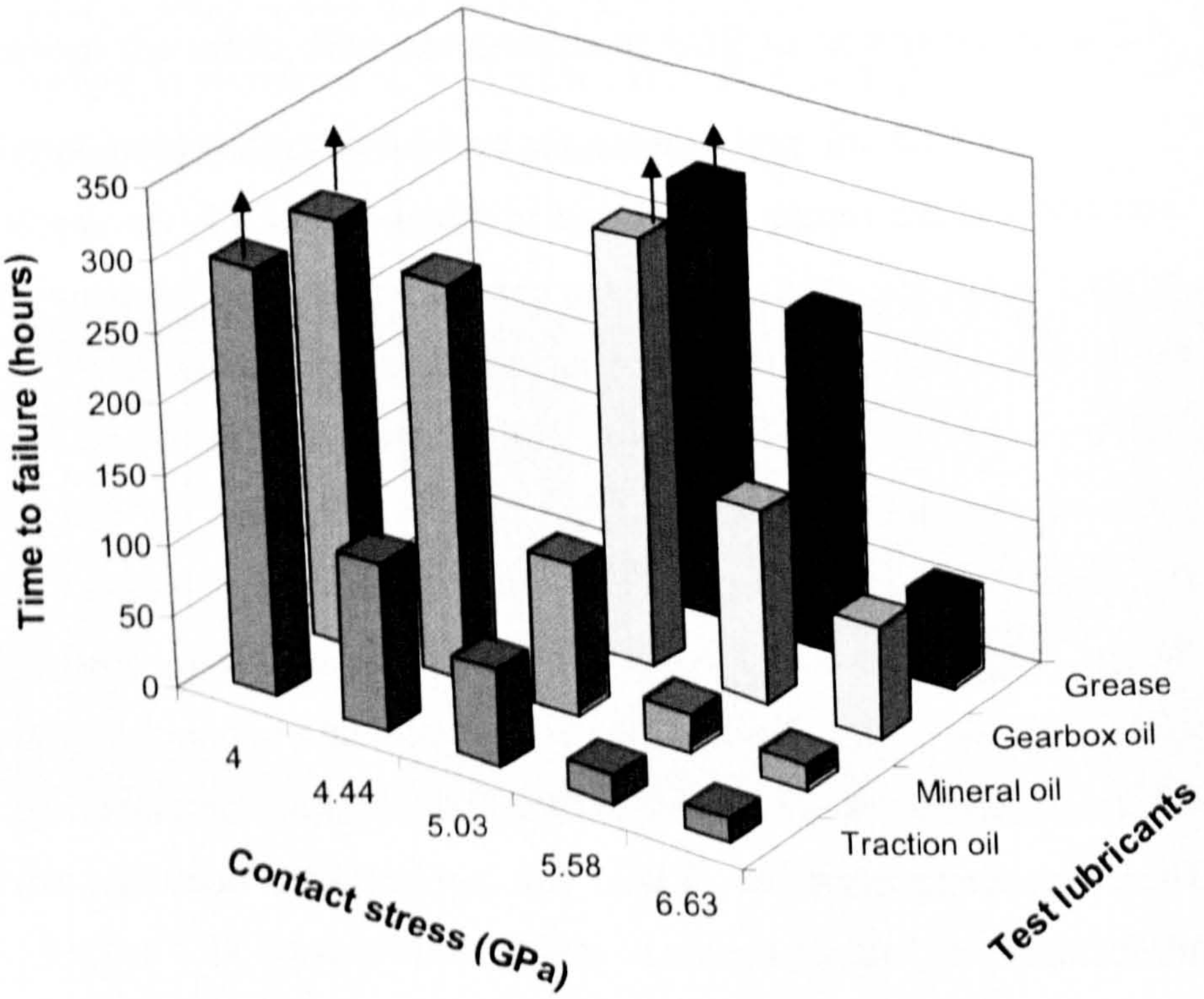

Figure 4.31 Comparison of RCF life with various lubricants and contact stresses.

The lubrication regime is studied using elasto-hydrodynamic theory and the results show that a full film exists. Therefore, for all these tests the oil film exists and fully separates the two surfaces. The use of grease may prevent the oil penetrating into the crack or delay penetration, and the crack face friction force is probably larger compared to the gearbox and traction oil. The crack face friction plays an important role in the formation of surface cracks (see Section 5.3 in Chapter 5). Increasing the crack face friction decreases the tensile stress at the contact circle, which prevents the surface cracks from forming. In addition, the mode II stress intensities along the crack front decreases with the increase of the crack face friction (see Section 5.4 in Chapter 5). This will reduce the crack

propagation rate. The test results also indicate the effect of the surface tangential traction on fatigue failure. Increasing surface tangential traction decreases rolling contact fatigue life. The use of traction fluid will increase the surface tangential traction. Higher surface traction make the crack grow fast due to the higher stress intensities caused by higher tangential traction. As a result the rolling contact fatigue life shortens.

Life-load relationship for traction fluid and mineral oils is shown in figure 4.32. Comparison of these two lubricants reveals that the RCF life performance with mineral oil is slightly better than that in traction oil. In addition, the experimental results indicate that the fatigue failure may not occur if the stress level is less than a certain value. For example, no fatigue failure is seen when the maximum contact stress is less than 4.0 GPa in the 20.25×10^7 stress cycles for both mineral oil and traction fluid.

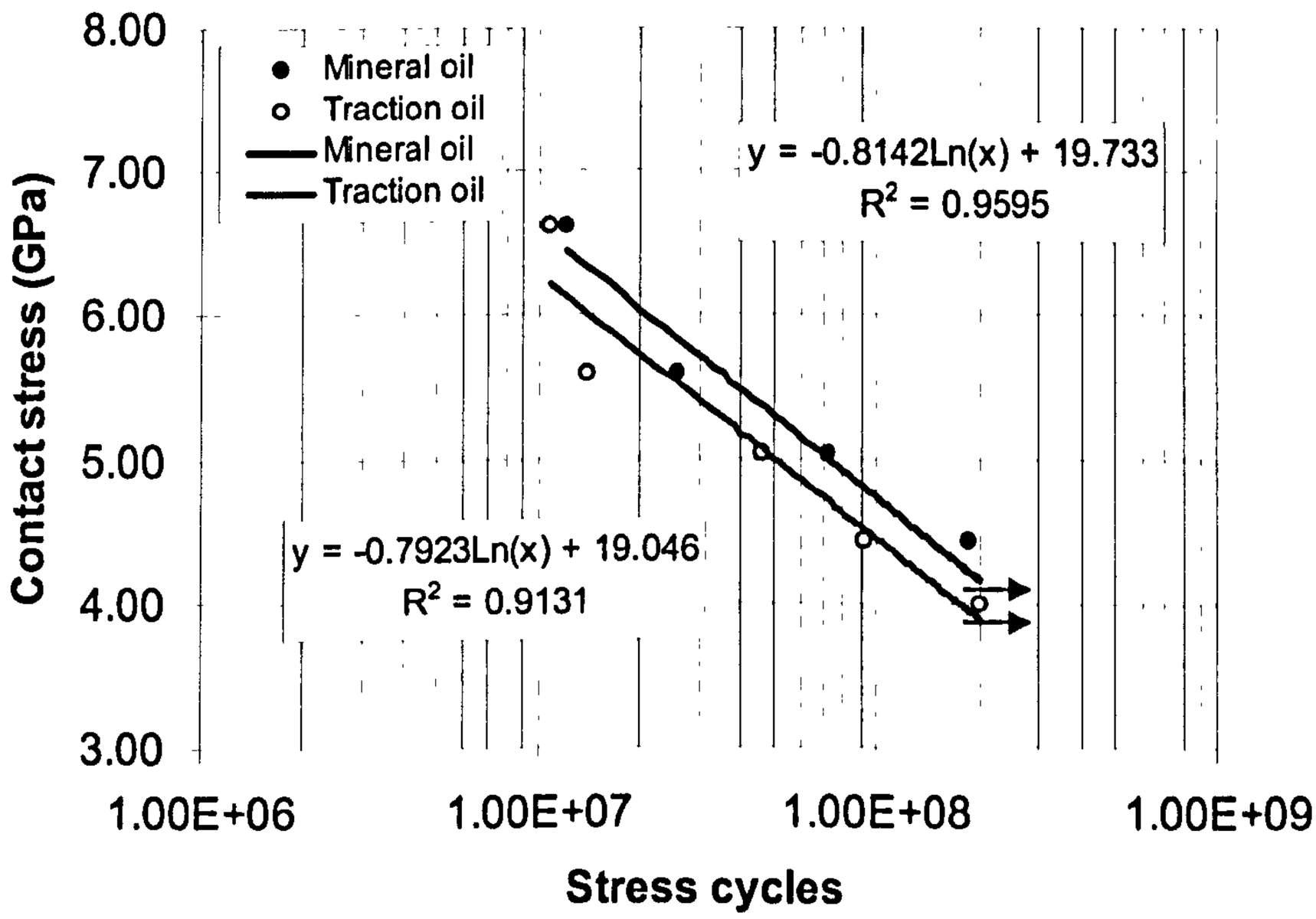

Figure 4.32 Load-life relationships with traction fluid and mineral oils.

4.3 RCF PERFORMANCE WITH ARTIFICIAL CRACKS

In the previous section, ceramic balls with naturally occurring surface ring cracks were tested using various lubricants. The rolling contact fatigue tests using natural cracks are time-consuming and subject to variability. The artificially produced surface defects are used here to study the mechanisms of rolling contact fatigue failure. The advantage of the artificial cracks is that the test conditions can be well-controlled. It is important to a fundamental understanding of the mechanisms of lubricated rolling contact fatigue failure. The crack generating device was used to produce artificial cracks as discussed in Chapter 2.

4.3.1 Influence of test lubricants

Two test lubricants, traction fluid and mineral oil, were used to examine their influence in RCF failure modes. The surface ring cracks were generated using material A balls (12.7mm diameter) impacting against material A balls (12.7mm diameter). The off-centre position 3 was selected. Table 4.6 describes detailed test conditions and results. All tests were conducted at 5000 rpm and a maximum contact pressure of 5.58 GPa. The crack orientation was in the normal position as shown in figure 3.4(a) in Chapter 3.

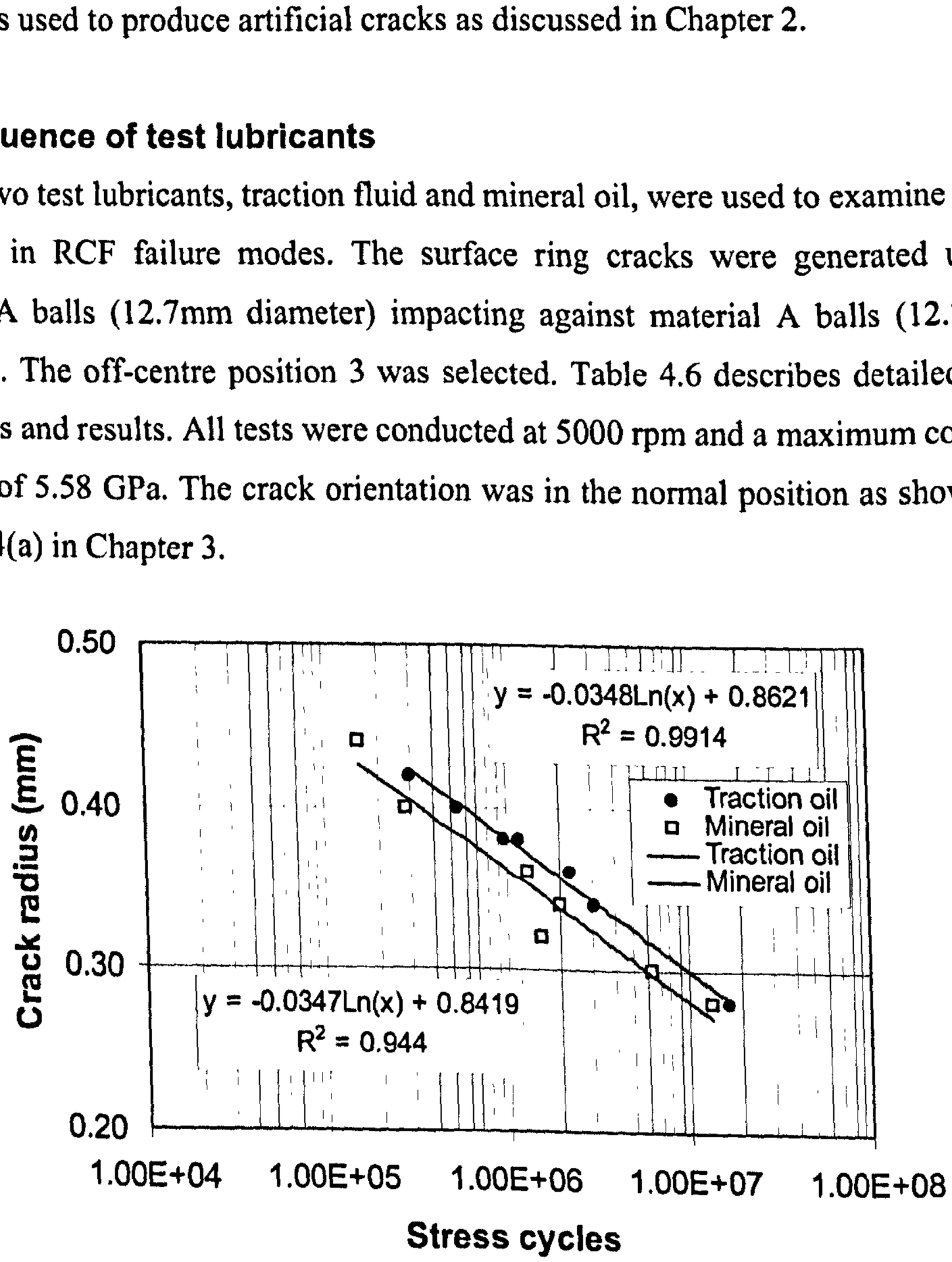

Figure 4.33 Comparison of fatigue life with traction and mineral oils

Table 4.6 Test conditions and results for the comparison of lubricant effect

Test No.	Test lubricants	Crack radius (mm)	Stress cycles ($\times 10^7$)	Test duration (Minutes)
1	Traction oil	0.42	0.03	27
2	Traction oil	0.40	0.054	48
3	Traction oil	0.38	0.099	88
4	Traction oil	0.38	0.12	107
5	Traction oil	0.36	0.225	200
6	Traction oil	0.34	0.311	276
7	Traction oil	0.28	1.665	1480
8	Mineral oil	0.44	0.016	14
9	Mineral oil	0.4	0.028	25
10	Mineral oil	0.36	0.132	117
11	Mineral oil	0.34	0.197	175
12	Mineral oil	0.32	0.156	139
13	Mineral oil	0.3	0.641	570
14	Mineral oil	0.28	1.361	1210

From figure 4.33, it can be seen that fatigue life performance is slightly different for the different lubricants. For the large cracks (artificially induced cracks), the RCF life when lubricated with the traction oil is slightly longer than that with the mineral oil. However, for the small cracks (natural cracks), the test results are different (see figure 4.32 of Section 4.2). The RCF life with traction oil was shorter than that with mineral oil lubrication. Two different failure mechanisms may be involved.

Detailed examination of surface damage was carried out using an optical and electronic scanning microscope to identify fatigue failure modes. The observation from Test 1 is shown in figure 4.34. Traction fluid was used as the lubricant. The ring crack after 12 minutes of testing is shown in figure 4.34(a). Fatigue spall occurred after 27 minutes of testing as illustrated in figure 4.34(b). The original conical face of the artificially induced crack was clearly seen at the right side of the micrograph. The failure mode for all the tests was spalling. Figure 4.35 is another example from Test 3.

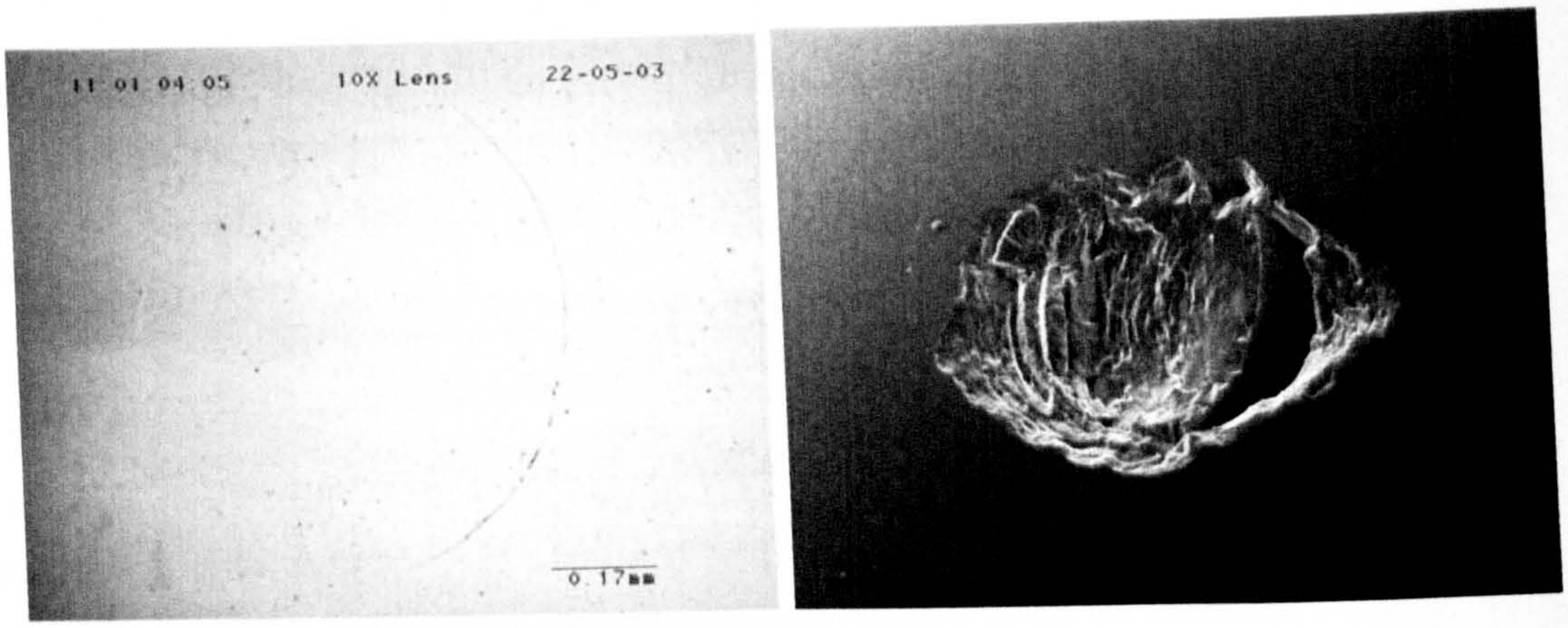

(a) After 12 minutes of testing (b) Overview of the spall (SEM)

Figure 4.34 Observation of surface damage from Test 1

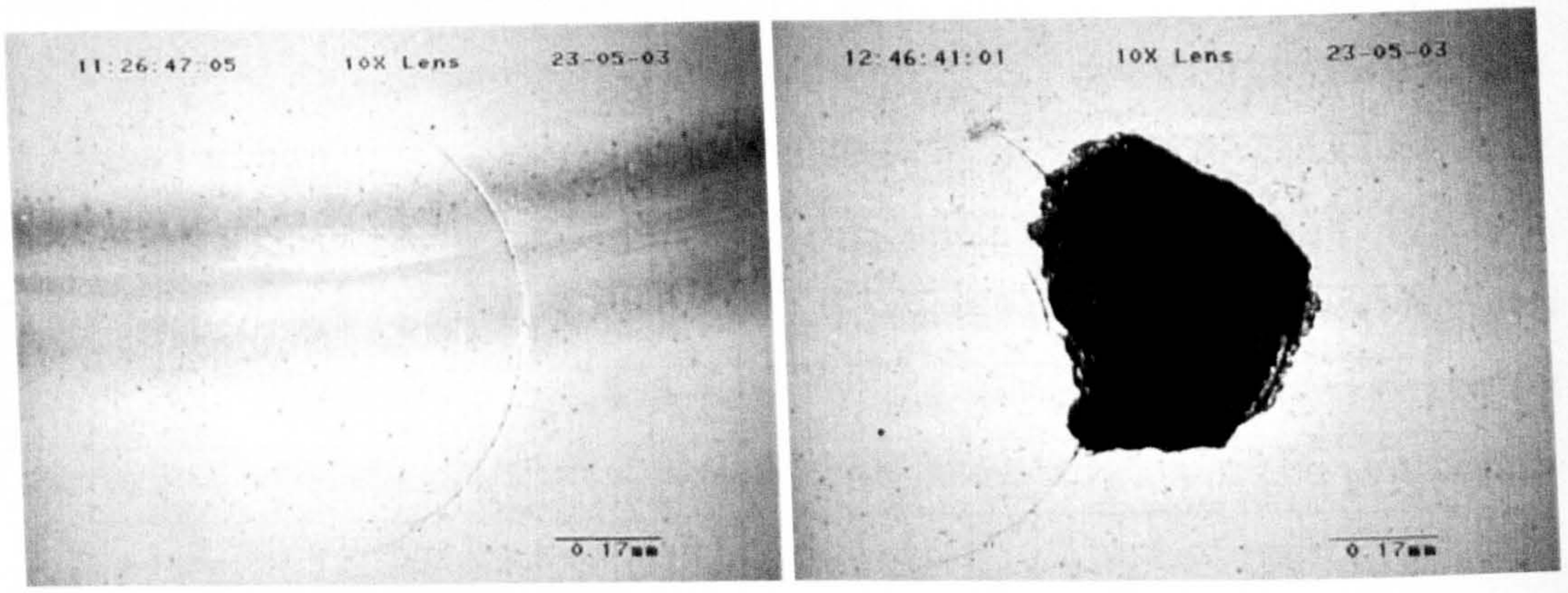

(a) After 20 minutes of testing (b) Overview of the spall (optical)

Figure 4.35 Observation of surface damage from Test 3

Figure 4.36 shows the observation from Test 8. The lubricant was a mineral oil. This is a multiple crack with the biggest crack radius of 0.44 mm (figure 4.36(a)). Therefore, the test only lasted 14 minutes and secondary cracks were seen around the spall (figure 4.36(b)). The failure mode was spalling. The spall contours could appear in either whole (figure 4.37) or half (figure 4.38) elliptical shapes.

Surface observations from Test 13 are shown in figure 4.39. Figure 4.39(a) shows an untested surface ring crack. Figure 4.39(b) shows the contact path and ring crack after one hour of testing. The spall images under the bright field and dark field light source are shown in figure 4.39(c) and 4.39(d).

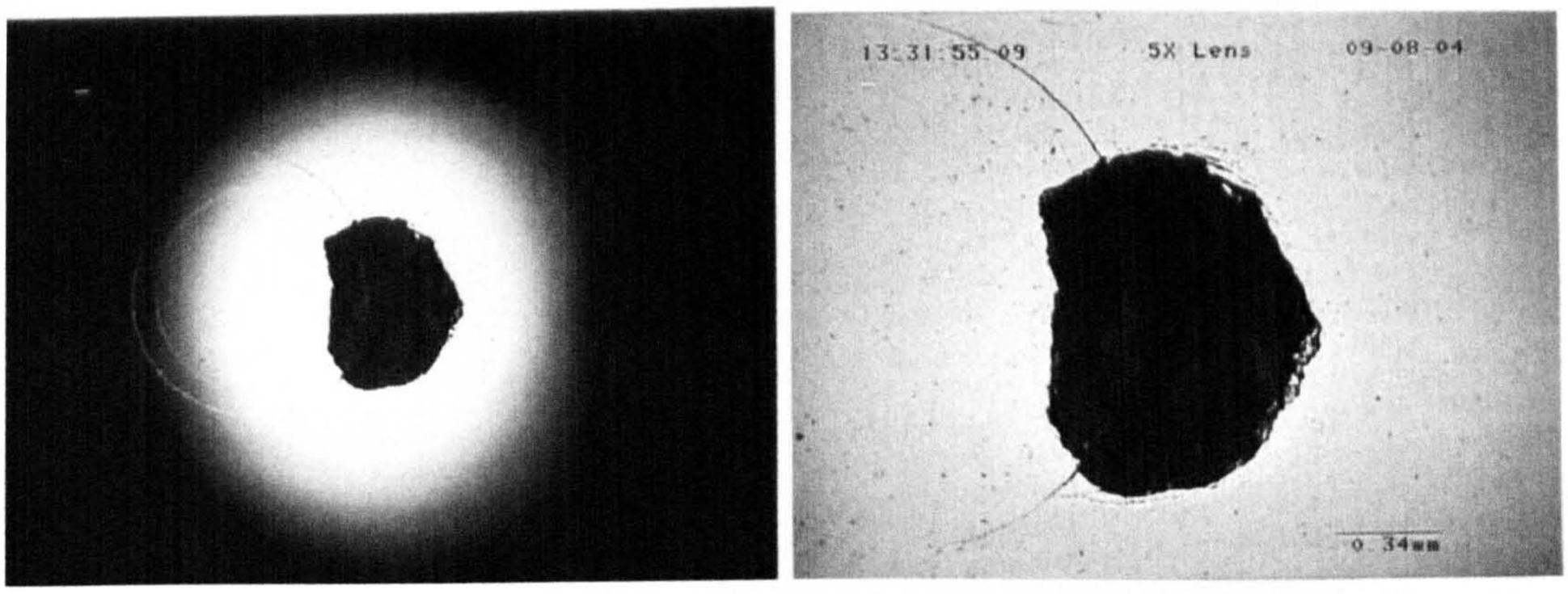

(a) After 14 minutes of testing (b) After 14 minutes of testing

Figure 4.36 Observation of surface damage from Test 8

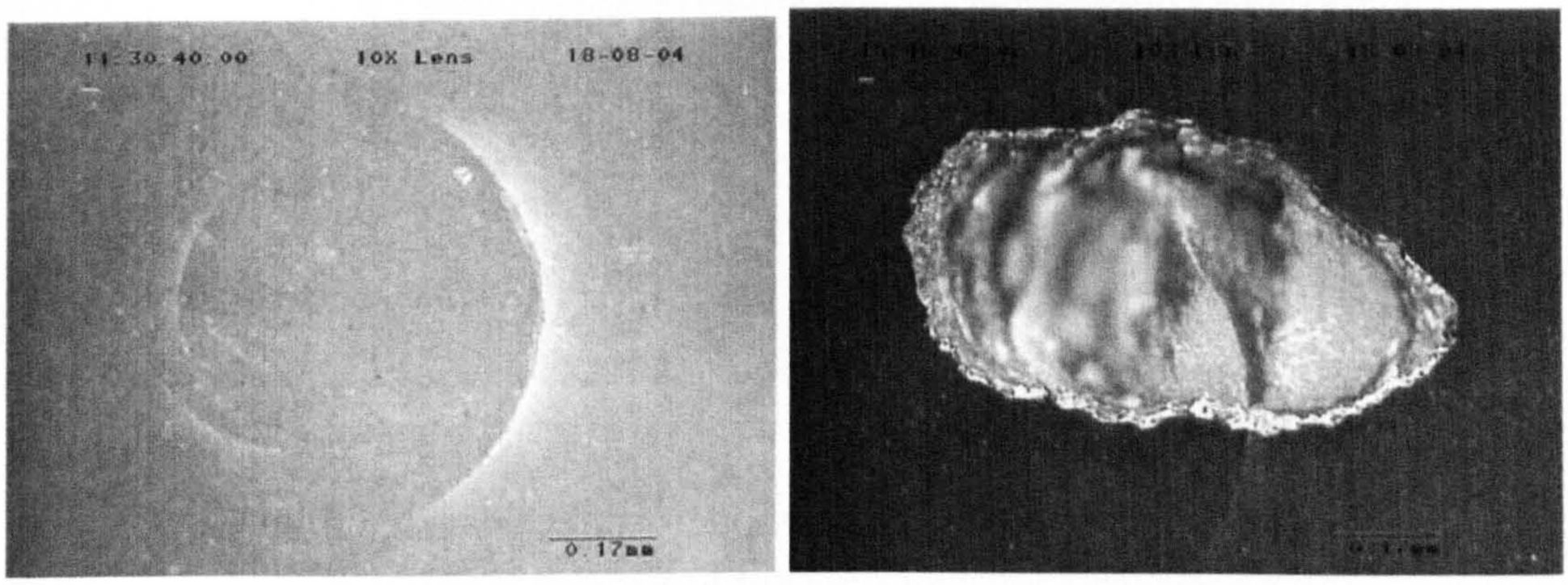

(a) Before testing. (b) After 117 minutes of testing

Figure 4.37 Observation of surface damage from Test 10

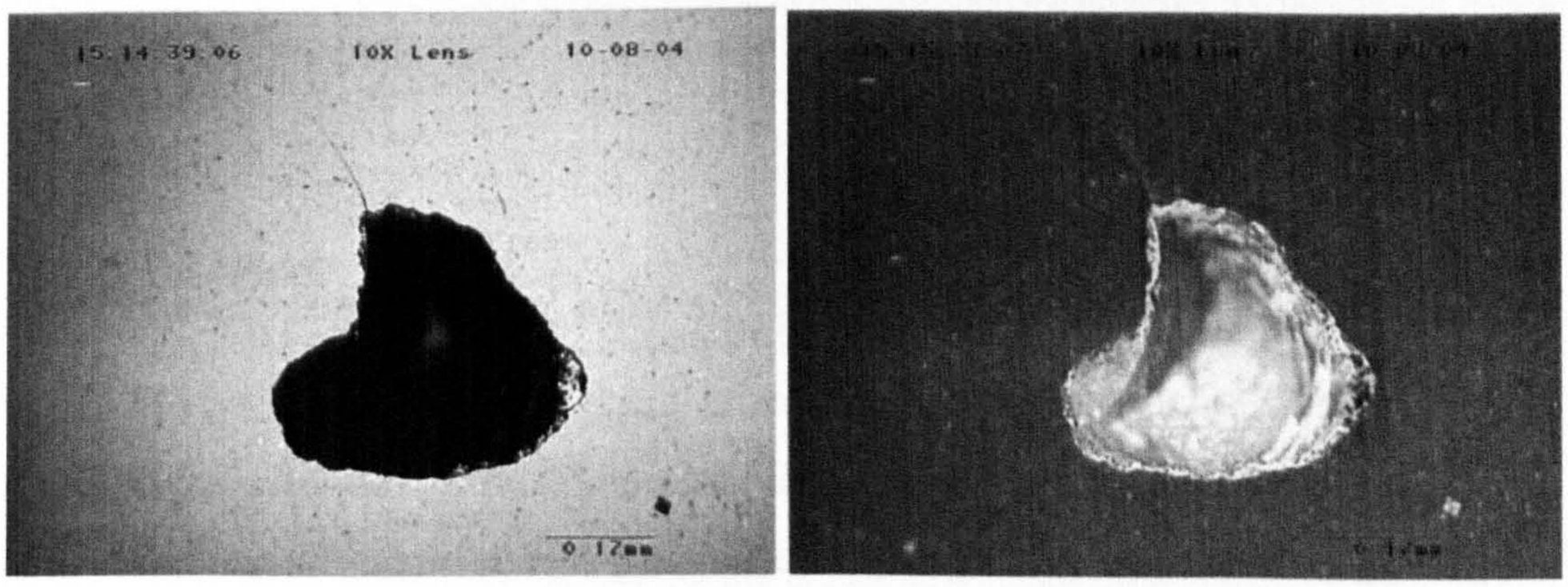

(a) Bright field image of the spall (b) Dark field image of the spall

Figure 4.38 Observation of surface damage from Test 11

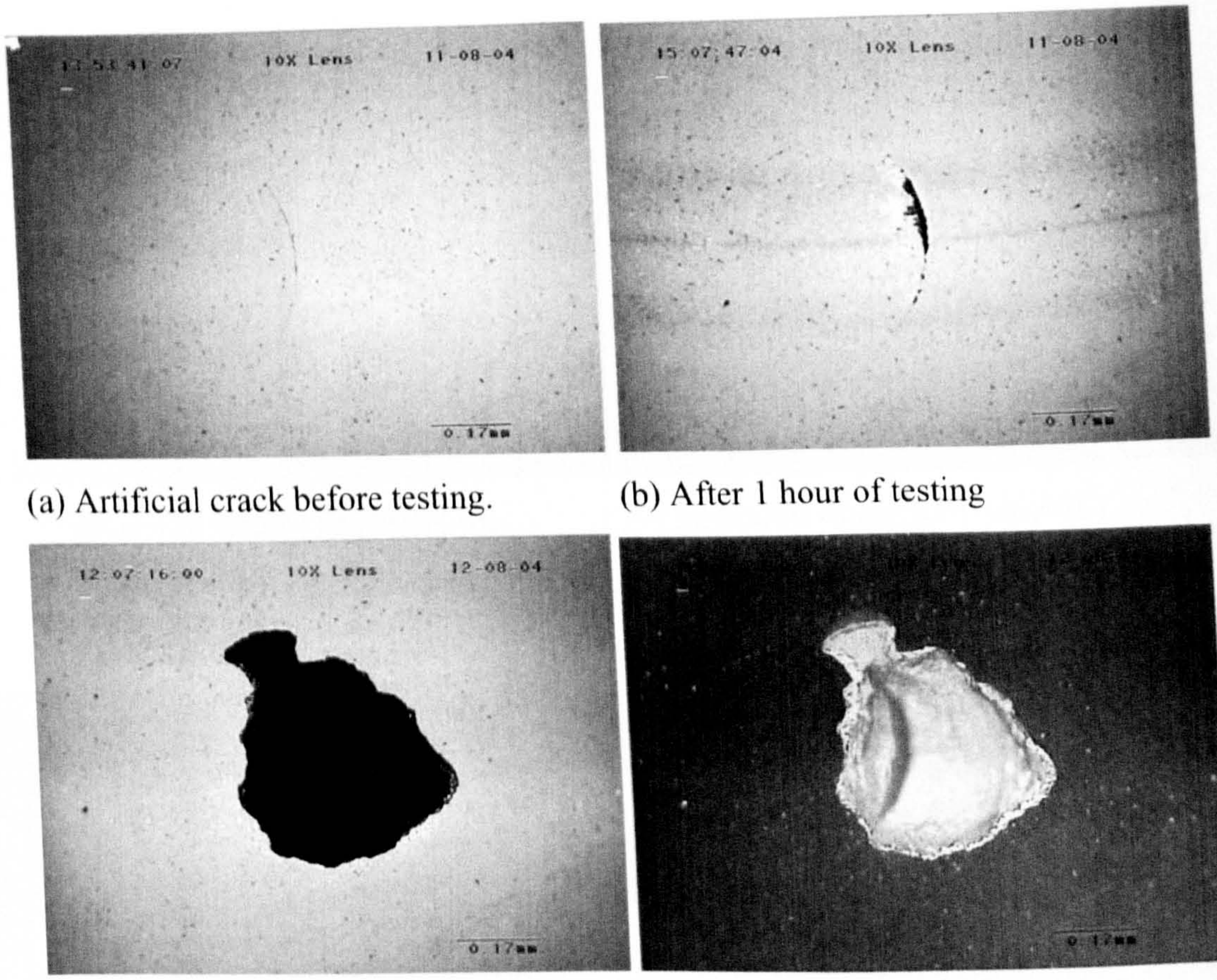

(a) Artificial crack before testing. (b) After 1 hour of testing

(c) After 9.5 hours of testing (d) After 9.5 hours of testing

Figure 4.39 Observation of surface damage from Test 13

4.3.2 Influence of ceramic materials

Test conditions for different ceramic materials are listed in table 4.7. Two types of silicon nitride ceramic ball, material A and material B, were used in order to test the effect of microstructure on rolling contact fatigue life. Figure 4.40 shows the microstructures of these two materials. Properties were described in Chapter 3, Table 3.1. All tests were conducted at the same stress level of 5.58GPa, and were lubricated by traction oil. The off-centre position 3 was selected. Different swing angles of the pendulum were selected to generate various crack sizes. The swing angles of the pendulum for material A balls were from 15° to 40°, for material B balls the angles were from 30° to 40° due to the different initiation strength of surface ring cracks.

Table 4.7 Test conditions and results for different ceramic materials

Test No.	Test materials	Crack radius (mm)	Stress cycles ($\times 10^7$)	Test duration (Minutes)
NB1	A	0.42	0.03	27
NB2	A	0.40	0.054	48
NB3	A	0.38	0.099	88
NB4	A	0.38	0.12	107
NB5	A	0.36	0.225	200
NB6	A	0.34	0.311	276
NB7	A	0.28	1.665	1480
T1	B	0.46	0.151	134
T2	B	0.46	0.177	157
T3	B	0.42	0.479	426
T4	B	0.42	0.72	640
T5	B	0.38	1.802	1602
T6	B	0.38	1.433	1274

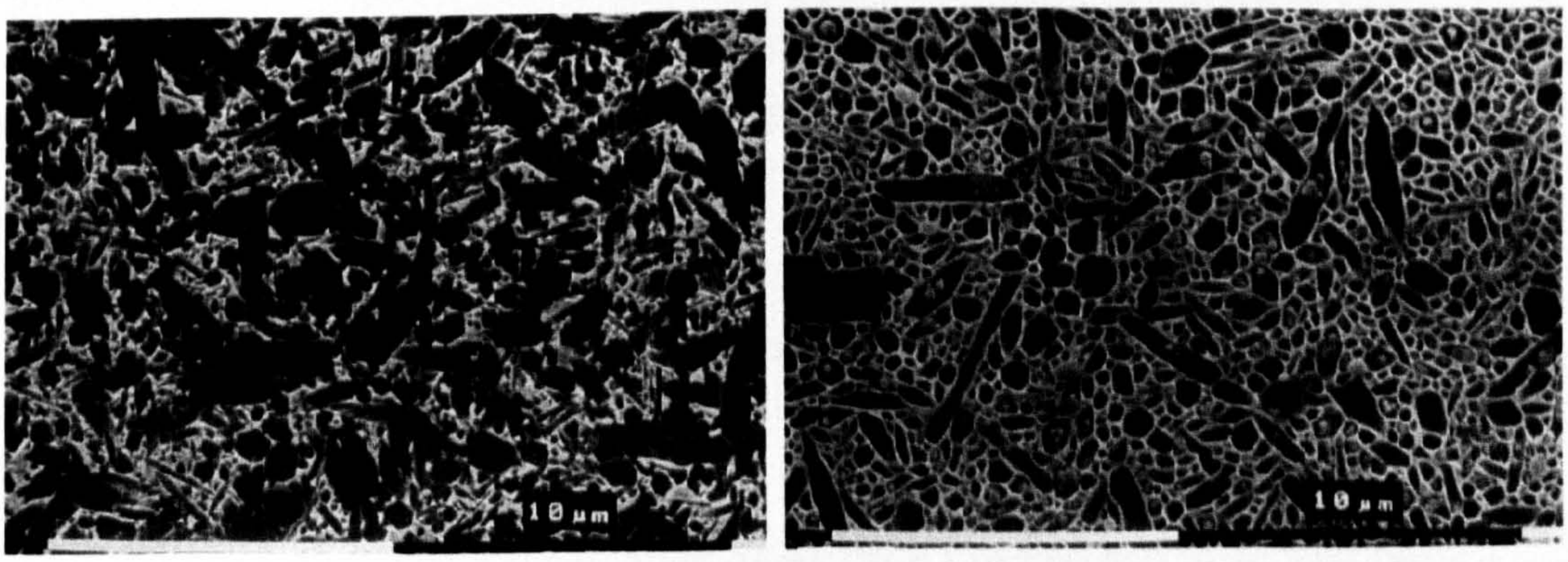

(a) Material A (b) Material B

Figure 4.40 Microstructures of ceramic materials (Courtesy of SKF)

Rolling contact fatigue life with various crack sizes was tested and the results are shown in figure 4.41. The failure mode for all the tests was spalling. There is a big difference in the fatigue life performance for these two materials. It can be seen

that type B material showed better fatigue life performance than type A material. The fatigue life of balls (material B) is about 15 times higher than the fatigue life of balls (material A). The fatigue testing results imply that silicon nitride material with higher initiation strength will display a longer fatigue life. The mechanism for this will be clearly understood in the numerical analysis, which is described in Chapter 5. For both materials, fatigue life decreases as the crack size increases. There is a high correlation between the fatigue life and crack size for both materials. Therefore, fatigue life performance at any other crack sizes may be predicted according to the following life-size relationship diagram (figure 4.41).

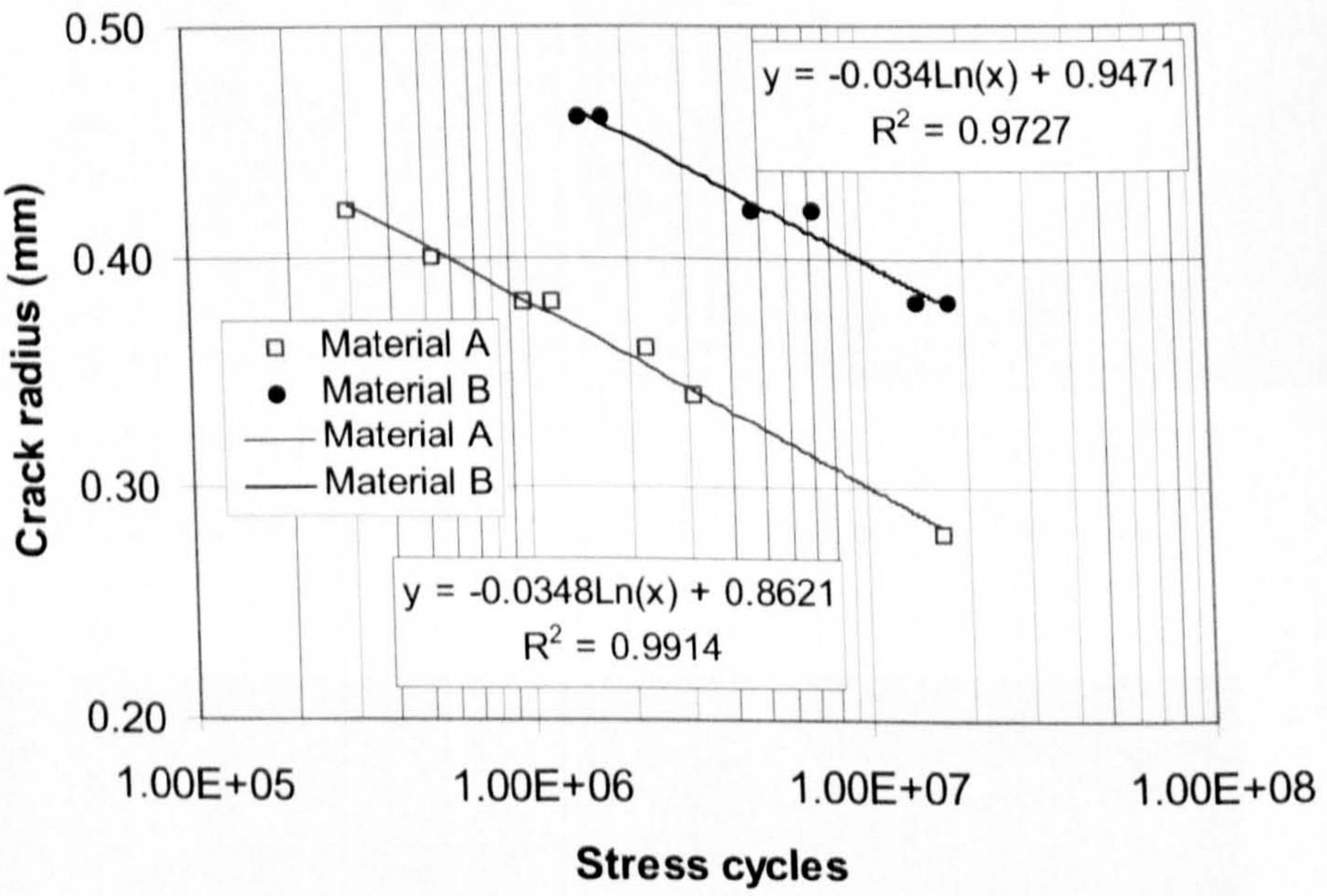

Figure 4.41 Influence of ceramic materials on fatigue life

Detailed examination of surface damage at different test stages has been carried out to understand the failure mechanisms. Figure 4.42 shows an example from material A. Unlike the natural cracks, the impact ring crack can be seen under a normal white light source. However, the ring crack becomes much clearer after a few minutes of testing. Figure 4.42(a) illustrates the crack and the contact track after

20 minutes of testing. Note that there were three cracks on the contact track, one was on the left and two were on the right. The contact track was dark. After 84 minutes of testing, the contact track became darker and the edge of the contact path was clear as shown in figure 4.42(b). No more wear was found except the initial surface damage. The overview of the fatigue spall was shown in figure 4.42(c). The detailed SEM image was shown in figure 4.42(d). The secondary surface cracks were clearly visible at the edge of the spall.

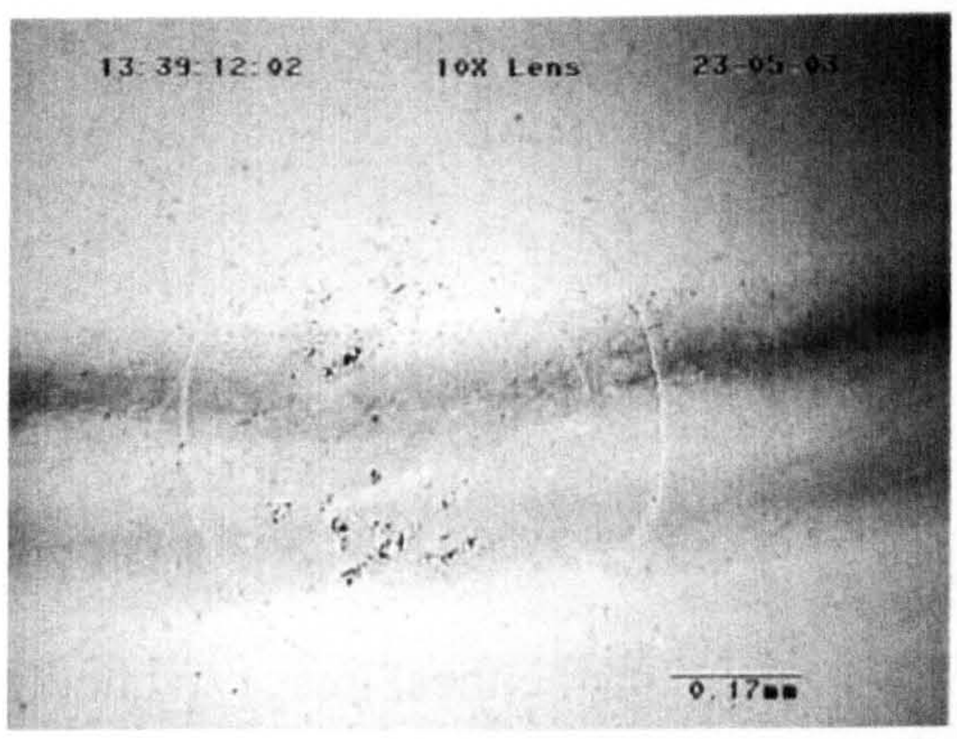

(a) After 20 minutes of testing

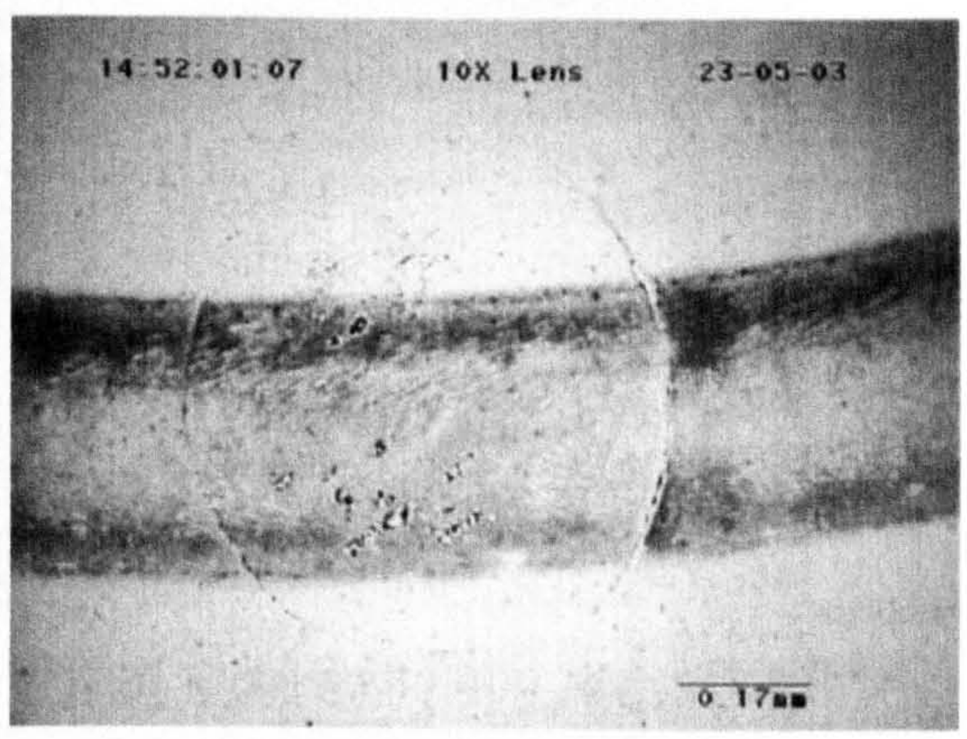

(b) After 84 minutes of testing

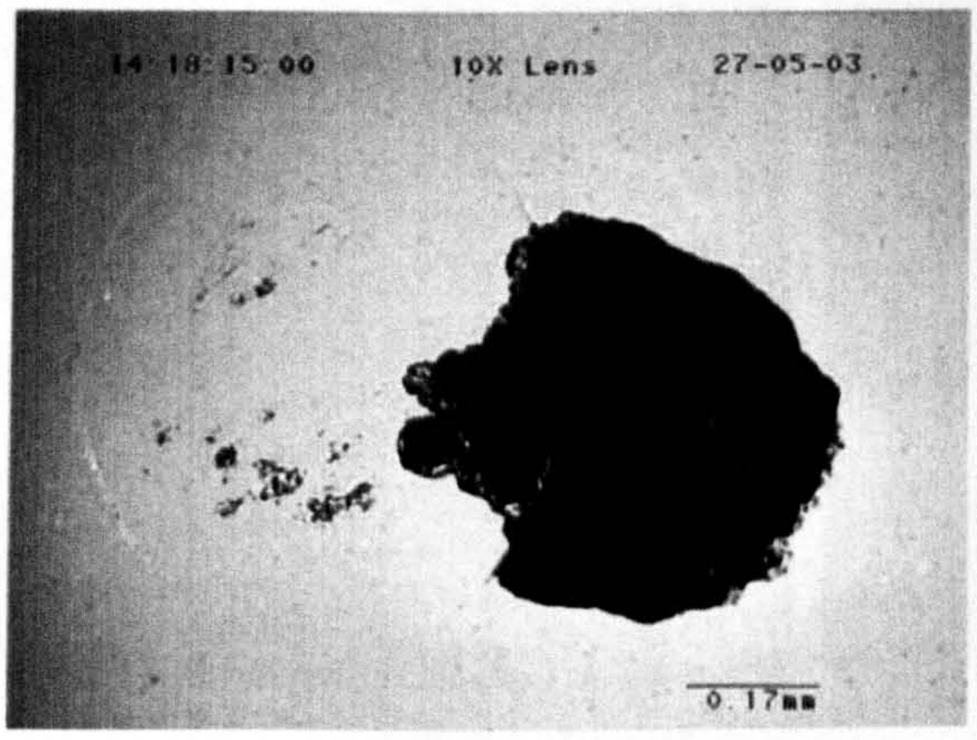

(c) Spall overview (107 minutes)

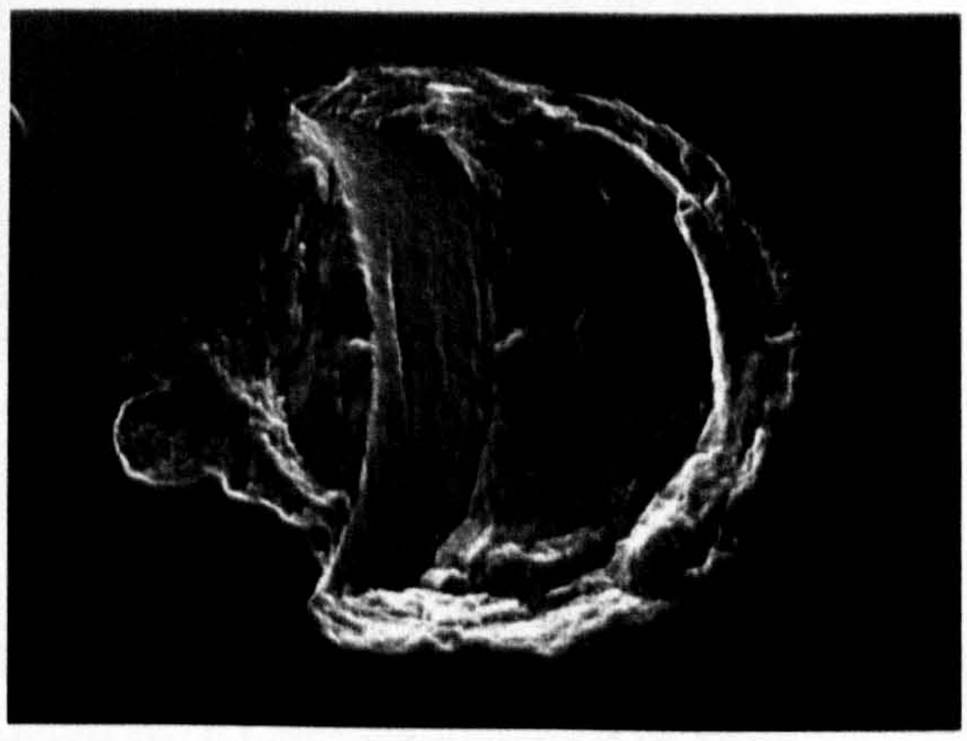

(d) Spall SEM micrograph

Figure 4.42 Surface observation of artificial cracked ball from Test NB4

Figure 4.43 shows the result from material B. This silicon nitride of material B has a good impact resistance compared with material A. The pre-test crack is shown in figure 4.43(a). Apart from the impact ring cracks, there was slight initial surface damage in the central zone. This initial damage looks like small pits

removed from the surface. This damage only happened when the drop height was big. There was no further wear observed around these pits. After 134 minutes of testing, the fatigue spall occurs as shown in figure 4.43(b) and (c). The detailed SEM image is shown in figure 4.43(d), on which the primary ring crack face and the secondary cracks are shown clearly.

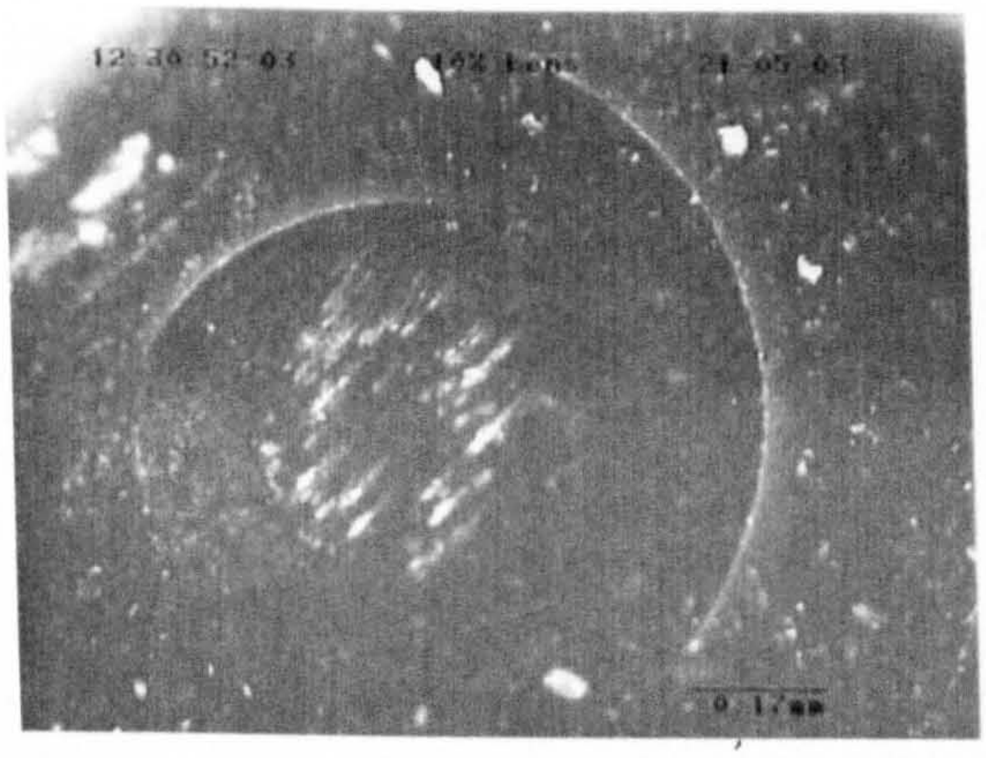

(a) Pre-test ring crack (dark light)

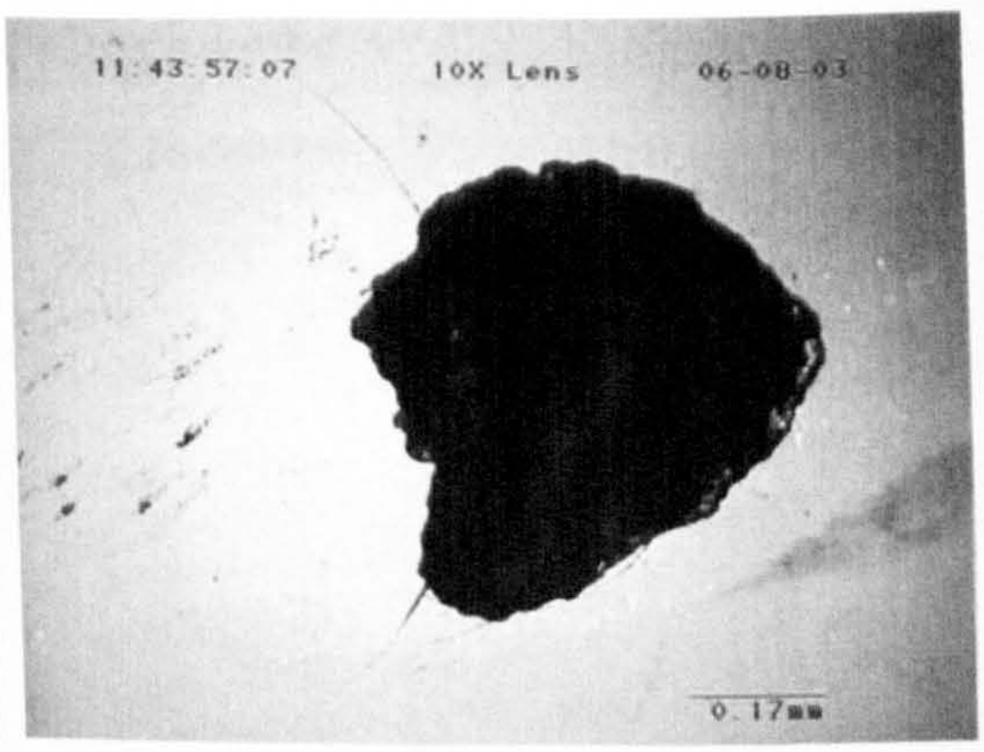

(b) Spall optical image (white light)

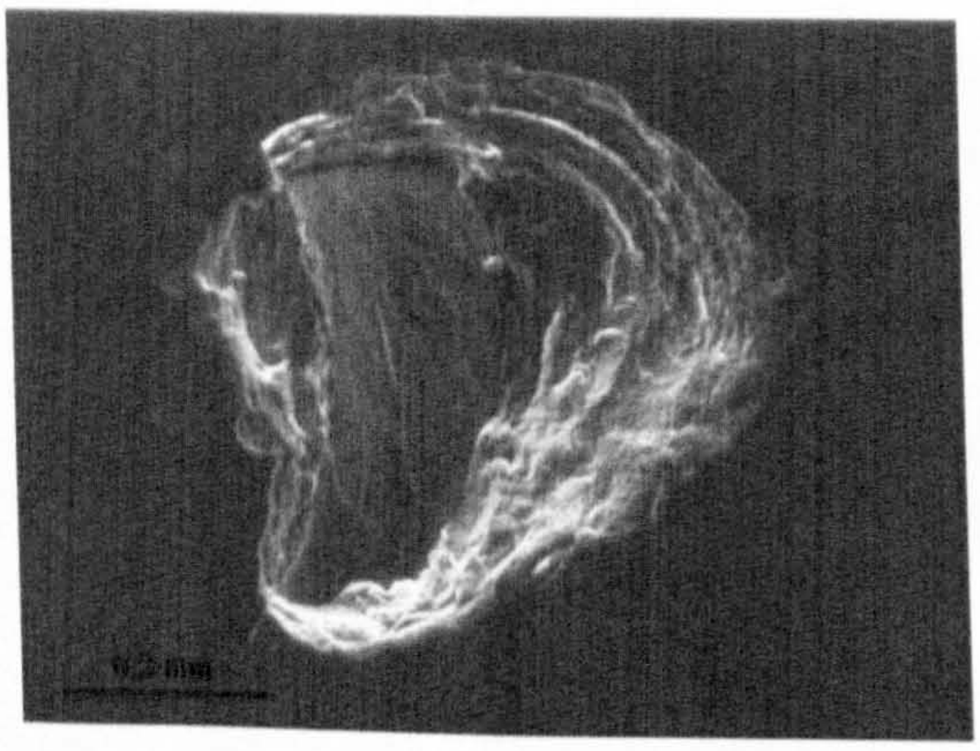

(c) Spall overview

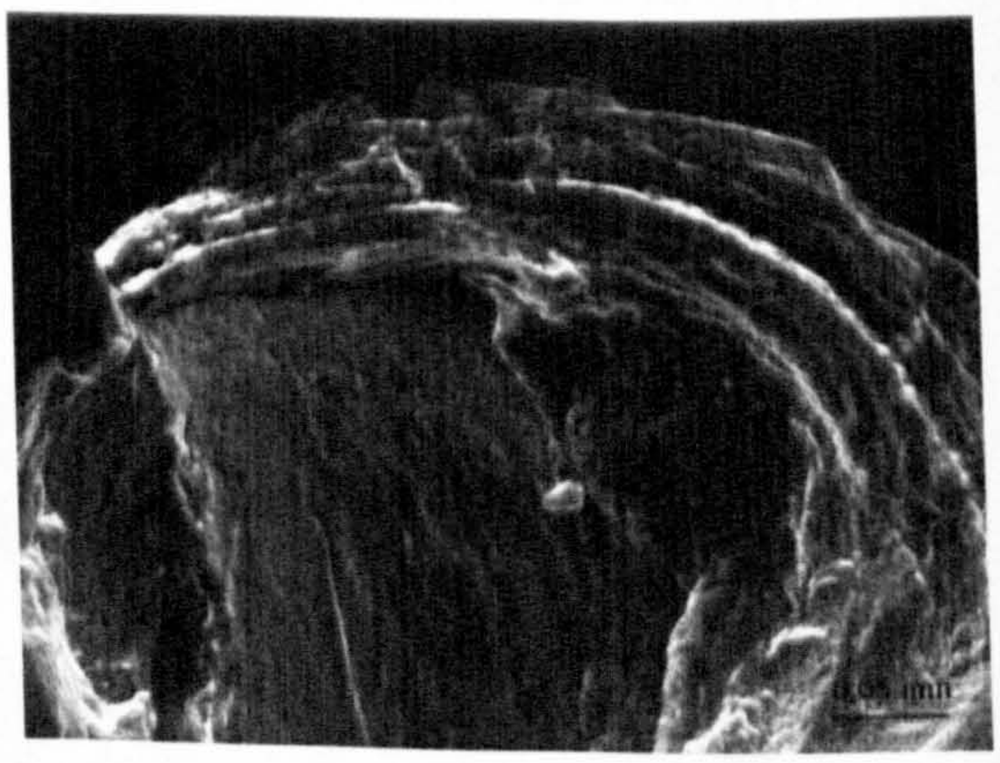

(d) Detailed SEM micrographs

Figure 4.43 Surface observation of artificial crack from Test T1

4.3.3 Influence of rolling directions

The influence of the rolling directions on the RCF failure in lubricated conditions was investigated experimentally. The test results are given in this section. Table 4.8 lists the test conditions. All samples were selected using 12.7mm balls (material A) impacting 12.7mm balls (material A). The off-centre position 2 was adopted to generate the surface ring cracks. The tests were performed at a speed of 5000 rpm and the maximum contact pressure of 5.58GPa. All the tests were lubricated using traction oil. Tests N1 to N7 were performed at the normal position, and Tests R1 to R7 were performed at the reverse position. The normal position is illustrated in Chapter 3, figure 3.4(a) and the reverse position is illustrated in Chapter 3, figure 3.4(b).

Table 4.8 Test conditions and results for different rolling directions

Test No.	Crack orientation	Crack radius (mm)	Stress cycles ($\times 10^7$)	Test duration (Minutes)
N1	Normal	0.42	0.014	12
N2	Normal	0.40	0.026	23
N3	Normal	0.38	0.068	60
N4	Normal	0.36	0.087	77
N5	Normal	0.32	0.27	241
N6	Normal	0.3	0.56	498
N7	Normal	0.28	0.68	608
R1	Reverse	0.44	0.007	6
R2	Reverse	0.42	0.006	5
R3	Reverse	0.38	0.064	57
R4	Reverse	0.36	0.052	46
R5	Reverse	0.32	0.208	185
R6	Reverse	0.28	1.673	1487
R7*	Reverse	0.28	6.07	5400*

* Test is suspended without spalling after 5400 minutes of testing

Figure 4.44 shows the life-size relationship for different rolling directions. The results indicate that the RCF life decreases as the crack radius increases for both rolling directions. No significant RCF life difference is seen between these two directions. The failure mode was by ceramic ball spalling for both rolling directions.

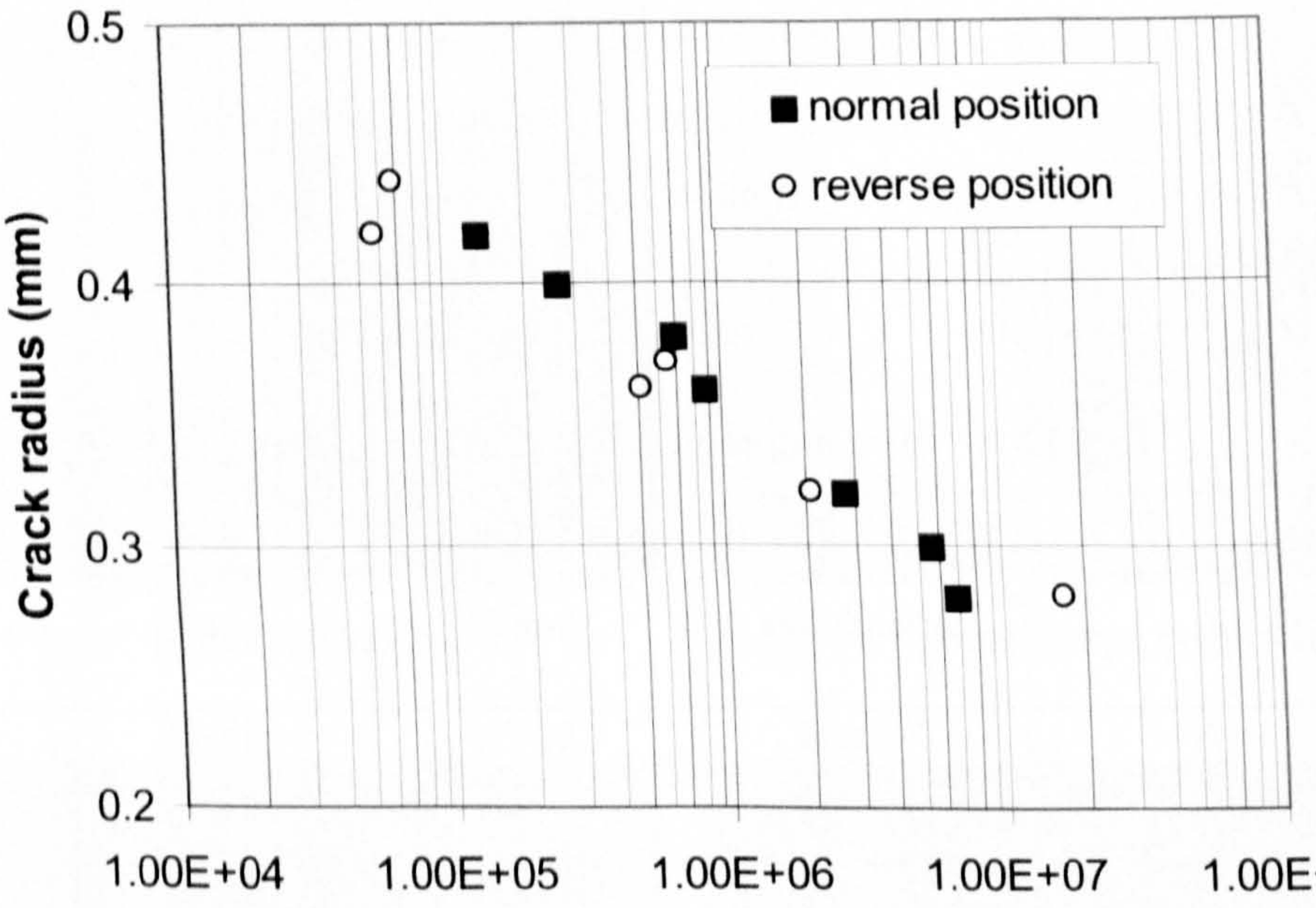

Figure 4.44 Influence of rolling direction on fatigue life

The silicon nitride balls, which failed during the fatigue test, were analysed in detail to determine the failure mechanism. The results of surface examinations from Test N1 are shown in figure 4.45. Figure 4.45(a) shows a typical artificially induced ring crack, illustrated by a microscopic image under normal light. The general spall morphology shown in figure 4.45(b) was typical of that seen previously on RCF tests. The spall origins and general ball surface conditions were determined on the SEM. As may be seen in figure 4.45(c), a spall would originate at crescent-shaped Hertzian cracks extending into the silicon nitride ball. The right side of the spall with delamination surface is shown in figure 4.45(d).

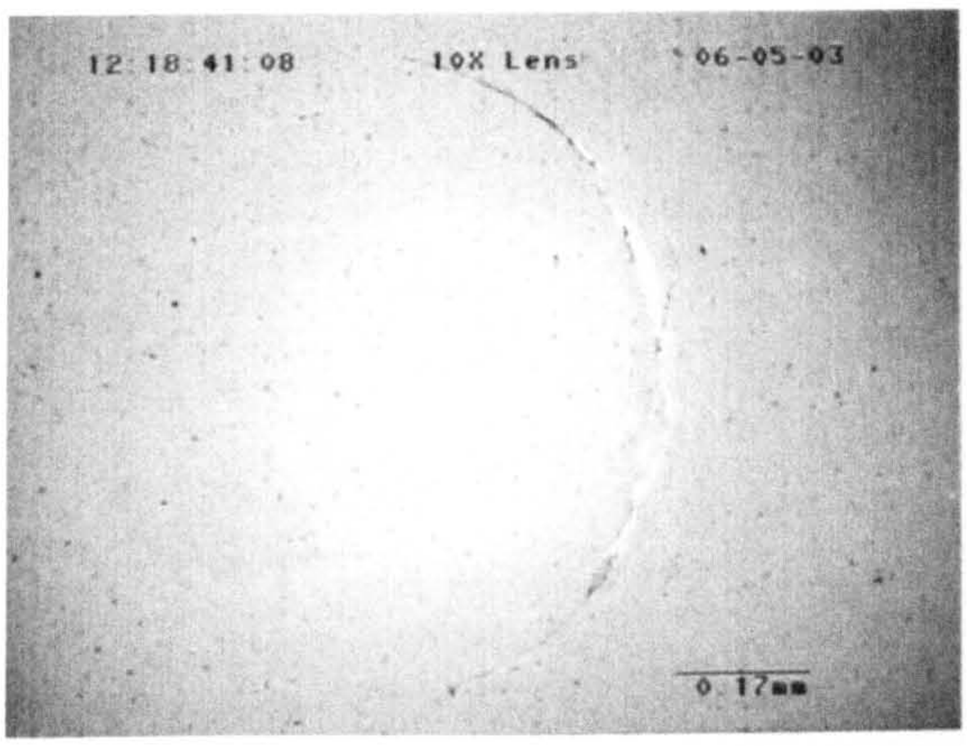

(a) Ring crack before test

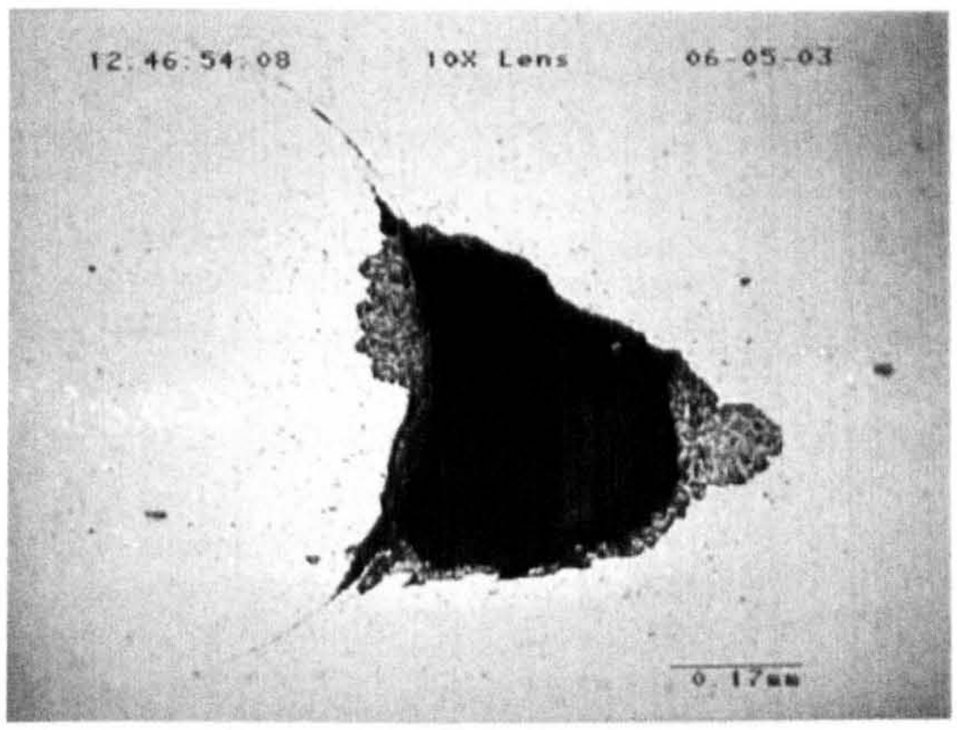

(b) Spall optical image (12 minutes)

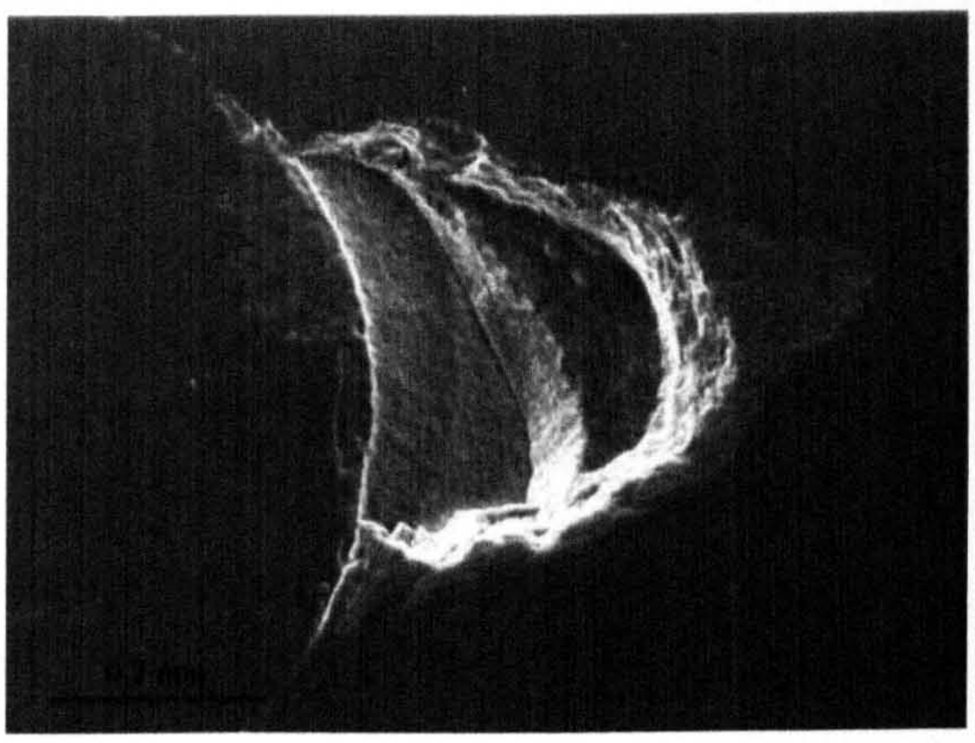

(c) Spall SEM micrograph

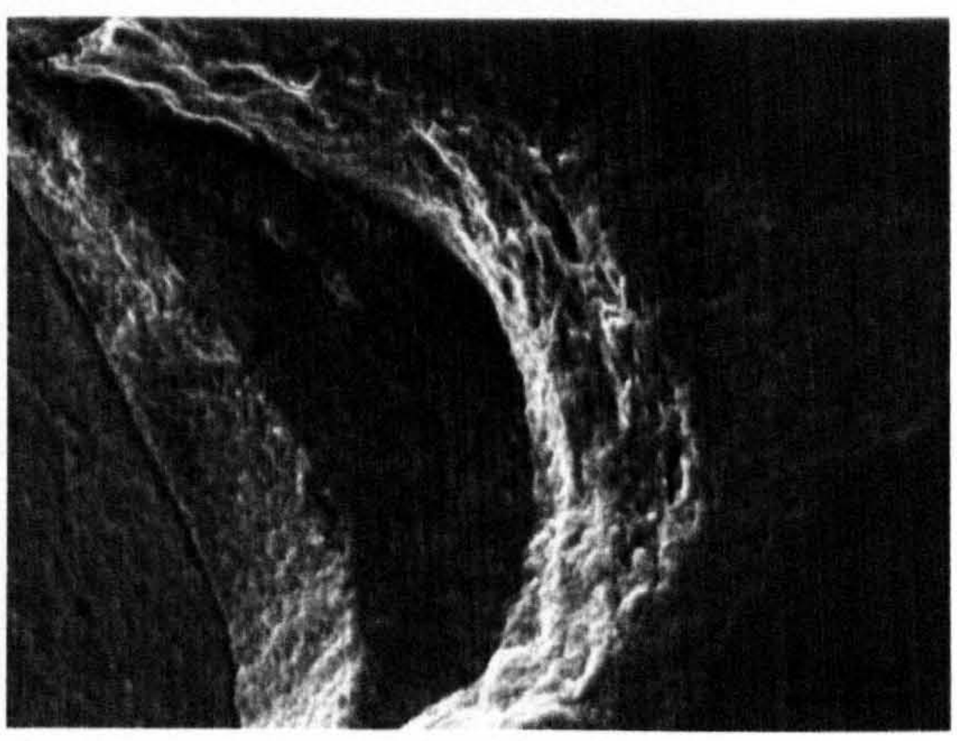

(d) Right side with delamination surface

Figure 4.45 Observation of surface damage from Test N1

Figure 4.46 shows surface damage micrographs from Test N2. The appearance of the ring crack after 10 minutes of testing is shown in figure 4.46(a). The contact path is right across the middle of the crack. Figure 4.46(b) illustrates an optical image of fatigue spall. SEM micrograph provides all details of fractured surface (figure 4.46(c)). On the left side, the original ring crack face shows a smooth surface. No fatigued crack growth is seen along the rolling direction. The fatigue crack only propagates opposite to the rolling direction. On the right side of figure 4.46(c), the fatigued surface is clearly visible. The high magnification of the curved striations is shown in figure 4.46(d). The traces of the secondary cracks are clearly seen on both edges.

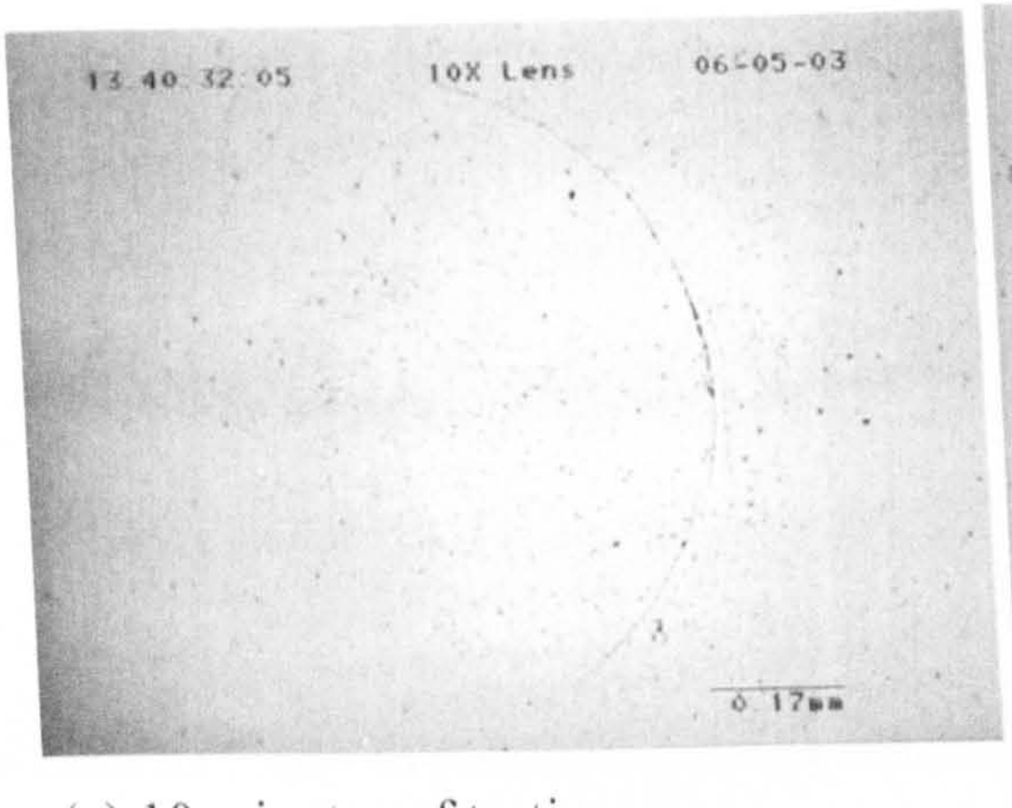

(a) 10 minutes of testing

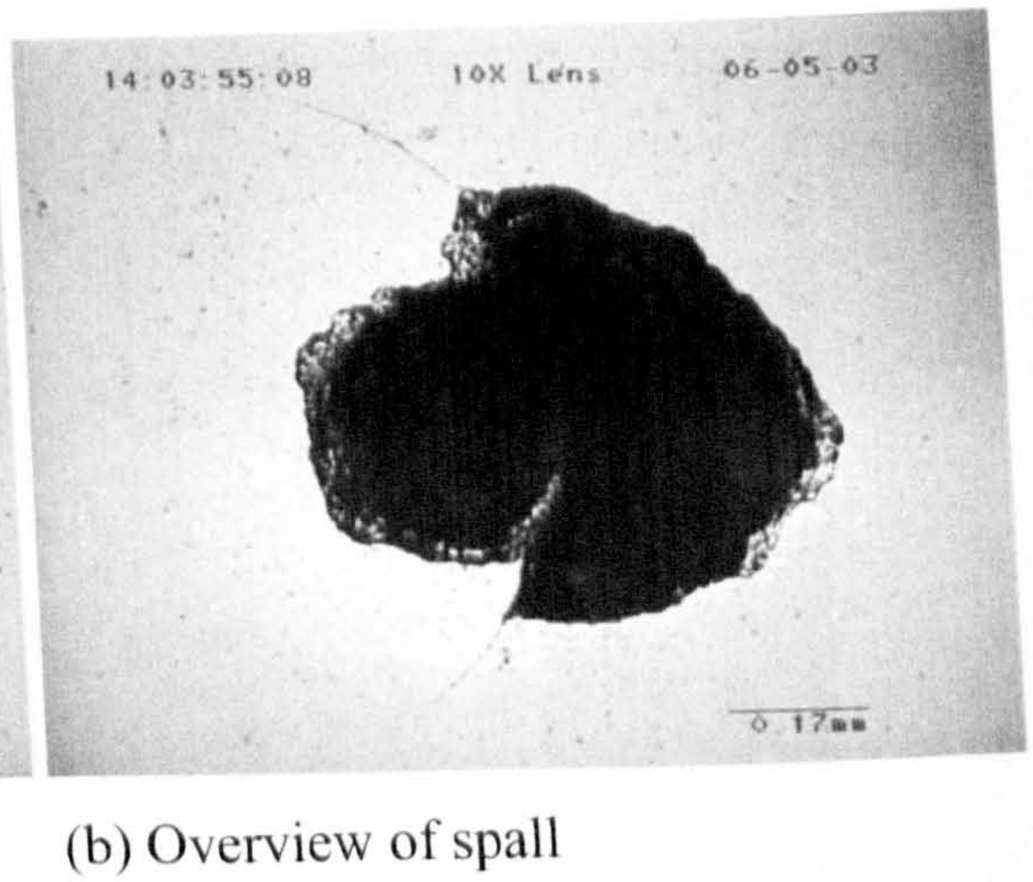

(b) Overview of spall

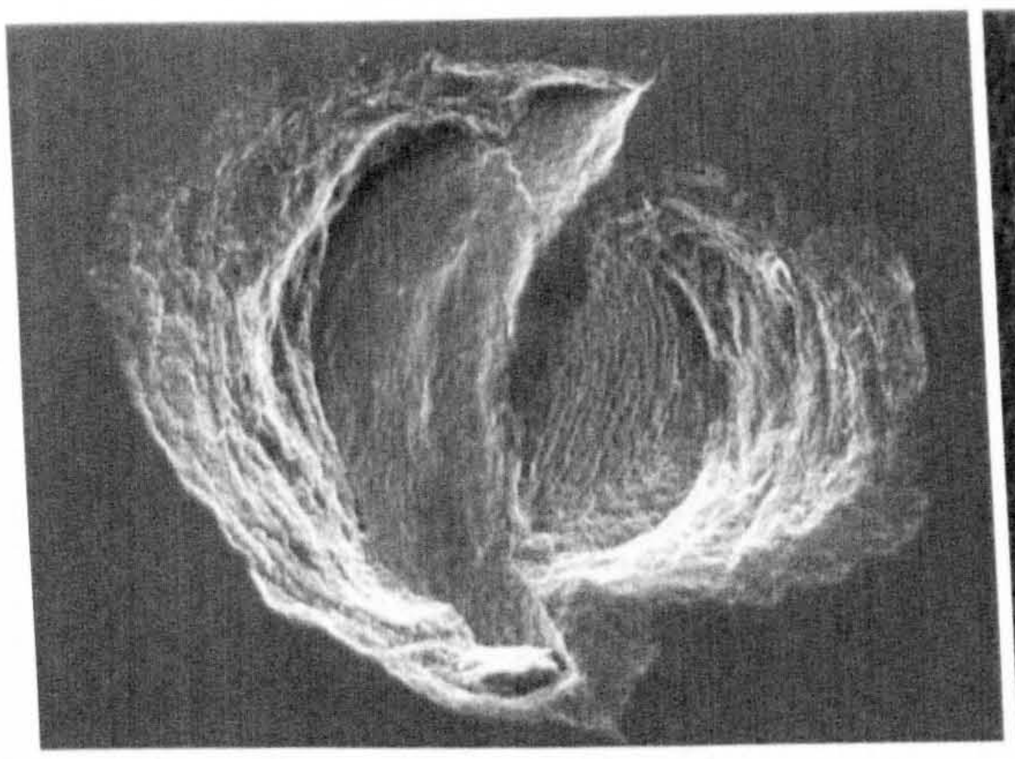

(c) SEM micrograph

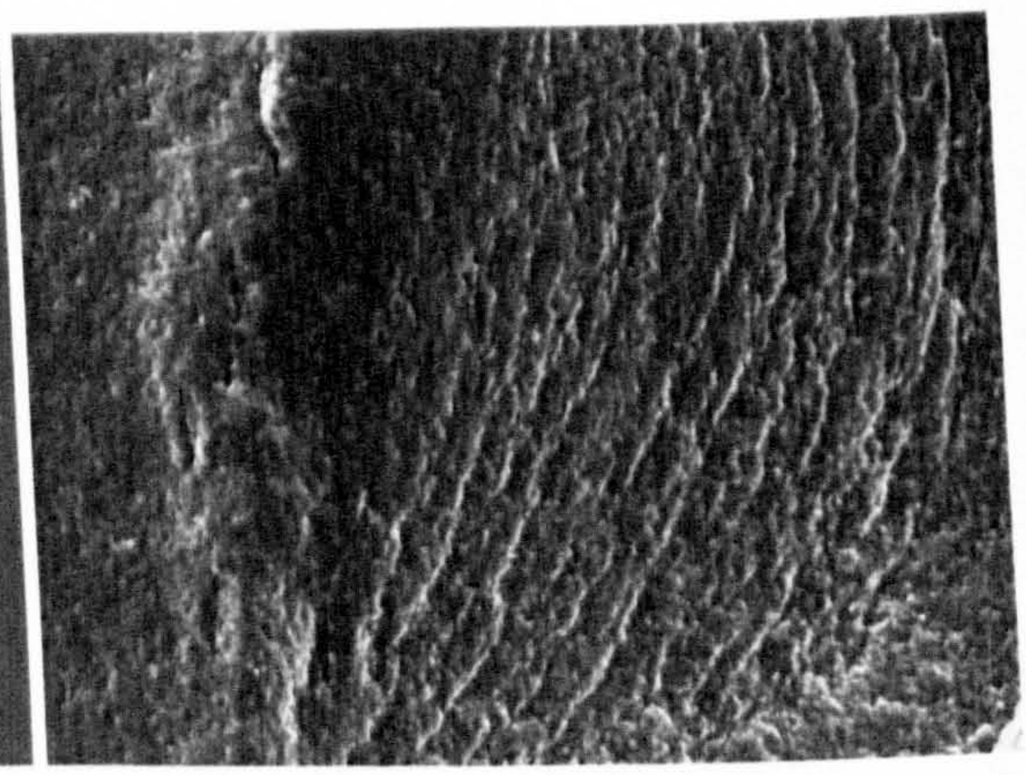

(d) Curved striations

Figure 4.46 Observation of surface damage from Test N2

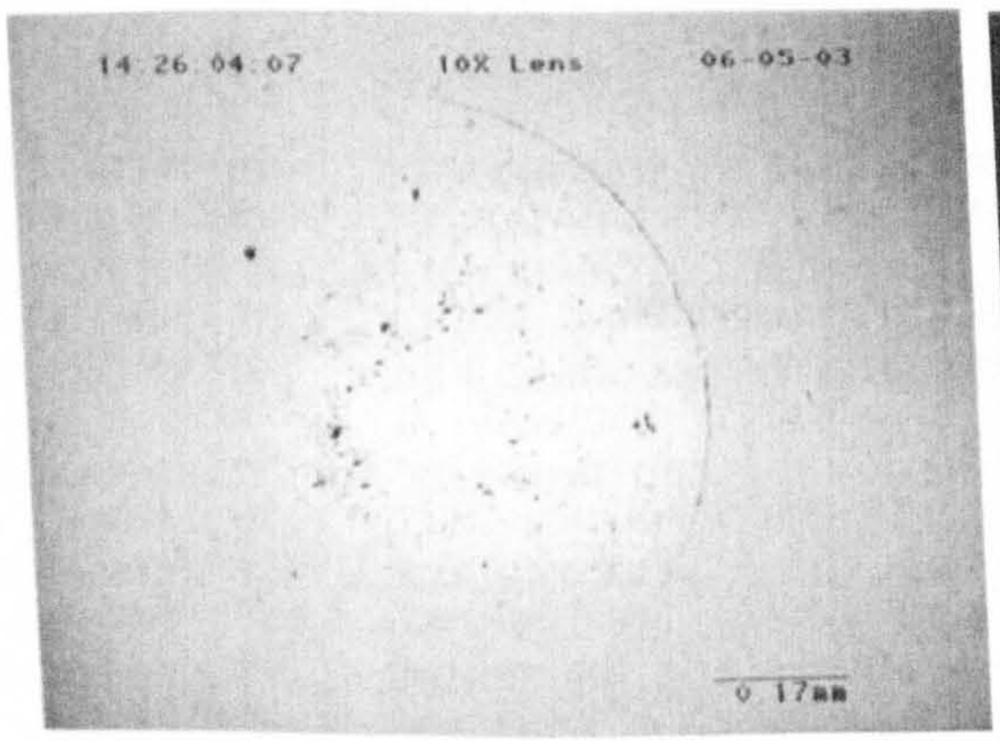

(a) Pre-test ring crack

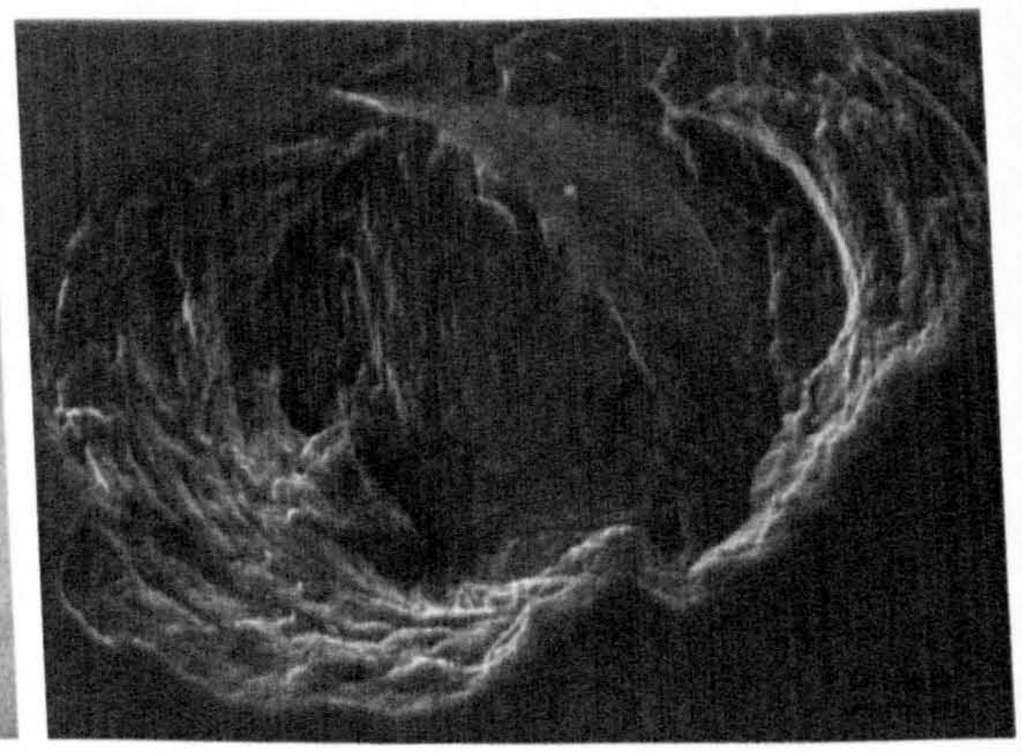

(b) SEM micrograph of a spall

Figure 4.47 Observation of surface damage from Test N3

Surface observation of the artificial crack from Test N3 is shown in figure 4.47. Figure 4.47(a) shows a pre-test ring crack. The fatigue spall is shown in figure 4.47(b). The original artificial crack is clearly seen in this photograph. The primary crack face is smooth when compared to the fatigued surface. The brittle fracture surface is apparent in the left part. The secondary cracks can be seen clearly on both sides.

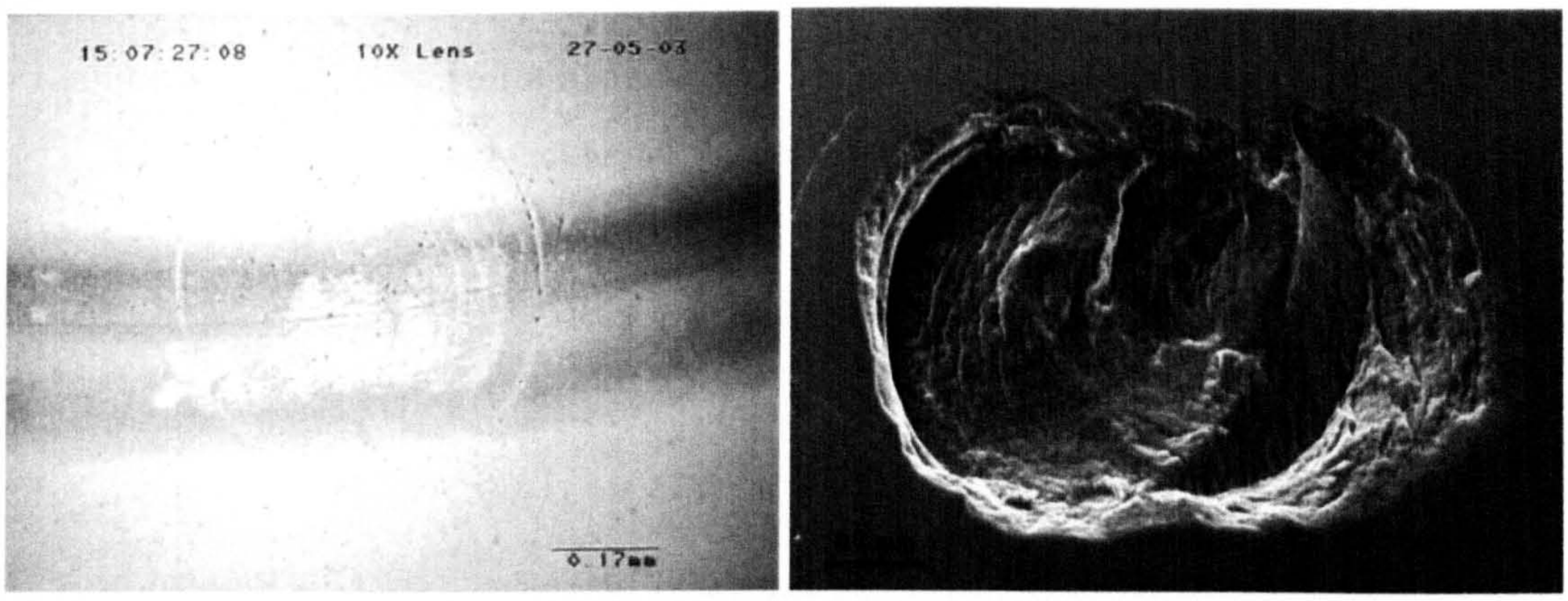

(a) After 20 minutes of testing

(b) After 77 minutes of testing

Figure 4.48 Observation of surface damage from Test N4

The post-test analysis of surface damage from Test N4 is shown in figure 4.48. It can be seen, the original crack with cone surface can still be identified clearly after spall formation. On the left side of the spall, the subsurface delamination with typical curved striations is exhibited clearly. The secondary surface cracks have developed beyond the curvature of the spall and can be seen clearly.

Test results from ceramic/steel rolling contact lubricated with a traction fluid and the reverse rolling direction are shown in figures 4.49 to 4.51. Test R1, with crack radius 0.44mm, failed after 6 minutes of testing as shown in figure 4.49. Test R3, with crack radius 0.38mm, failed after 57 minutes of testing (figure 4.50). All the tests performed in reverse position confirmed that the rolling direction is not the key factor in rolling contact fatigue life compared with the tests performed in normal position.

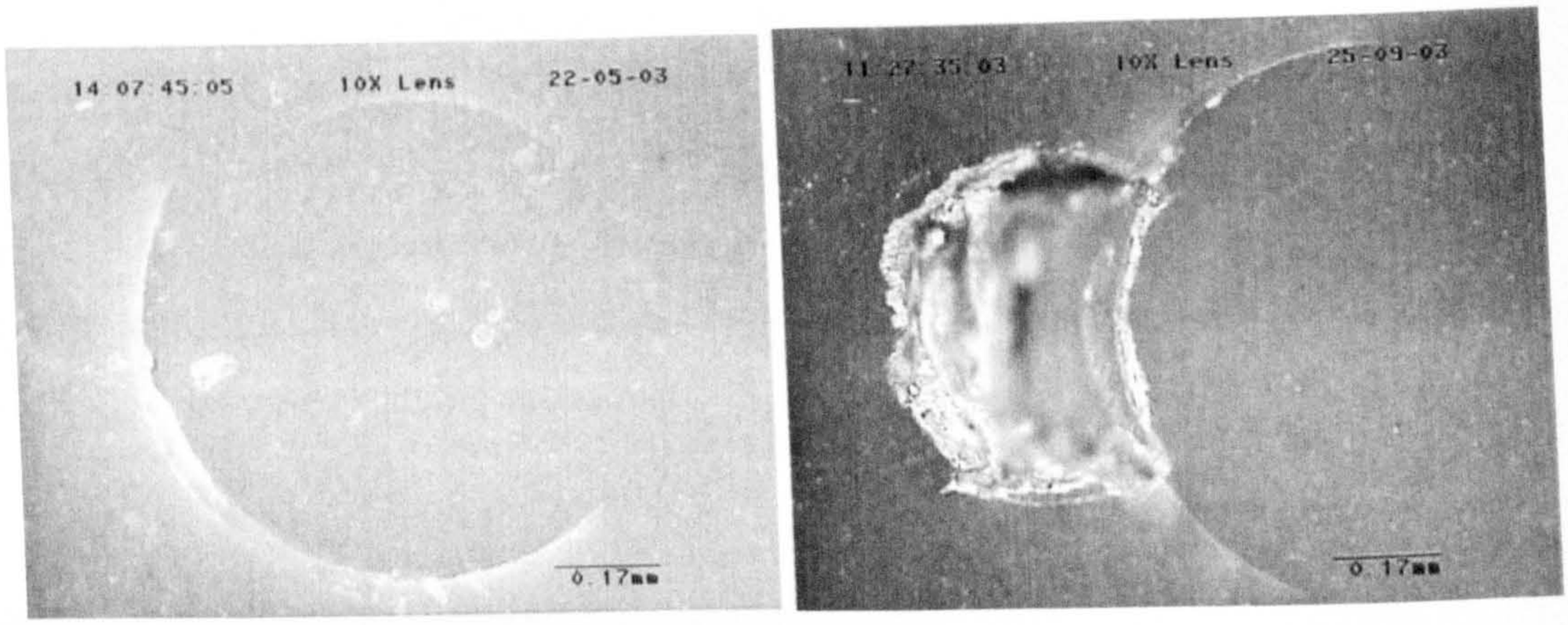

(a) Artificial crack before test (b) Failure overview (6 minutes)

Figure 4.49 Observation of surface damage from Test R1

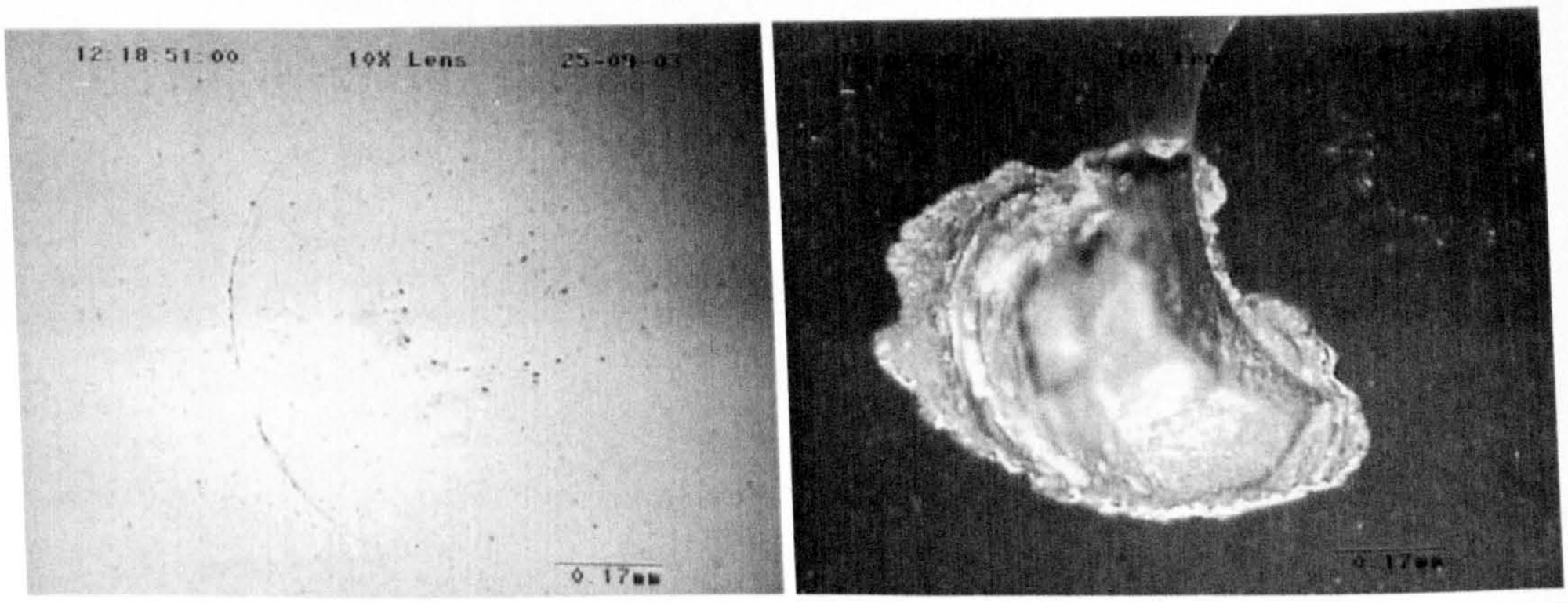

(a) After 7 minutes of testing (b) After 57 minutes of testing

Figure 4.50 Observation of surface damage from Test R3

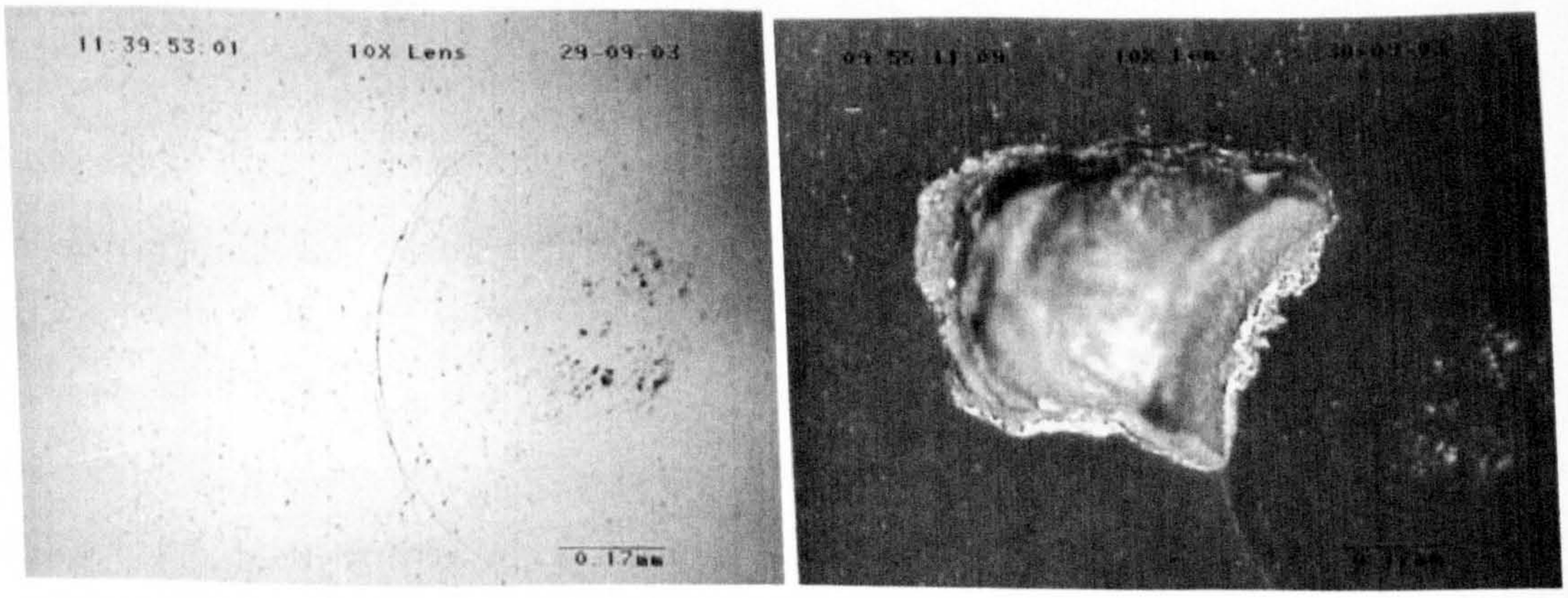

(b) After 10 minutes of testing (b) Dark field image (46 minutes)

Figure 4.51 Observation of surface damage from Test R4

4.3.4 Influence of crack angle

The influence of the crack angles on the RCF failure was investigated experimentally. The test results are discussed in this section. Table 4.9 lists the test conditions and results. All samples were selected using 12.7mm balls (material A) impacted against similar balls. The off-centre positions 2 and 3 were selected to generate different crack angles. Subsurface examinations show that artificial cracks formed at position 3 normally have a larger crack angle compared to position 2 (Chapter 2). The tests were performed at a speed of 5000 rpm and the maximum contact pressure was 5.58GPa. All the tests were lubricated using a traction fluid.

Table 4.9 Test conditions and results for various crack angles

Test No.	Off-centre position	Crack radius (mm)	Stress cycles ($\times 10^7$)	Test duration (Minutes)
P2-1	2	0.42	0.0135	12
P2-2	2	0.4	0.0259	23
P2-3	2	0.38	0.0675	60
P2-4	2	0.35	0.0866	77
P2-5	2	0.32	0.271	241
P2-6	2	0.30	0.56	498
P2-7	2	0.28	0.684	608
P3-1	3	0.42	0.03	27
P3-2	3	0.40	0.054	48
P3-3	3	0.38	0.099	88
P3-4	3	0.38	0.12	107
P3-5	3	0.36	0.225	200
P3-6	3	0.34	0.311	276
P3-7	3	0.28	1.665	1480

Figure 4.52 presents the test results of the crack angle influence in rolling contact fatigue failure. As described in Chapter 2, the impact cracks formed at position 3 show a larger crack angle compared to position 2. It can be seen that the larger the crack angle the longer the fatigue life. This relationship is seen in all ranges of the crack radius.

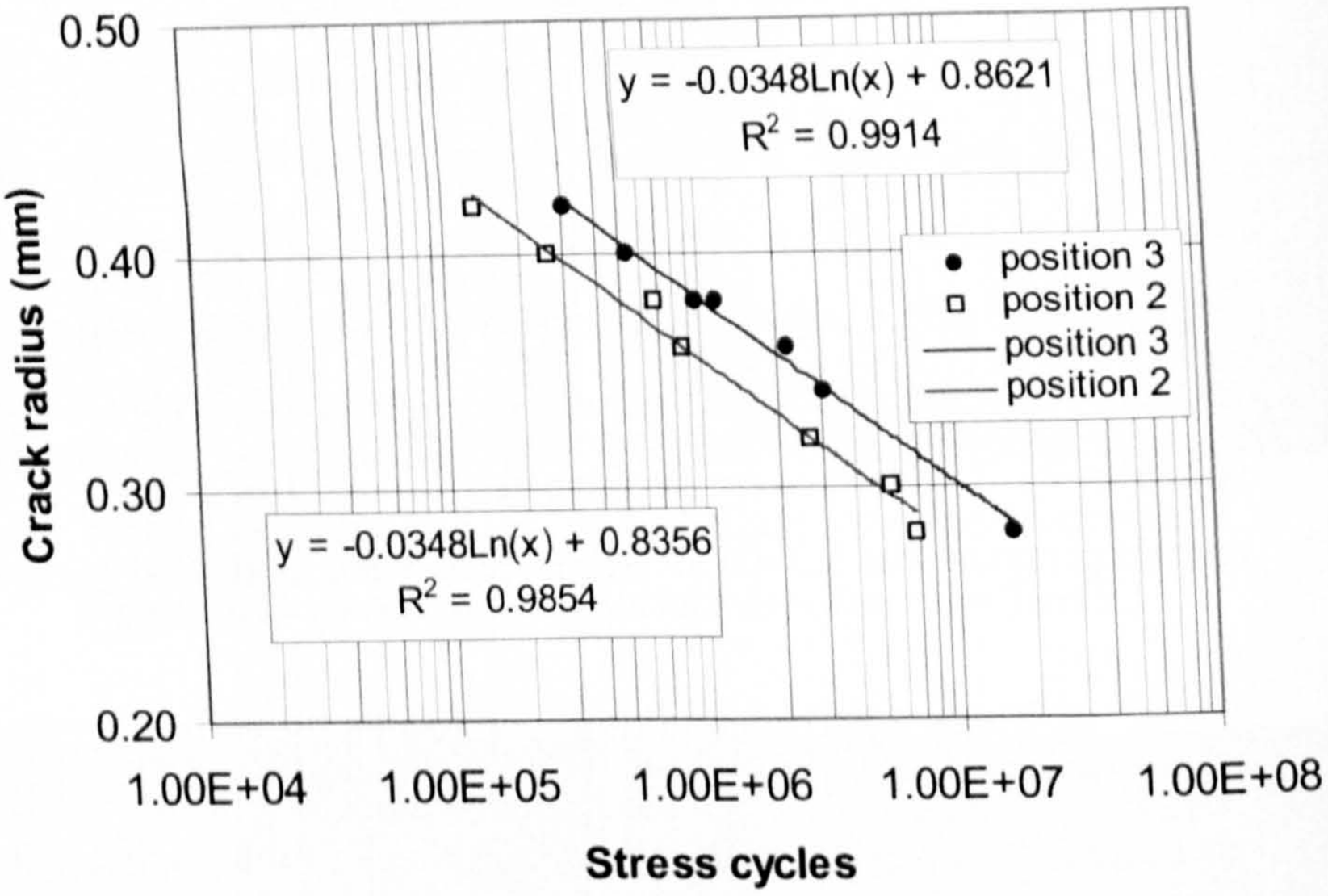

Figure 4.52 Influence of crack angle on fatigue life

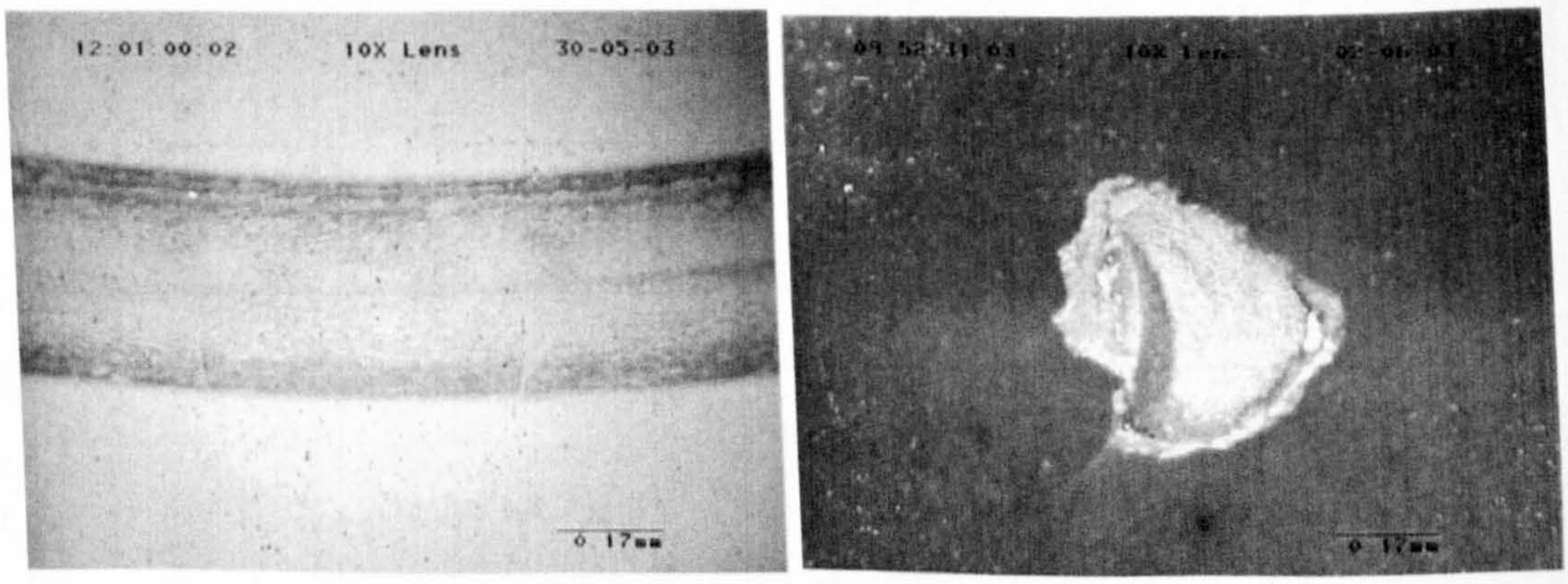

(a) After 40 minutes of testing

(b) After 241 minutes of testing

Figure 4.53 Surface observation of silicon nitride ball (Test P2-5)

Detailed examination of surface damage was carried out in order to identify fatigue failure modes. The results reveal that the failure mode for all the tests was spalling. The surface contours can be a whole elliptical shape or a half-elliptical shape.

The observation results from smaller crack angles (position 2) are shown in figures 4.53 to 4.55. For example, the observation from Test P2-5 is shown in figure 4.53. This is a double crack with a crack radius of 0.32 mm. After 40 minutes of testing, the cracks are clearly seen on the contact track. The fatigue spall with half-elliptical shape appears after 241 minutes of testing. Figure 4.54 is an other example of the half-elliptical spall. The spall can also appear in whole-elliptical like shape (figure 4.55).

The observation results from the larger crack angles (position 3) are shown in figures 4.56 to 4.58. The appearance of surface damage is the same as in the case of position 2. The surface contours can be a whole elliptical shape (figures 4.56 and 4.58), or a half-elliptical shape (figure 4.57).

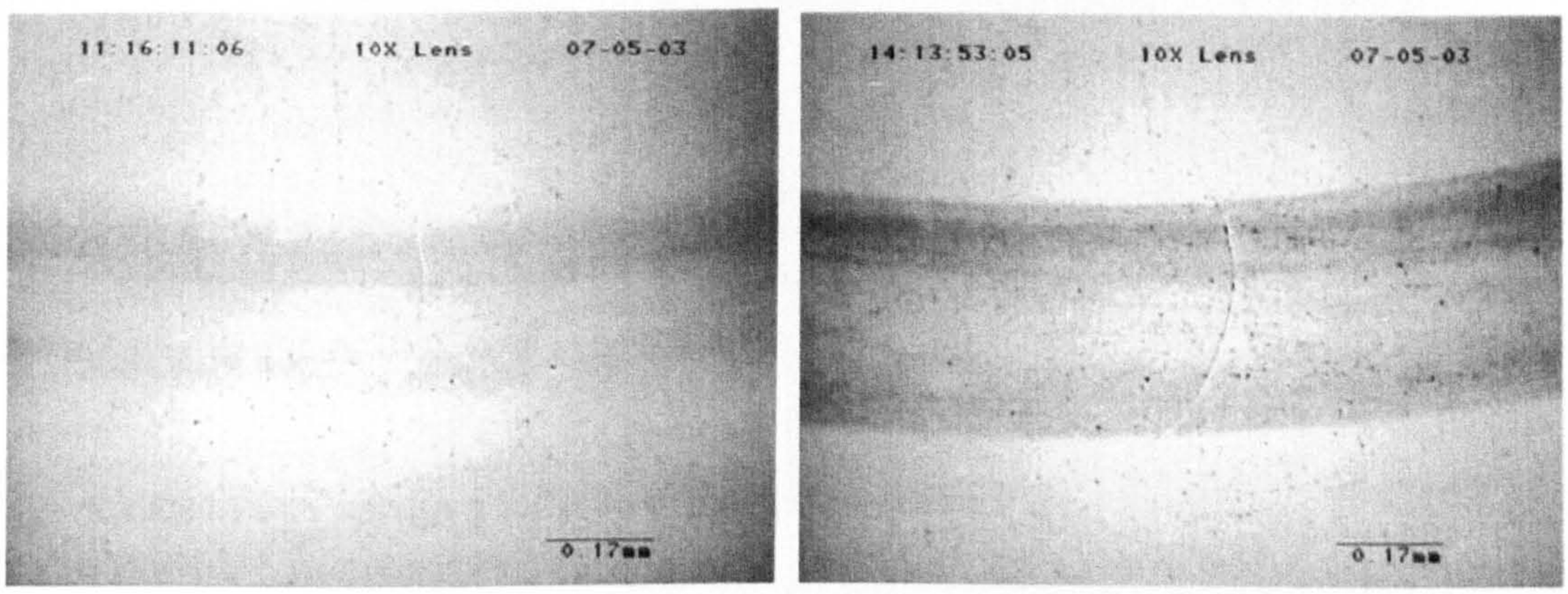

(a) After 15 minutes of testing

(b) After 3 hours 2 minutes of testing

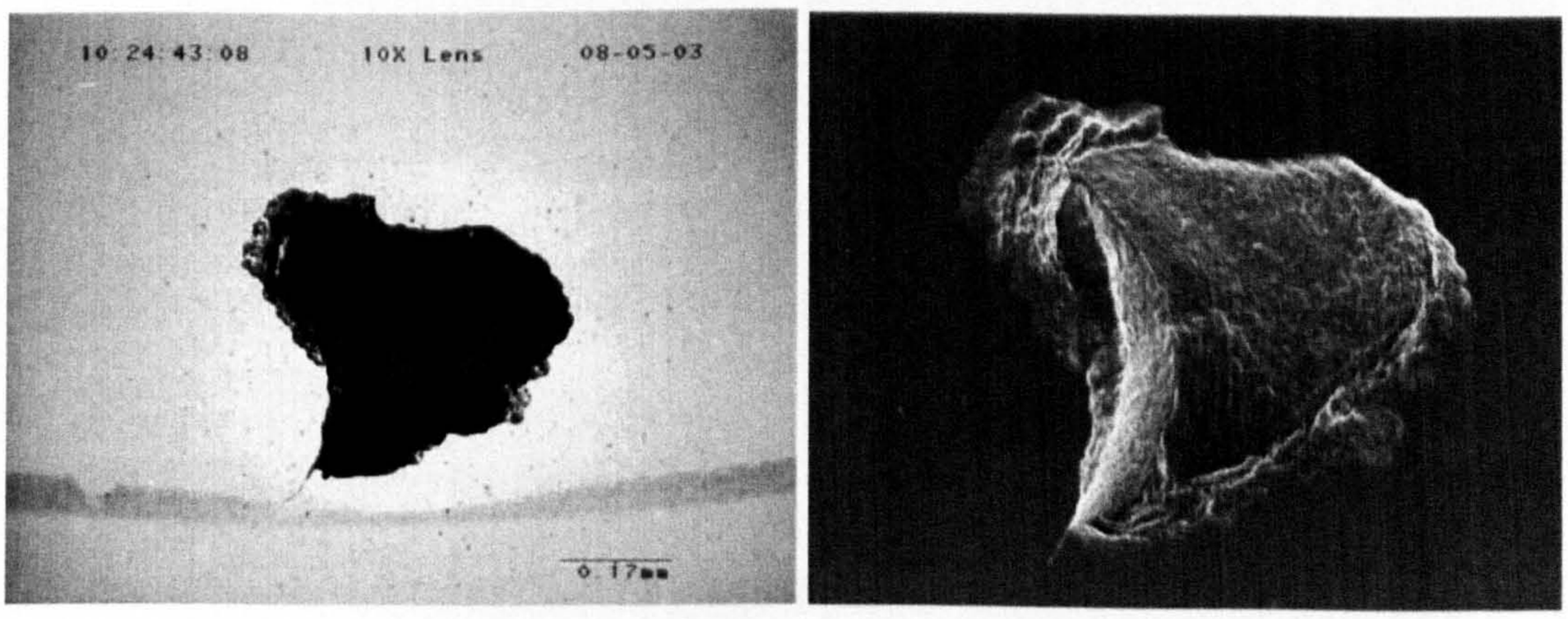

(c) After 498 minutes of testing

(d) Spall SEM image

Figure 4.54 Surface observation of silicon nitride ball (Test P2-6)

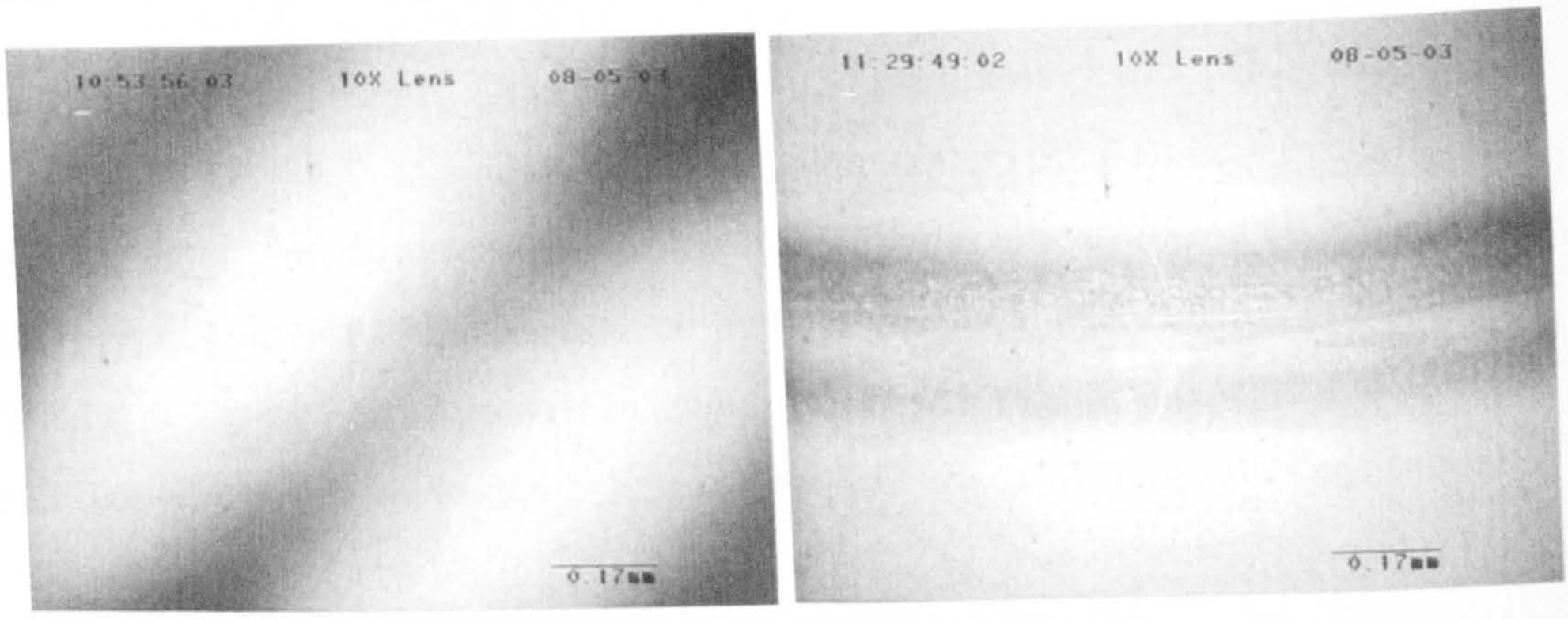

(a) Before testing (b) After 22 minutes of testing

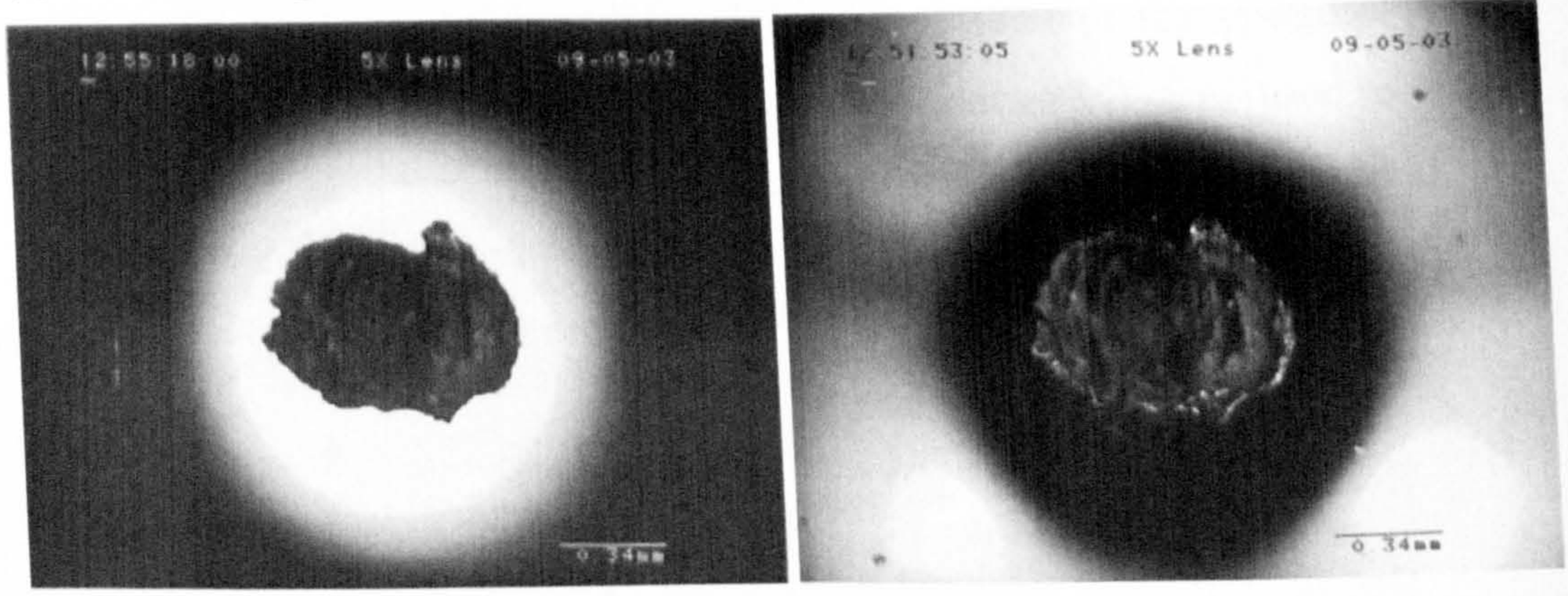

(c) Bright field image (608 minutes) (d) Dark field image of fatigue spall

Figure 4.55 Surface observation of silicon nitride ball (Test P2-7)

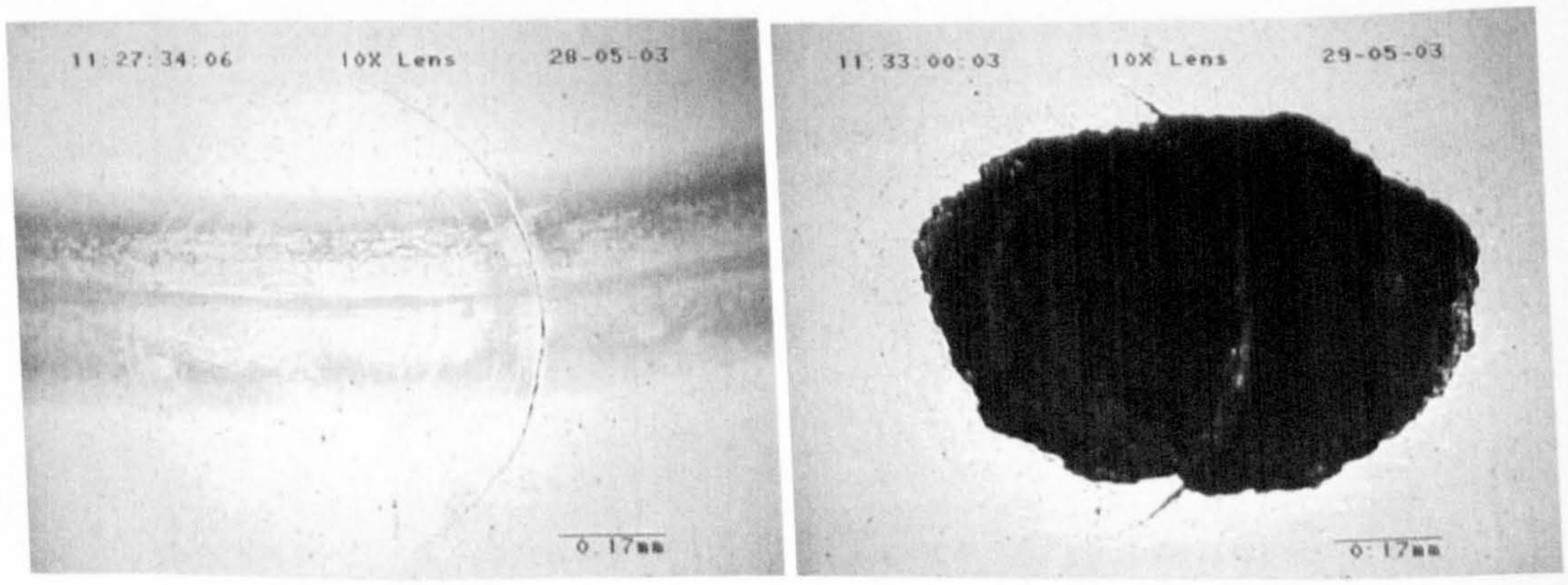

(a) After 20 minutes of testing (b) Fatigue spall

Figure 4.56 Surface observation of silicon nitride ball (Test P3-2)

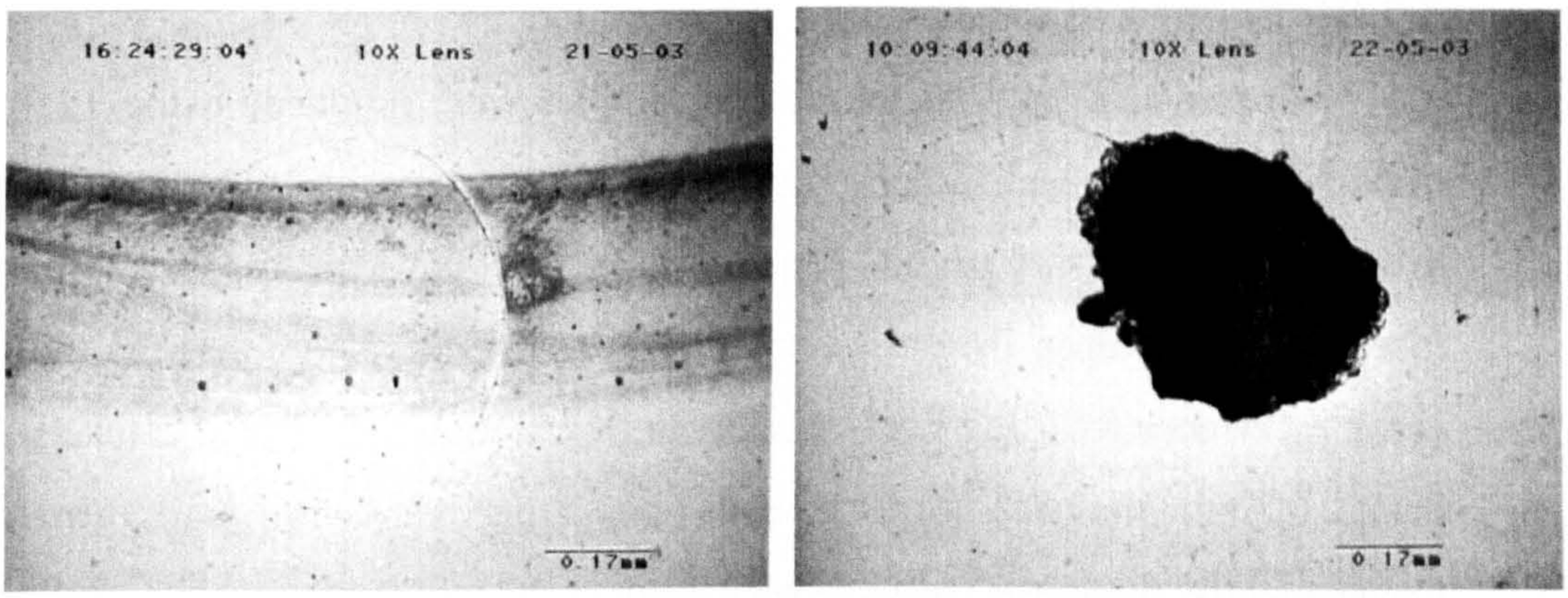

(a) After 3 h 42 minutes (b) After 4 h 36 minutes

Figure 4.57 Surface observation of silicon nitride ball (Test P3-6)

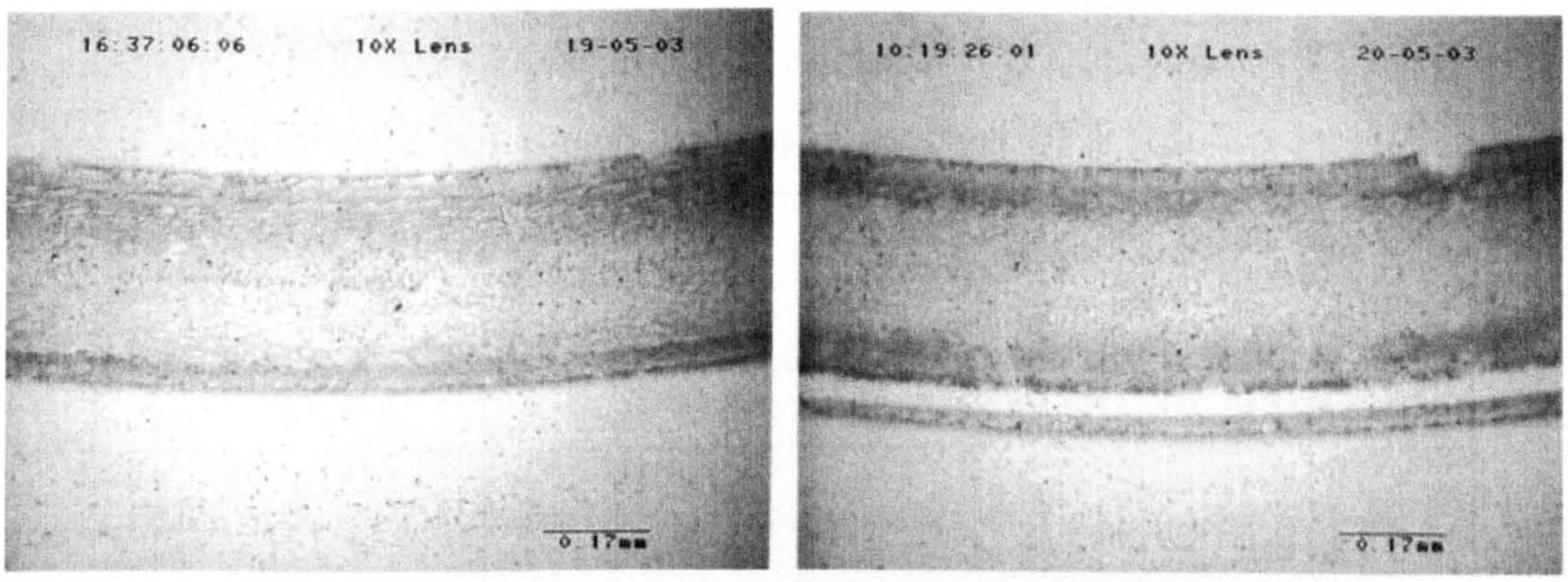

(a) After 1 h 8 minutes (b) After 3 h 42 minutes

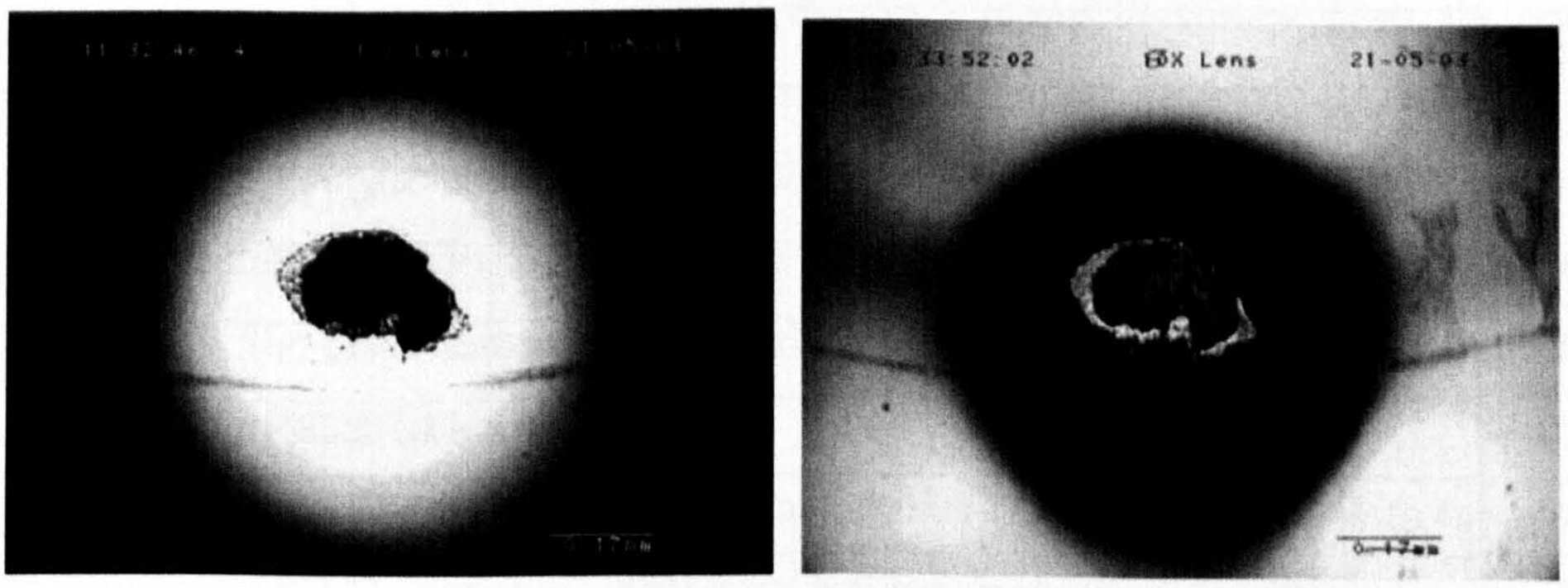

(c) Bright field image of fatigue spall (d) Dark field image of fatigue spall

Figure 4.58 Surface observation of silicon nitride ball (Test P3-7)

4.3.5 Influence of crack size

In previous sections all the test samples were produced using 12.7mm balls impacting against each other. The size of the surface crack is controlled by the different drop heights of the pendulum. In this way, the radius of the crack is increased as the drop height increases. The test results show that the radius of the crack influences RCF life performance. In this section the surface cracks were made using 6.3mm tungsten carbide balls impacting 12.7 mm balls (material A). Consequently, the crack radius is very close to the radius of a natural ring crack. The tests were performed at a speed of 5000 rpm and the maximum contact pressure was 5.58GPa. All the tests were lubricated using traction oil. The test conditions are listed in table 4.10.

Table 4.10 Test conditions and results for different crack sizes

Test No.	Off-centre position	Crack radius (mm)	Stress cycles ($\times 10^7$)	Test duration (Minutes)
D1-1	1	0.28	0.066	59
D1-2	1	0.26	0.105	93
D1-3	1	0.23	0.143	127
D1-4	1	0.225	0.231	205
D1-5	1	0.20	4.995	4440
D1-6	1	0.22	0.375	333
D2-1	2	0.28	0.110	98
D2-2	2	0.24	0.209	186
D2-3	2	0.26	0.158	140
D2-4	2	0.21	0.285	253
D2-5	2	0.22	1.856	1650
D2-6	2	0.20	0.714	635
D2-7	2	0.21	0.380	338
D2-8	2	0.20	4.779	4248

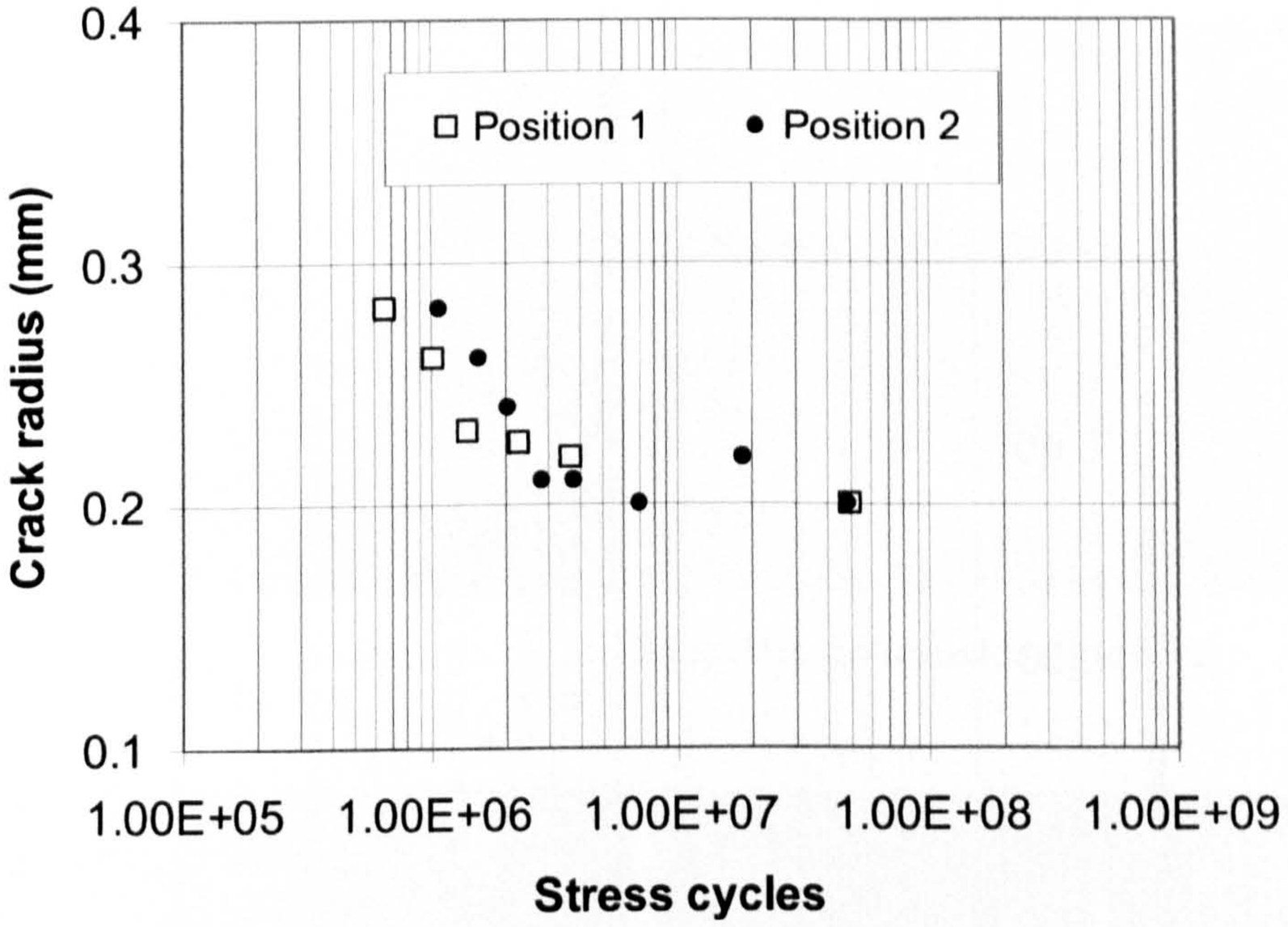

Figure 4.59 Influence of crack sizes on RCF life

The influence of crack size on rolling contact fatigue life is shown in figure 4.59. As in the case of 12.7mm ceramic balls impacting each other, rolling contact fatigue life is increased significantly as the crack radius decreases. Also, the crack angle affects the RCF life performance as described in the previous section.

To investigate how the size of the crack influences the RCF failure, the test results (traction oil lubrication only) are plotted together as shown in figure 4.60. Apparently, the crack dimensions strongly influence the rolling contact fatigue life of silicon nitride ceramic elements.

The RCF life decreases as the crack radius increases whether with the group of large cracks (12.7mm ball impacting against each other) or with the group of small cracks (6.35mm ball impacting against 12.7mm ball). The crack sizes (radius and length) from the impact of same diameter balls (two 12.7mm) are much larger than those from the two different diameter balls (6.35 and 12.7mm). However, the RCF life for those balls with the larger cracks is much longer than for the balls with the smaller cracks. The question arises here: why does the large crack show a good

fatigue life performance? The reason is that the subsurface geometry of the cracks in the two groups is different from each other. This is discussed later in Chapter 5.

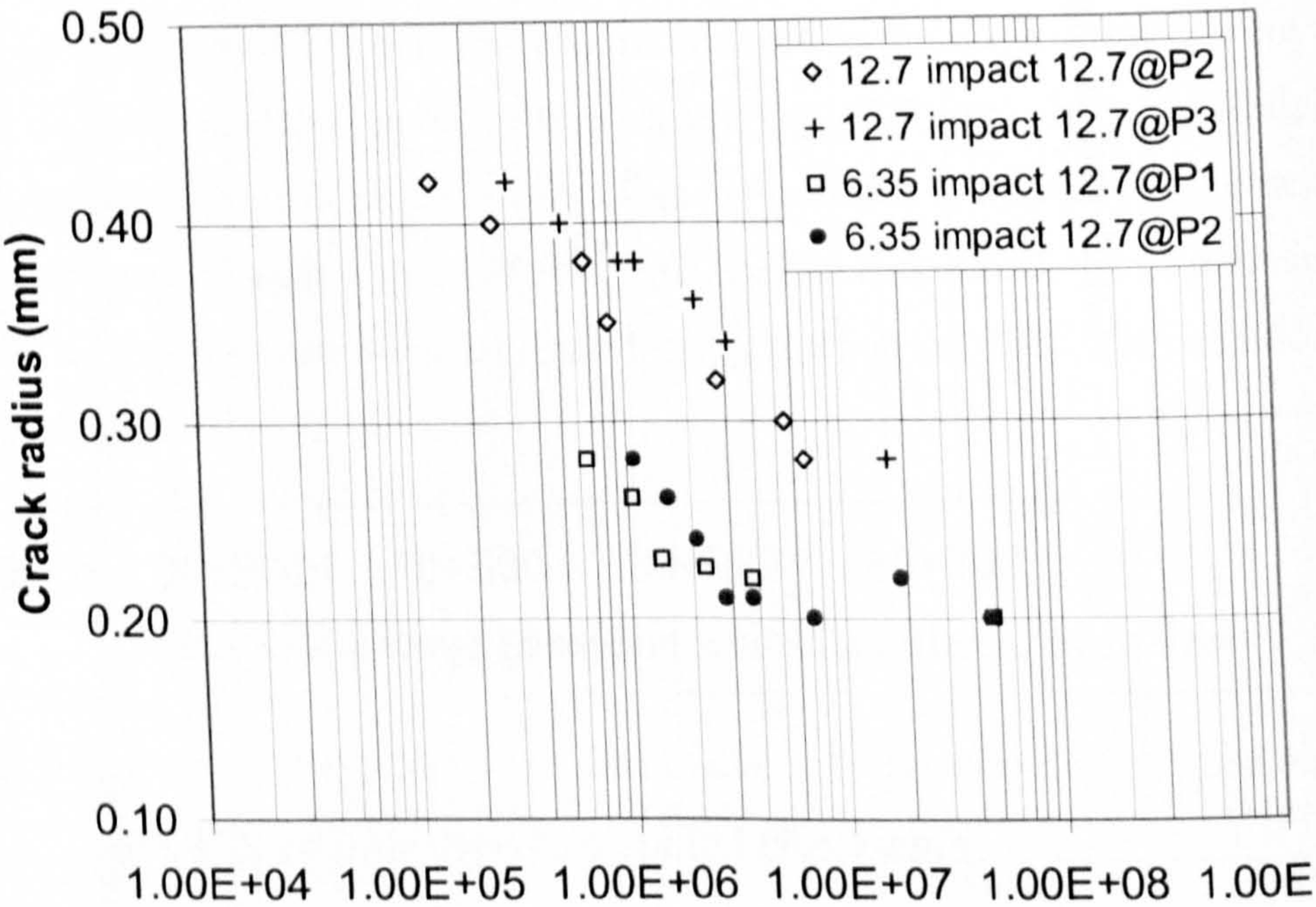

Figure 4.60 Comparison of RCF life at various crack dimensions

Surface observations of fatigue failure from the artificial cracks (12.7mm ceramic ball impacting against each other) have been shown in previous sections. In this section we focus on the balls with small cracks from 6.35mm balls impacting against 12.7 balls.

Figure 4.61 shows the surface observations from Test D1-1. The surface ring crack can be seen before testing under the normal light conditions (figure 4.61(a)). The contact track becomes darker as the test proceeds (figure 4.61(b)). A typical fatigue spall that developed on the ball surface can be in a whole elliptical profile (figure 4.61(c)). The original ring crack can still be clearly seen after the fatigue spalling (figure 4.61(d)). Fatigue crack propagation initiates from the original ring crack and grows outward in both directions. The right side of figure 4.61(d) shows fracture surface.

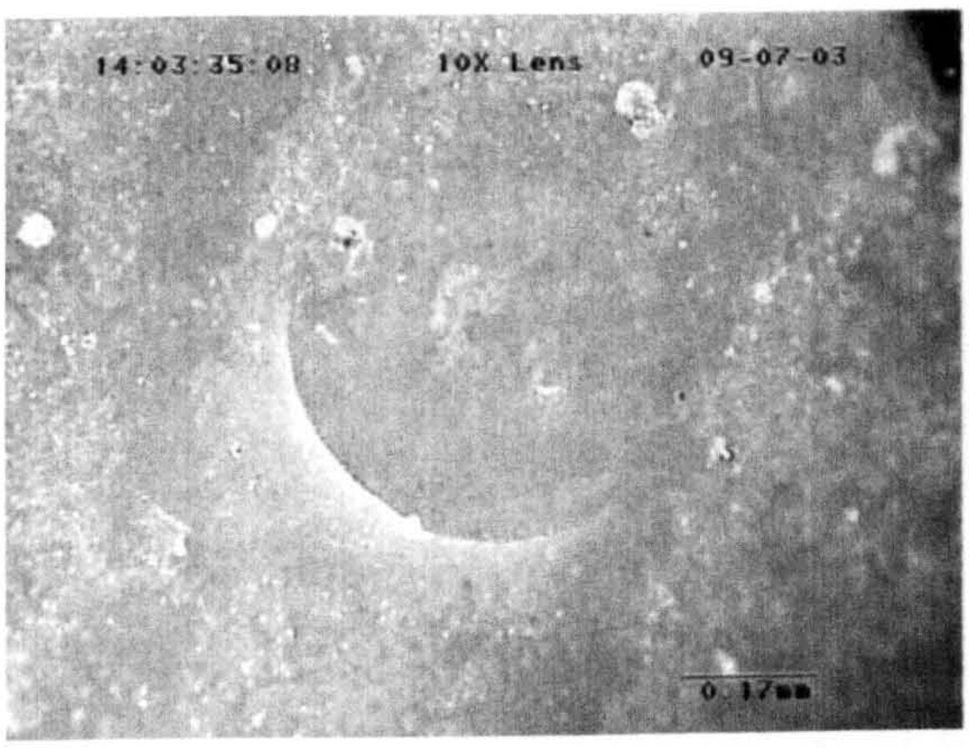

(a) Before testing

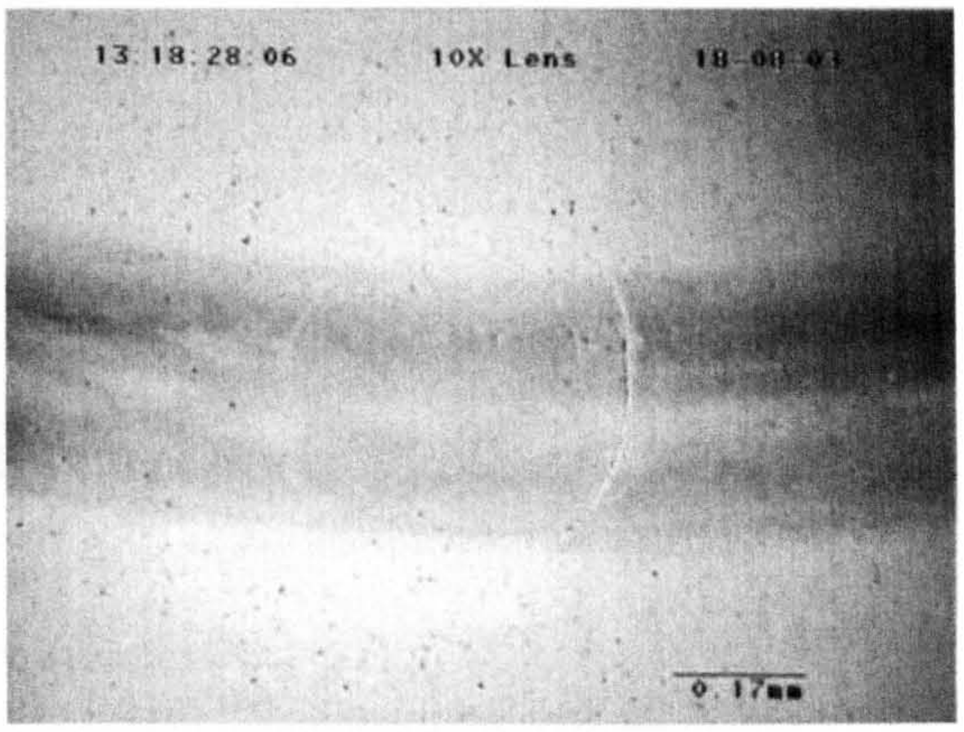

(b) After15 minutes of testing

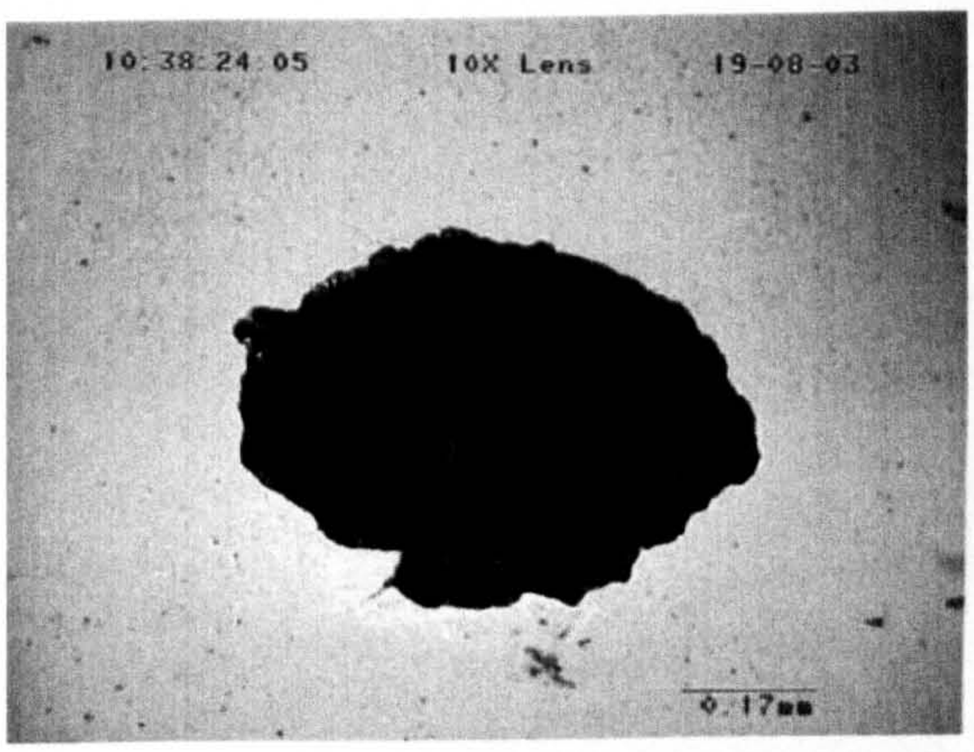

(c) Spall overview (white light)

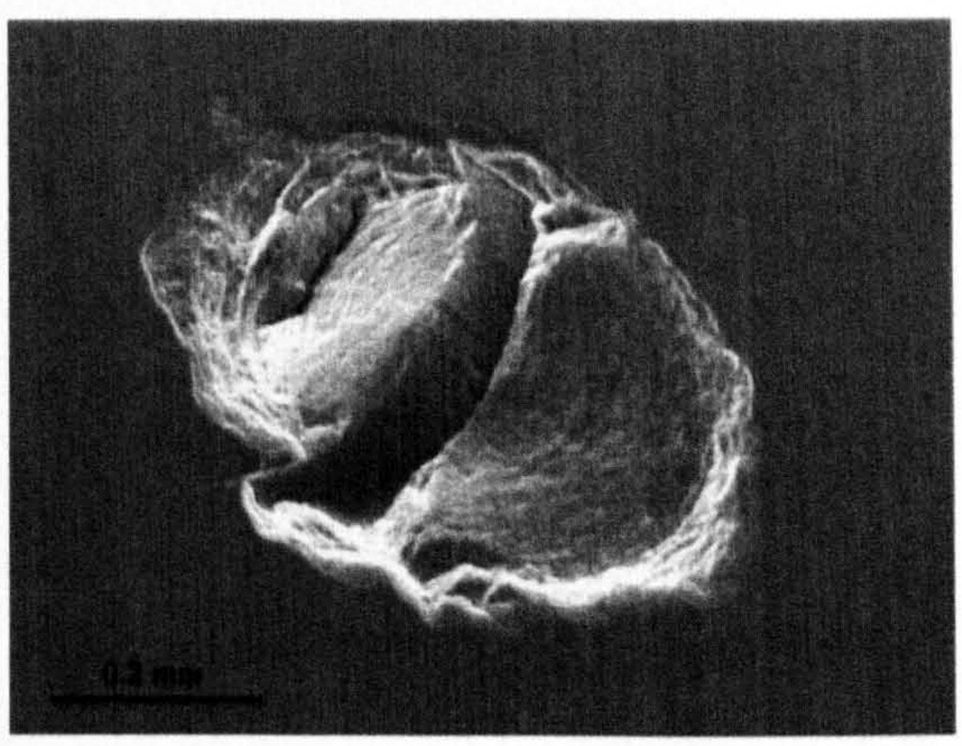

(d) SEM micrograph

Figure 4.61 Observation of surface damage from Test D1-1

In figure 4.62, observations results from Test D1-2 are presented. The radius of the crack is slightly smaller than that in Test D1-1. The crack depth is smaller. The pre-test image of the crack is shown in figure 4.62(a). An overview of a spall with the half-elliptical profile is clearly shown in figure 4.62(b). As can be seen, the surface is still in a very good condition and has the appearance of an untested surface. The conical face of the crack can still be seen after the spall has formed.

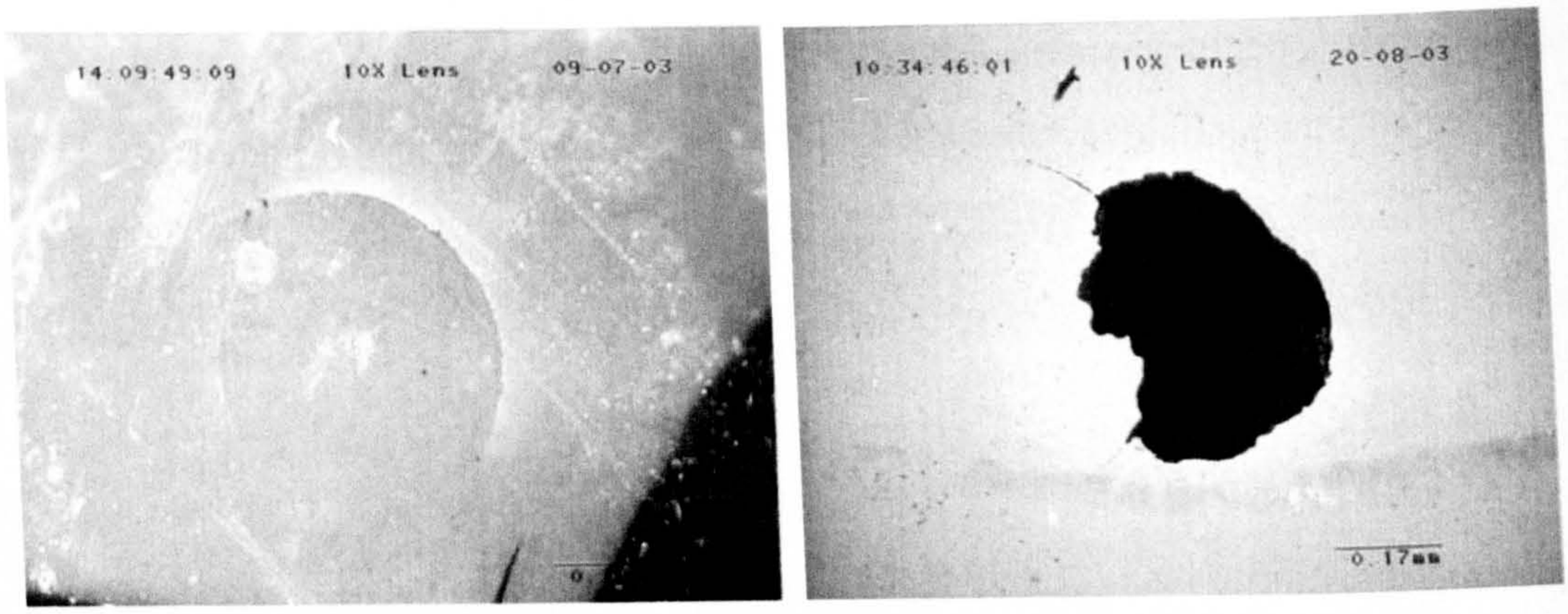

(a) Artificial crack before test (b) overview of fatigue spall

Figure 4.62 Observation of surface damage from Test D1-2

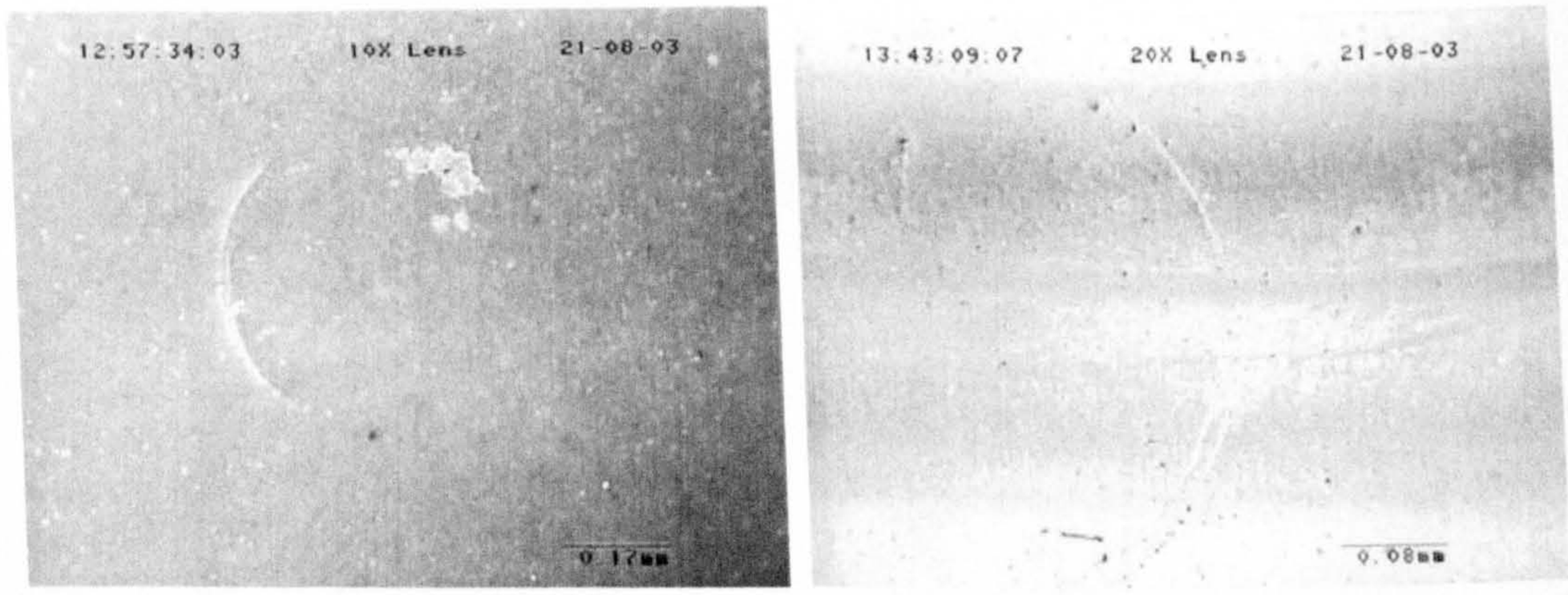

(a) Artificial crack before test (b) 15 minutes of fatigue test

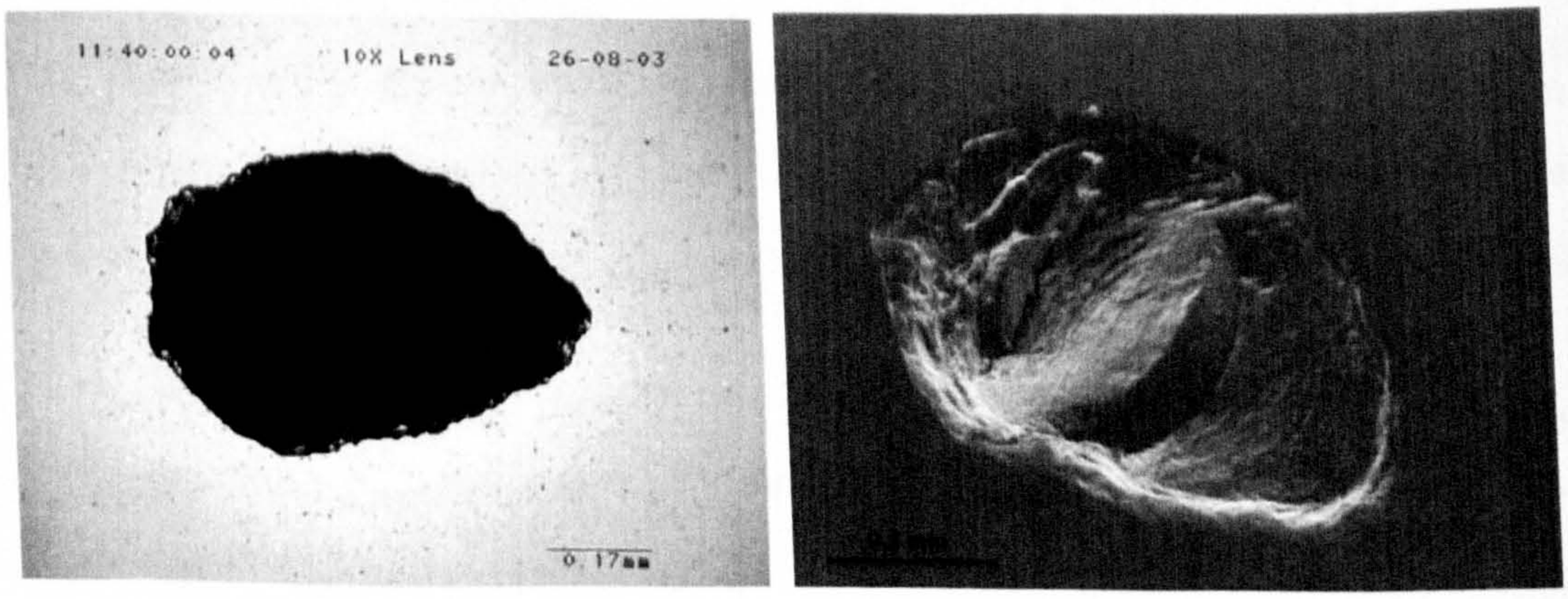

(c) Failure overview (d) Spall SEM micrograph

Figure 4.63 Observation of surface damage from Test D1-4

The optical images of the crack before test and during the testing have been shown in figure 4.63(a) and figure 4.63(b). The optical and SEM images of a failed ceramic ball after 205 minutes of testing are shown in figure 4.63(c) and figure 4.63(d). The fatigue life is much longer than in Test D1-1 and Test D1-2 due to the fact that the crack radius is much smaller than in the above two tests. In this micrograph, the original crack can be identified clearly. It is obvious that the crack propagated in two directions.

Figure 4.64 shows the observation of surface damage from Test D2-2. The ring crack and contact path after 15 minutes of testing are shown in figure 4.64(a). Failure overviews of optical and SEM images are presented in figure 4.64(b) and figure 4.64(c). The left side of the spall with circle-like striations is shown in figure 4.64(d).

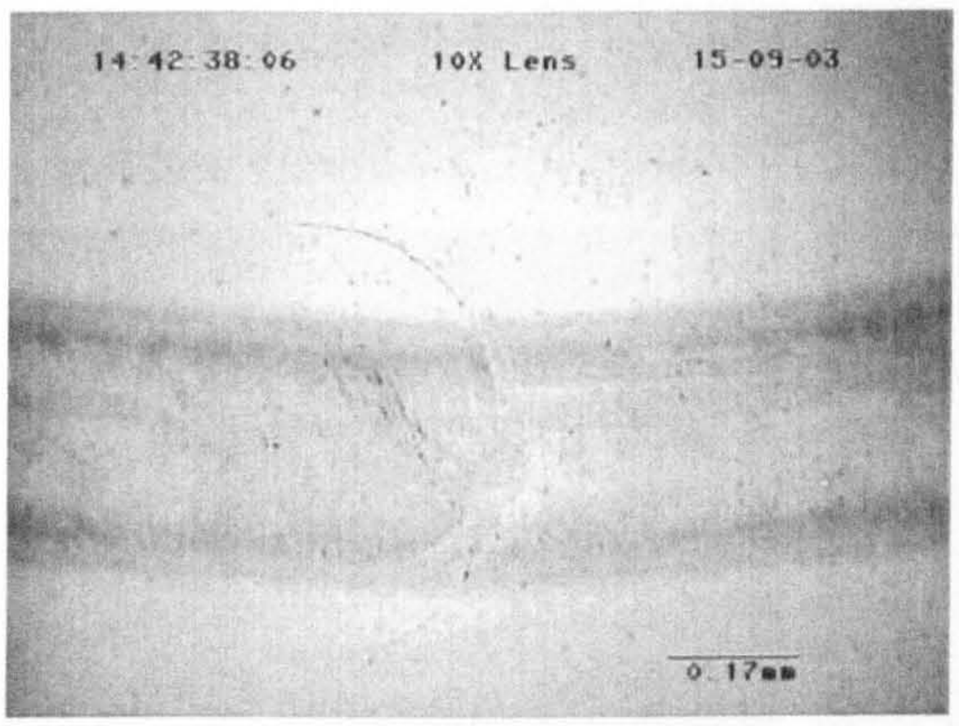

(a) After 15 minutes of testing

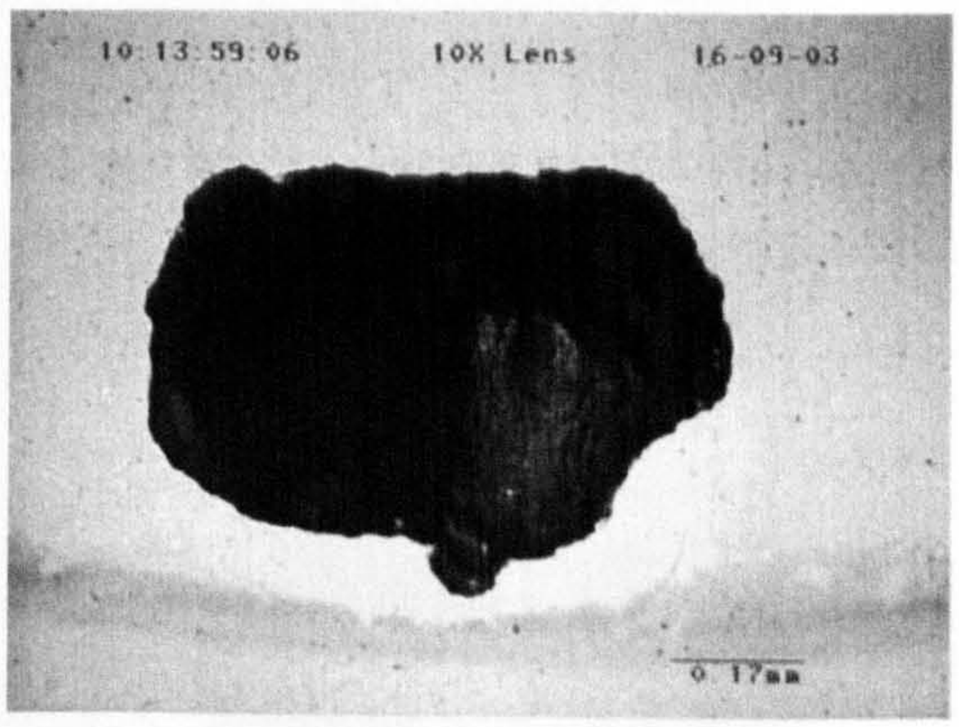

(b) Failure overview

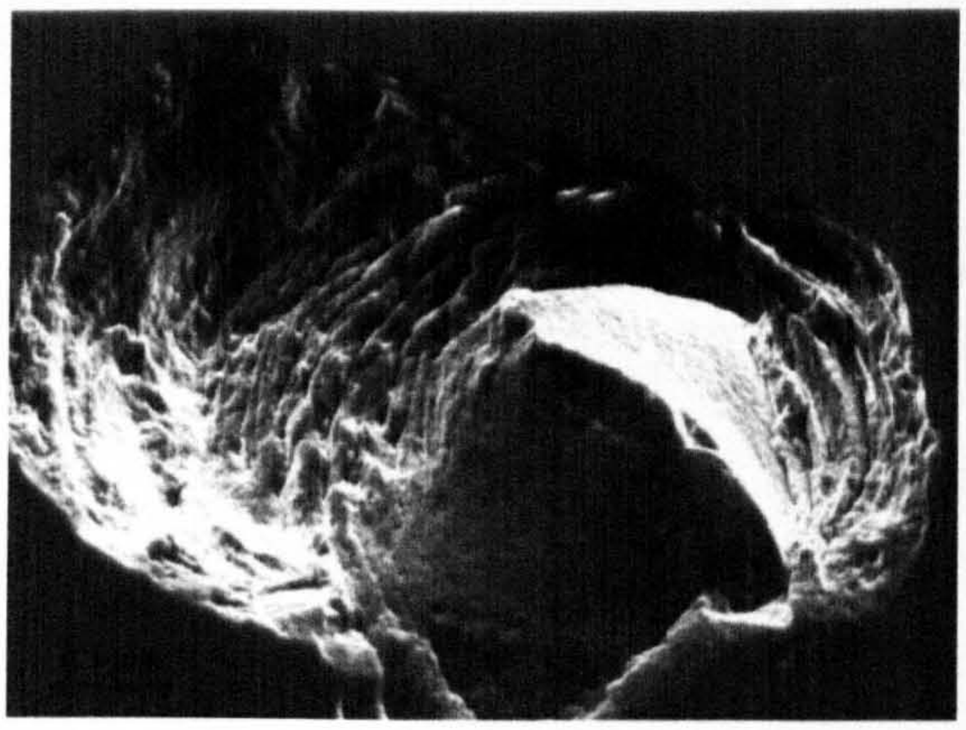

(c) SEM micrograph of spall

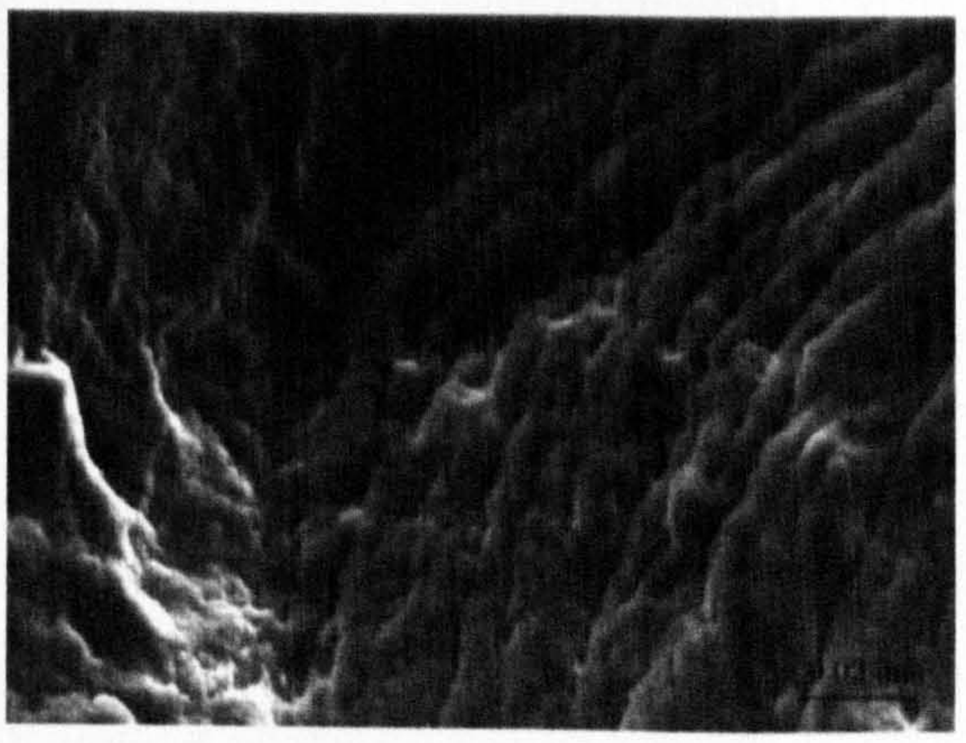

(d) Left side of spall

Figure 4.64 Observation of surface damage from Test D2-2

Results of surface observation from Test D2-8 are shown in figure 4.65. The crack radius generated on this ball is similar in size to the natural ring crack as shown in figure 4.65(a). Figure 4.65(b) shows the ring crack and contact path after 25 minutes of fatigue testing. The optical image of the spall is shown in figure 4.65(c) and the SEM image is shown in figure 4.65(d).

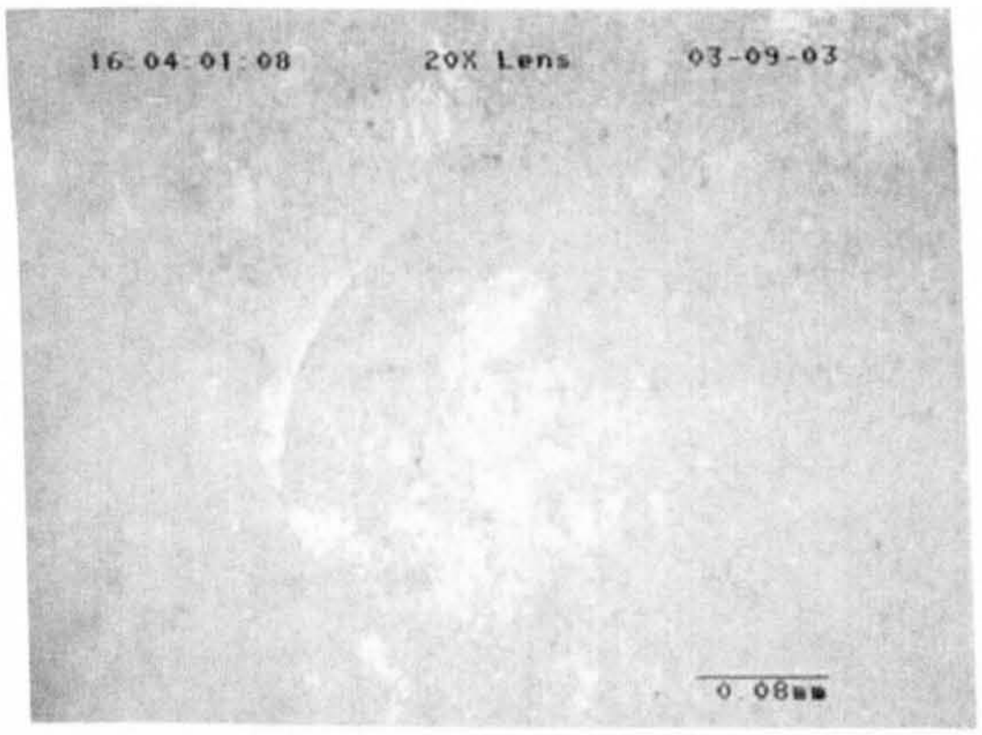

(a) Artificial crack before test

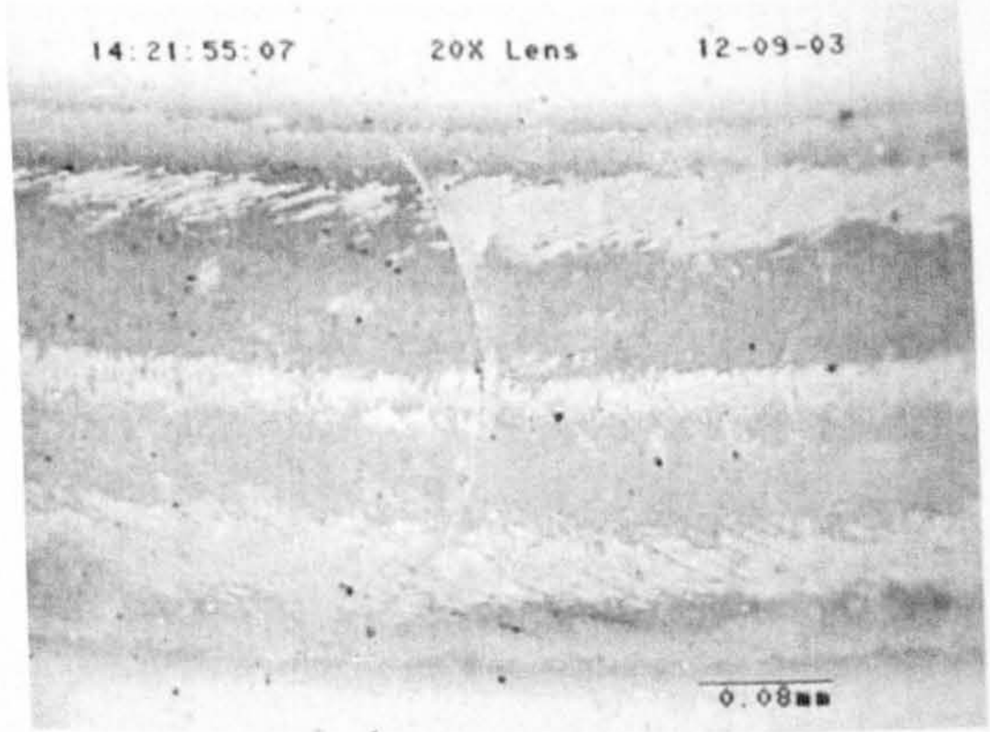

(b) Ring crack after 25 minutes of testing

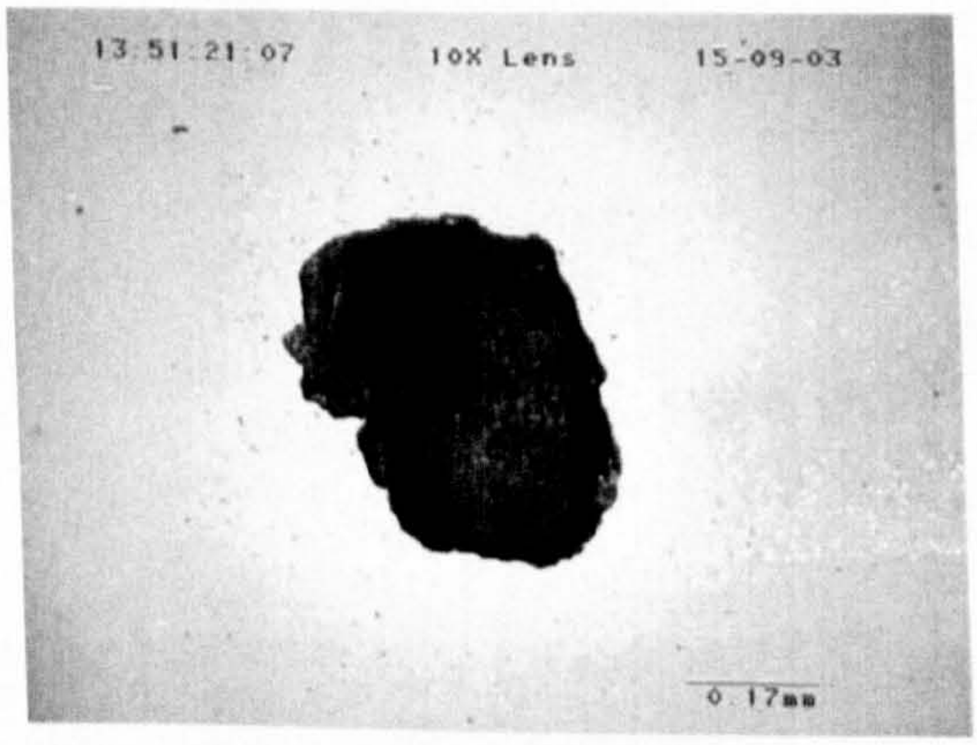

(c) Failure overview (white light)

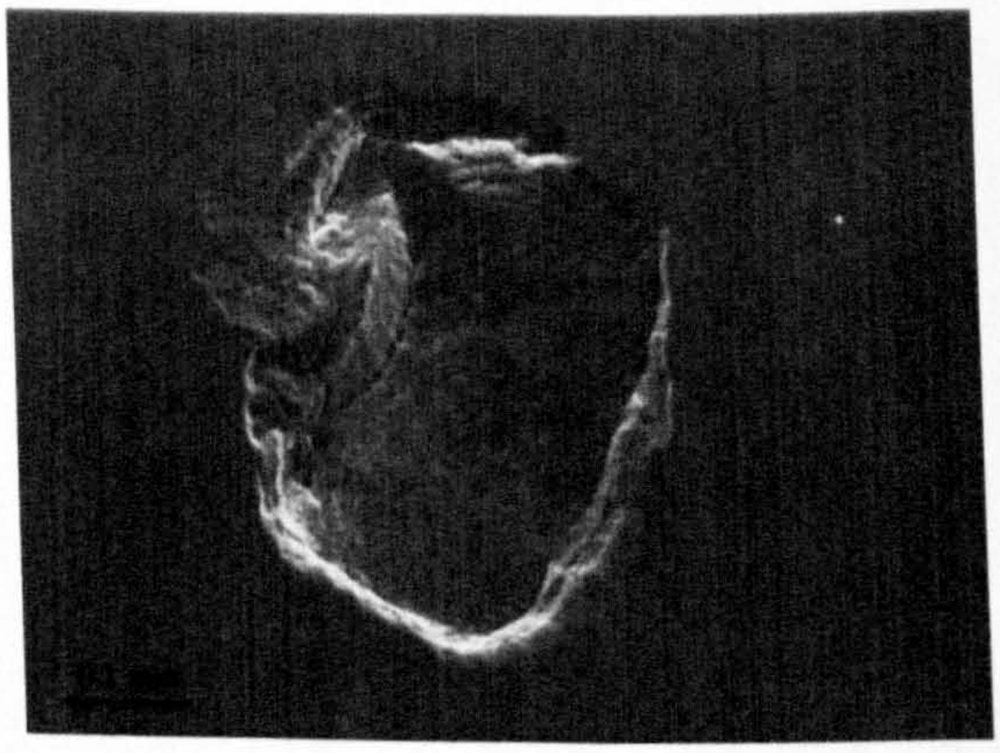

(d) SEM micrograph

Figure 4.65 Observation of surface damage from Test D2-8

4.3.6 Influence of contact load

The influence of the contact load on the RCF failure modes was investigated experimentally. All samples were 12.7mm material A balls with artificially induced cracks. The cracks were produced by 12.7mm balls impacting against the similar balls. The off centre position 3 was adopted to generate the surface ring cracks. The tests were performed at a speed of 5000 rpm. Contact pressures were 5.58 and 4.0GPa, respectively. Table 4.11 lists the test conditions and results. All the tests were lubricated using mineral oil. The reverse position of the crack was selected as illustrated in Chapter 3, figure 3.4(b). To investigate the effect of crack orientation on failure modes at low contact stresses, Test I was performed with the normal crack position (see figure 3.4(a)).

Table 4.11 Test conditions for various contact loads

Test No.	Contact load (GPa)	Crack radius (mm)	Stress cycles ($\times 10^7$)	Test duration (Minutes)
A	5.58	0.4	0.0034	3
B	5.58	0.36	0.012	11
C	5.58	0.32	0.132	117
D	5.58	0.3	0.357	318
E	4.0	0.42	0.247	220
F	4.0	0.32	2.78	2478
G	4.0	0.3	20.25*	18000*
H	4.0	0.28	20.25*	18000*
I	4.0	0.32	1.12	995

* The test was suspended with no spalling

Figure 4.66 shows a huge difference in the fatigue life when the contact loads are different. At the low contact stresses the ceramic balls show a very long life. The main reasons are: (a) low surface tensile stresses at the edge of the contact circle and (b) the low stress intensities along the crack front (these aspects will be discussed in Chapter 5). It is interesting to note that when the crack radius is less

than a certain size there is no fatigue failure at a contact pressure of 4.0 GPa. The result predicts that the fatigue curve may become asymptotic when the crack is smaller than a critical size. A fatigue limit may exist for a given crack size.

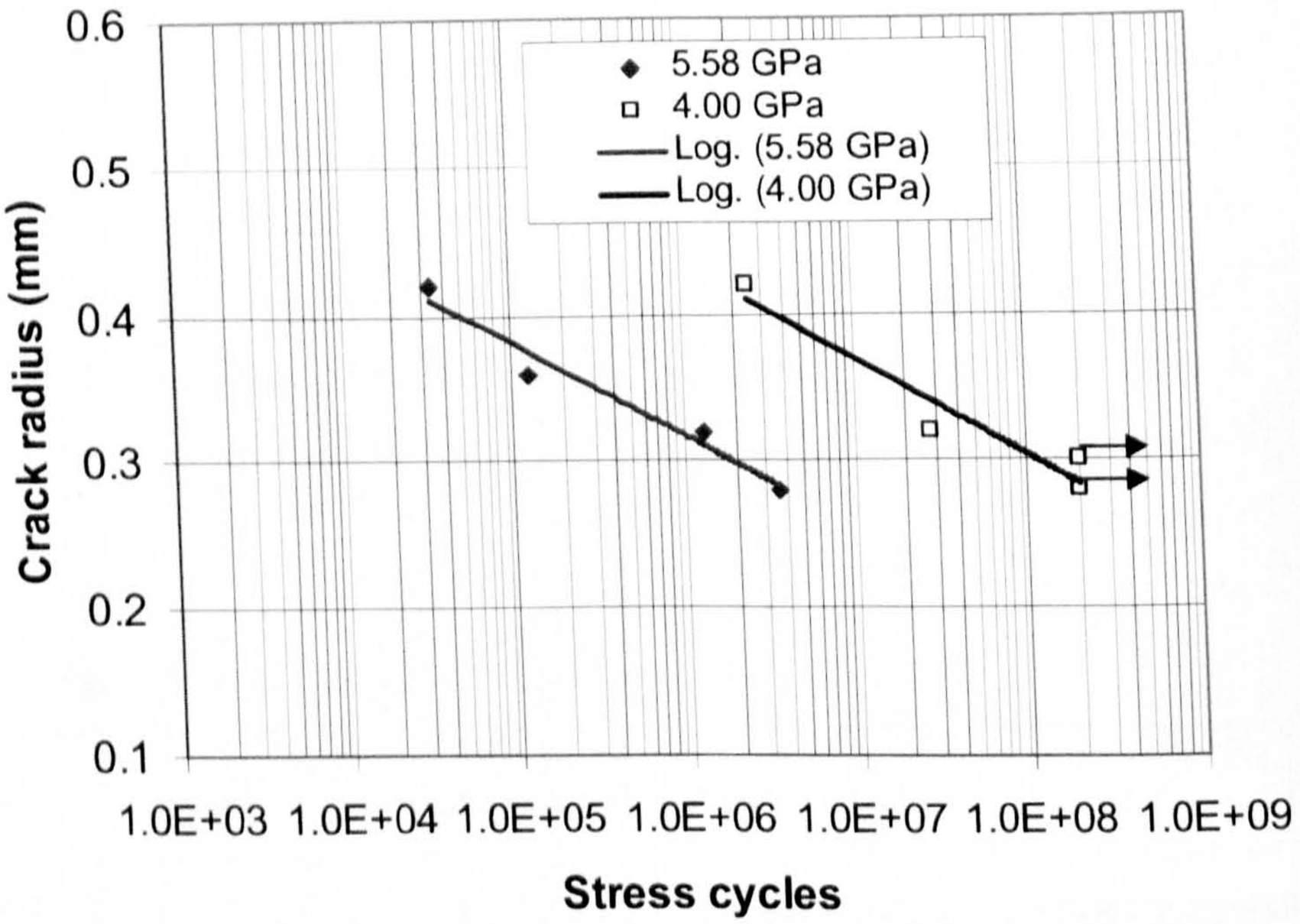

Figure 4.66 Influence of contact stress on fatigue life

Detailed surface examinations during tests were performed using an optical microscope. Figures 4.67 to 4.70 show the results of surface observations from a contact stress of 5.58GPa. For a large crack, secondary surface cracks form very quickly if the contact load level is high. The reason for the quick failure is because the maximum principal stresses at the contact circle are high enough to initiate the secondary surface cracks. These secondary surface cracks dominate the failure modes. Fatigued subsurface crack growth may not be involved. Figure 4.67 shows an example of the observations from the large cracks. The test ball fails only after 3 minutes of testing. The result is fairly consistent with the numerical analysis. Figure 4.68 shows another example of the observations from the large crack, which fails after just 11 minutes of testing.

As the crack radius decreases the RCF life increases. The results of surface observations from small cracks are shown in figures 4.69 and 4.70. The subsurface

crack growth is involved when the crack is small.

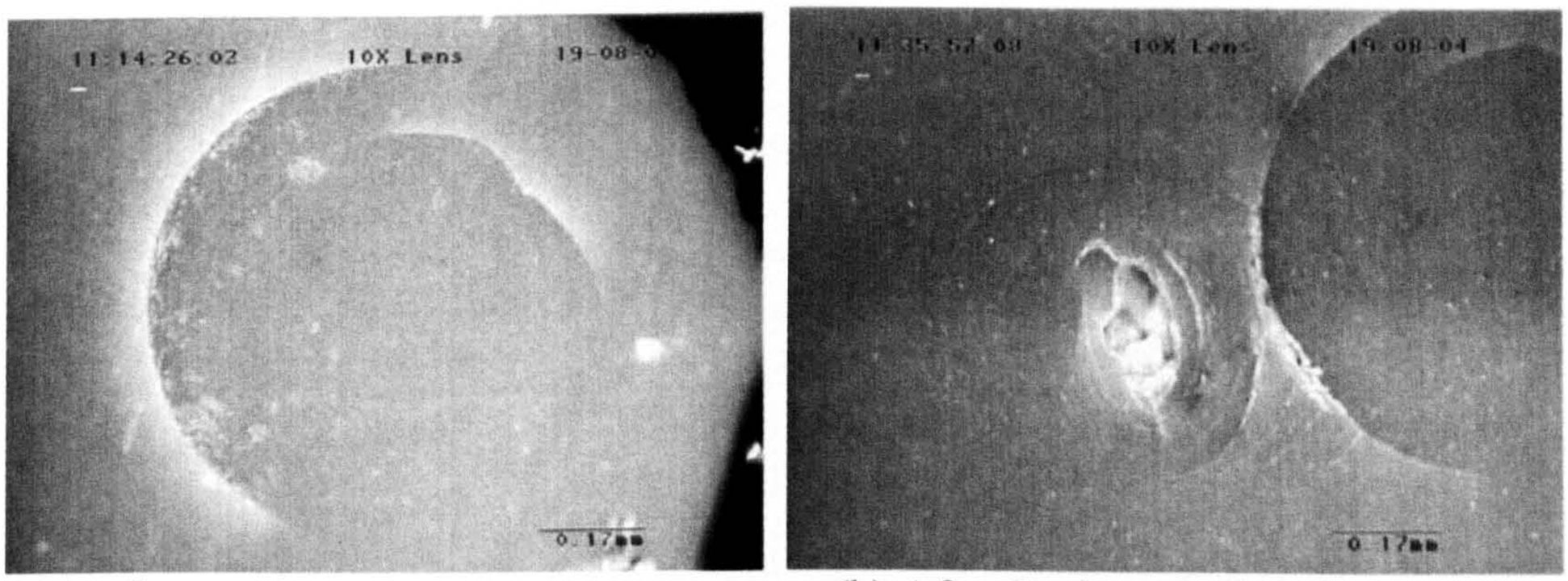

(a) Before testing (b) After 3 minutes of testing

Figure 4.67 Surface observation of silicon nitride ball (Test A)

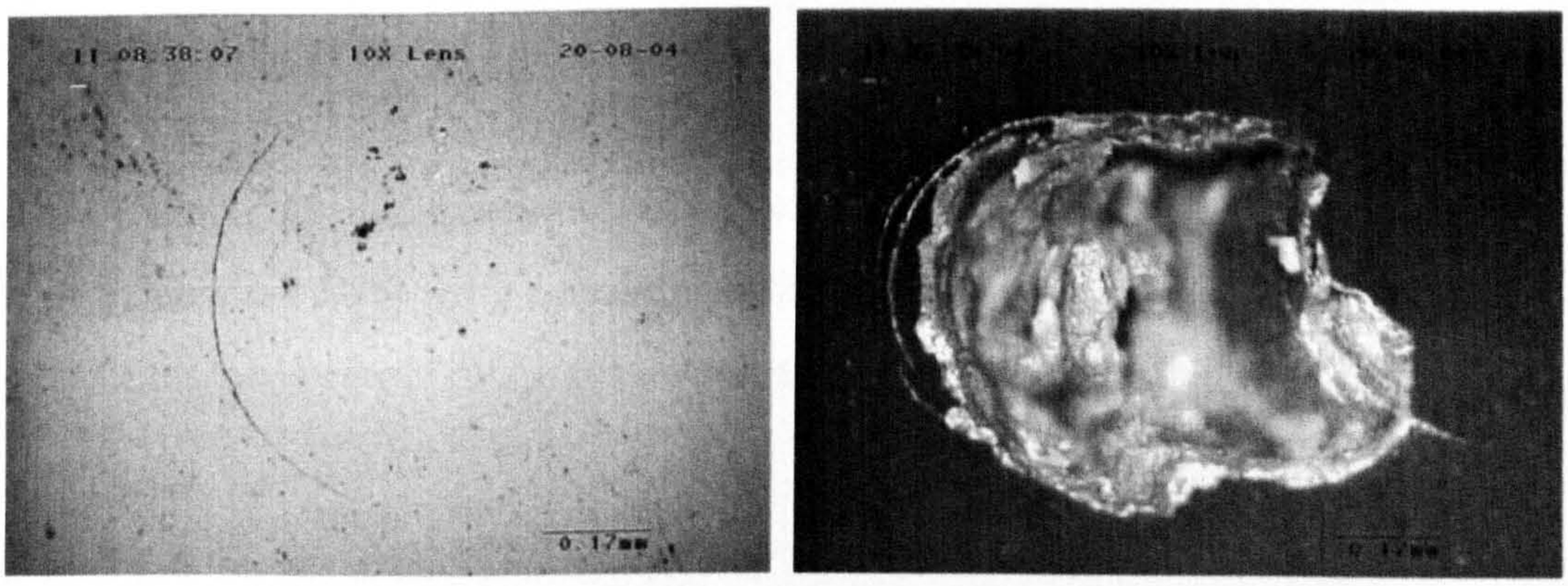

(a) Before testing (b) After 11 minutes of testing

Figure 4.68 Surface observation of silicon nitride ball (Test B)

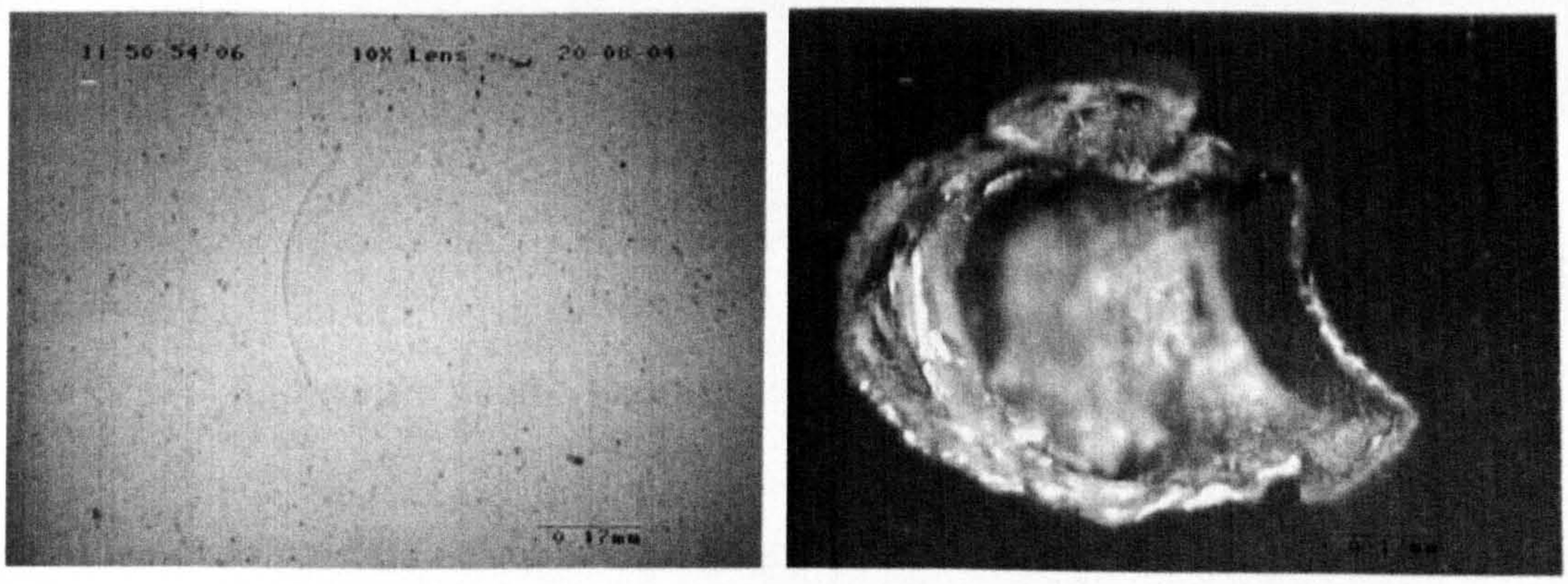

(a) Before testing (b) After 117 minutes of testing

Figure 4.69 Surface observation of silicon nitride ball (Test C)

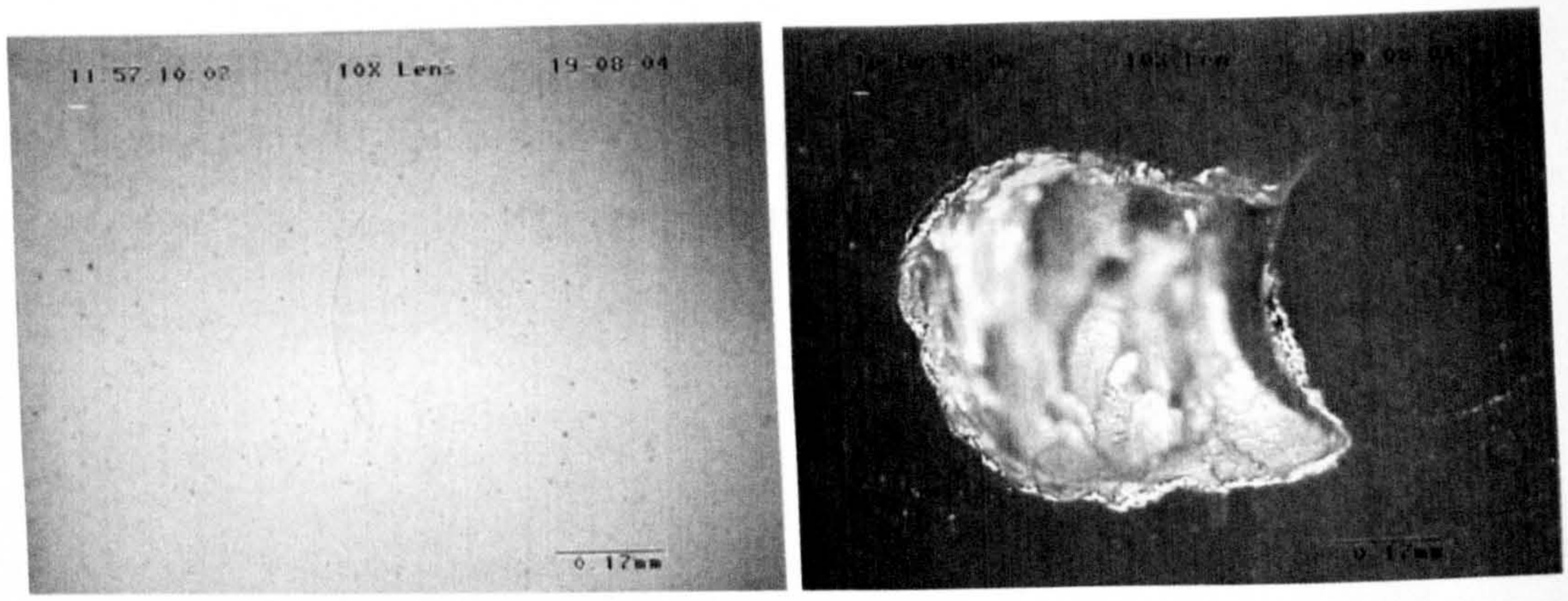

(a) Before testing (b) After 318 minutes of testing

Figure 4.70 Surface observation of silicon nitride ball (Test D)

The contact stress is decreased to 4.0 GPa to attempt long cycle failure modes. Figure 4.71 illustrates the results of surface observations from Test F. The shape of the spall implies that a long distance of subsurface crack growth exists. Numerical analysis shows that the surface tensile stress is less than the value required for the formation of the secondary cracks when the contact stress is less than 4.0 GPa. The subsurface crack continues to grow until the crack gap reaches a critical value. Consequently, a long shape of fatigue spall is formed.

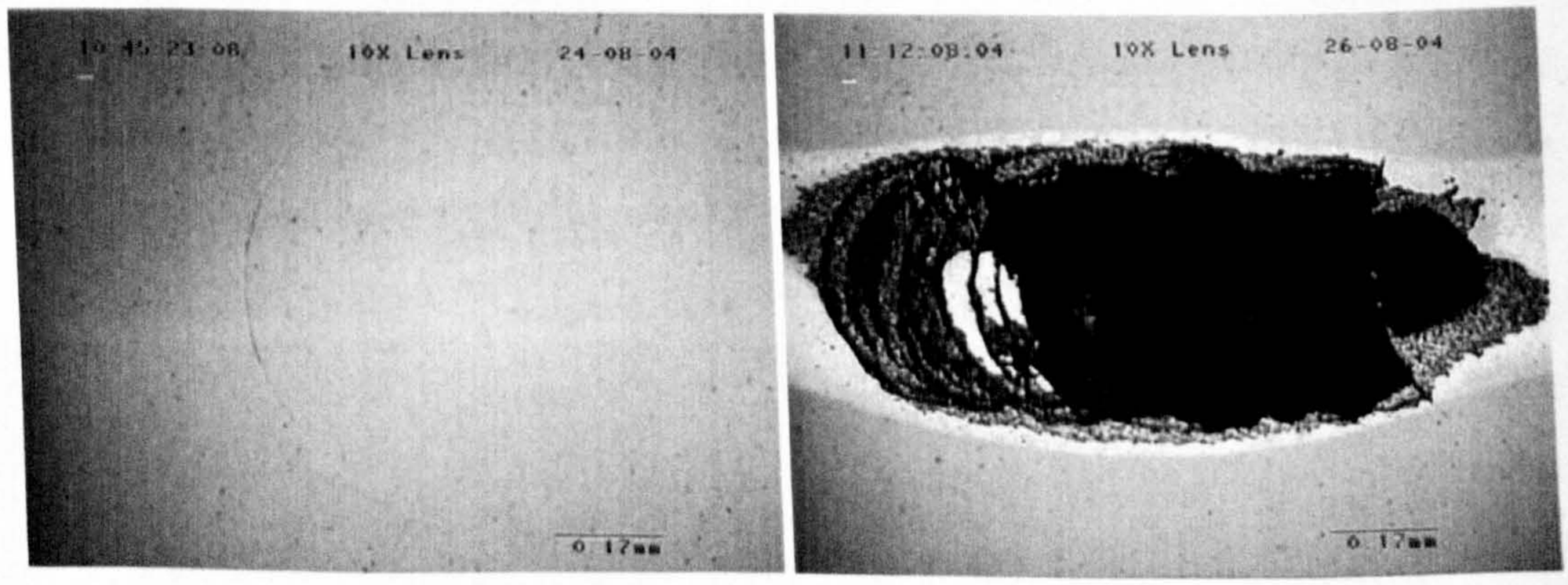

(a) Before testing (b) After 2478 minutes of testing

Figure 4.71 Surface observation of silicon nitride ball (Test F)

Figure 4.72 shows the results of surface observations from Test I. The crack orientation is the opposite of that in Test F. The fatigued crack propagates in two directions (right and left). Again, the shape of the spall implies that a long distance

of subsurface crack growth exists. The optical image of the pre-test crack is shown in figure 4.72(a). After 205 minutes of testing, the contact path is covered by lubricant deposit (figure 4.72(b)). Unlike the deposit formed in traction fluid, the lubricant deposit here is very easy to remove. The overview of the spall is shown in figure 4.72(c) and the dark field image is shown in figure 4.72(d). The original ring crack is clearly visible. The curved striations are seen on both sides of the ring crack.

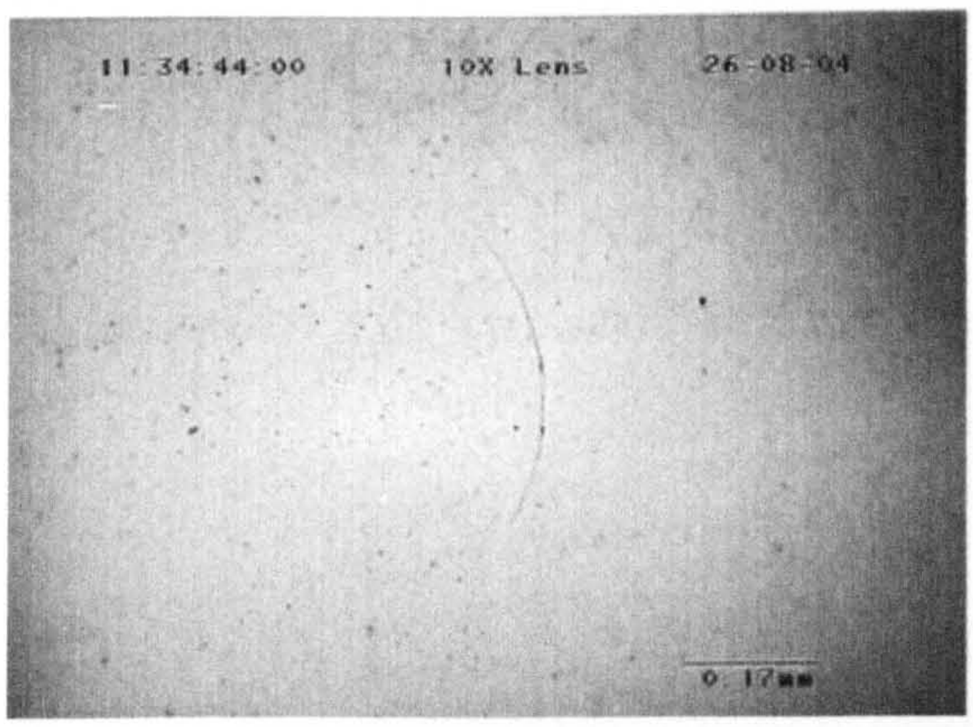

(a) Before testing

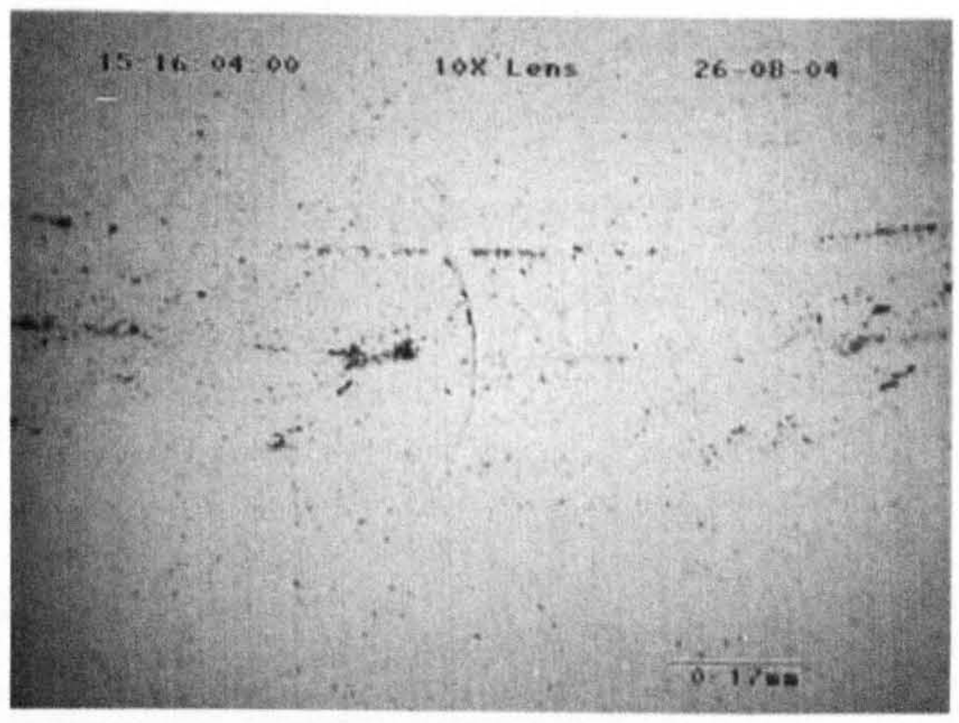

(b) After 205 minutes of testing

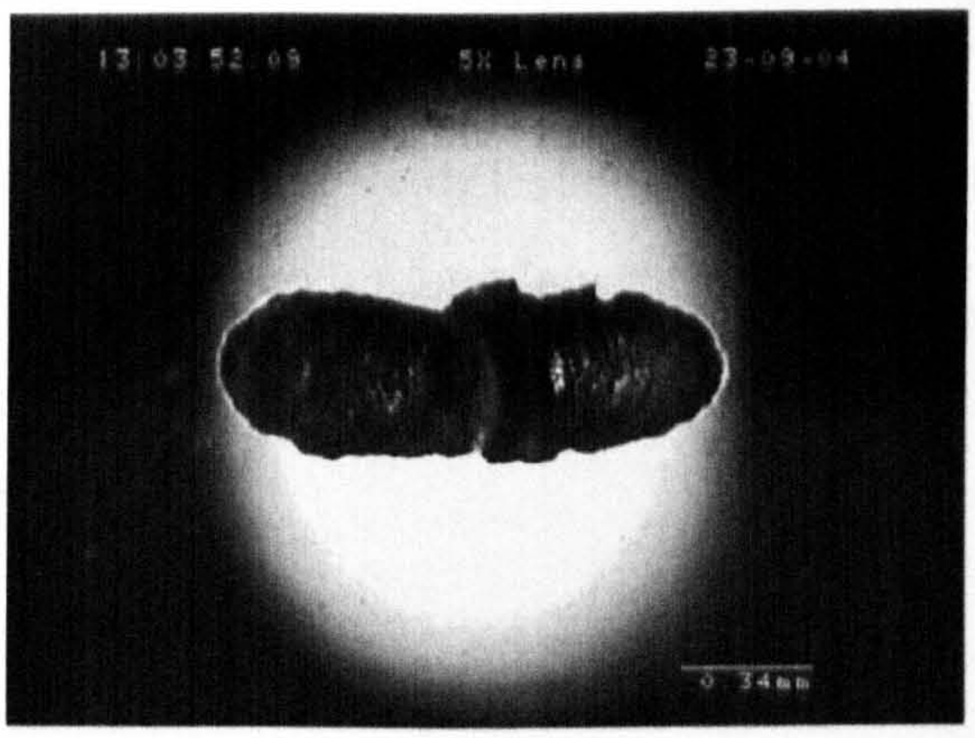

(c) After 995 minutes of testing

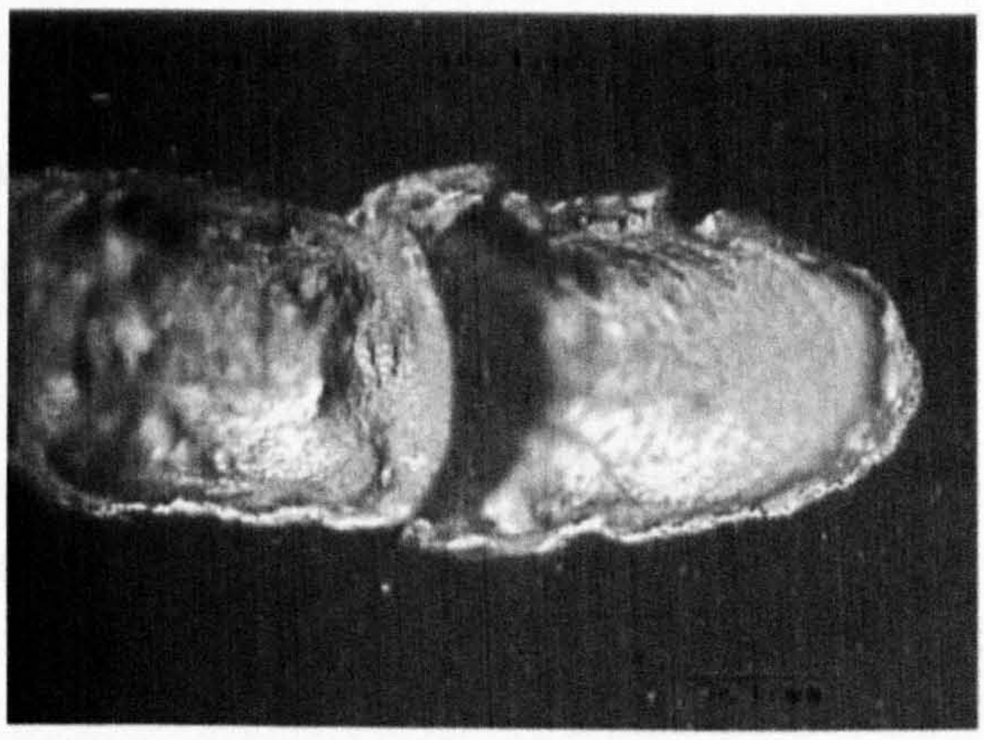

(d) Dark field image of a spall

Figure 4.72 Surface observation of silicon nitride ball (Test I)

4.4 SURFACE CHARACTERISATION OF ROLLING CONTACT FATIGUE

Observations of surface damage were carried out to determine the failure mechanisms of rolling contact fatigue in relation to the surface ring cracks. The experimental observations have confirmed that the failure mode is fatigue spalling. This section details failure progressions from four aspects: (a) secondary surface cracks, (b) fatigue spall contours, (c) fatigued crack propagation profile and (d) fatigue fracture surface features.

4.4.1 Secondary surface cracks

Numerous observations have revealed that surface secondary cracks almost always occur on a damaged surface around the spall. The understanding of how these cracks are formed is a key to revealing the mechanisms of ceramic rolling contact fatigue failure. Surface studies on balls with all test conditions have been performed using the optical and electron microscopes. The surface observations before, during and after testing were carried out to ascertain the formation process of the fatigue spall. Detailed investigations of failure processes of surface cracks are described below.

Figure 4.73 shows an example (Section 4.2, Table 4.2, Test GOL-2) of a fatigue test lubricated with gearbox oil. The maximum contact pressure was 5.58GPa. The initial ring crack cannot be seen without ultra-violet light. As the test proceeds the crack becomes more visible. Figure 4.73(a) illustrates the surface after 39.8 hours of testing. It can be seen that the crack is clearly visible due to wear around the crack mouth. Figure 4.73(b) shows the image after 68.8 hours of testing. Figure 4.73(c) shows an overview of the spall. The original ring crack is still clear after the fatigue spall was formed. Also the secondary surface cracks are found on the damaged area. The SEM micrographs clearly show those secondary surface cracks indicated by arrows (figures 4.73(e) and 4.73(f)). In this case the spall appeared beside the original crack, this may be caused by the secondary surface crack propagation. The distance between the secondary crack and the original crack is approximately 0.032mm, and the distance between two secondary cracks is about 0.036mm.

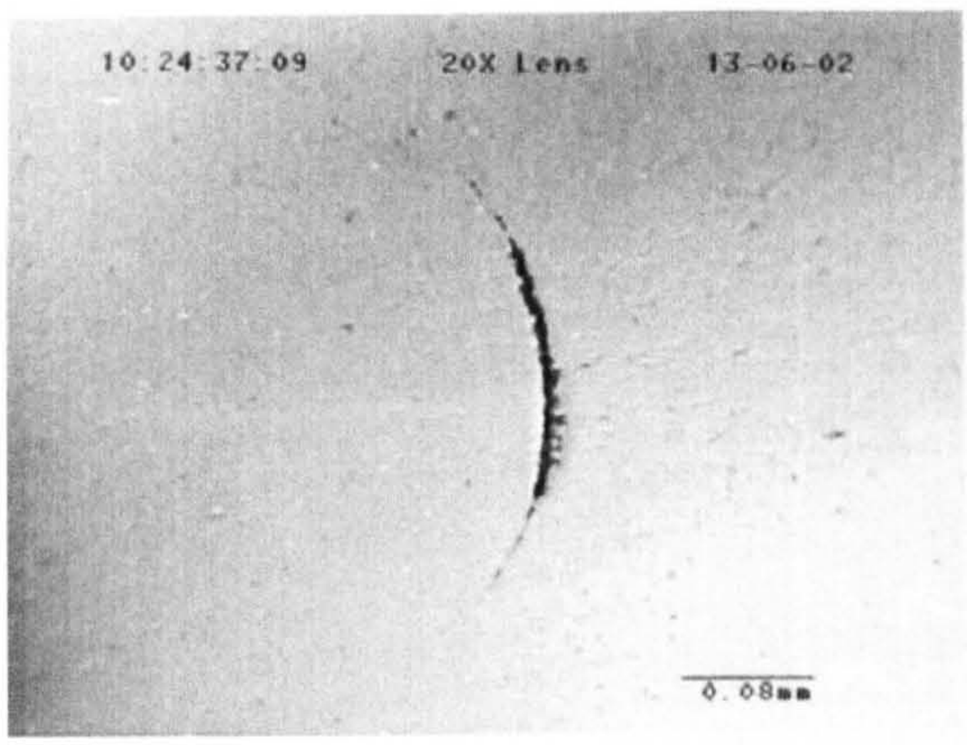

(a) After 39.8 hours of testing

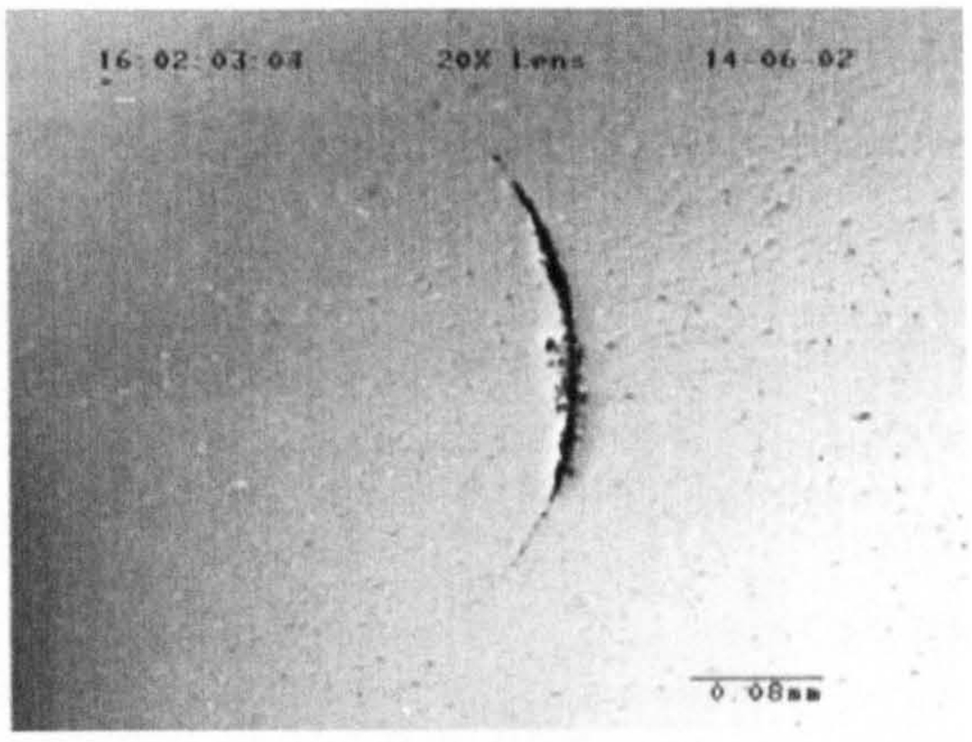

(b) After 68.8 hours of testing

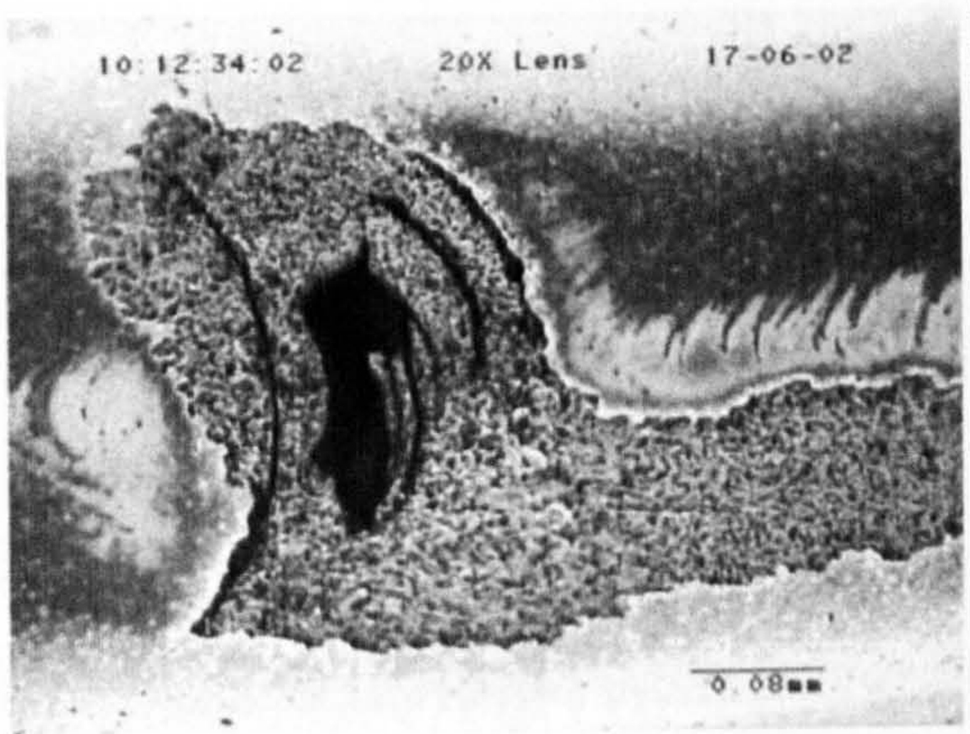

(c) Failure overview (134.33 hours)

(d) SEM image (134.33 hours)

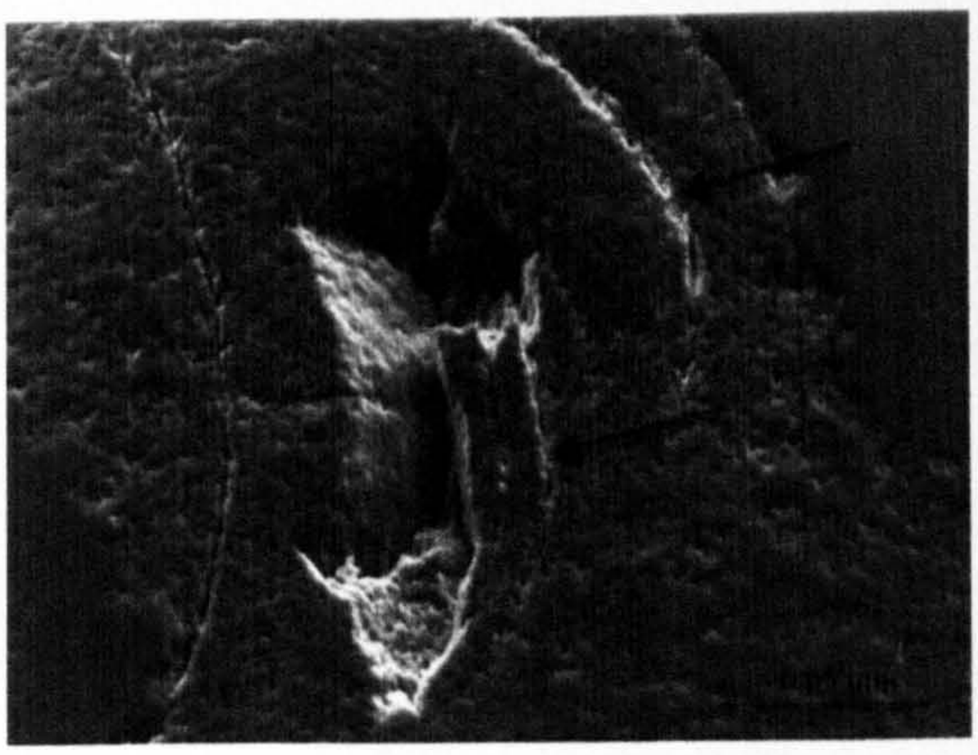

(e) Further magnified micrograph

(f) High magnification

Figure 4.73 Observation of surface damage (Test GOL-2, Table 4.2)

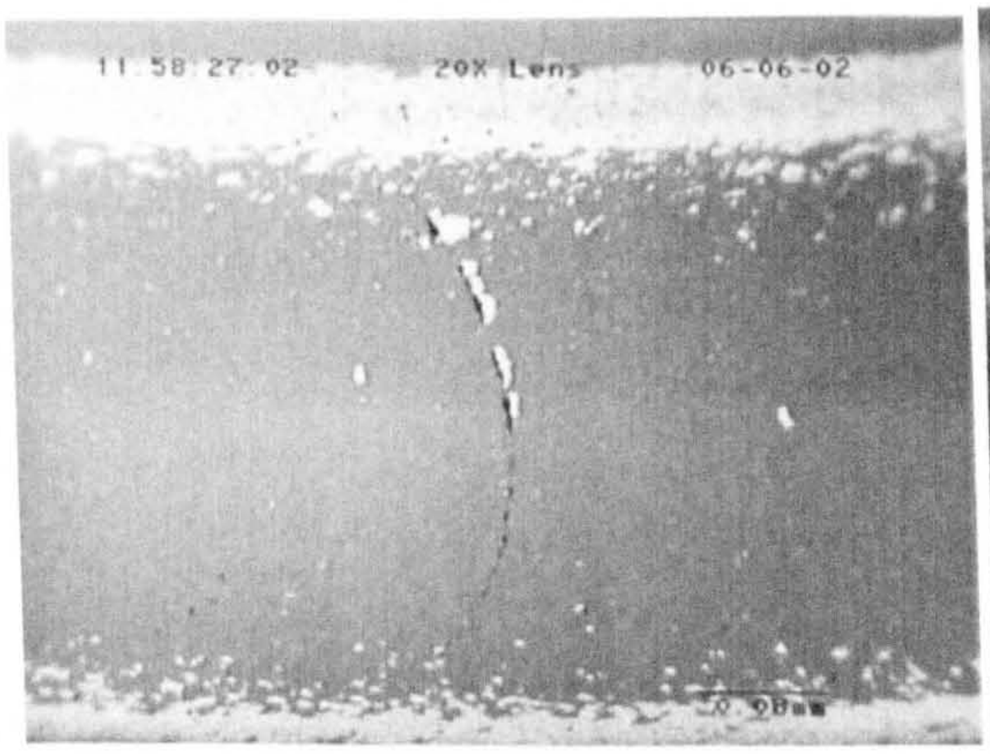

(a) After 114 hours of testing

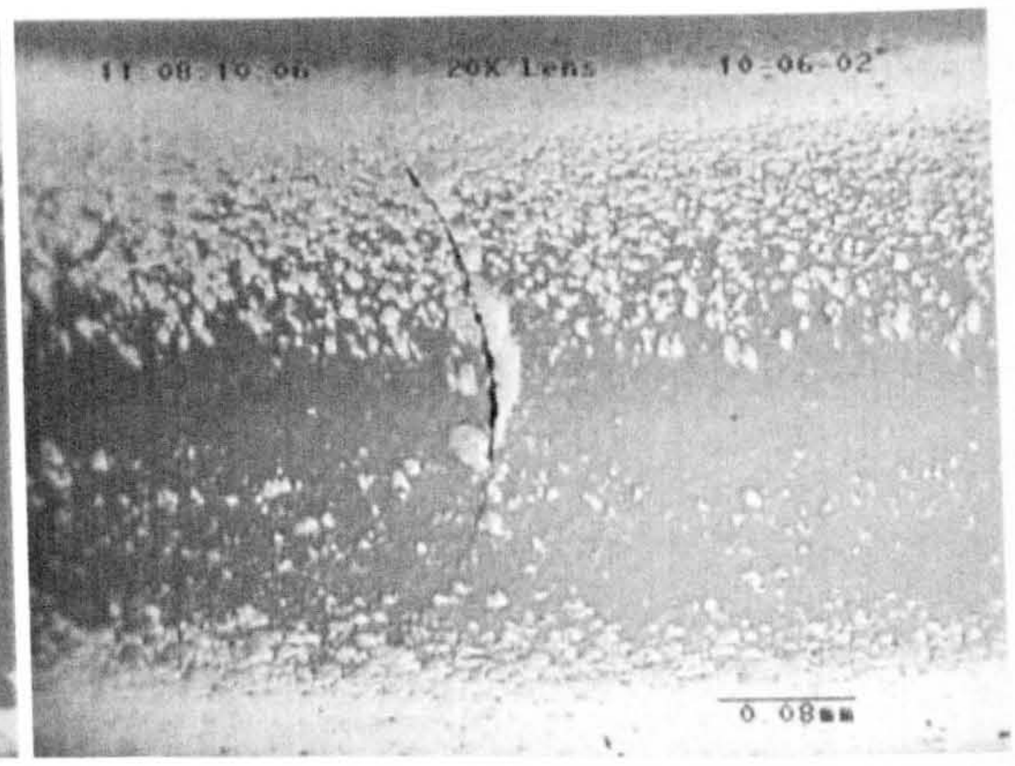

(b) After 208 hours of testing

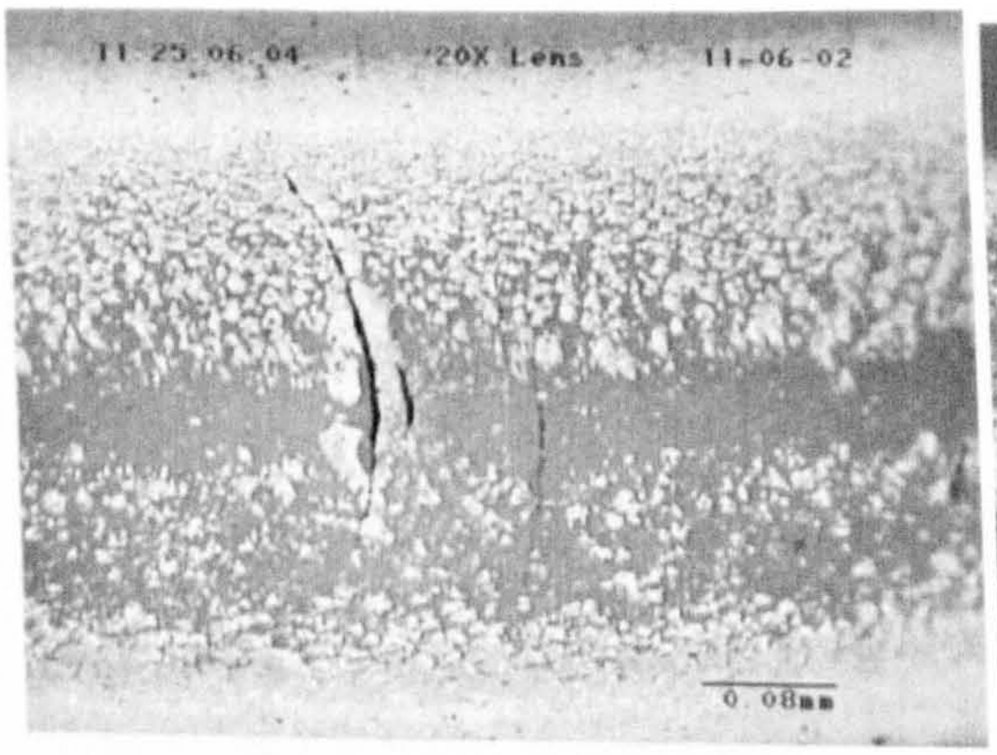

(c) After 231 hours and 20 minutes

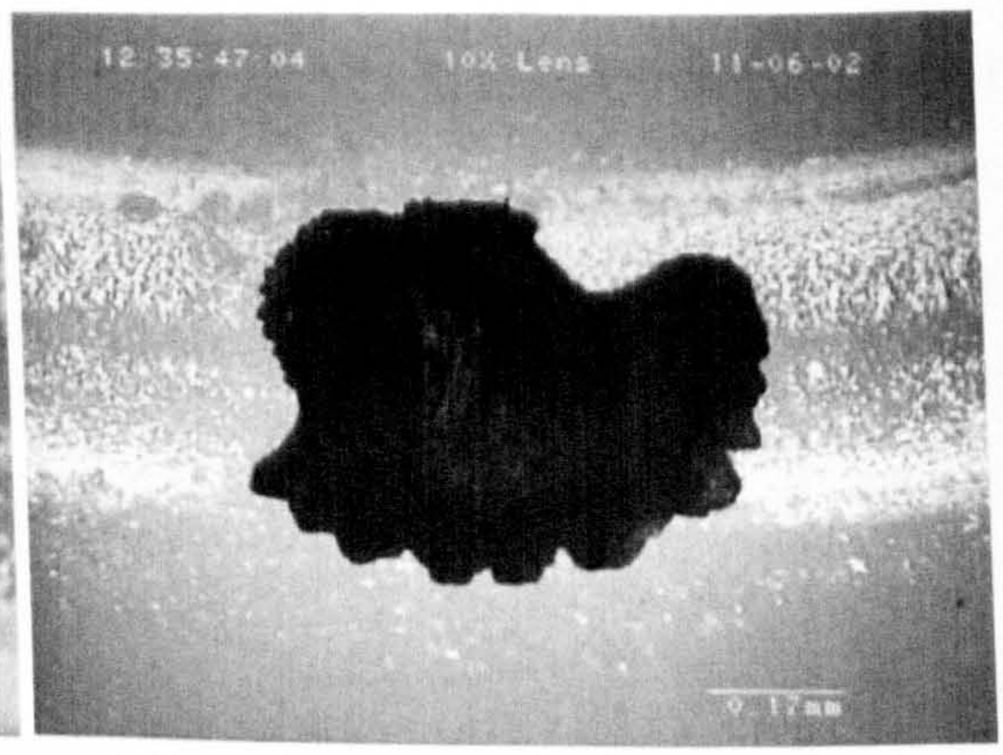

(d) After 231 hours and 40 minutes

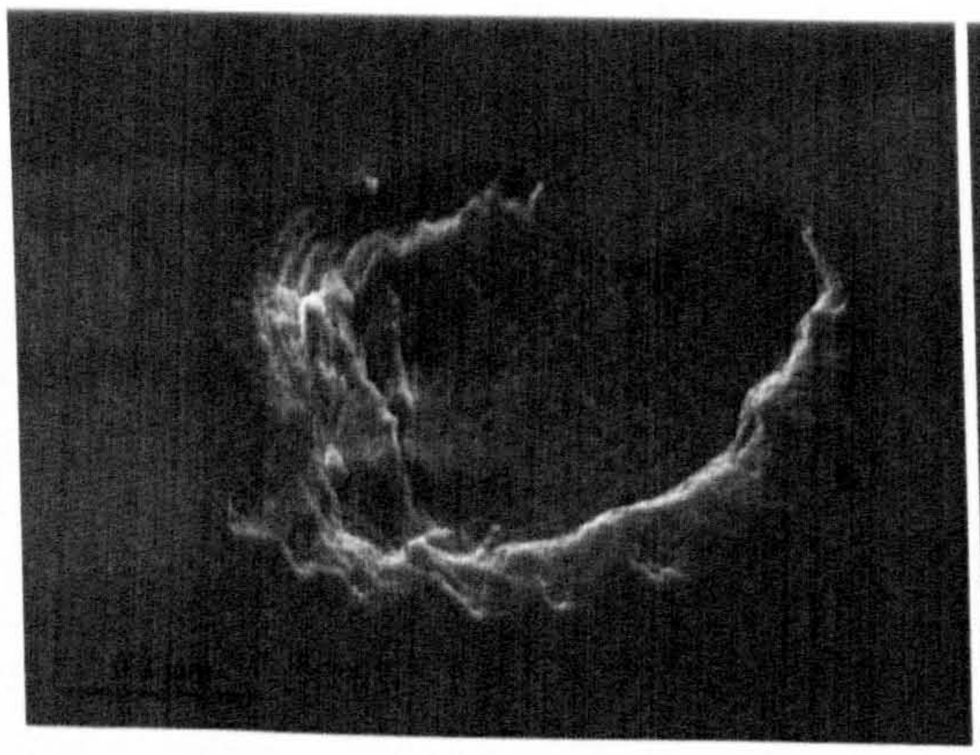

(e) SEM image of spall

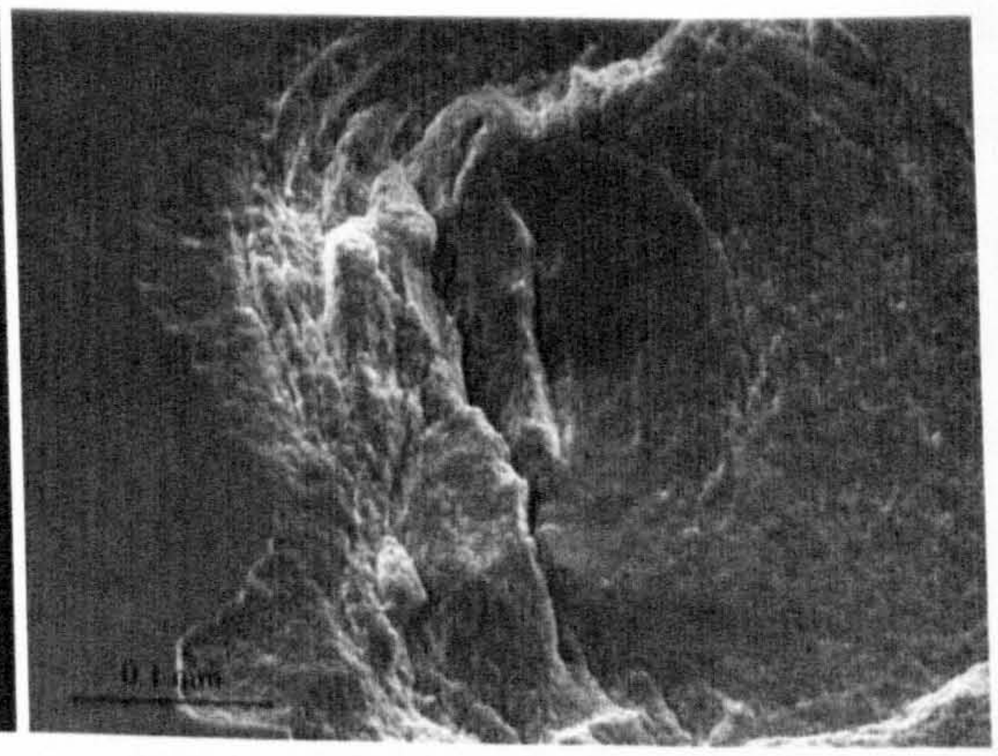

(f) Further magnified

Figure 4.74 Surface observation of silicon nitride ball (Test Grease-2, Table 4.3)

Figure 4.74 shows the surface images from Test Grease-2 (Table 4.3 of Section 4.2) at different test durations. This test was carried out at a contact pressure of 5.58GPa with grease lubrication. Figure 4.74(a) shows the ball surface after 114 hours of testing. The ring crack after 208 hours of testing is shown in figure 4.74(b). No evidence of crack growth is found along the original ring circle on the surface after completion of different test times. But the observation provides experimental evidence of the existence of the crack gap. Comparison of figures 4.74(a) and 4.74(b) reveals that the gap of the crack is proportional to the test time. The secondary surface cracks occur when the gap reaches a certain level. Figure 4.74(c) shows that the secondary surface cracks appeared on the ball surface after 231 hours and 20 minutes of testing. The distance between the secondary crack and the original crack was approximately 0.022mm. The distance between two secondary cracks was about 0.08mm. These secondary surface cracks propagate conically away from the original ring crack and connect each other to form a broken crack network. Spalling occurs from this broken network. In addition, the spall occurred just 20 minutes after the secondary surface cracks appeared on the ball surface (figure 4.74(d)). Therefore, the secondary surface cracks may play an important role in rolling contact fatigue performance.

Detailed SEM analysis of the spall is shown in figures 4.74(e) and (f). After fatigue spall, the secondary cracks have mostly gone. However, the trace of those secondary cracks can still be seen as shown in figure 4.74(f). The crack propagation forming a branch crack pattern is clearly displayed on fatigue surfaces. The mechanism of the ring crack growth must be related to the formation of fatigue striations. Fatigue mechanics will be discussed in Chapter 5.

Since the original crack was a small natural crack, the secondary cracks cannot be formed easily. The initiation of secondary surface cracks requires a certain crack size. This will be explained from numerical analysis, discussed in Chapter 5. Therefore, the small cracks (natural and small artificial) often involve the initiation and propagation of fatigue cracks.

The observations from large cracks (artificially induced cracks) are shown in figures 4.75 to 4.78. These results contain various sizes of the cracks tested under different conditions. Figure 4.75 shows the result from Test A of table 4.11. The

crack radius was 0.4mm and the crack length was approximately 0.23mm. The crack length is estimated according to the results of subsurface geometry studies. The lubrication fluid was mineral oil. The reverse position was used in this test. As expected, the large cracks can easily cause the secondary surface cracks (figure 4.75). This test only lasted three minutes.

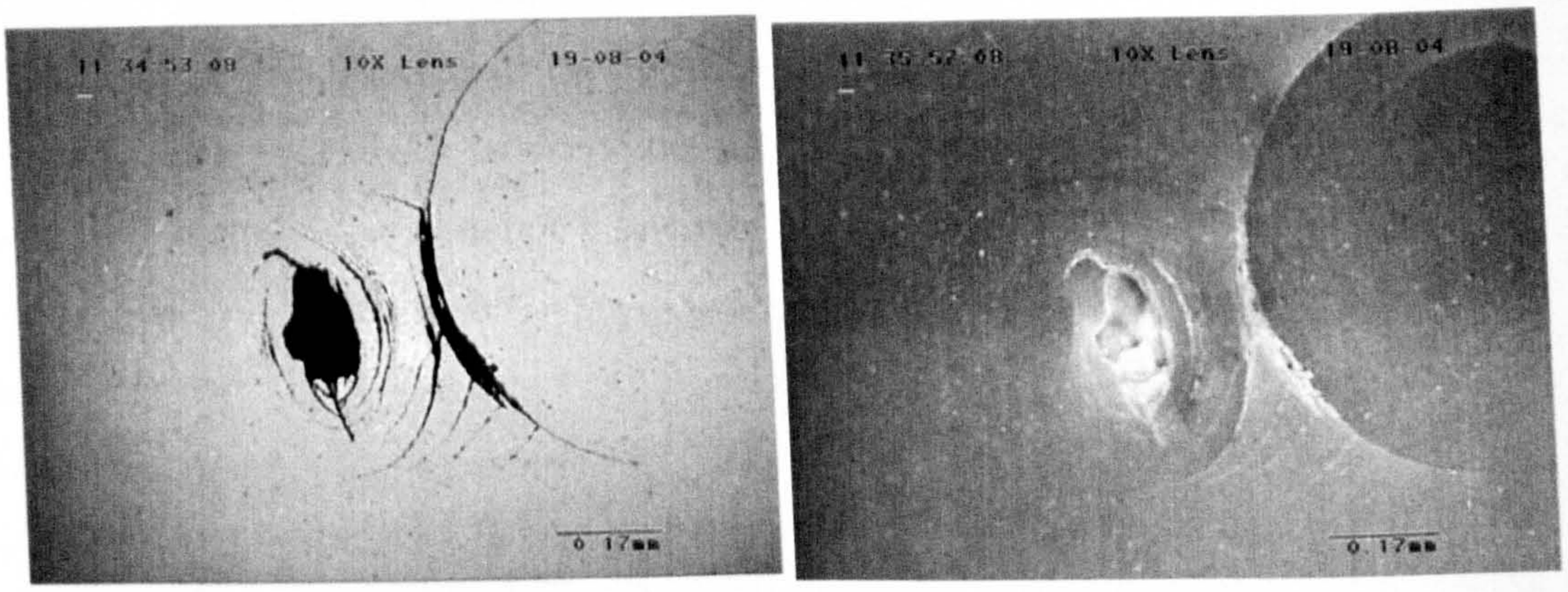

(a) After 3 minutes of testing (b) Dark field image

Figure 4.75 Surface observation of silicon nitride ball (Test A, Table 4.11)

Figure 4.76 is an example showing the secondary surface cracks from Test 9 of table 4.6. The crack radius and length are the same as in previous tests (Test A). Lubrication fluid was mineral oil. The normal crack orientation was used. The crack before testing is shown in figure 4.76(a). After 25 minutes of testing the secondary surface cracks appear on the ball surface around the primary crack (figure 4.76(b)). These secondary surface cracks occur on both sides of the primary crack and cracks were very close to each other. The radius of the secondary cracks is also similar to each other. The fact that secondary surface cracks appear on the left side of the primary crack implies a subsurface crack underneath. Figure 4.77 is another example showing the secondary surface cracks. The original ring crack is still visible on the right edge. A number of surface cracks are left on the surface (left edge) because most of the cracks have spalled away. The traces of the secondary cracks can be clearly seen at both the left and right edges of the spall.

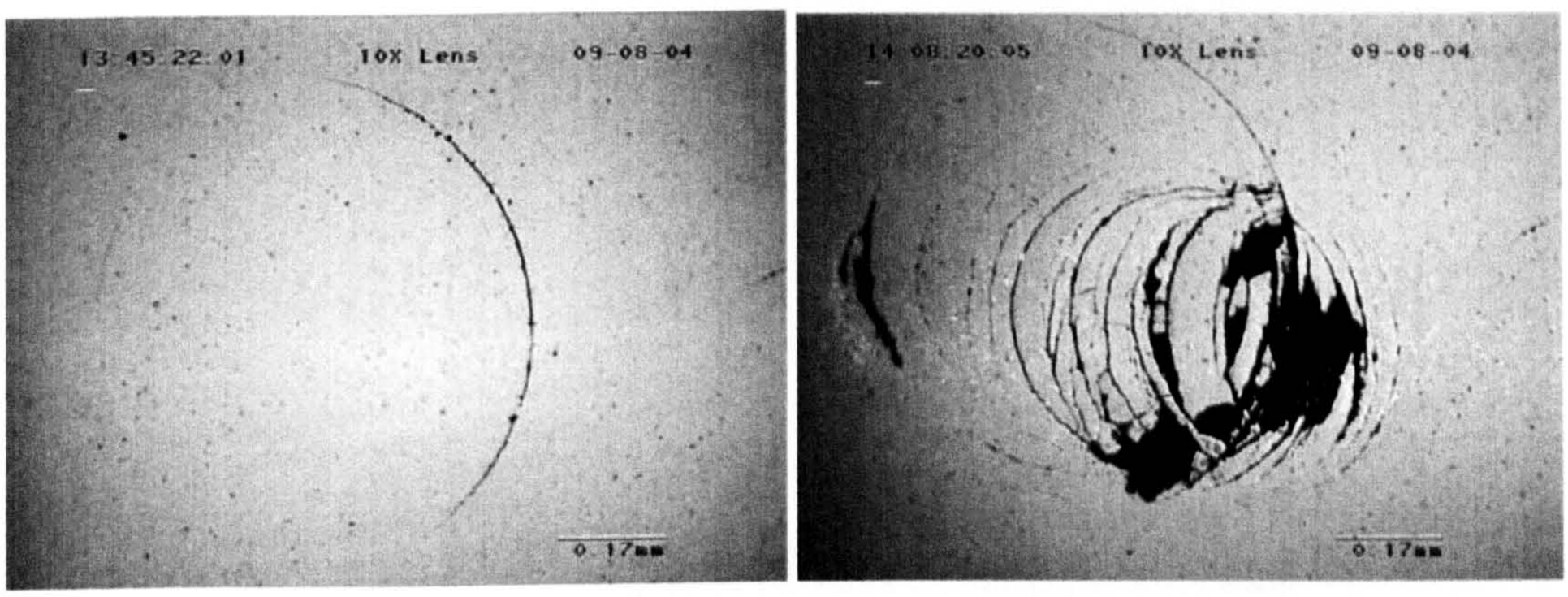

(a) Before testing (b) After 25 minutes of testing

Figure 4.76 Surface observation of silicon nitride ball (Test 9, Table 4.6)

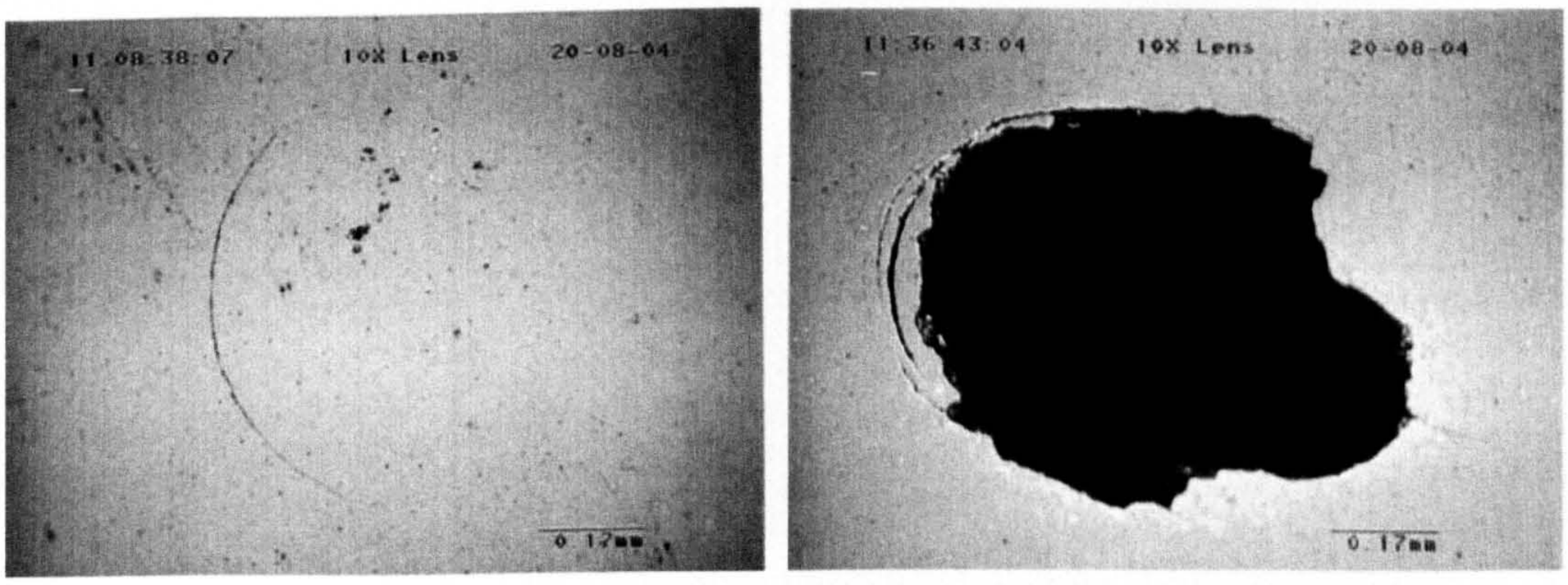

(a) Before testing (b) After 11 minutes of testing

Figure 4.77 Surface observation of silicon nitride ball (Test B, Table 4.11)

Results of surface observation from Test F (maximum contact stress 4.0GPa) are shown in figure 4.78. The crack before the test can be seen under normal white light (figure 4.78(a)). Figure 4.78(b) shows the ring crack and contact track after 23 hrs and 10 minutes of fatigue testing. The ring crack became more visible and the crack gap became bigger. This observation provides evidence of crack gap enlargement. Eventually the ball failed after 41 hours and 18 minutes of testing (figure 4.78(c)). The primary crack is seen clearly and the fatigued crack propagates almost parallel to the surface. Detailed secondary cracks are shown in figure 4.78(d).

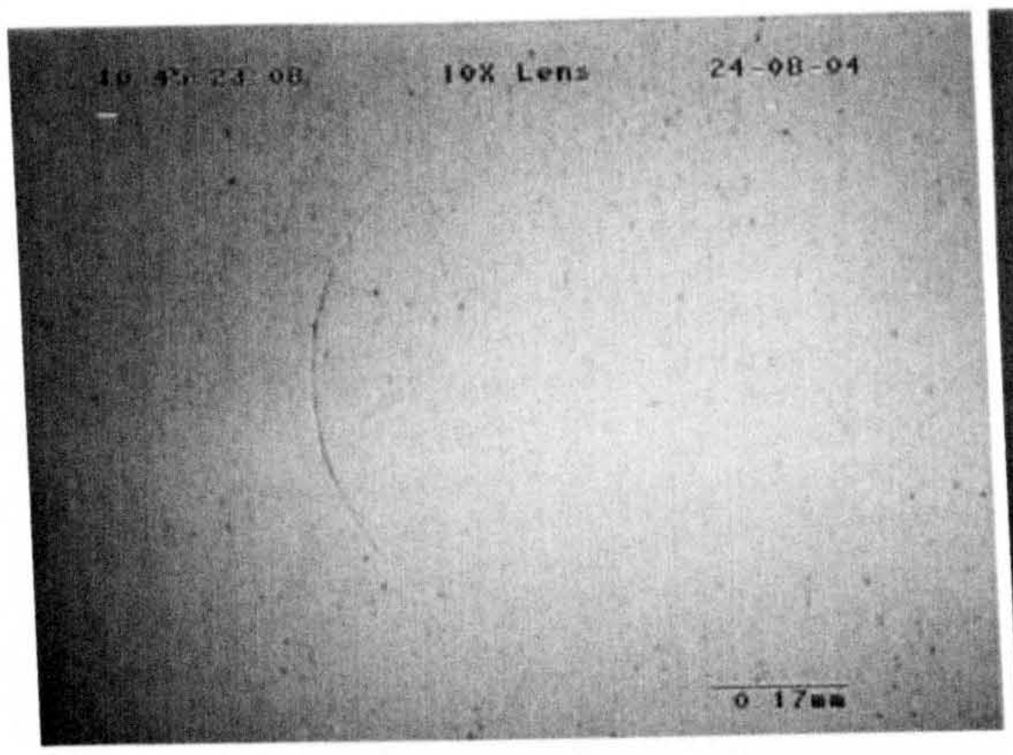

(a) Before testing

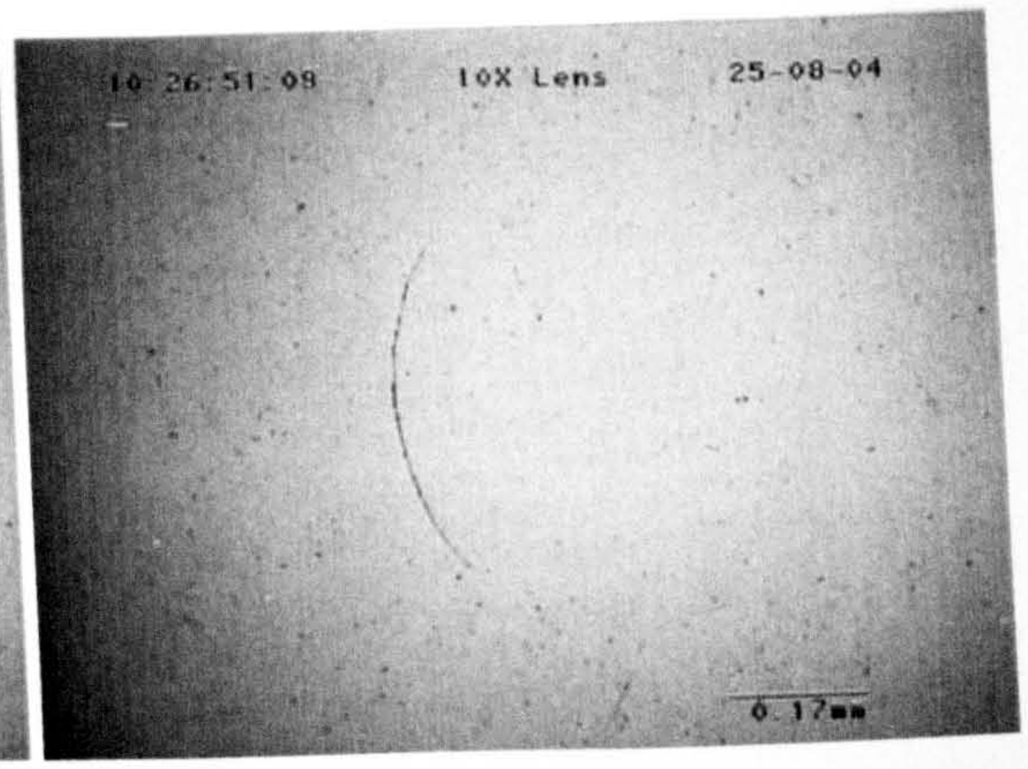

(b) After 23h and 10 minutes

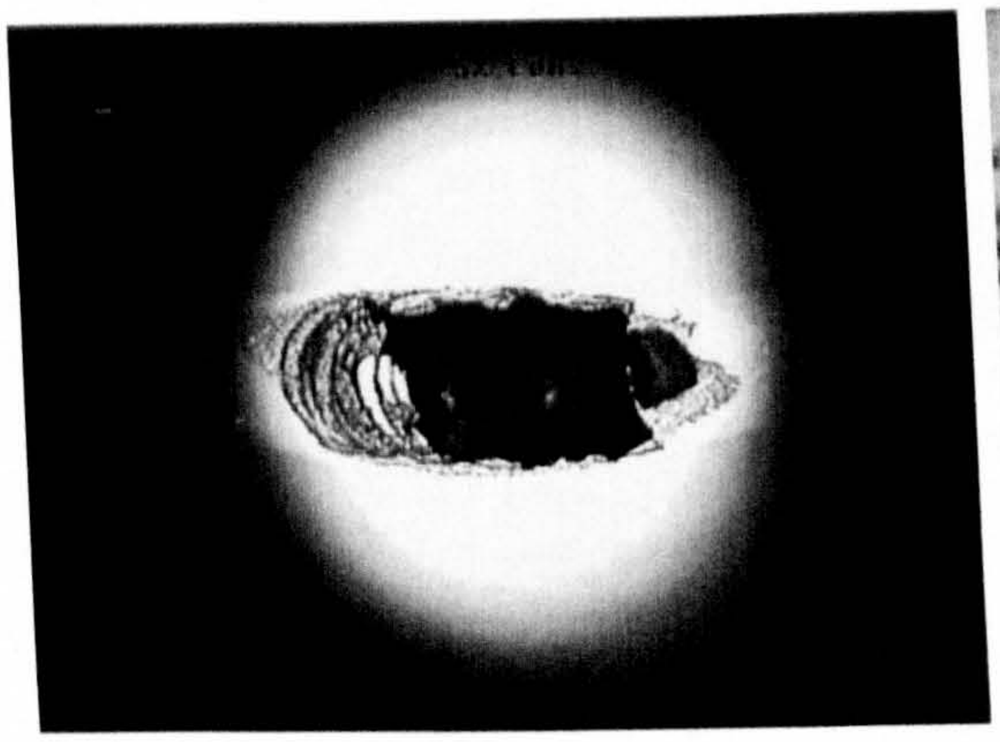

(c) After 41h and 18 minutes

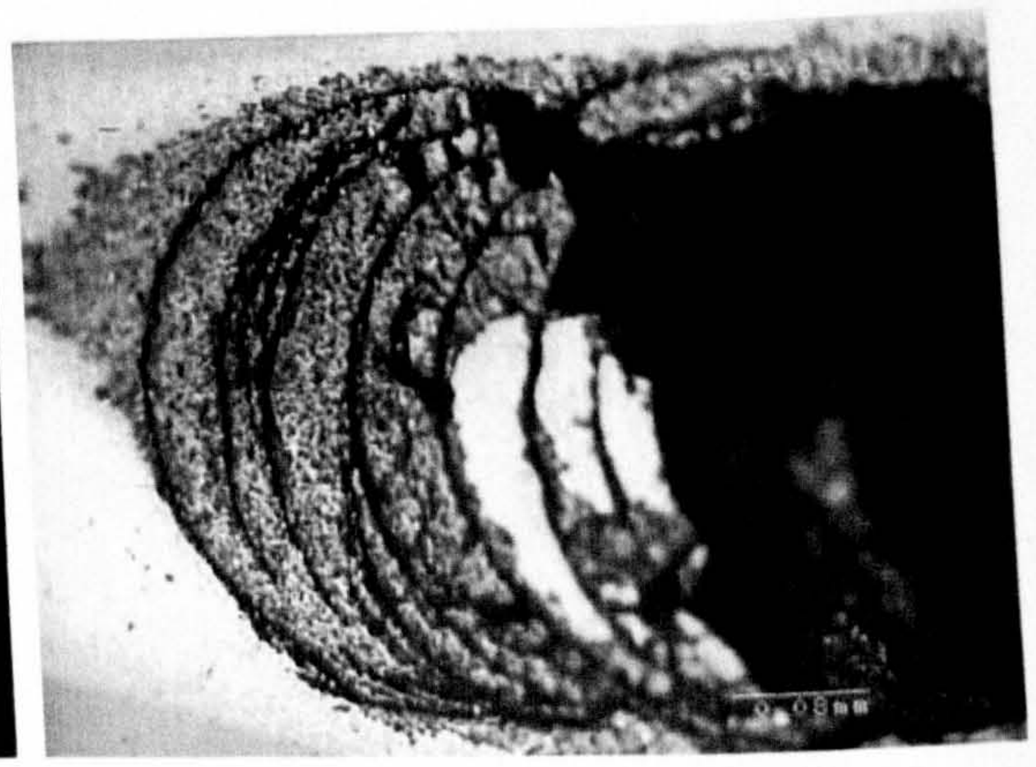

(d) Further magnified image

Figure 4.78 Surface observation of silicon nitride ball (Test F, Table 4.11)

Figure 4.79 shows the results from Test N3 using traction oil lubrication. This test was performed at a contact pressure of 5.58GPa. Unlike the previous observations, only a few secondary surface cracks are left on the surface because of the extensive spalling. Figure 4.79(a) shows the ring crack and contact track after 31 minutes of fatigue testing. Due to fatigue spalling the secondary surface cracks cannot be seen directly on the ball surface. However, the traces of these cracks are clearly displayed on the fracture surface as shown in figure 4.79(b). Figures 4.79(c) and (d) demonstrate further images of secondary surface cracks at higher magnification.

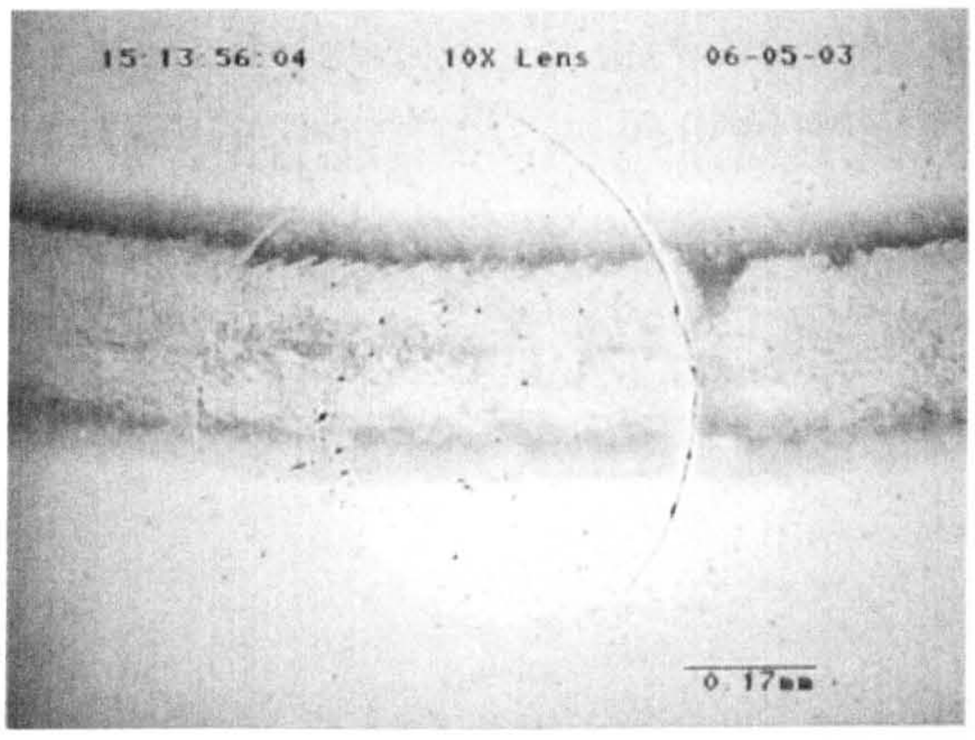

(a) After 31 minutes of testing

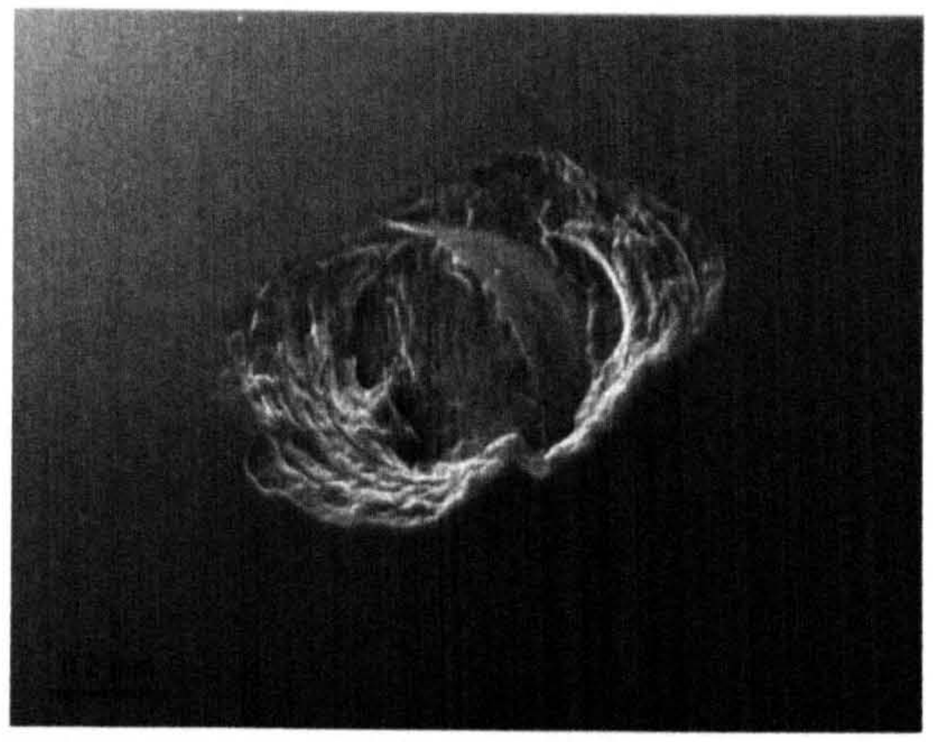

(b) After 60 minutes of testing

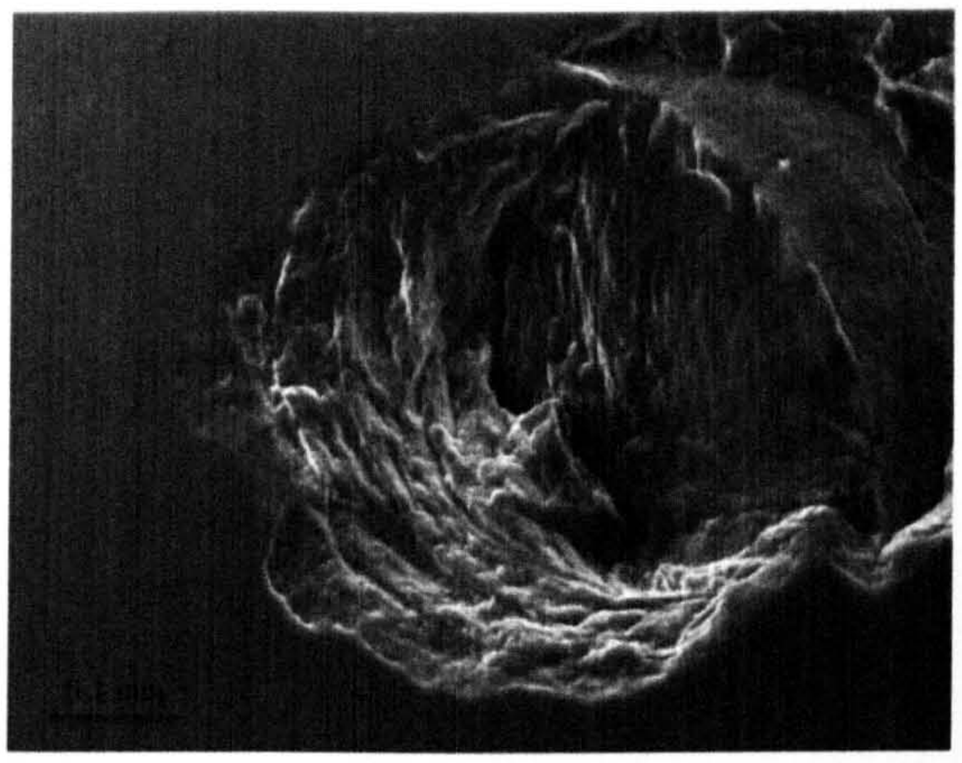

(c) Magnified image of left side

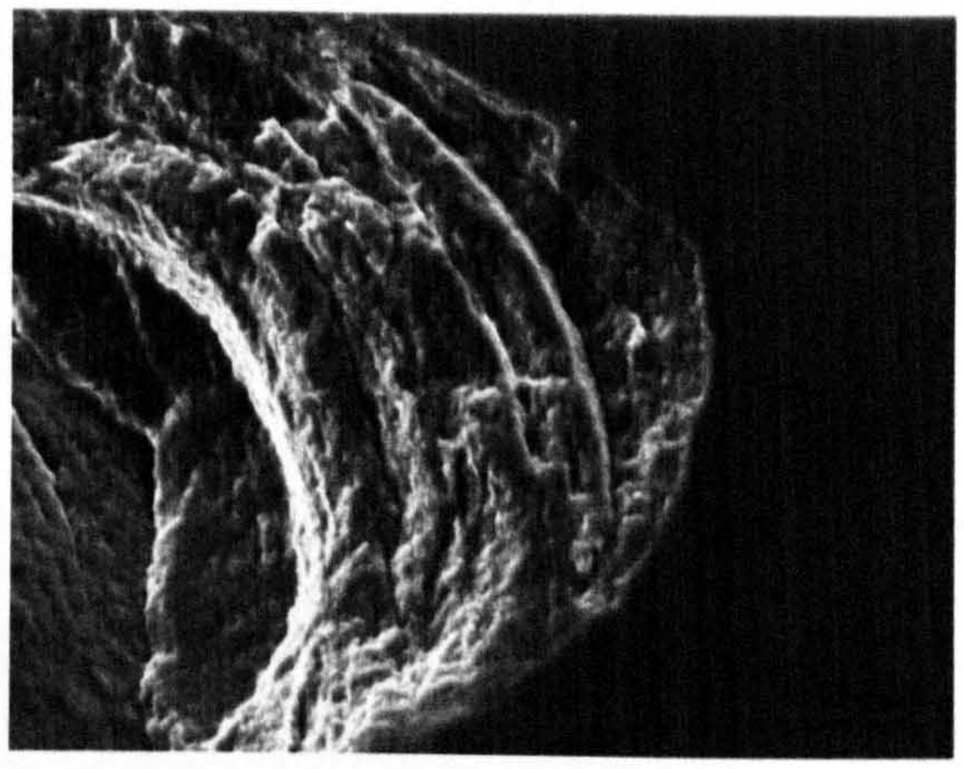

(d) Magnified image of right side

Figure 4.79 Surface observation of silicon nitride ball (Test N3, Table 4.8)

4.4.2 Fatigue spall contours

A fatigue spall normally takes the form of an ellipse. Sometimes it may take the form of a half ellipse. The shape of the ellipse depends on the rolling direction, crack size and contact stresses. To express those factors clearly, some terms need to be stated first. The long axis of the ellipse represents the x axis, which is parallel to the contact path (or rolling direction). The short axis of the ellipse represents the y axis, which is perpendicular to the contact path (or rolling direction). The short axis is approximately equal to the contact radius. The long axis is dependent upon the contact stresses and crack sizes.

The shape of the spall depends on the rolling direction. When a surface ring crack is located in the normal position (figure 3.4(a)), the spall can take the form of either: (a) a half ellipse (figure 4.80(a)) or (b) a whole ellipse (figure 4.80(b)). However, when the crack is located in the reverse position (figure 3.4(b)), the spall contour only takes the form of a half ellipse due to the favoured crack propagation direction, as shown in figure 4.81.

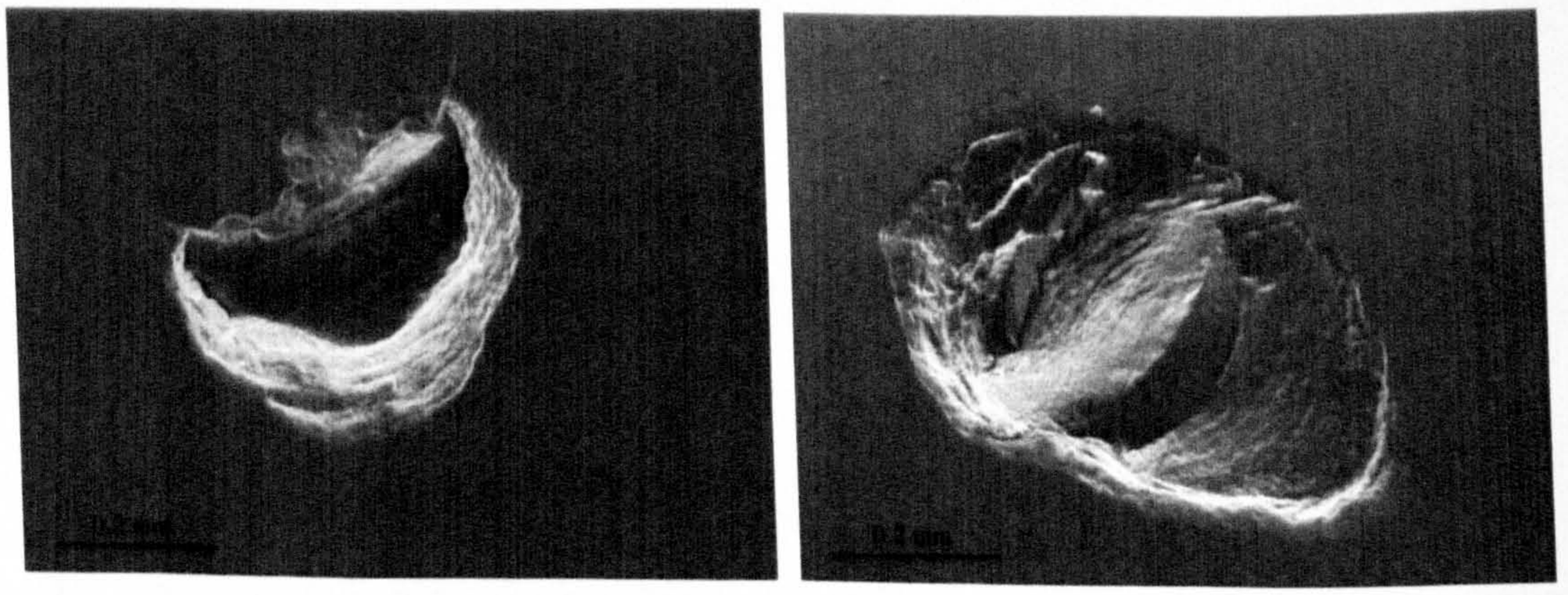

(a) Half ellipse (Test D1-2, Table 4.10) (b) Whole ellipse (Test D1-4, Table 4.10)

Figure 4.80 Fatigue spall profile with normal position (Table 4.10)

Crack sizes significantly affect the spall contour of ceramic balls. For a large crack, the long axis of the ellipse becomes shorter compared to a small crack. In other words, the x axis value (the long axis of the ellipse) decreases as the radius of a crack increases. This is because the large crack normally results in the high maximum principal stresses at the edge of the contact circle (see Chapter 5). This high tensile stress leads to the formation of secondary surface cracks. The secondary

surface cracks dominate the failure processes. Subsurface crack growth is normally not involved. Figure 4.82 illustrates two examples of fatigue spall which come from the large crack. Fatigue failure is dominated by secondary surface cracks.

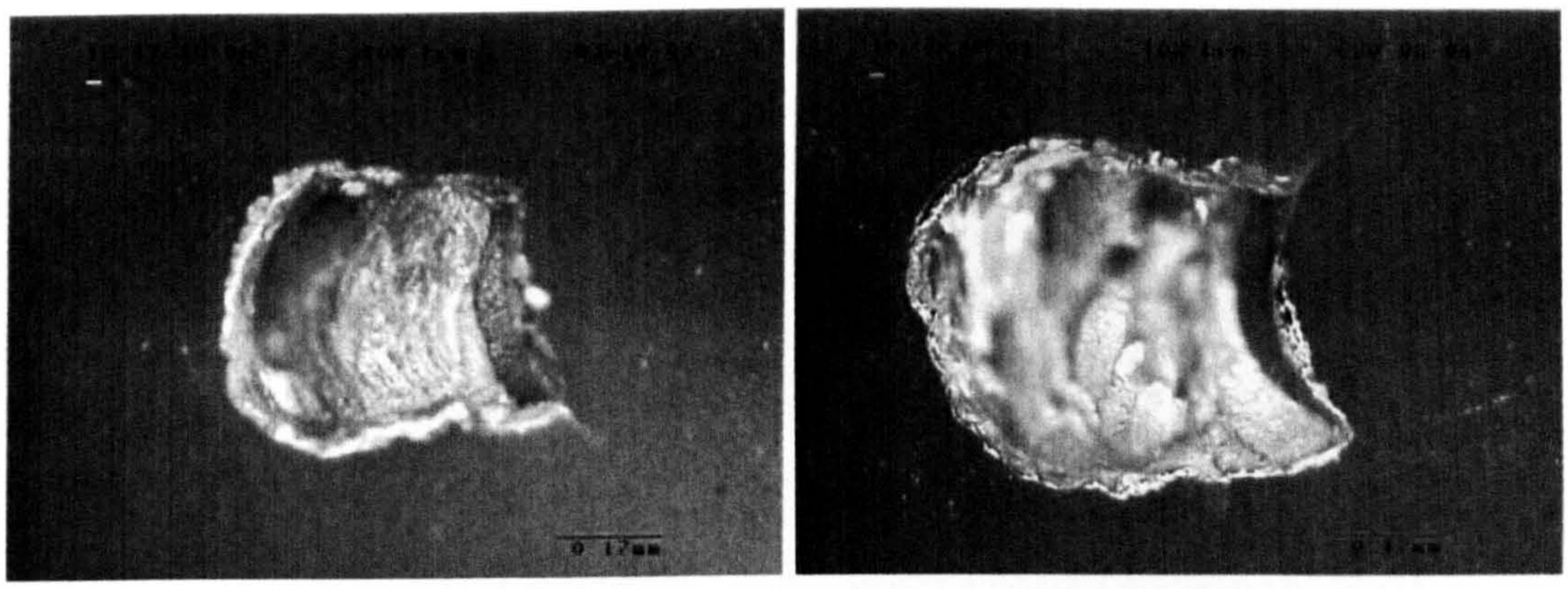

(a) Half ellipse (Test R6, Table 4.8)　　(b) Half ellipse (Test D, Table 4.11)

Figure 4.81 Surface contour of fatigue spall with the reverse position

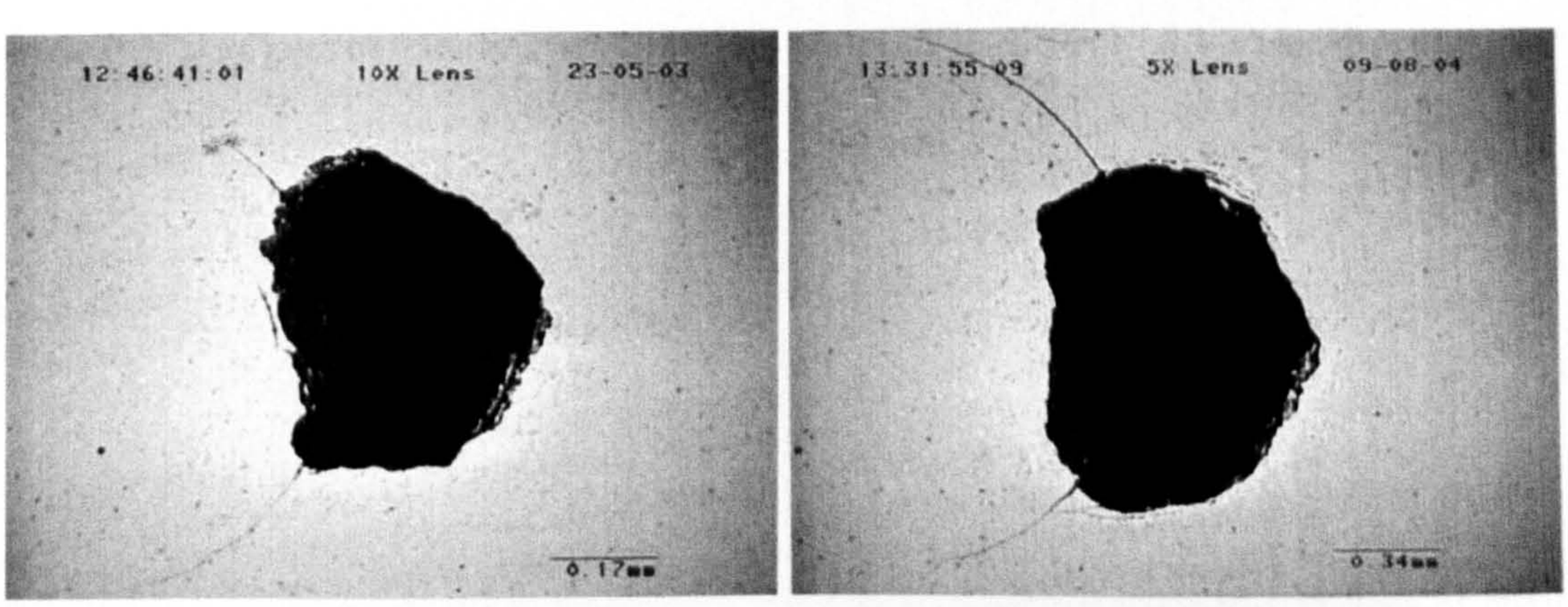

(a) Test 3 in Table 4.6　　(b) Test 8 in Table 4.6

Figure 4.82 Surface contour of a spall with a large crack radius

The spall contour is considerably influenced by the contact stresses. The long axis of the ellipse becomes longer and longer as the contact stress decreases. Numerical analysis (Chapter 5) predicts that the surface tensile stress is less than the value required for the formation of the secondary surface cracks when the contact stress is small. As a result the subsurface fatigued crack continues to grow until the crack gap reaches a critical value. When the crack gap reaches the critical value the secondary surface cracks are generated to form a final spall. Figures 4.83 and 4.84

are two examples of a fatigue spall at a low contact stress. In figure 4.83, the fatigued crack grows in the opposite direction of the rolling direction. Crack propagation is towards the inside of the ball or parallel to the surface (The crack propagation will be discussed in the next section). The failure is caused by the secondary surface cracks.

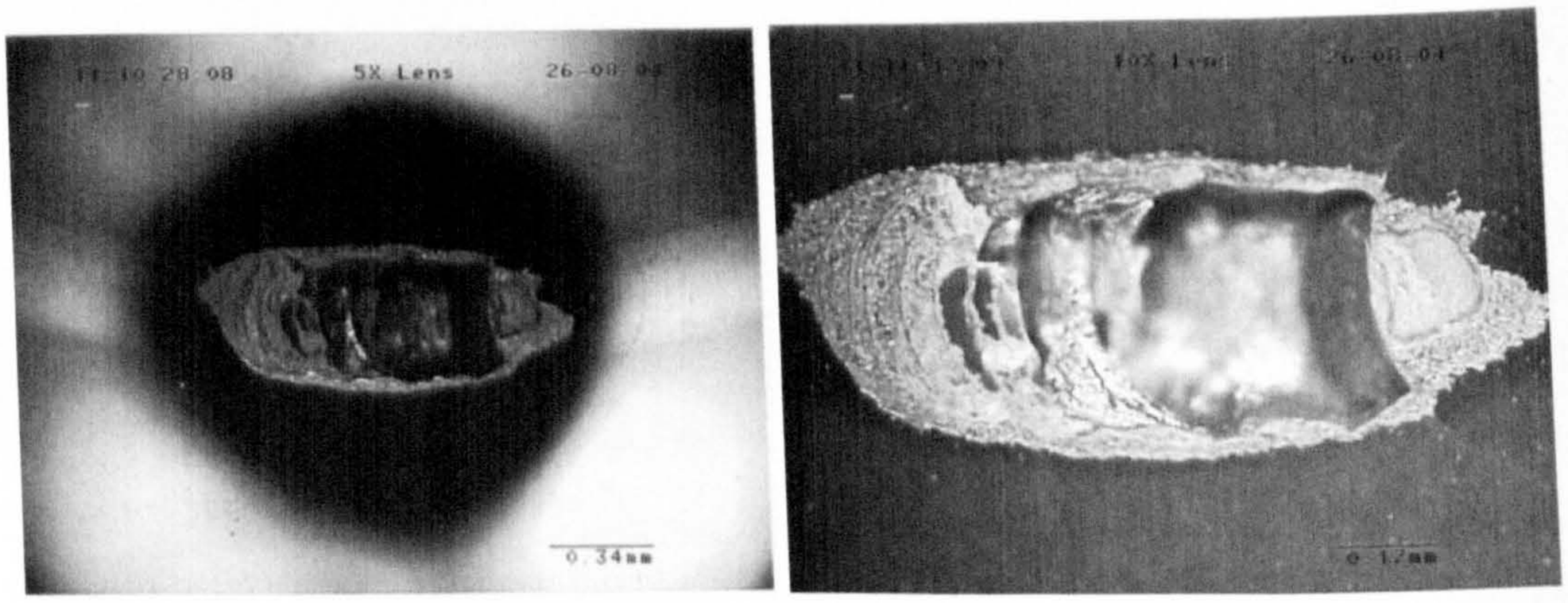

(a) Overview of a spall (b) Further magnified image

Figure 4.83 Profile of fatigue spall with low contact stress (Test F, Table 4.11)

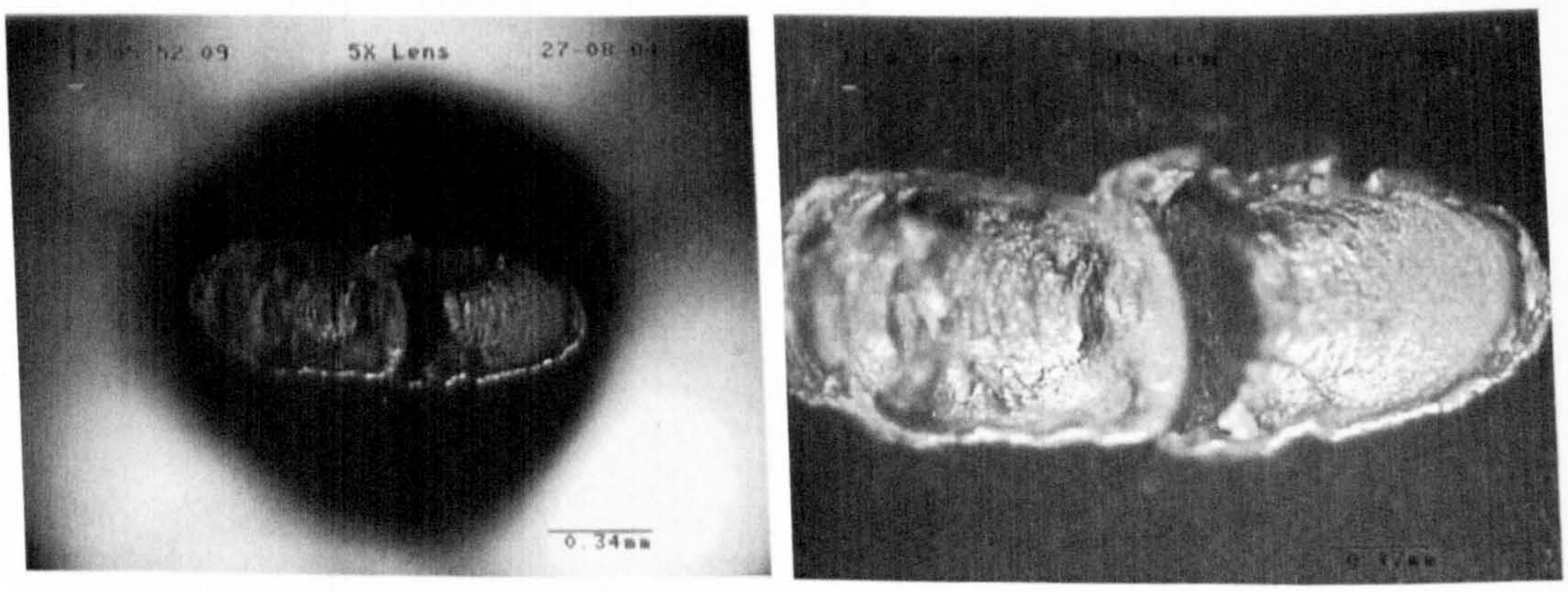

(a) Overview of a spall (b) Further magnified image

Figure 4.84 Profile of fatigue spall with low contact stress (Test I, Table 4.11)

In figure 4.84, the fatigue crack propagates in both directions. Since the orientation of the crack is in the normal position, as discussed above, for this position the fatigue crack can propagate either along the rolling direction or opposite to the rolling direction. When the crack grows along the rolling direction, crack propagation is parallel to the surface or slightly towards the surface.

4.4.3 Fatigue crack propagation profile

Although the optical and SEM images can provide a detailed surface texture, they cannot display the profile of fatigue fracture surface. Profiles of the fatigue paths are important in the study of failure mechanisms and fatigue life. In the following discussion, the profile of a fatigued surface is measured using a WYKO laser profilometer.

Figure 4.85 gives details of the experimental results from Test R4 of table 4.8. Figure 4.85(a) shows an overview of the spall. The primary ring crack can be seen clearly. Figure 4.85(b) shows a 3D profile of the spall. It can be seen that the maximum depth is approximately 69 microns. To obtain the whole view of the fatigued surface, scans are made in three directions as indicated by the arrows, shown in figure 4.85(c) to (e). The crack propagates approximately 0.25mm at a depth of 0.074mm (figure 4.85(d). The growth path is almost parallel to the surface. The crack angle is about 31.8° (figure 4.85(c)).

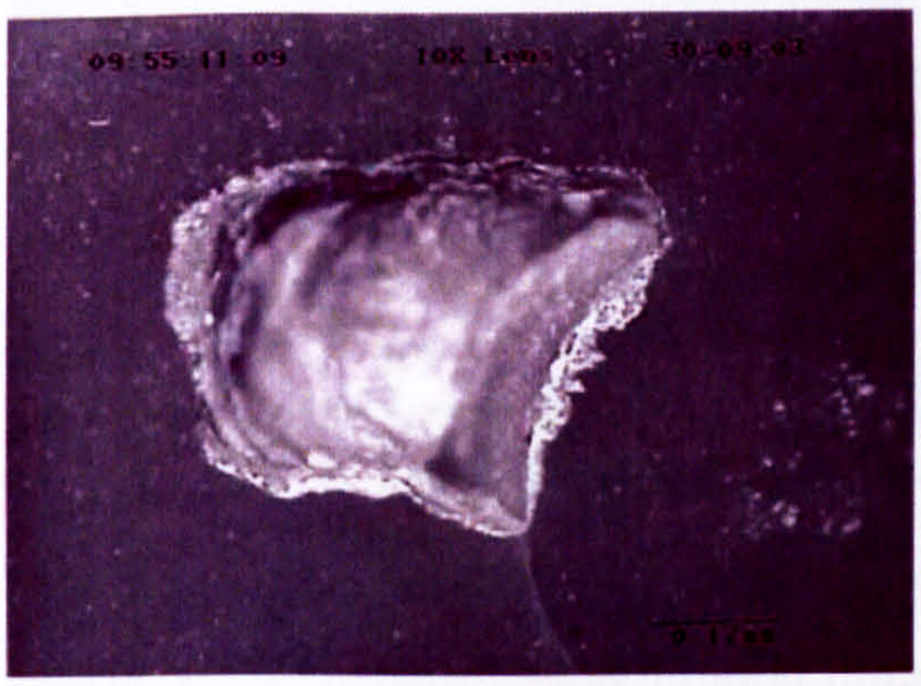

(a) Overview of fatigue spall

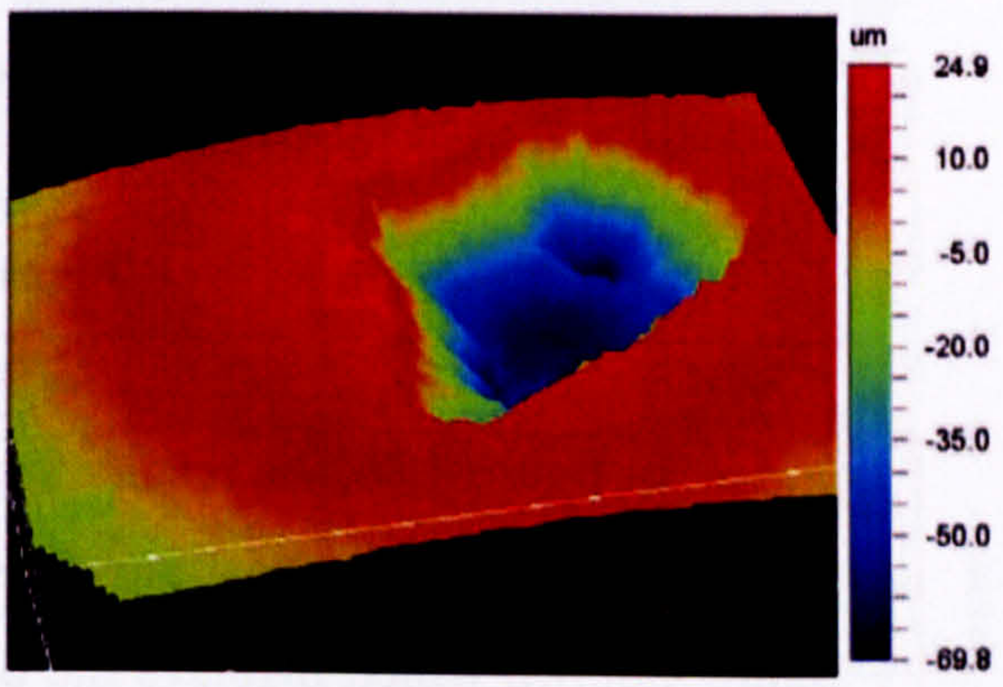

(b) 3D profile of fatigue spall

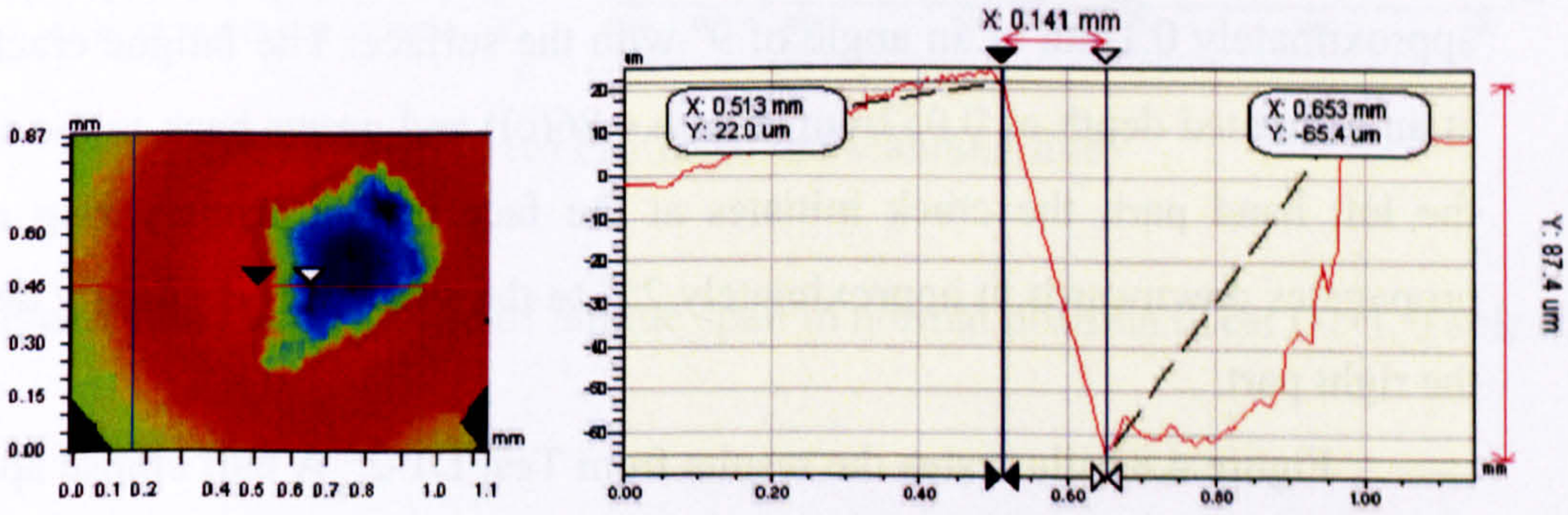

(c) Profile of the scanning line

Figure 4.85 Depth profile of fatigue spall in reverse position (Test R4, Table 4.8)

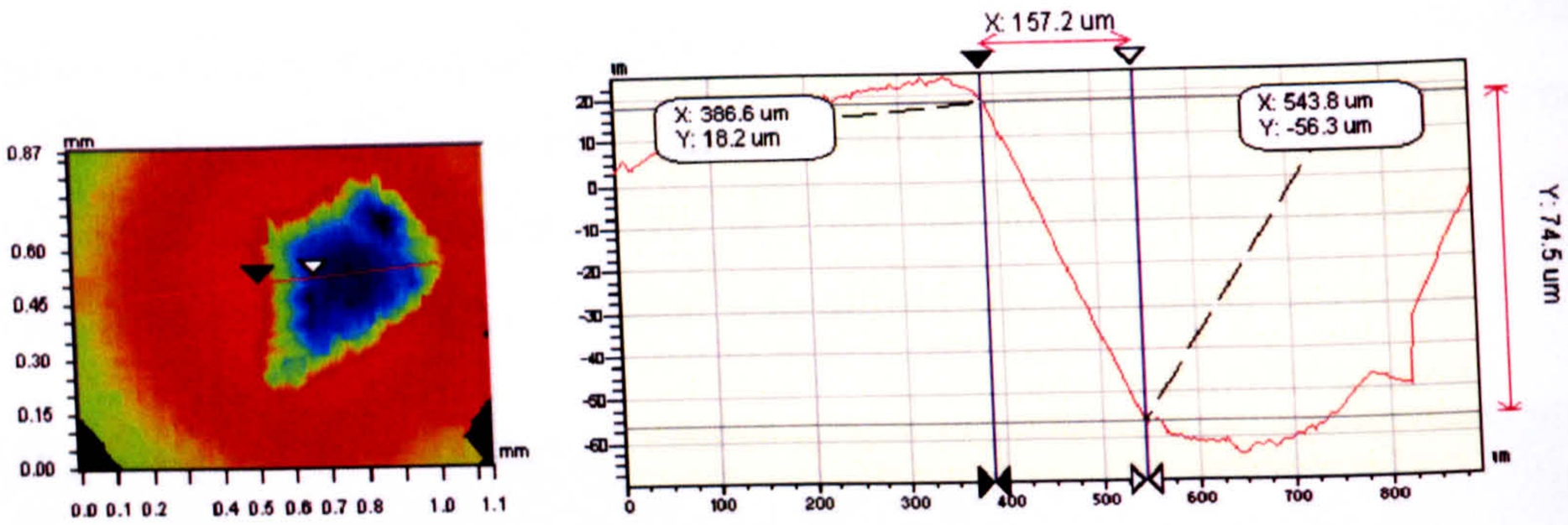

(d) Profile of the scanning line

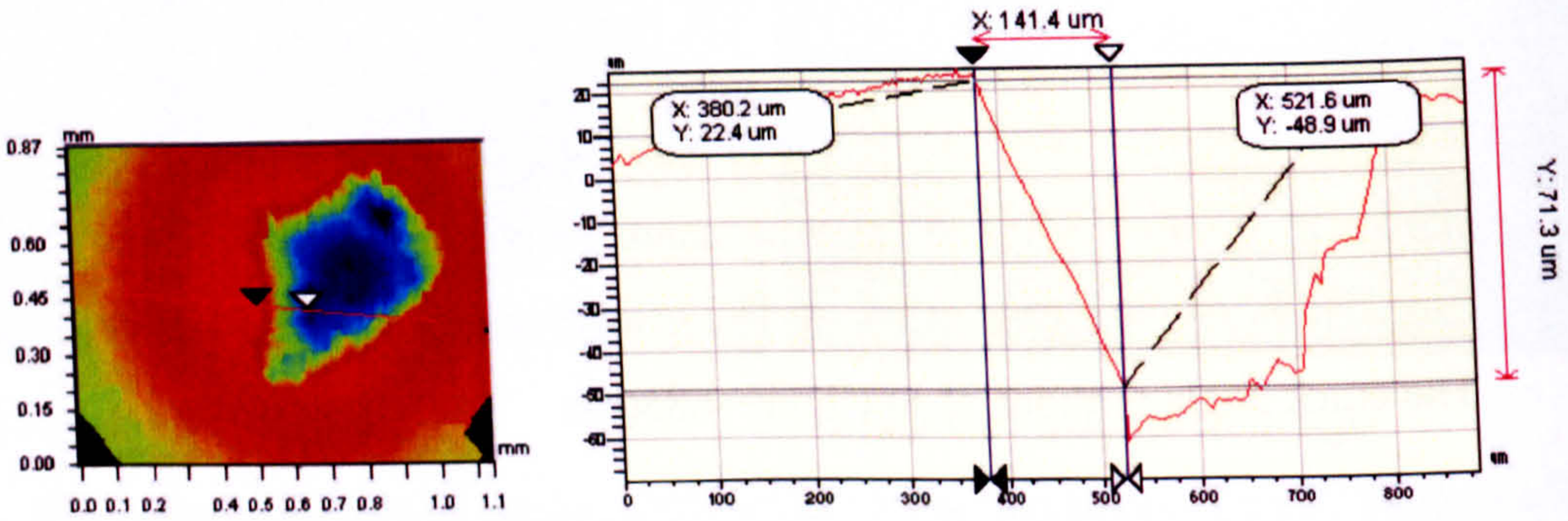

(e) Profile of the scanning line

Figure 4.85 continued

In figure 4.86, the results from Test D1-1 are presented. The overview of the fatigue spall is shown in figure 4.86(a). The 3D profile of the spall is shown in figure 4.86(b), which displays the depth contours. The fatigue crack grows in both directions (left and right). In the right hand part, the fatigue crack propagates approximately 0.1mm at an angle of 9° with the surface. The fatigue crack initiates at an estimated depth of 0.052mm (figure 4.86(c)) and grows back to the surface. In the left hand part, the crack initiates at the face of the primary ring crack and propagates downwards at approximately 25° to the surface. It is slightly deeper than the right part.

Figure 4.87 illustrates the results from Test D1-2. A half ellipse appears. No subsurface fatigue crack propagation is seen. The secondary surface cracks play a significant role in fatigue spalling. Compared with Test D1-1, the spall is deeper, approximately 0.09mm (figure 4.87(b) and (c)).

WYKO analysis results from Test D1-3 are shown in figure 4.88. Again, figure 4.88(a) shows an overview of the spall. The 3D profile of the spall is shown in figure 4.88(b). The fatigue crack grows in both directions (left and right). In the right part, the fatigue crack propagates approximately 0.1mm at an angle of 9° with the surface. The fatigue crack initiates at a depth of 0.070mm (figure 4.88(c) and then grows towards to the surface. In the left part, the crack initiates at the face of the primary ring crack and propagates downwards at approximately 25° to the surface.

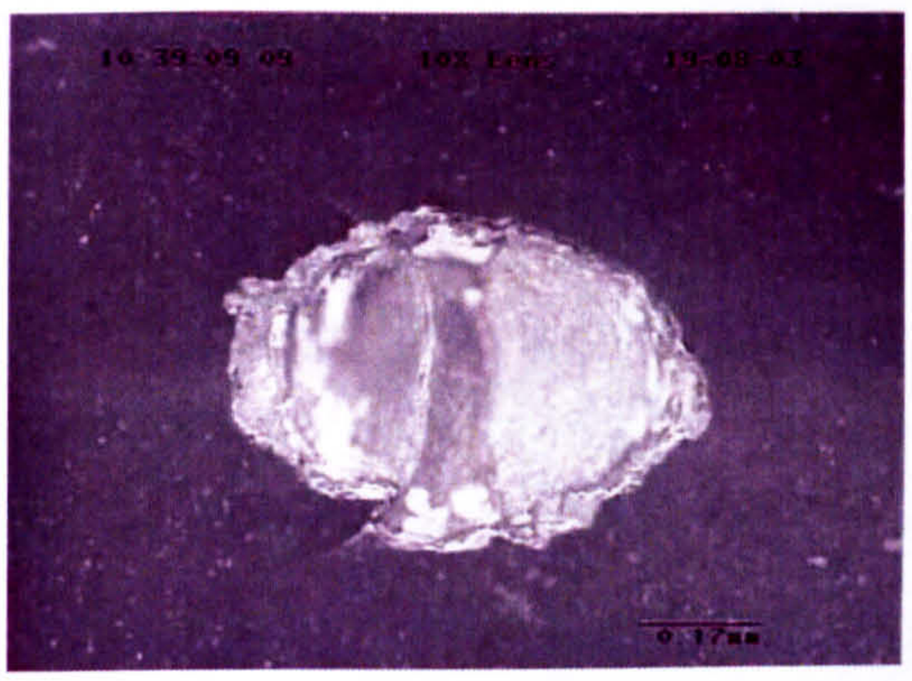

(a) Overview of a spall

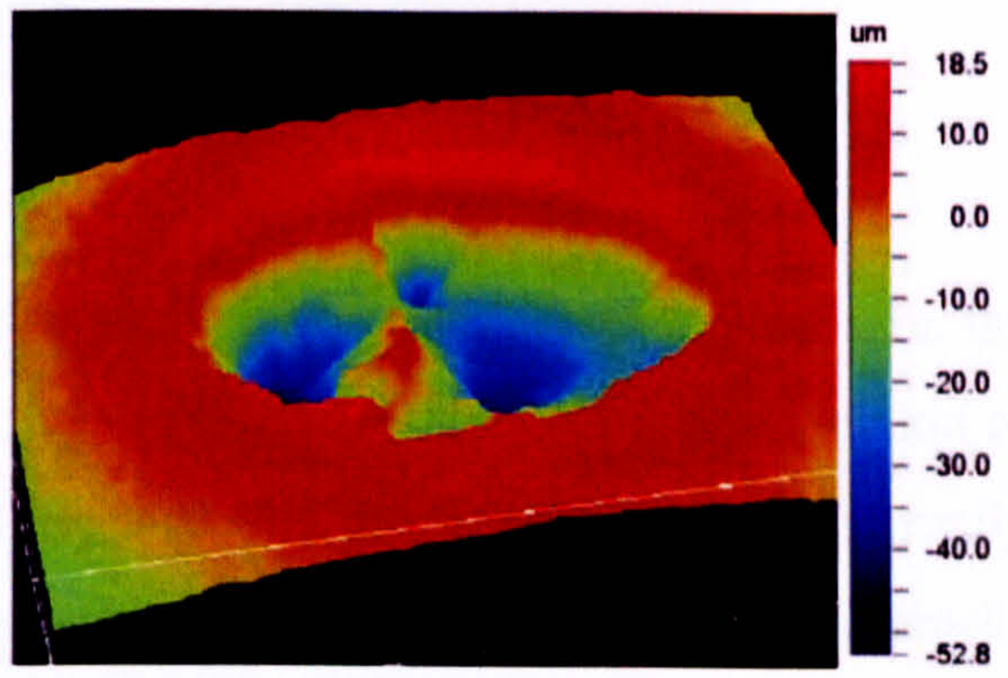

(b) 3D profile of fatigue spall

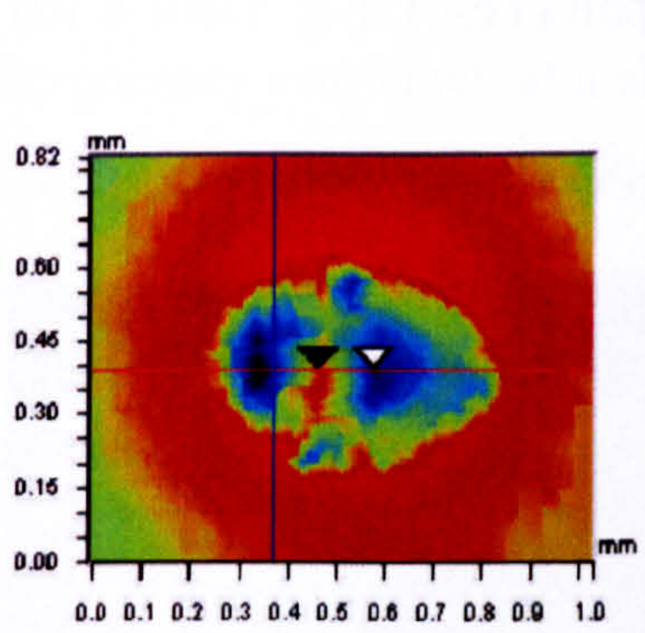

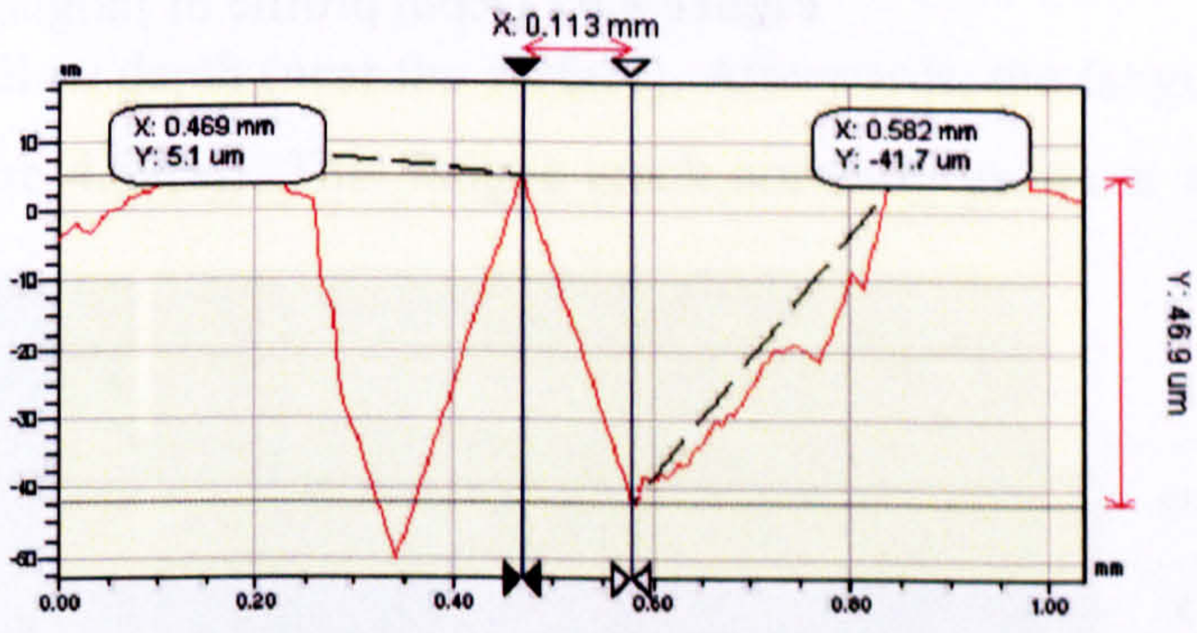

(c) Profile of the scanning line

Figure 4.86 Depth profile of fatigue spall in normal position (Test D1-1, Table 4.10)

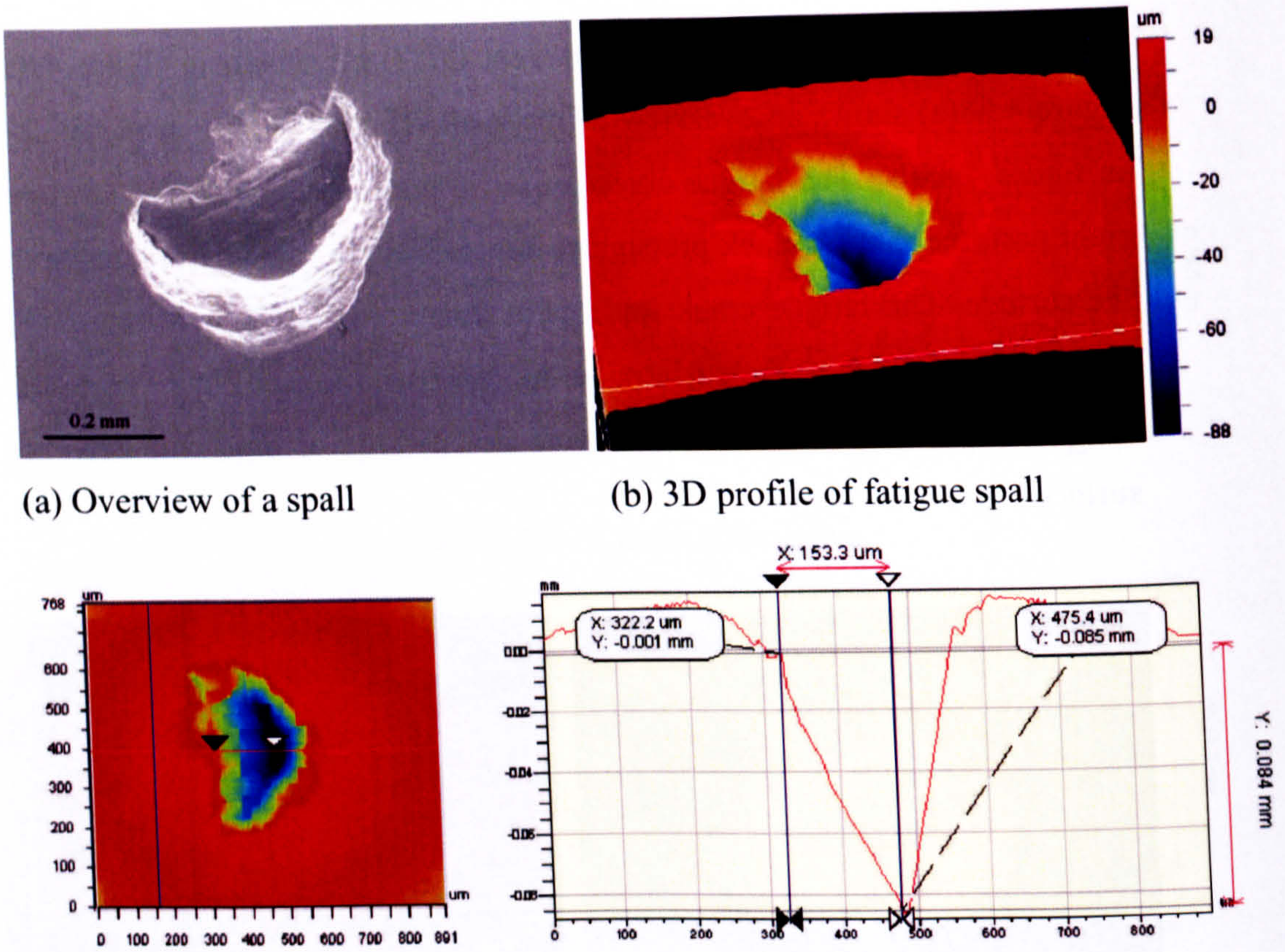

(a) Overview of a spall (b) 3D profile of fatigue spall

(c) Profile of the scanning line

Figure 4.87 Depth profile of fatigue spall (Test D1-2, Table 4.10)

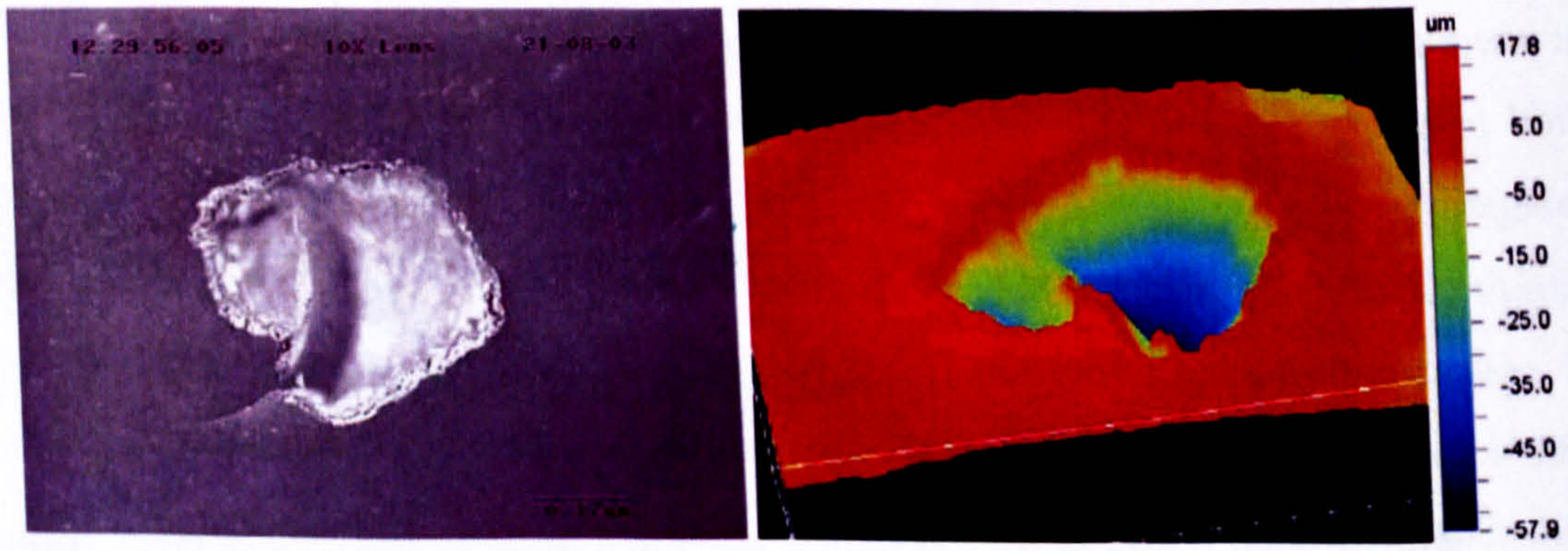

(a) Overview of a spall (b) 3D profile of fatigue spall

Figure 4.88 Depth profile of fatigue spall (Test D1-3, Table 4.10)

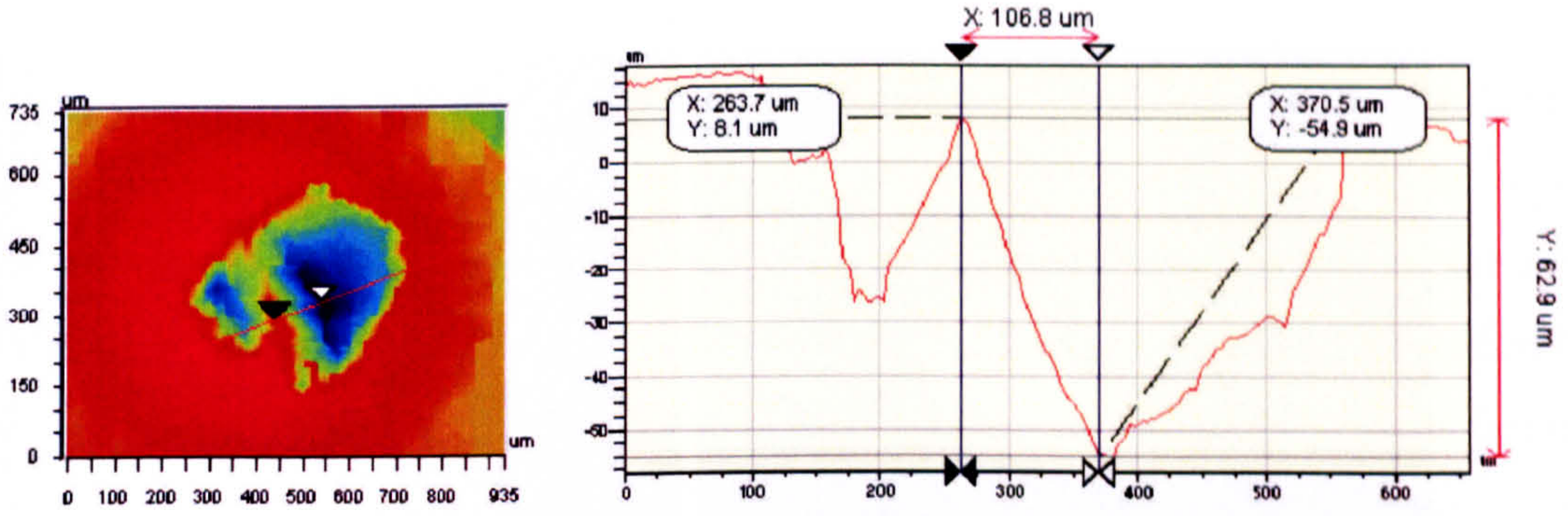

(c) Profile of the scanning line

Figure 4.88 continued

Figures 4.89 to 4.92 give other examples of the WYKO analysis. For the crack orientation (normal position, figure 3.4(a)), when the propagation direction of the fatigue crack is the same as the rolling direction, the fatigue crack is normally initiated at approximately 30 and 60 micron below the surface. The small cracks often correspond to shallower depths (figures 4.90 and 4.92). When the propagation direction is opposite to the rolling direction, a crack is first initiated on the face of the primary ring crack at a shallow depth (near the surface). Afterwards, the fatigue crack grows downwards (Figure 4.89(a)). This fatigue crack normally grows at an angle 25° to 30° with the surface.

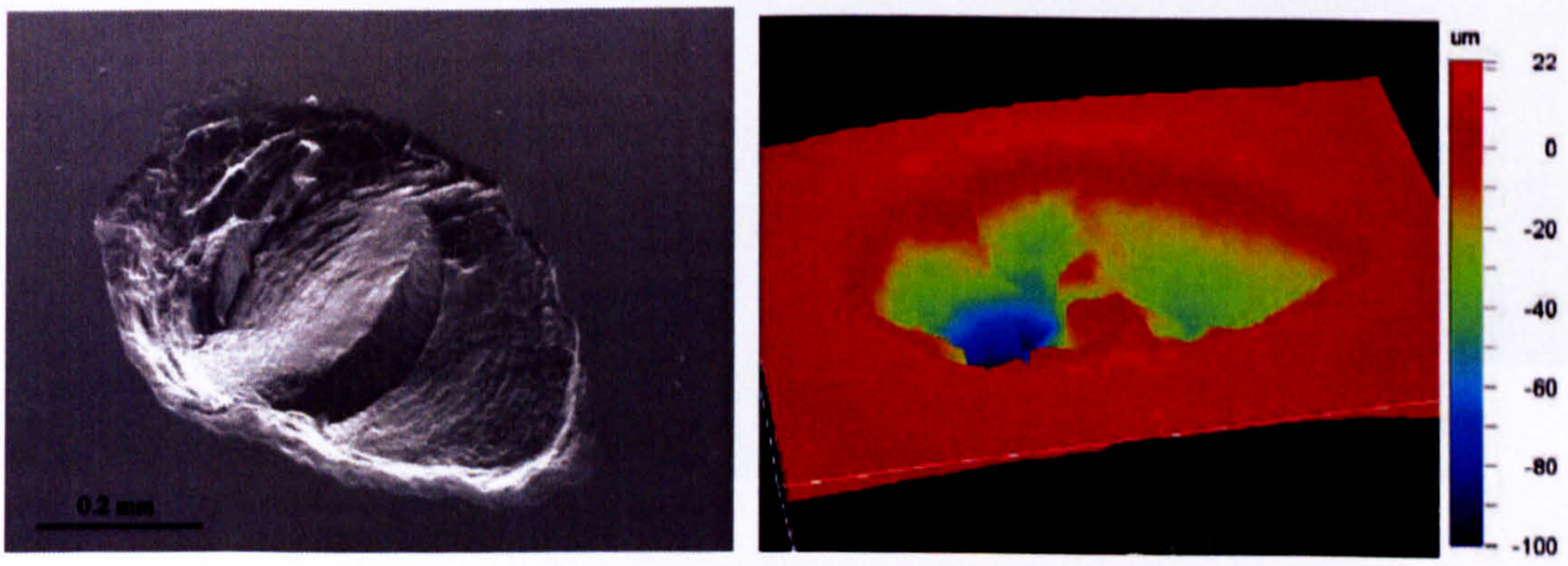

(a) Overview of a spall

(b) 3D profile of fatigue spall

Figure 4.89 Depth profile of fatigue spall (Test D1-4, Table 4.10)

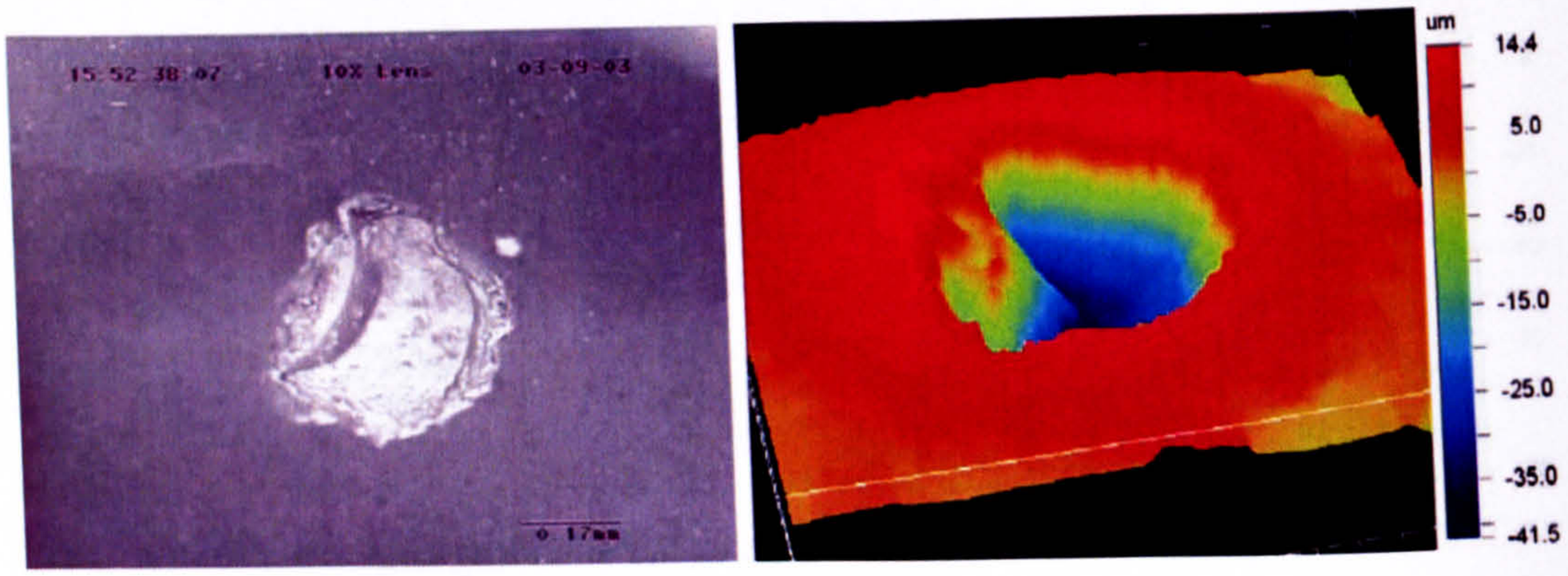

(a) Overview of a spall (b) 3D profile of fatigue spall

Figure 4.90 Depth profile of fatigue spall (Test D1-6, Table 4.10)

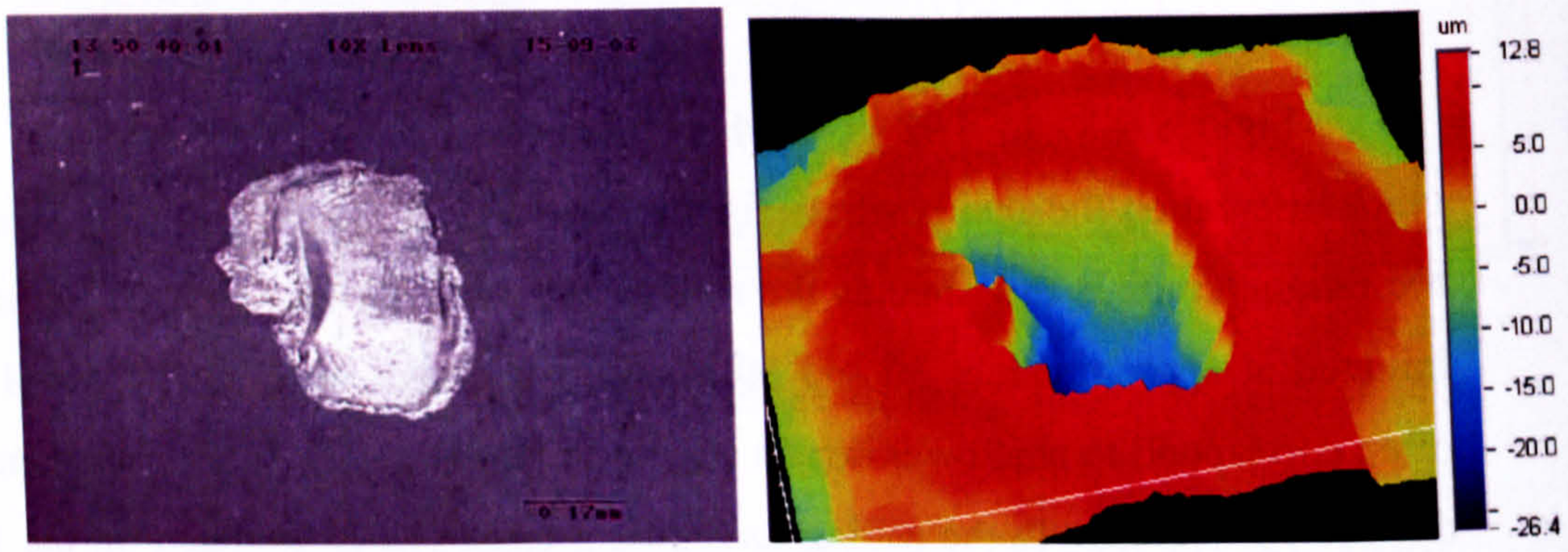

(a) Overview of a spall (b) 3D profile of fatigue spall

Figure 4.91 Depth profile of fatigue spall (Test D2-8, Table 4.10)

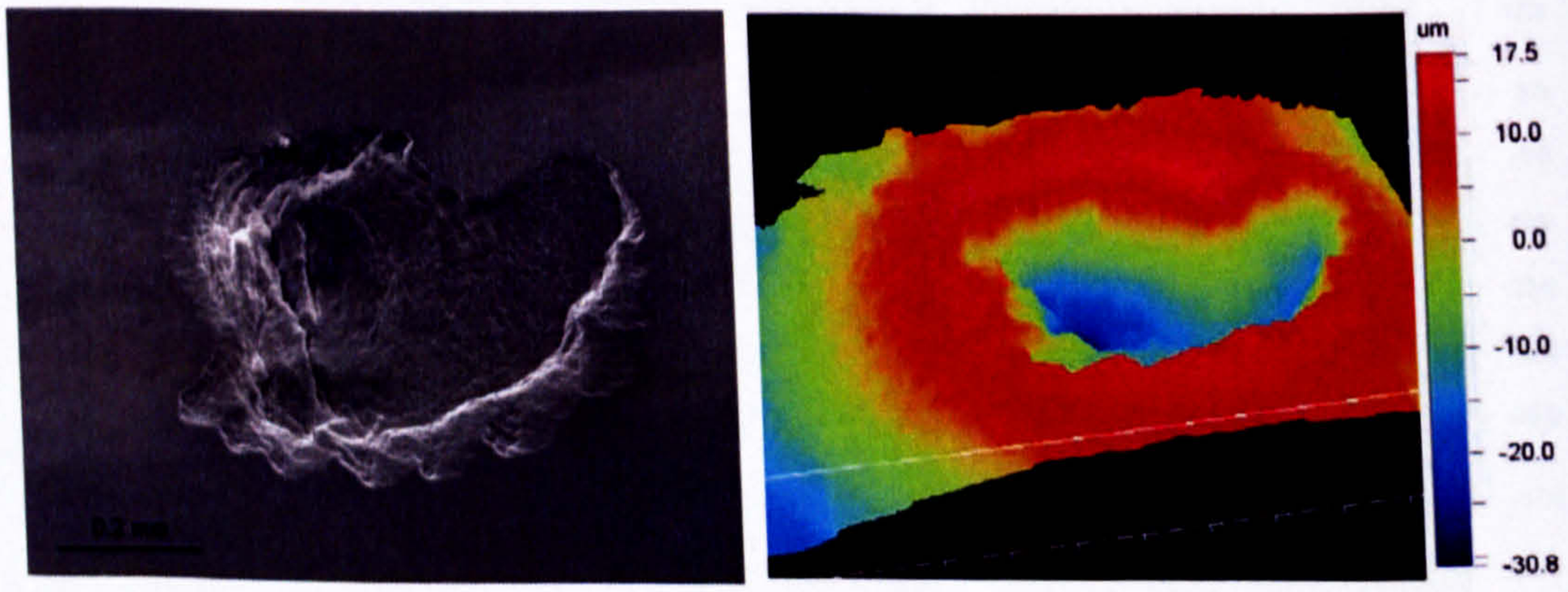

(a) Overview of a spall (b) 3D profile of fatigue spall

Figure 4.92 Depth profile of fatigue spall (Test Grease-2, Table 4.3)

4.4.4 Fracture surface features

Post-test analysis of fracture surface is important in determining failure modes in rolling contact fatigue. A fatigue crack may propagate in the same direction as the rolling direction or in the opposite direction. The fatigued surfaces from these two rolling directions will show different fracture features. Detailed SEM investigation of the test balls was carried out and the results are shown in figures 4.93 to 4.100.

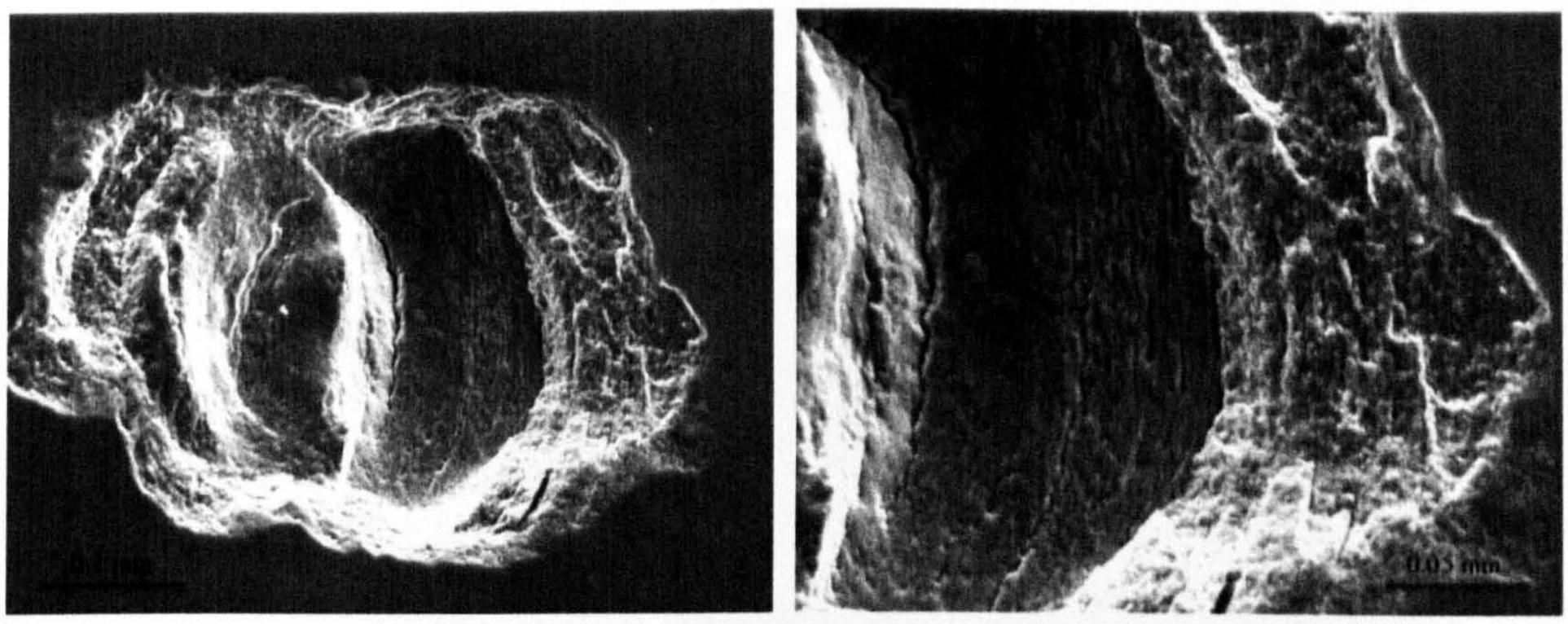

(a) SEM image of a spall (b) Detailed views of fracture surface

Figure 4.93 SEM micrographs of fatigue spall (Test TT9-4, Table 4.5)

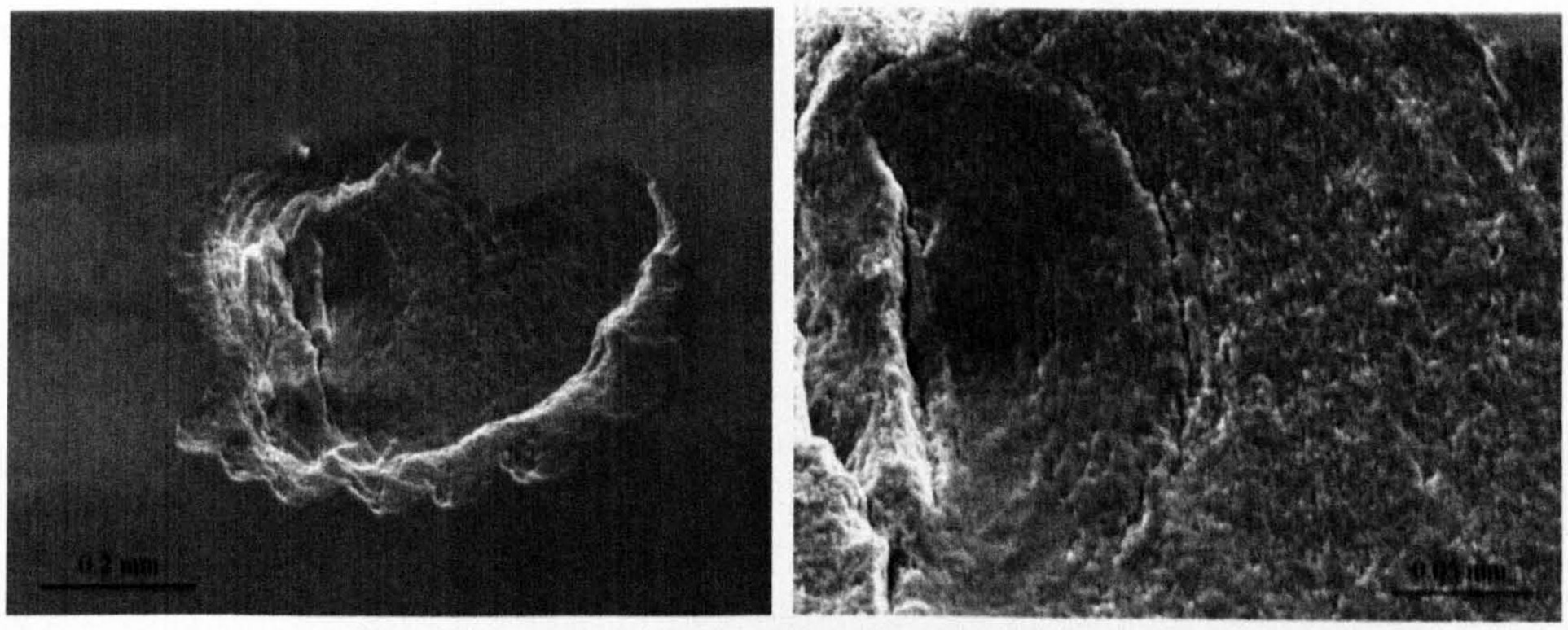

(a) SEM image of a spall (b) Detailed views of fracture surface

Figure 4.94 SEM micrographs of fatigue spall (Test Grease-2, Table 4.3)

Figure 4.93 shows the results of scanning electron microscope analysis of a spalled ball with a natural crack (Test TT9-4). The primary ring crack is still clear after spalling. The fatigue crack grows outwards both directions. Crack propagation

forming a striation-like pattern is clearly displayed on fatigue fracture surfaces (figure 4.93(b)). The striations formed in ceramics under rolling contact show apparent branch cracks. The branch crack geometry always takes the shape of the pre-existing crack fronts. The mechanisms of fatigue crack growth must somehow be related to the formation of those striations. Fracture mechanics analysis of crack propagation will be described in Chapter 5. The symptom of secondary surface cracks is clearly seen on the right edge. Figure 4.94 shows the results of scanning electron microscope analysis from Test Grease-2. Again, fracture appearances for these two tests are similar to each other. The striations formed on the fracture face always take the shape of the primary ring crack.

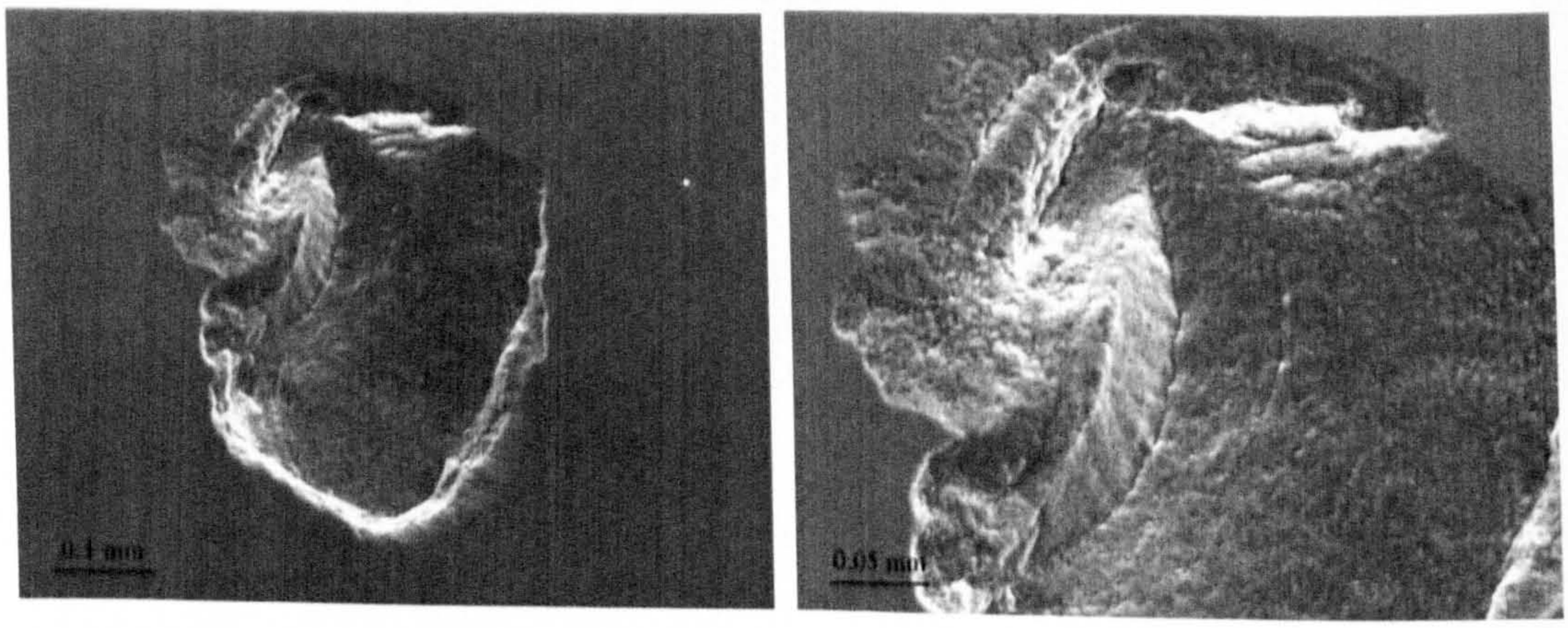

(a) SEM image of a spall (b) Detailed views of fracture surface

Figure 4.95 SEM micrographs of fatigue spall (Test D2-8, Table 4.10)

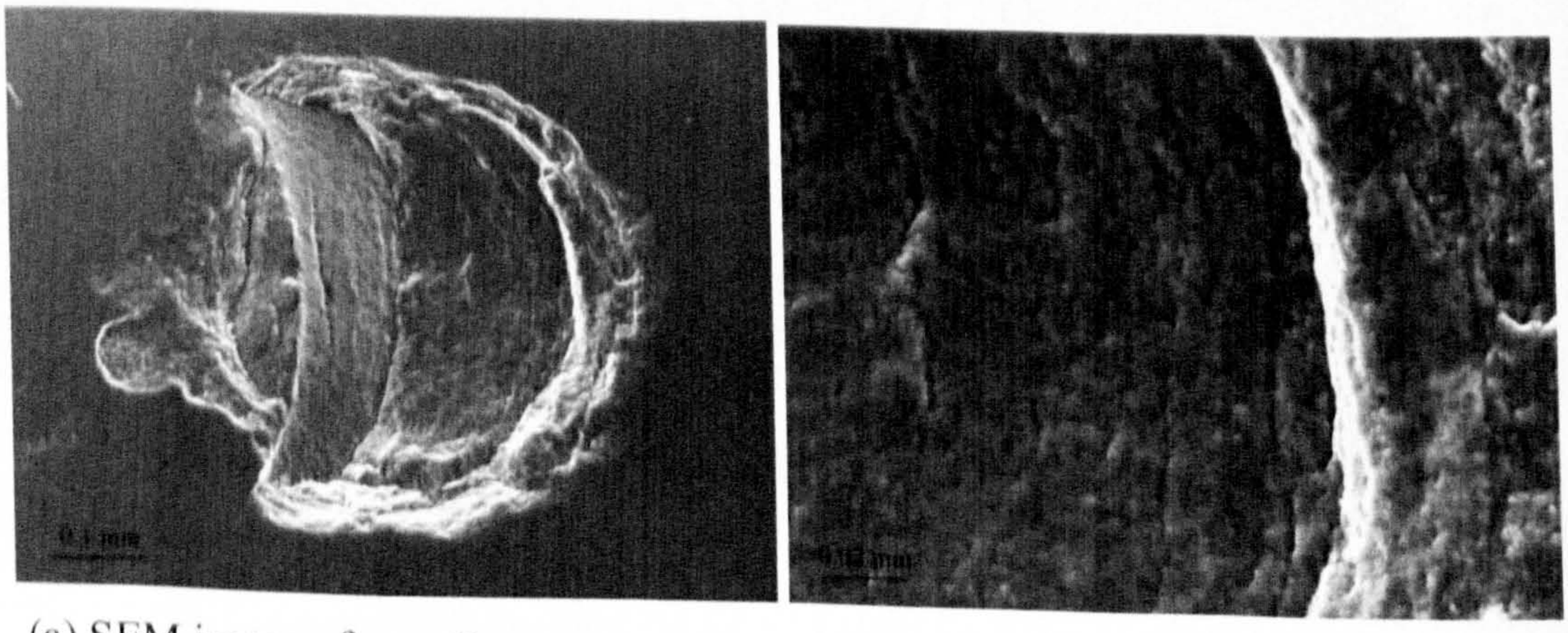

(a) SEM image of a spall (b) Detailed views of fracture surface

Figure 4.96 SEM micrographs of fatigue spall (Test NB4, Table 4.7)

In figures 4.95 and 4.96, the results of SEM analysis from the artificial cracks are presented. Similarly, fatigue crack propagation initiates from the site of the original conic face. Crack growth forms the fracture surfaces which contain the striated patterns.

Figure 4.97 illustrates the results of SEM analysis from the artificial cracks (Test N4). The SEM image of the spall overview is shown in figure 4.97(a). The original ring crack can be identified clearly. Crack growth is towards the left (opposite rolling direction). Figure 4.97(b) enhances the magnification of the micrograph. The characteristic of fatigue fracture is apparent and subsurface branch cracks are clearly displayed on the spall surface. The geometry of the subsurface branch cracks is influenced by the contact circle and will normally inherit the geometry of that circle. The distance between two striations is around 5-10 μm. Figure 4.98 shows another example of surface SEM analysis from the artificial cracks.

The surface characteristic of the fatigue spall varies with the rolling direction. Comparison of the results from two rolling directions reveals that when the crack grows in a direction opposite to the rolling direction, the fracture surfaces display large sharp striations.

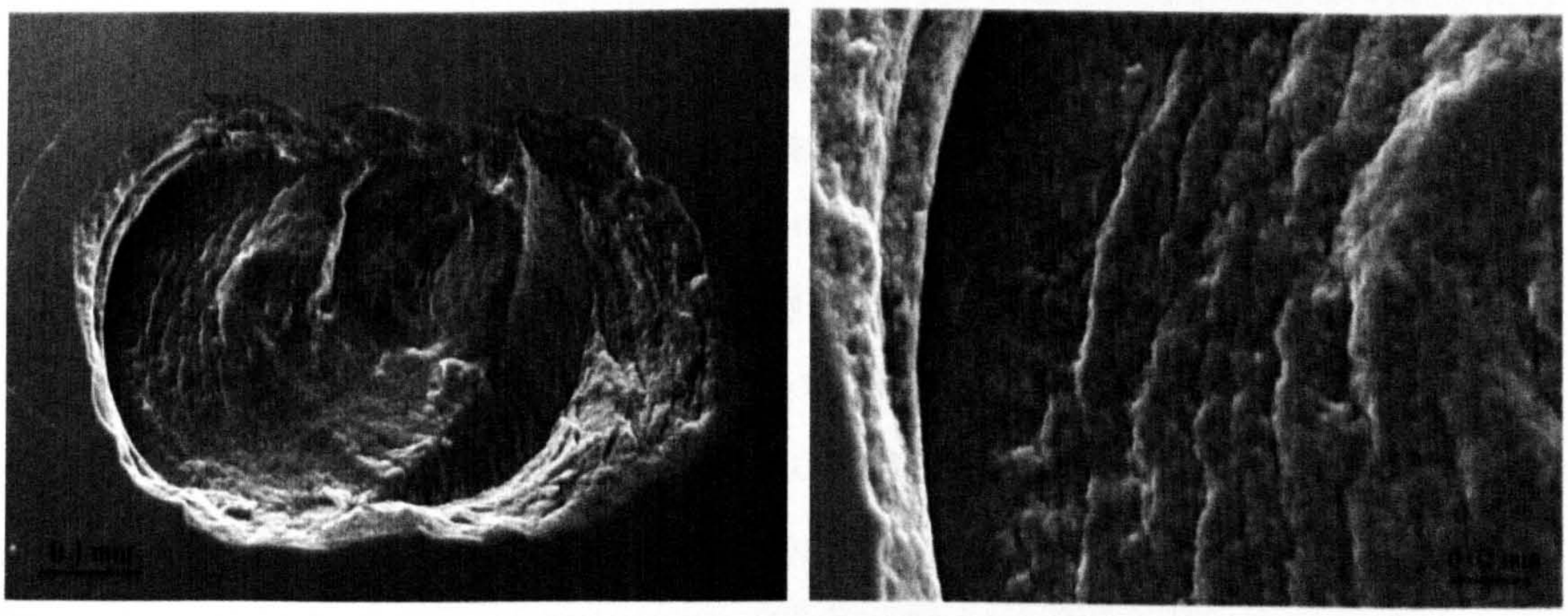

(a) SEM image of a spall (b) Detailed views of fracture surface

Figure 4.97 SEM micrographs of fatigue spall (Test N4, Table 4.8)

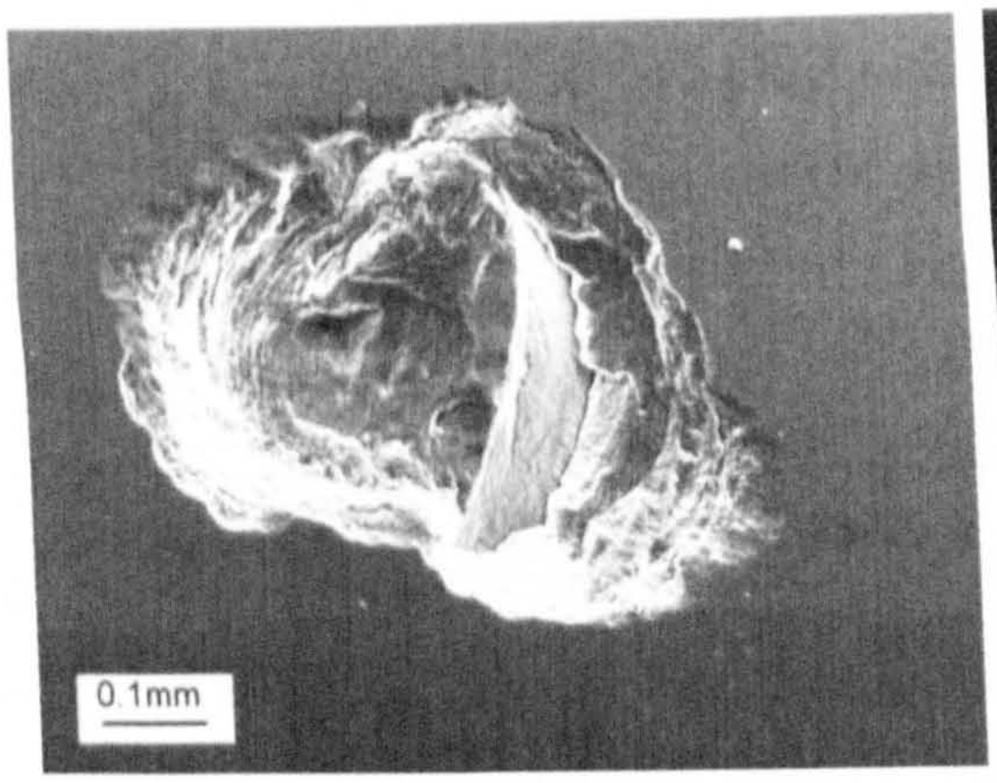

(a) SEM image of a spall

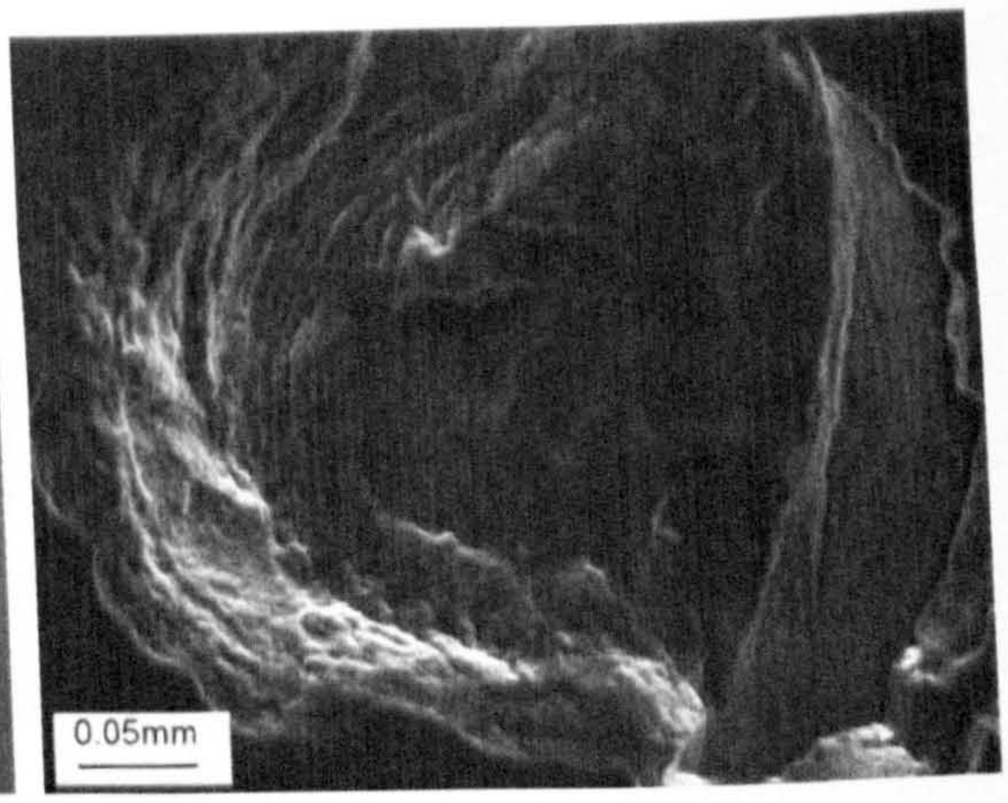

(b) Further magnified image

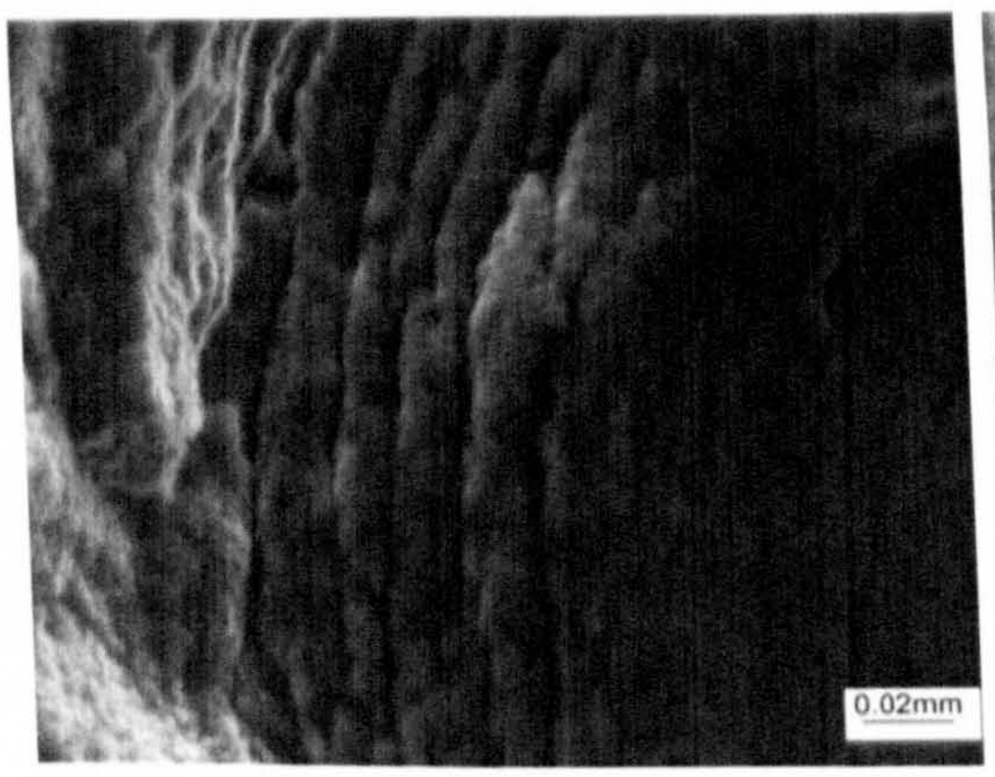

(c) Fatigued surface

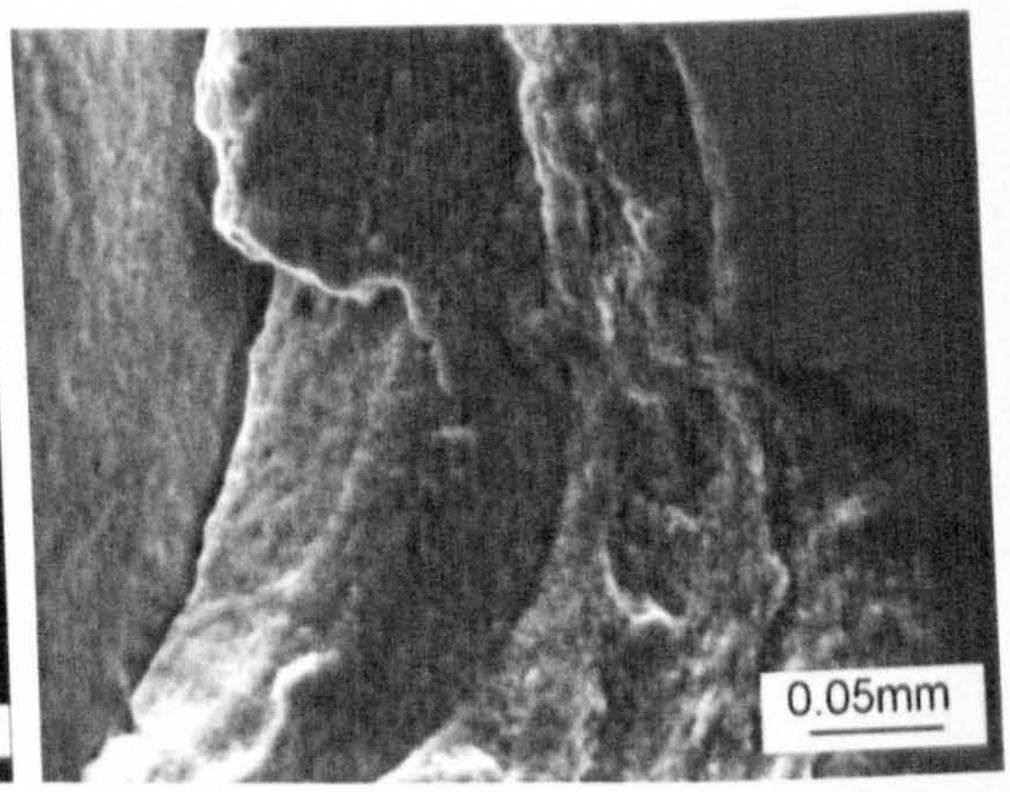

(d) High magnification of right edge

Figure 4.98 SEM micrographs of fatigue spall (Test T3, Table 4.7)

Figure 4.99 shows the images scanned from Test D1-2. The primary ring crack circle and crack face can be identified clearly. A subsurface crack is seen on the crack face (figure 4.99(a). A high magnification image of this crack is shown in figure 4.99(b). This crack is normally initiated near the surface and propagates downwards at an angle of approximately 25 - 30°.

Figure 4.100 shows another example from Test P3-6. Crack growth is in both directions (the left and the right) as shown in figure 4.100(a). The circle-like striations formed on the fracture surface are also seen. Figure 4.100(b) enhances the magnification of the micrograph. The characteristic of cracking fracture is apparent and is displayed clearly in the middle of figure 4.100(b).

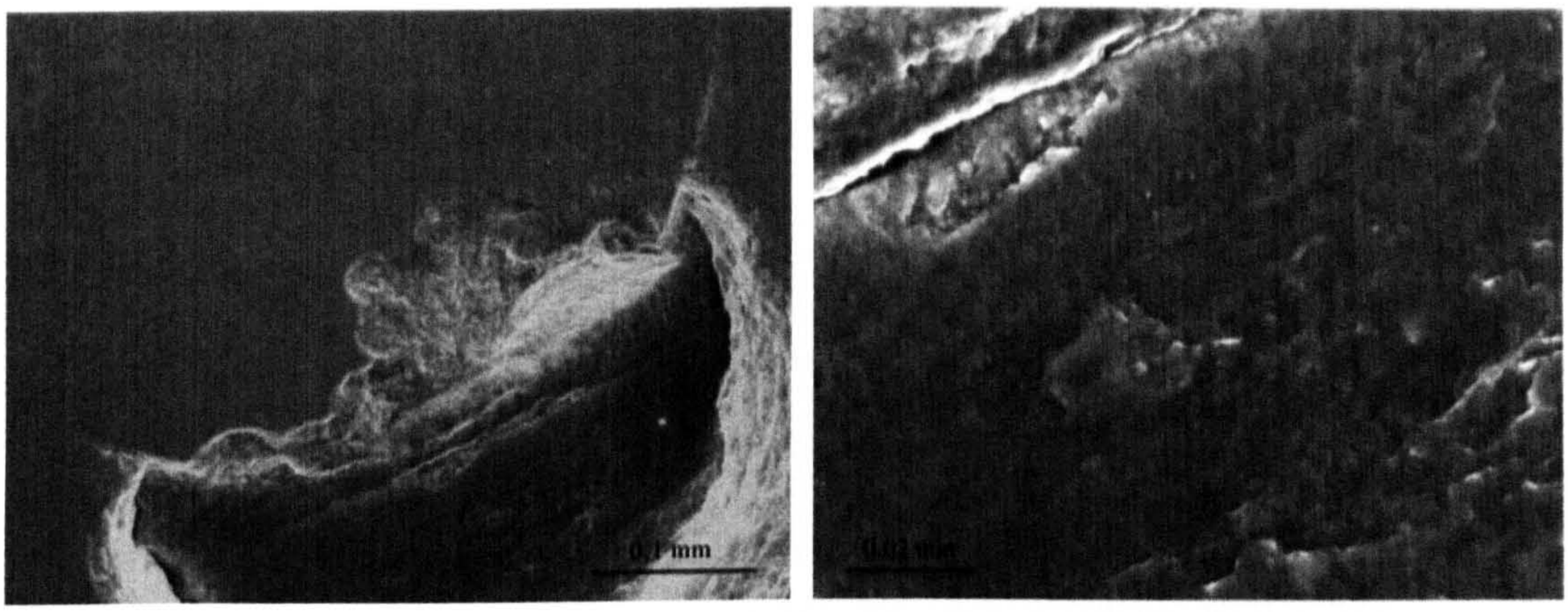

(a) Overview of subsurface cracks (b) High magnification

Figure 4.99 SEM micrographs of fatigue spall (Test D1-2, Table 4.10)

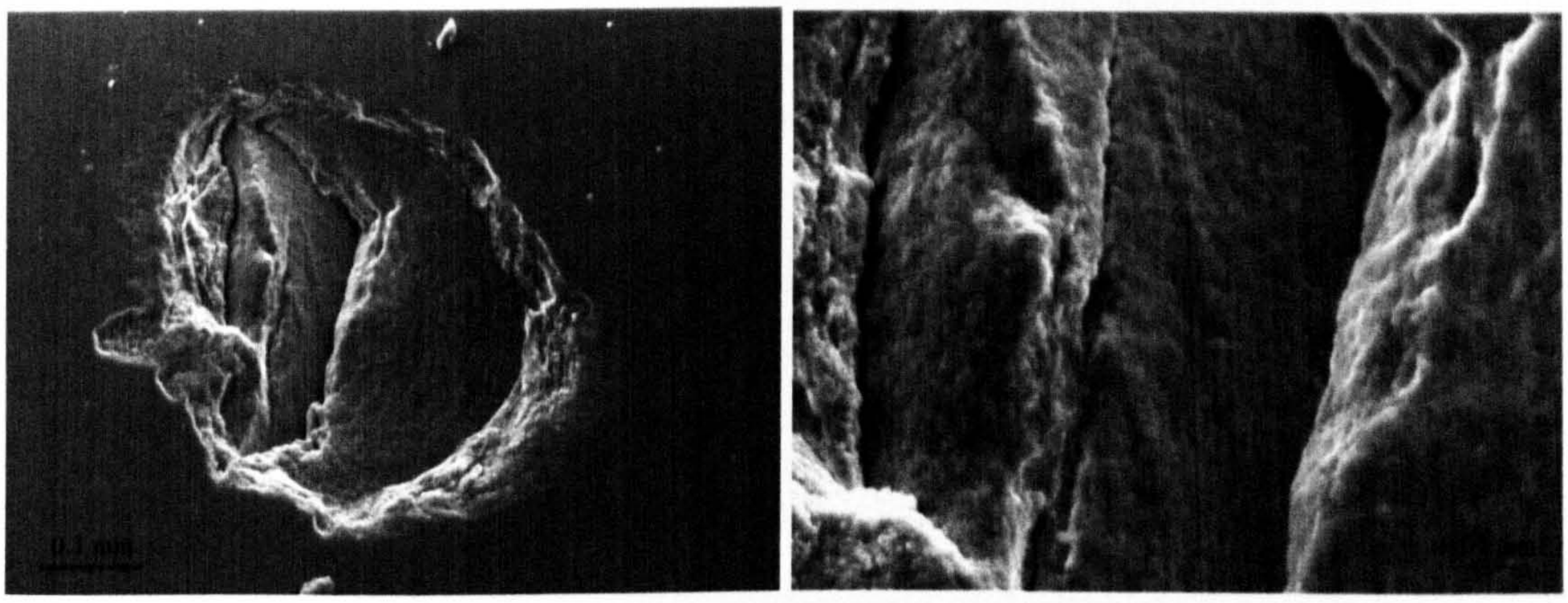

(a) SEM image of a spall (b) Detailed views of subsurface cracks

Figure 4.100 SEM micrographs of fatigue spall (Test P3-6, Table 4.9)

4.5 SUBSURFACE OBSERVATION OF FAILURE PROCESSES

4.5.1 Cracks with incipient spall

Subsurface study is very important in the understanding of the mechanical process of ring crack spalling. The experimental observation of subsurface crack propagation has been carried out to ascertain the crack growth path. A typical transition process from normal to a spall is shown in figure 4.101. All the images in figure 4.101 are from Test GOL-2, described in table 4.2. After 90.7 million stress cycles, new surface cracks are found beside the original ring crack (figure 4.101(b)). These new cracks are called secondary surface cracks in this study. The ball was sectioned and polished to investigate the subsurface crack propagation behaviour. Figure 4.101(c) is a surface view of the failure ball, which shows the section positions to be observed.

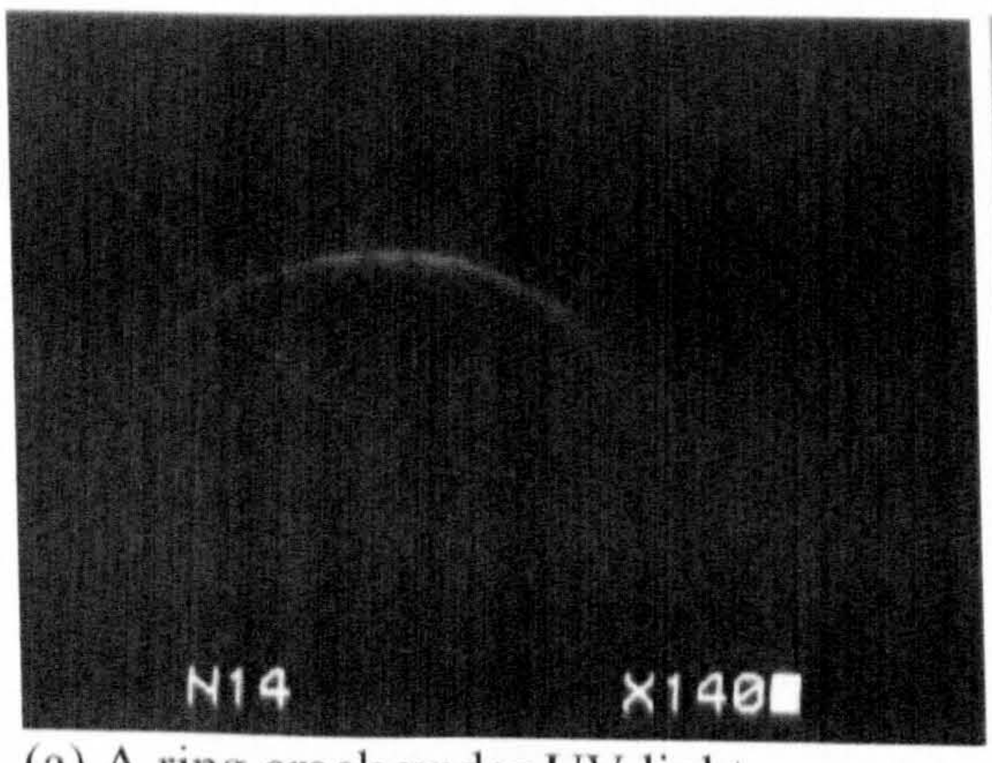

(a) A ring crack under UV light

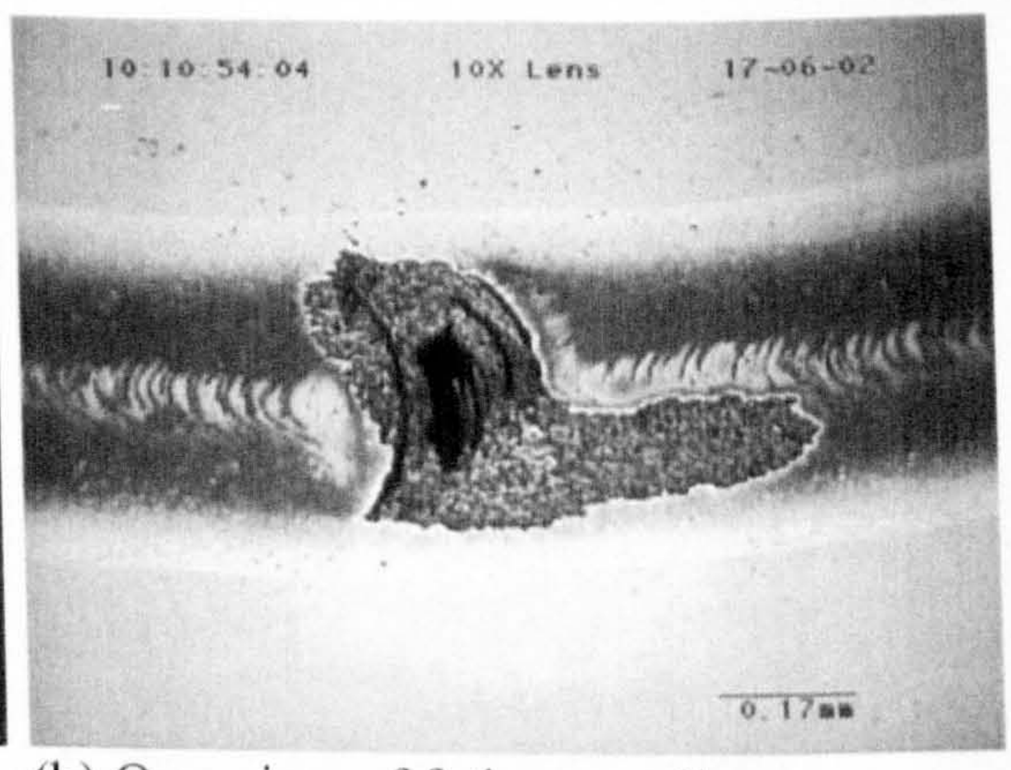

(b) Overview of fatigue spall

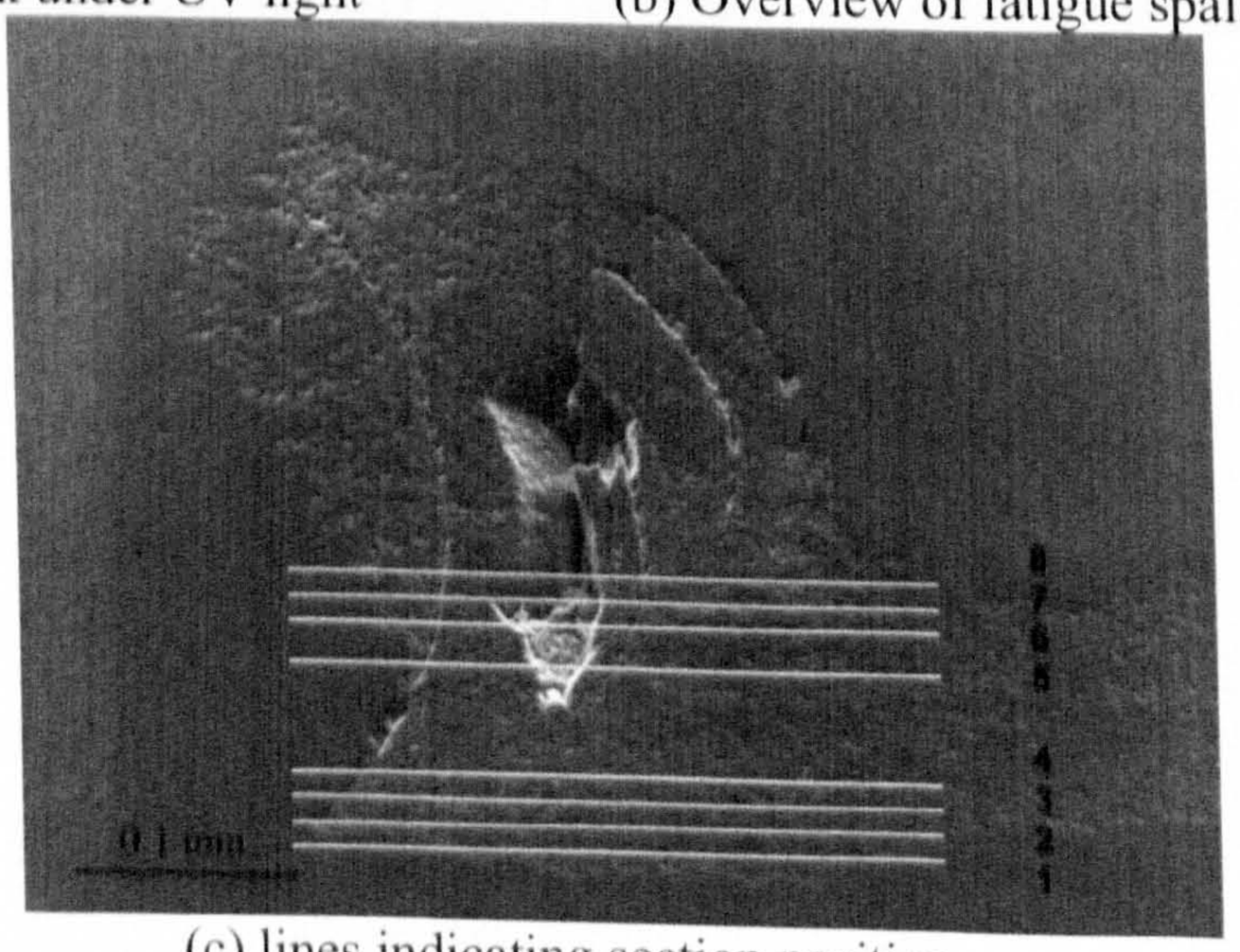

(c) lines indicating section position

Figure 4.101 Surface observation of incipient failure (Test GOL-2, Table 4.2)

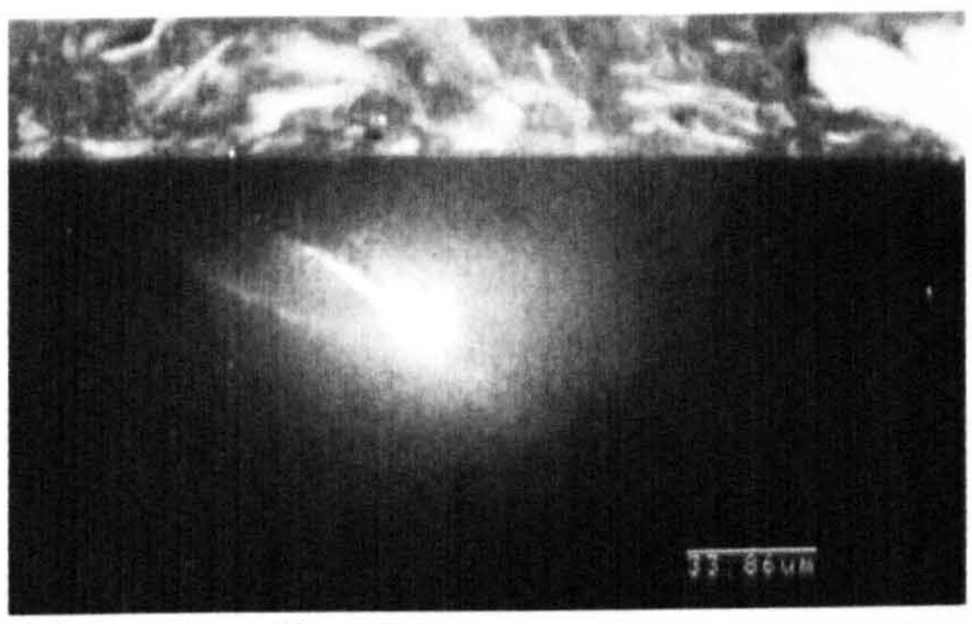

(a) Section line 1

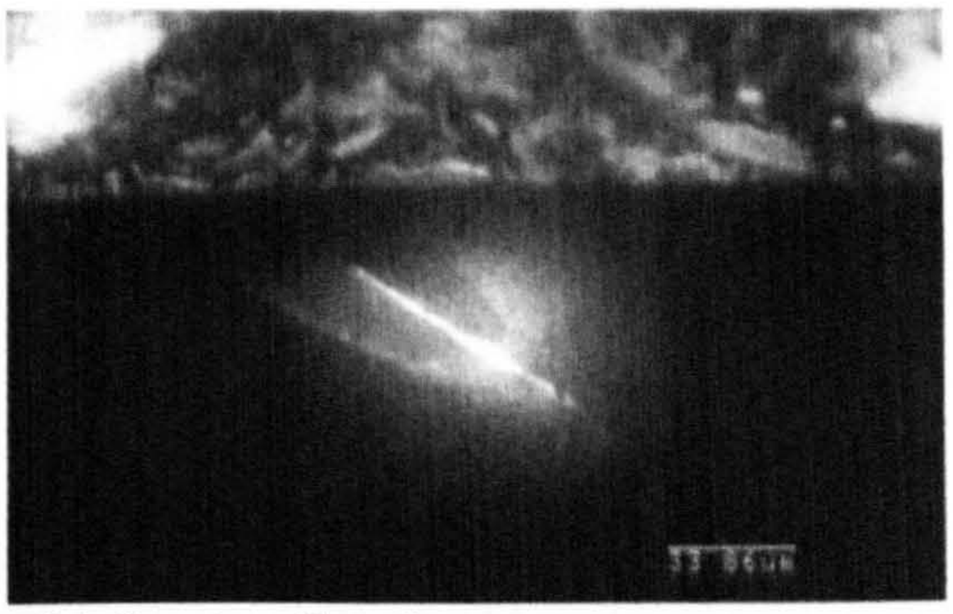

(b) Section line 2

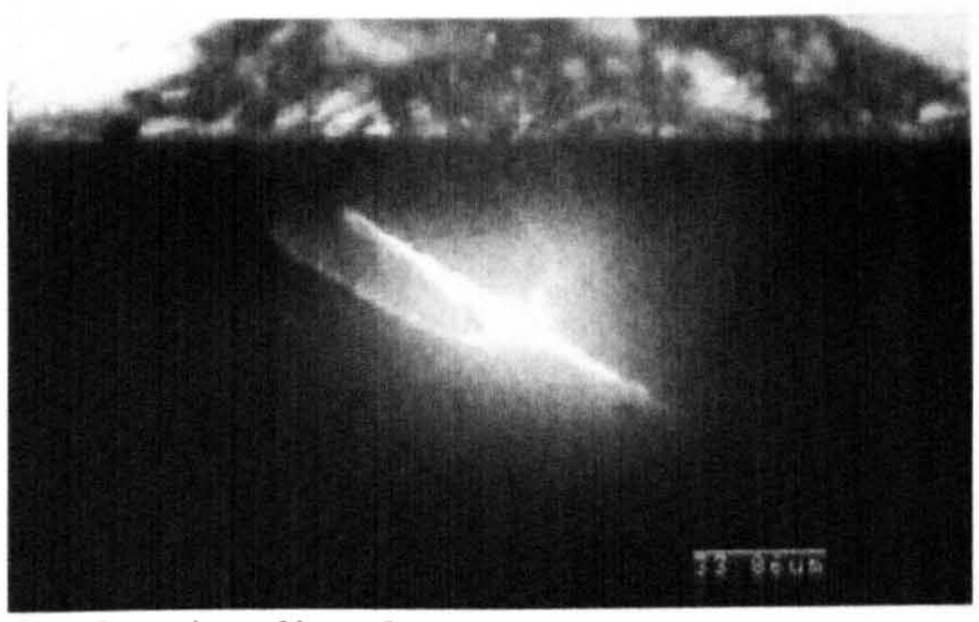

(c) Section line 3

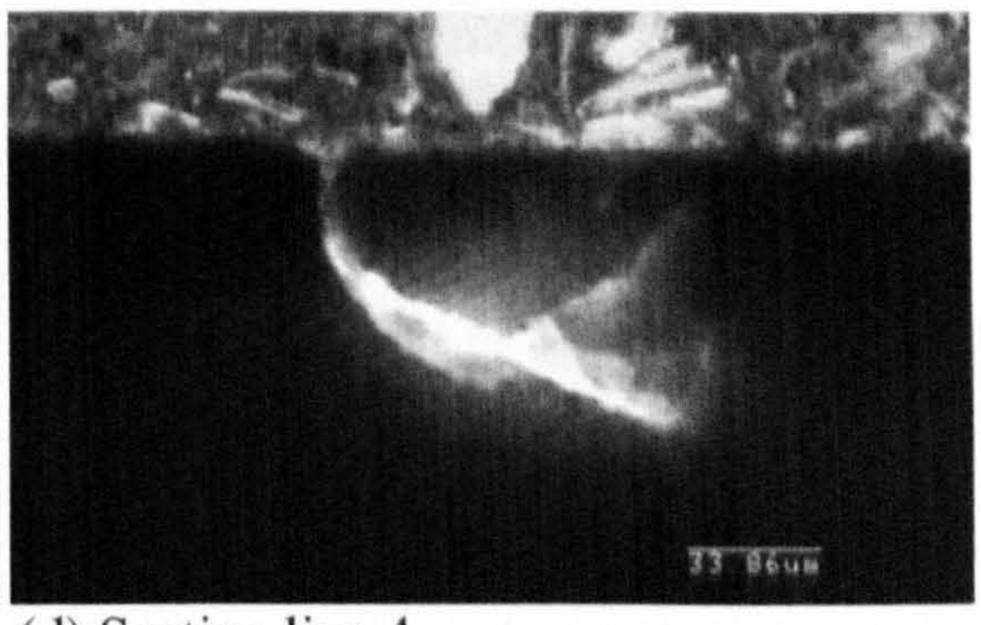

(d) Section line 4

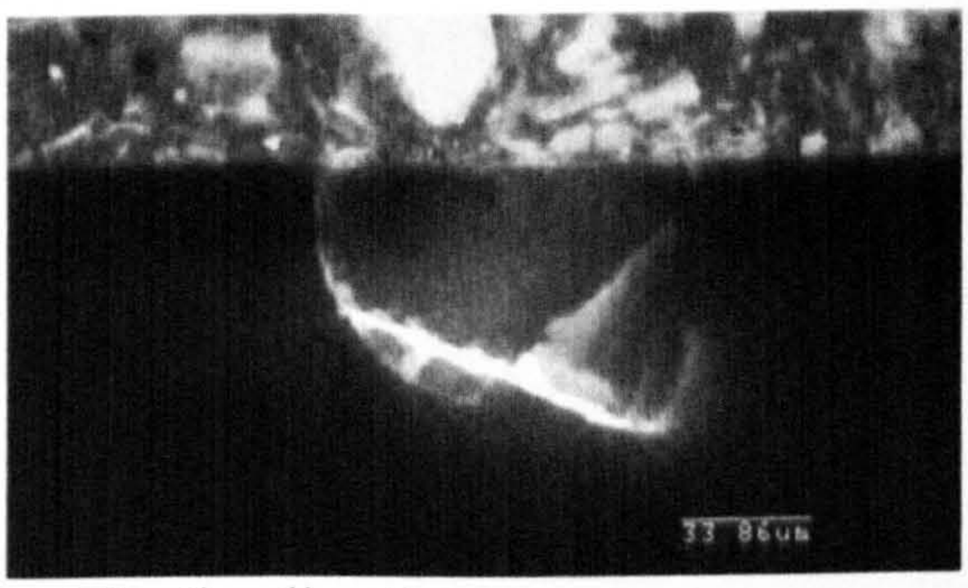

(e) Section line 5

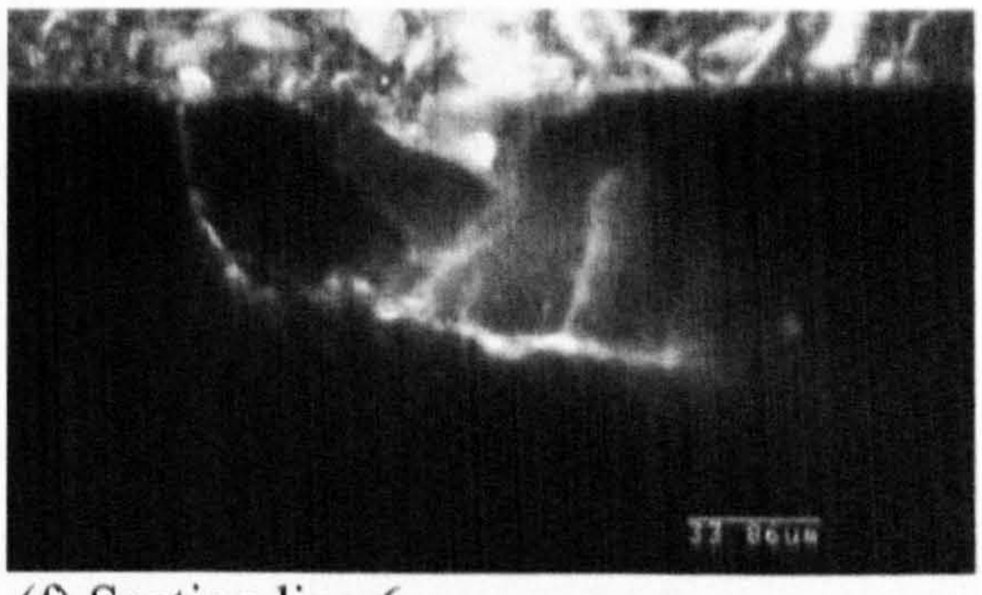

(f) Section line 6

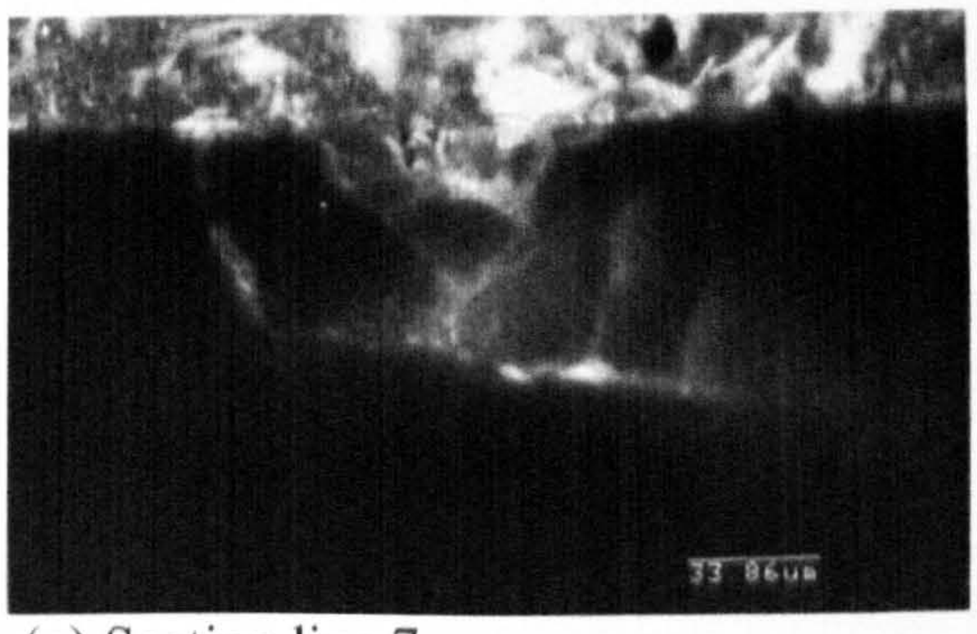

(g) Section line 7

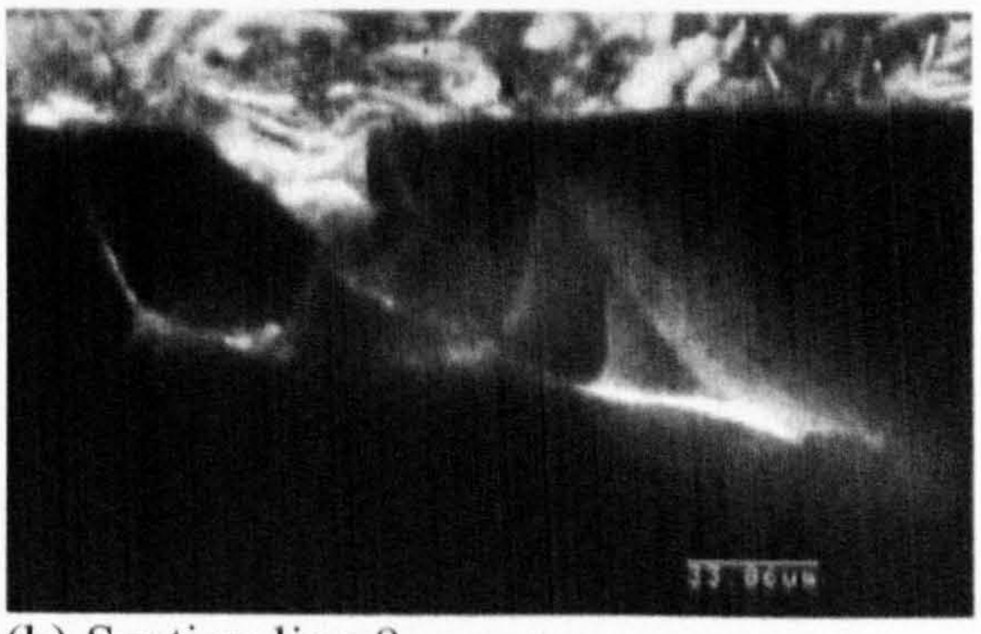

(h) Section line 8

Figure 4.102 Subsurface observations of crack growth and secondary surface cracks (Test GOL-2, Table 4.2)

The ball was sectioned near the crack and then polished gradually across the cracks to examine the profiles of crack propagation. There are eight lines on figure 4.101(c). These lines show the sites at which the section images were taken. The subsurface image from the first section (line 1) is shown in figure 4.102(a), using microscopic analysis with ultra-violet light. Figures 4.102(b) and 4.102(c) show images taken at lines 2 and 3. The bright straight line is a defect. Figure 4.102(d) shows the image taken at the fourth line. The branched crack appears and propagates towards to the surface. At the section of line 5, another branched crack occurs at the tip and propagates towards the surface as shown in figure 4.102(e). As the subsurface crack grows a new branched crack appears (figure 4.102(f) and (g)). The secondary cracks can be seen clearly and they propagate conically towards the material. Then a flake of material comes off. A detailed crack network is clearly exhibited. Figure 4.102(h) reveals that the secondary surface cracks propagate conically towards the material. They may pass through the branched cracks and reach the bottom to form a crack network. The branched cracks are formed along the crack growth path.

Subsurface observations reveal that the fatigue spall is mainly caused by two factors. One is from secondary surface crack propagation. The secondary surface cracks propagate conically away from the surface and will meet the main crack growth path. Branched cracks can also be generated on the faces of each secondary crack and these cracks connect with each other to form a broken crack network. Spalling occurs eventually when material flakes out from the broken crack network. Another contributing factor is from subsurface branch crack propagation. These branched cracks formed on the upper crack face may grow towards the ball surface. Aspects of crack growth mechanics will be discussed in Chapter 5.

4.5.2 Cracks with spall

Figure 4.103 shows the subsurface observation of a ball with an artificial ring-crack. This crack was produced at a swing angle of 20 degrees, using two 12.7mm balls (material A) impacting each other at position 2. The ball failed after 498 minutes of testing under a contact pressure of 5.58GPa, lubricated with traction

oil. Figure 4.103(a) shows a SEM image of fatigue spall. The ball was sectioned near the ring crack and polished gradually across the ring crack to the middle as shown in figure 4.103(b). The subsurface image from the section is shown in figure 4.103(c), using microscopic analysis with dark field illumination. The fatigue crack propagates back to the surface in this case. The secondary cracks can still be seen as shown in figure 4.103(d).

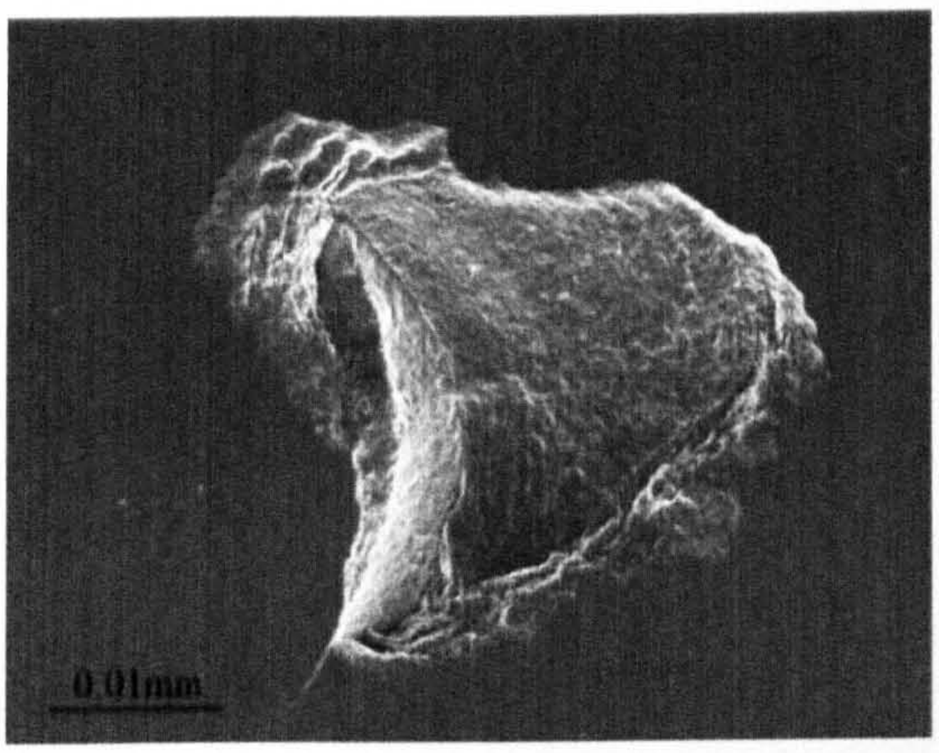

(a) SEM image

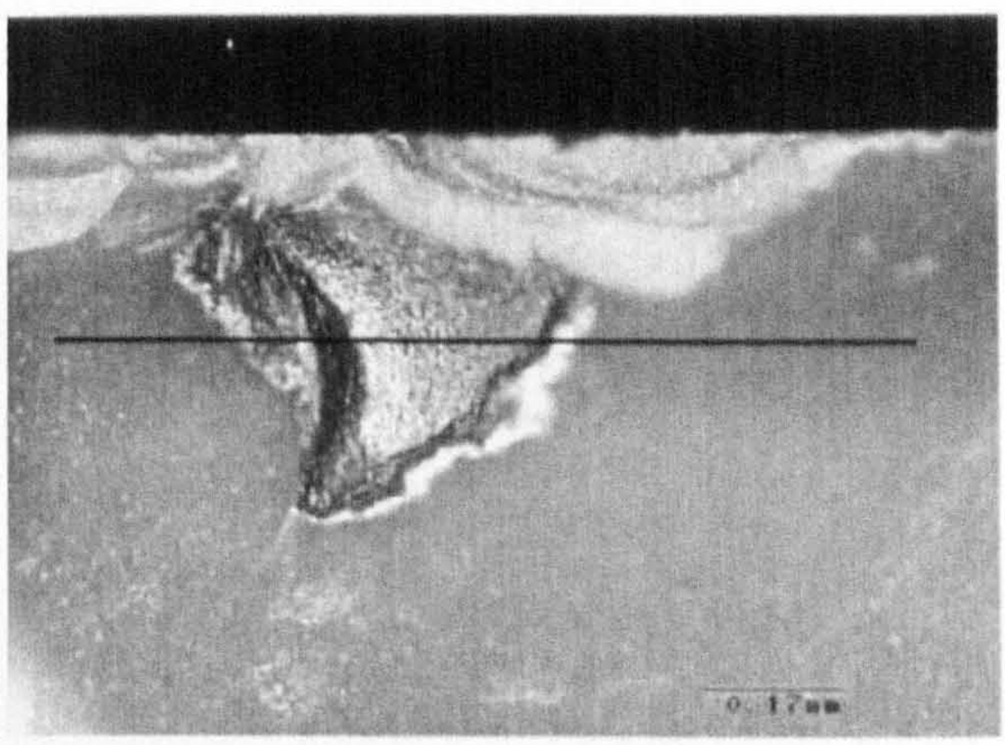

(b) Section position

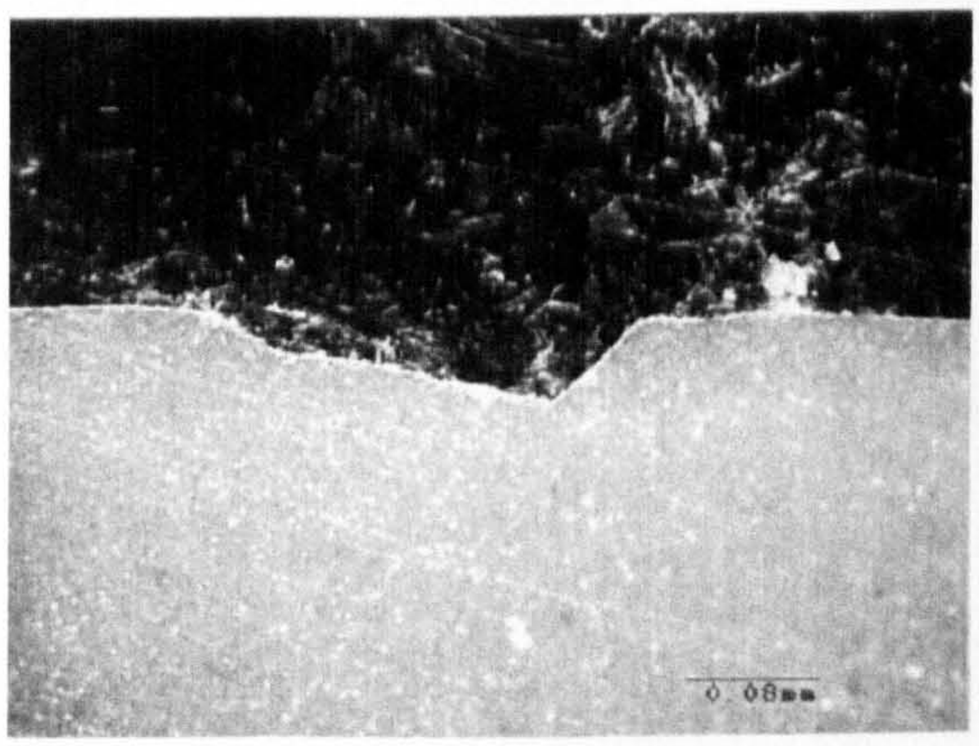

(c) Dark field image

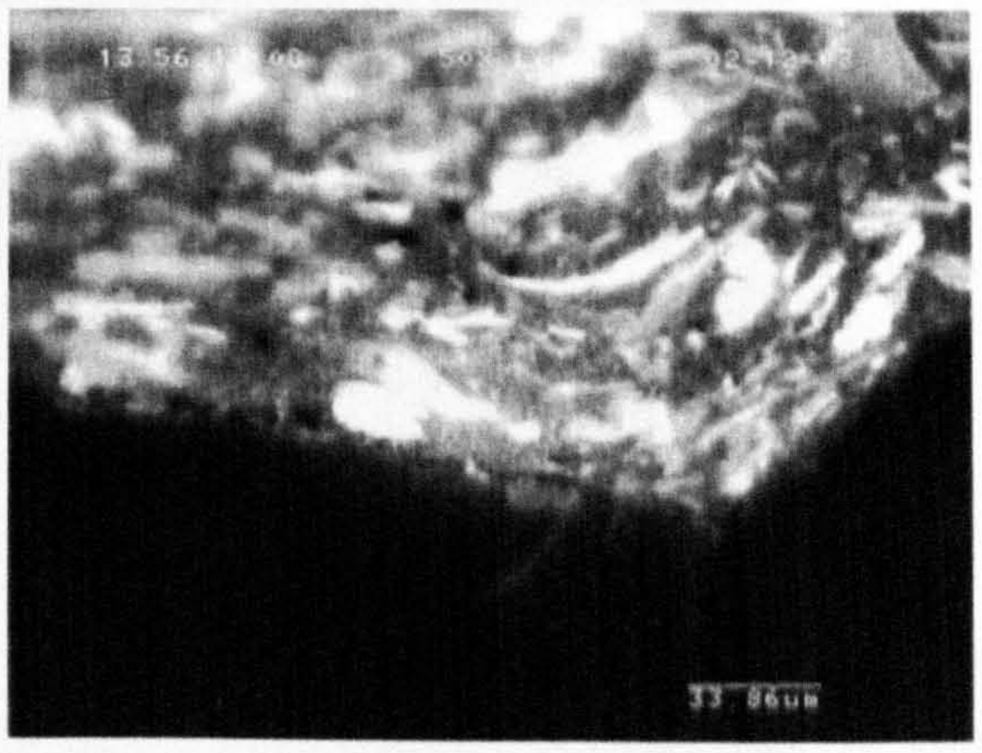

(d) With UV light

Figure 4.103 Subsurface observations of fatigue spall (Test N6, Table 4.8)

Figure 4.104 is an example of subsurface observations from Test N2 (Table 4.8). Figure 4.104(a) shows an overview of the spall. There are three lines on figure 4.104(b), which shows the sites at which the section images are taken. The subsurface image at the section line 1 is shown in figure 4.104(c), using microscopic

analysis with ultra-violet light. Figure 4.104(d) shows the dark field image taken at the line 2, which shows the profile of the sectioned plane. The left side shows the path of fatigue crack propagation. The right side is the primary crack path. Figure 4.104(e) indicates no branched crack at the tip. Figure 4.104(f) shows the image taken at the third line. The path of crack growth is clearly displayed. The primary crack still exists underneath as shown in figure 4.104(g). Secondary surface cracks are seen in the sectioned plane. The surface image corresponding to this part is shown in figure 4.104(h).

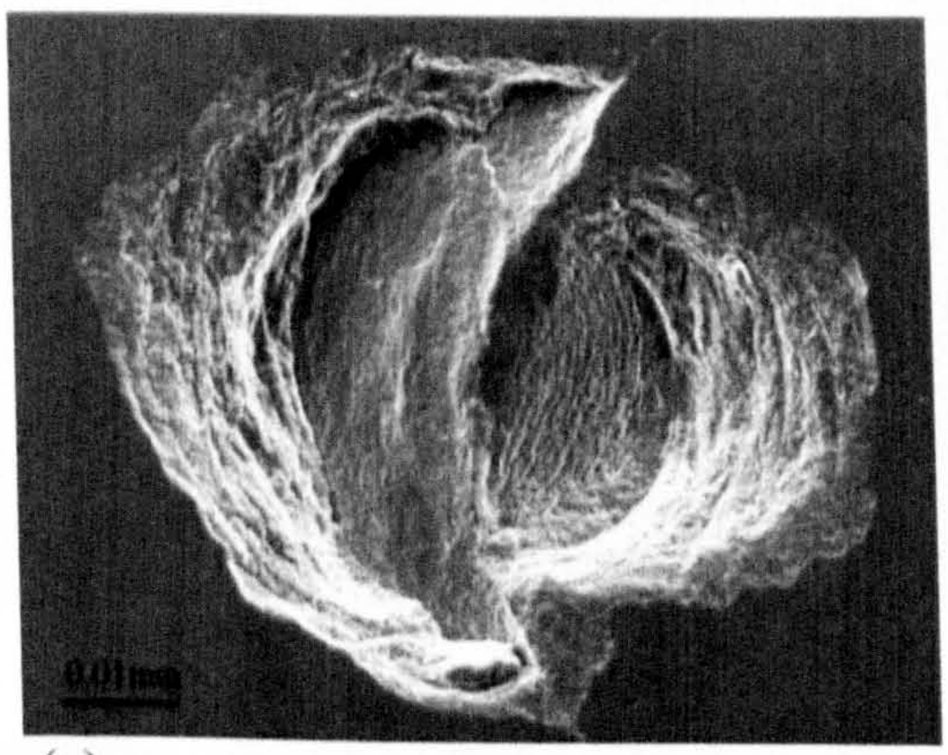

(a)

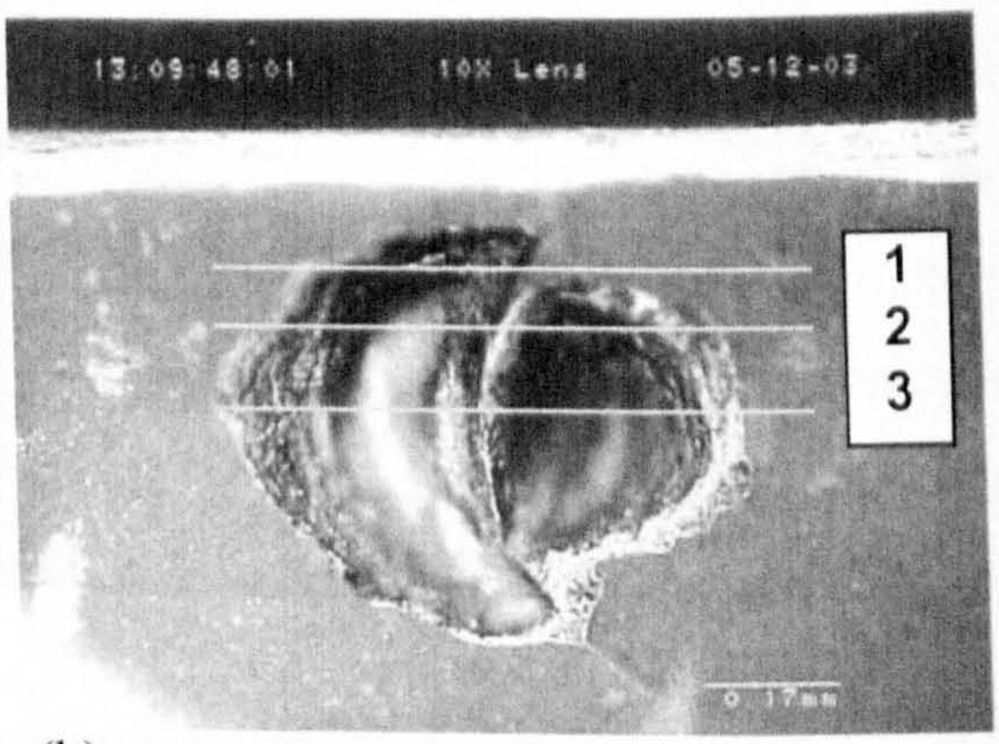

(b)

(c) Section line 1

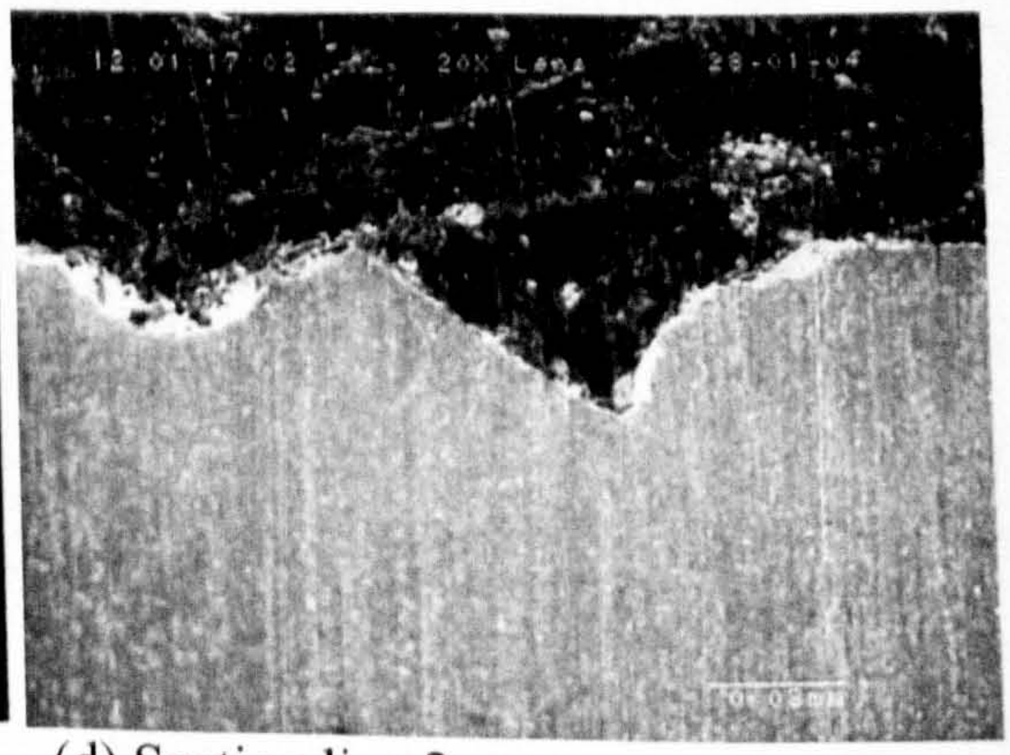

(d) Section line 2

Figure 4.104 Subsurface observations of crack growth and secondary surface cracks (Test N2, Table 4.8)

(e) Section line 2

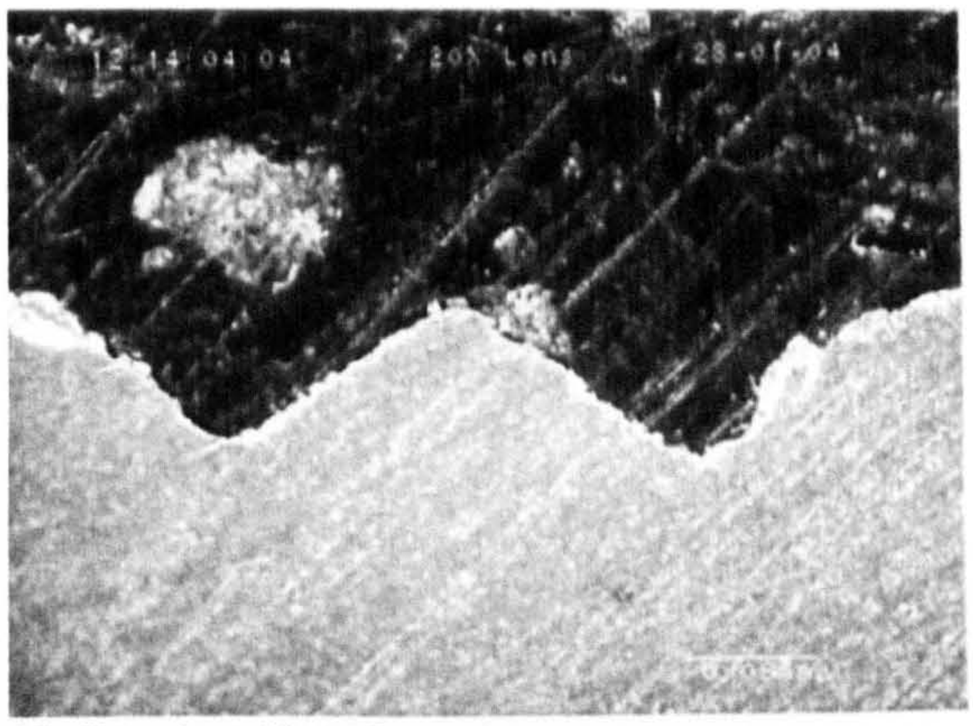

(f) Section line 3

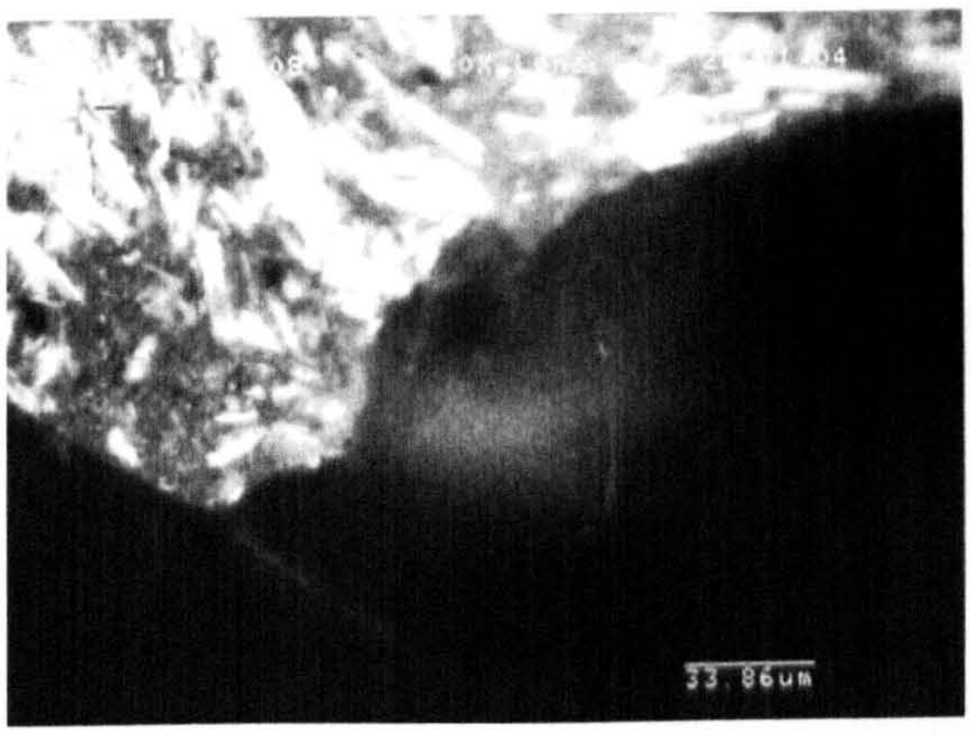

(g) Section line 3

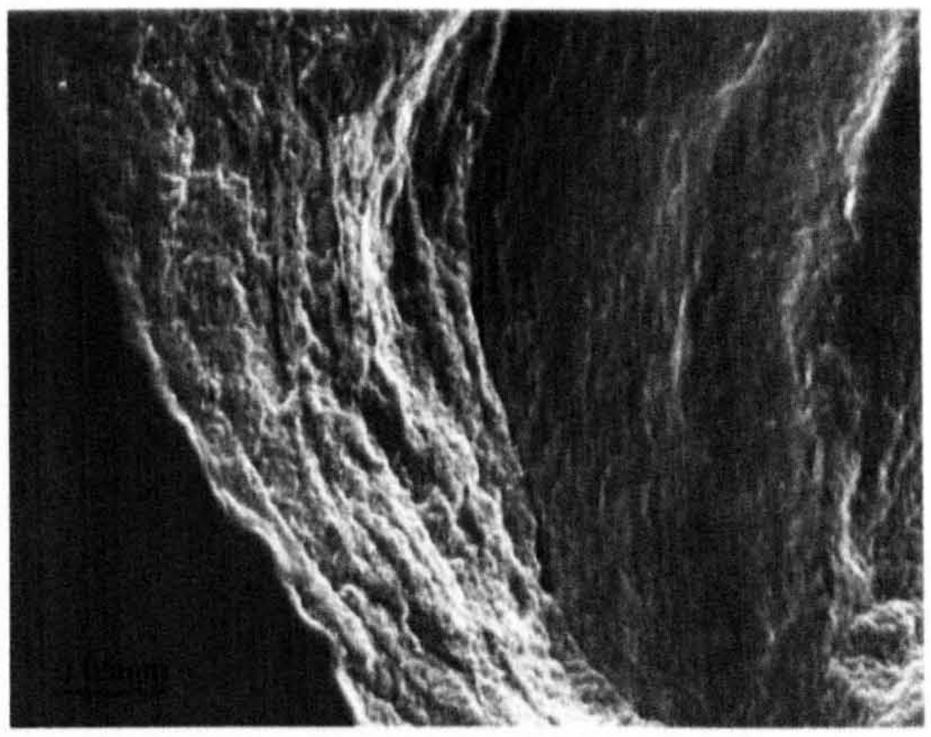

(h) Surface image corresponding to (g)

Figure 4.104 continued

4.5.3 Cracks with no spall

The tested balls without fatigue spall were also sectioned to examine whether or not the fatigue crack had propagated. The balls were sectioned near the crack and then polished gradually across the crack to inspect the profile of the subsurface crack.

Figure 4.105 presents the subsurface observations from the ball with a natural crack. The fatigue test was performed at contact pressure of 5.03GPa and was lubricated with mineral oil. The test was suspended after 116 hours of testing. Figure 4.105(a) is a surface view showing the ring crack and contact track. The surface view at the section site is shown in figure 4.105(b). The subsurface observations indicate that this natural crack had a length of approximately 0.05mm

(figure 4.105(c) and (d)). No subsurface crack growth is seen in this observation.

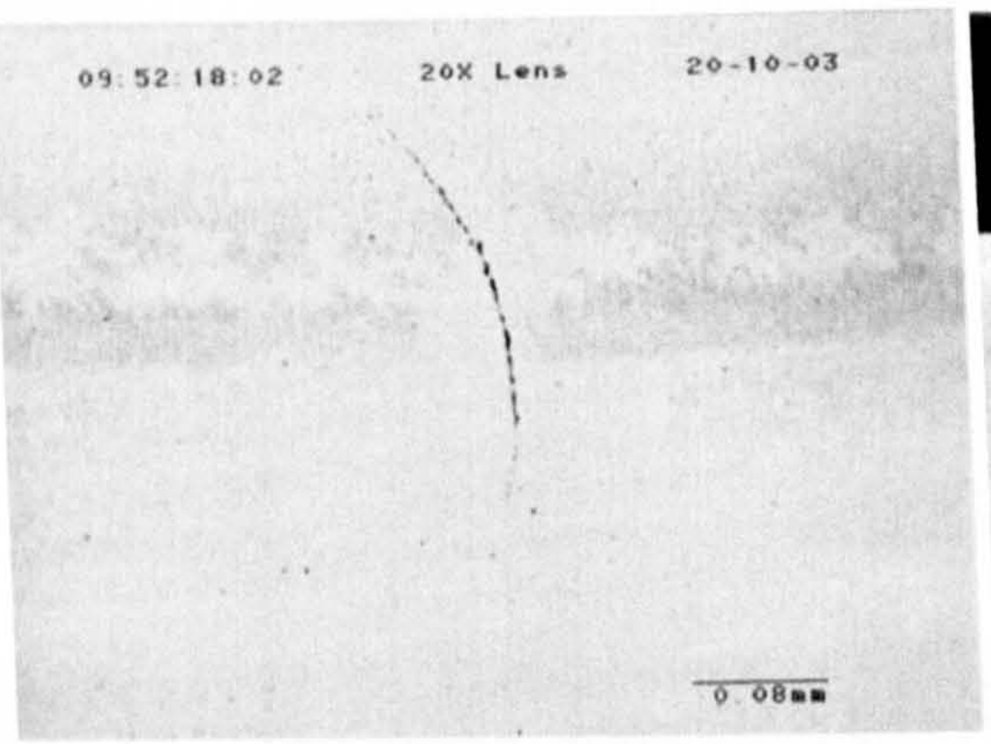

(a) Contact path

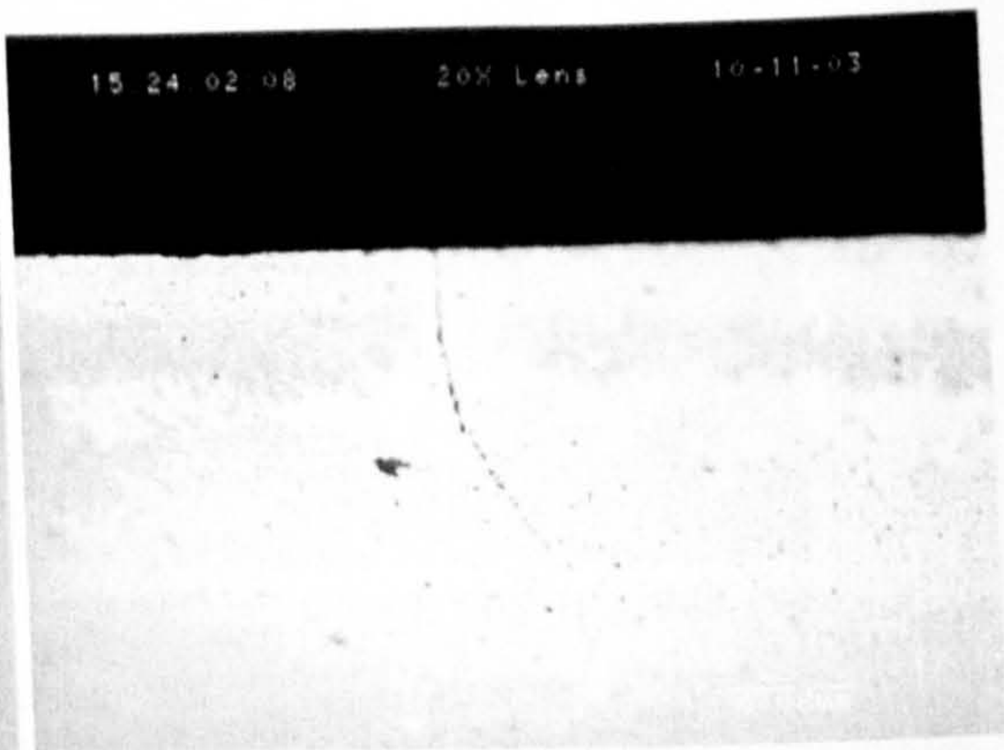

(b) Surface view of section site

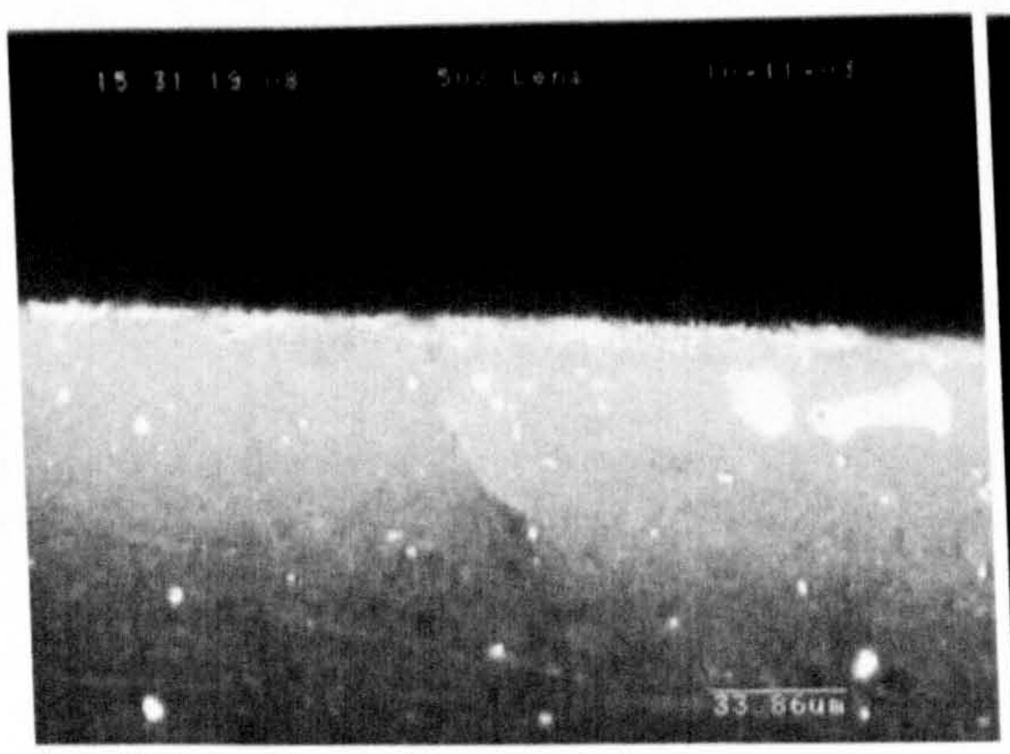

(c) Subsurface observation

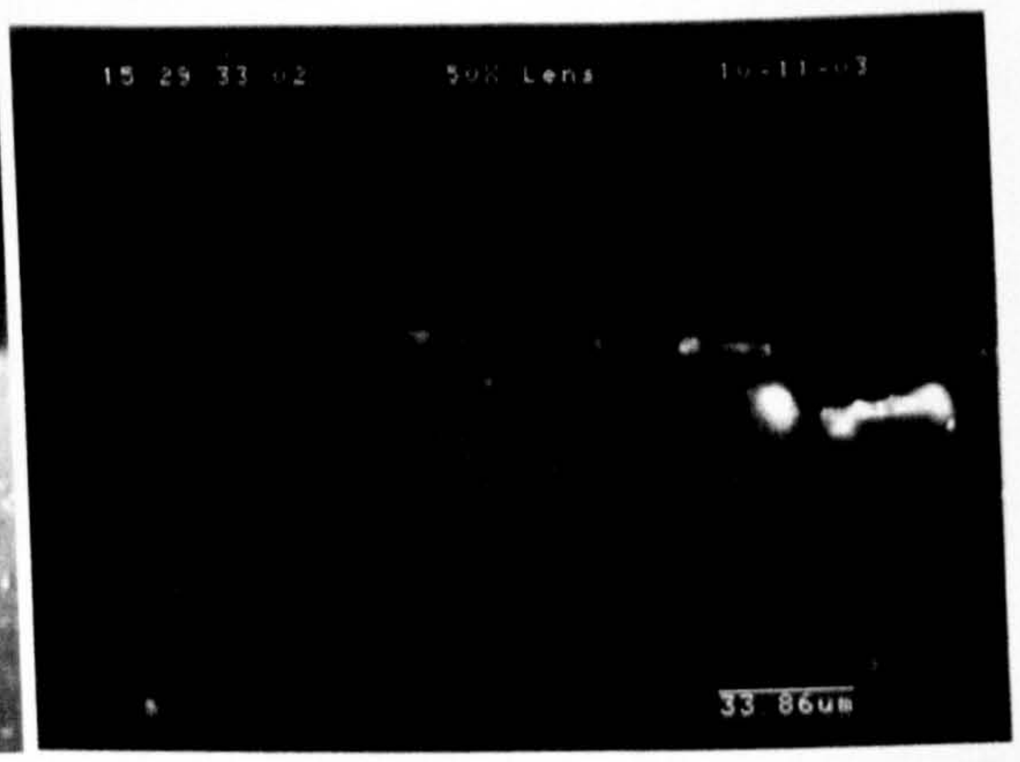

(d) With UV light

Figure 4.105 Subsurface observations of crack growth (Test TT9-6, Table 4.5)

Figure 4.106 shows the subsurface observation of a crack from Test GOL-1. It is a small crack (natural ring crack). This test was performed at the contact pressure of 5.03GPa and was suspended after 300 hours (approximately 2×10^8 stress cycles). Figure 4.106(a) presents a surface view of the contact track and ring crack. There are three lines (figure 4.106(a)), which show the sites at which the section images are taken. The subsurface image at the section line 1 is shown in figure 4.106(b), using microscopic analysis with ultra-violet light. The depth is very shallow at the beginning of sections. As the section plane moves to the middle, the depth of the crack becomes deeper as shown in figure 4.106(c). No subsurface crack growth is seen at this section. Two branched cracks at the tip are seen when the

section moves to the middle of the ring crack as shown in figure 4.106(d).

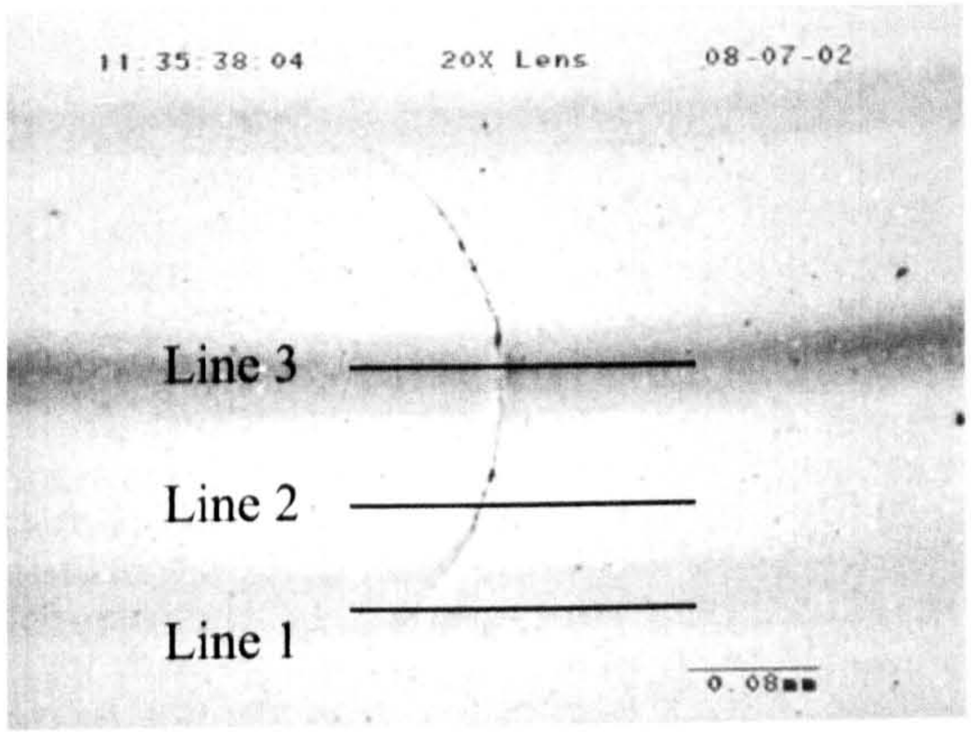

(a) Line indicating section position

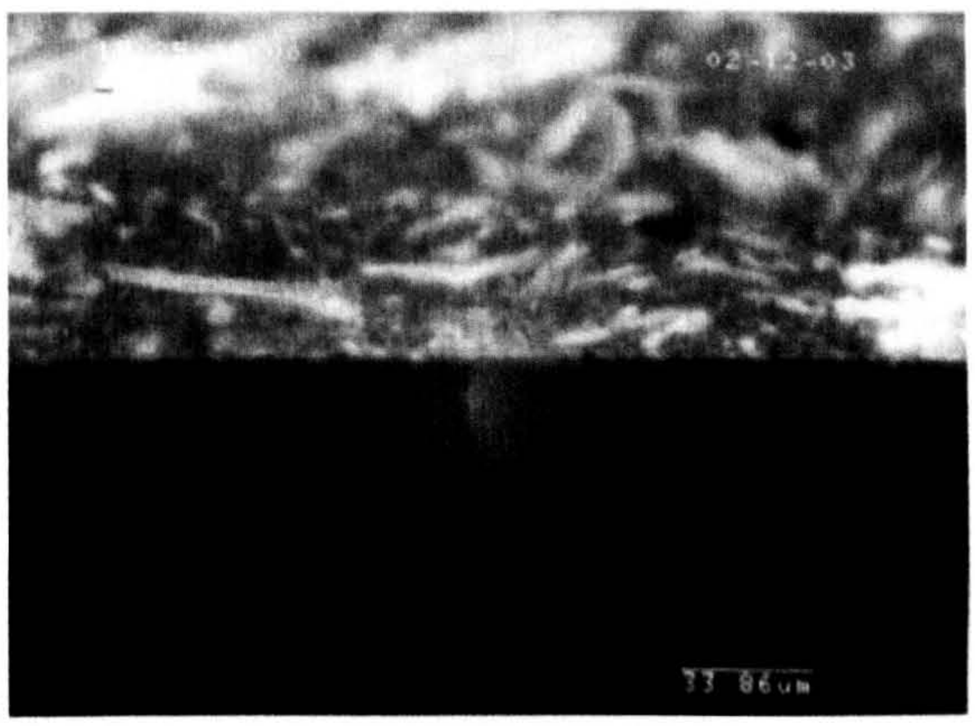

(b) Shallow depth (line 1)

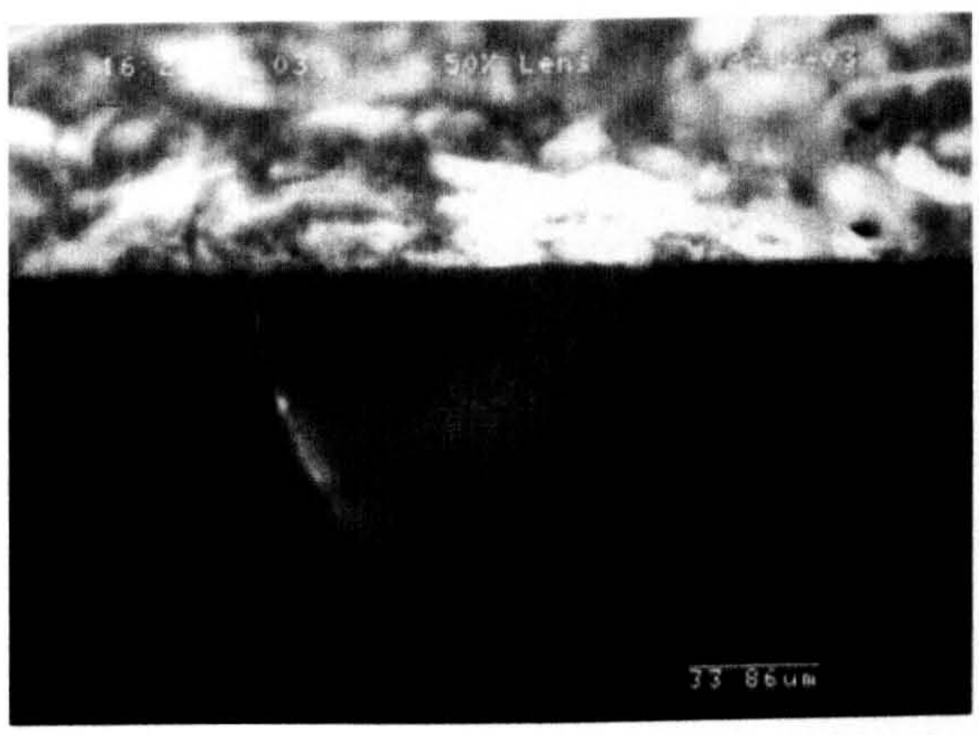

(c) Becoming deeper (line 2)

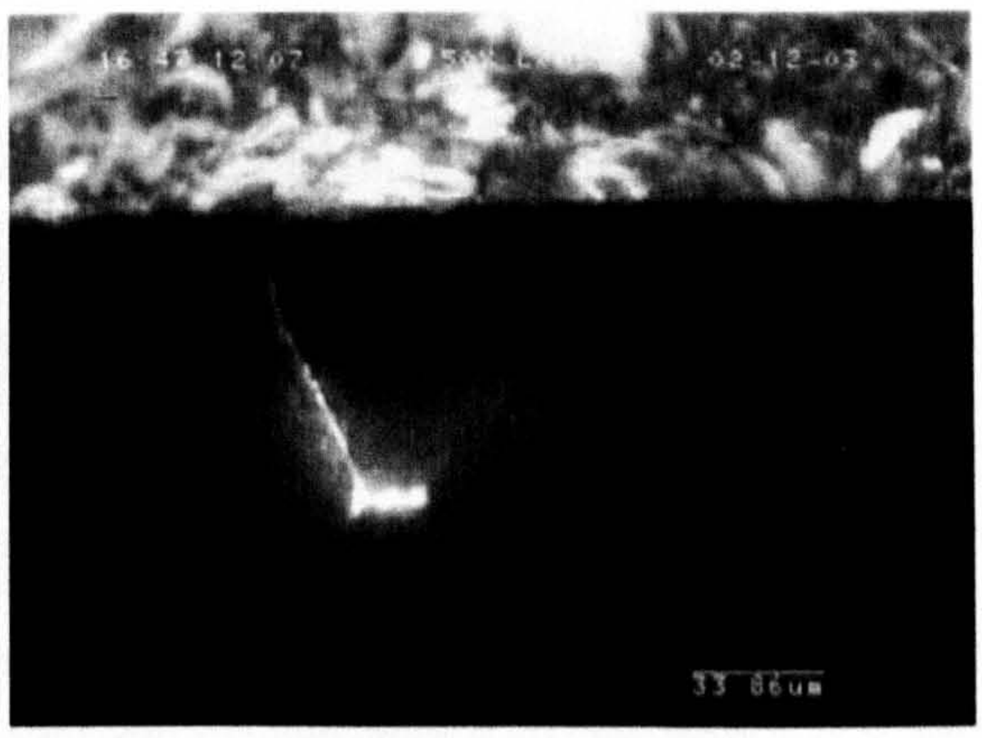

(d) Branched cracks seen (line 3)

Figure 4.106 Subsurface observations of crack growth (Test GOL-1, Table 4.2)

4.6 SUMMARY FROM EXPERIMENTAL WORK

The RCF tests of silicon nitride balls with surface ring cracks showed that their life was strongly influenced by load/contact stress, crack size, lubricant and material type. Whilst the strong dependence of life on load and crack size could be expected, the effects of lubricant and material type were not so straightforward. The shorter life with traction fluid can be explained by higher surface traction stresses leading to higher stress intensities around the crack. The better performance of

grease and gearbox oil compared to mineral oil may be due to penetration of lubricant into the crack faces. Therefore, the effect of crack face friction was included in the modelling studies described in Chapter 5.

The surface and subsurface examination of cracks (tested and untested), incipient spalls and full spalls provided valuable information on the failure mechanisms. Previously, it was thought that spalling failure occurred as a result of growth of the original crack towards the surface under cyclic loading. In this study, secondary cracks, generally parallel to the original crack, were shown to form on the surface. At the same time, there is subsurface propagation of the original crack, often laterally parallel to the ball surface. Crack branching was shown to occur both from the propagated (fatigue) crack and secondary cracks leading to a subsurface crack network which eventually leads to break-out of material and spalling.

As a consequence, modelling work on the RCF behaviour of balls with ring cracks in the following chapter was focussed on two main aspects. One was the analysis of surface tensile stresses necessary for the formation of secondary cracks and the other was a study of the factors involved in subsurface fatigue crack propagation. In addition it was hoped that the modelling could explain the difference in RCF behaviour of the ball materials used in this study, both of which were high quality materials with similar physical and material properties.

CHAPTER 5
MODELLING OF ROLLING CONTACT FATIGUE FAILURE

An analytical study of ceramic rolling contact fatigue is presented in this chapter. A boundary element analysis is carried out to increase understanding of rolling fatigue failure processes. The analytical model is presented and described in section 5.1. The physical considerations and modelling strategy are addressed. A three-dimensional boundary element model is developed and described in section 5.2. Contact stresses due to surface ring cracks are analysed. The influencing factors such as crack face friction, crack geometry and contact stresses are described in section 5.3. The calculation results predict the conditions for the secondary surface cracks and interpret the failure mechanism of ceramic rolling contact fatigue.

Stress intensity factors (SIF) are computed according to the three-dimensional fracture model. SIF solutions along the crack front are described in Section 5.4. The effect of crack face friction is discussed in Section 5.4.1. The effect of crack geometry on the stress intensity factors is described in Sections 5.4.2. The effects of crack position and crack gap on the stress intensity factors are also described in Section 5.4.3 and Section 5.4.4. The effects of normal load and tangential traction on the stress intensity factors are described in Section 5.4.5 and Section 5.4.6. The SIF calculation when the crack is outside the contact circle is outlined in Section 5.4.7.

5.1 MODEL DESCRIPTION

5.1.1 Loading condition

The loading configuration of the testing environment for the modified four-ball machine was described in the previous section (see figure 3.3, Chapter 3, Section 3.3). The surface loading traverses the surface ring crack repeatedly. Based on this loading configuration, a three-dimensional contact fatigue model is considered as shown in figure 5.1, where a surface containing a ring crack is subjected to a Hertzian point contact loading moving across its surface. The normal

pressure distribution $p(x, y)$ is given by the Hertz theory (Johnson 1985),

$$p(x,y) = p_0\sqrt{1-\frac{x^2+y^2}{a^2}} \tag{5.1}$$

where p_0 and a are the maximum Hertzian pressure and contact radius respectively. The tangential traction $q(x, y)$ is expressed as

$$q(x,y) = fp(x,y) \tag{5.2}$$

where f is the coefficient of traction. The traction coefficient $f < 0$ if the surface loading traverses from right to left , and the traction coefficient $f > 0$ if traversing from left to right. Various values of the traction coefficients are selected to simulate different scenarios. The symbol d represents the distance from the contact circle to the ring crack circle.

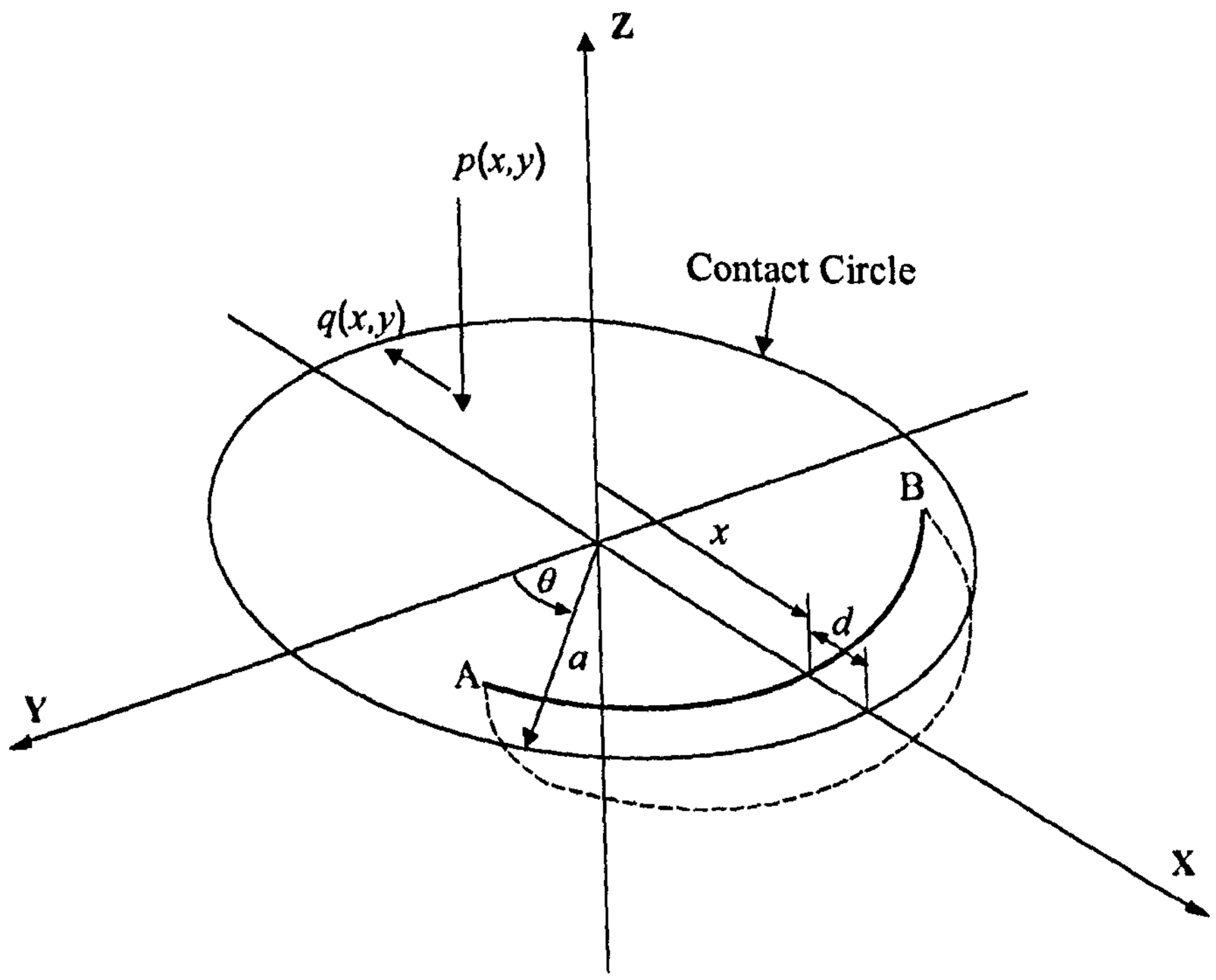

Figure 5.1 Analytical model and global co-ordinate system

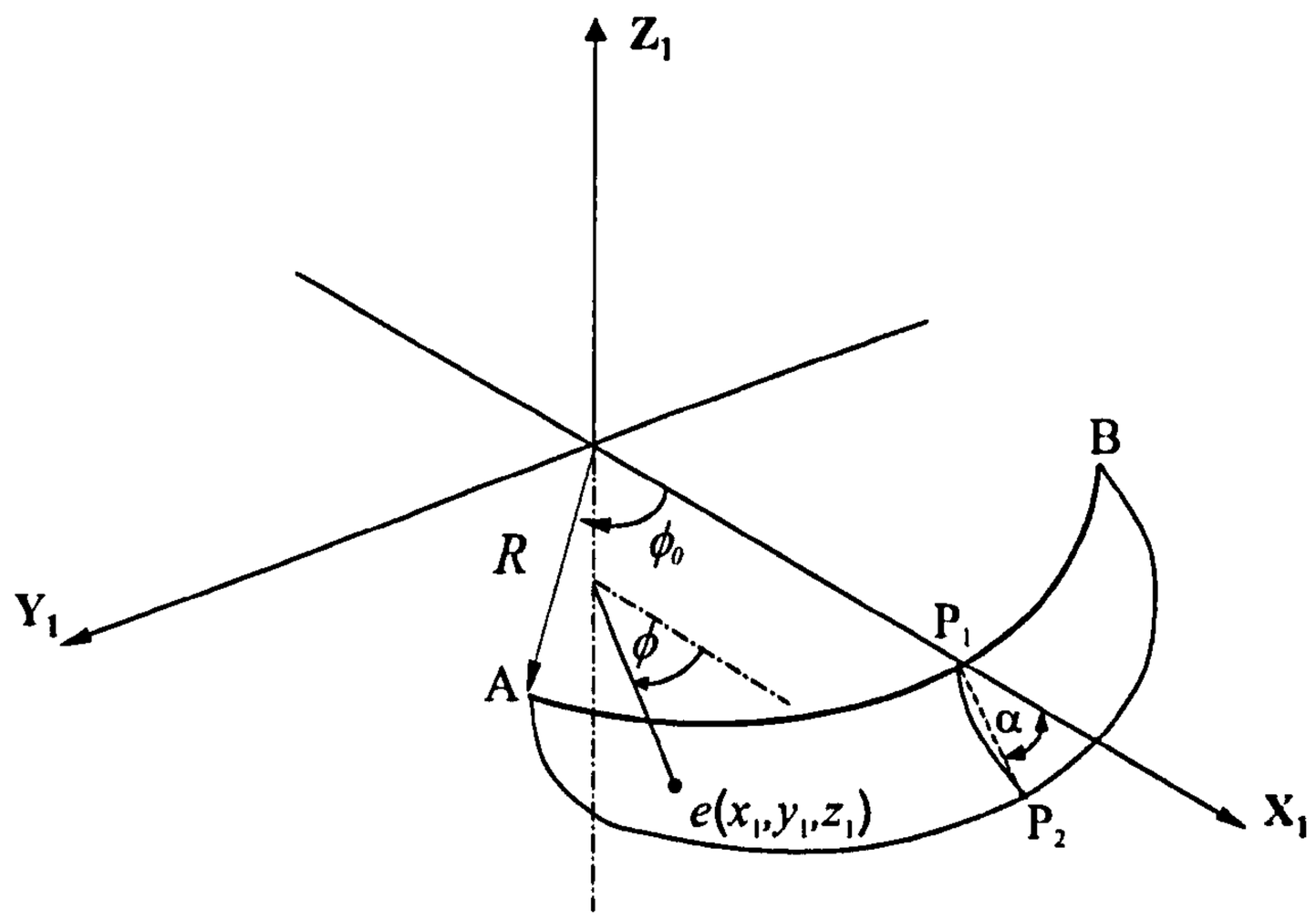

Figure 5.2 Local co-ordinate system describing the geometry of a ring crack (Wang and Hadfield 2000a)

5.1.2 Crack geometry

The crack geometry has a significant effect on fracture mechanics analysis and will be considered carefully. The crack geometries used in the numerical calculation are defined by the modified equations (4.5) to (4.7) (see Chapter 4, Section 4.1.4), which is written below as equations (5.3) to (5.5), as shown in figure 5.2 (Wang and Hadfield 2000a),

$$x_1 = (R + l\sqrt{1 - (\frac{\phi}{\phi_0})^2}\cos\ \alpha)\cos\ \phi \qquad (5.3)$$

$$y_1 = (R + l\sqrt{1 - (\frac{\phi}{\phi_0})^2}\cos\ \alpha)\sin\ \phi \qquad (5.4)$$

$$z_1 = \sqrt{\frac{l\cos\alpha}{S}\sqrt{1-(\frac{\phi}{\phi_0})^2}} \qquad (5.5)$$

where l denotes the crack length, $0 < l <$ maximum crack length (line P_1P_2), R is the radius of the ring crack, α is the angle of line P_1P_2 to the ball surface, $0< \alpha < \pi/2$, ϕ represents the angle of an element position on the crack face, $-\phi_0 < \phi < \phi_0$ and ϕ_0 denotes half the angle of ring crack arc AB, $0 < \phi_0 < \pi/2$. The S is the shape constant, which is used to describe the subsurface profile.

5.1.3 Crack face friction

As the surface loading moves across the surface ring crack, the crack will undertake various stress states. When the crack lies in the contact area, the faces of the crack became contacting, and therefore friction forces act between them. The Coulomb's law is used to model crack face friction. The crack face coefficient f_c, depends on the contact condition of the crack faces. Choosing different crack face friction coefficients simulate their effect on the stresses ahead of the crack.

According to the experimental observations, there is a gap as defined by the maximum separation at the ball surface. This gap will increase due to the wear of the crack faces as fatigue testing. It is felt that the understanding of the crack gap effect on failure modes is the key to revealing the nature of ring crack fatigue damage. To analyse how the gap affects the contact behaviour, different gaps are adopted for the numerical analysis.

5.2 BOUNDARY ELEMENT ANALYSIS

5.2.1 Boundary element modelling

The three-dimensional contact fatigue model for fracture mechanics analysis is presented in the previous discussion. In general, analytical solutions to the problems in fracture mechanics are limited to a small number of idealised situations in which the domain is considered to be infinite, homogeneous and isotropic and the loading relatively simple. However, in practical situations the geometry and loading encountered in three-dimensional crack problems is too complex for the stress intensity factors to be solved analytically (Wang and Hadfield 2004). The calculation of the stress intensity factors is further complicated because it is influenced by the crack size and shape, type of loading and geometry of the

structure. This has frequently led to numerical approaches such as the boundary element method and finite element method. In this study, a boundary element method based computer modelling package BEASY (Computational Mechanics BEASY 1998) was employed to perform fracture mechanics analysis.

The boundary element method (Appendix 4) is now widely used in many engineering disciplines as an alternative numerical technique to the finite element method (Brebbia and Dominguez 1992). The advantage of using boundary element analysis in fracture mechanics analysis is that the fracture model is largely reduced in the dimensionality of the problem; for three-dimensional problems, only the surface of the domain needs to be discretized. This means that the boundary element analysis results in a substantial reduction in data preparation. Another important feature of the boundary element formulation is that it provides a continuous modelling of the interior since no discretization of the interior is required; this leads to a high resolution of interior stresses and displacements.

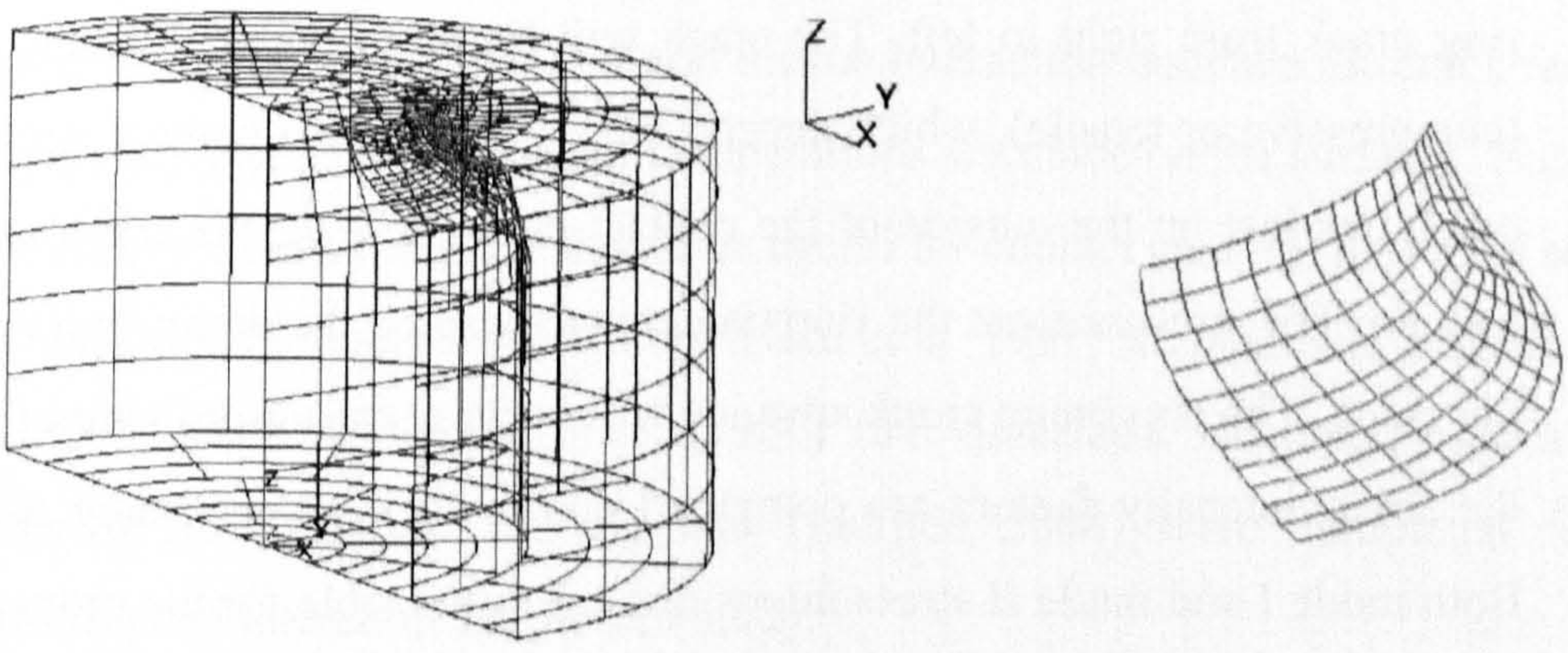

(a) Overview of the model (b) Detailed view of the crack mesh

Figure 5.3 Three-dimensional boundary element model

The three-dimensional boundary element model used in the present study is a small volume of the ceramic ball in order to reduce the size of the model as shown in figure 5.3. The prescribed boundary displacements and stresses in the concentrated contact zone were extracted from the analysis of the ceramic and steel ball contact. An axisymmetric boundary element model was adopted to perform this analysis (Appendix 5). The use of the small volume leads to a significant reduction in numbers of boundary elements. This simplification makes it feasible for the complex three-dimensional contact and crack problems. The three-dimensional contact fatigue model also incorporates a vertical symmetry plane through the middle of the disk to reduce the number of elements used in the model. There is no need to place the elements on the symmetry plane and as a result of that, this further reduces the size of the model.

5.2.2 Fracture analysis

As described in the three-dimensional contact fatigue model (figure 5.1), the crack will undertake a dynamic loading when the surface loading moves across the ring crack from right to left. The crack will be acted under different stress states (compressive or tensile), which depend the position of the contact circle. When the crack lies just on the outside of the contact circle ($x \geq a$), the crack mouth will be opened. The stresses from the Hertzian contact will be the driven force to propagate the crack. The maximum crack advance will occur at the co-ordinate of $x = a$, where the stress intensity factors are computed due to their values being the maximum. Both mode I and mode II stress intensities are responsible for the propagation of the crack.

When the crack lies in the contact circle ($-a < x < a$), the crack front receives the compressive stress. The mode I stress intensity (K_I) does not play any role in crack growth due to $K_I \leq 0$. Therefore the mode II (K_{II}) will dominate the crack propagation behaviour. The magnitude of the stress intensity (K_{II}) is a function of co-ordinate x. Also, the interaction between the crack faces becomes more important for the determination of the stress intensity values. The friction exists between the

crack faces and will significantly influence the crack propagation behaviour. Clearly, fatigue crack propagation and surface cracking are affected by the co-ordinate x and can be a rather complex process due to the cyclic Hertzian loading

The calculation of the stress intensity factors for the crack being outside contact circle has been carried out by Wang and Hadfield (2000a). In that study, the natural crack was adopted in the model and crack growth was analysed using the dual boundary element method. No attempt was made to compute the stress intensity factors where the crack lies in the contact circle because the numerical method is only valid for the crack faces being open. The calculation results were successfully used to explain the experimental observations of the crack orientation effect on fatigue spalling. However, the calculations could not explain why the spall size is often larger than the numerical prediction. This is because the calculation of the stress intensity factors did not take into account the situations where the crack lies in the contact circle.

When the crack lies in the contact circle (compressive zone) the mode II stress intensity will dominate the crack propagation because the mode I stress intensity becomes zero. The crack face friction plays an important role in determining the magnitude of the mode II stress intensity. The crack face contact is considered for the boundary condition for the interaction between the crack faces. In the boundary element analysis, all computations are made on the surfaces. Naturally, the boundary element method should be useful for contact analysis problems and has been discussed by many investigators (Niku et al. 1991, Aliabadi and Brebbia 1993, Man 1994) since Andersson et al. (1980) first described. However, only a small number of investigations (Wang and Hadfiled 2004) were completed for the situations encountered in the present study.

In the present study, the computation of the stress intensity factors will concentrate on the situations where the crack lies in the contact circle. In other words, the calculation of the stress intensity (K_{II}) with complex ring crack geometry and loading conditions in ceramics is the main purpose of the study, which has not been done by any other investigators.

The importance of the stress intensity factor in determining stress fields around the crack tip was first demonstrated by Irwin (1957). The stress intensity

factors have been addressed by numerous authors (Aliabadi 1991) since then and different numerical methods have been developed for the calculation of the stress intensity factors. In Irwin's equations, the stress and displacement are given near a crack tip in terms of the stress intensity factor at the crack tip. Thus if these stress and displacement fields are known from the boundary element analysis, the stress intensity factors can be calculated. The near-tip stress field for mode II is given by the following expression (Aliabadi 1991):

$$\sigma_{xx} = \frac{K_{II}}{\sqrt{2\pi r}} \sin\frac{\theta}{2}(2 + \cos\frac{\theta}{2}\cos\frac{3}{2}\theta)$$

$$\sigma_{yy} = \frac{K_{II}}{\sqrt{2\pi r}} \sin\frac{\theta}{2}\cos\frac{\theta}{2}\cos\frac{3}{2}\theta)$$

$$\sigma_{xy} = \frac{K_{II}}{\sqrt{2\pi r}} \cos\frac{\theta}{2}(1 - \sin\frac{\theta}{2}\sin\frac{3}{2}\theta) \quad . \qquad (5.6)$$

The near-tip displacement field for mode II is

$$u_x = \frac{K_{II}}{\mu}\sqrt{\frac{r}{2\pi}} \sin\frac{\theta}{2}[\frac{1}{2}(\kappa + 1) + \cos^2\frac{\theta}{2}]$$

$$u_y = \frac{K_{II}}{\mu}\sqrt{\frac{r}{2\pi}} \cos\frac{\theta}{2}[\frac{1}{2}(1 - \kappa) + \sin^2\frac{\theta}{2}]. \qquad (5.7)$$

The mode II (sliding mode) stress intensity factor is the limit

$$K_{II} = \lim_{r\to 0}\sqrt{2\pi r}\sigma_{xy} \ (r,\theta=0).$$

The true value of K_{II} is the value at $r = 0$, which can be extrapolated from the plot of K_{II} against r (the distance from the crack tip) using the boundary element modelling. The calculation results regarding the mode II stress intensity factor (K_{II}) will be discussed in Section 5.4.

5.3 CONTACT STRESSES DUE TO SURFACE RING CRACKS

The numerical results contain two parts: the analysis of stress intensity factors and the stress distribution analysis on the surface in the region of the crack. The analysis of the stress intensity factors will be presented in Section 5.4. In this section, the analysis of the stress distributions on the surface is shown. As a surface ring crack exists, the stresses ahead the crack on the ball surface cannot be solved analytically using the Hertz elastic contact theory. Therefore a numerical solution is required in the calculations. It is felt that the understanding of how an exiting crack affects the stress distributions ahead the crack is crucial important for determining surface cracking behaviour of a cracked ceramic ball. The purpose of the following discussion is to establish a fundamental understanding of failure mechanisms of ceramic balls that contain different crack size. The numerical results are expected to explain the experimental observations.

The experimental results in Chapter 4 showed the great importance of the secondary surface cracks in the processes of fatigue damage. In other words, for the balls with the larger ring cracks, the fatigue failure is dominated by the secondary surface cracks; and for the balls with the smaller ring cracks, the fatigue failure is dominated by subsurface fatigue crack propagation and secondary surface cracks. Also, the experimental results indicated that the material with high Hertzian fracture strength always showed a good fatigue life performance. Therefore the analysis of the stress distributions on the cracked ball may be able to reveal the nature of ring crack contact fatigue in ceramics. Based on the experimental tests (Chapter 2), the Hertz fracture strength required the formation of the surface ring cracks is 2.07 GPa for material B and 1.51 GPa for material A. These critical values will be used to determine whether the surface cracks form or not for a given load.

The numerical analysis of surface stresses on the cracked ceramic balls, using a boundary element method, was addressed by Wang and Hafield (2004). They selected a natural crack size (crack radius = 0.21 mm) as a modelling object and only two crack lengths were analysed. In their calculations, the influencing factors such as contact load, crack geometries (crack radius, arc length, crack angles etc) and surface traction were not fully considered since the investigation into each

influencing factor requires the different models to compute. The model preparation and three-dimensional computation are time-consuming. Consequently the results based on the limited geometries and loading configurations cannot reflect the practical situations tested in the experiments such as larger surface ring/cone cracks. In the present analysis, all those factors are considered in the modelling work. The corresponding experimental tests were done and discussed in the experimental results.

5.3.1 Influence of crack face friction

It is well known that lubrication fluids have a significant effect on fatigue failure in rolling contacts. Different mechanisms have been proposed to explain why lubrication fluid increases the rate of the fatigue crack propagation in rolling contact since Way (1935) published his work. For example, lubricating oil penetrates into the crack to produce a hydraulic effect. The lubrication pressure was assumed to prise the crack open and to force the crack to grow back to the surface (Keer and Bryant 1983, Murakami et al. 1985, Kaneta and Murakami 1987). Also sufficient lubrication fluid was taken to exist in the crack so that the crack face friction was zero which increased Mode II crack propagation. In all of these analyses, fatigue crack propagation behaviour was thought to be the only cause of fatigue spall. The fracture analyses seem to explain the observation that pitting is most often observed on the following rather than the driving roller and that cracks are inclined in the direction of motion. Cracks inclined away from the direction of motion will also be initiated, but will not propagate since the contact motion squeezes fluid from the crack faces rather than entrapping the fluid.

Crack face friction coefficient f_c is used to present the magnitude of the crack face friction. The greater the friction coefficient is, the higher is the crack face friction. Small (natural) and large (artificial) cracks were selected to investigate their effect on the stresses. For the small crack, the arc length of the crack is smaller than the width of the contact path. The entire crack is within the contact track. For the

large crack the crack arc length is larger than the contact path. Therefore, the contact circle cannot cover the whole crack. The calculation is performed at a fixed crack length for each case. For the purpose of the calculation, the gap between the crack faces is assumed to be zero. The calculation conditions and the crack geometry are listed in Table 5.1.

Table 5.1 Crack geometry and calculation conditions

Case No	Contact stress (GPa)	Crack position d (mm)	f	f_c	Crack geometry			
					R (mm)	l (mm)	ϕ_0 (degree)	S
1-1	5.58	0.0468	-0.05	0 to 0.9	0.21	0.098	45	20
1-2	5.58	0.0468	-0.05	0 to 0.3	0.38	0.082	35	20

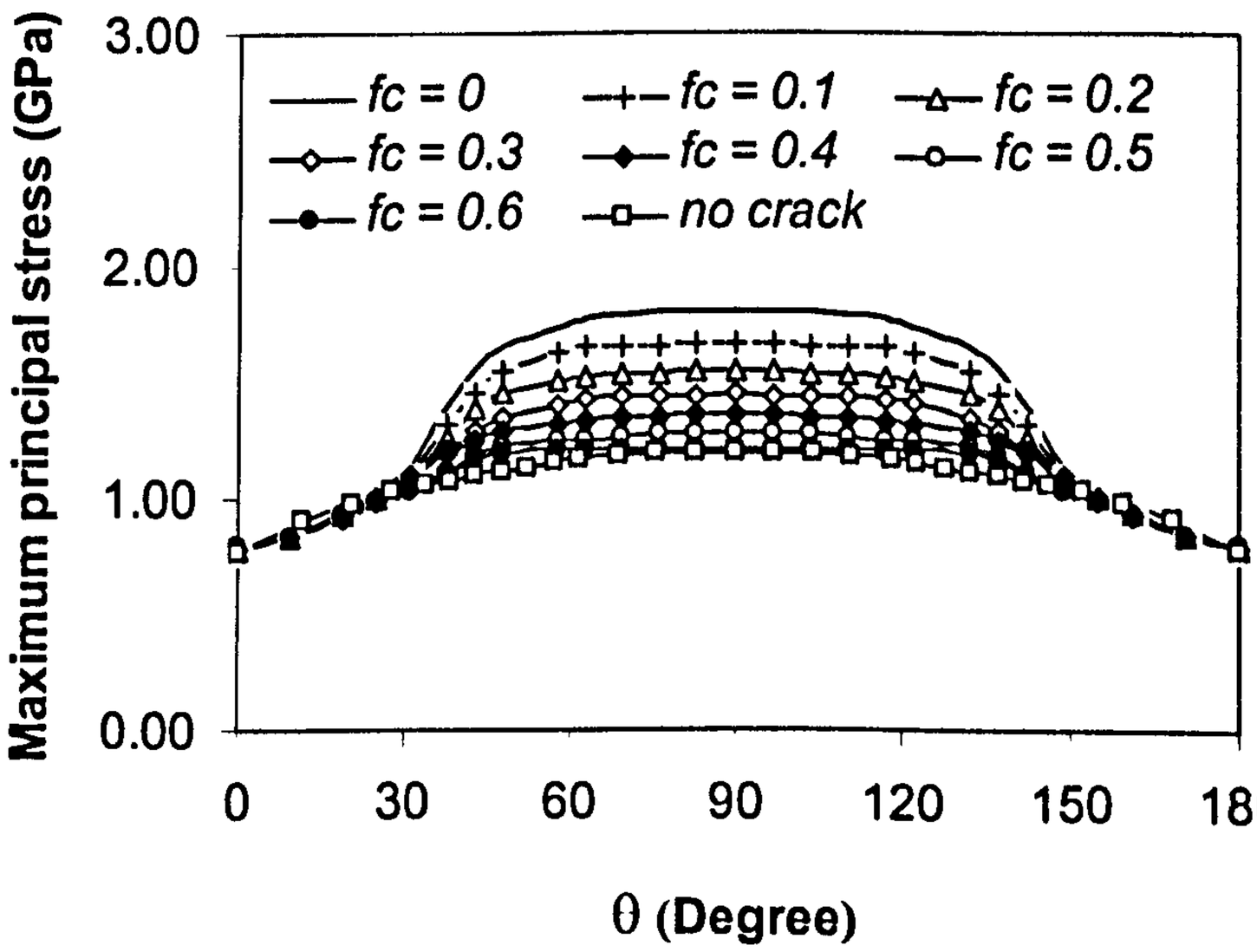

Figure 5.4 Maximum principal stresses along the contact circle of R = 0.21mm (Case 1-1)

Figure 5.4 shows the maximum principal stresses (tensile stress) along the circle of $R = 0.21$mm. It can be seen from figure 5.4, the maximum principal stress is a function of the angle θ and reaches the maximum value at $\theta = 90^{\circ}$. The high tensile stresses are developed at the location of the angle θ approximately between 45° and 135°. The maximum principal stresses decrease as the crack face friction increases. When the crack face friction rises to a certain level, e.g. $f_c = 0.6$, the maximum tensile stress decreases to a value almost identical to that of no crack. Figure 5.4 also indicated that in the range of 0° to 30° and 150° to 180° approximately there are hardly any changes in the magnitude regardless of crack face friction since there is no crack underneath at this area. However, the maximum principal stress considerably increases as the crack face friction decreases, e.g. $f_c = 0$, which approximates to 1.81 GPa. This tensile stress is the main contributor to the initiation of the secondary surface cracks.

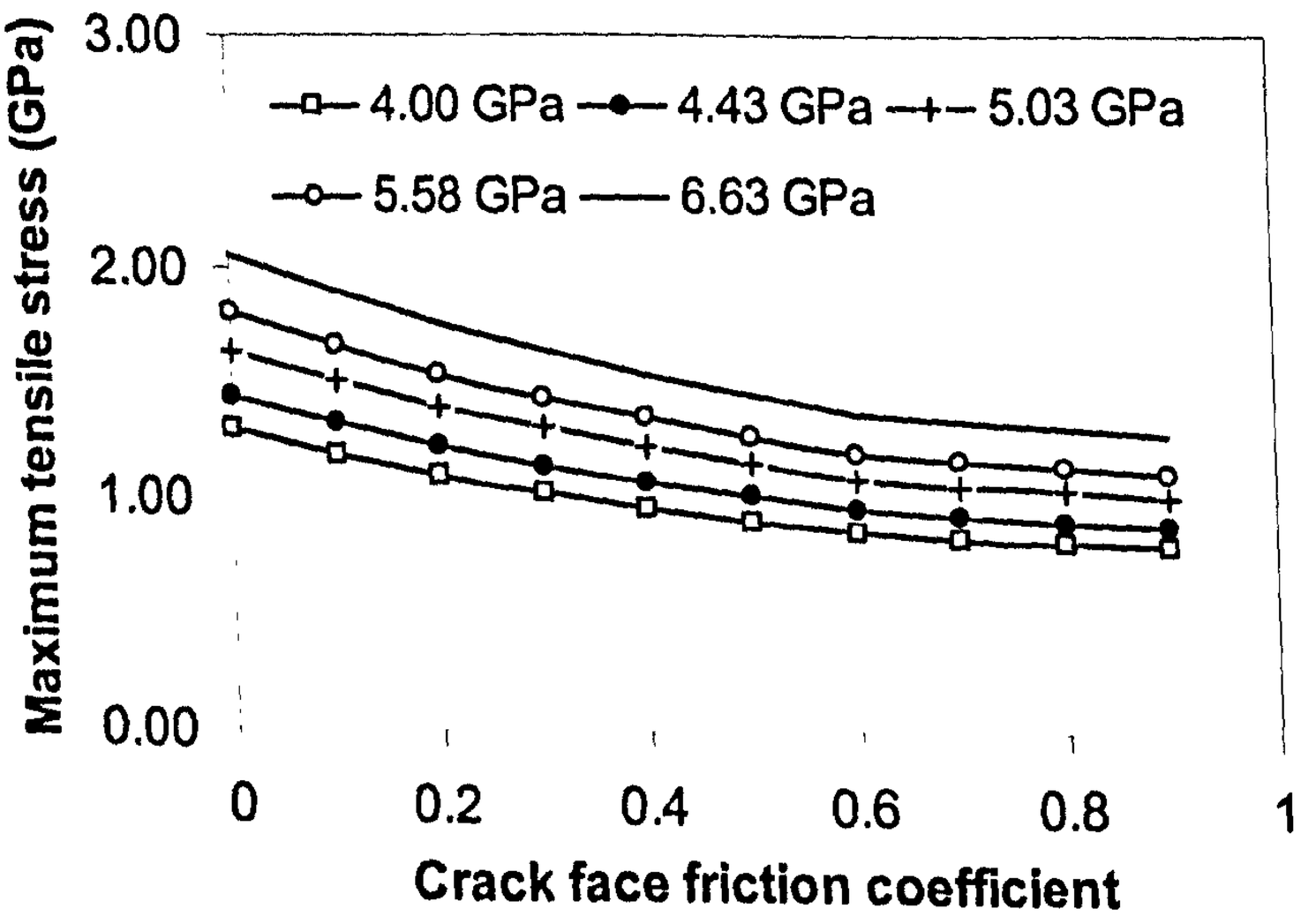

Figure 5.5 Maximum tensile stress against crack face fiction coefficient (at $\theta = 90^{\circ}$) for different loads (Case 1-1)

Figure 5.5 shows the effect of the contact pressure on the maximum tensile stress (the maximum principal stress at $\theta = 90^{\circ}$). The maximum tensile stress increases as the contact pressure increases. Increasing crack face friction decreases

the maximum tensile stress. The calculation results are now studied in detail. When the maximum contact pressure is less than 5.03 GPa, the maximum tensile stress is below the initiation tensile strength of surface ring crack (1.51-1.82 GPa). Consequently, it is difficult to form a spall because the secondary surface cracks are difficult to form. This prediction is consistent with the experimental observation. For example, there is no fatigue failure for gearbox oil and grease when the contact stress is below 5.03 GPa. Obviously, any factors which prevent oil from penetrating the crack, may lead to an increase in the crack face friction. As a result the maximum tensile stresses decrease and the likelihood of the formation of the secondary surface cracks is lower. The use of grease can inhibit the amount of oil that can enter a crack and friction acting between the faces of the crack increases. The results of the experiment agree well with the calculation. Generally, the secondary surface cracks have a circular shape and a similar radius to the original ring crack circle. These secondary surface cracks grow downward as soon as they form, join and connect with the fatigued crack. A spall is eventually formed. This may explain why the spall contours always take the ellipse shape. Figure 5.6 shows an example of the stress contours around the contact area.

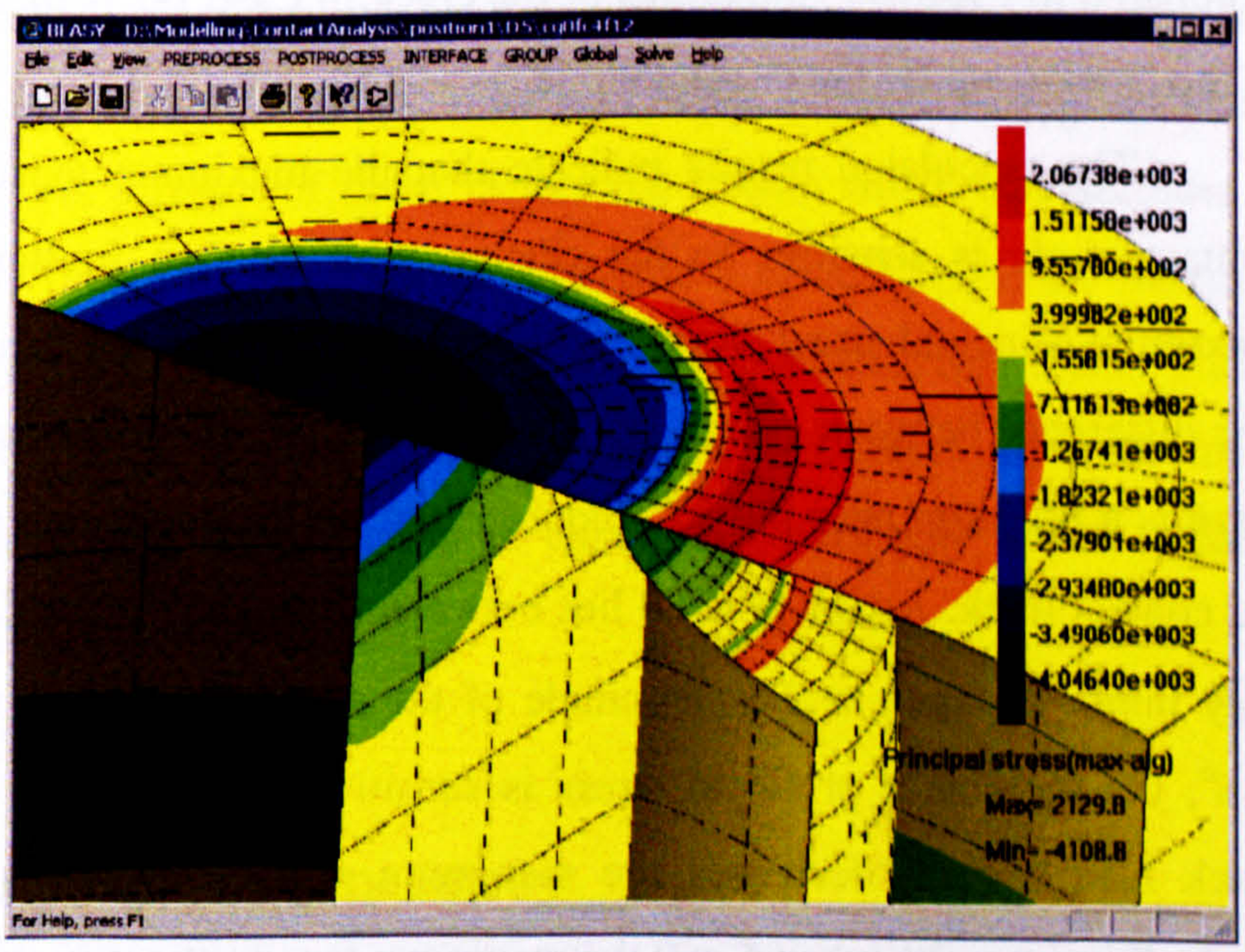

Figure 5.6 Maximum principal stress contours around the contact region for f_c= 0.2, f= -0.05 and p_0= 5.58GPa (Case 1-1)

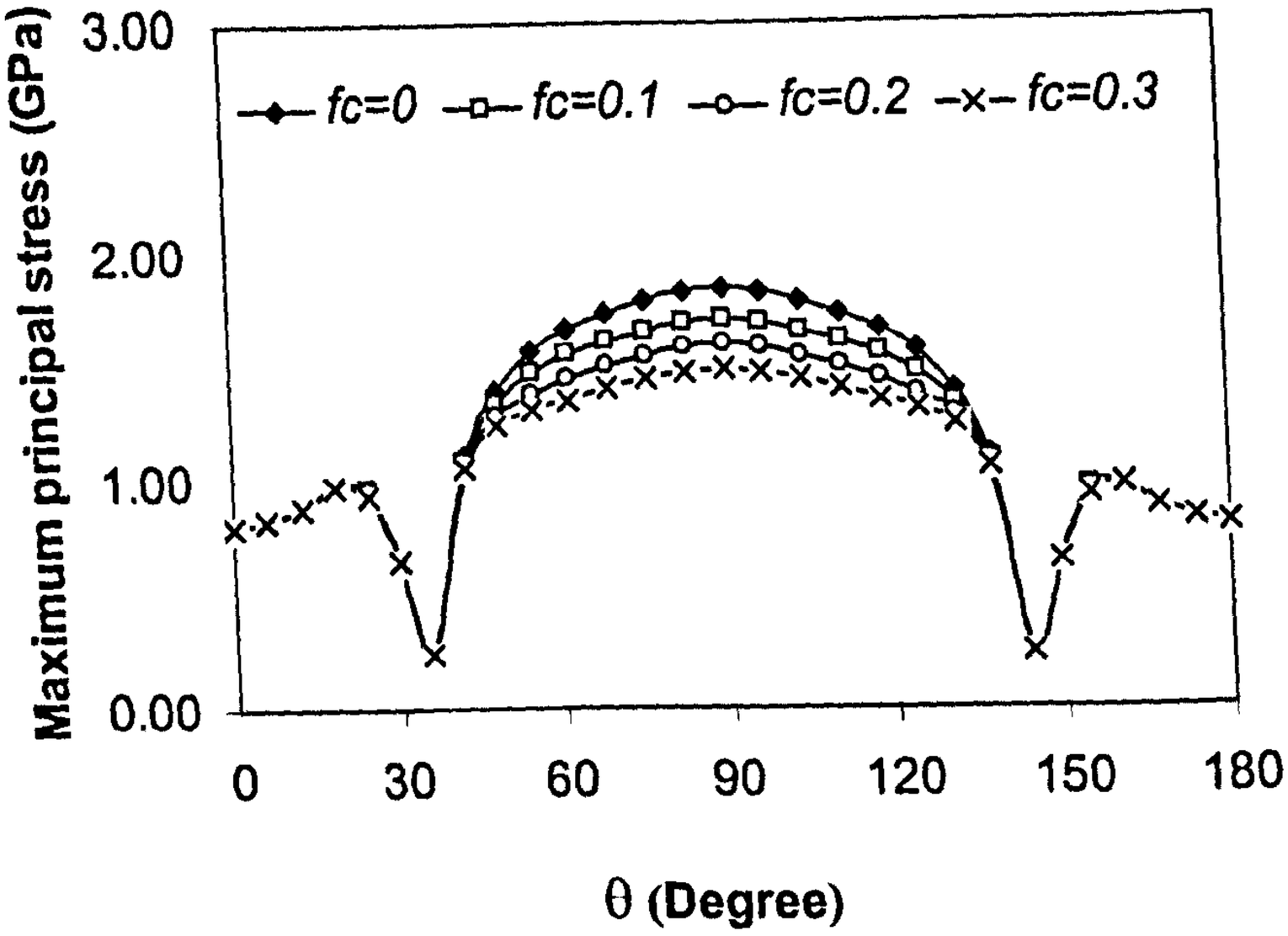

Figure 5.7 Maximum principal stresses along the contact circle (Case 1-2)

Consider the results from Case 1-2. The stresses on the ball surface for the crack radius of 0.38mm are computed and the results are shown in figure 5.7. The stress distribution contour around the contact region is shown in figure 5.8. Compared to Case 1-1, the radius of the crack in Case 1-2 is much larger. Only part of the crack is under the contact circle.

The calculated results indicate that the maximum tensile stress along the contact circle is sensitive to the change in crack face friction coefficients. The maximum principal stress significantly increases as the crack face friction decreases. The difference between case 1-1 and case 1-2 is the stress distribution. For case 1-2, there is a big drop near the 35° and 145° thresholds due to the crack being outside the contact track. Again, when θ lies between 0° and 35° or 145° and 180°, there are only minor changes in the magnitude of the stresses. When θ is between 45° and 135°, the maximum principal stress is sensitive to crack face friction. Increasing crack face friction decreases the maximum principal stresses along the contact circle. For example, when $f_c = 0$ the maximum tensile stress is approximately to 1.84 GPa while the maximum tensile stress is 1.4 GPa when $f_c = 0.3$.

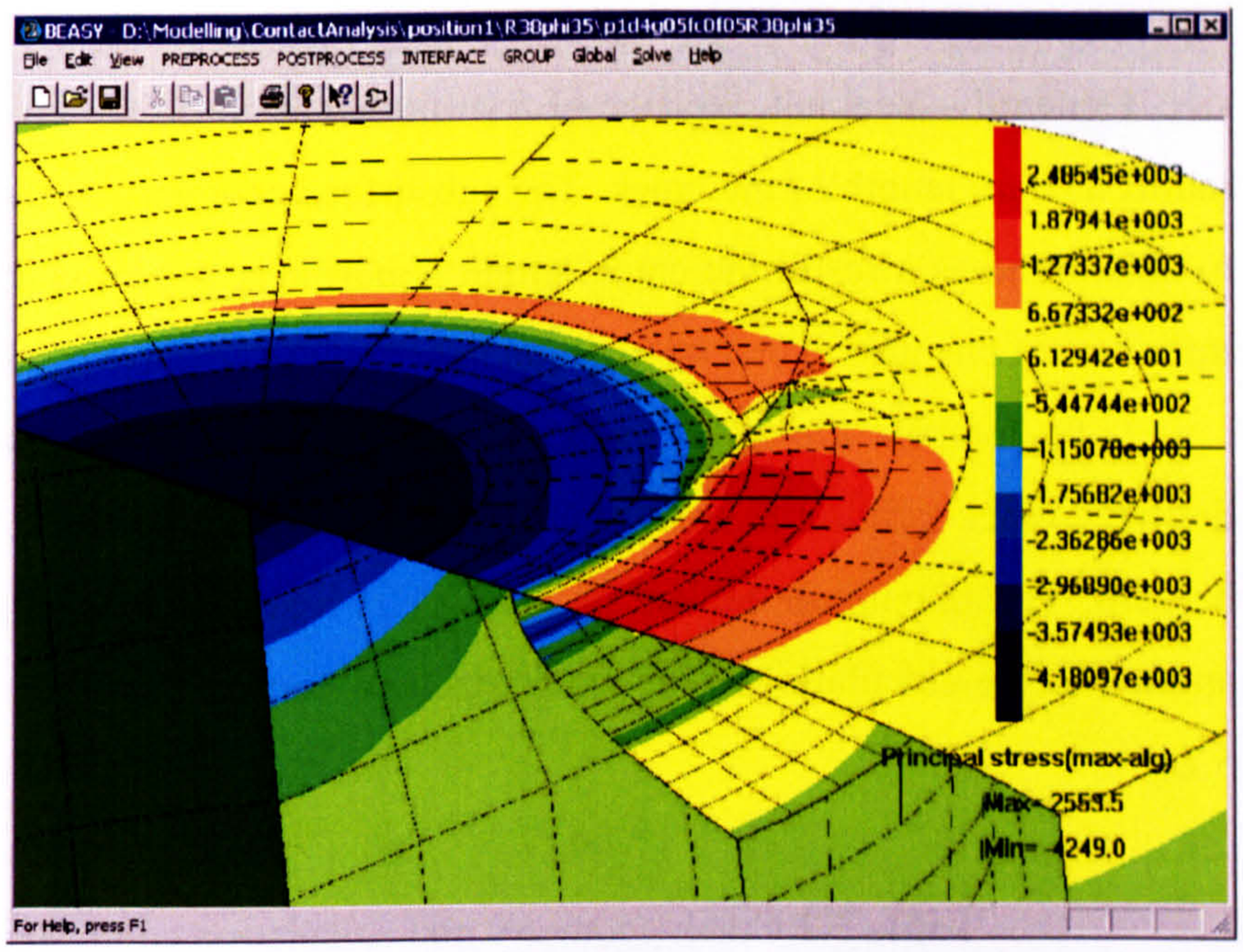

Figure 5.8 Maximum principal stress contours around the contact region (Case 1-2, f_c= 0)

The calculation results from both cases indicate that the maximum tensile stresses at the contact circle decrease with the increase of crack face friction. Therefore, increasing the crack face friction will decrease the likelihood of the formation of the secondary surface cracks. In other words, any factors which prevent oil penetrating inside the crack, may lead to the increase of the crack face friction coefficient. As a result of these factors the tensile stress will decrease. When the friction coefficient of the crack face rises to a critical level, the maximum tensile stress decreases to a value identical to that of no surface ring crack. There is a very slight change in the maximum tensile stress on the contact circle for different crack radii. Hence, crack face friction is the main contributor to the initiation of the secondary surface cracks.

5.3.2 Influence of crack geometry

5.3.2.1 Crack length

To determine critical crack size, the size effect is addressed in the following discussion. The crack size is important for predicting rolling element fatigue damage.

The fatigue life of cracked ceramic balls can be evaluated according to the crack size. Generally speaking, the size of a surface ring crack can be described using the radius and arc length of the crack. The subsurface geometry of the crack is very hard to obtain and as a result the crack length is normally not known before testing. The influence of changes in crack length on the stresses is discussed as follows.

To compare the effect of the crack length, the calculations are conducted at the fixed crack radius and arc length. The gap between the crack faces is assumed to be zero. The maximum contact pressure p_0 is assigned to a value of 5.58GPa and applied to the calculations. The crack size and contact conditions are listed in table 5.2.

Table 5.2 Crack geometry and calculation conditions

Case No	Contact stress (GPa)	Crack position d (mm)	f	f_c	Crack geometry			
					R (mm)	l (mm)	ϕ_0 (degree)	S
2-1	5.58	0.0468	-0.1	0	0.21	0.03 to 0.098	45	20

Figure 5.9 shows the distribution of the maximum principal stress (tensile stress) at the contact circle. The calculated results indicate that the maximum principal stress is a function of the angle θ and reaches the maximum value at $\theta = 90^0$. The high tensile stresses are developed when the value of the angle θ falls in the approximate range 30^o to 150^o.

In figure 5.10, the comparison of the maximum principal stress at $\theta = 90^o$ is shown. It can be seen that the maximum tensile stress significantly increases as the crack length increases. When the length of the crack is small, e.g. $l = 0.03$ mm, the tensile stress is not high enough to generate the secondary surface cracks. The required tensile stress is not reached until the crack length exceeds a certain value. It is also interesting to note that the tensile stress reaches a maximum value at a certain length and is not able to increase further. The experimental results indicate that the

large length crack displays shorter fatigue life than the small length cracks. The numerical prediction is consistent with the experimental observations.

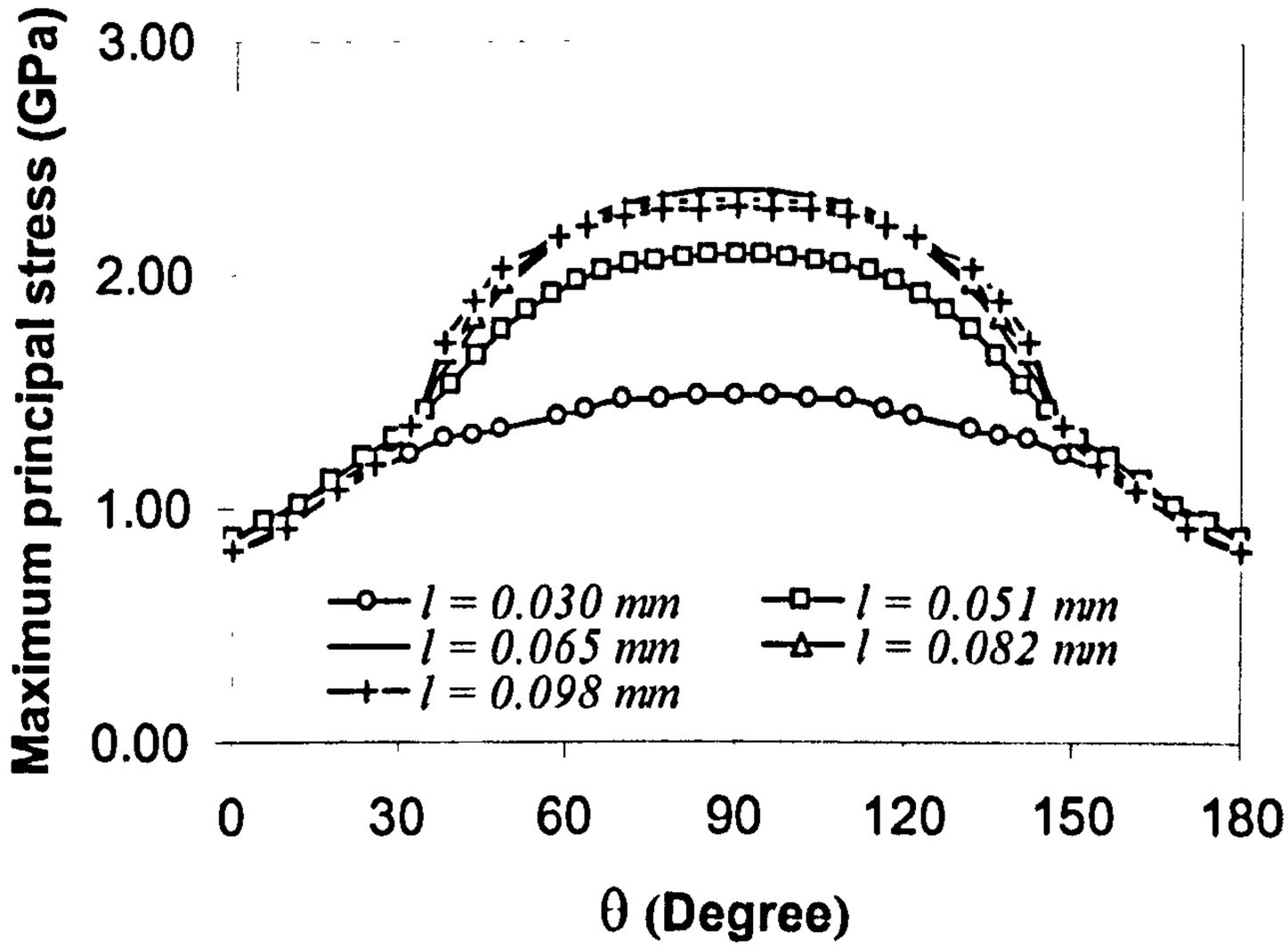

Figure 5.9 Maximum principal stresses along the contact circle (Case 2-1)

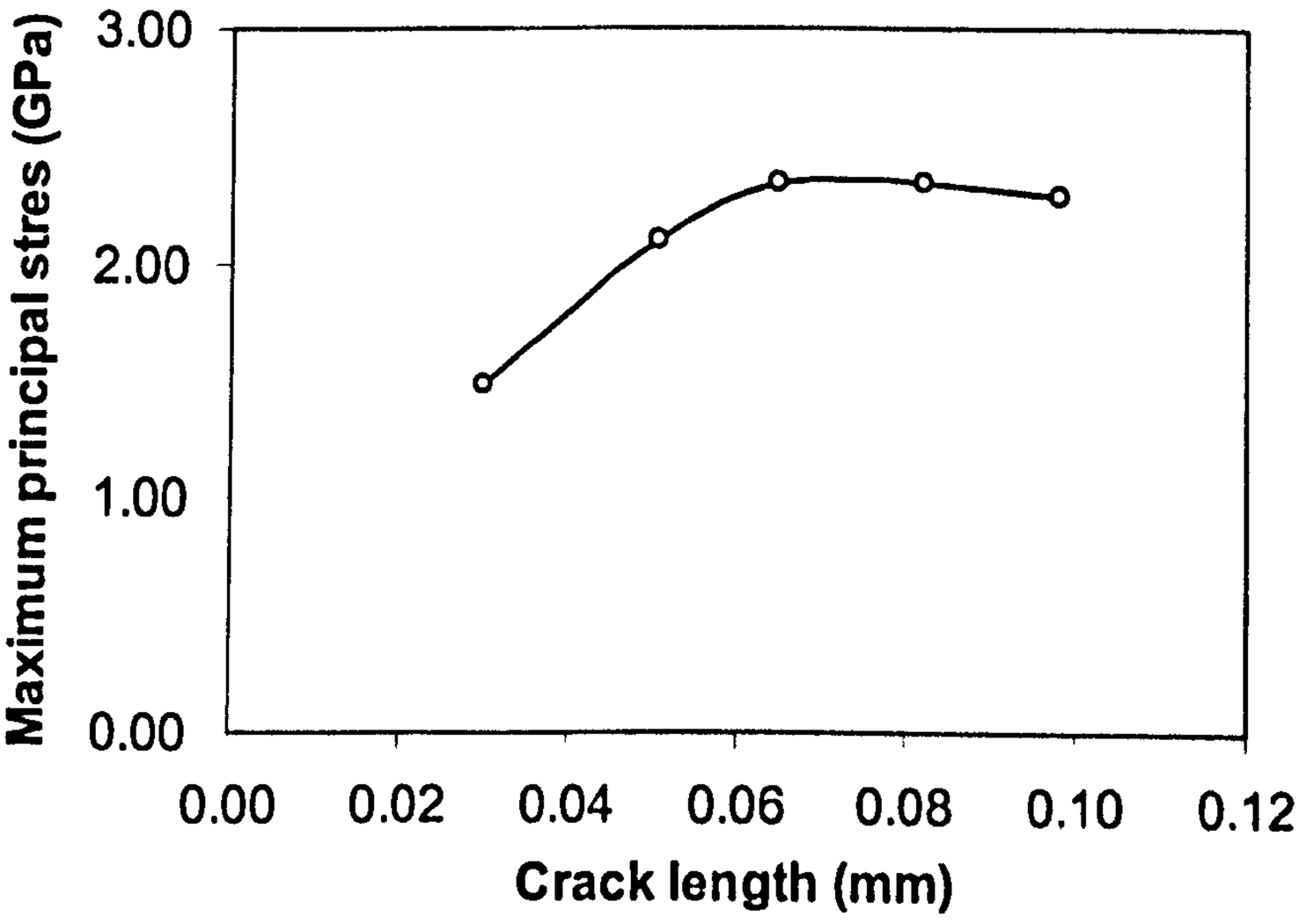

Figure 5.10 Maximum principal stresses against crack length (Case 2-1)

5.3.2.2 Arc length

The influence of the arc length is now investigated. The crack length and radius are fixed in order to compare the effect of the crack arc length. The maximum contact pressure p_0 is 5.58 GPa. Two groups of the cracks are selected to compare the arc length effect. In group one, the crack radius and length are 0.21mm and 0.051mm, respectively. Three lengths of the arc are computed. In group two, the crack radius and length are 0.38 and 0.082 mm, respectively. Two lengths of arc are selected. Detailed conditions are listed in table 5.3.

Table 5.3 Crack geometry and calculation conditions

Case No	Contact stress (GPa)	Crack position d (mm)	f	f_c	Crack geometry			
					R (mm)	l (mm)	ϕ_0 (degree)	S
3-1	5.58	0.0468	-0.1	0	0.21	0.051	35 45 55	20
3-2	5.58	0.0468	-0.05	0	0.38	0.082	24 35	20

The calculation results indicate that there is practically no effect on the maximum tensile stress ($\theta = 90^\circ$) as shown in figure 5.11. However, the distribution of the maximum principal stresses along the contact circle is changed as the arc length changes. The calculated results imply that the formation of the secondary cracks is easier when the arc length is larger.

In figure 5.12, the crack radius is 0.38mm and the arc length is 0.318 mm ($\phi_0 = 24^\circ$) and 0.464 mm ($\phi_0 = 35^\circ$). Again, there is no significant change for these two arc lengths. There is a considerable drop near the 35° and 145° thresholds for the larger arc length since the crack is bigger than the contact circle.

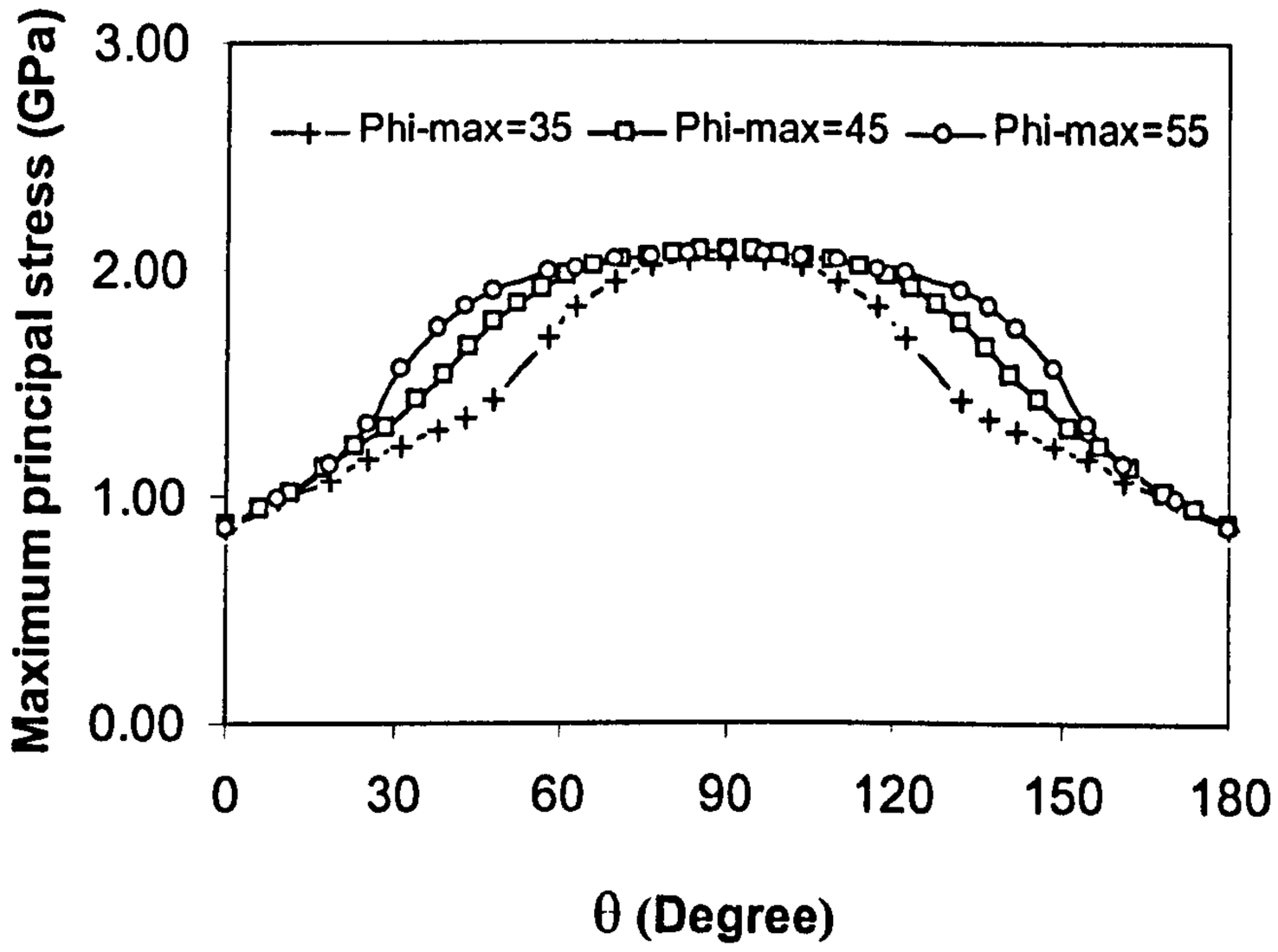

Figure 5.11 Comparison of the maximum principal stresses (Case 3-1)

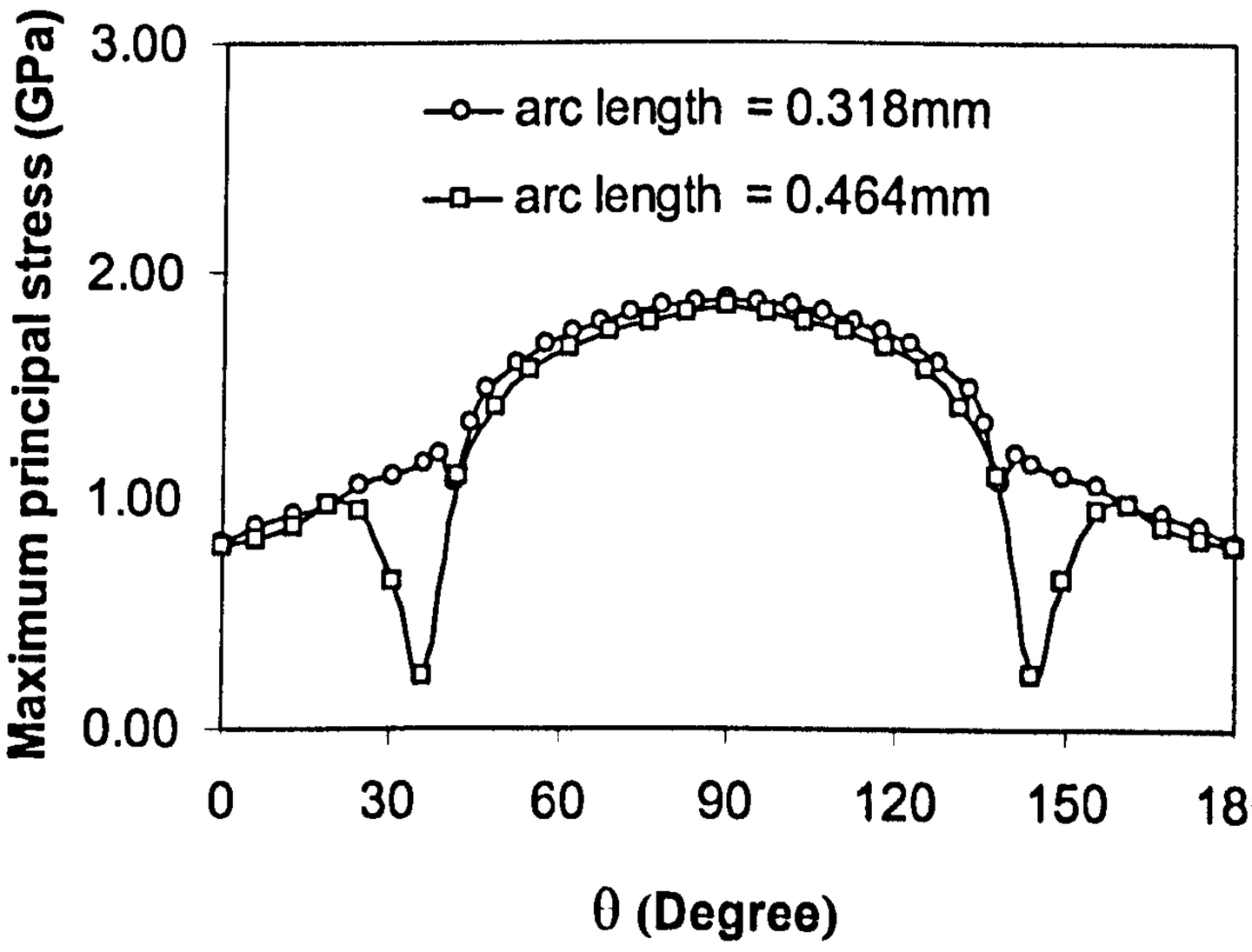

Figure 5.12 Comparison of the maximum principal stress (Case 3-2)

5.3.2.3 Crack radius

The influence of crack radius is also investigated. To compare the influence of the crack radius, the calculations are conducted at fixed crack length and arc length. Two types of crack are chosen to simulate both natural and artificial cracks. For artificial cracks, the arc length is 0.464mm while the crack radius is assumed to be 0.32, 0.38 and 0.44mm. For natural cracks, the arc length is 0.318mm while the crack radius is assumed to be 0.21 and 0.38mm, respectively. The maximum contact pressure 5.58GPa is applied to the calculations. Table 5.4 lists detailed calculation conditions.

Table 5.4 Crack geometry and calculation conditions

Case No	Contact stress (GPa)	Crack position *d*(mm)	*f*	f_c	Crack geometry			
					R (mm)	*l* (mm)	*Arc length* (mm)	*S*
4-1	5.58	0.0468	-0.05	0	0.32 0.38 0.44	0.082	0.464	20
4-2	5.58	0.0468	-0.05	0	0.21 0.38	0.082	0.318	20

Figure 5.13 shows the distribution of the maximum principal stresses (tensile stress) at the contact circle. The calculated results indicate that the maximum principal stress is a function of the angle θ and reaches the maximum value at θ = 90°. The high tensile stresses are developed when the value of the angle θ falls between 40° and 140°. The crack radius has a slight effect on the maximum tensile stresses when the cracks take the same length. Note that the calculated result here is made under the assumption that the crack length is the same.

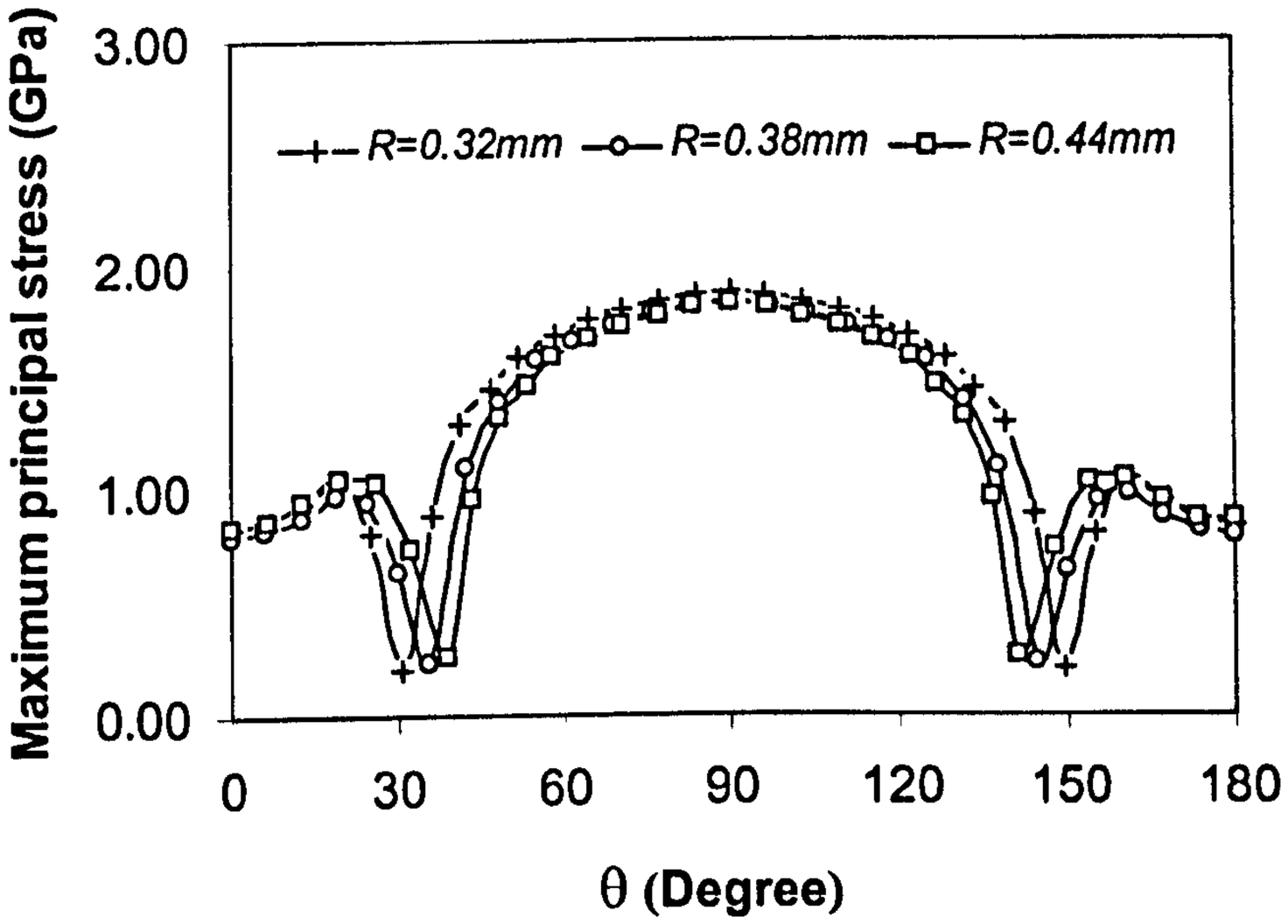

Figure 5.13 Influence of crack radius on maximum principal stress (Case4-1)

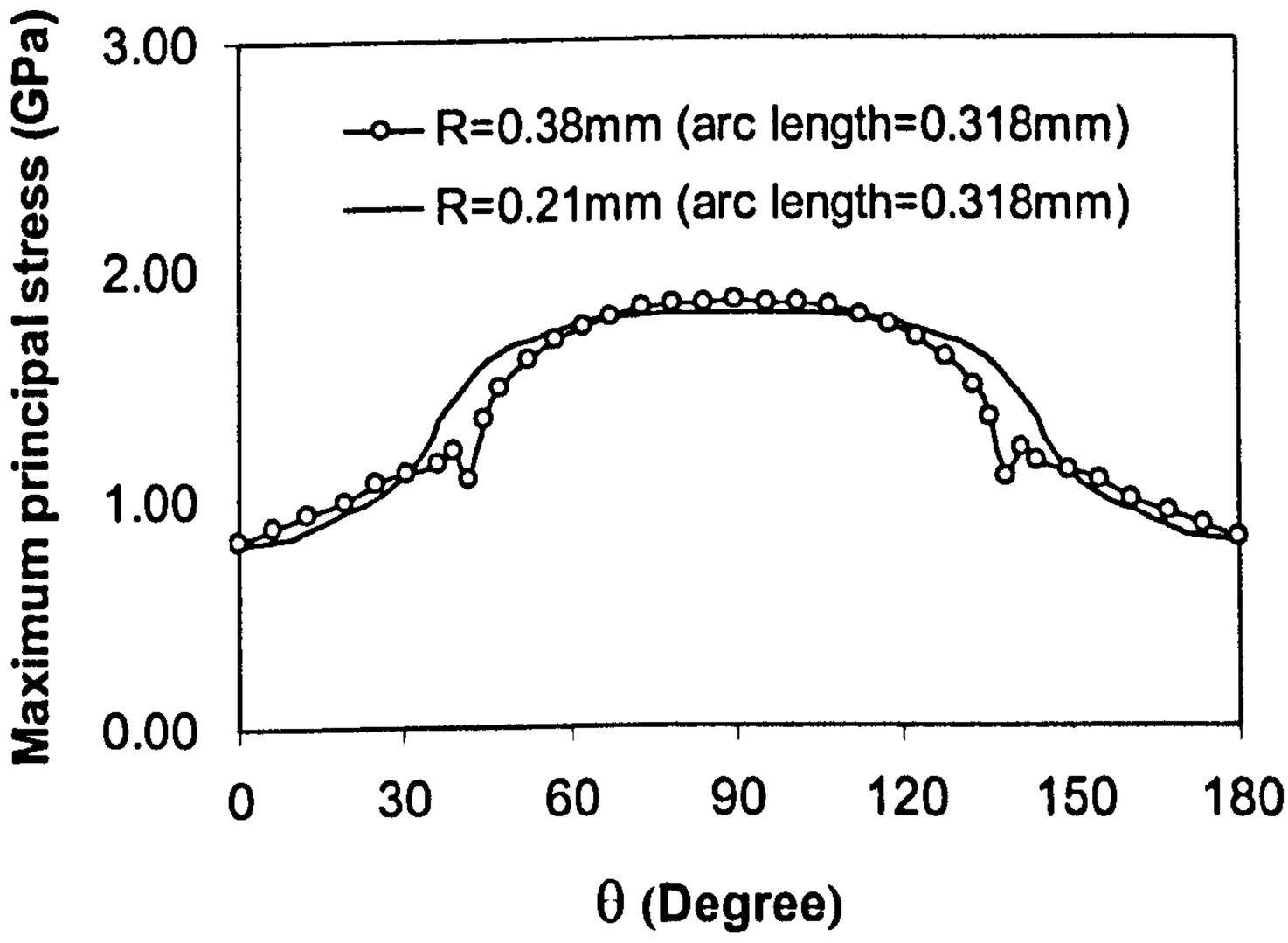

Figure 5.14 Comparison of maximum principal stresses (Case 4-2)

Figure 5.14 shows the comparison of the maximum principal stresses for two different sizes of crack radius. Again, the results indicate that the maximum

principal stress is a function of the angle θ and reaches the maximum value at θ = 90°. The changes in the crack radius do not significantly affect the maximum tensile stresses when the cracks take the same length.

As discussed in the previous section, the larger crack radius always corresponded with a larger crack length and the tensile stress significantly increases with the increase of the crack length. Therefore, fatigue life decreases with the increase of the crack radius due to the large crack length.

5.3.2.4 Crack angle

The influence of crack angle on surface stresses is computed in the following discussion. The calculations are conducted at fixed crack length and arc length. Referring to figure 5.2, the crack angle is related to the shape factor of the crack. The calculations indicate that when S = 50, 20, 10 and 5, the corresponding angles of the crack are 34.4°, 51.1°, 64.° and 75.9° respectively. These angles are selected to investigate their effect. The crack dimensions and loading conditions are listed in table 5.5.

Table 5.5 Crack geometry and calculation conditions

Case No	Contact stress (GPa)	Crack position d(mm)	f	f_c	Crack geometry			
					R (mm)	l (mm)	ϕ_0 (degree)	S
5-1	5.58	0.0468	-0.05	0	0.21	0.051	45	5 10 20 50

Figure 5.15 illustrates the distribution of the maximum principal stresses along the contact circle. Apparently, the maximum principal stresses are sensitive to the change of the crack angle. At the beginning, the magnitude of the stresses increases as the crack angle increases. When the crack angle reaches a critical value the maximum principal stress reaches the maximum value. And then, the maximum

principal stress decreases as the crack angle increases as shown in figure 5.16.

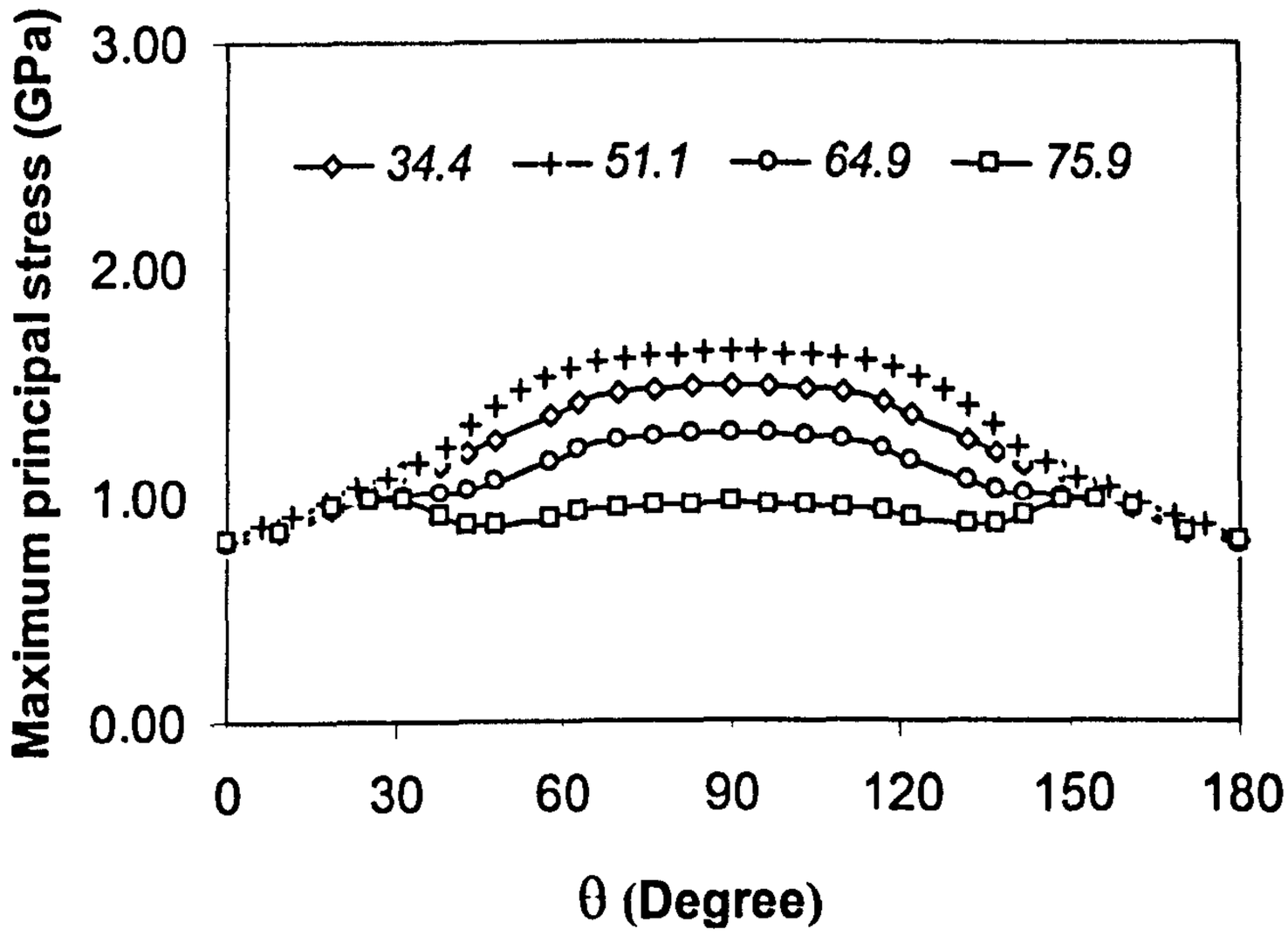

Figure 5.15 Influence of crack angle on maximum principal stresses

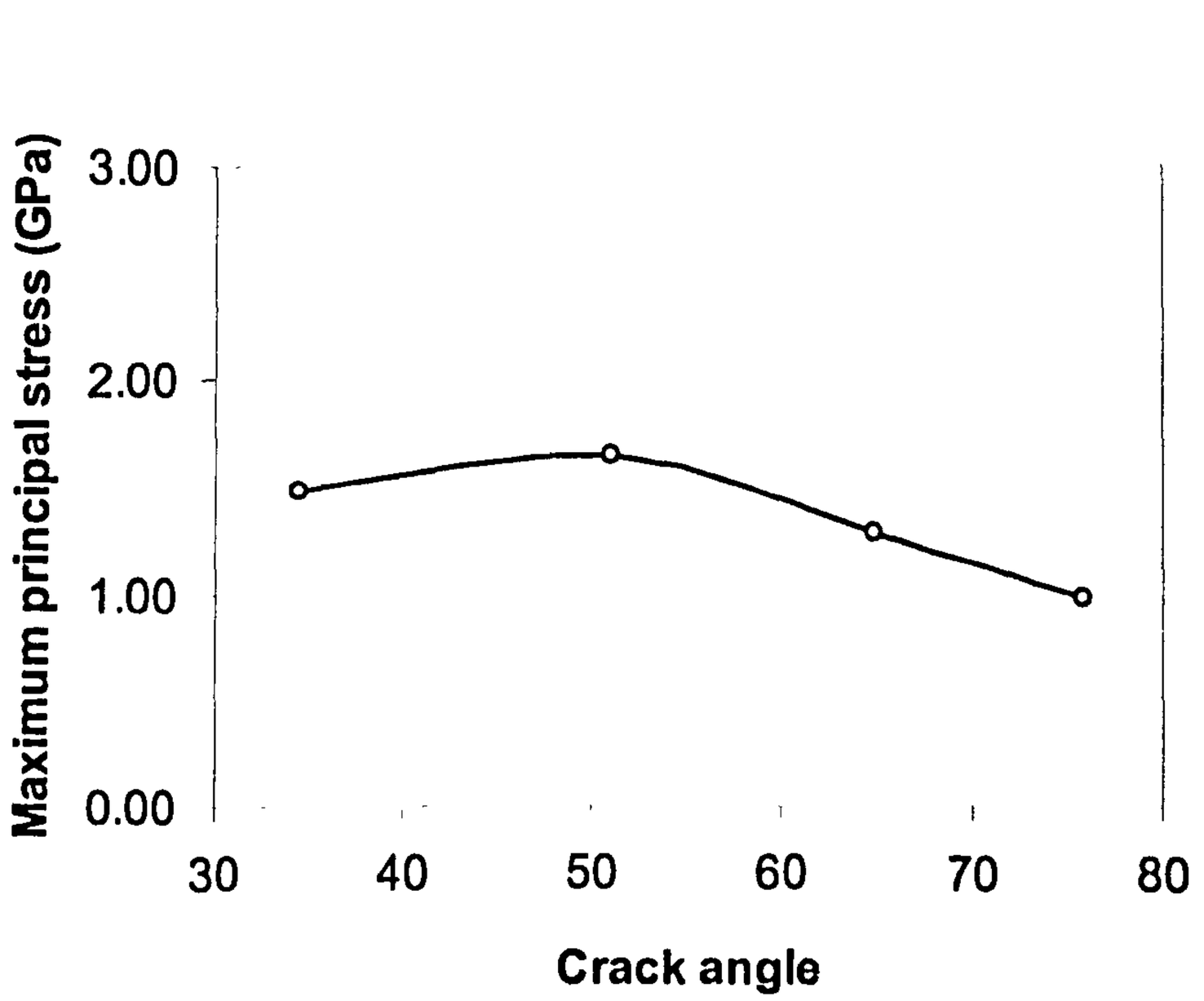

Figure 5.16 Influence of crack angle on maximum principal stress at $0 = 90^{o}$

5.3.3 Influence of crack gaps

Experimental observations show that the larger the crack radius the easier the crack is to locate. Generally speaking, larger radius cracks lead to larger gaps between crack faces. As a result of this, the crack is more easily seen. The effect of the crack gap on the surface stresses is now investigated. In this study, the crack dimension is listed in table 5.6.

Table 5.6 Crack geometry and calculation conditions

Case No	Contact stress (GPa)	Crack position d (mm)	f	f_c	Crack geometry			
					R (mm)	l (mm)	ϕ_0 (degree)	S
6-1	5.58	0.0468	-0.05	0	0.21	0.051	45	20
6-2	5.58	0.0468	-0.05	0	0.32	0.082	42	20

Figure 5.17 shows the distribution of the maximum principal stresses at the surface along the contact circle. This is a small crack (natural crack range). There are hardly any changes in the magnitude and distribution of stresses along the contact circle for any gap (0, 0.2 and 0.5 microns) when θ is between 0° and 30°, or between 150° and 180°. However, the tensile stresses will increase significantly as the crack gap increases when θ is between 30° and 150°. When the gap is 0.2μm, the tensile stress will reach 1.8GPa. The secondary surface cracks will be initiated due to this high tensile stress exceeding Hertz fracture strength. The experimental observation confirmed that the crack gap increased as the test proceeded (see Chapter 4) and the crack gap is possible to reach 0.2μm due to the wear of the contacting crack faces.

At this stage the situation when the crack size is in the artificial size range (case 6-2, figure 5.18) was considered. Like natural cracks, there are hardly any changes in the magnitude and distribution of stresses along the contact circle for any gap (0, 0.1, 0.3 and 0.5 micron) when θ is between 0° and 30°, or between 150° and 180°. However, the tensile stresses will increase significantly as the crack gap increases when θ is between 30° and 150°.

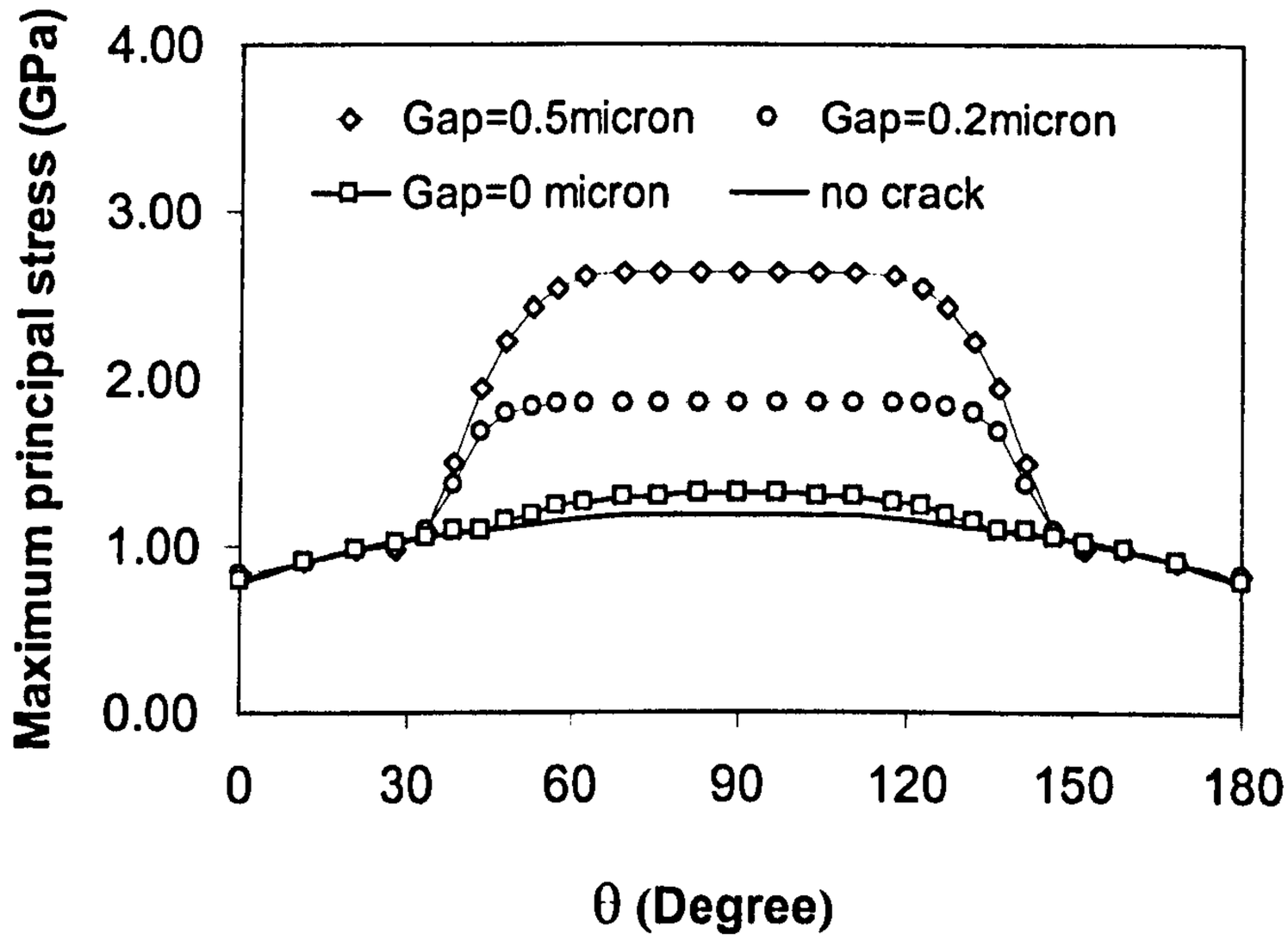

Figure 5.17 Influence of crack gap on maximum principal stresses (case 6-1)

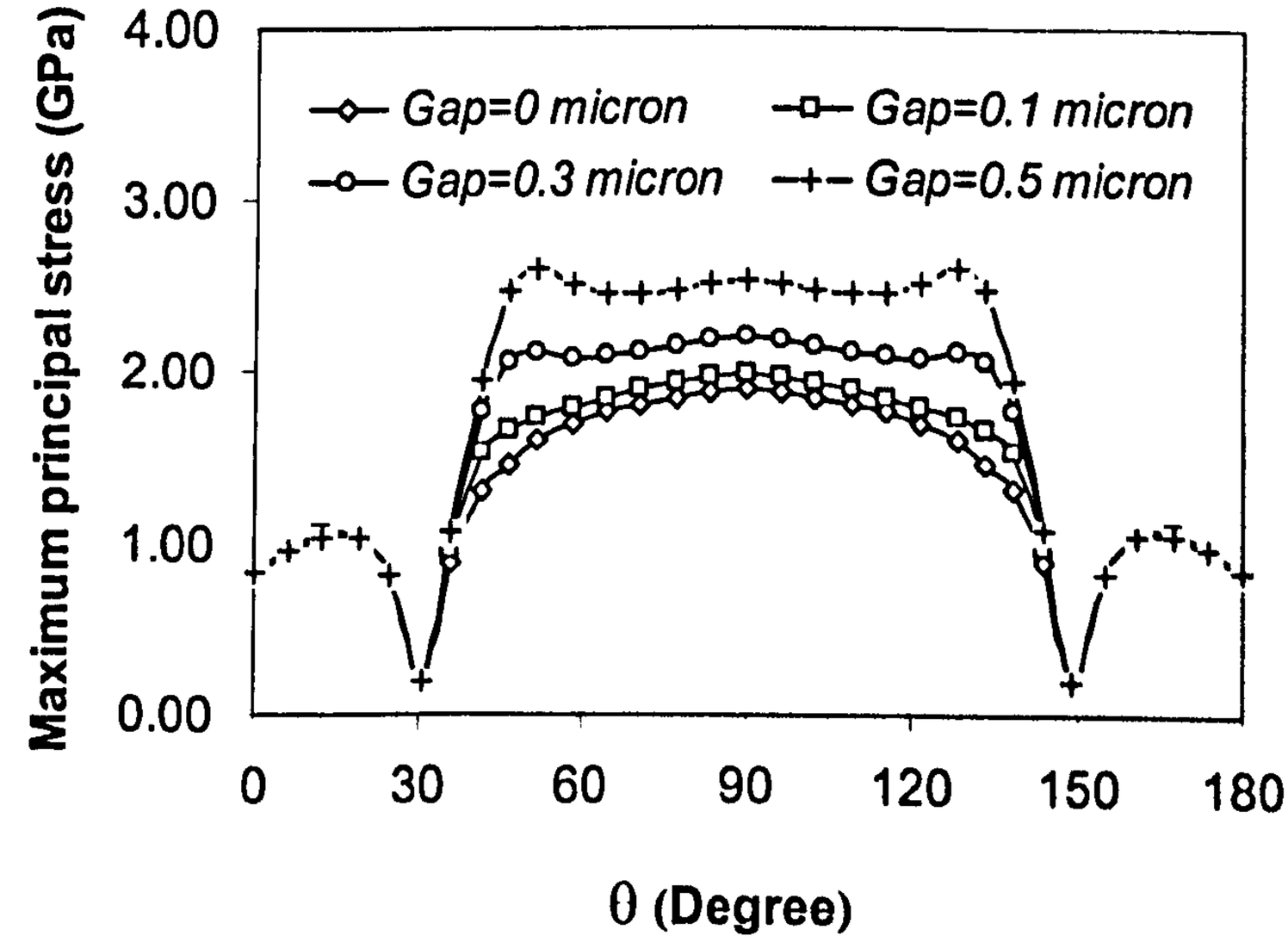

Figure 5.18 Influence of crack gap on maximum principal stresses (case 6-2)

In terms of the numerical calculation, the tensile stress around the contact circle increases considerably with the increase of the gap between the crack faces. When the crack gap reaches a certain value, this tensile stress will exceed Hertz fracture strength. As a result, the secondary cracks are initiated around that circle. This is why for brittle material secondary surface cracks are circular and are of a similar radius to the contact circle. As soon as the secondary surface cracks are initiated, they will grow towards materials to form a crack network, and therefore a spall is generated. The numerical analysis here provides the fundamental basis for an explanation of why the secondary surface cracks almost always is of the characteristic of the partial circle.

5.3.4 Influence of contact stress

The influence of the contact stresses on rolling contact fatigue failure is discussed in the following section. It will be focused on one size of crack to study the effect of the contact load on the surface stresses. For the purpose of the calculation, the gap between the crack faces is assumed to be zero. The detailed calculation conditions are listed in table 5.7.

Table 5.7 Crack geometry and calculation conditions

Case No	Contact stress (GPa)	Crack position d (mm)	f	f_c	Crack geometry			
					R (mm)	l (mm)	ϕ_0 (degree)	S
7-1	4.0 4.4 5.03 5.58 6.63	0.0468	-0.05	0 to 0.9	0.21	0.098	45	20

Figure 5.19 illustrates the relationship between the maximum principal stress and contact stresses for the various crack face friction coefficients. Apparently, the maximum tensile stresses increase as the contact stress increases. The effect of crack

face friction on the stresses is also shown in figure 5.19. Increasing crack face friction decreases tensile stresses on the surfaces. When the contact stress is less than 4 GPa it is very hard to form secondary surface cracks unless the crack gap reaches a critical value. This is very consistent with the experimental observation.

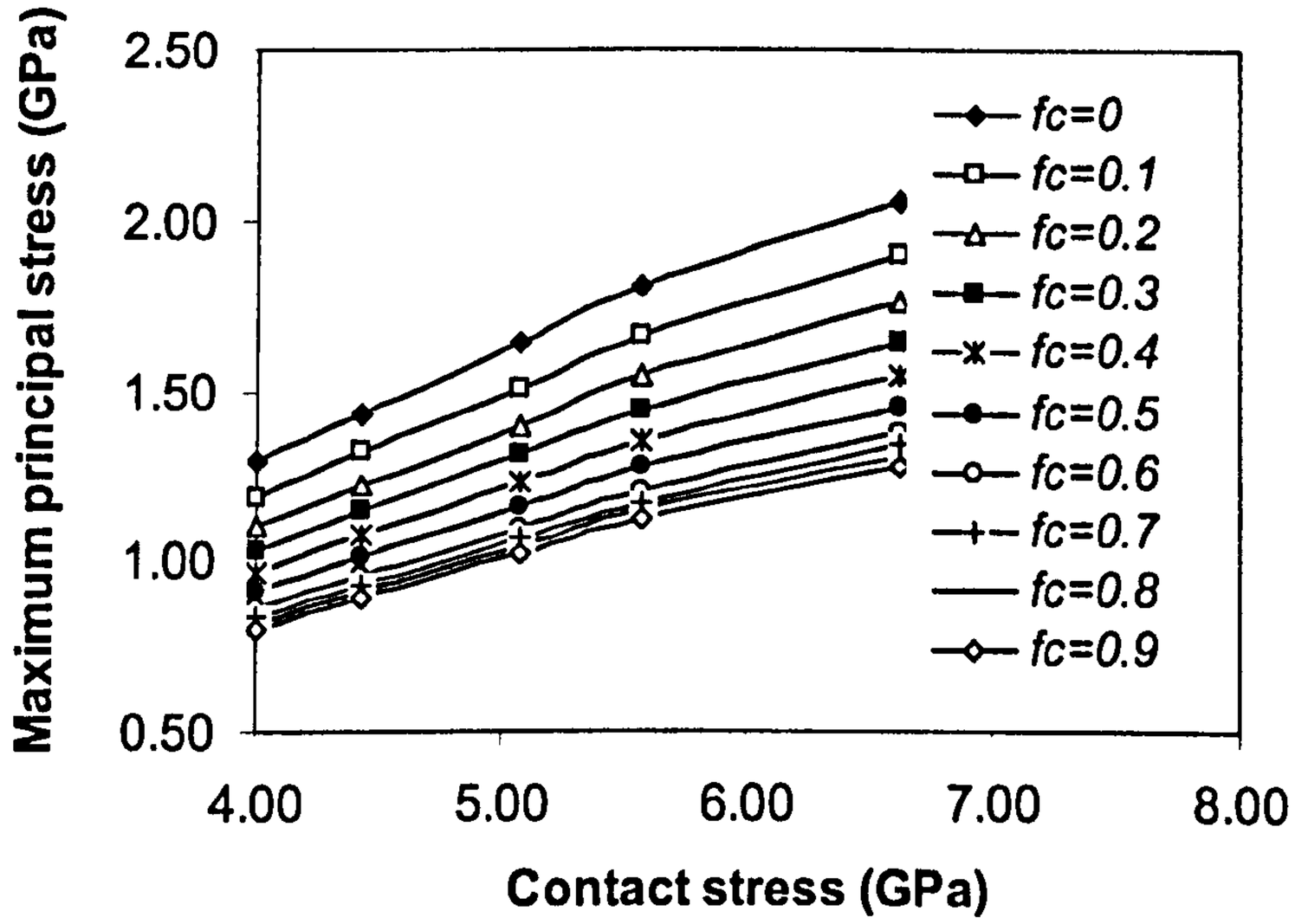

Figure 5.19 Maximum principal stress against contact stress for various crack face coefficients

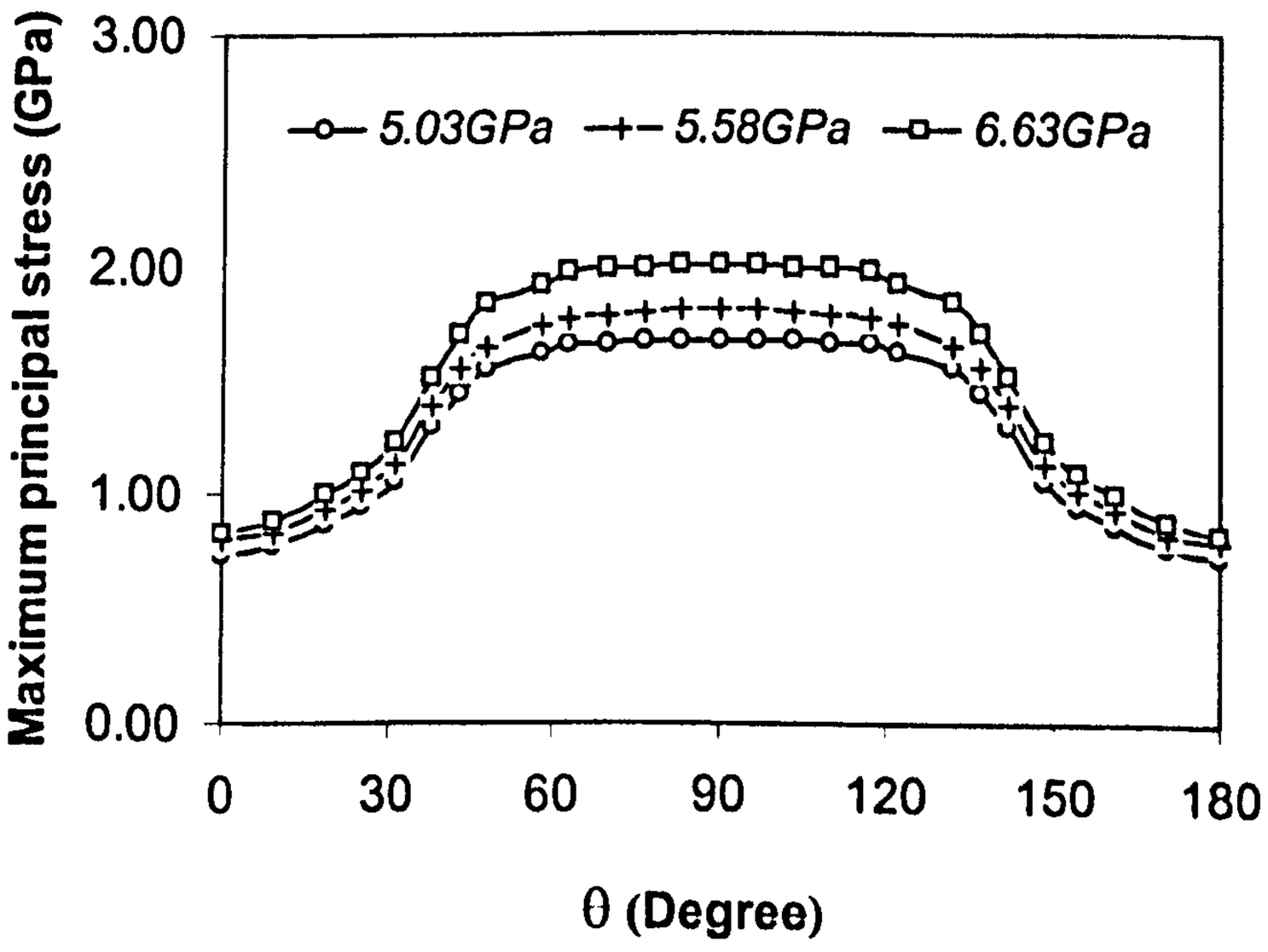

Figure 5.20 Maximum principal stress distribution along the contact circle

In figure 5.20, the calculation results indicated that the maximum principal stress is a function of the angle θ and reaches the maximum value at θ = 90° (x axis). The high tensile stresses are developed at the location of the angle θ in the approximate range 45° to 135°.

5.3.5 Influence of shear traction

The influence of the surface shear traction on the magnitude and distribution of the maximum tensile stresses on the surface is also investigated. Again, the traction coefficient f is utilised to describe the magnitude of the surface shear traction. The bigger the traction coefficient f, the higher the surface shear traction is. The detailed calculation conditions and crack geometry are listed in table 5.8.

Table 5.8 Crack geometry and calculation conditions

Case No	Contact stress (GPa)	Crack position d (mm)	f	f_c	Crack geometry			
					R (mm)	l (mm)	ϕ_0 (degree)	S
8-1	4.0 to 6.63	0.0468	0 to -0.12	0	0.21	0.098	45	20
8-2	5.58	0.0468	-0.05 to 0.05	0	0.32	0.082	42	20

For the maximum contact pressure of 5.58GPa, the calculation result is shown in figure 5.21. The calculated results indicate that the maximum principal stress increases as surface traction increases. The maximum value is attained at the angle $\theta = 90°$. Unlike the stress distribution in figure 5.4, the stress value increases at all the locations along the contact circle from $\theta = 0°$ to $\theta = 180°$. There is a large

increase in the maximum principal stress within the crack region (45^0 to 135^0) and a small increase outside the contact region.

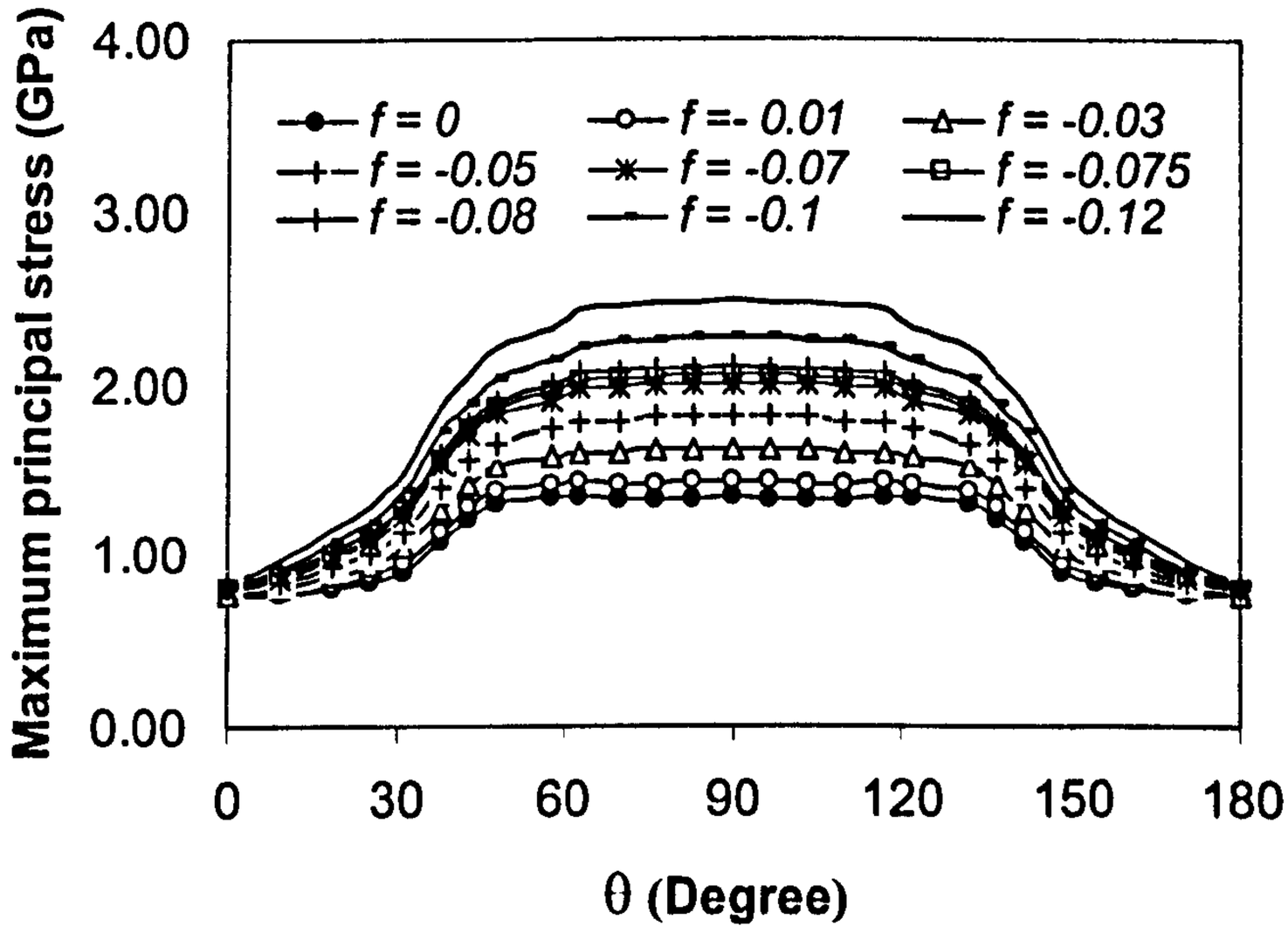

Figure 5.21 Maximum principal stresses along the contact circle for the maximum contact pressure of 5.58GPa (Case 8-1)

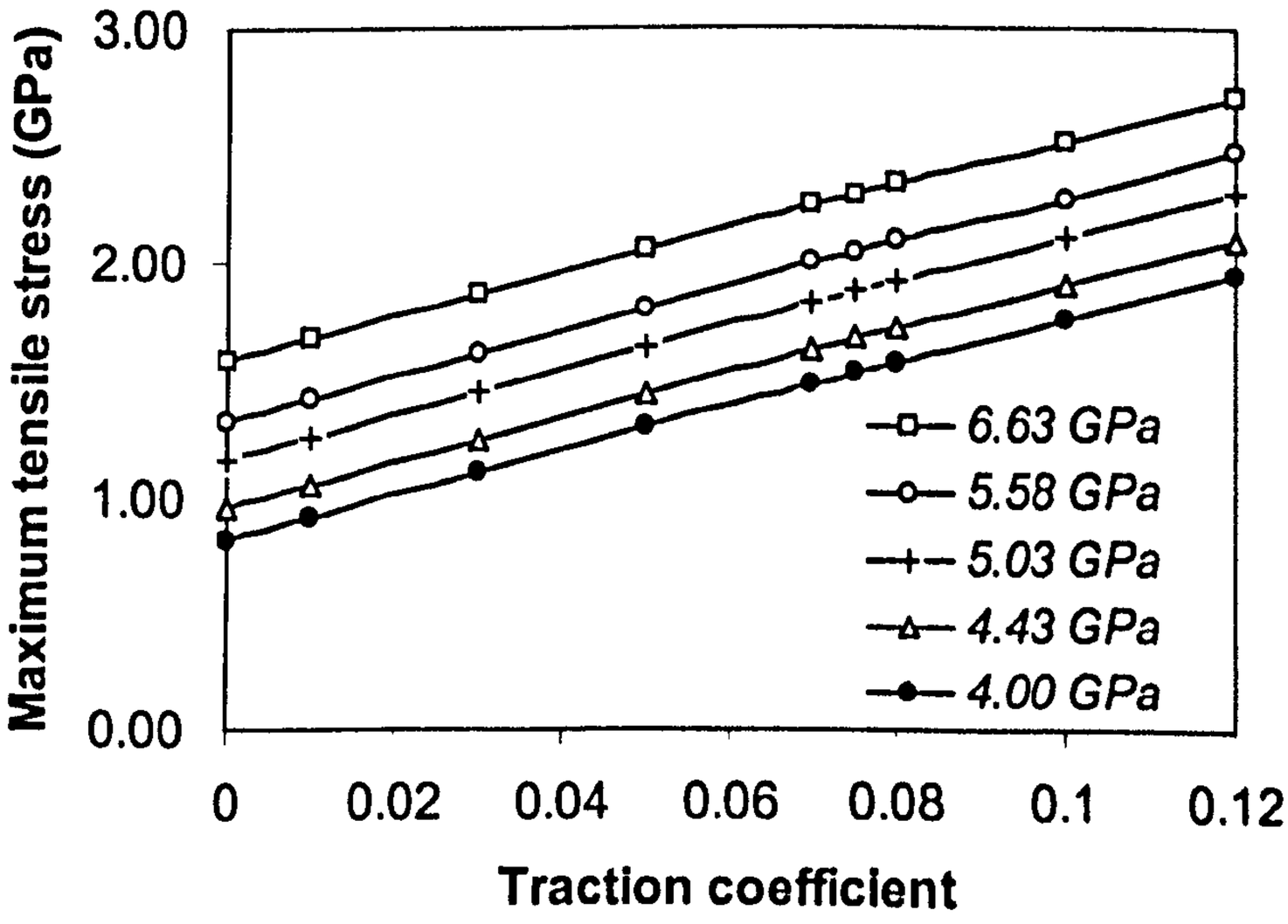

Figure 5.22 Maximum tensile stresses against traction coefficient for $f_c = 0$ and $\theta = 90^0$ (Case 8-1)

Figure 5.22 shows the relationship between the contact pressure, traction coefficient and the maximum tensile stress. As can be seen from figure 5.22, for various contact stresses, the plotted lines are parallel to each other. This diagram is useful to predict whether the secondary surface cracks will form or not. The surface traction has a significant effect on rolling contact fatigue failure. The experimental result for the traction oil is a good example which verifies the numerical prediction.

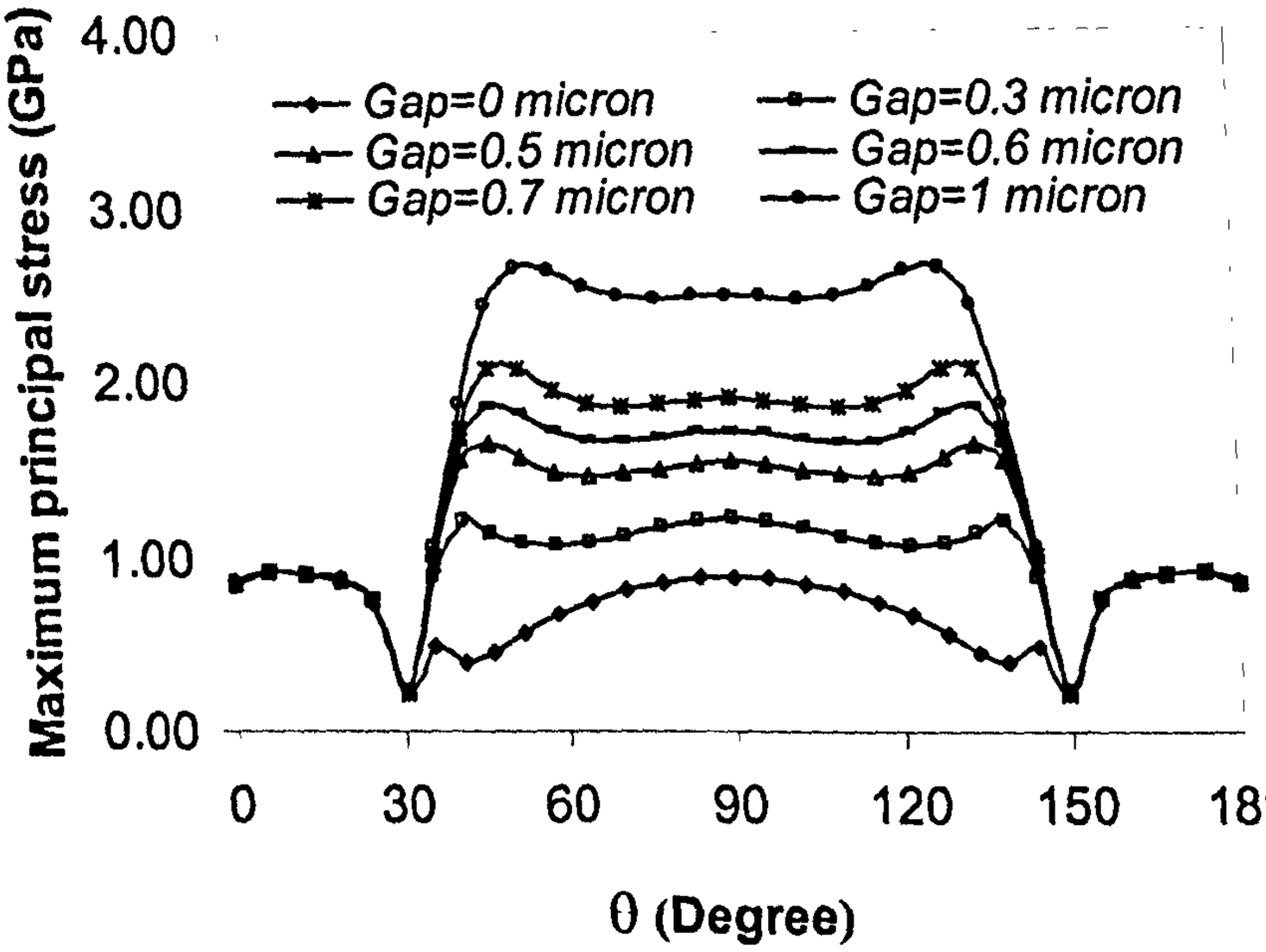

Figure 5.23 Maximum principal stresses at the contact circle (Case 8-2, $f = +0.05$)

The influence of the traction direction on the surface stresses is investigated and the results are shown in figures 5.23 and 5.24. As stated in the previous section, the signs of traction coefficient represent the rolling directions. In Case 8-2, two traction directions are computed.

In figure 5.23, the result from a positive traction coefficient is shown. The result from a negative coefficient has been shown previously (see figure 5.18). As it can be seen that one direction increases the surface tensile stresses while another direction decreases the tensile stresses on the surface. The maximum principal stress along the contact circle will decrease significantly as the traction direction is changed. Therefore, the potential for the formation of the secondary surface cracks will be lower. Consequently, the fatigue life will be influenced by the change of the

rolling direction. However, there is still the possibility of producing the secondary surface cracks if the crack gap exceeds 0.5 μm. Figure 5.24 shows the comparison of the calculated results from two traction directions. The stress contour around the contact region is shown in figure 5.25.

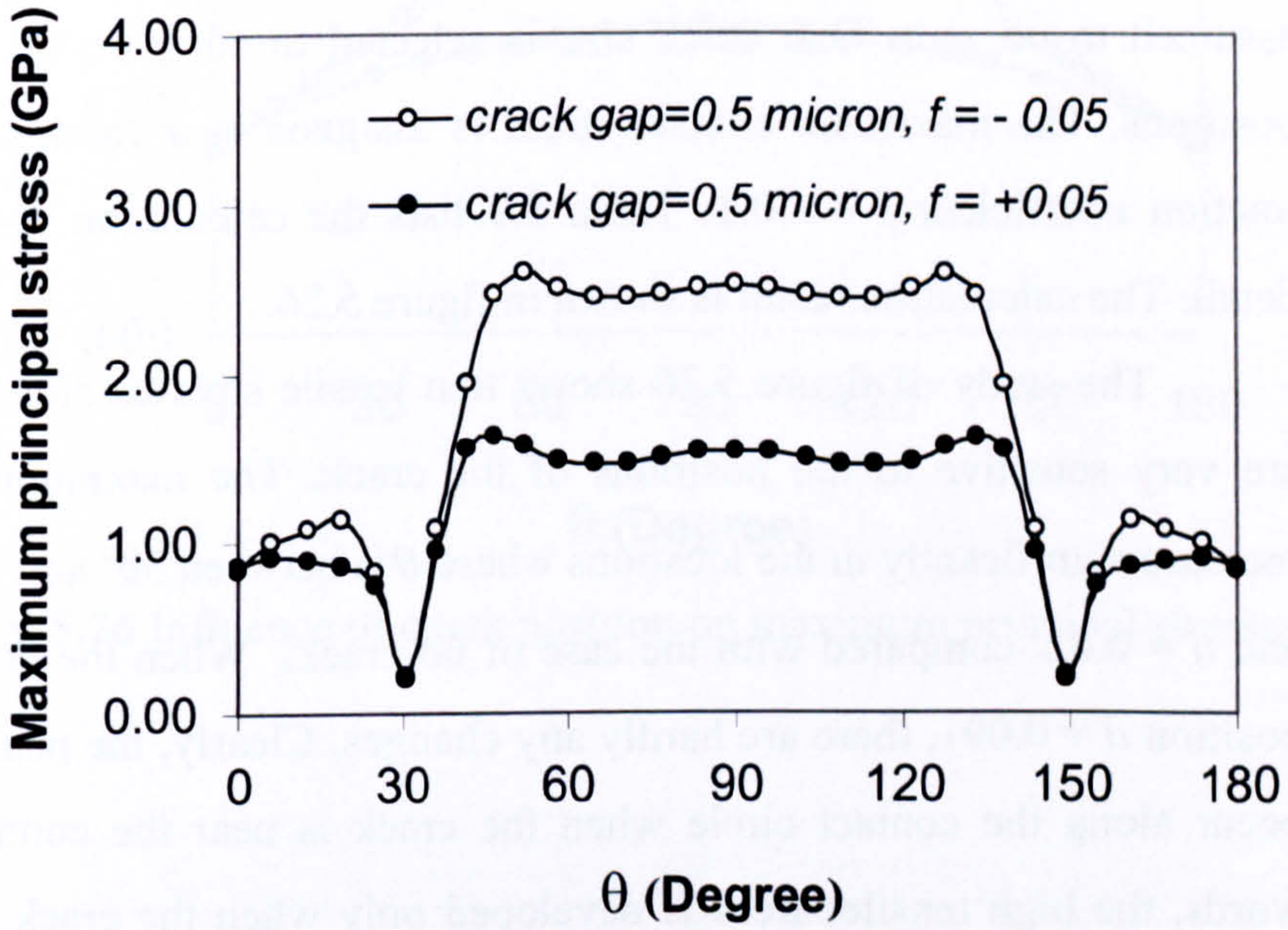

Figure 5.24 Comparison of maximum principal stresses (Case 8-2)

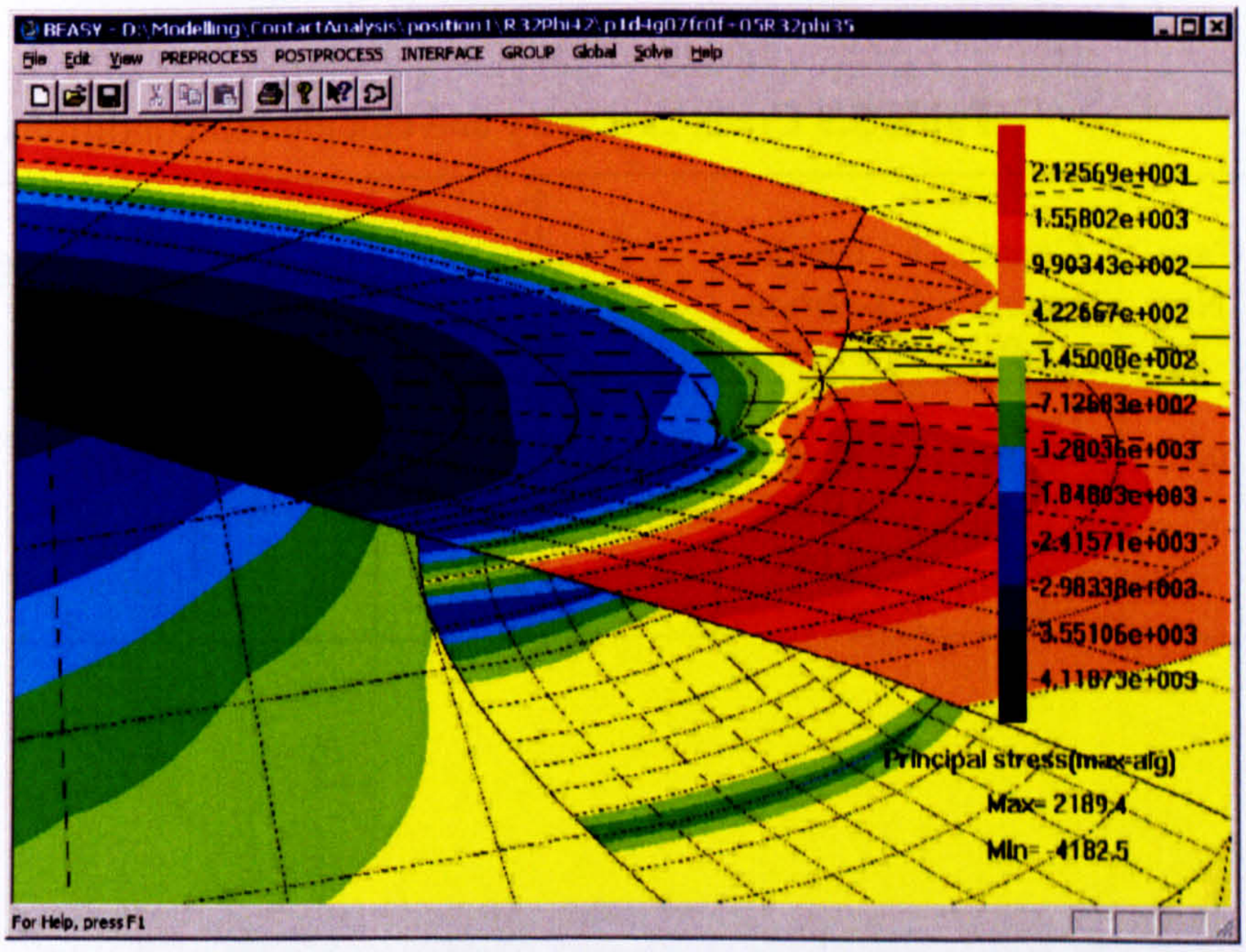

Figure 5.25 Maximum principal stress contours around the contact region (Case 8-2, crack gap = 0.7μm and $f = +0.05$)

5.3.6 Influence of the position of the crack

Contact stresses on the surface are sensitive to the position of the crack. The different positions will create different contact stresses on the surface. The influence of the crack position on the maximum tensile stress along the contact circle is computed. For the purpose of the calculation, the gap between the crack faces is assumed to be zero. One crack size is selected to compare the effect of different positions. The maximum contact stress is assigned to a value of 5.58GPa and the traction coefficient f = - 0.1. Table 5.9 lists the calculation conditions with great detail. The calculation result is shown in figure 5.26.

The study of figure 5.26 shows that tensile stresses along the contact circle are very sensitive to the positions of the crack. The maximum principal stresses increase significantly in the locations where θ is between 30° and 150° for d = 0.0468 and d = 0.02, compared with the case of no crack. When the crack moves into the position d = 0.091, there are hardly any changes. Clearly, the peak stresses will only occur along the contact circle when the crack is near the contact circle. In other words, the high tensile stress is developed only when the crack is near the contact circle. The maximum tensile stress at the edge of the contact area cannot be affected when the crack is located just near the centre.

Table 5.9 Crack geometry and calculation conditions

Case No	Contact stress (GPa)	Crack position d (mm)	f	f_c	Crack geometry			
					R (mm)	l (mm)	ϕ_0 (degree)	S
9-1	5.58	0.02 0.0468 0.091	-0.1	0	0.21	0.051	45	20

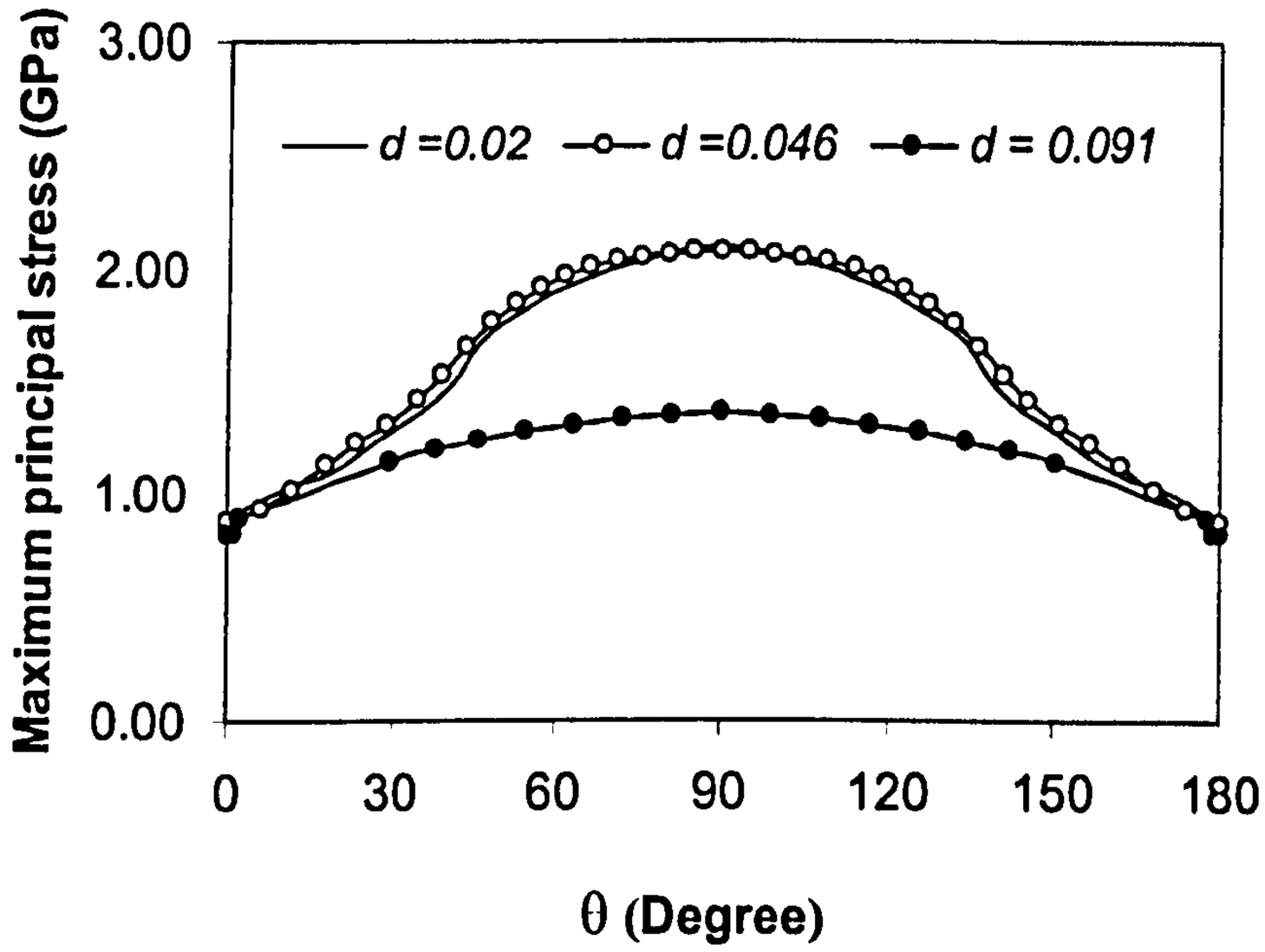

Figure 5.26 Influence of crack position on maximum principal stresses

5.4 STRESS INTENSITY FACTOR ANALYSIS

As discussed in the previous section, the crack front will pass from compressive to tensile stress as the surface loading passes over the crack from right to left, repeatedly. The crack will open its mouth when it is outside the contact circle at $d = 0$ (see figure 5.1). The calculation of the stress intensity factors for the crack being outside the contact circle has been carried out by Wang and Hadfield (2000b, 2004). In their studies, the natural crack was selected in the model and crack growth was analysed using a dual boundary element method. As the calculation method is not valid in the compressive stresses, the stress intensities for the crack being in the contact circle were not computed. Consequently, the numerical calculations were limited because the situations where the crack lies in the contact circle were not taken into account. The results cannot be used in evaluating the crack propagation behaviour when the crack lies in the contact circle as the mode I stress intensity was assumed to propagate crack.

In the following discussion, the calculated results of the stress intensity factors are based on the situations where the crack lies in the contact circle. The stress intensity factor (K_{II}) along the crack front under loading conditions and various geometries is discussed. A standard boundary element method is used in fracture modelling and the extrapolation technique is used to obtain the stress intensity (K_{II}) along the crack front. Compared with the dual boundary element method (Appendix 4), the stress intensity calculation here is complex and time-consuming. The modelling work here is different from the previous studies by Wang and Hadfield (2000b and 2004).

5.4.1 Effect of crack face friction

When the crack is under the compressive stress (within the contact circle), the faces of the crack are in contact, and friction forces therefore act between them. Here, the crack face friction is modelled using Coulomb's law, with a coefficient f_c. The greater the crack face friction coefficient, the higher the crack face friction. The crack dimensions and calculation conditions are listed in table 5.10.

Table 5.10 Crack geometry and calculation conditions

Case No.	Contact stress (GPa)	Crack position d (mm)	f	Crack geometry			
				R (mm)	l (mm)	ϕ_0 (degree)	S
10-1	5.58	0.0468	-0.05	0.21	0.098	45	20
10-2	5.58	0.091	-0.05	0.21	0.03 to 0.098	45	20

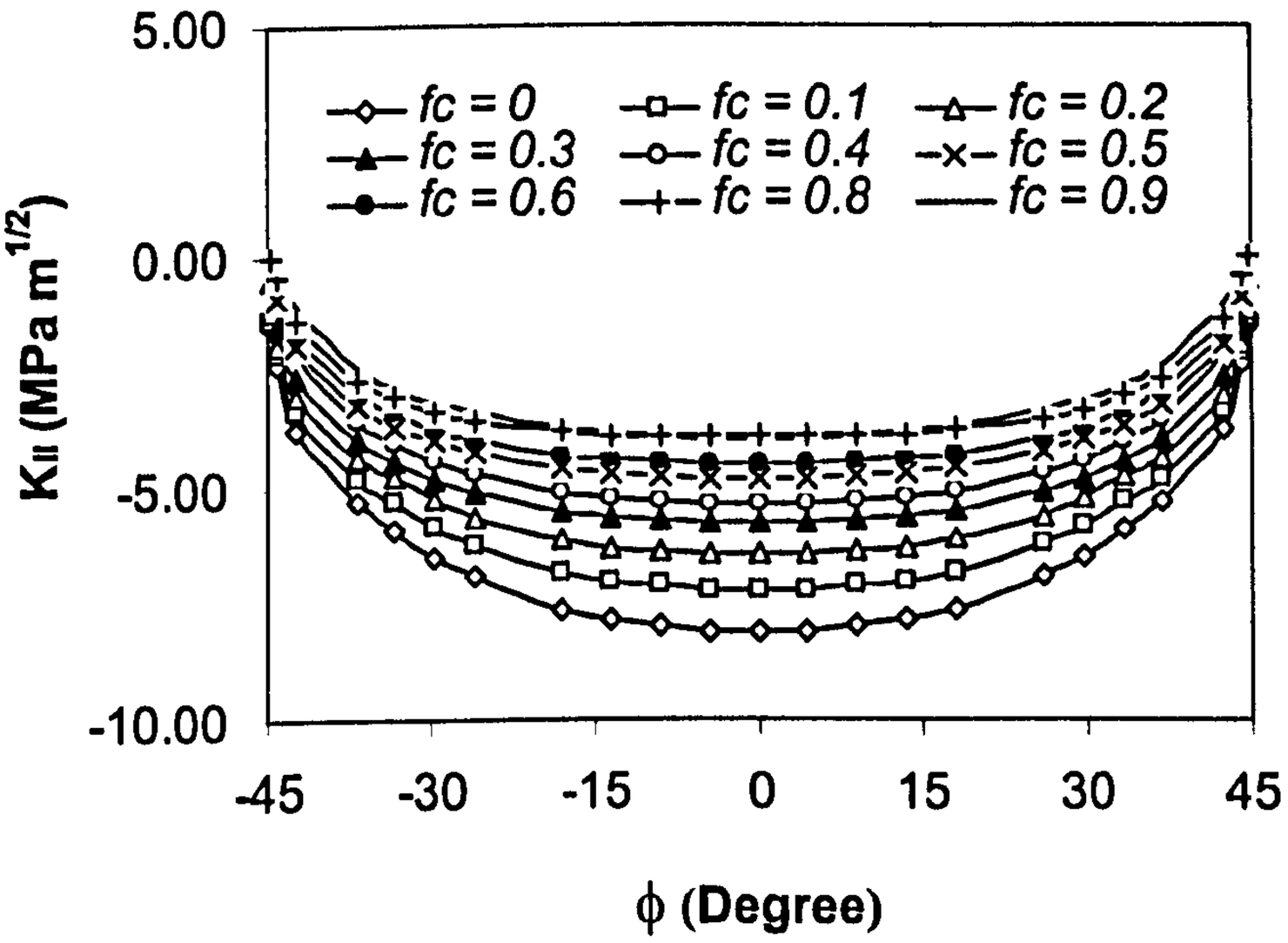

Figure 5.27 Influence of crack face friction coefficient on K_{II} (Case 10-1)

The calculation results indicate that the mode II stress intensity factor (K_{II}) is very sensitive to the change of the crack face friction. Increasing crack face friction significantly decreases the magnitude of the stress intensities (K_{II}) along the crack front. Figure 5.27 shows the calculation results from Case 10-1. Figure 5.28 shows the result from Case 10-2 at l = 0.098 mm. In Case 10-2, the influence of the crack face friction on the stress intensities is larger than that in Case 10-1. This is probably because the crack is fully under the contact circle for Case 10-2 while only half of

the crack is underneath the contact circle in Case 10-1. Figure 5.29 shows the comparison of the stress intensities at $\phi = 0$ for these two cases at $l = 0.098$ mm. It can be seen from figure 5.29 that a large variation rate exists at the beginning for Case 10-2.

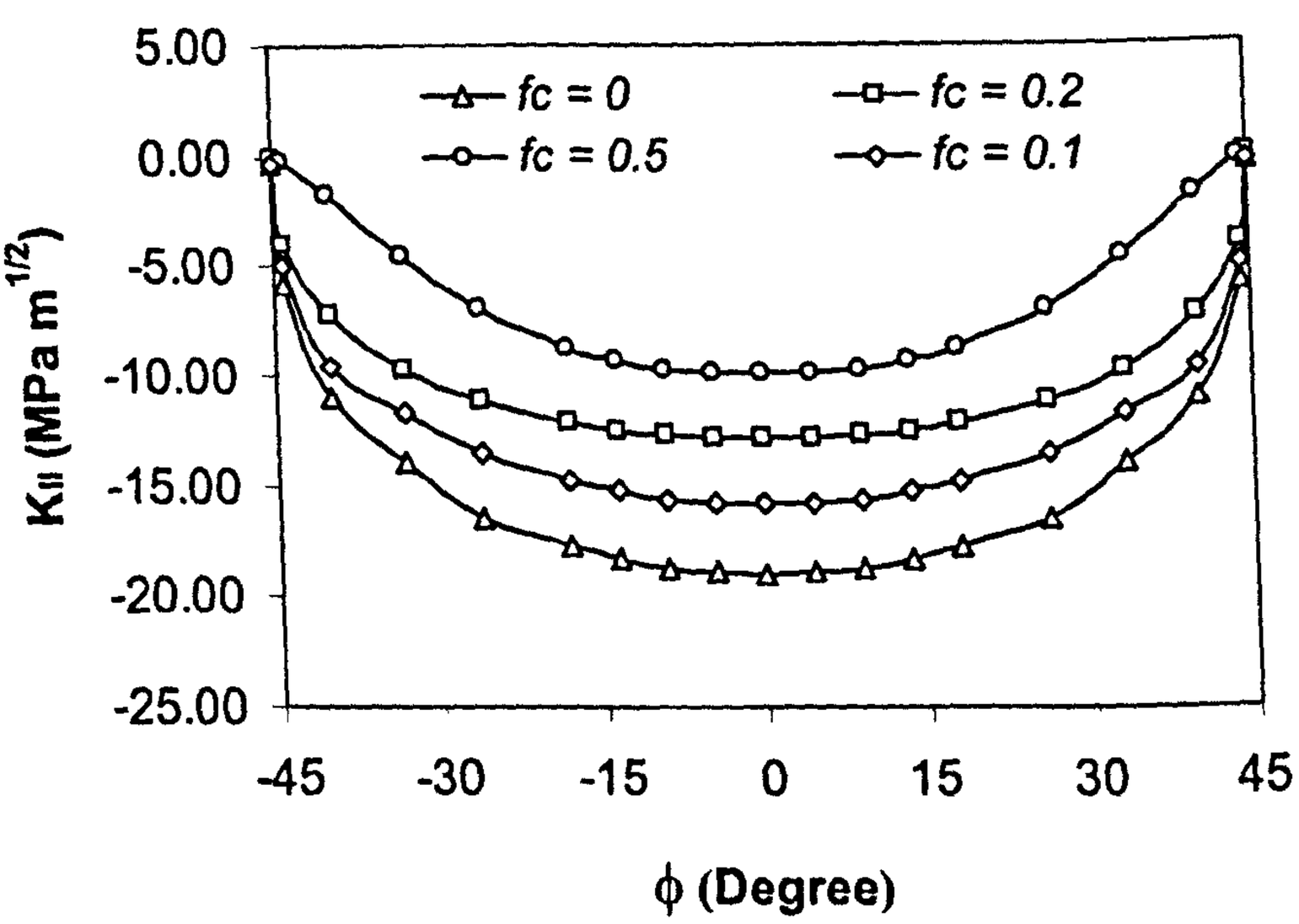

Figure 5.28 Influence of crack face friction coefficient on K_{II}
(Case 10-2, $l = 0.098$ mm)

Figure 5.30 and figure 5.31 show the results when crack lengths are 0.051 and 0.03 mm from Cases 10-2. Since the crack is fully under the contact circle, the effect of crack face friction is very significant. The calculated results show that K_{II} value approaches zero ($f_c = 0.5$) when the crack length is very small (figure 5.31). The crack is not able to propagate with a lack of driving force to crack growth. The numerical analysis predicts that fatigue is hardly to appear if the crack size is very small such as the small natural cracks. This is because in the present analysis the mode II stress intensity is considered to be the crack driven force. Figure 5.32 shows the comparison of K_{II} for different cases.

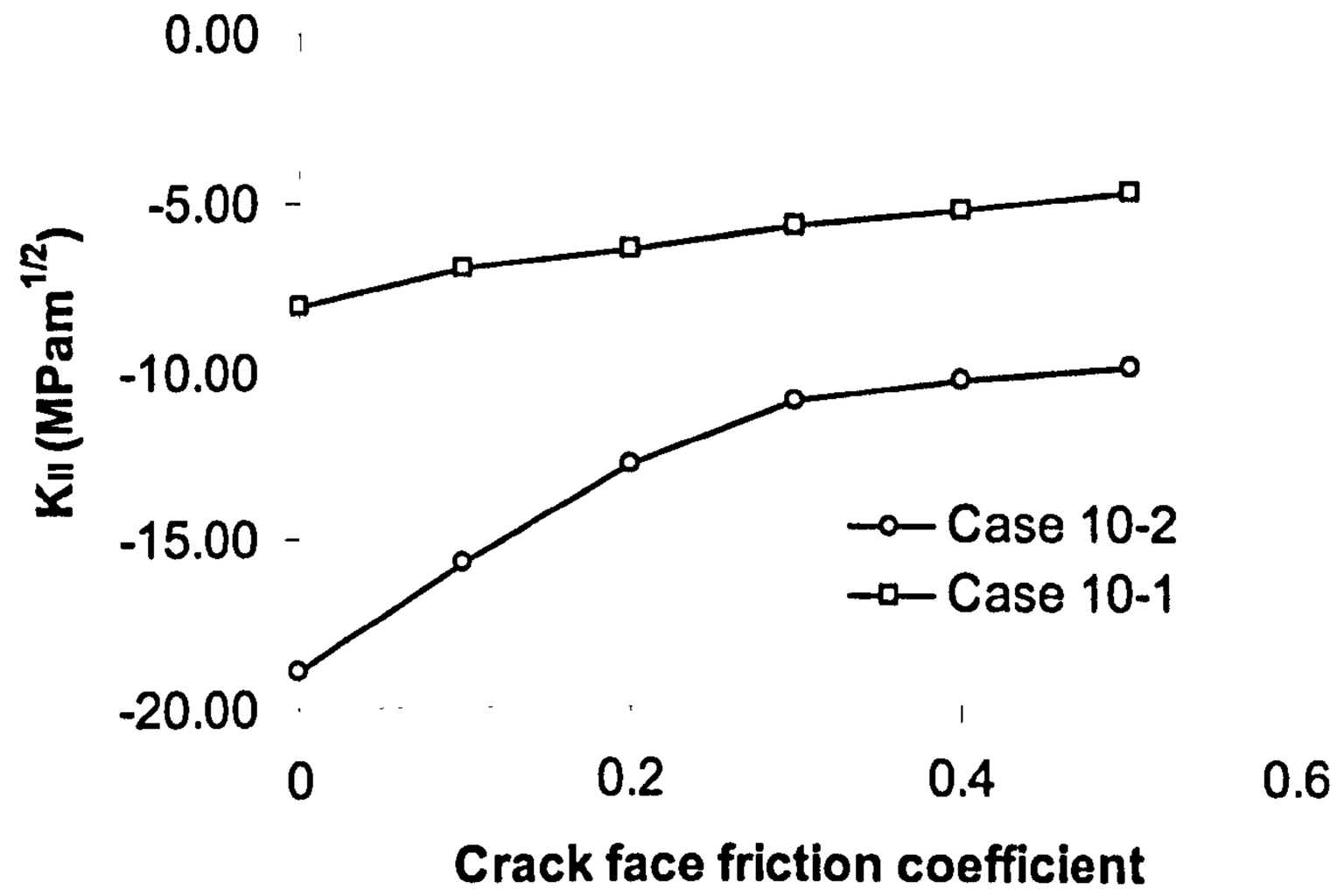

Figure 5.29 Comparison of K_{II} at $\phi = 0°$ for Case 10-1 and Case 10-2 (l = 0.098 mm)

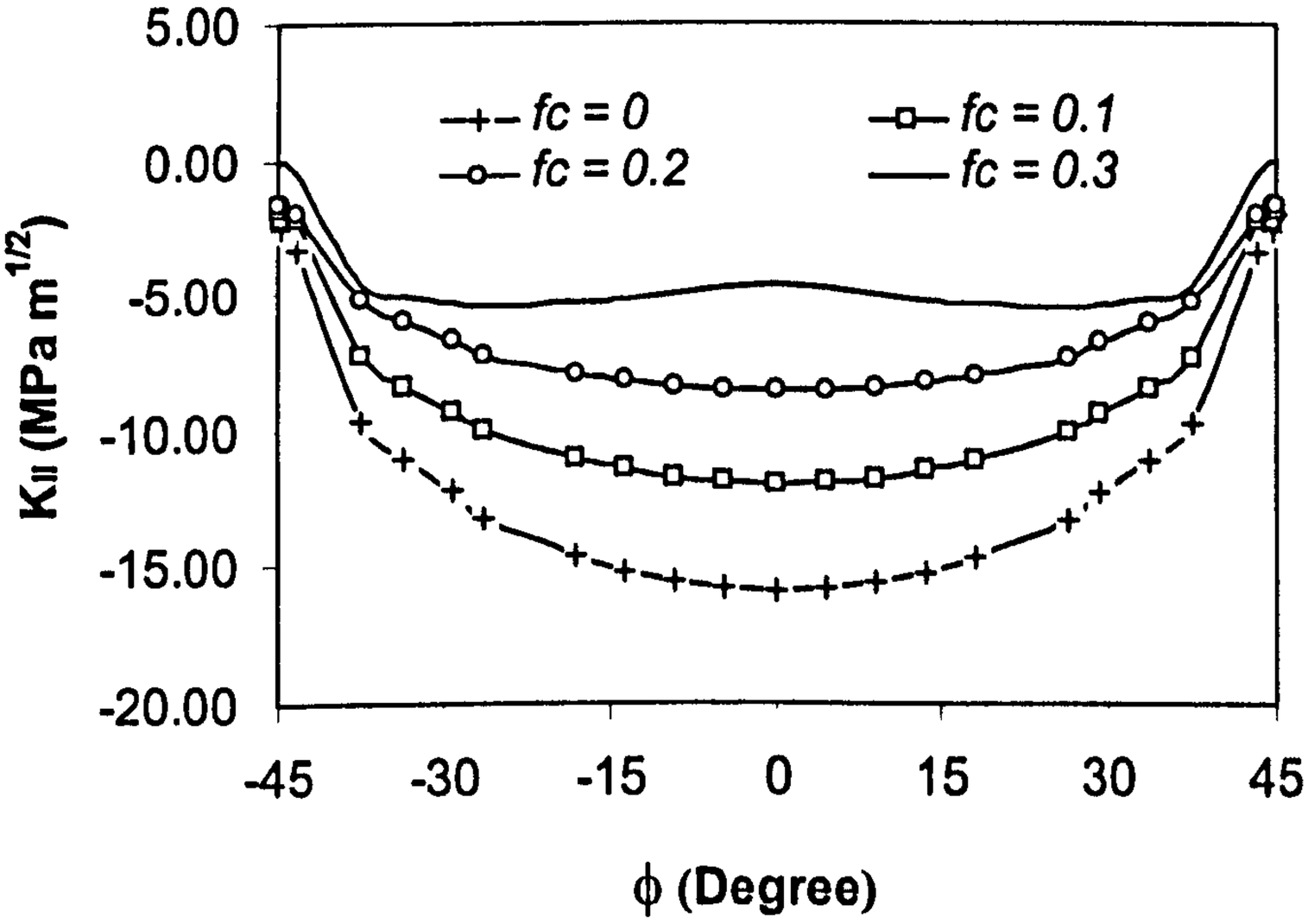

Figure 5.30 Influence of crack face friction coefficient on K_{II} (Case 10-2, l = 0.051 mm)

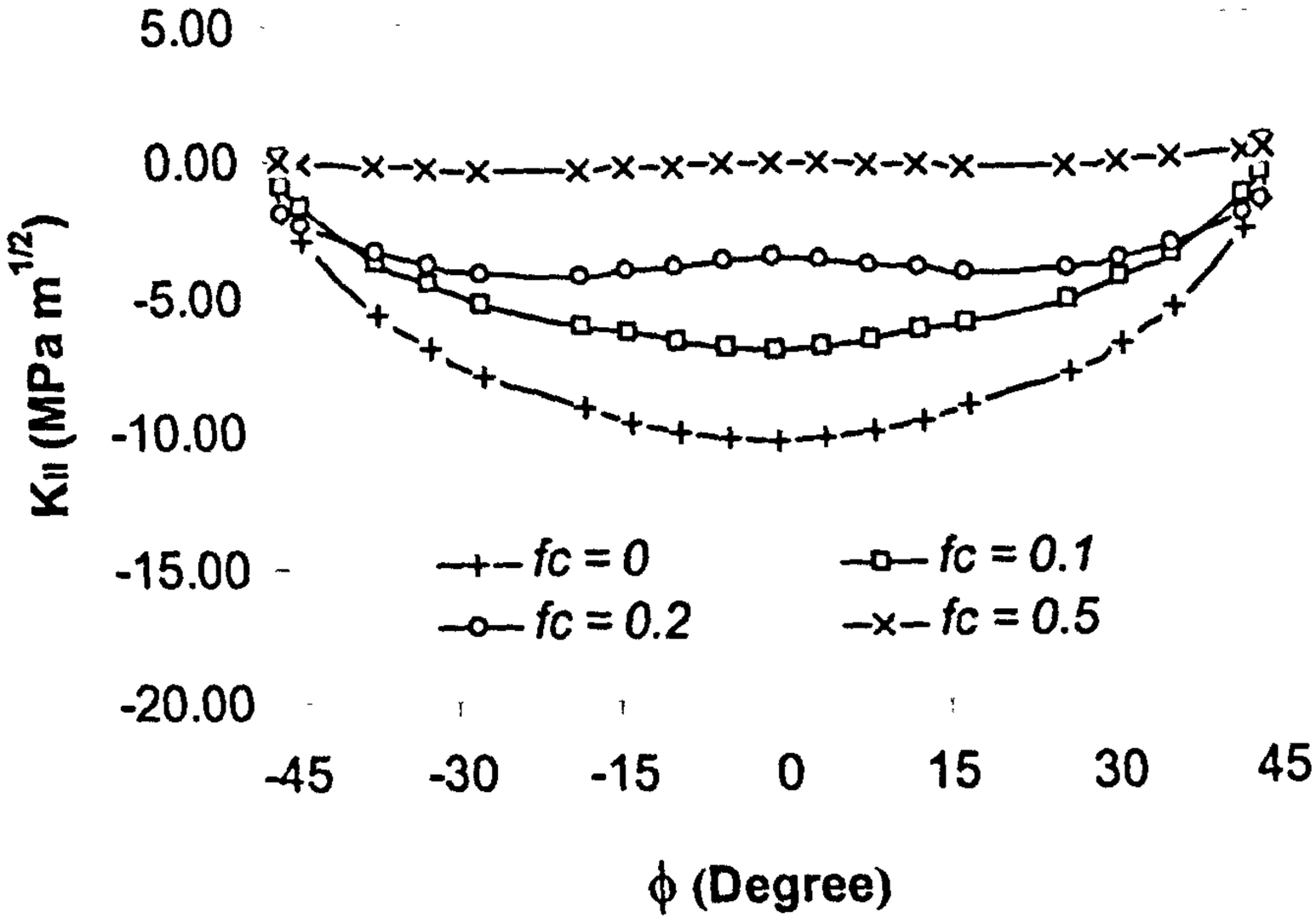

Figure 5.31 Influence of crack face friction coefficient on K_{II} (Case 10-2, l = 0.03mm)

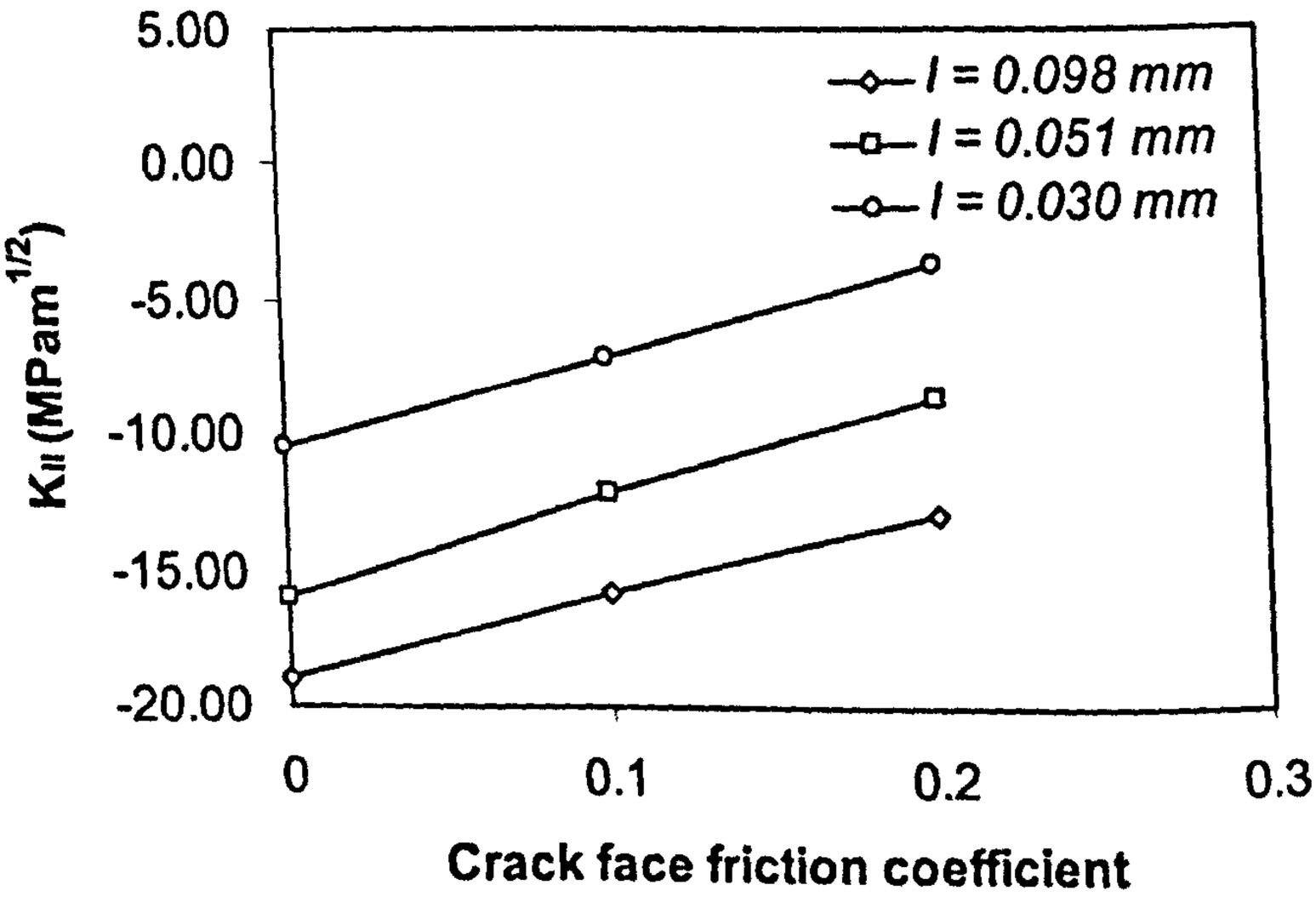

Figure 5.32 Comparison of K_{II} at $\phi = 0^{o}$ for different crack lengths (Case 10-2)

5.4.2 Effect of crack geometry

5.4.2.1 Crack length

The crack size is crucial important in determining rolling contact fatigue life. The following sections examine how a crack length affects the stress intensity factors. The calculation conditions are detailed in table 5.11. Two crack positions are selected to investigate the effect of crack geometry on the stress intensities. The crack gap is assumed to be zero and applied to the calculations.

Table 5.11 Crack geometry and calculation conditions

Case No	Contact stress (GPa)	Crack position d (mm)	f	f_c	Crack geometry			
					R (mm)	l (mm)	ϕ_0 (degree)	S
11-1	5.58	0.091	-0.05	0 to 0.2	0.21	0.03 to 0.098	45	20
11-2	5.58	0.4668	-0.05	0	0.21	0.051 to 0.12	45	20

The calculation result from Case 11-1 is shown in figure 5.33. It can be seen that as the length of the crack increases the stress intensity (absolute value) increases. When the crack length increases to a certain value the increments of stress intensity factor value become small. The results predict that the stress intensity will not increase when the crack reaches a certain length. In other words, the crack will propagate at a constant rate in a stable way. Figure 5.34 illustrates the variation of stress intensity at different crack face friction.

Figures 5.35 and Figure 5.36 show the result from Case 11-2. Since the crack position changes K_{II} becomes positive. Again, the value of K_{II} increases as the crack length increases. The K_{II} value increases quickly at the beginning (shallow crack) and increases slowly as the length grows. The K_{II} will reach a stable level when the length reaches a certain value.

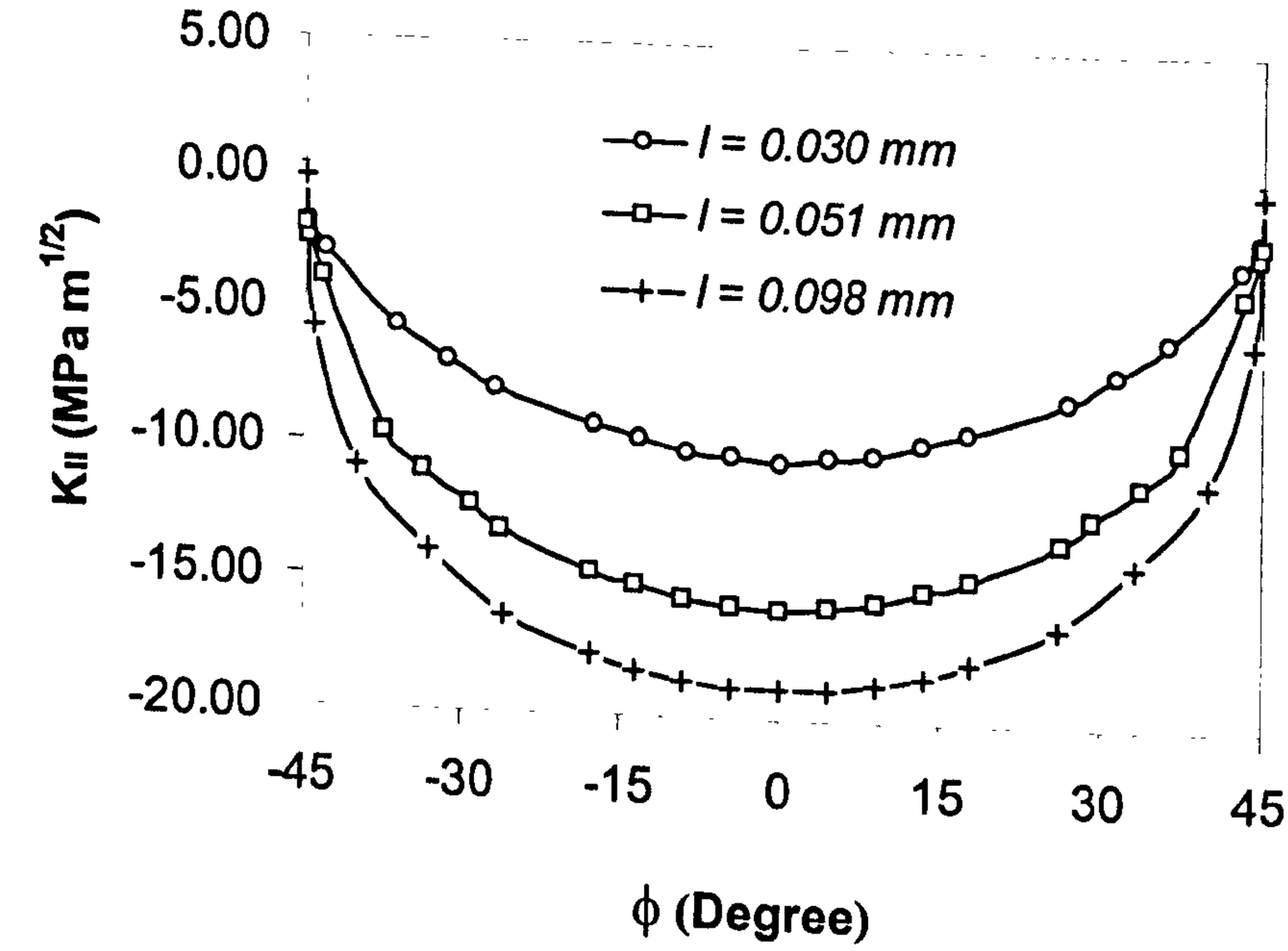

Figure 5.33 Influence of crack length on K_{II} (Case 11-1, $f_c = 0$)

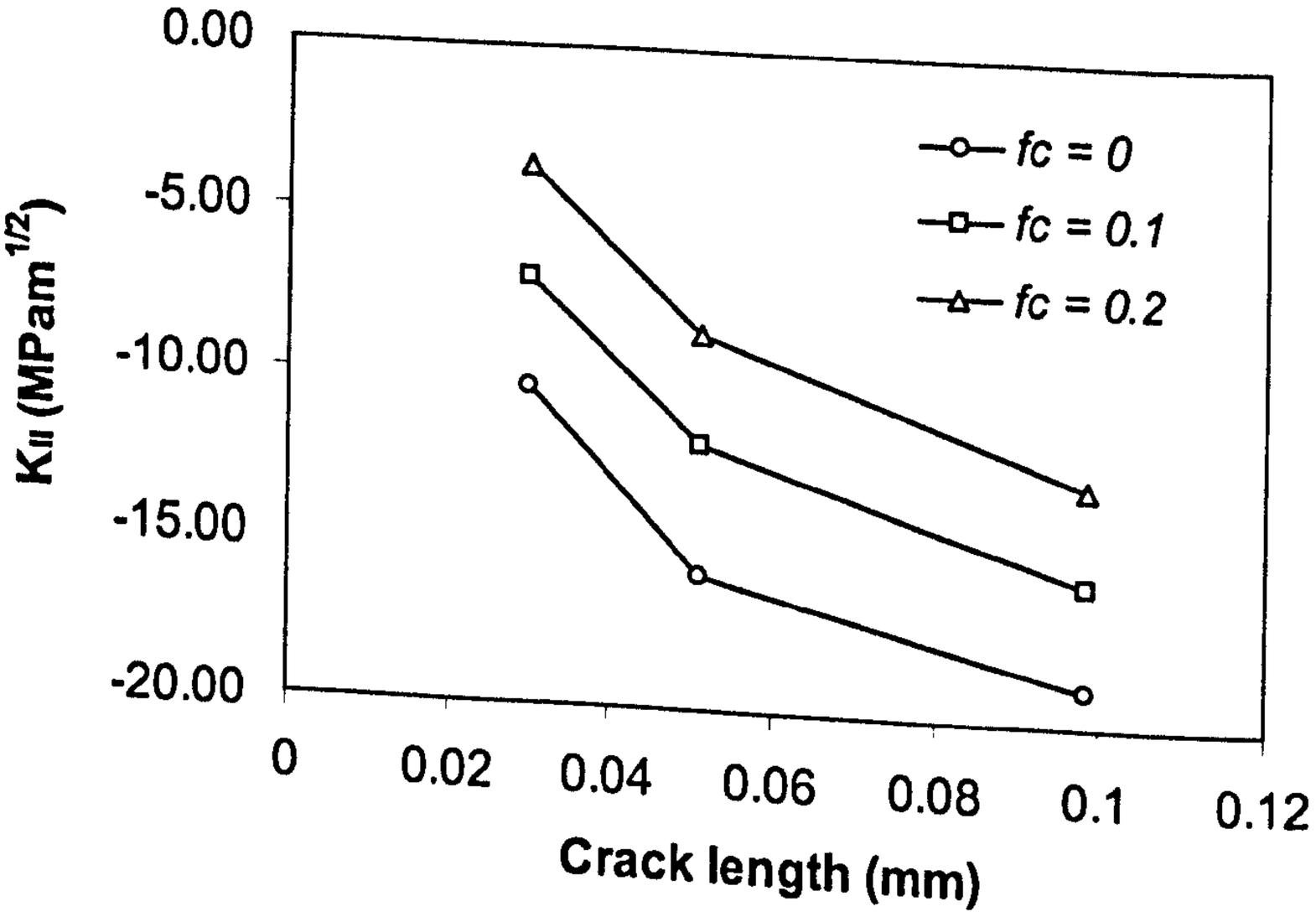

Figure 5.34 Influence of crack length on K_{II} at $\phi = 0°$ (Case 11-1)

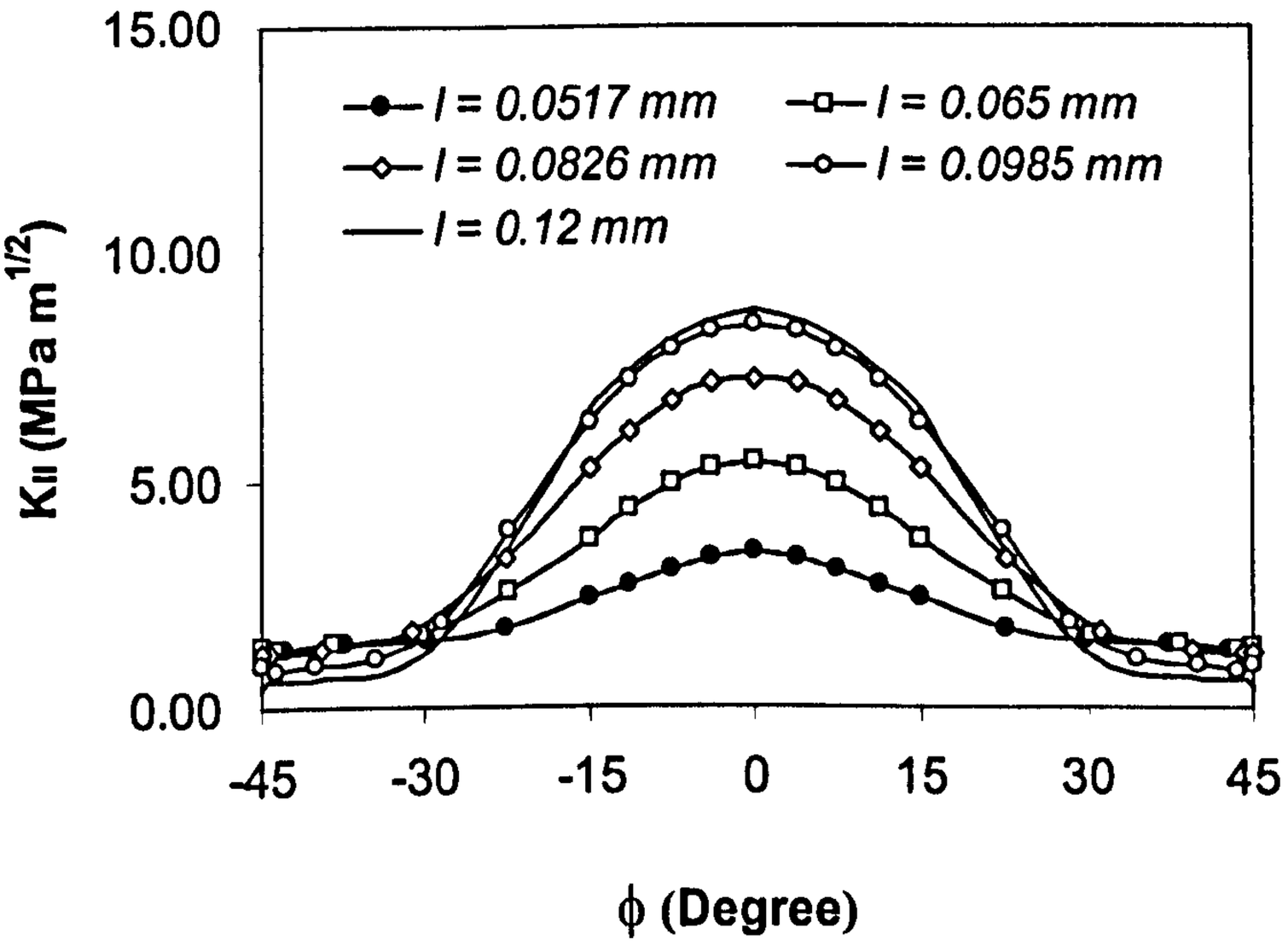

Figure 5.35 Influence of crack length on K_{II} (Case 11-2, $f_c = 0$)

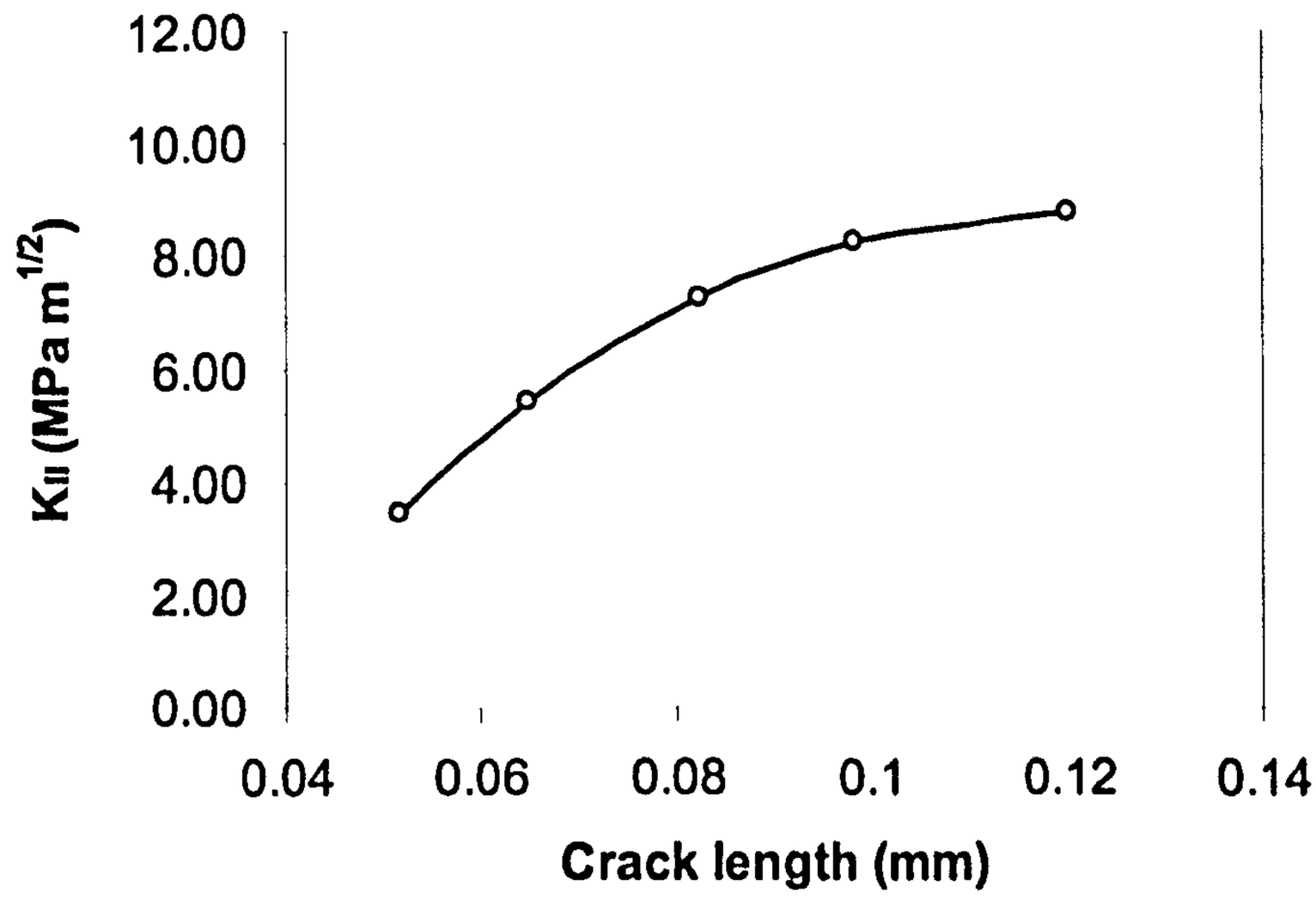

Figure 5.36 Influence of crack length on K_{II} at $\phi = 0^o$ (Case 11-2, $f_c = 0$)

5.4.2.2 Crack radius

Table 5.12 lists the calculation conditions for the study of the influence of crack radius on mode II stress intensities. The arc length and length of the crack are fixed. Only one variable component, the radius of the crack, is selected to investigate its effect. In addition, the crack gap is assumed to be zero and is applied to the calculations. Two cases of the crack scale are chosen. One is an artificial crack scale and another is a natural crack scale. For an artificial size scale, the crack arc length is bigger than the width of the contact path. For a natural size scale, the crack is covered by the contact circle.

Table 5.12 Crack geometry and calculation conditions

Case No	Contact stress (GPa)	Crack position d (mm)	f	f_c	Crack geometry			
					R (mm)	l (mm)	ϕ_0 (degree)	S
12-1	5.58	0.0468	-0.05	0	0.32 0.38 0.44	0.082	42 35 30	20
12-2	5.58	0.0468	-0.05	0	0.21 0.38	0.082	45 24	20

Figure 5.37 shows the calculated results from large cracks (Case 12-1). Since the crack radius is different, the ϕ_0 value must be different to keep the same arc length. As can be seen from the plot, K_{II} value is a function of ϕ. The SIF solutions change very slightly as the crack radius changes. The stress intensity factor of K_{II} is slightly different at $\phi = 0^o$ (lower point) for different crack radii. It can be concluded that the effect of the crack radius on K_{II} is not significant while the crack length and arc length are the same.

Figure 5.38 shows the calculated results from small cracks (Case12-2), which is a natural size scale. Again the ϕ must be different in order to have the same length of arc. Similarly with the case of an artificial size, the SIF solutions change

very slightly as the crack radius changes. The stress intensity factor of K_{II} is slightly different at $\phi = 0^{o}$ (lower point) for different crack radii. Therefore, the crack radius has little effect on K_{II} while the crack length and arc length are the same.

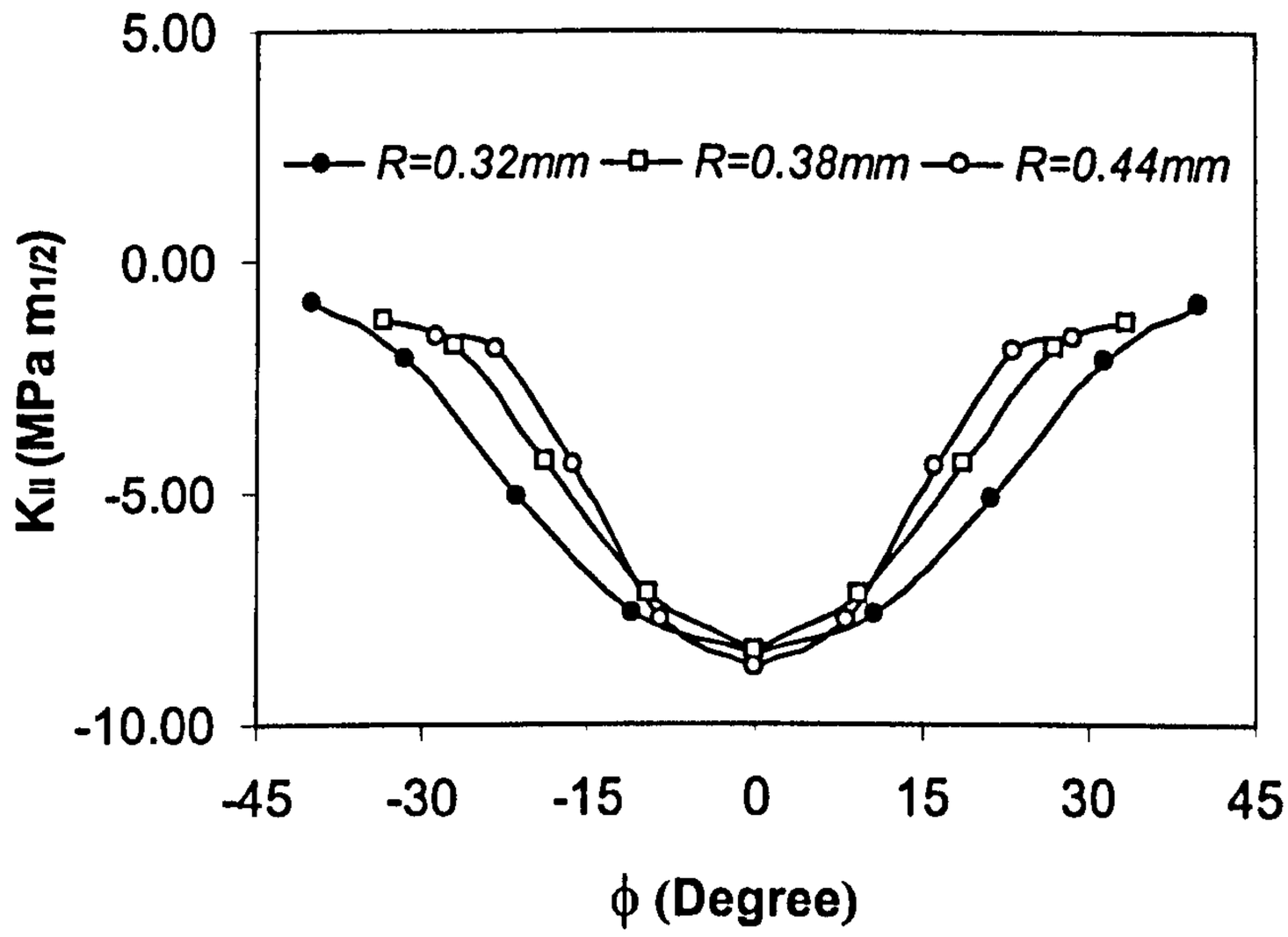

Figure 5.37 Influence of crack radius on K_{II} for large cracks (Case 12-1)

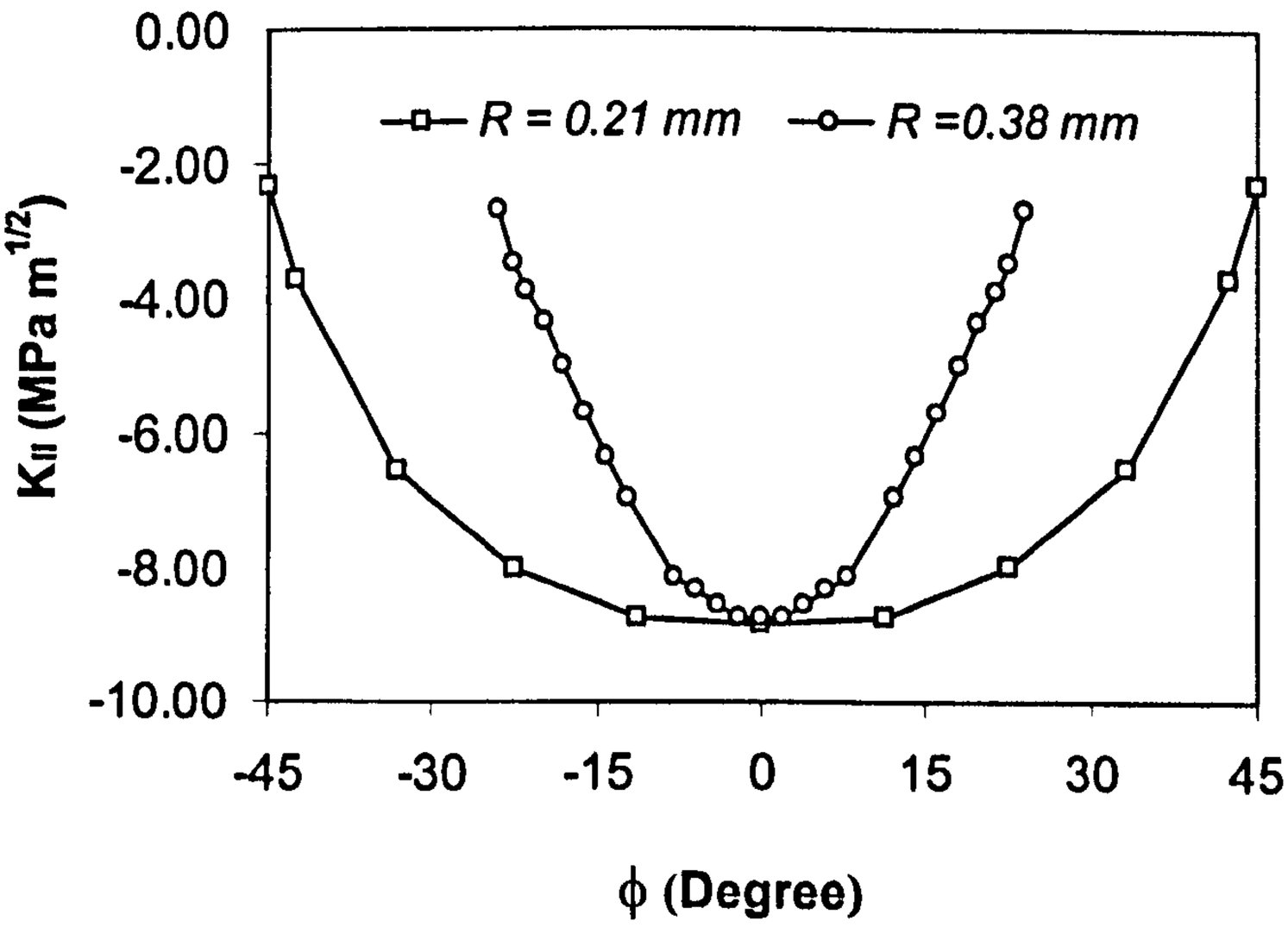

Figure 5.38 Influence of crack radius on K_{II} for small cracks (Case 12-2)

5.4.2.3 Crack angle

Table 5.13 lists the calculation conditions for the study of the influence of crack angle on mode II stress intensities. The constant S is changed to get different crack angles. The corresponding crack angles for S = 50, 20 and 10 are 34.4°, 51.4° and 64.9° respectively. The crack radius, crack length and arc length are the same. The crack gap is zero and applied to the calculations.

Table 5.13 Crack geometry and calculation conditions

Case No	Contact stress (GPa)	Crack position d (mm)	f	f_c	Crack geometry			
					R (mm)	l (mm)	ϕ_0 (degree)	S
13-1	5.58	0.0468	-0.05	0	0.21	0.051	45	10 20 50

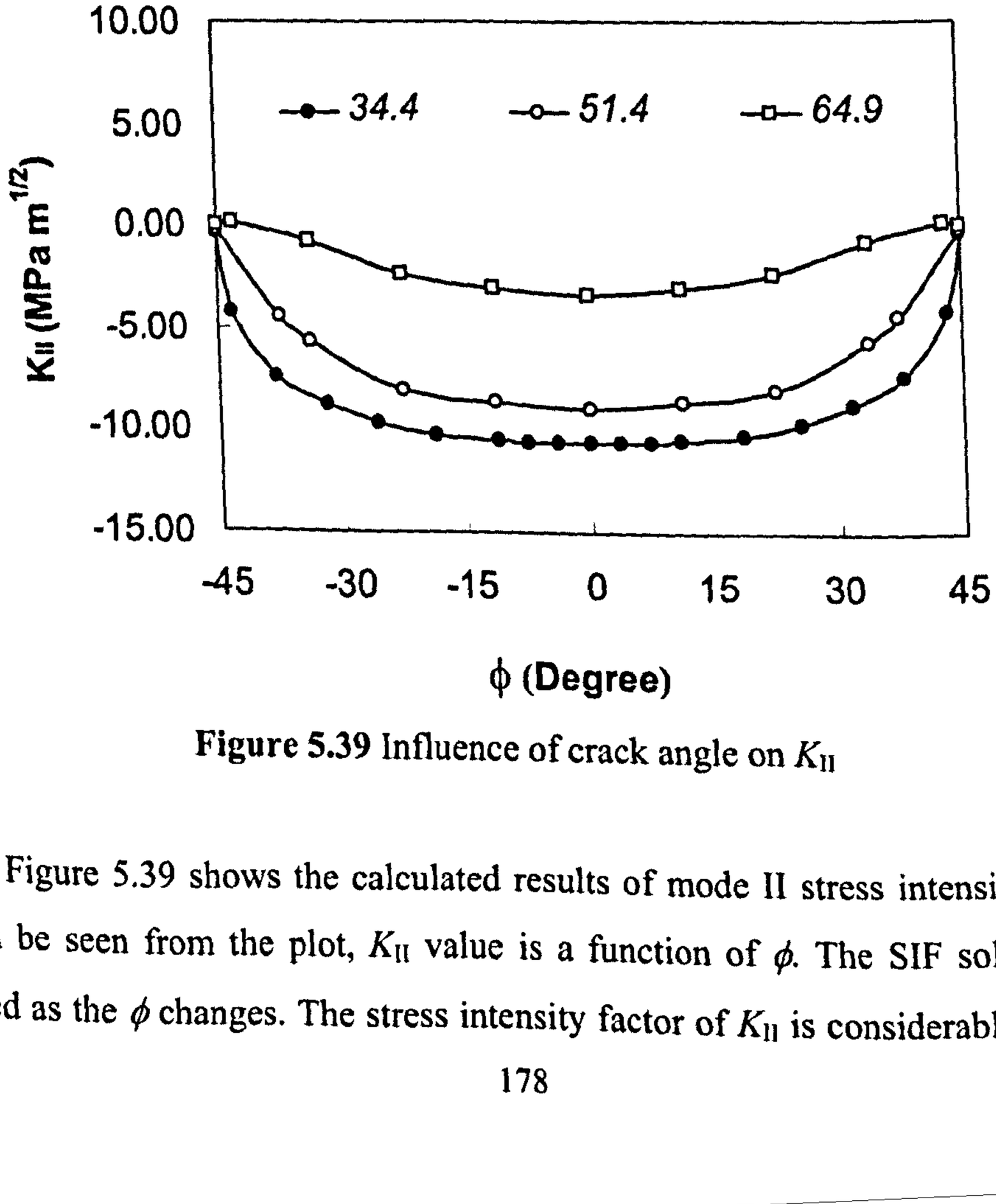

Figure 5.39 Influence of crack angle on K_{II}

Figure 5.39 shows the calculated results of mode II stress intensity factors. As can be seen from the plot, K_{II} value is a function of ϕ. The SIF solutions are changed as the ϕ changes. The stress intensity factor of K_{II} is considerably changed

as the crack angle changes. The crack angle has a significant effect on the mode II stress intensity. The calculations indicate that a large angle crack leads to a small K_{II} (absolute value). The calculated results here predict that a large angle crack may have a good RCF life compared with a small angle crack. This has been confirmed by experimental observations (see Chapter 4)

5.4.2.4 Arc length

Table 5.14 lists the calculation conditions for the study of the influence of crack arc length on mode II stress intensities. The radius and length of the crack are fixed. Only one variable component, the length of the arc, is selected to investigate its effect. The crack gap is assumed to be zero and is applied to the calculations. Two lengths of crack are selected to compare their effect.

Table 5.14 Crack geometry and calculation conditions

Case No	Contact stress (GPa)	Crack position d (mm)	f	f_c	Crack geometry			
					R (mm)	l (mm)	ϕ_0 (degree)	S
14-1	5.58	0.0468	-0.1	0	0.21	0.051	35 45 55	20
14-2	5.58	0.0468	-0.05	0	0.38	0.082	24 35	20

Figures 5.40 to 5.41 show the calculated results of mode II stress intensity factors. Since the crack radius is the same, the ϕ_0 value must be different in order to obtain the different arc lengths. As can be seen from the plot, the value of K_{II} is a function of ϕ. The SIF solutions for longer arc length are slightly higher than for the shorter arc length. It can be concluded that the effect of the arc length on K_{II} is not significant while the crack length is the same.

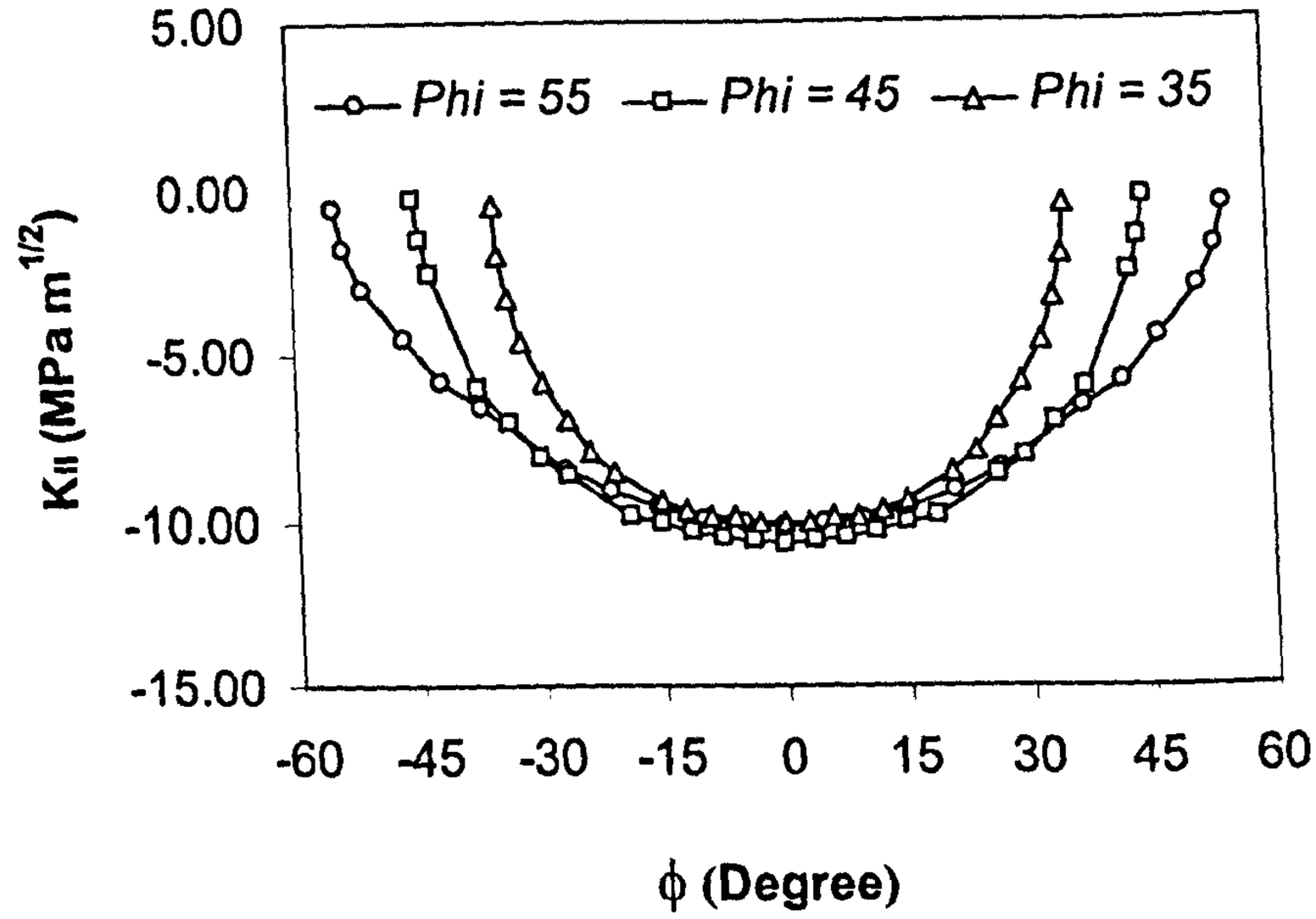

Figure 5.40 Influence of crack arc length on K_{II} (Case 14-1)

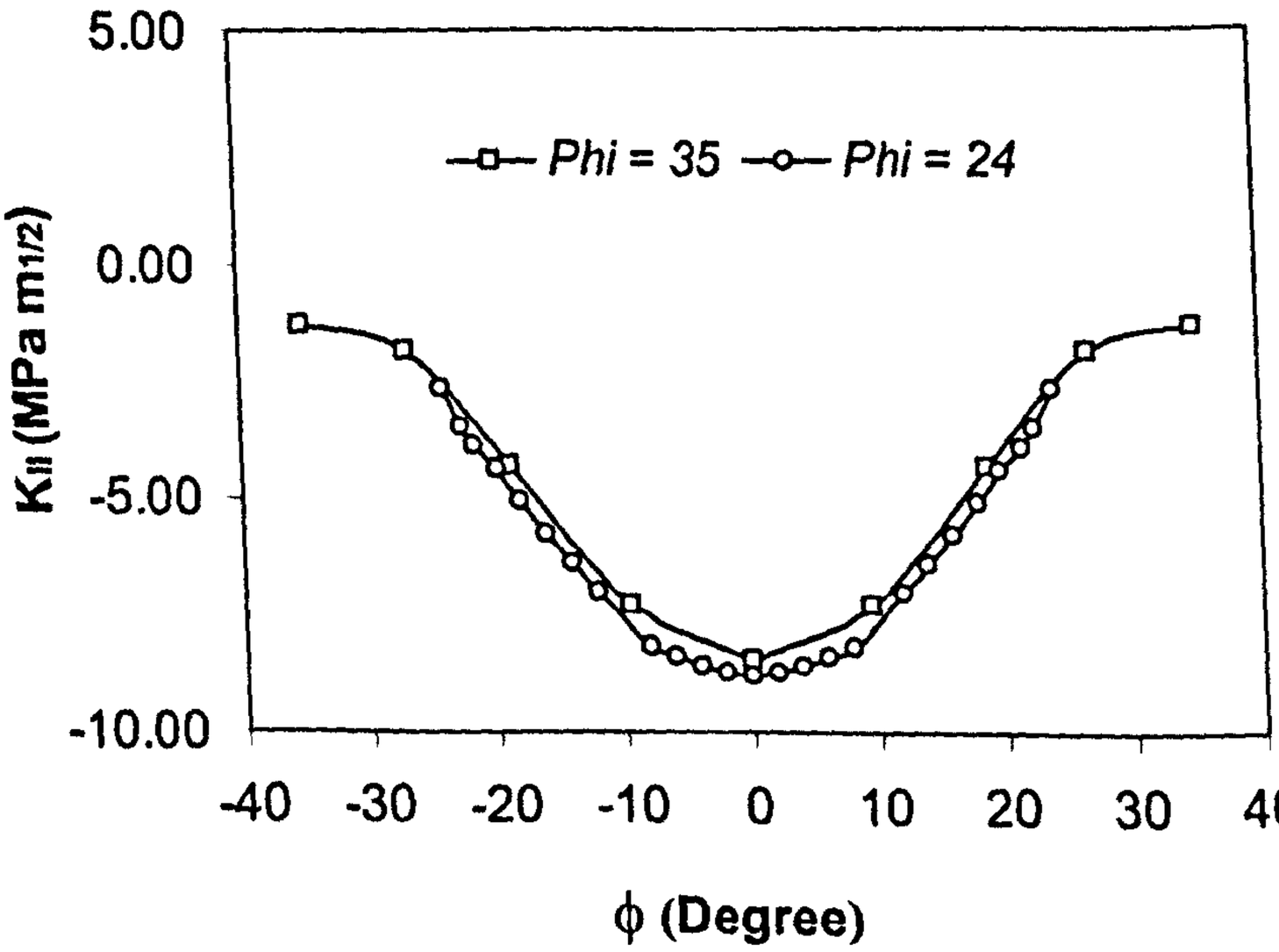

Figure 5.41 Influence of crack arc length on K_{II} (Case 14-2)

5.4.3 Effect of crack position

When the crack lies in the contact circle (compressive region) the mode I stress intensity becomes zero. The mode II stress intensity will dominate the crack propagation. Clearly, subsurface crack propagation is affected by the change of co-ordinate x. In this section the effect of co-ordinate x on the stress intensity K_{II} is discussed below. Table 5.15 lists the calculation conditions. It will be focused on one crack to compare their effect. The crack gap and crack face friction coefficient are assumed to be zero.

Table 5.15 Crack geometry and calculation conditions

Case No	Contact stress (GPa)	Crack position d (mm)	f	f_c	Crack geometry			
					R (mm)	l (mm)	ϕ_0 (degree)	S
15-1	5.58	0.0468 0.0910 0.3468 0.4668	-0.05	0	0.21	0.098	45	20

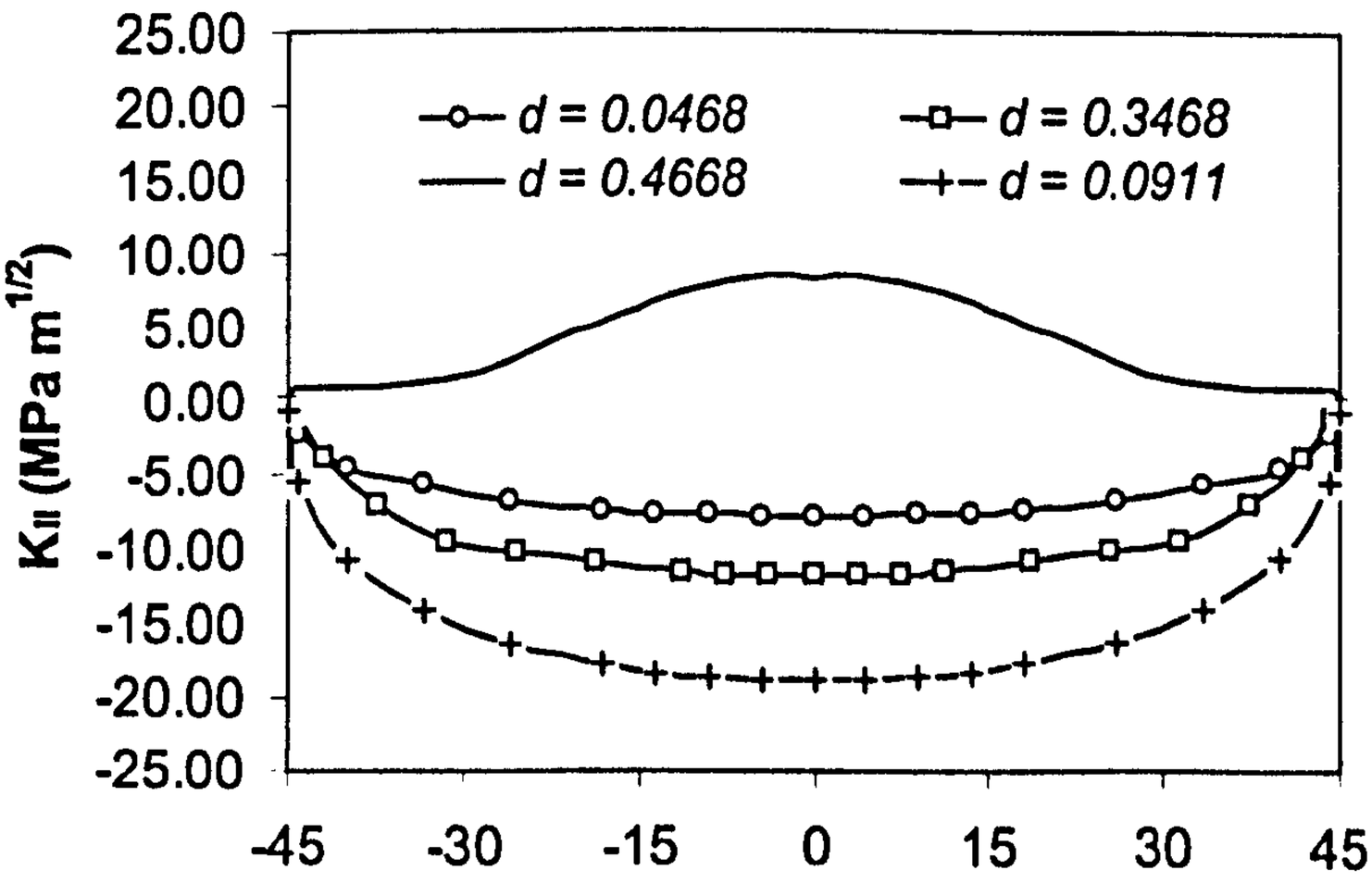

Figure 5.42 Influence of crack position on K_{II}

Figures 5.42 and 5.43 show the calculation results of mode II stress intensity factors. It can be seen that K_{II} value is very sensitive to crack positions within the contact circle. In addition, the sign of K_{II} changes from negative to positive when the contact load passes the crack. The history of K_{II} is very complicated as the crack position changes. It is still possible to find one position in which the absolute value is the maximum. This position can be considered as the worst case to determine whether the crack propagates or not. Mode II stress intensity takes the maximum value at a position of $d = 0.091\text{mm}$ ($d = a - x$).

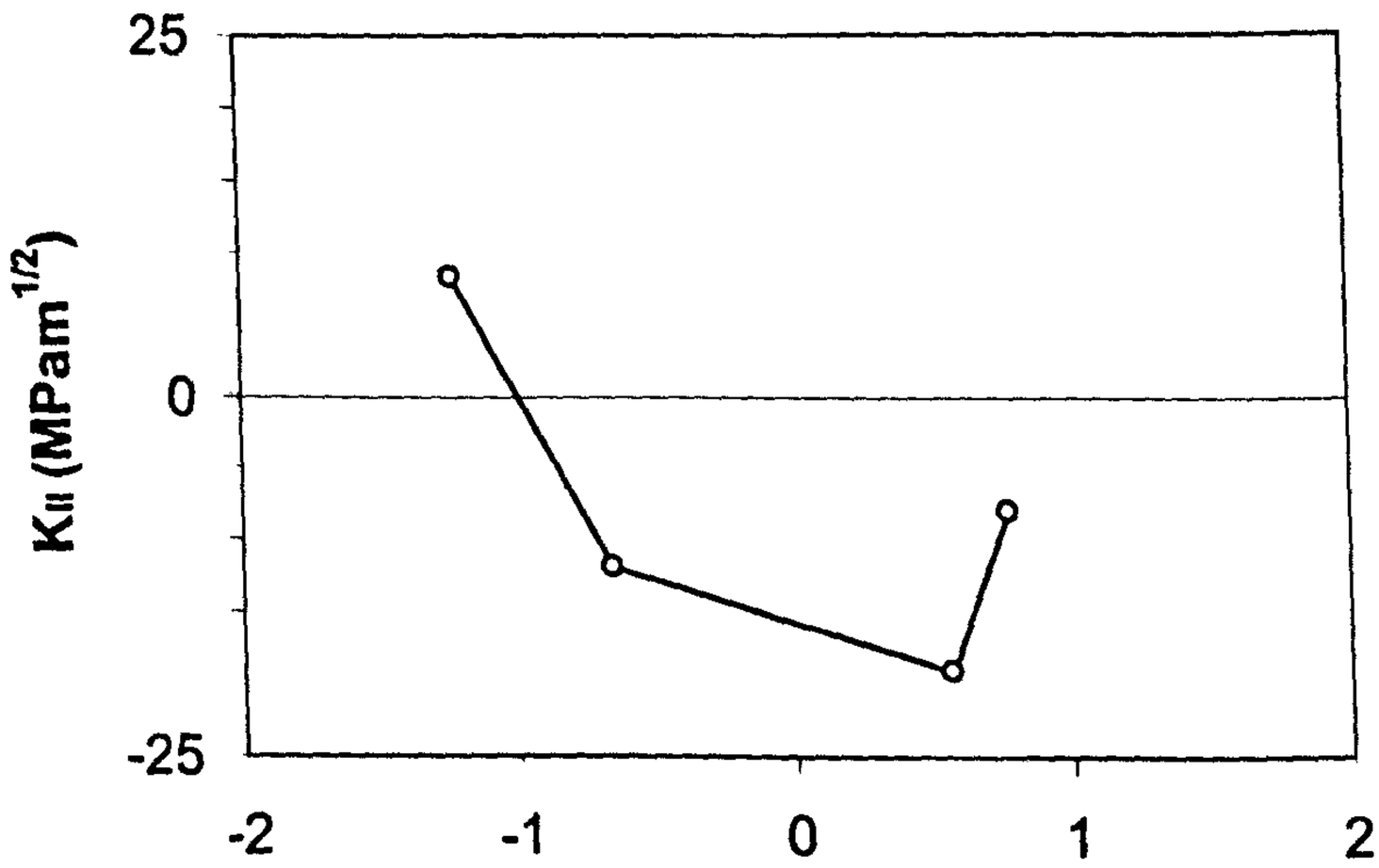

Figure 5.43 Influence of crack position on K_{II} ($\phi = 0°$)

5.4.4 Effect of crack gaps

Two sizes of crack (natural and artificial) are used to investigate the effect of the gap on stress intensities. Table 5.16 lists the crack geometry and calculation conditions.

Figure 5.44 shows the result from Case 16-1. As can be seen from the plot, K_{II} value is a function of ϕ. At the surface points ($\phi = \pm 45°$), K_{II} (absolute value)

takes the minimum value. The maximum value (absolute value) appears at $\phi = 0$. The K_{II} value (absolute value) for the big crack gap is higher than that of the small crack gap. Therefore, it can be concluded that the crack gap has a significant effect on the stress intensities.

Table 5.16 Crack geometry and calculation conditions

Case No.	Contact stress (GPa)	Crack position	f	f_c	Crack geomctry			
					R (mm)	l (mm)	ϕ_0 (degree)	S
16-1	5.58	0.091	0.05	0	0.21	0.098	45	20
16-2	5.58	0.0468	-0.05	0	0.32	0.082	42	20

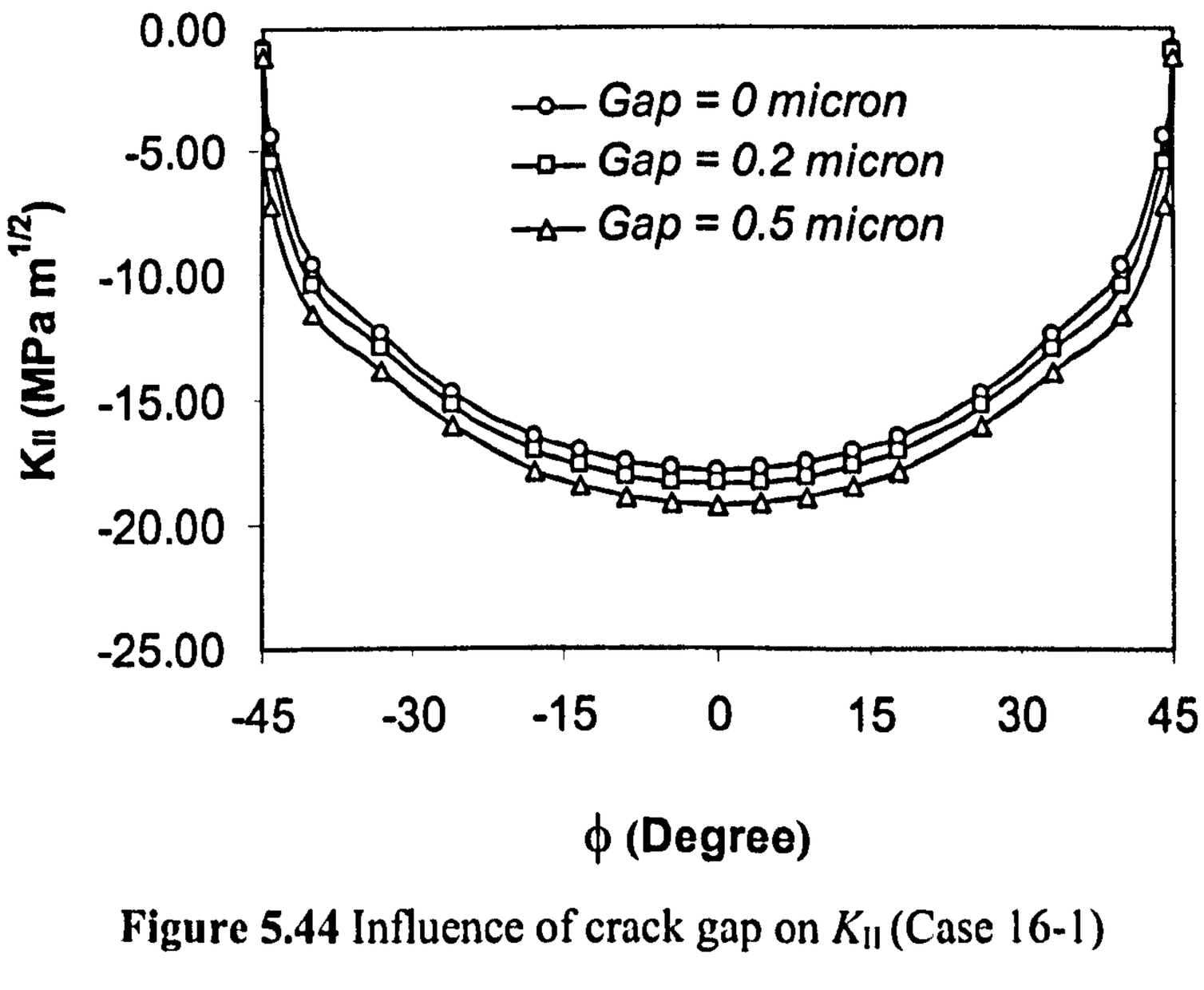

Figure 5.44 Influence of crack gap on K_{II} (Case 16-1)

Figure 5.45 shows the result from Case 16-2. Again, K_{II} value is a function of ϕ. At the surface points ($\phi = \pm 45^{\circ}$), K_{II} takes the minimum value. The maximum value appears at $\phi = 0$. The crack gap has a significant effect on stress intensity factor value. Increasing crack gap increases mode II stress intensities.

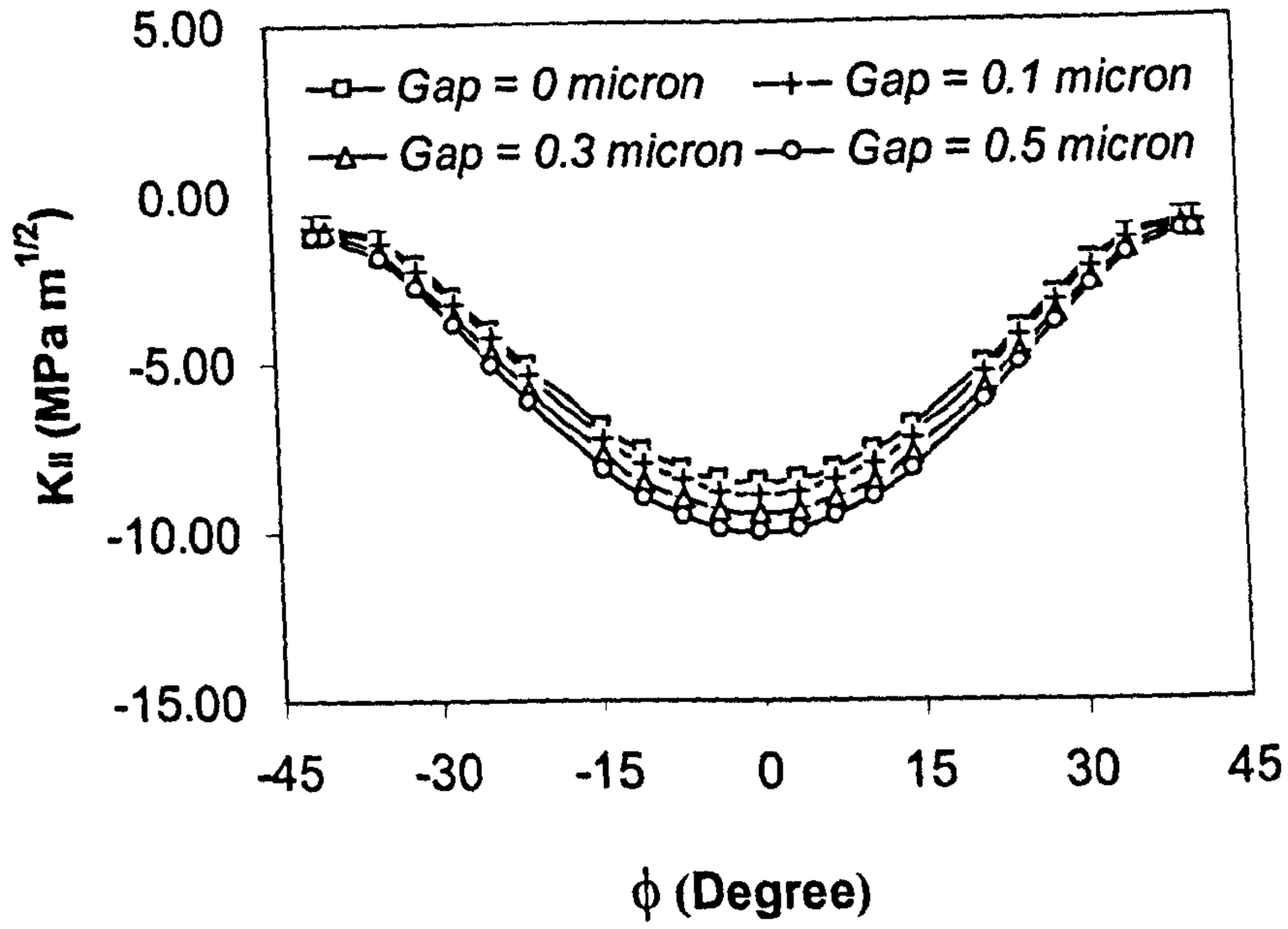

Figure 5.45 Influence of crack gap on K_{II} (Case 16-2)

5.4.5 Effect of contact stress

The following discussion focuses on the effect of contact stresses on SIFs. The crack gap is assumed to be zero and is applied to the calculations. Various crack face friction coefficients are selected to compare their effect on K_{II} stress intensity factors. Detailed conditions are given in table 5.17.

Table 5.17 Crack geometry and calculation conditions

Case No.	Contact stress (GPa)	Crack position d (mm)	f	f_c	Crack geometry			
					R (mm)	l (mm)	ϕ_0 (degree)	S
17-1	5.03 5.58 6.63	0.0468	-0.05	0 0.2 0.4	0.21	0.098	45	20

Figure 5.46 shows the result of K_{II} stress intensity factor. As can be seen from the plot, at the surface points ($\phi = \pm 45^{\circ}$), K_{II} (absolute value) takes the

minimum value. The maximum value (absolute value) appears at $\phi = 0$. The K_{II} value (absolute value) increases as contact stresses increase. Figure 5.47 illustrates the influence of the contact stress and crack face friction on the K_{II} stress intensity factor.

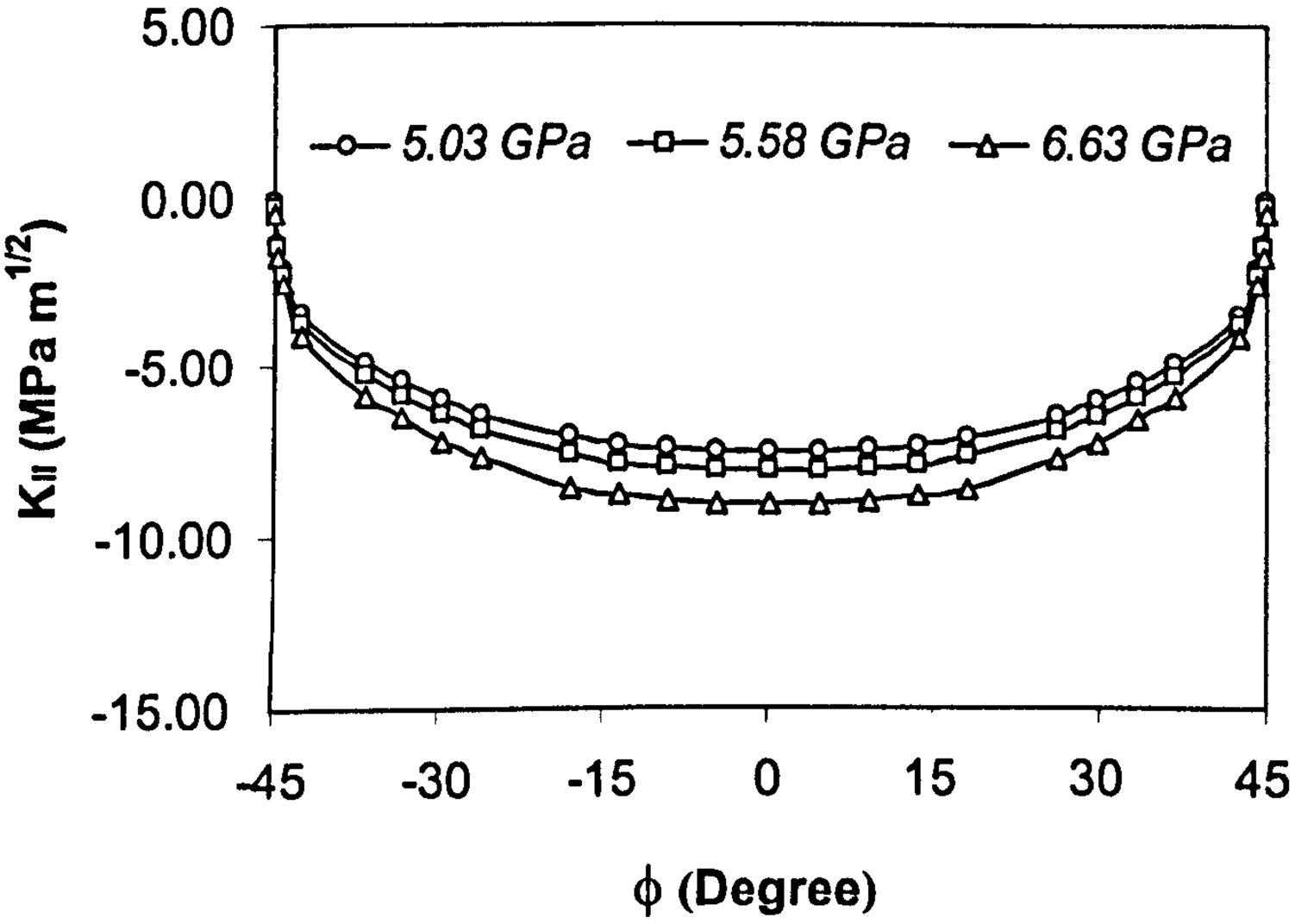

Figure 5.46 Influence of contact stress on K_{II}

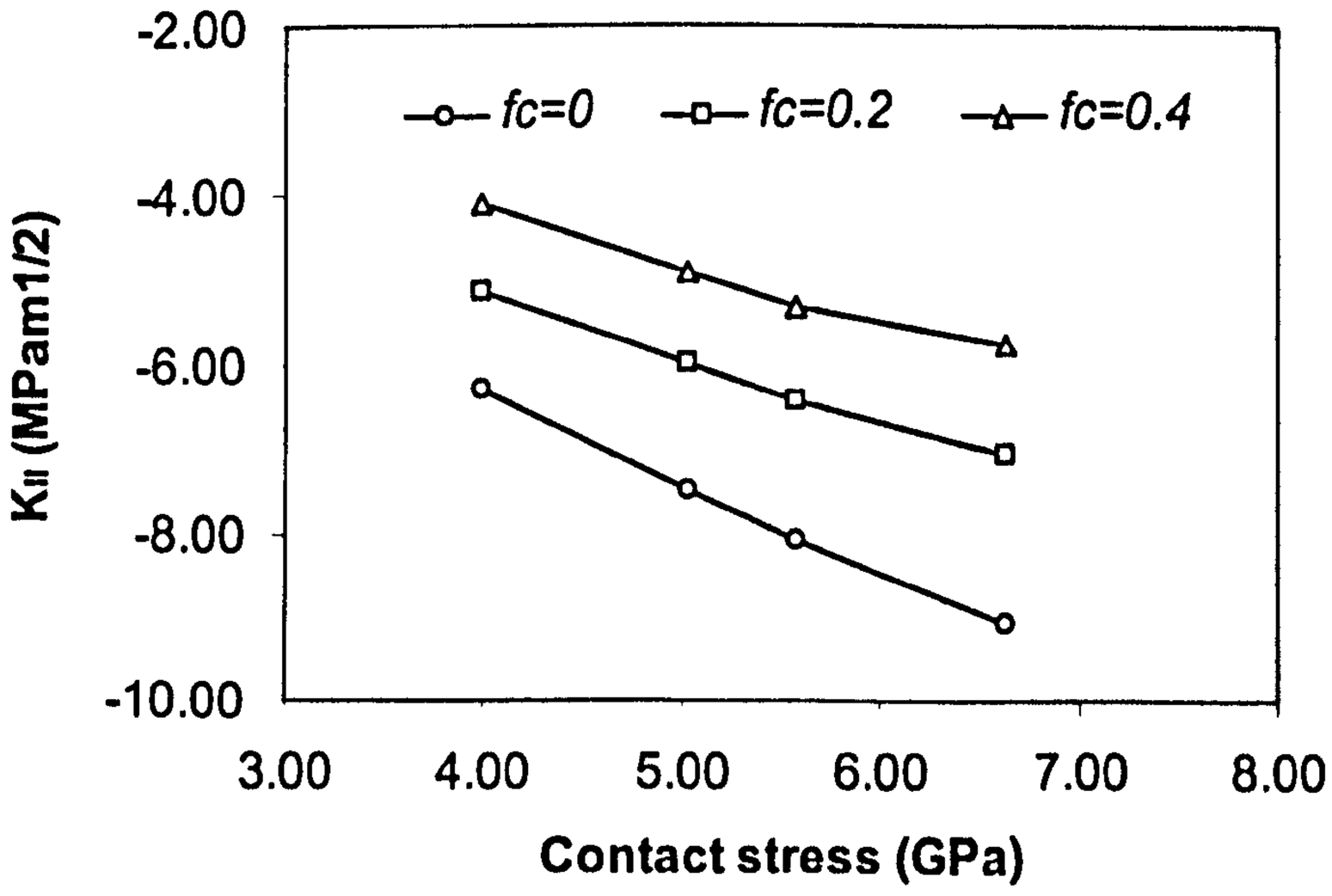

Figure 5.47 Influence of contact stress and crack face friction on K_{II} ($\phi = 0^{o}$)

5.4.6 Effect of shear traction

The influence of shear traction on stress intensity factors is investigated. The magnitude and direction of tangential traction are determined in terms of the traction coefficients. Both positive and negative traction coefficients are selected to investigate their effect on stress intensity factors. Detailed conditions are listed in table 5.18.

Table 5.18 Crack geometry and calculation conditions

Case No.	Contact stress (GPa)	Crack position d (mm)	f	f_c	Crack geometry			
					R (mm)	l (mm)	ϕ_0 (degree)	S
18-1	5.58	0.091	+0.05 -0.05	0	0.21	0.098	45	20

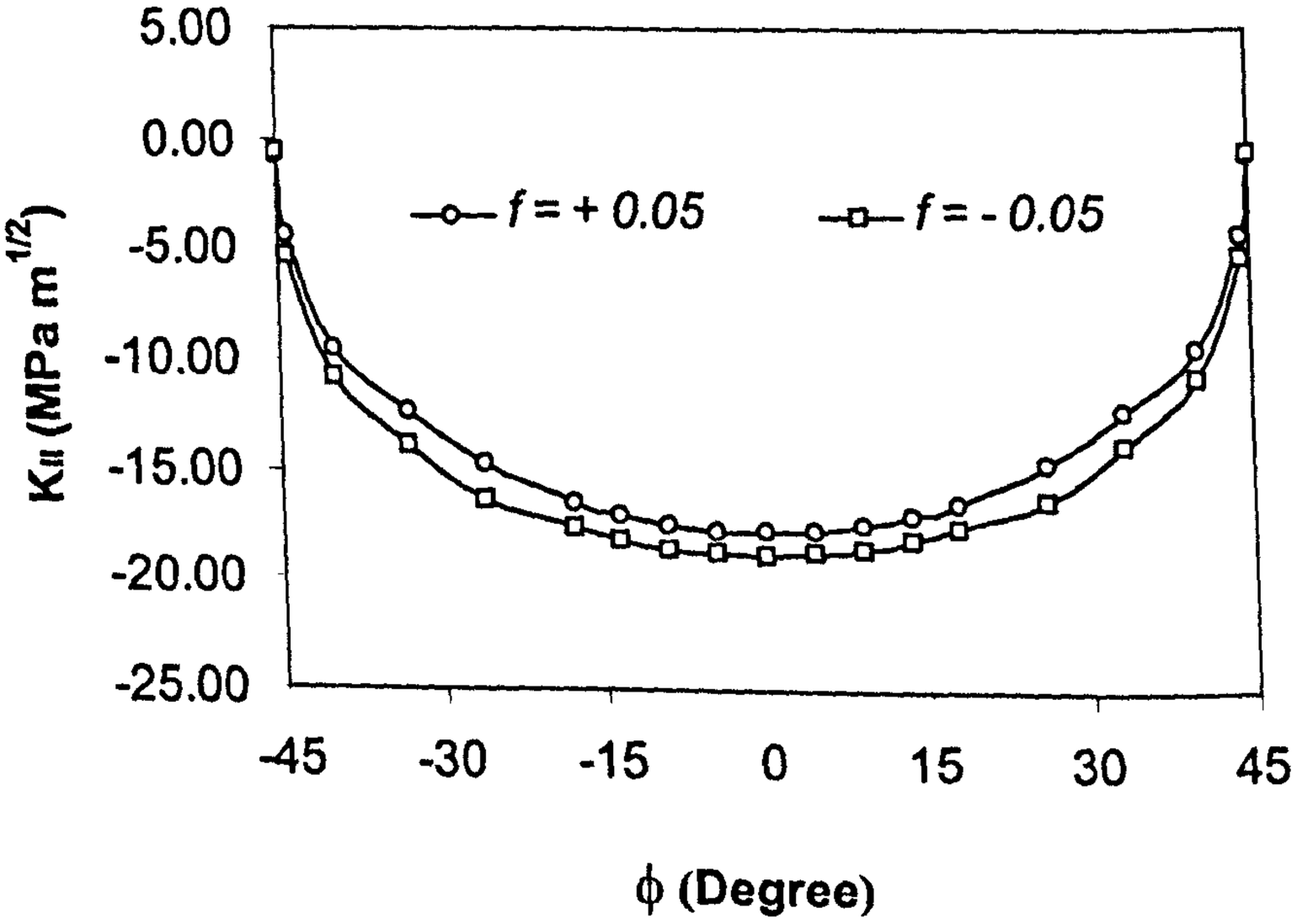

Figure 5.48 Influence of friction direction on K_{II}

In figure 5.48, the comparison of K_{II} values is presented. There is a slight variation in the magnitude of the stress intensity when traction coefficient changes from +0.05 to -0.05. This small change may not have a significant impact. However,

this minor change still may result in a difference in crack propagation. Figure 5.49 illustrates K_{II} variations at different traction coefficients of the crack faces. The results show that the plotted lines are nearly parallel to each other.

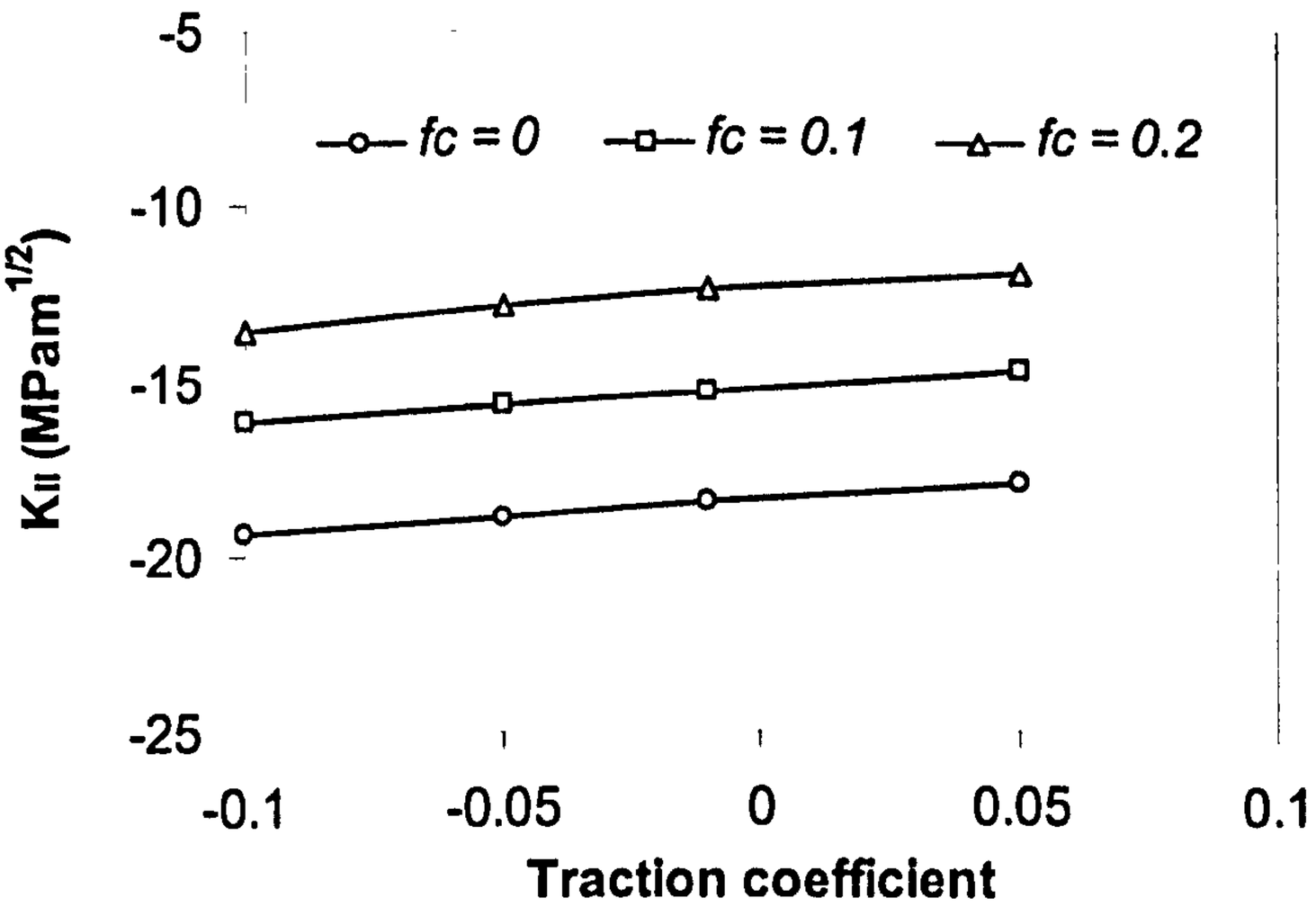

Figure 5.49 Influence of friction direction on K_{II} ($\phi = 0^{o}$)

5.4.7 SIF analysis - crack outside the contact circle

In previous sections, the stress intensity factor calculations deal with where the crack lies in the contact circle. When the crack lies in the contact circle (compressive zone) the mode II stress intensity will dominate the crack propagation because the mode I stress intensity becomes zero. The crack face friction plays an important role in determining the magnitude of the mode II stress intensity. To compare the results from two situations (inside and outside the contact circle), the following discussion focuses on the case where the crack lies outside the contact circle. The analysis of the stress intensity factor has been extensively carried out by Wang and Hadfield (2000, 2004) using a dual boundary element method. Therefore the contact load and friction coefficients are concentrated only in the preset investigation.

5.4.7.1 Effect of contact load

Since the contact radius changes as the contact stress, this introduces some difficulties into the stress intensity factor calculations. To accommodate the situations with various contact conditions, the surface ring crack is placed at the same distance away from the contact circle in order to compare the calculation results. Detailed calculation conditions are listed in table 5.19.

Table 5.19 Crack geometry and calculation conditions

Case No.	Contact stress (GPa)	f	Crack geometry			
			R (mm)	l (mm)	ϕ_0 (degree)	S
19-1	4.0 to 7.6	-0.05	0.21	0.051	45	20

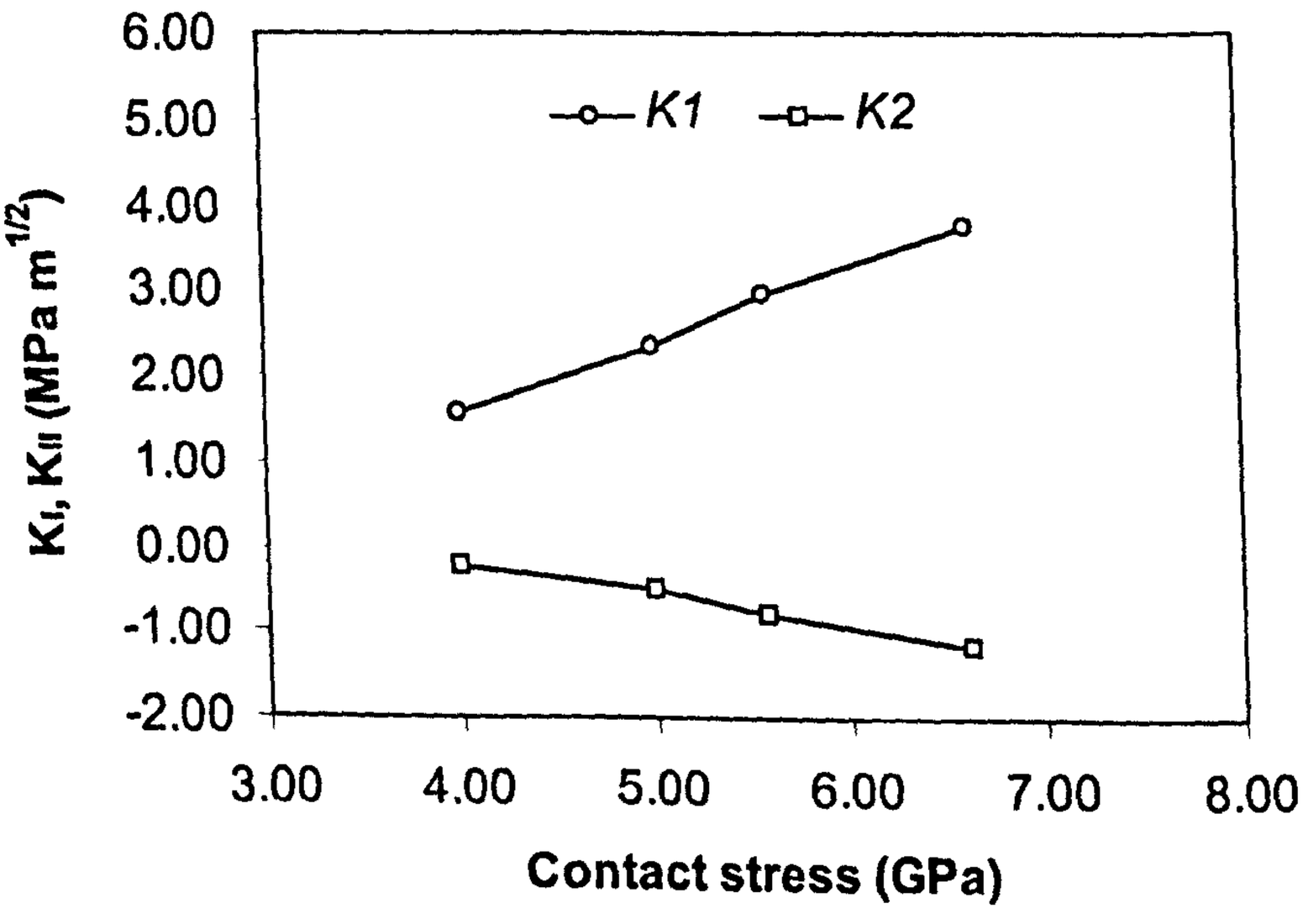

Figure 5.50 Influence of contact stress on stress intensities ($\phi = 0^{\circ}$)

In figure 5.50, K_I and K_{II} are plotted. As can be seen from the plot, mode I stress intensity K_I is much higher than mode II stress intensity K_{II}, in fact approximately three times higher, e.g. for the contact stress 5.6 GPa. The calculated

results indicate that when the crack is outside the contact circle the mode I stress intensity (K_I) plays an important role in crack growth. It is reasonable to assume that the mode I stress intensity will dominate the crack growth behaviour. The calculated results also indicate the K_I increases as the contact stress increases and predict that when the contact stress is less than 4 GPa the crack is hard to propagate due to very low stress intensity (ΔK_{th} = 2-3 $MPam^{1/2}$)(Bar-On and Beals 1990). The prediction is consistent with experimental observations as discussed in Chapter 4.

5.4.7.2 Effect of shear traction

As discussed above, the mode I stress intensity K_I plays an important role in crack growth where the crack lies outside the contact circle and it is reasonable to consider that the stress intensity K_I will dominate crack propagation. The influence of shear traction on K_I is now investigated in the following discussion. The crack geometry and calculation conditions are given in table 5.20.

Table 5.20 Crack geometry and calculation conditions

Case No.	Contact stress (GPa)	Crack position d (mm)	f	Crack geometry			
				R (mm)	l (mm)	ϕ_0 (degree)	S
20-1	5.58	0	-0.05 to +0.05	0.21	0.051	45	20

From figure 5.51, it can be seen that the shear traction significantly affects the magnitude of the stress intensity K_I. The K_I value increases with the increase of the traction coefficient when the contact circle moves from right to left (see figure 5.1) and the K_I decreases as the traction coefficient increases when the contact circle moves from left to right. The calculated results imply that the crack propagation behaviour is influenced by the crack orientation because of different stress intensity factor values. Also, the K_I value is sensitive to the magnitude of the traction coefficient.

In the previous sections, the analysis of the mode II stress intensity (K_{II}) shows the K_{II} is not sensitive to the direction and magnitude of tangential traction. On the other hand, the shear traction effect is not significant when the crack is inside the contact circle, while the shear traction effect is significant when the crack is outside the contact circle. The experimental tests using natural cracks (Section 4.2.6) showed that the use of traction fluid often demonstrated a short fatigue life performance. This may be the traction fluid increasing the traction coefficient, the K_I value is increased and therefore fatigue crack is easily initiated and propagated. For artificial cracks, however, the interaction (crack face friction coefficient) between the crack faces plays an important role in fatigue crack growth and fatigue damage mechanism is also different.

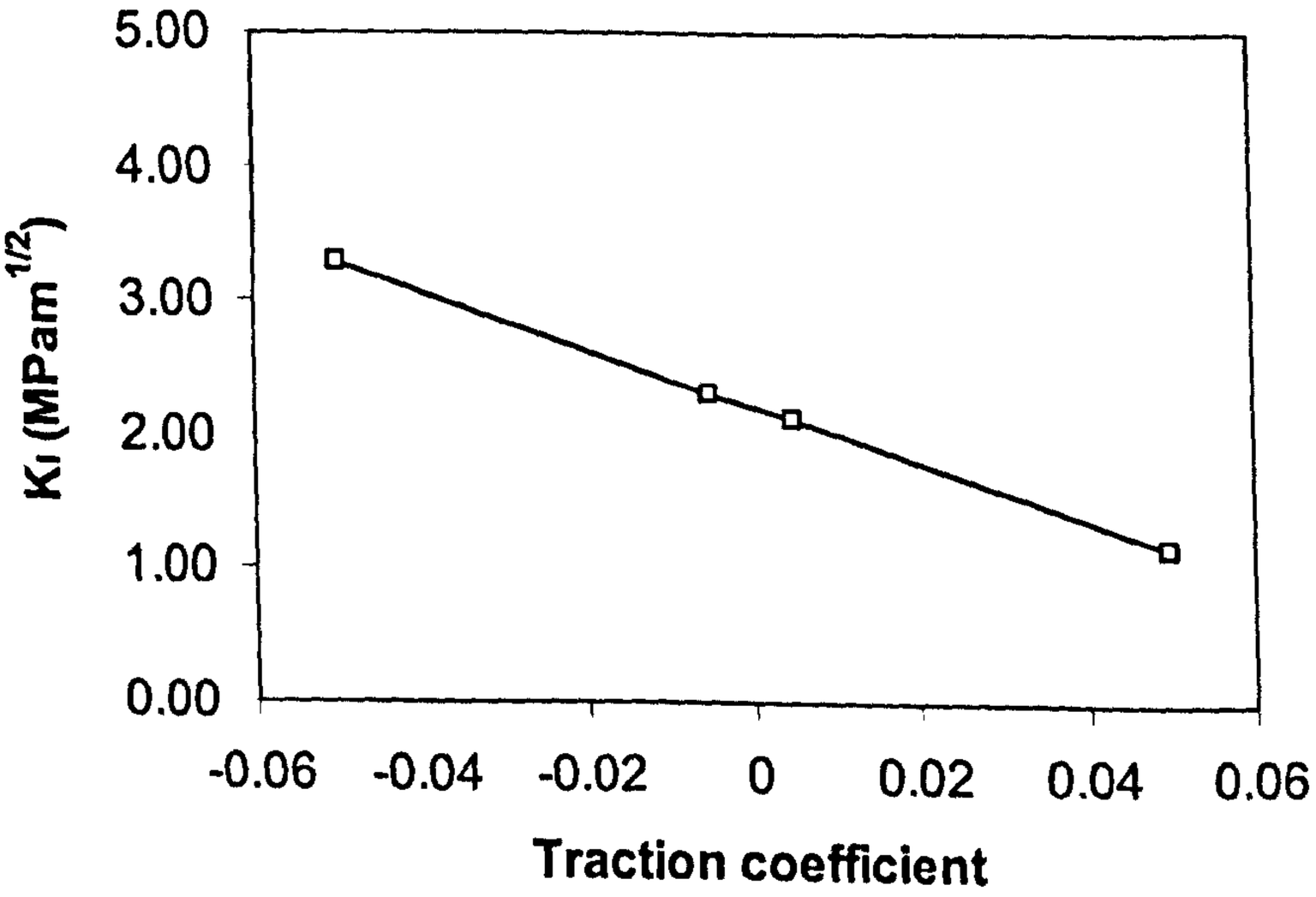

Figure 5.51 Influence of friction direction on stress intensity factor K_I ($\phi = 0^o$)

CHAPTER 6
DISCUSSION AND CONCLUSIONS

6.1 DISCUSSION

6.1.1 Secondary cracks

Secondary surface cracks generally paralleling the original ring cracks were observed on many tested balls particularly on those tested at high loads. These cracks were typically 0.02-0.03 mm in front of the original ring crack with a spacing of 0.02-0.03 mm between cracks (see figures 4.73 to 4.79). The contact model showed high tensile surface stresses ahead of the crack. The magnitude of these stresses is calculated to be more than 2 GPa under some conditions which will exceed the surface tensile strength of the material. Post-test examination of failed and un-failed balls showed that the secondary cracks could join up with sub-surface fatigue cracks and branched cracks leading to a crack network from which material could break out to initiate a spalling failure. For large cracks, the spalling failure was mostly dominated by the formation of the secondary surface cracks (figure 6.1) while for small cracks the spalling failure was dominated by both crack propagation behaviour and secondary surface cracks (figure 6.2).

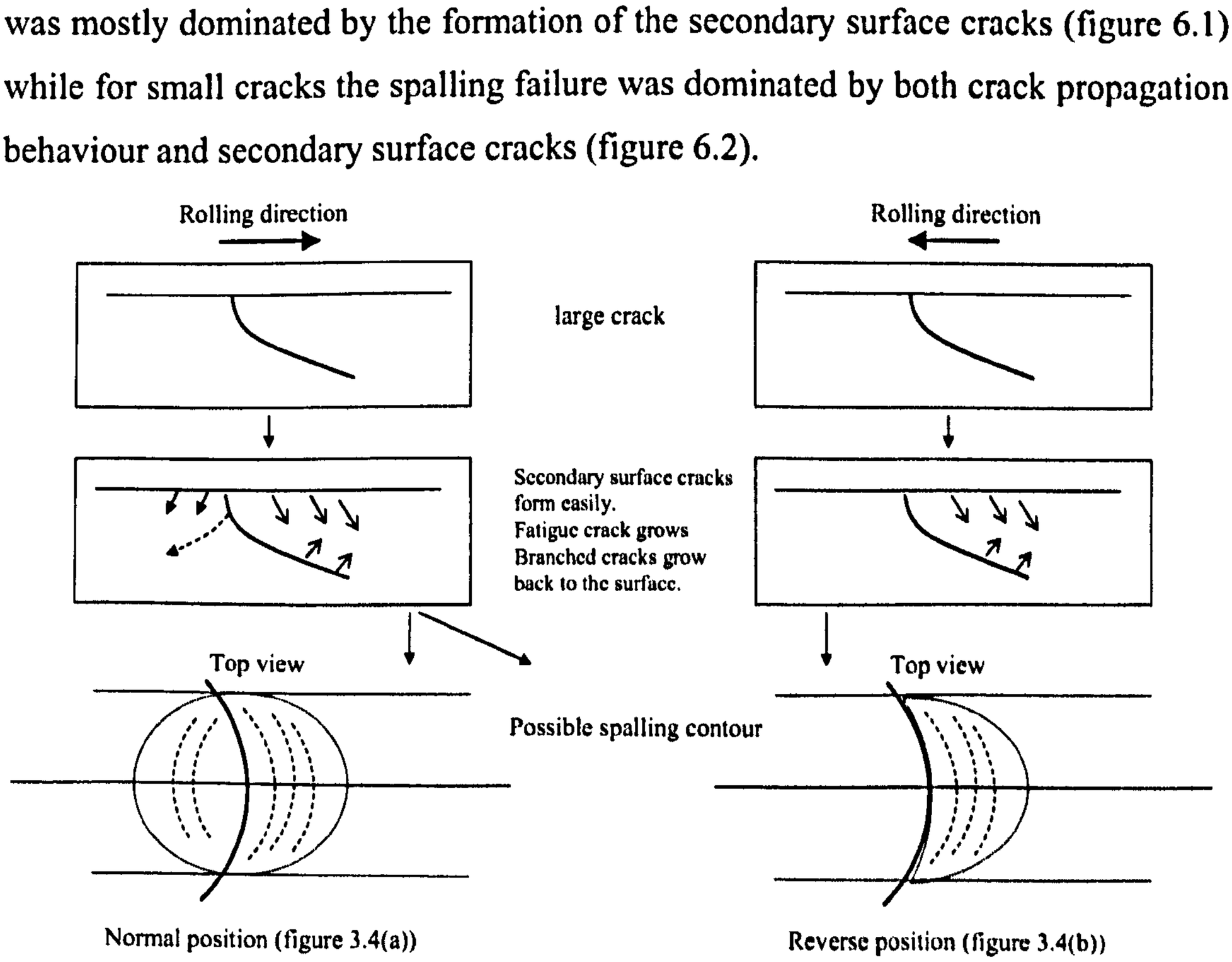

Figure 6.1 Processes of large ring crack spalling failure

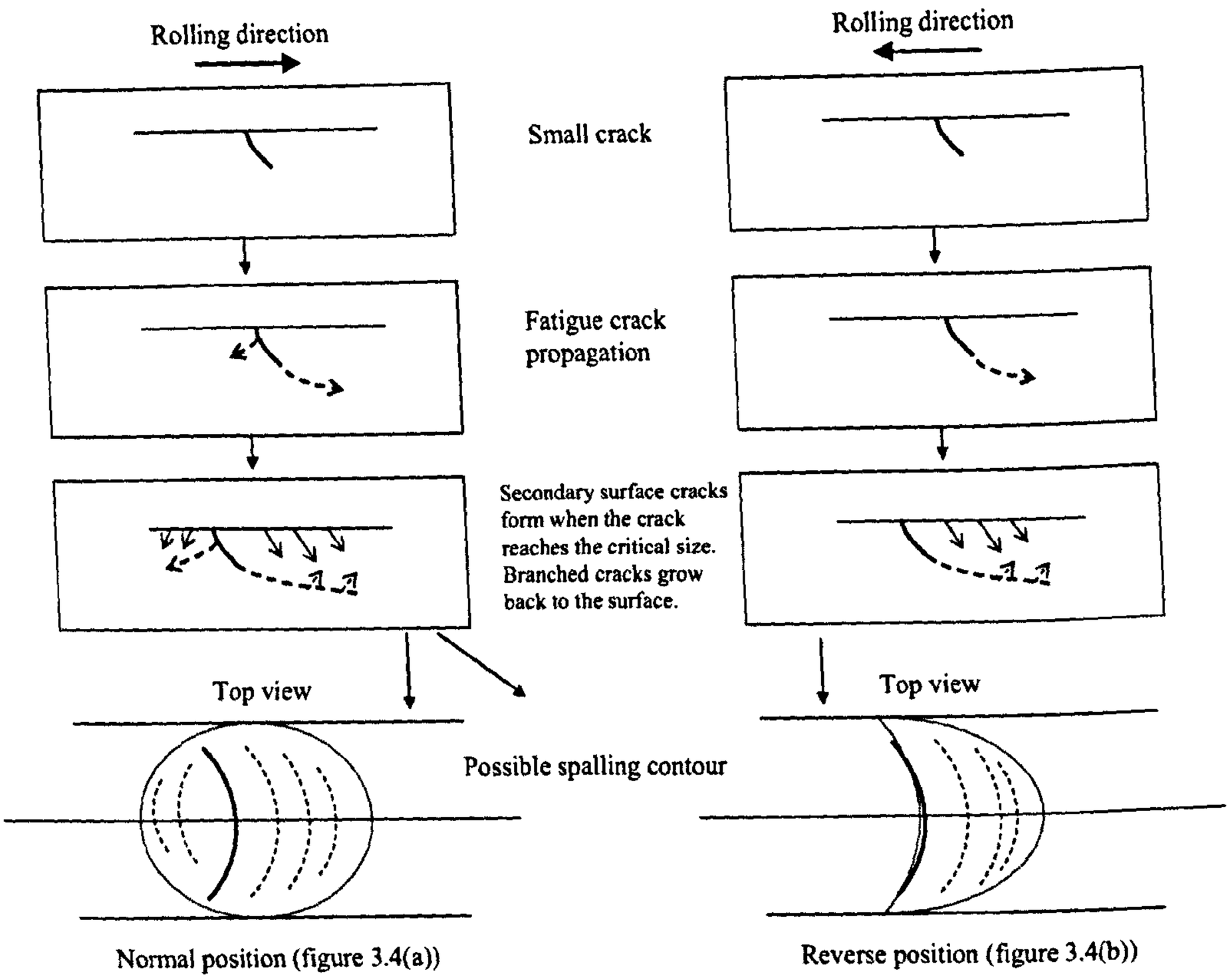

Figure 6.2 Processes of small ring crack spalling failure

6.1.2 Crack propagation

The conventional view of ceramics materials subject to static stress conditions is that the material will either accommodate the stresses or fail immediately since ceramics have virtually no capacity of plastic deformation to arrest crack growth. It was previously thought that under dynamic loading, ceramic balls or rollers in bearings would either continue to run indefinitely or fail very quickly if the contact stress exceeded a critical value. The crack growth period was thought to be very short. However, the results in this study have shown that crack growth is a relatively slow process. The consistency of the results and the reproducibility where duplicate tests were carried out indicates that the crack growth is a stable process. Plots of cycles to failure against crack radius showed a consistent gradient and a high degree of correlation. Sub-surface examination of tested balls showed extensive fatigue crack growth from the original ring crack. Typically the fatigue crack propagated laterally, parallel to the surface, but there was also evidence of alternative crack growth both towards the surface and away from the

surface (see figure 4.102). In addition, the fatigue cracks (and secondary cracks) could branch and form a network.

6.1.3 Crack size and geometry

Crack size as defined by crack radius had, after contact stress, the most effect on RCF performance of balls with ring cracks. Both the arc length and the crack length were observed to increase as the crack radius increased. Although the surface geometry of a crack can be easily measured, the sub-surface geometry is much more difficult to determine and factors such as crack angle and crack length cannot be deduced from the surface geometry. Nevertheless, observations showed that crack length generally increases with crack radius. The crack generating device was designed and manufactured to produce larger cracks than the natural cracks present on commercially available silicon nitride balls. In most cases cracks were formed from the impacts between balls of the same size using different degrees of offset to vary the crack geometry. Testing of balls with both natural and artificial cracks gave consistent results with a good correlation between crack size and fatigue life.

Ring cracks formed as a result of static loading of ceramic balls tend to have relatively shallow angles of 25 - 30°. However, ring cracks on silicon nitride balls tend to be higher due to traction effects with off-set impacts - both 'natural' impacts in ball finishing (50 - 65°) and 'artificial' impacts in the crack generating device (40 - 50°). Experimental studies showed that shallow angle cracks were worse for fatigue performance and that high angle cracks above 60° would be relatively harmless. The modelling studies indicated that crack angle had an effect on maximum principal stress (see figures 5.15 and 5.16). The K_{II} models indicated that crack angles above 60° had virtually no effect and that there was relatively little difference in the range 30° to 50° (see figure 5.39).

Modelling work showed that the crack length was a more important parameter than crack angle. Increasing the crack length for given crack radius resulted in higher absolute K_{II} values and also gave higher values of maximum principal stress. Crack radius and arc length had very little effect on both K_{II} and

maximum principal stress, but it should be noted that the calculations were based on change in radius and arc length with the crack length kept constant. Since a larger radius crack will usually be accompanied by increased crack length (and arc length), it will be the longer crack length that results in lower fatigue life. Balls with cracks produced by impacts of 6.35 mm tungsten carbide balls failed at significantly lower lives than those that had cracks from the impact of two silicon nitride balls of the same diameter (figure 4.60). Tungsten carbide has an elastic modulus nearly twice that of silicon nitride which, combined with the difference in ball diameter, resulted in cracks with the same radius as natural cracks but increased crack lengths.

6.1.4 Crack gap and crack face friction

The modelling work indicated that crack gap, as defined by the maximum separation at the ball surface, had a significant effect on maximum principal stress. Maximum principal stress with a crack gap of 0.5 microns was shown in some instances to be more than double that of a crack with zero width (figures 5.17 - 18). K_{II} also increased in absolute magnitude as the crack gap increased but less significantly (see figures 5.44 - 45). Crack face friction which will be influenced by crack width also has a significant effect on stress and stress intensity parameters. Increasing the crack face friction decreased both the maximum principal stress and absolute magnitude of K_{II}, as shown for example in figures 5.4 and 5.27.

Measurement of crack widths or gaps before or after testing is extremely difficult. At the stressed surface, micro-delamination can give an overestimate of the crack gap when measured after testing. It is estimated that typical crack gaps are of the order of 0.1 micron. Silicon nitride balls typically have compressive surface stresses of 100 - 300 MPa after ball finishing operations which is one of the reasons why the cracks are narrow or 'tight'. Low viscosity fluids such as kerosene and fluorescent dye penetrants can readily penetrate into the cracks, but higher viscosity lubricating fluids may not be able to do so.

6.1.5 Different materials

The two materials (materials A and B) from which the balls used in this

study were made were both bearing grades of silicon nitride, commonly used for balls and rollers in hybrid bearings. Both had similar physical and mechanical properties, had similar optical microstructures and met the relevant specifications. However, when balls with ring cracks were tested the material B balls had significantly better fatigue lives (see figure 4.41). The main differences between the materials were that different additives to promote densification (sintering aids) were used as well as different densification processes. Material B was processed by a sinter + HIP method while the material A was densified by a direct HIP process. Yttria and alumina were used as sintering aids in material B and magnesia in the case of material A.

The two materials whilst having similar hardness and toughness properties differed in impact behaviour with balls made from material B having a greater impact resistance than material A balls. The results from impact tests can be used to estimate the effective surface tensile strength of the material. These gave values of tensile strength of 2.07 GPa for material B and 1.51 GPa for material A. Also, plasma etching was used to show the microstructure in more detail. SEM photos of etched samples, figure 4.40, compares the structure of the two materials. Material B has a more acicular (needle-like) structure than material A which has larger and more equiaxed grains of silicon nitride.

These factors can be used to explain the difference in RCF behaviour between the materials. The lower surface strength of material A will allow the formation of secondary cracks at lower loads/contact stresses than materials B. The interlocking needle structure of material B should provide more of an obstacle to fatigue crack propagation than the larger grained structure of material A and result in a slower fatigue crack growth rate.

6.1.6 RCF testing and service life

In the RCF tests carried out in this study, ring cracks on silicon nitride balls were placed precisely in the contact path in the most harmful orientation. Each crack was over-rolled 2.25 times per cycle. In a radially loaded ball bearing, each ball becomes fully loaded once per cycle and the ball can move at random during the

unloaded part of the cycle. Since a single crack occupies a very small proportion of the surface area of a ball, it will become fully loaded or stressed much less frequently. The possibility for a crack being on the contact track is only 2%. Balls in thrust loaded angular contact bearings are all loaded all the time, but generally the load on each ball is less than in a radially loaded ball bearing. In any case, balls in service would be expected to have lives many times, even orders of magnitude, greater than those experienced in the RCF tests.

6.1.7 Effect of load

The applied load and resulting contact stress will obviously dominate the RCF life of a silicon nitride ball with a ring crack defect. The loads applied in the RCF tests resulted in contact stresses in the range 4.0 to 6.6 GPa. Bearings in service rarely experience contact stresses above 3 GPa, but testing at low applied loads would been prohibitively time consuming. The use of higher loads (and resulting contact stresses) in this study therefore allows a margin of safety in applying the results to bearings in service.

6.1.8 Effect of lubricant

The lubricants investigated included a typical grease used in hybrid bearings as well as mineral and gearbox oils. A traction fluid and kerosene were also studied. The effect of kerosene on RCF could not be evaluated since the failure mode was surface wear, whereas balls tested in the lubricants and traction fluid failed by spalling of the ring crack. At a given contact stress, traction fluid and the mineral oil gave lower lives than grease and the gearbox oil. The poor performance of the traction fluid can be explained in the higher surface traction stresses induced by such a fluid and it would be expected that these stresses would increase stress intensities in the cracks. The reason for the better performance of grease and gearbox oil lubrication compared to that of the mineral oil, which was typically used in bearings, can be explained in terms of crack face friction. The modelling work showed that the mode II stress intensity K_{II} is considerably affected by the amount of

friction between the faces of the crack. Increasing the crack face friction decreases the magnitude of K_{II}. Lubricating greases are essentially a mixture of a mineral oil and a filler such as soap or polyurea. The mineral oil may have a low viscosity but it is surmised that the filler blocks ingress of oil into the crack thus maintaining a high level of crack face friction. Similarly, the gearbox oil with a higher viscosity (101.2 cSt @40°C) than mineral oil (9.4 cSt @40°C) would be less likely to penetrate the crack while the 'thinner' mineral oil would be more likely to do so and decrease crack face friction. It should be noted that the ring cracks are very 'tight' cracks with an initial width of less than 0.1 microns.

6.2 CONCLUSIONS

A crack generating device has been designed and manufactured which can produce various sizes and shapes of the surface ring/cone cracks. Various crack geometries were selected to identify the mechanisms of fatigue initiated from such surface cracks.

Rolling contact fatigue (RCF) life was influenced most by load, lubricating fluid and crack size. The original ring crack propagated during fatigue testing and that crack branching occurred. Also, secondary surface cracks were observed to form especially under high loads/contact stresses. The consistency of results showed that crack growth was an integral part of the failure mechanism.

A boundary element analysis showed that principal surface stresses could reach very high levels in the zone ahead of the ring crack. Such high stresses therefore will lead to the initiation of secondary cracks at the ball surface in front of the original ring crack. These surface stresses naturally increase with load and crack size. Increasing crack face friction decreases the surface stresses.

The calculations also showed that wider crack gaps would increase surface stresses partly as a result of decreasing the crack face friction. Lubricants with less ability to penetrate a crack and thereby increase crack face friction should therefore give a better RCF performance. In practice, this would mean either higher viscosity oils or grease where the filler can provide a barrier to lubricant penetration.

The most important factor of crack geometry was shown to be the (subsurface)

crack length with crack radius, angle and arc length having relatively little effect. Although it is not yet possible to measure crack length non-destructively, the length increases with crack size as defined by crack radius and/or arc length. Therefore crack radius can be used an index of crack severity.

Tests on balls made from different grades of silicon nitride material showed significant differences in RCF performance. Impact tests showed that one material required greater input energy to produce artificial ring cracks than the other, indicating a higher effective surface tensile strength. Balls made from this material had substantially longer RCF lives for a given load and crack size. Therefore, it is concluded that materials with higher surface tensile strength will be more resistant to secondary crack initiation.

Fatigue crack propagation can be a rather complex process due to Hertzian loading in a cyclic fashion. When the crack lies outside the contact circle, the mode I stress intensity K_I shows a significant effect on crack growth. The magnitude of K_I was shown to be increased only by applied load and contact traction for a given crack size. When the crack lies in the contact circle (compressive stress zone), the mode I stress intensity K_I becomes zero and is therefore of importance only at one part of the stress cycle.

The mode II stress intensity K_{II} therefore dominates crack propagation. The K_{II} values were mainly affected by load, crack length and crack face friction. Increasing the load or crack length resulted in an increase in absolute K_{II} values, but high crack face friction led to lower K_{II}. As with the principal surface tensile stresses, any factors which prevent oil from penetrating the crack will benefit RCF behaviour. Similarly wider crack openings (gaps) will have a detrimental effect.

6.3 FURTHER WORK

It is found that the RCF life increases with the effective surface strength of the silicon nitride material from which the balls are made. Further study of the influence of this surface strength is needed. Experiments using various types of material with different microstructures and ball diameters are necessary.

Residual stresses on the surface are important in determining the effective surface strength. Further study on residual stresses of the silicon nitride material is needed. The influence of the residual stresses on surface ring crack propagation also requires further study.

This study has provided information on the magnitude of stress intensity factors, but additional work is needed to determine the values or levels that lead to crack propagation. Also, there is currently no data on the rate of crack propagation of ring cracks under cyclic fatigue loading.

The interaction of the crack faces with the trapped lubricants also requires further study. This has important implications for the determination of crack face friction coefficients.

APPENDIX 1
ROLLING CONTACT FATIGUE TEST METHODS

Fatigue of silicon nitride elements in rolling contact is almost always initiated from surface crack defects. Over the past four decades, many attempts have been made to identify rolling contact fatigue using various test machines namely modified four-ball (Scott et al. 1971, Scott and Blackwell 1973, Tourret and Wright 1977, Hadfield et al. 1993a, Hadfield et al. 1993b, Hadfield 1998, Wang and Hadfield 2000a, Wang and Hadfield 2004), five-ball (Carter and Zaretsky 1960, Parker and Zaretsky 1975), balls-on-rod (Lucek 1990, Allen 1994, Burrier 1996, Chao et al. 1998), disc-on-rod (Baumgartner 1974, Lucek and Cowley 1978), contacting rings (Akazawa and Kato 1988, Braza et al. 1989, Akazawa et al. 1986), ball-on-plate (Fujiwara et al. 1989, Kikuchi et al.1984). Experiments conducted on silicon nitride elements generally exhibited considerable scatter in number of stress cycles to failure. This difficulty arises as a consequence of the variability associated with testing techniques. A recent developed test method (Wang and Hadfield 2000a) is useful as the crack orientation/location is precisely positioned. This novel test method using four-ball machine (Wang and Hadfield) is summarised below.

A1.1 Ring crack orientation in the contact path

Figure A1.1 shows the loading configuration of the modified four-ball machine and the geometric position of a crack within the contact path. The ring cracks distribute randomly on the ball surface and therefore they can occur in any positions when two balls contact each other. Therefore, the probability for the crack being in the contact area is calculated using the following expression (Wang and Hadfield 2000a)

$$\rho = A / A_0 \qquad \text{(A1.1)}$$

where ρ is contact probability, A_0 is area of ball surface, A is area of contact track and the A is approximately calculated by

$$A = 4\pi a R_1 \sin\omega \qquad \text{(A1.2)}$$

where a is the contact radius, R_1 is the radius of the ceramic ball. If R_1 = 6.35 mm, a = 0.21, mm $\omega = 35.3^{\circ}$, hence $\rho = 0.02$. As can be seen from the calculated result, the possibility of a crack being on the contact track is only two percent. Consequently, it is nearly impossible to guarantee the crack being on the contact path if the ceramic ball is just randomly placed in the collet.

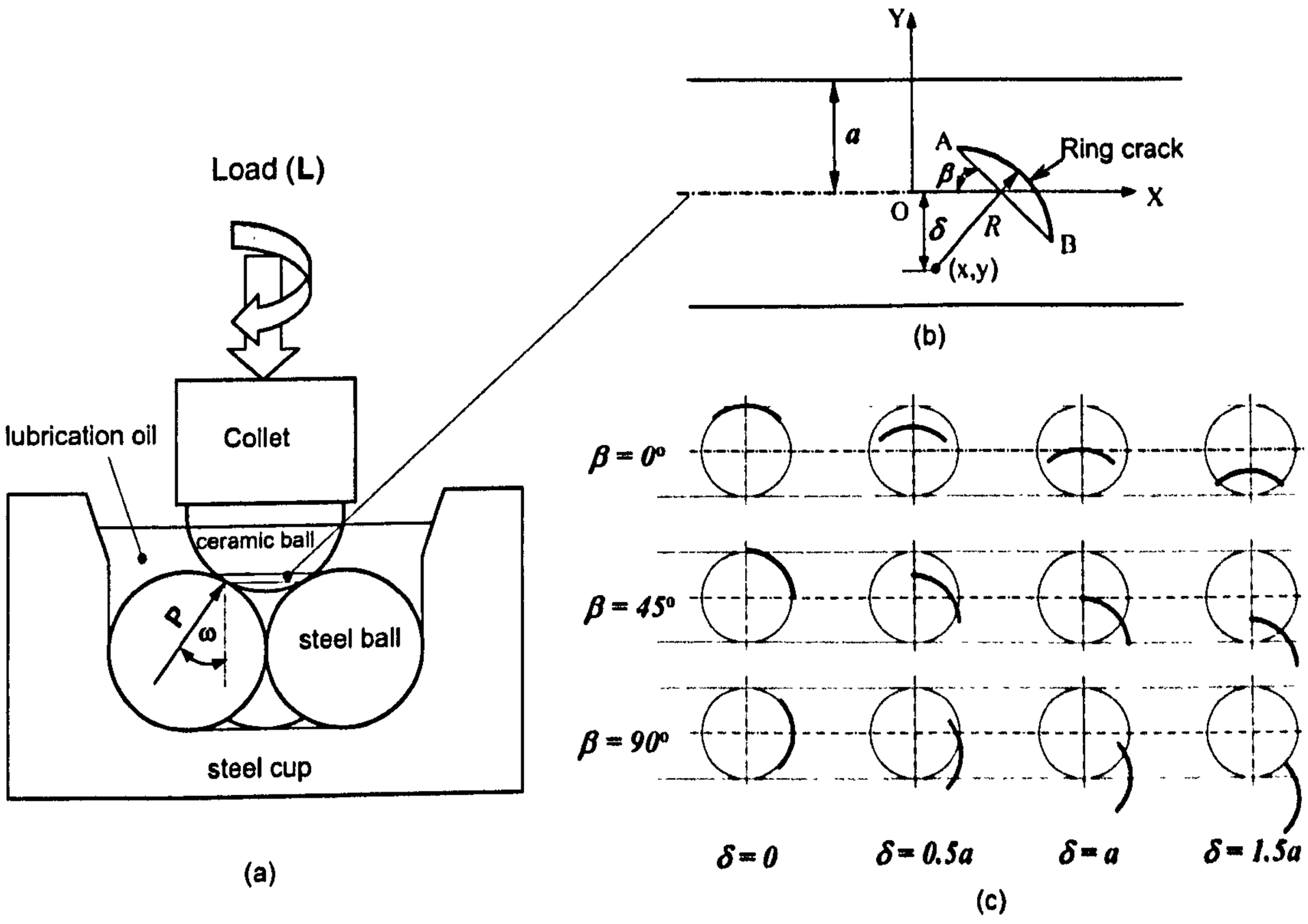

Figure A1.1 Loading configuration and ring crack position within the contact path (Wang and Hadfield 2000a)

The geometric position of the crack is described using two geometrical parameters as shown in figure A1.1(b). One is δ, which represents the distance from the centre of the crack circle to the central line of the contact track. Another is β, which is the angle of the chord of ring crack (arc AB) to the central line. From a mathematical viewpoint, the positions are infinite and twelve typical locations are shown (figure A1.1c). Tests must comply with certain experimental procedures to

ensure the crack is on the contact path. This is will be addressed in the followings.

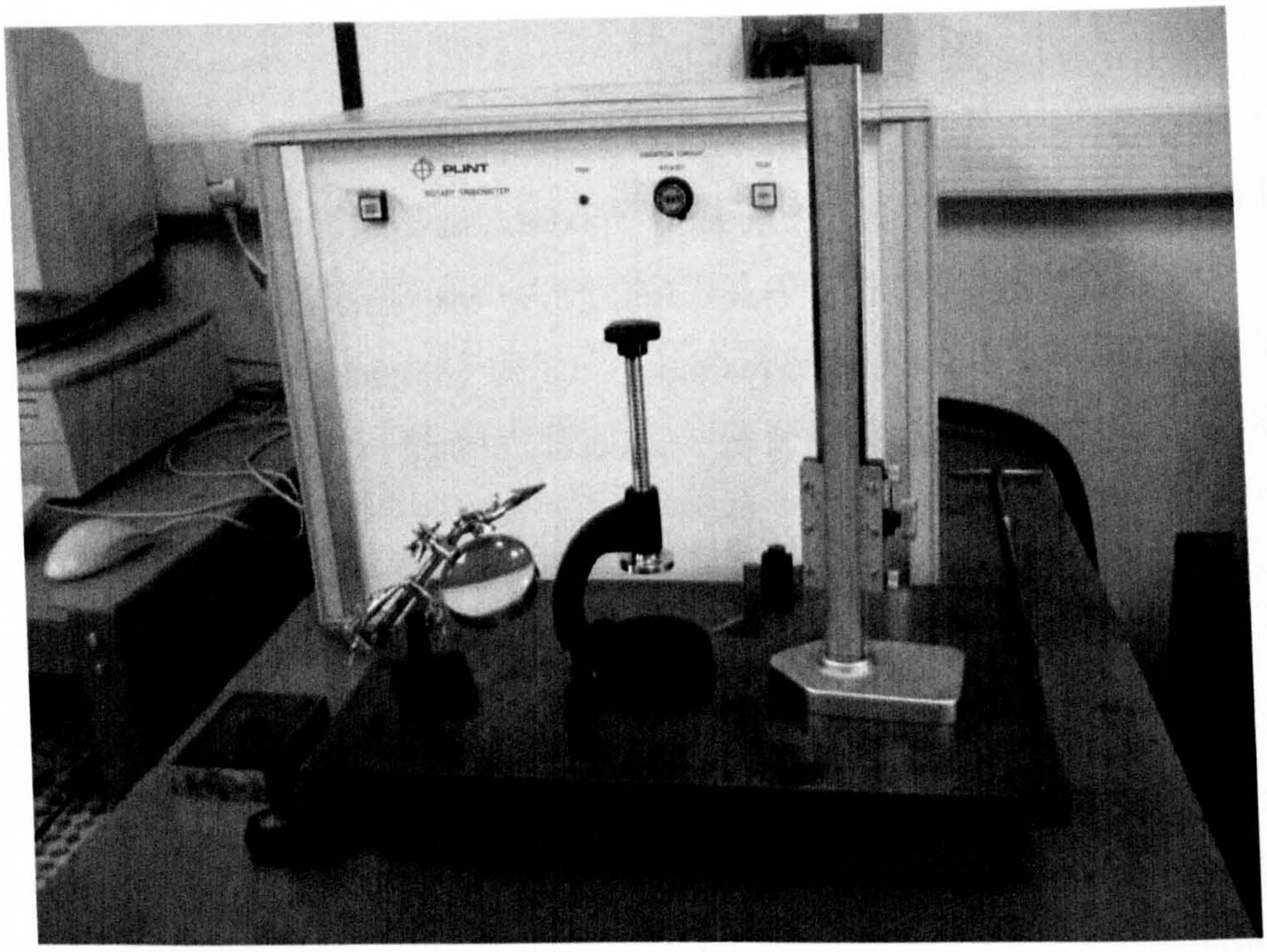

Figure A1.2 The rig for determining crack location

A 1.2 The method for positioning a ring crack

The crack orientation is critical important in rolling contact fatigue and it is a key to investigating failure mechanisms. The crack should be in the same position to each test. To achieve this, the crack location tool (figure A1.2) should be used. The experimental procedure for crack location is described as follows (Wang and Hadfiled):

1. Observe the ring crack under a microscope with UV light, and at the same time, draw a circle line around the crack (1-2mm diameter) indicating its direction.
2. Put the marked ceramic ball on the location setting tool as shown in figure A1.2.
3. Measure the height (1.17mm) starting from the top surface of the ball and turn the ball in the direction indicated.
4. The height (h) is calculated by equation $h = radius - (radius \times cos\varphi)$ (see figure A1.3). In the present study, $radius = 6.35$mm, contact angle $\varphi = 35.3^0$, hence $h =$

1.17mm.

5. Press the ball into the collet.

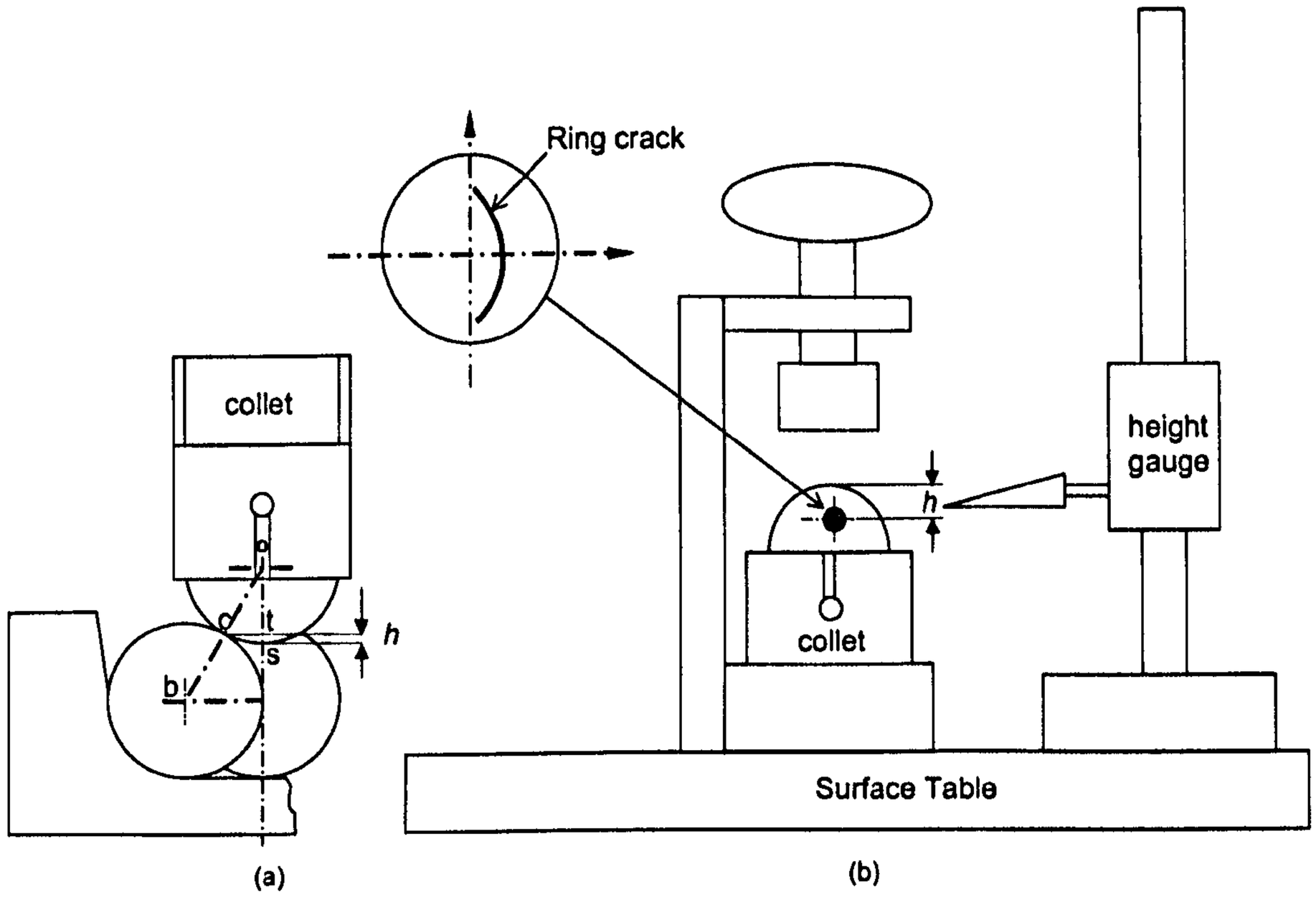

Figure A1.3 Schematic illustration showing how a crack is located on the target position (Wang and Hadfield 2000a)

APPENDIX 2
CONTACT STRESS FIELDS

The stress fields within the Hertzian elastic contact field are well documented (Huber 1904, Lawn and Wilshaw 1975, Timoshenko and Goodier 1951, Johnson 1985) and are given by the following expressions, in cylindrical coordinates r, θ, z:

$$\frac{\sigma_r}{p_m} = \frac{1-2\nu}{2}\left(\frac{a}{r}\right)^2\left[1-\left(\frac{z}{u^{1/2}}\right)^3\right]+\frac{3}{2}\left(\frac{z}{u^{1/2}}\right)^3\frac{a^2u}{u^2+a^2z^2}$$

$$+\frac{3}{2}\frac{z}{u^{1/2}}\left[u\frac{1-\nu}{a^2+u}+(1+\nu)\frac{u^{1/2}}{a}\arctan\left(\frac{a}{u^{1/2}}\right)-2\right] \qquad \text{(A2.1a)}$$

$$\frac{\sigma_\theta}{p_m} = -\frac{1-2\nu}{2}\left(\frac{a}{r}\right)^2\left[1-\left(\frac{z}{u^{1/2}}\right)^3\right]$$

$$-\frac{3}{2}\left(\frac{z}{u^{1/2}}\right)\left[2\nu+\frac{1-\nu}{a^2+u}-(1+\nu)\frac{u^{1/2}}{a}\arctan\left(\frac{a}{u^{1/2}}\right)\right] \qquad \text{(A2.1b)}$$

$$\frac{\sigma_z}{p_m} = -\frac{3}{2}\left(\frac{z}{u^{1/2}}\right)^3\left(\frac{a^2u}{u^2+a^2z^2}\right) \qquad \text{(A2.1c)}$$

$$\frac{\tau_{rz}}{p_m} = -\frac{3}{2}\left(\frac{rz}{u^2+a^2z^2}\right)^3\left(\frac{a^2u^{1/2}}{a^2+z}\right) \qquad \text{(A2.1d)}$$

where

$$u = \frac{1}{2}\left\{(r^2+z^2-a^2)+[(r^2+z^2-a)^2+4a^2z^2]^{1/2}\right\} \qquad \text{(A2.1e)}$$

The principal normal stresses, defined such that $\sigma_1 \geq \sigma_2 \geq \sigma_3$ nearly everywhere, are:

$$\sigma_1 = \frac{\sigma_r + \sigma_z}{2} + \left\{ \left[\frac{(\sigma_r - \sigma_z)}{2} \right]^2 + \tau_{rz}^2 \right\}^{1/2} \qquad \text{(A2.2a)}$$

$$\sigma_2 = \sigma_\theta \qquad \text{(A2.2b)}$$

$$\sigma_3 = \frac{\sigma_r + \sigma_z}{2} - \left\{ \left[\frac{(\sigma_r - \sigma_z)}{2} \right]^2 + \tau_{rz}^2 \right\}^{1/2} \qquad \text{(A2.2c)}$$

The maximum principal shear stress is:

$$\tau_{max} = \frac{1}{2}(\sigma_1 - \sigma_3). \qquad \text{(A2.3)}$$

The angle α between the crack path and specimen free surface is found from:

$$\tan 2\alpha = -\frac{2\tau_{rz}}{(\sigma_1 - \sigma_3)} \qquad \text{(A2.4)}$$

The stress trajectories of σ_2, being a hoop stress, are circles around the z axis. Stress trajectories for σ_1 and σ_3 can be determined from equation (A2.4). The important feature of the indentation stress field for the initiation of a conical fracture in brittle materials is the tensile region in the specimen surface just outside the area of contact. Hertzian cone cracks tend to follow the minimum principal stress σ_3 trajectory since it is orthogonal to the maximum principal stress σ_1.

APPENDIX 3

MECHANICAL AND PHYSICAL PROPERTIES OF SILICON NITRIDE

Table A3.1 Mechanical and physical properties of silicon nitride (Jahanmir 1994)

Properties	Processing route				
	Sintered	Hot-pressed	Reaction-bound	Sintered reaction-bound	Hot isostatic pressing
Density (g/cm^3)	3.2	3.2	2.5	3.3	3.2
Flexural strength (MPa)	600	800	210	825	1000
Fracture toughness ($MPa\ m^{1/2}$)	4.5	5.0	3.6	-	6.0
Elastic modulus (GPa)	276	317	165	297	310
Poisson's ratio	0.24	0.28	0.22	0.28	0.28
Hardness (GPa)	14	20	10	19	20
Thermal expansion coefficient ($\times 10^{-6}\ ^oC$)	3.4	3.2	2.8	3.5	3.5
Thermal conductivity ($W\ m^{-1}\ ^oC^{-1}$)	28	30	6	30	32

APPENDIX 4

BOUNDARY ELEMENT METHOD

A4.1 INTRODUCTON

The boundary element method (BEM) also known as the boundary integral equation method is now widely used in many engineering disciplines as an alternative numerical technique to the finite element method (Brebbia at al 1984, Trevelyan 1994). The boundary integral equation method was proposed for the fluid applications in the 1950's, and was applied to mechanical analysis in the late 1960's. The boundary element method emerged as a more generally applicable technique during the 1970's, and has been developed substantially in the following years. The attraction of the boundary element method can be largely attributed to the reduction in the dimensionality of the problem; for three-dimensional problems, only the surface of the domain needs to be discretized. This means that the boundary element analysis results in a substantial reduction in data preparation. Furthermore, this simpler description of the body means that region of high stress concentration can be modelled more efficiently as the necessary high concentration of grid point is confined to one less dimension. Another important feature of the boundary element formulation is that it provides a continuous modelling of the interior since no discretization of the interior is required; this leads to a high resolution of interior stresses and displacements (Brebbia and Dominguez 1992).

A4.2 THE BOUNDARY ELEMENT FORMULATION IN ELASTICITY

A4.2.1 Applying the reciprocal theorem

The direct boundary element formulation for elastostatic problems can be derived from the reciprocal theorem, or Betti's reciprocal theorem. The reciprocal theorem states that, for any two possible loading conditions which are applied independently to a structure such that it remains in equilibrium, the work done by taking the forces from the first load case and the displacements from the secondary

load case is equal to the work done by the forces from second load case on the displacements from the fist load case. The reciprocal theorem can be expressed as

$$\int_{\Omega} b^{*} u d\,\Omega + \int_{\Gamma} t^{*} u d\,\Gamma = \int_{\Omega} b u^{*} d\Omega + \int_{\Gamma} t u^{*} d\Gamma \,, \quad \text{(A4.1)}$$

where the domain Ω with boundary Γ and the domain Ω^{*} with boundary Γ^{*} encompass the states (u, t, b) and (u^{*}, t^{*}, b^{*}) respectively, u and u^{*} are displacements; t and t^{*} are tractions and b and b^{*} are body forces. A special case in which there are no body forces in one state (real load case), i.e. b = 0, is now considered. So, the reciprocal theorem becomes

$$\int_{\Omega} b^{*} u d\,\Omega + \int_{\Gamma} t^{*} u d\,\Gamma = \int_{\Gamma} t u^{*} d\Gamma \quad \text{(A4.2)}$$

We can choose the right form of the complementary load case to make the equations much simpler, and to lead to the boundary integral equation.

A4.2.2 Choosing the complementary load case

The load case (u, t, b) represents the real loading for which we are trying to find the stresses and displacements. The load case (u^{*}, t^{*}, b^{*}) is completely arbitrary and can be chosen carefully to make the equations much simpler. It is very helpful to choose the complementary load case a type of point force. The form the point force takes a Dirac delta function, which is of a mathematical convenience than an engineering reality. It represents a point force acting over an infinitesimally small area at some position p in the domain Ω. The Dirac delta function for all points y in the domain Ω is defined as follows

$$\Delta(p,y) = \begin{cases} 0 & y \neq p \\ \infty & y = p \end{cases} \quad \text{(A4.3)}$$

$$\int_{\Omega} \Delta(p, y) d\Omega = 1 \quad \text{(A4.4)}$$

The volume integral term in equation (A4.2) can be removed using this choice of complementary load case. This integral term can be rewritten as

$$\int_{\Omega} \Delta(p, y) u d\,\Omega$$

Since the integral of the Dirac delta function is equal to 1, and the value of the displacement u at p is u(p), the entire volume integral reduce to

$$\int_{\Omega} \Delta(p, y) u d\Omega = u(p)$$

Hence, the equation (A4.2) becomes

$$u(p) + \int_{\Gamma} t^{*} u d\Gamma = \int_{\Gamma} t u^{*} d\Gamma \qquad \text{(A4.5)}$$

A4.2.3 The boundary integral equation

The direct boundary element formulation relating the boundary displacements to boundary tractions can be obtained from equation (A4.5) by considering the limiting process as an internal point goes to the boundary. Introducing a multiplier $c(p)$, which depends on the boundary geometry at the point force, we can write (Brebbia at al 1984)

$$c(p) u(p) + \int_{\Gamma} t^{*} u d\Gamma = \int_{\Gamma} t u^{*} d\Gamma \qquad \text{(A4.6)}$$

The multiplier $c(p) = 1$ when the fictitious point is completely inside the domain, c(p) = 0 when it is completely outside the domain, and c(p) = 0.5 on a smooth boundary. It can be difficult to calculate the c(p) term analytically, and it is often best to avoid this calculation by using the row-sum method to find the diagonal terms in the influence matrix.

A4.3 THE FUNDAMENTAL SOLUTIONS

As shown in the previous section, the existence of the point force solutions is crucial important in the formulation of boundary element method. The choice of the Dirac delta function eliminates the volume integral in the reciprocal theorem statement, and therefore leads the way to the boundary-only description. In the following discussion some of the important fundamental solutions for the problems are given.

The traction and displacement components at any field point y when a point force of this type is applied at a source point p can be obtained from classical theory. The most versatile fundamental solutions known as Kelvin's solution (Brebbia, 1984), which describe the displacement and traction fields (u^{*} and t^{*}) in infinite materials as a result of this applied load, is given by the following expressions.

For two-dimensional problems:

$$u_{ij}^{*} = \frac{1}{8\pi\mu(1-\nu)}\left[(3-4\nu)\ln\frac{1}{r}\delta_{ij} + r_i r_j\right], \tag{A4.7}$$

$$t_{ij}^{*} = \frac{-1}{4\pi\mu(1-\nu)r}\left\{[(1-2\nu)\delta_{ij} + 2r_i r_j]\frac{\partial r}{\partial n} - (1-2\nu)(r_i n_j - r_j n_i)\right\}. \tag{A4.8}$$

And for three-dimensional problems:

$$u_{ij}^{*} = \frac{1}{16\pi\mu(1-\nu)r}\left[(3-4\nu)\delta_{ij} + r_i r_j\right], \tag{A4.9}$$

$$t_{ij}^{*} = \frac{-1}{8\pi\mu(1-\nu)}\left(\frac{1}{r^2}\right)\left\{\frac{\partial r}{\partial n}((1-2\nu)\delta_{ij} + 3r_i r_j) - (1-2\nu)(r_i n_j - r_j n_i)\right\} \tag{A4.10}$$

where μ is the shear modulus and r is the distance between the source point p and the field point y. r_i and r_j are the components of r in the i and j directions. δ_{ij} is simply a multiplier which takes the value 1 when $i = j$ and 0 when $i \neq j$.

A4.4 NUMERICAL DISCRETIZATION

The boundary integral equation (A4.6) describes the displacement and traction distributions around the boundary in terms of the integrals around the boundary Γ of the fundamental solutions. The integrations cannot be solved analytically except for special cases and therefore a numerical solution is required. The boundary Γ is divided into N boundary elements, so that the equation (A4.6) becomes (Brebbia at al 1984)

$$c(p)u(p) + \sum_{n=1}^{n} \int_{\Gamma_n} t^{*} u d\Gamma_n = \sum_{n=1}^{n} \int_{\Gamma_n} u^{*} t d\Gamma_n \tag{A4.11}$$

On each element, the unknown displacement field u and the traction t field are approximated using interpolation functions. So for an element having m nodes, the displacement u at any point on the element can be found from the values of displacement (u_1, u_2, ..., u_m) at the modes:

$$u = \phi_1 u_1 + \phi_2 u_2 + \ldots + \phi_m u_m$$

where the ϕ terms are the interpolation functions. The u can be written in the vector form:

$$u = \Phi^T \mathbf{u} \qquad \text{(A4.12)}$$

where $\Phi^T = [\phi_1, \phi_2, \ldots, \phi_m]$ and $\mathbf{u}^T = [u_1, u_2, \ldots + u_m]$. A similar equation for the traction can be expressed in:

$$t = \Phi^T \mathbf{t} \qquad \text{(A4.13)}$$

Replacing u and t in equation (A4.11) by the vector forms of equations (A4.12) and (A4.13), then the equation (A4.11) can be rewritten as follows (Trevelyan 1994).

$$c(p)u(p) + \sum_{n=1}^{n} \left(\int_{\Gamma_n} t^* \Phi^T d\Gamma_n \right) \mathbf{u} = \sum_{n=1}^{n} \left(\int_{\Gamma_n} u^* \Phi^T d\Gamma_n \right) \mathbf{t} \qquad \text{(A4.14)}$$

In the equation A4.14, t^* and u^* are known for any pair of a source point p and a field point as they are simply fundamental solutions as given in equations A4.7 to A4.10. The Φ vectors are simple functions based on the position of a point on an element. These functions are able to be integrated. The integrals of the fundamental solutions u^* and t^*, multiplied by the interpolation functions, will be a series of coefficients which multiply the nodal values of displacement and traction. These coefficients are called h^*_{ij} for the results of integrating the t^* type fundamental solution and g_{ij} for the u^* type function. The i refers to the node at the source point, and the j refers to the node at the field point. When the integrations are performed over every element for any position of the source point, a simple equation relating all the nodal values of displacement and traction by a series of coefficients will be given. Having defined following expression (Trevelyan 1994).

$$h_{ij} = \begin{cases} h^*_{ij} + c(p) & i = j \\ h^*_{ij} & i \neq j \end{cases},$$

the whole system of equations can be written in the simple form

$$\mathbf{H}\,\mathbf{u} = \mathbf{G}\,\mathbf{t} \qquad \text{(A4.15)}$$

$$\begin{bmatrix} h_{11} & h_{12} & . & h_{1n} \\ h_{21} & h_{22} & . & h_{2n} \\ . & . & . & . \\ h_{n1} & h_{n2} & . & h_{nn} \end{bmatrix} \begin{bmatrix} u_1 \\ u_2 \\ . \\ u_n \end{bmatrix} = \begin{bmatrix} g_{11} & g_{12} & . & g_{1n} \\ g_{21} & g_{22} & . & g_{2n} \\ . & . & . & . \\ g_{n1} & g_{n2} & . & g_{nn} \end{bmatrix} \begin{bmatrix} t_1 \\ t_2 \\ . \\ t_n \end{bmatrix}$$

$$\mathbf{H} \qquad \mathbf{u} \quad = \quad \mathbf{G} \qquad \mathbf{t}$$

These matrices **H** and **G** are called the influence matrices, and the terms inside them influence coefficients.

The boundary integral equation has been reduced to a matrix form (A4.15). To solve the matrix equation, the n boundary conditions need to specify to reduce the n unknowns. This can be done by specifying the displacements and tractions.

A4.5 THE DUAL BOUNDARY ELEMENT METHOD

The dual boundary element method (Portela et al. 1992) is based on dual equations, which are the displacement and traction boundary integral equations. The dual boundary element method allows fracture mechanics problems to be solved when the two surface of the crack are part of the same zone. The advantages are: (1) the interface line or surface, which takes time to define as part of model, is removed; (2) the crack can extend an arbitrary length and direction in order to analyse the next step in crack propagation. The use of the dual boundary element method in three-dimensional crack growth analysis was presented by Mi and Aliabadi (1992), Mi and Aliabadi (1994) and Mi (1996).

The displacement equation is the same as the boundary integral equation (Cruse 1977)

$$c(p)u(p) + \int_{\Gamma} t^{*} u d\Gamma = \int_{\Gamma} t u^{*} d\Gamma \quad . \qquad \text{(A4.16)}$$

The traction equation which is formed over one set of nodes defining the crack surface is the derivative of this equation

$$\frac{1}{2} t_j(p) + n_i(p) \int_{\Gamma} T^{*}_{kij} u_k d\Gamma = n_i(p) \int_{\Gamma} U^{*}_{kij} k_k d\Gamma \quad . \qquad \text{(A4.17)}$$

The term T^* is the derivation of the traction fundamental solution t^* and U^* is the derivation of the displacement fundamental solution u^*. Equations (A4.16) and (A4.17) constitute the basis of the dual boundary element method.

APPENDIX 5

CONTACT ANALYSIS

Contact analysis is performed using a boundary element method based computer modelling package BEASY (Computational Mechanics BEASY 1998). Figure A5.1 illustrates the model of a ceramic upper ball contacting with a steel lower ball. This model is axisymmetric, which simplifies the geometric requirements to a plane model, rotated about the load axis. The reason for this consideration is that the friction coefficient is extremely low in lubricated rolling contact and hence its influence on the stress field is limited. Lubrication regime analysis indicates that a full film exists, which implies that a frictionless model is valid.

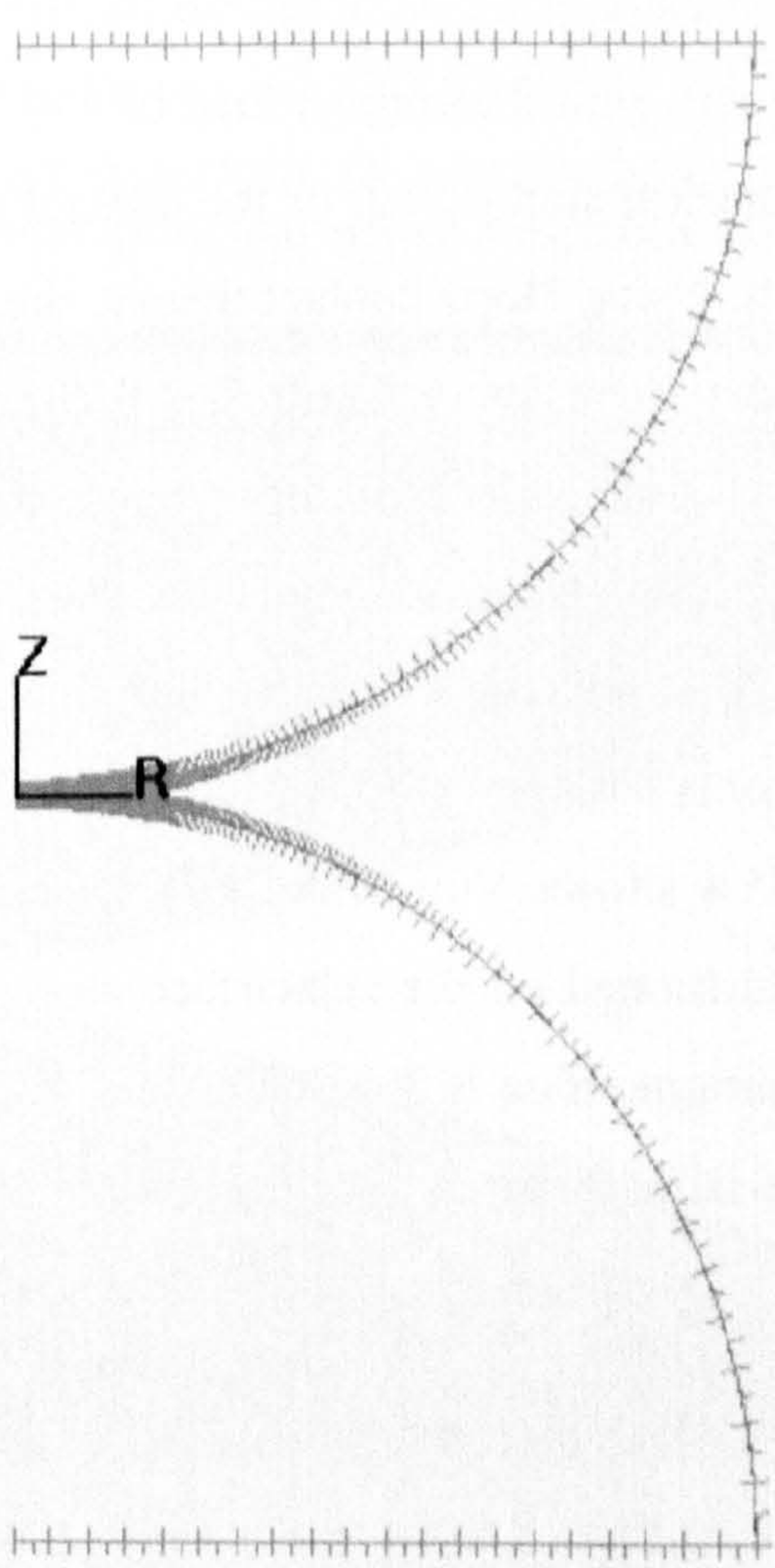

Figure A5.1 The axisymmetric model for contact analysis

The main objective for development by the analytical models of the contact problem is to obtain stress fields and displacements around the contact zone. The displacements are extracted from a specified area and applied to a three-dimensional contact volume model at a later stage. The accuracy of the numerical calculation at this stage is very important to eliminate any accumulated errors. To determine the numerical error, Hertz theory is used to validate the boundary element model.

First of all, the influence of contact load on the maximum contact stress and contact radius is studied. Numerical calculations with different load are compared with the theoretical calculations using Hertz theory and the numerical calculation results are very close to analytical results. For example, the error is approximately 0.15 percent for the maximum contact stress, and the error is 0.49 percent for contact radius. This means that the BEM model can provide highly accurate results.

Figures A5.2 and A5.3 demonstrate the maximum principal stress and direct radial stress contours with the contact load of 490 N. The maximum tensile stress is positioned on a surface slightly out of the contact circle, and it reaches a maximum value of 860 MPa. Using Hertz contact theory, the analytical result with this load is 857 MPa. The numerical contact radius is 0.205 mm for this load; the analytical result is 0.204 mm. Comparison of both calculated results shows that the numerical calculation result is very consistent with the analytical result. The maximum compressive stress is 5992 MPa and the analytical result for this load is 5589 MPa. Therefore the error is 0.05 percent only.

Figure A5.4 shows Von-Mises (VM) stress contour. The maximum Von-Mises stress is positioned on the subsurface along the load axis at a depth of 0.12 mm and the maximum value is 3.44 GPa. The shear stresses contours are shown in figure A5.5. The BEM predicts that the maximum shear stress is at 45° from the centre of contact, which is consistent with the analytical analysis in terms of Hertz contact theory.

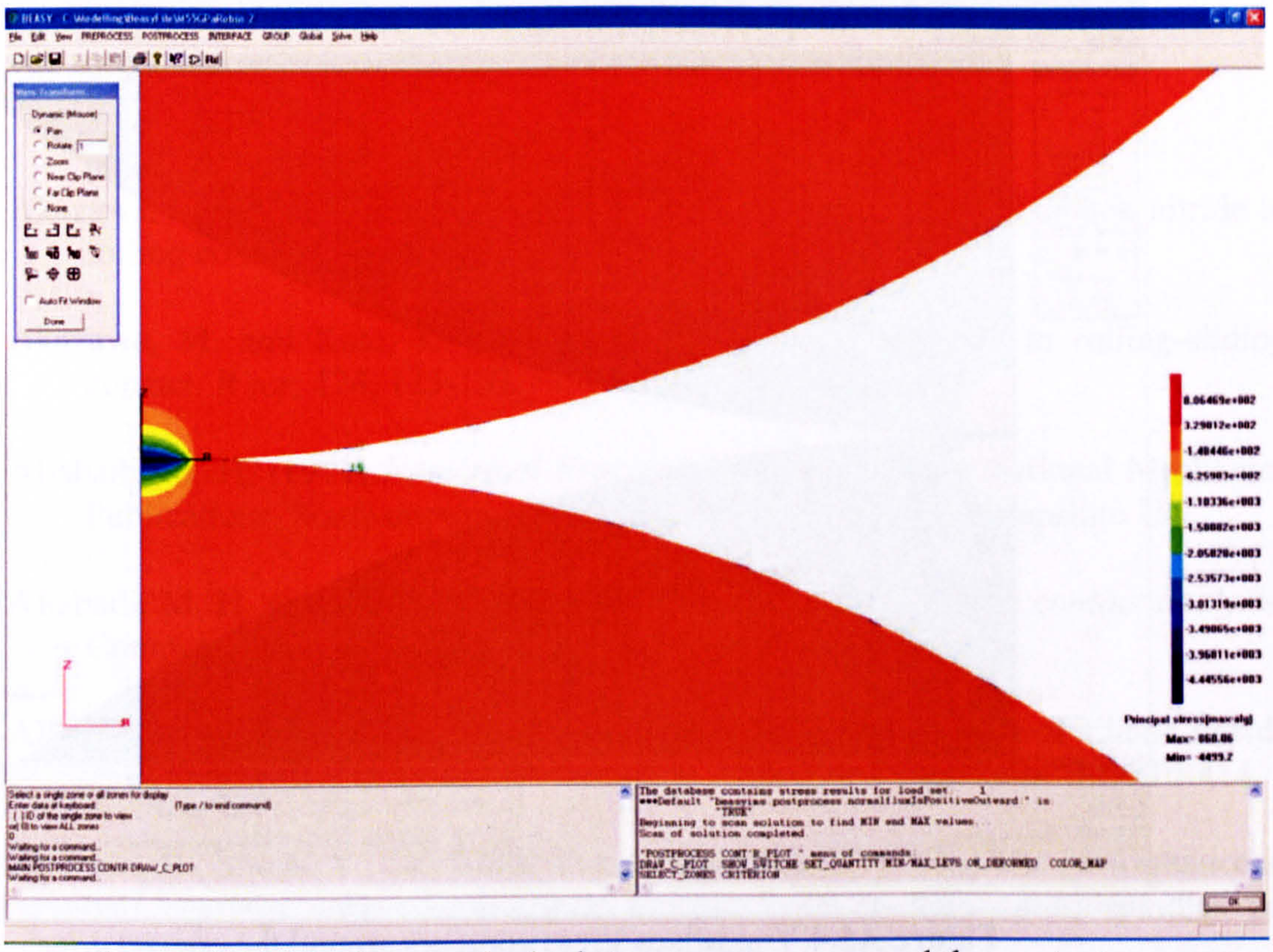

Figure A5.2 Maximum principal stress contours around the contact zone

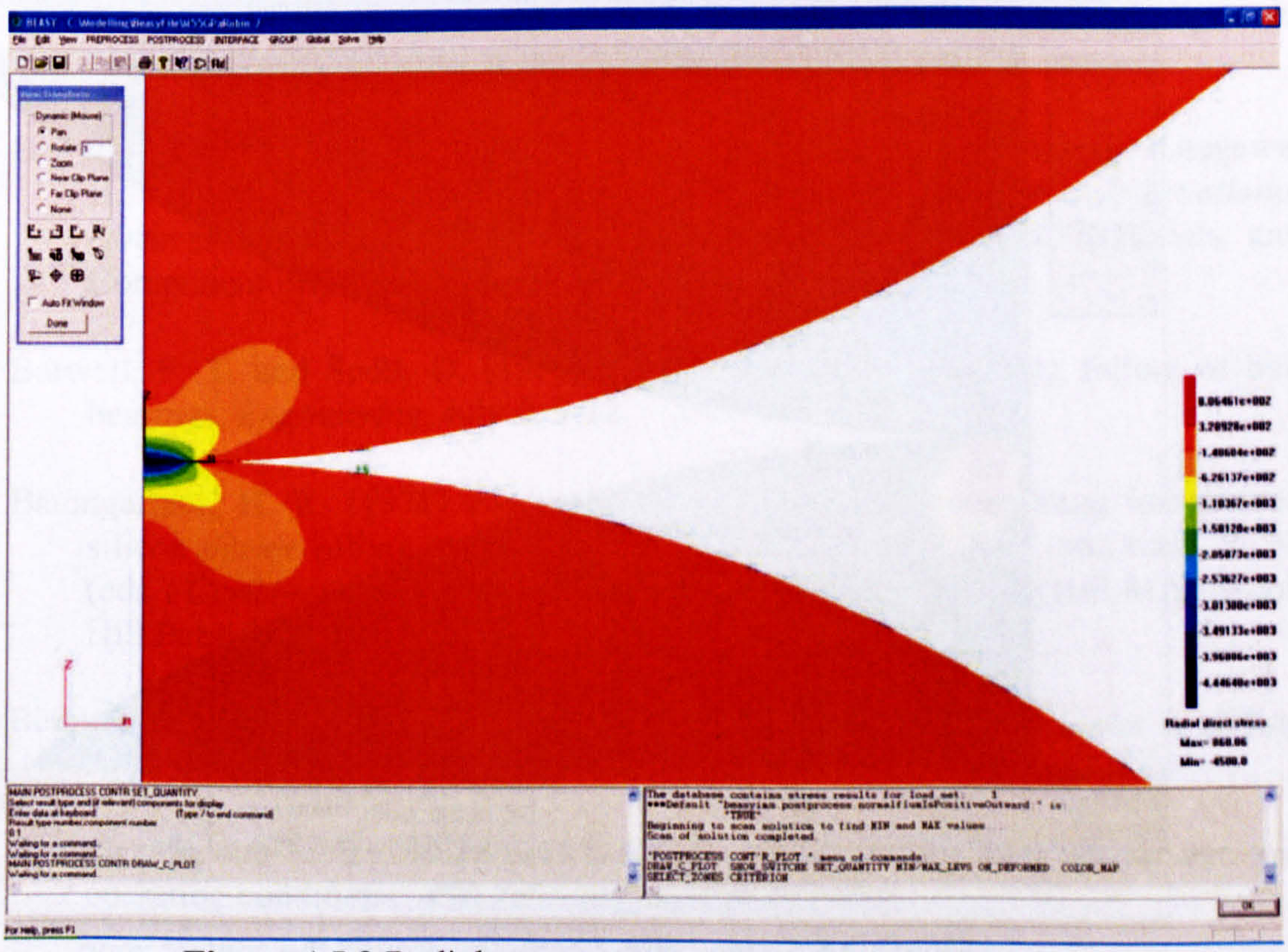

Figure A5.3 Radial stress contours around the contact zone.

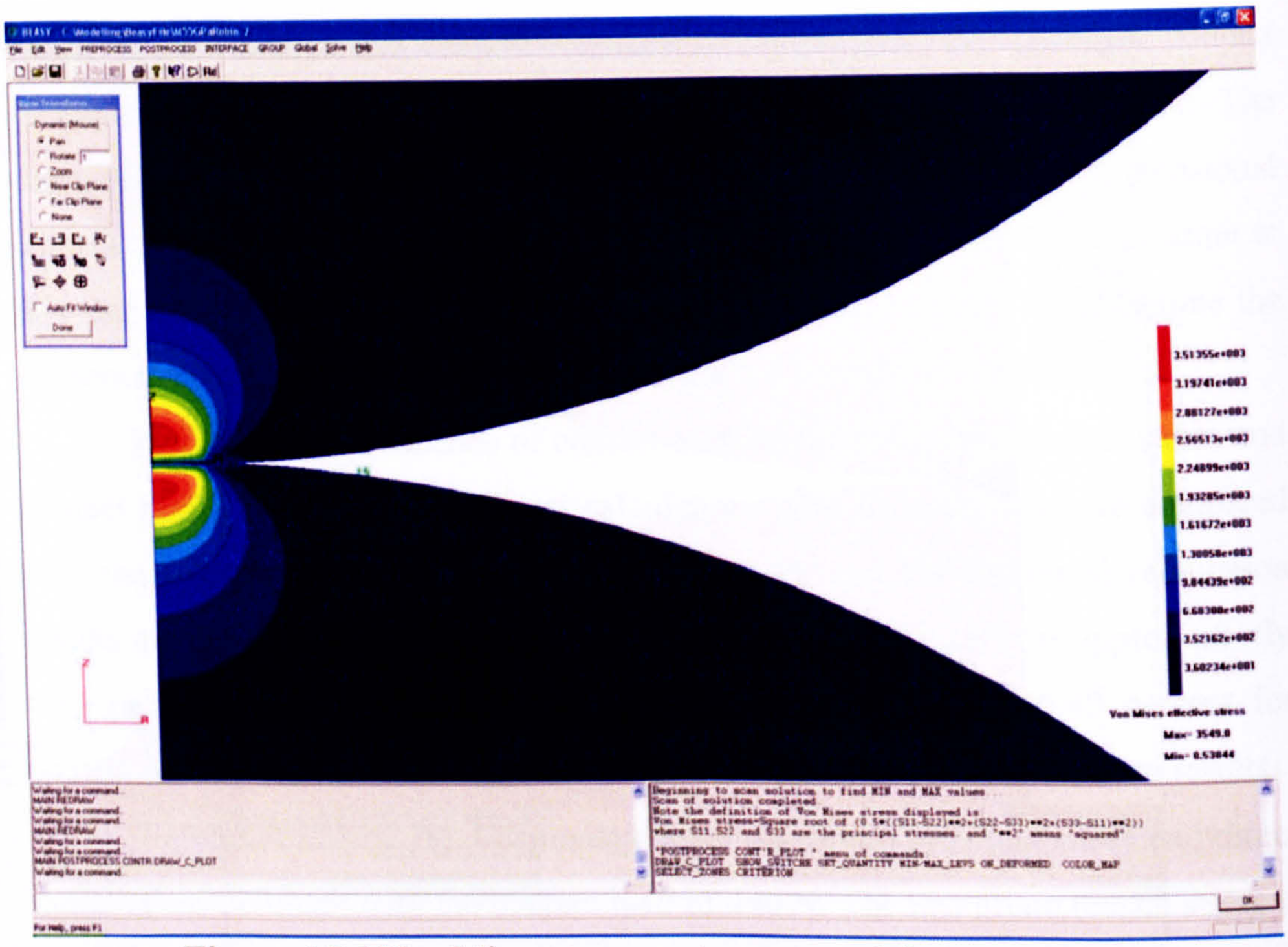

Figure A5.4 Von Mises stress contours around the contact zone.

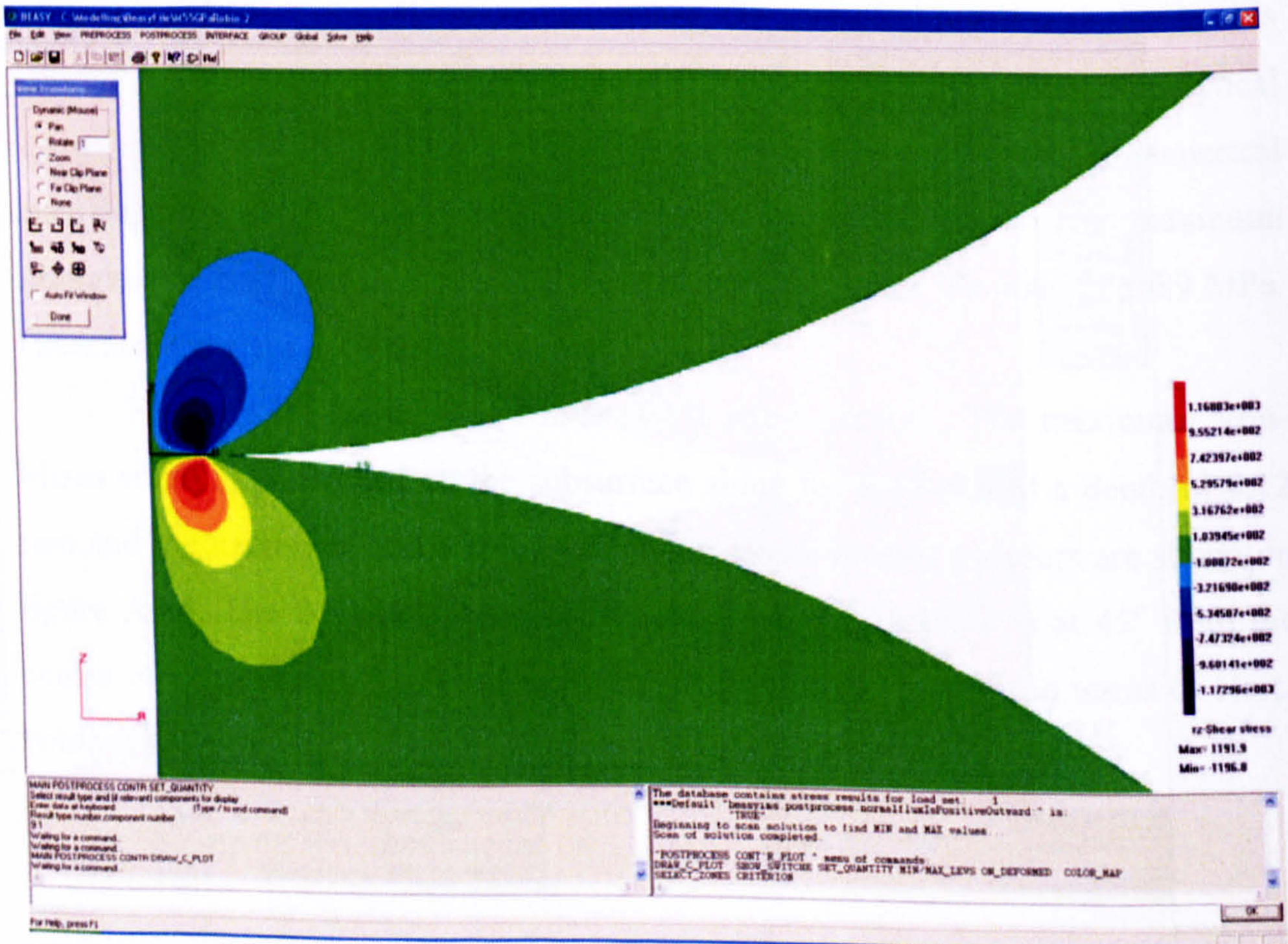

Figure A5.5 Shear stress contours around the contact zone.

REFERENCES

Akazawa, M., Kato, K. and Umeya, K. (1986) Wear properties of silicon nitride in rolling contact. *Wear*, 110, 285-293

Akazawa, M. and Kato, K. (1988) Wear properties of Si3N4 in rolling-sliding contact. *Wear,* 124, 123-132.

Aliabadi, M. H. (1991) *Numerical Fracture Mechanics,* Computational Mechanics Publications, Southampton UK and D. P. Rooke, R. A. E. Hampshire UK.

Aliabadi, M. H. and Brebbia, C. A. (1993) *Boundary elements in contact analysis,* Computational Mechanics Publications.

Allen, D. L. (1994) Effect of composition and physical properties of silicon nitride on rolling wear and fatigue performance. *Tribology Transaction*, 37, 410-414.

Aramaki, H., Shoda, Y., Morishita, Y. and Sawamoto, T. (1988) The performance of ball bearings with silicon-nitride ceramic balls in high speed spindles for machine tools. *J. of Tribology,* 110, 693-698.

Andersson, T., Fredriksson, B. and Persson, B. G. A. (1980) In *New Developments in Boundary Element Methods*. Computational Mechanics Publications.

Bar-On, I. and Beals, J. T. (1990) Fatigue in silicon nitride bend bars. In: Kitagawa, H. and Tanaka, T. (eds.) *Fatigue 90: Proceedings of 4th International conference on fatigue and fatigue thresholds*. Edgbaston, Materials and Component Engineering Publications. 793-798

Barwell, F. T. and Scott, D. (1956) Effect of lubricant on pitting failure of ball bearings. *Engineering*, July 6, 9-12.

Baumgartner, H. R. (1974) Evaluation of roller bearings containing hot-pressed silicon nitride rolling elements. In: Burke, J. J., Gorum, A. E. and Katz, R. N. (eds.) *Ceramics for high performance applications*. Chestnut Hill MA, Brook Hill Publishing. 713-727.

Bethune, B. J. (1971) The surface cracking of glassy polymers under a sliding spherical indenter. *J. Mater. Sci.* 11, 199-205.

Bhushan, B. and Sibley, L. B. (1981) Silicon nitride rolling bearings for extreme operating conditions. *ASL Transactions,* 25, 417-428.

Bower, A. F. (1988) The influence of crack face friction and trapped fluid on surface initiated rolling-contact fatigue cracks. *Journal of Tribology; Transactions of the ASME*, 110(4), 704-711.

Braza, J. F., Cheng, H. S. and Fine, M. E. (1989a) Silicon nitride wear mechanisms: rolling and sliding contact. *Tribology Transactions*, 32(4), 439-446.

Braza, J. F., Cheng, H. S., Fine, M. E., Gangopadhyay, A. K., Keer, L. M. and Worden, R. E. (1989b). Mechanical failure mechanisms in ceramic sliding and rolling contacts. *Tribology Transactions*, 32(1), 1-8.

Brebbia, C. A., Tells, J. C. F. and Wrobel, L. C. (1984) *Boundary element Techniques: Theory and Applications in Engineering*. Springer-Verlag.

Brebbia, C. A. and Dominguez, J. 1992. *Boundary elements: An introductory course.* Southampton UK and Boston USA, Computational Mechanics Publications.

Bryant, M. D., Miller, G. R. and Keer, L. M. (1984) Line contact between a rigid indenter and a damaged elastic body. *Q. J. Mech. Appl. Math. 37(3)*, 468-478.

Burrier, H. I. (1996) Optimising the structure and properties of silicon nitride for rolling contact bearing performance. *Tribology Transactions*, 39(2), 276-285.

Carter, T. L. and Zaretsky, E. V. (1960) Rolling contact fatigue life of a crystallized glass ceramic. *NASA TN D-259.*

Chao, L-Y., Lakshminarayanna, R., Iyer, N., Lin, G.-Y. and Shetty, D. K. 1998. Transient wear of silicon nitride in lubricated rolling contact. *Wear*, 223, 58-65.

Chaudhri, M. and Phillips, M. A. (1990) Quasi-static indentation cracking of thermally tempered soda-lime glass with spherical and Veckers indenters. *Phil. Mag. A* 62(1), 1-27.

Chen, S. Y., Farris, T. N. and Chandrasekar, S. (1995) Contact mechanics of Hertzian cone cracking. *International Journal of Solids and Structures*, 32, 329-340.

Computational Mechanics BEASY (1998) *BEASY user guide*. Southampton UK.

Cruse, T. A. (1977) Mathematical formation of the boundary integral equation methods in solid mechanics. *Report No. AFOSR-TR-77-1002.* Pratt and Whitney Aircraft Group.

Cundill. R. T. (1990) Rolling element bearings into 21st century, in: Proceedings of IMechE Seminar, London 1990.

Cundill, R T. (1992) Material selection and quality for ceramic rolling elements, 4*th international symposium on ceramic materials & components for engines*.

Cundill, R. T. (1997) Impact resistance of silicon nitride balls, in: Proceedings of the Sixth *International Symposium on Ceramic Materials & Components for*

Engines, Japan Fine Ceramics Association, Tokyo, pp556-561.

Dauskardt, R. H., James, M. R., Porter, J. R. and Ritchie, R. O. (1992) Cyclic fatigue crack growth in a SiC-whisker-reinforced alumina ceramic composite: long crack and small crack behaviour. *J. Am. Ceram. Soc.*, 75(4), 759-771.

Fleming, J. R. and Suh, N. P. (1977) Mechanics of crack propagation in delamination wear. *Wear*, 44, 39-56.

Frank, F. C. and Lawn, B. R. (1967) On the theory of Hertzian fracture. *Proc. Roy. Soc. A,* 299, 291-306.

Fujiwara, T., Yoshioka, T., Kitahara, T., Koizumi, S., Takebayashi, H. and Tada, T. (1989) Study on load rating property of silicon nitride for rolling bearing material. *Journal of JSLE International Edition* 10, 81-86.

Galbato, A. T., Cundill, R. T. and Harris, T. A. (1992) Fatigue life of silicon nitride balls. *Lubrication Engineering,* 48(11), 886-894.

Hadfield, M. (1998) Failure of silicon nitride rolling elements with ring crack defects. *Ceramics International,* 24, 379-386.

Hadfield, M. and Stolarski, T. A. (1994a) Observations of delamination fatigue on pre-cracked ceramic elements in rolling contact. *Ceramics International,* 21, 125-130.

Hadfield, M., Tobe, S. and Stolarski, T. A. (1994b) Subsurface crack investigation on delaminated ceramic elements. *Tribology International,* 27, 359-367.

Hadfield, M., Stolarski, T. A. and Cundill, R. T. (1993a) Failure modes of ceramics in rolling-contact. *Proc. R. Soc. London, Ser. A,* 443, 607-621.

Hadfield, M., Stolarski, T. A., Cundill, R. T. and Horton, S. (1993b) Failure modes of ceramic elements with ring-crack defects. *Tribology International,* 26(3), 157-164.

Hadfield, M. and Stolarski, T. A. (1993c) Failure modes of pre-cracked ceramic elements under rolling contact. *Wear,* 169, 69-75.

Hadfield, M. and Stolarski, T. A. (1995) The effect of the test machine on the failure mode in lubricated rolling contact of silicon nitride. *Tribology International*, 28(6), 377-382.

Hamburg, G., Cowley, P. and Valori, R. (1981) Operation of an all-ceramic main-shaft roller bearing in J-402 gas-turbine engine. *J. ASME, Lubrication Engineering,* 37, 407-415.

Hamilton, G. M. and Goodman, L. E. (1966) The stress field created by a circular sliding contact. *Journal of applied mechanics*, 33, 371-376.

Hills, D. A. and Ashelby, D. W. (1979) A fracture mechanics approach to rolling contact fatigue. *Tribology International*, 115-119.

Hsu, S. M. and Shen, M. (2004) Wear prediction of ceramics. *Wear*, 256, 867-878.

Hu, S., Chen, Z. and Mecholsky, J. J. (1996) On the Hertzian fatigue cone crack propagation in ceramics. *International Journal of Fracture*, 79, 295-307.

Huber, M. T. (1904) Zur Theorie der Berührung fester elastische körper. *Ann. Phys. Lpz.*, 14, 153.

Ichikawa, M., Takamatsu, T., Matsuo, T., Okabe, N. and Abe, Y. (1995a) Intra-Ball and Inter-Ball Variability of Ring Crack Initiation Load of Silicon-Nitride Bearing Balls. *Jsme International Journal Series a-Mechanics and Material Engineering*, 38, 231-235.

Ichikawa, M., Takamatsu, T., Shindou, N., Okabe, N. and Abe, Y. (1995b) Ring crack initiation load of silicon nitride bearing balls. *JSME International Journal, Series A: Mechanics and Material Engineering*, 38, 226-230.

Irwin, G. R. (1957) Analysis of stresses and strains near the end of a crack traversing a plate. *Trans. ASME J. Appl. Mech.*, 24, 361-364.

Jahanmir, S. (1994) Friction and Wear of Ceramics, Marcel Dekker, Inc. New York.

Johnson, K. L. (1985) *Contact Mechanics*, Cambridge University Press, Cambridge.

Kalin, B. and Vizintin, J. (2004) Advantages of using the ball-on-flat device in rolling contact testing of ceramics. *Journal of the European Ceramic Society* 24, 11-15.

Kaneta, M. and Murakami, Y. (1987) Effects of oil hydraulic pressure on surface crack-growth in rolling sliding contact. *Tribology International*, 20, 210-217.

Katz, R. N. and Hannoosh, J. G. (1987) Ceramics for high performance rolling element bearing: a review and assessment. *Materials & Design*, 8, 108-112.

Keer, L. M. and Bryant, M. D. (1983) A pitting model for rolling-contact fatigue. *Journal of Lubrication Technology-Transactions of the ASME*, 105, 198-205.

Keer, L. M., Bryant, M. D. and Haritos, G. K. (1982) Subsurface and surface cracking due to Hertzian contact. *Journal of Lubrication Technology-Transactions of the ASME*, 104(3), 347-351.

Keer, L. M. and Worden, R. E. (1990) A qualitative model to describe the

microchiping wear mode in ceramic rollers. *Tribology Transactions*, 33, 411-417.

Kikuchi, K., Yoshioka, T., Kitahara, T., Ozaki, K., Nakayama, K. and Fujiwara, T. (1984) Rolling contact fatigue life of ceramics for rolling bearing materials. *J. JSLE Int. Ed.*(5), 137-142.

Kim, S. S., Kato, K., Hokkirigawa, K. and Abe, H. (1986) Wear mechanism of ceramic materials in dry rolling friction. *Transactions of the ASME*, 108, 522-526

Lawn, B. R. (1967) Partial cone crack formation in a brittle material loaded with a sliding spherical indenter. *Proc. R. Soc. Lond.*, A299, 307-316.

Lawn, B. R. (1998) Indentation of ceramics with spheres: a century after Hertz. *J. Am. Ceram. Soc.*, 81, 1977-1994.

Lawn, B. R. and Wilshaw, T. R. (1975) Indentation fracture: Principles and application. *J. Mater. Sci.*, 10, 1049-81.

Lee,W. E. and Rainforth, W. M. (1994) *Ceramic microstructures: property control by processing*, Chapman & Hall, London.

Li, Y. Z. and Hills, D. A. (1991) The Hertzian cone crack. *Journal of Applied Mechanics-Transactions of the ASME*, 58, 120-127.

Lucek, J. W. (1990) Rolling wear of silicon nitride bearing materials. *ASME paper No.*, 90-GT-165.

Lucek, J. W. and Cowley, P. E. (1978) Investigation of the use of ceramic material in aircraft engine bearings. *Dept. of Navy, Code AIR-52032A*. Washington.

Man, K. W. (1994) *Contact Mechanics Using Boundary Elements*, Computational Mechanics Publications, Southampton UK and Boston USA.

Mi, Y. (1996) Three-dimensional analysis of crack growth. *Topics in Engineering*, 28, Computational Mechanics Publ., Southampton, UK.

Mi, Y. and Aliabadi, M. H. (1992) Dual boundary element method for three-dimensional fracture mechanics analysis. *Engineering Analysis with Boundary Elements*, 10, 161-171.

Mi, Y., and Aliabadi, M. H. (1994) Three-dimensional crack growth simulation using BEM. *Computer & Structure*, 52, 871-878

Miner, J. R., Grace, W. A. and Valori, R. (1981) A demonstration of high-speed gas turbine bearing using silicon nitride rolling elements. *Lubrication Engineering*, 37(8), 473-478.

Morrison, F. R., McCool, J. I. and Yonushonis, T. M. (1984) The load-life relationship for M50 steel bearings with silicon nitride ceramic balls. *J. of ASLE, Lubrication Engineering*, 40, 153-159.

Mouginot, R. and Maugis, D. (1985) Fracture indentation beneath flat and spherical punches. *J. Mater. Sci.* 20, 4354-76.

Murakami, Y., Kaneta, M. and Yatsuzuka, H. (1985) Analysis of surface crack-propagation in lubricated rolling-contact. *ASLE Transactions,* 28, 60-68.

Niku, S. M., Adey, R. A. and Baynham, J. M. W. (1991) In *Boundary Element Technology VI*(Ed, Brebbia, C. A.) Computational Mechanics Publications.

Ohgushi, K. and Ichikawa, M. (1996) Fracture mechanics study of ring crack initiation in ceramics by sphere indentation. *JSME International Journal, Series A: Mechanics and Material Engineering* 39(4), 489-495.

Parker, R. and Zaretsky, E. V. (1975) Fatigue life of high-speed ball bearings with silicon nitride balls. *Trans. of the ASME, J. of Lub. Tech.* (July), 350-357.

Portela, A., Aliabadi, M. H. and Rooke, D. P. (1992) The dual boundary element method: effective implementation for crack problems. *Int. J. Num. Meth. in Eng.,* 23, 1269-1287.

Reece, M. and Guiu, F. (1991) Indentation fatigue of high-purity alumina in fluid environments. *J. Am. Ceram. Soc.*, 74(1), 148-154.

Ritchie, R. O. and Dauskardt, R. H. (1991) Cyclic fatigue of ceramics - a fracture mechanics approach to subcritical crack-growth and life prediction. *Nippon Seramikkusu Kyokai Gakujutsu Ronbunshi - Journal of the Ceramic Society of Japan*, 99(10), 1047-1062.

Roesler, F. C. (1956) Brittle fracture near equilibrium. *Proc. Phys. Soc. Lond.* B69, 981-1012.

Rosenfield, A. R. (1980) A fracture mechanics approach to wear. *Wear*, 61, 125-132.

Scott, D., Blackwell, J. and McCullagh, P. J. (1971) Silicon nitride as a rolling bearing material - A preliminary assessment. *Wear*, 17, 73-82.

Scott, D. and Blackwell, J. (1973) Hot pressed silicon nitride as a rolling bearing material - A preliminary assessment. *Wear*, 24, 61-67.

Thoma, K., Rohr, L., et al. (2004) Material failure mechanisms of hybrid ball bearings with silicon nitride balls. *Tribology International* 37, 463-471.

Thomsen, N. B. and Karihaloo, B. L. (1996) Subsurface and surface cracks under contact loading in transformation-toughened ceramics. *J. Mech. Phys. Solids,*

44(2), 207-231.

Tillett, J. P. A. (1956) Fracture of glass by spherical indenters. *Proc. Phys. Soc.* B69, 47-54.

Timoshenko, S. and Goodier, J. N. (1951) *Theory of Elasticity,* McGraw-Hill, New York.

Tourret, R. and Wright, E. P. (1977) *Rolling contact fatigue: performance testing of lubricants,* Heyden & son LTD.

Trevelyan, J. (1994) *Boundary elements for engineers: theory & application,* Southampton UK , Computational Mechanics Publications.

Ueda, K. (1989) Deformation and fracture of ceramics in contact stress field. *Journal of Japanese Society of Tribologists,* 34, 82-87.

Wang, Y. and Hadfield, M. (2000a) The influence of ring crack location on the rolling contact fatigue failure of lubricated silicon nitride: experimental studies. *Wear,* 243, 157-166.

Wang, Y. and Hadfield, M. (2000b) The influence of ring crack location on the rolling contact fatigue failure of lubricated silicon nitride: fracture mechanics analysis. *Wear,* 243, 167-174.

Wang, Y. and Hadfield, M. (2001) Ring crack propagation in silicon nitride under rolling contact. *Wear,* 250, 282-292.

Wang, Y. and Hadfield, M. (2002a) *Rolling contact fatigue of ceramics.* ASM Handbook.

Wang, Y. and Hadfield, M. (2002b) A study of line defect fatigue failure of ceramic rolling elements in rolling contact. *Wear,* 253, 975-985

Wang, Y. and Hadfield, M. (2003) A mechanism for nucleating secondary fractures near a pre-existing flaw subjected to contact loading *Wear,* 254, 597-605.

Wang, Y. and Hadfield, M. (2004) Failure modes of ceramic rolling elements with surface crack defects. *Wear,* 256, 208-219.

Wang, Y. L., Fernandez, J. E. and Cuervo, D. G. (1996) Rolling-contact fatigue lives of steel AISI 52100 balls with eight mineral and synthetic lubricants. *Wear,* 196, 110-119.

Warren, P. D., Hills, D. A. and Dai, D. N. (1995) Mechanics of Hertzian cracking. *Tribology International,* 28, 357-362.

Way, S. (1935) Pitting due to rolling contact. *Journal of applied mechanics, ASEM,* 2, A49-A58.

Warren, R. (1978) Measurement of the fracture properties of brittle solids by Hertzian indenters. *Acta Metall* 46, 1759-1769.

Wilshaw, T. R. (1971) The Hertzian fracture test. *J. Phys. D: Appl. Phys.,* 4, 1567-1581

Zeng, K., Breder, K. and Rowcliffe, D. J. (1992) The Hertzian stress field and formation of cone cracks: 1. Theoretical approach. *Acta Metallurgica Et Materialia*, 40(10), 2595-2600.

BIBLIOGRAPHY

Akama, M. and Susuki, I. (2000) Fatigue crack growth simulation and estimation for rolling contact. *Key Engineering Materials*, 183-187, 1035-1040.

Arnell, R. D., Davies, P. B., et al. (1991) *Tribology: Principle and Design Application.* Macmillan Education Ltd.

Andersson, M. (1996) Stress distribution and crack initiation for an elastic contact including friction. *International Journal of Solids and Structures*, 33(25), 3673-3696.

Bower, A. F. and Fleck, N. A. (1994) Brittle fracture under a sliding line contact. *J. Mech. Phys. Solids*, 42(9), 1375-1396.

Chen, Z., Cuneo, J. C., Mecholsky, J. J. and Hu, S. F. (1996) Damage processes in Si_3N_4 bearing material under contact loading. *Wear*, 198(1-2), 197-207.

Cheng, W., Cheng, H. S., Mura, T. and Keer, L. M. (1994) Micromechanics modelling of crack initiation under contact fatigue. *Journal of Tribology, Transactions of the ASME*, 116(1), 2-8.

Chiang, Y., Brinie, D. P. and Kingery, W. D. (1997) *Physical ceramics*. John Wiley & Sons, Inc., New York, Chichester, Toronto, Brisbane, Singapore.

Chiu, Y. P., Pearson, P. K. et al. (1996) Fatigue life and performance testing of hybrid ceramic ball bearing. *Lubrication Engineering* 52 (3), 198-204.

Dill, S. J., Bennison, S. J. and Dauskardt, R. H. (1997) Subcritical crack growth behaviour of borosilicate glass under cyclic loads: evidence of a mechanical fatigue effect. *Journal of the American Ceramic Society*, 80(3), 773-776.

Dowson, D. and Higginson, G. R. (1966) *Elasto-Hydrodynamic Lubrication.* Pergamon Press.

Dusza, J. and Steen, M. (1999) Fractography and fracture mechanics property assessment of advanced structural ceramics. *International materials reviews*, 44(5), 165-215.

Eberhardt, A. W. and Kim, B. S. (1998) Crack face friction effects on mode II stress intensities for a surface-cracked coating in two-dimensional rolling contact. *Tribology Transactions*, 41(1), 35-42.

Ebert, F. J. (1990) Performance of silicon nitride components in aerospace bearing applications. *ASME*, 90-GT-166.

Flasker, J., Fajdiga, G. et al. (2001) Numerical simulation of surface pitting due to contact loading. *International Journal of Fatigue* 23, 599-605.

Evans, A. G. (1980) Fatigue in Ceramics. *International Journal of Fracture*, 16(6), 485-498.

Franklin, F. J., Widiyarta, I., et al. (2001) Computer simulation of wear and rolling contact fatigue. *Wear* 251, 949-955.

Fleming, J. R. and Suh, N. P. (1977) The relationship between crack propagation rates and wear rates. *Wear*, 44, 57-64.

Gilbert, C. J., Dauskardt, R. H. and Ritchie, R. O. (1995) Behaviour of cyclic fatigue cracks in monolithic silicon-nitride. *Journal of the American Ceramic Society*, 78(9), 2291-2300.

Gilbert, C. J. and Ritchie, R. O. (1998) Transient fatigue-crack growth behaviour following variable-amplitude loading in a monolithic silicon nitride ceramic. *Engineering Fracture Mechanics*, 60(3), 303-313.

Goryacheva, I. G. (1998) *Contact mechanics in tribology*. Kluwer Acad.Publrs.

Green, D. J. (1998) *An Introduction to the mechanical properties of ceramics*. Cambridge, Cambridge University Press.

Hadfield, M. and Tobe, S. (1998) Residual stress measurements of hot isostatically pressed silicon nitride rolling elements. *Ceramics International* 24, 387-392.

Hanson, M. T. and Keer, L. M. (1992) An analytical life prediction model for the crack propagation occurring in contact fatigue failure. *ASLE Trans.*, 35, 451-461.

Harris, T. (1991) *Rolling Bearing Analysis*. John Wiley and Sons, Inc. New York, Chichester, Brisbane, Toronto, Singapore.

Hearn, E. J. (1985) *Mechanics of Materials*. Pergamon Press, Oxford, New York, Toronto, Sydney, Frankfurt.

Hirst, W. and Richmond, J. W. (1988) Traction in elasto-hydrodynamic contacts. *Proc Instn Mech Engrs*, 202(C2), 129-144.

Hutchings, I. M. (1992) *Tribology - Friction and Wear of Engineering Materials*. Arnold, London, Sydney, Auckland.

Ioannides, E. and Harris, T. A. (1985) A new fatigue life model for rolling bearings. *ASME Journal of Tribology* 107, 367-378.

Johnson, K. L., O'Connor, J. J. and Woodward, A. C. (1973) The effect of the indenter elasticity on the Hertzian fracture of brittle materials. *Proc. R. Soc. Lond. A.*, 334, 95-117.

Kelly, A. and Macmillan, N. H. (1986) *Strong solids*. Oxford University Press, Oxford.

Kim, D. K., Jung, Y. G., Peterson, I. M. and Lawn, B. R. (1999) Cyclic fatigue of intrinsically brittle ceramics in contact with spheres. *Acta Materialia*, 47(18), 4711-4725.

Kishimoto, H., Ueno, A. and Matsunaga, A. (1998) Cyclic-fatigue crack initiation and propagation in smooth alumina specimens. *Journal of American Ceramics Society*, 81(1), 55-60.

Knott, J. F. (1973). *Fundamentals of fracture mechanics*. Butterworths, London Boston Sydney Wellington Durban Toronto.

Kocer, C. and Collins, R. E. (1998) Angle of Hertzian cone cracks. *Journal of the American Ceramic Society*, 81(7), 1736-1742.

Kuo, C. H., Keer, L. M. and Bujold, M. P. (1997) Effects of multiple cracking on crack growth and coalescence in contact fatigue. *Journal of Tribology-Transactions of the ASME*, 119(3), 385-390.

Lawn, B. (1993) *Fracture of brittle solids. 2nd edition*. Cambridge, Cambridge University Press.

Marshall, D. B., Evans, A. G., Khuri, B. T., Tien, J. W. and King, G. S. (1983) The nature of machining damage in brittle materials. *Proc. R. Soc. Lond*, A385, 461-475.

Mukai, D. J. (2000) An analysis of a near-surface crack branching under a rigid indenter. *Journal of Tribology-Transaction of the ASME*, 122, 23-29.

Murakami, Y. (1987) *Stress intensity factors handbook.* Pergamon Press, Oxford, New York, Beijing, Frankfurt.

Murakami, Y., Sakae, C. and Inchimaru, K. (1994) Three-dimensional fracture mechanics analysis of pit formation mechanism under lubricated rolling sliding contact loading. *ASLE Trans.*, 37, 445-454.

Paris, P. and Erdogan, F. (1963) A critical analysis of crack propagation laws. *Transactions of the ASME Journal of Basic Engineering*, 528-534.

Plint, M. A. (1967) Traction in elasto-hydrodynamic contacts. *Proc Instn Mech Engrs*, 182(14), 300-307.

Rooke, D. P. and Cartwright, D. J. (1976) *Compendium of stress intensity factors*, London, H.M.S.O.

Rose, L. R. F. (1987) The mechanisms of transformation toughening. *Proc. R. Soc. Lond.*, A412, 169-197.

Schijve, J. (2003) Fatigue of structures and materials in the 20th century and the state of the art. *International Journal of Fatigue*, 25, 679-702.

Scott, D. (1963) Study of the effect of lubricant on pitting failure of balls. *IMechE, Lub. and Wear Convention*, 463-468.

Sheppard, S., Barber, J. R. and Comninou, M. (1987) Subsurface cracks under conditions of slip, stick, and separation caused by a moving compressive load. *J. Appl. Mech.*, 54, 393-398.

Sih, G. C. (1991) *Mechanics of Fracture Initiation and propagation.* Kluwer, Academic Publishers, New York.

Suresh, S. (1998) *Fatigue of materials.* Cambridge University Press, Cambridge

Tallian, T. E. (1972) The theory of partial elasto-hydrodynamic contacts. *Wear*, 21, 49-110.

Wachtman, J. B. (1996) *Mechanical properties of ceramics*, John Wiley & Sons, Inc., New York, Chichester, Brisbane, Toronto, Singapore.

Wilde, A. (2000) *A dual boundary element formulation for three-dimensional fracture analysis.* Southampton UK, Computational Mechanics Pulications.

Williams, J. K. (1994). *Engineering tribology.* Oxford University Press, Oxford, New York, Tokyo.

Yoffe, E. H. (1986) Stress field of radial shear traction applied on elastic half-space. *Philos. Mag.*, A 54(1), 115-29.